

**The Response of Biophysical Model Systems
to High Pressure Conditions:
A Study of Lipids and Proteins
Using Diffraction Methods**

Dissertation

zur Erlangung des akademischen Grades eines

**Doktor der Naturwissenschaften
(Dr. rer. nat.)**

vorgelegt von

Christoph G. Jeworrek

geboren am 05. Juli 1982 in Duisburg

eingereicht bei der
Technische Universität Dortmund
Fakultät Chemie

Dortmund
05. Juli 2011

Die vorliegende Arbeit wurde in der Zeit von Februar 2008 bis Mai 2011 am Lehrstuhl für Physikalische Chemie I (Biophysikalische Chemie) der Technischen Universität Dortmund unter Betreuung von Herrn Prof. Dr. R. Winter angefertigt.

Dissertation eingereicht am: 05. Juli 2011
Tag der mündlichen Prüfung: 29. September 2011

Amtierender Dekan: Prof. Dr. H. Rehage

Prüfungskommission:

Prof. Dr. R. Winter	(Erstgutachter)
Prof. Dr. H. Rehage	(Zweitgutachter)
Prof. Dr. C. M. Niemeyer	(Vorsitzender)
PD Dr. C. Czeslik	(wissenschaftlicher Mitarbeiter)

*Omnes scientiae sunt connexae et fovent auxiliis sicut partes ejusdem totius,
quarum quaelibet opus suum peragit non propter se sed pro aliis.*

*All sciences are connected;
they lend each other material aid as parts of one great whole,
each doing its own work, not for itself alone, but for the other parts;
as the eye guides the body and the foot sustains it and leads it from place to place.*

Roger Bacon (1219-1292)

Acknowledgements

This thesis was the occasion for numerous acquaintanceships. I would like to take the opportunity to acknowledge all the people I came across during this time.

First and foremost, I would like to express my deepest gratitude to **Prof. Dr. Roland Winter** for his constant support and guidance throughout my PhD work. I would like to thank him for giving me the interesting subjects, many valuable discussions, and for supporting me whenever he could.

I have to thank **Prof. Dr. Heinz Rehage** for his work as the second examiner of this thesis.

I owe thanks to **PD Dr. Claus Czeslik** for introducing me to reflectometry, for numerous discussions and for his support, especially during experiments at the Helmholtz-Zentrum Berlin and with the construction of the high pressure neutron reflectometry sample cell.

I would like to thank **Dr. Werner Horstmann** for helping me to overcome numerous bureaucratic barriers during my work. His work enabled me to focus mainly on scientific issues.

Andrea Kreusel was an invaluable help at all the formal concerns, duties and necessities such as ordering substances and material, communicating with companies, and completing forms. Without her, the work in the group would not have been nearly as smooth as it was.

Many thanks are given to **Dr. Katrin Weise, Dr. Matthias Pühse, Dr. Andrea Gohlke, Mirko Erkkamp, Sebastian Grobelny** for the successful cooperation projects and their support during various synchrotron- and neutron diffraction experiments.

I would also like to thank the other members of our group, in no particular order: **Dr. Daniel Sellin, Christian Denter, Shobhna Kapoor, Juny Koo, Jonas Markgraf, Janine Seeliger, Alexander Werkmüller, Yong Zhai, Simone Möbitz, Bertina Schuppan, and Milan Saskovic** for the good and constructive working atmosphere.

The time of my studies would have been much harder without my two good friends at the university, **Sabine Leick** and **Sascha Hempel**. I have to sincerely thank both of them for countless constructive discussions during one or the other lunch break as well as for lifting my spirits whenever necessary.

Most projects involved in my thesis were conducted in cooperation with professors and students from other departments or universities. Without their contributions this work would not have been possible. Here, I want to express my gratitude to all of these capable scientists:

- First and foremost, **Dr. Florian Evers** for the highly successful collaboration in many XRR and GIXD projects and above all for a very good time during these experiments.
- I learned a lot and enjoyed the time during synchrotron SAXS experiments at the ESRF with the scientists from Imperial College London, **Prof. Dr. John Seddon, Prof. Dr. Richard Templer, PD Dr. Oscar Ces, Dr. Nick Brooks, Dr. Dora Tang, Arwen Tyler, Natalia Goering** among others.
- I appreciated working with **Martin Schroer** during several SAXS projects.

- **Prof. Dr. Aphrodite Kapurniotu** from the “Wissenschaftszentrum Weihenstephan für Ernährung, Landnutzung und Umwelt” at TU München for providing the peptides, A β and IAPP.
- **Prof. Dr. Parkson Lee-Gau Chong** from the Department of Biochemistry, Temple University School of Medicine in Philadelphia (Pennsylvania, USA) for isolating the archaeal lipids (PLFE).
- **Prof. Dr. Klaus Brandenburg** from the “Leibniz-Zentrum für Medizin und Biowissenschaften”, Forschungszentrum Borstel for providing glycolipids (LPS).
- **Prof. Dr. Catherine Royer, Jean Baptiste Rouget and Julien Roche** from the “Centre de Biochimie Structurale” at the Université de Montpellier for expressing different staphylococcal nuclease variants as well as for a number of pleasant discussions.
- **Prof. Dr. Bertrand Gracia-Moreno and Victor Khangulov** from the Department of Biophysics at the John Hopkins University (Baltimore, MD, USA) for expressing further staphylococcal nuclease variants and a great time during the synchrotron experiments at DELTA in Dortmund.
- and finally **Prof. Dr. Kazuyuki Akasaka, Kazumi Hata, Akihiro Maeno** from the High Pressure Research Center at Kinki University (Wakayama, Japan) for the complementary high pressure NMR measurements on different staphylococcal nuclease variants.

The crew of the mechanical workshop, **Holger Konopka, Klaus Langner, Markus Weste**, and all other co-workers there did a fantastic job and gave me a lot of valuable advice, especially during the construction of the new high pressure neutron reflectometry cell. Without their work several projects would have been impossible to conduct.

Any problems with electrical devices were quickly and directly sorted out by the electronic workshop. Thanks to **Ralf Maserski, Ali Fent**, and all the other staff members there.

This work would not have been possible without the beamline crews at the different synchrotron- and neutron-sources. Here, I would like to thank them for their excellent and tireless work:

- **Dr. Michael Sztucki, Dr. Narayanan Theyencheri, and Jacques Gorini** from the beamline ID02 at the ESRF in Grenoble (France). It was always a pleasure to work at this beamline.
- **Dr. Oleg Konovalov and Dr. Alexei Vorobiev** from the beamline ID10B at the ESRF, where the support was as perfect as at beamline ID02 – even on a Sunday in the middle of the night.
- **Dr. Roland Steitz and Dr. Ralf Köhler** from the instrument V6 as well as **Dr. Uwe Keiderling and Dr. Karsten Voggt** from the instrument V4 at the Helmholtz-Zentrum Berlin for the assistance during neutron experiments.
- **Dr. Bernd Struth** from beamline BW1 at DESY (HASYLAB) in Hamburg for giving me the opportunity to learn so much about beamline instrumentation and software.
- **Dr. Javier Perez** from the SWING beamline at Soleil (Giv sur Yvette, France) for introducing us to his new beamline.
- **Dr. Michael Paulus and Dr. Christian Sternemann** from beamline BL9 of the synchrotron source DELTA at TU Dortmund University for excellent support during the experiments.
- Finally, the **machine crews** of ESEF, DESY, Soleil, HMI, and DELTA for providing synchrotron radiation and a platform for our experiments without major difficulties.

Last but not the least, I owe my immense gratitude to **my friends and family** for their continuous support and encouragement throughout my research work.

Contents

Acknowledgements	I
Contents	III
1 Introduction	1
2 Small-angle X-ray scattering	3
2.1 Introduction	3
2.2 SAXS of colloidal solutions	4
2.2.1 Scattering of diluted solutions	4
2.2.2 The characteristic and the pair distance distribution function	5
2.3 The intra-particle form factor	7
2.3.1 Form factor of a sphere	8
2.3.2 Form factor of a cylinder	8
2.3.3 Scattering intensity of complex structures – the Debye method	8
2.4 The Guinier approximation	9
2.5 Information directly obtainable from the scattering curve	10
2.6 The static structure factor	12
2.7 <i>Ab initio</i> particle shape reconstruction	12
2.7.1 The multipole expansion method	13
2.7.2 Multi-bead modelling	14
2.7.3 The dummy-residue method	16
2.8 Scattering of lipid dispersions	17
2.8.1 Basics of crystallography	17
2.8.2 Lamellar lipid systems	18
2.8.3 Non-lamellar periodic lipid systems	19
2.9 Measuring procedure and data treatment	19
2.9.1 Data collection	20
2.9.2 Data evaluation and correction	21
2.9.3 Data analysis	22
2.9.4 Solution structure modelling	23
3 Grazing incidence X-ray diffraction and X-ray reflectometry	25
3.1 X-ray reflectometry (XRR)	26

3.1.1	Basics of XRR	26
3.1.2	Bragg's equation	27
3.1.3	Kiessig oscillations	27
3.1.4	Parratt's recursive method	28
3.1.5	The kinematic approach	29
3.1.6	X-ray reflectivity data collection and treatment	29
3.1.7	<i>Excursus</i> : X-rays vs. neutrons	30
3.2	Grazing incidence X-ray diffraction (GIXD)	31
3.2.1	Basics of GIXD	31
3.2.2	Bragg peaks – two-dimensional crystallography	31
3.2.3	Bragg rods	33
3.2.4	The horizontal and vertical coherence lengths	34
3.2.5	Plane groups and their GIXD patterns	34
3.2.6	Grazing incidence X-ray diffraction data collection and treatment	35
4	Biological macromolecules - proteins and lipids	37
4.1	Proteins	37
4.1.1	General	37
4.1.2	SNase variants	39
4.1.3	Gramicidin D	40
4.1.4	Fusion peptides	40
4.1.5	MsP1	42
4.1.6	IAPP, A β , and the small-molecule inhibitor resveratrol	42
4.2	Lipids	44
4.2.1	General	44
4.2.2	Lamellar lipid phases	46
4.2.3	Inverse hexagonal lipid phases	47
4.2.4	Inverse bicontinuous cubic lipid phases	47
4.2.5	Bicellar lipid mixtures	51
4.2.6	Sterols	52
4.2.7	Phospholipids	53
4.2.8	Monoolein	54
4.2.9	Glycolipids	55
4.2.10	Archaeal lipids	56
4.3	Effect of pressure on biomolecules	58
4.3.1	General	58
4.3.2	Pressure effect on lipids	59
4.3.3	Pressure effect on proteins	59
5	Design and construction of a novel high pressure sample cell for neutron reflectometry	61
5.1	Key design parameters	61
5.2	Cell design and specifications	62
5.2.1	Cell body	62

5.2.2	Cell windows	63
5.2.3	Sealings	64
5.2.4	Inner sample cell	64
5.2.5	Overall HP experimental setup	65
5.2.6	Neutron reflectivity data collection	66
5.3	First studies using the high pressure NR sample cell	67
5.3.1	Pressure-induced phase transitions of lipid films	67
5.3.2	Protein adsorbate at an aqueous-solid interface under high pressures	68
6	Investigations of pure lipid systems	71
6.1	Bicellar lipid mixtures	71
6.1.1	Introduction	71
6.1.2	Materials and methods	72
6.1.3	Results of the static measurements	74
6.1.4	Results of the pressure-jump induced trSAXS measurements	80
6.1.5	Conclusions	84
6.2	Influence of ergosterol on the phase behaviour of DPPC	86
6.2.1	Introduction	86
6.2.2	Materials and methods	87
6.2.3	Results	87
6.2.4	Conclusions	90
6.3	Three-component lipid raft membrane	90
6.3.1	Introduction	91
6.3.2	Materials and methods	92
6.3.3	Results	94
6.3.4	Conclusions	104
6.4	Five-component lipid raft membrane	106
6.4.1	Introduction	106
6.4.2	Materials and methods	106
6.4.3	Results	107
6.4.4	Conclusions	110
6.5	Monoolein under limited hydration conditions	111
6.5.1	Introduction	111
6.5.2	Materials and methods	111
6.5.3	Results and discussion	112
6.5.4	Conclusions	120
6.6	Archaeal lipids	121
6.6.1	Introduction	121
6.6.2	Materials and methods	121
6.6.3	Results and discussion	122
6.6.4	Conclusions	127
6.7	Glycolipids	128
6.7.1	Introduction	128

6.7.2	Materials and methods	128
6.7.3	Results and discussion	129
6.7.4	Conclusions	137
7	Investigations of proteins in solution	139
7.1	<i>Ab initio</i> shape reconstruction of Staphylococcal nuclease variants in solution	139
7.1.1	Introduction	140
7.1.2	Materials and methods	140
7.1.3	Results	141
7.1.4	Discussion and conclusions	148
7.2	Peroxidase MsP1	151
7.2.1	Introduction	151
7.2.2	Materials and methods	151
7.2.3	Results	152
7.2.4	Discussion and conclusions	153
8	Investigations of lipid-peptide interactions	155
8.1	Interaction of gramicidin D with archaeal lipids	155
8.1.1	Introduction	155
8.1.2	Materials and methods	156
8.1.3	Results and discussion	156
8.1.4	Conclusions	158
8.2	Interaction of monoolein with fusion peptides	158
8.2.1	Introduction	159
8.2.2	Materials and methods	159
8.2.3	Results and discussion	160
8.2.4	Conclusions	179
8.3	Further studies of lipid-peptide interactions	180
8.3.1	Interaction of IAPP with resveratrol at an anionic lipid raft monolayer	180
8.3.2	Cross-interaction of A β and IAPP with an anionic raft monolayer	184
8.3.3	Interaction of IAPP with glycolipids	191
9	Summary & Zusammenfassung	193
9.1	Summary	193
9.2	Zusammenfassung	195
	Bibliography	197
	APPENDIX	a1
A	MATLAB code examples	a1
A.1	Introduction	a1
A.2	Splitting of spec-files from synchrotron sources	a1
A.3	GUI: manual identification of space groups from Bragg peaks	a4

A.3.1	Graphical user interface (GUI)	a4
A.3.2	Programming code	a5
A.4	Advanced processing of SAXS data - main routine	a10
A.5	GUI of a program identifying space groups automatically from Bragg patterns	a14
A.6	XRR raw data processing	a16
A.6.1	Data measured at beamline BW1 at Hasylab, Hamburg	a16
A.6.2	Data measured at beamline ID10B at the ESRF	a19
A.7	Converting GIXD raw data to MATLAB structures	a24
A.8	Advanced processing of GIXD data	a26
B	List of symbols and abbreviations	a33
C	List of publications	a41
D	List of Figures	a43
E	List of Tables	a47
F	Curriculum vitae	a49
	Selbstständigkeitserklärung	a51

CHAPTER 1

Introduction

X-ray diffraction methods offer the opportunity to investigate biomolecules with high spatial and temporal resolution in their natural environments – aqueous solutions. Whereas bulk systems can be studied by small-angle X-ray scattering (SAXS), information about layer systems – especially molecular monolayers at the water interface – are also accessible via X-ray reflectometry (XRR) and grazing incidence X-ray diffraction (GIXD).

Using SAXS, detailed parameters of the unit cells of crystalline systems in solution can be obtained. However, in non-crystalline systems information about the particles in solution are also available; for example, the radius of gyration, the particle envelope, characteristic distances, or even the molecular mass of the scattering particle.

Details of the laterally averaged layer structure of (monomolecular) biofilms, like the electron density, thickness, and interfacial roughness of each layer, can be obtained by XRR. GIXD probes only for crystalline structures in such a layer system and reveals the corresponding crystallographic unit cells as well as the horizontal and vertical dimensions of the crystalline domains, which makes this technique highly suitable for the detection of ordered lipid domains in a generally disordered lipid monofilm.

Natural biomembranes are highly complex two-dimensional solutions consisting of different lipid types, steroids, carbon hydrates, and a large quantity of different proteins. A comprehensive study of such complex systems is nearly impossible. Instead, simple model systems, which reflect the desired characteristics of the complex biomembranes, are chosen for basic studies. These systems usually contain only a few different molecules, allowing the development of a molecular understanding of the underlying processes.

Proteins are involved in nearly every biological process. Their manifold functions include specific catalysis, selective transport of substances, mechanic support of structures, control over functions like growth and immune defence, and many more. But observing isolated proteins in solution is often a too simplistic approach, since a large fraction of proteins fulfil their biological function in or on the surface of biomembranes. Therefore it is vital to investigate the interaction of proteins and peptides with model lipid systems, revealing a significant influence of the lipid membrane on the protein's behaviour.

From the results obtained in the model systems often important conclusions can be perceived about essential processes *in vivo* – which should always be the main objective of biophysical studies.

The thematic focus of this thesis was:

- the development of a high pressure sample cell for neutron reflectometry as a platform for future studies of biologically relevant systems,
- the phase behaviour and phase transition kinetics of lipid systems as a function of temperature, lateral film pressure, and high hydrostatic pressure,
- the lateral organisation and structure of monomolecular lipid films (phospho-, archaeal-, glycolipids),
- the effect of sterols (cholesterol and ergosterol) on the phase behaviour and heterogeneity of phospholipid membranes,
- *ab initio* shape reconstruction of proteins in solution,
- the interaction of peptides with lipid mesophases and model membrane systems.

To be able to follow the interpretation of the results presented in this thesis, both a certain theoretical knowledge of the applied methods as well as a basic understanding of the studied molecules are necessary. The theory of SAXS is introduced in chapter 2 and a brief introduction into XRR and GIXD is given in chapter 3. Insights into the structure and behaviour of different biomolecules as well as their response to high hydrostatic pressure are presented in chapter 4.

In chapter 5 the construction of a novel high pressure sample cell for neutron reflectometry is described and first measurements performed with this cell are presented.

The results of several studies are shown in the following chapters. All sections presenting results are written with the intention to be autonomously understandable without information from other sections of the thesis. Otherwise a cross reference was placed to point to related text passages in other sections.

In chapter 6 studies of pure lipid systems, specifically different phospholipid mixtures, monoolein, archaeal lipids as well as glycolipids, are presented. Investigations of pure proteins in solution are compiled in chapter 7. Finally, the interaction of different proteins and peptides with lipid systems was researched, as shown in chapter 8.

To conclude the main part of the thesis, a two-page summary in English and German is given in chapter 9.

In the appendix additional information about several programmed MATLAB scripts are given, a curriculum vitae can be found, and lists of publications, used abbreviations, as well as figures and tables of this thesis are provided.

Finally some concluding remarks: First, this thesis is written in British English. Further, it should be noted that nearly all projects presented in this thesis have been published previously in scientific journals. The corresponding sections are often based on these publications, which are referenced in the preamble of the respective section. Also all other scientists, who contributed to the particular project and especially to the presented results, are named there.

CHAPTER 2

Small-angle X-ray scattering

In this chapter the basic theory of small-angle X-ray scattering (SAXS) is introduced. The focus will be mainly on the scattering of colloidal particles – like proteins – in solution. Afterwards, the scattering of lipid solutions is presented. At the end of the chapter, the data treatment procedure as well as details of the used equipment and beamlines are described. For a more detailed study of small-angle X-ray scattering the reader is referred to the literature [1–10]. The theory of small-angle neutron scattering (SANS) is nearly identical to the theory of X-ray scattering. The essential differences between both techniques – using X-rays or neutrons – are pointed out in section 3.1.7 (page 30).

2.1 Introduction

One of the main advantages of small-angle X-ray scattering is the ability to study proteins in nearly any desired solvent and to follow changes of the protein structure as a response to a variety of stimuli, i.e. pH, pressure or temperature, addition of cosolvents, chemical or genetic modifications, and so forth. A further advantage of this technique is that SAXS provides direct information on the global structure of the proteins in solution without specific artefacts from labels or dyes (spectroscopy), coatings (electron microscopy) or necessary additives (crystallography). Additionally, SAXS is not limited to small particles as for example nuclear magnetic resonance (NMR), where the size limitation of proteins is around 18 - 20 kDa.^[6] Furthermore, time-resolved SAXS (trSAXS) can provide information with high time-resolution (up to 5 ms at a synchrotron source) of dynamic processes as observed in temperature- or pressure-jumps. Especially the combination of trSAXS with the pressure-jump relaxation technique is a powerful tool to study the kinetics of protein unfolding / refolding or lipid phase transitions.^[3, 11, 12]

Small-angle X-ray scattering provides structural information about inhomogeneities of the electron density with characteristic dimensions between a few Ångströms and several hundred nanometres.^[3] These dimensions of the observed colloidal particles are much larger than inter-atomic distances. As a consequence, the scattering objects can be described using a continuous electron density, which is determined by the chemical composition of the object.^[3] This assumption holds true as long as there are no strong variations in the electron density within the scattering object, which is given for most proteins as the electron density and packing of all amino acids is basically the same. In the presence of heavier atoms several levels of electron density have to be introduced, e.g. iron in a heme group, as well as for more complex, heterogeneous particles.

Scattering curves from particles in solution only contain low-resolution information. The maximal resolution of a SAXS pattern of randomly oriented particles in solution is given by the average dimension, d_{av} , of the particles. Roughly, the scattering will be small at scattering angles larger than λ/d_{av} , where λ is the wavelength of the X-rays.^[6] Only few parameters can be directly obtained from the scattering curve, e.g. the radius of gyration, R_G , the particle surface and accordingly the particle volume as well as the maximal dimension of the particle, D_{max} . A common way of further analysis is modelling of particle envelope or structure, but this method can by no means guarantee uniqueness of the result.^[13]

2.2 SAXS of colloidal solutions

The theory presented in this part can only be applied to diluted systems without interaction between the particles in solution. In such a system each single scattering object can be considered as isolated, resulting only in intra-particle scattering, whereas in a concentrated solution the interaction of the particles, displaying spatial correlations, contributes to the scattering intensity (so-called inter-particle scattering).^[3] In SAXS experiments only coherent, elastic (Thomson-) scattering is considered, i.e. there is no energy exchange between the photon and the electron during the scattering process contrary to the inelastic Compton scattering.^[6] In the following, the validity of the kinematic approximation is presumed, which means, the interaction of the incident intensity with the particles is weak and therefore the interaction of the scattered wave with the primary wave as well as multiple scattering can be neglected.

2.2.1 Scattering of diluted solutions

In this chapter it is generally assumed that the system is highly diluted and therefore the particles can be regarded as isolated. Hence, the scattering of a single particle in solution is observed.

The kinematics of a scattering experiment is shown in Figure 2.1. The sample is illuminated by an incident beam (plane wave) with the wave vector \vec{k}_0 ($|\vec{k}| = 2\pi/\lambda$), the wavelength of radiation λ , and the energy E_0 . The intensity of the scattered radiation (spherical wave) with the wave vector \vec{k}_1 and the energy E_1 is measured as a function of the scattering angle 2θ .

In case of fully elastic scattering ($\Delta E = 0$; $|\vec{k}_1| = |\vec{k}_0|$) the magnitude of the wave vector transfer is given by:

$$|\vec{q}| = q = 2 \left| \vec{k}_0 \right| \sin \theta = \frac{4\pi}{\lambda} \sin \theta = 2\pi s. \quad (2.1)$$

Instead of q often the magnitude of the scattering vector, $s = |\vec{s}|$, is used, where $\vec{s} = (\vec{k}_1 - \vec{k}_0)/2\pi$.

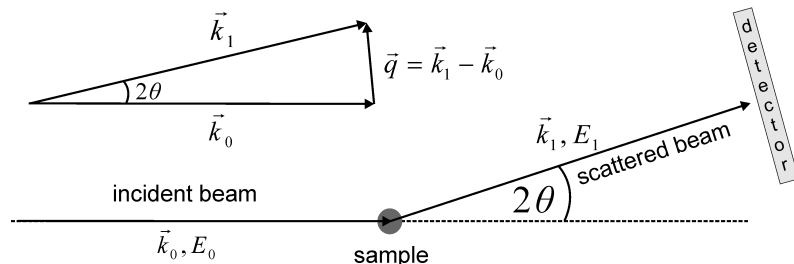


Figure 2.1: Kinematics of the scattering process and definition of the wave vector transfer \vec{q} .^[14]

The scattering amplitude of radiation $A(\vec{s})$ with the wave vector \vec{k}_0 illuminating the volume V_p of a particle with the electron density $\rho(\vec{r})$ at the point \vec{r} at distances much larger than the dimension of the particle is given by:^[3]

$$A(\vec{s}) = \int_{V_p} \rho(\vec{r}) \cdot e^{-2\pi i \vec{s} \vec{r}} dV_p. \quad (2.2)$$

The amplitude of the scattered wave is proportional to the scattering length (product of the classical electron radius, r_e , and the electron density, ρ_e) of the electron-photon interaction. With an experimental resolution lower than the atomic scale and a large number of atoms composing a particle, the sum of scattering lengths in the particle can be described by a continuous electron density distribution, $\rho(\vec{r})$.^[6] From equation 2.2 it is obvious that the scattering amplitude, $A(\vec{s})$, is the Fourier transform of the electron density distribution, $\rho(\vec{r})$, where the contributions are independent from the particle shape and internal structure.^[3, 5, 6]

The scattering amplitude at $\vec{s} = 0$ is

$$A(0) = \int_{V_p} \rho(\vec{r}) dV_p = n_e, \quad (2.3)$$

where n_e is the number of electrons in the volume V_p .

The scattered intensity normalised to the scattering of a single electron is given by the square of the scattering amplitude resulting from the summation of all the amplitudes of scattered X-rays,

$$I(\vec{s}) = A(\vec{s}) \cdot A^*(\vec{s}) = |A(\vec{s})|^2. \quad (2.4)$$

$A^*(\vec{s})$ is the complex conjugate of the scattering amplitude, $A(\vec{s})$. In a scattering experiment only the intensity, which is proportional to the absolute square of the scattering amplitude, is experimentally accessible, i.e. we are facing a ‘‘phase problem’’. The phase information of the scattered wave is lost and therefore a reconstruction of the electron density of the sample in real space by a simple Fourier transformation is not possible.

For $\vec{s} = 0$ and a two-phase system (solute in solvent) the exponential term in equation 2.2 vanishes. Therefore, $I(0)$ is proportional to the squared absolute excess scattering length of the particle,^[5]

$$I(0) = \Delta \bar{\rho}^2 V_p^2 = \Delta n_e^2. \quad (2.5)$$

Δn_e is the number of excess electrons, i.e. the difference between the number of electrons of the scattering particle and the number of solvent electrons in the volume of solvent displaced by the particle.^[3]

2.2.2 The characteristic and the pair distance distribution function

The autocorrelation function $V_p \gamma(\vec{r})$ of the electron density, $\rho(\vec{r})$, was denoted by Debye and Bueche in 1949 as characteristic function. This function is the direct representation of the measured intensity, $I(\vec{s})$, in real space and gives the probability to find a distance between \vec{r} and $\vec{r} + d\vec{r}$ ($\vec{R} = \Delta \vec{r} = \vec{r} - \vec{r}'$) inside the volume V_p of a homogeneous particle.^[3, 5, 15] It is defined as

$$\gamma(\vec{r}) = \frac{1}{V_p} \int_{V_p} \rho(\vec{r}) \rho(\vec{r} + \vec{r}') dV_p. \quad (2.6)$$

From equation 2.4 and equation 2.6 we obtain for the scattering intensity $I(\vec{s})$:

$$I(\vec{s}) = \int_V V \gamma(\vec{r}) e^{-2i\pi \vec{R} \vec{s}} dV. \quad (2.7)$$

The scattering of particles in solution originates only from the electron density difference $\Delta\rho(r) = \rho(r) - \rho_0$ between the electron density of the particles, $\rho(\vec{r})$ ($\approx 0.44 \text{ e}^- / \text{\AA}^3$ for proteins), and the homogeneous electron density of the solvent surrounding the particles, ρ_0 ($\approx 0.33 \text{ e}^- / \text{\AA}^3$ for pure water).^[7] This small difference in electron density of proteins in water leads to just a weak scattering signal. As an example, an 1 mg/ml protein solution (of 40 kDa molar mass) scatters in the order of only 1 photon per 100000 incident photons.^[16]

In case of solution scattering the sample is isotropic, i.e. the particles take all possible orientations relative to the incident beam. The angle α between the vectors \vec{r} and \vec{s} is therefore different for every scattering particle, which leads to the loss of information about the relative orientations of inter-atomic vectors and therefore to the observed low information content and resolution of SAXS patterns.^[4] Thus, the obtained scattering patterns are isotropic and only the spherical average of the intensity, $\langle I(\vec{s}) \rangle$, is experimentally accessible. To calculate this measurable intensity, the phase factor $\exp[2\pi i \vec{r} \vec{s}]$ (q.v. equation 2.2) has to be averaged spherically. The distribution function of the angles α is $(\sin \alpha)$:

$$\langle e^{2\pi i \vec{r} \vec{s}} \rangle = \langle e^{2\pi i r s \cos \alpha} \rangle = \frac{\int_0^{180^\circ} e^{2\pi i r s \cos \alpha} \sin \alpha d\alpha}{\int_0^{180^\circ} \sin \alpha d\alpha}. \quad (2.8)$$

From $\cos \alpha = x$ and its derivative $\frac{dx}{d\alpha} = -\sin \alpha$ follow the relations $\alpha = 0^\circ \rightarrow x = 1$ as well as $\alpha = 180^\circ \rightarrow x = -1$. Accordingly, equation 2.8 can be transformed to

$$-\frac{1}{2} \frac{1}{2\pi i r s} e^{2\pi i r s x} \Big|_1^{-1} = -\frac{1}{2} \frac{1}{2\pi i r s} (e^{-2\pi i r s} - e^{2\pi i r s}) = \frac{\sin(2\pi r s)}{2\pi r s}. \quad (2.9)$$

With equation 2.2 and equation 2.9 the spherically averaged intensity can finally be written as:

$$\langle I(s) \rangle = \langle A(\vec{s}) \cdot A^*(\vec{s}) \rangle = 4\pi \int_0^\infty p(r) \frac{\sin(2\pi r s)}{2\pi r s} dr. \quad (2.10)$$

Due to the spherical averaging the magnitude of the scattering vector, s , is used instead of the vector \vec{s} .^[5] The term $p(r)$ is called pair distance distribution function, which is the spherically averaged auto-correlation function of the excess electron density. The scattering intensity $I(s)$ and the function $p(r)$ are related by:^[3, 5, 17]

$$p(r) = r^2 V \gamma(r) = \frac{1}{\pi} \int_0^\infty r s \cdot I(s) \sin(2\pi r s) ds = \frac{1}{2\pi^2} \int_0^\infty r q \cdot I(q) \sin(qr) dq. \quad (2.11)$$

For homogeneous particles ($\rho(r) = \text{constant}$) the function $p(r)$ is the histogram of distances between all pairs of points within the particle.^[3, 18] The value of the $p(r)$ -function is obviously zero when r exceeds D_{max} , the maximal dimension of the particle.^[5, 6, 18] The approach of the indirect Fourier transformation, introduced by O. Glatter in 1977,^[19] calculates the $p(r)$ -function from the measured data by using a linear combination of spline functions, e.g. a Fourier series or Hermite polynomials.^[3]

The radius of gyration, R_G , of the particle can be calculated directly from the pair distance distribution function, $p(r)$:

$$R_G^2 = \frac{\int r^2 p(r) dr}{2 \int p(r) dr}. \quad (2.12)$$

The radius of gyration is the mean squared distance between the scattering centres – the electrons – and the centre of gravity of the particle:

$$R_G^2 = \frac{1}{V_p} \int_{V_p} r^2 dV = \frac{\int_{V_r} \Delta\rho(r) r^2 dV_r}{\int_{V_r} \Delta\rho(r) dV_r}. \quad (2.13)$$

Theoretically, the characteristic function as well as the pair distance distribution function could be directly calculated from the experimental scattering curve by Fourier transformation, but this is generally not very reliable, because the measured data consist only of a finite number of points between the limits $[s_{\min}, s_{\max}]$ rather than the needed range for integration of $[0, \infty]$.^[5] For the computation as well as the analysis of the $p(r)$ -function the program GNOM written by D.I. Svergun can be used.^[4, 20, 21] The function $p(r)$ is calculated indirectly by inverse Fourier transformation according to equation 2.10 in the interval $[0, D_{\max}]$. For this purpose the program parametrises the $p(r)$ -function by a linear combination of two orthogonal functions.^[6, 20]

Guinier was able to show that the scattering intensity, $I(s)$, of a highly diluted, homogeneous solution of monodisperse, colloidal particles equals the sum of the scattering of all individual particles, $I_i(s)$, in solution, $I(s) = N \cdot I_i(s)$, where N is the number of particles in the illuminated volume.^[1]

2.3 The intra-particle form factor

The scattering of a homogeneous particle with constant electron density in a homogeneous solvent can be described by its intra-particle form factor, $F(s)$. Between the form factor, $F(s)$, and the scattering factor, $P(s)$, the simple relation, $P(s) = F(s) F^*(s)$, can be found.

The measured overall scattering intensity of a colloidal solution without inter-particle interactions is given by the product of the forward scattering, $I(0)$, and the scattering factor, $P(s)$, of the particles. The forward scattering is directly proportional to the number of particles, N , in solution, the average electron density contrast ($\overline{\Delta\rho} = \rho_{\text{particle}} - \rho_{\text{solvent}}$) and the volume of the particles, V_p :

$$I(0) = N \cdot (\overline{\Delta\rho} \cdot V_p)^2 = N \cdot K^2. \quad (2.14)$$

The term K is usually denoted as the contrast factor. The overall scattering intensity of an infinitely diluted solution of homogeneous particles can be described by:

$$I(q) = N \cdot K^2 \left(\frac{1}{V_p} \int_{V_p} \frac{\sin(qr)}{qr} dV \right)^2. \quad (2.15)$$

In this chapter only the intra-particle form factors of a sphere and a cylinder will be discussed. Further form factors can be found in the literature, e.g. [2, 10, 16, 22].

2.3.1 Form factor of a sphere

The form factor of a sphere can be calculated analytically, which is only possible for fully rotationally symmetrical bodies. With the volume of a sphere given by $V = 4\pi R^3/3$, the form factor can be calculated:

$$F(q, R) = \frac{1}{V} \int_0^R \frac{\sin(qr)}{qr} dV. \quad (2.16)$$

With $dV = 4\pi r^2 dr$ and equation 2.16, the scattering factor of a sphere is given by

$$P(q, R)_{\text{sphere}} = \left[\frac{3(\sin(qR) - 2\pi qR \cos(qR))}{(qR)^3} \right]^2. \quad (2.17)$$

2.3.2 Form factor of a cylinder

The scattering of a cylindrical body is calculated as an example of a geometrical body that is not completely rotationally symmetrical with respect to its centre.

The form factor of a cylinder with uniform scattering length density, radius R , length L_{cyl} and volume $V_{\text{cylinder}} = \pi R^2 L_{\text{cyl}}$ is given by^[23]

$$F_{\text{cylinder}}(\vec{q}, R, L_{\text{cyl}}, \theta_{\text{or}}) = V_{\text{cylinder}} \frac{2J_1(\vec{q}R \sin \theta_{\text{or}})}{\vec{q}R \sin \theta_{\text{or}}} j_0(\vec{q}R \cos \theta_{\text{or}}), \quad (2.18)$$

where $j_0(x)$ is the zero order spherical Bessel function and $J_1(x)$ is the first order Bessel function. θ_{or} is defined as the angle between the cylinder main axis and \vec{q} .

To obtain the scattering intensity (normalised to the cylinder volume) of a monodisperse solution of randomly oriented cylinders as described by equation 2.18, the integral over all possible orientations of θ_{or} relative to \vec{q} has to be calculated:

$$I_{\text{cylinder}}(q, R, L_{\text{cyl}}, \Delta\rho) = \frac{1}{V_{\text{cylinder}}} \int_0^{\pi/2} (\rho_{\text{cylinder}} - \rho_{\text{solvent}})^2 F_{\text{cylinder}}^2(\vec{q}, R, L_{\text{cyl}}, \theta_{\text{or}}) \sin \theta_{\text{or}} d\theta_{\text{or}}. \quad (2.19)$$

2.3.3 Scattering intensity of complex structures – the Debye method

The shape of many real scattering objects cannot be reasonably approximated by a simple geometrical body. A possible solution is to construct a model composed of several subunits of simple geometrical structure. The scattering amplitudes of the individual constituent subunits are calculated analytically and are added afterwards according to the particular orientation in the model. The total amplitude is squared and averaged over all orientations. In the Debye method the particle is described by an ensemble of N equal spheres.^[6, 24] The total scattering intensity, $I(q)$, of the model is then given by^[6]

$$I(q) = I(q)_{\text{sphere}} \left[N + 2 \left\langle \sum_{j=1}^N \sum_{k=1}^N \frac{\sin(qr_{jk})}{qr_{jk}} \right\rangle \right], \quad (2.20)$$

where $r_{jk} = |\vec{r}_j - \vec{r}_k|$ is the distance between the centres of two subunits. Therefore, the sum is only calculated for pairs of j and k denoting different spheres, i.e. $j \neq k$. $I_{\text{sphere}}(q)$ is the scattering intensity of a single subunit, which is defined by $I(q) = I(0)P(q)$ (q.v. equations 2.14 and 2.17).

2.4 The Guinier approximation

A fast and easy way to find a first approximation for the radius of gyration of a particle directly from the scattering curve is given by the Guinier approximation.^[25] This relation is based on the fact that the function $I(s)$ is an even function, i.e. $I(s) = I(-s)$, which can be expanded to a series of even powers of s . The Guinier approximation relies on the assumption of a monodisperse and ideal solution. If the interaction between the particles are not negligible (contribution of inter-particle scattering), the scattering data follow no longer the Guinier approximation. Therefore this relation can be also used to test for polydispersity and interaction or aggregation of particles in solution.

The term $\sin(x)/x$ with $x = (2\pi rs)$ in the definition of the orientational averaged scattering intensity (equation 2.15) can be described by a series expansion,^[26]

$$\frac{\sin(x)}{x} = 1 - \frac{x^2}{3!} + \frac{x^4}{5!} - \dots + (-1)^n \frac{x^{2n+1}}{(2n+1)! \cdot x} \pm \dots, \quad (2.21)$$

yielding another expression of equation 2.15, by considering only the first two terms of the series expansion:

$$I(s) = I(0) \cdot \left(\frac{1}{V_p} \int_{V_p} [1 - \frac{1}{6} (2\pi rs)^2] dV \right)^2 = I(0) \cdot \left(1 - \frac{1}{6} (2\pi s)^2 \frac{1}{V_p} \int_{V_p} r^2 dV \right)^2. \quad (2.22)$$

According to the definition of the radius of gyration (equation 2.13) equation 2.22 can be written as:

$$I(s) = I(0) \cdot \left(1 - \frac{1}{6} (2\pi R_G s)^2 \right)^2 = I(0) \cdot \left(1 - \frac{4\pi^2}{3} R_G^2 s^2 + \frac{16\pi^4}{36} R_G^4 s^4 \right). \quad (2.23)$$

The term in the brackets in equation 2.23 equals the first three terms of the series expansion of the function e^z .^[26] Therefore it can be approximated by:

$$I(s) \cong I(0) \cdot \exp\left(-\frac{4\pi^2}{3} R_G^2 s^2\right) = I(0) \cdot \exp\left(-\frac{1}{3} R_G^2 q^2\right). \quad (2.24)$$

Equation 2.24 shows that the scattering curve of an isolated particle in solution at very small scattering angles can be approximated by a Gaussian function. The width of this Gaussian is proportional to the squared radius of gyration of the particle.^[3] In practise, the radius of gyration is approximated by fitting a line to the linear region of the data in a plot of $\ln[I(s)]$ versus s^2 . This plot is generally known as Guinier plot. The Guinier approximation (equation 2.24) of spherical particles is only valid for values of s up to $s^2 \cdot R_G^2 \leq 1.0$ or for values of q to a maximal value of $q \cdot R_G \leq 1.3$, respectively.^[5, 7] From the intercept of the Guinier plot the forward scattering intensity, $I(0)$, can be obtained, whereas the slope yields the radius of gyration.^[5, 7, 27]

This method to determine the radius of gyration cannot be used for polydisperse solutions or solutions where the interaction between the particles cannot be neglected. Also for unstructured, loosely packed chains – like unfolded proteins – this method cannot be applied.^[5] The radius of gyration calculated from

the pair distance distribution function, $p(r)$, is always more reliable than the values obtained from the Guinier plot, which uses only a small fraction of the scattering curve for the calculation. In contrast, the $p(r)$ -function includes the complete dataset into the calculation. Therefore, it is less susceptible to effects of particle-particle interaction or partial aggregation, which both have an influence on the region of low q -values of the scattering curve.^[5]

2.5 Information directly obtainable from the scattering curve

Beside the radius of gyration and the maximal dimension of the particle, several other parameters can be directly derived from the measured scattering curve:

The Porod invariant

The autocorrelation function (q.v. equation 2.11) for $R = 0$ is^[3]

$$V\gamma(0) = 2 \int_0^{\infty} s^2 I(s) ds \quad (2.25)$$

and for $\gamma(R)$ (equation 2.6) at $R = 0$ we obtain

$$\gamma(0) = \frac{1}{V} \int_{V_r} \Delta\rho(r) \Delta\rho(r) dV_r = \overline{\Delta\rho^2}, \quad (2.26)$$

where $\overline{\Delta\rho^2}$ is the mean square contrast of the electron density of the particle. Equations 2.25 and 2.26 yield finally an expression for the so-called Porod invariant \tilde{Q} :^[3, 28, 29]

$$V\gamma(0) = V \overline{\Delta\rho^2} = \int_0^{\infty} q^2 I(q) dq = \tilde{Q}. \quad (2.27)$$

The Porod invariant is only dependent on the mean square contrast of the particle's electron density, but independent of its structure.^[3]

The particle volume and surface area

The forward scattering intensity, $I(0)$, as described in equation 2.14, can be written for a single particle as $I(0) = (V\overline{\Delta\rho})^2$.^[3] In case of a homogeneous particle, the relation $(\overline{\Delta\rho})^2 = \overline{\Delta\rho^2}$ is valid and therefore the so-called Porod volume, which is the volume of the dissolved and hydrated particle, can be calculated by:^[5]

$$V_{\text{Porod}} = \sqrt{\frac{I(0)}{\gamma(0)}} = \frac{I(0)}{\tilde{Q}}. \quad (2.28)$$

The forward scattering $I(0)$ can be derived from the $p(r)$ -function using equation 2.10 by integrating between $[0, D_{\text{max}}]$. Typically, the value of the Porod volume of a protein in nm^3 is roughly twice as large as its molar mass in kDa.^[7, 30]

Porod also found a relation between the scattering intensity at high angles and the interfacial area, A_S , between the particle surface and the solvent. For a particle with a homogeneous electron density and a sharp interface with the solvent, the scattering intensity of a monodisperal solution oscillates around a straight line at high scattering angles and for $\rho_{\text{solvent}} \neq 0$ given by Porod's law:^[3, 5, 28, 31]

$$8\pi^3 \lim_{s \rightarrow \infty} [s^4 I(s)] = A_S \overline{\Delta\rho^2} + C s^4. \quad (2.29)$$

C is a correction term, accounting for short-distance density fluctuations as well as experimental fluctuations of the scattering intensity at high scattering angles. Plotting $s^4 I(s)$ versus s^4 yields a linear curve with the slope C . By subtracting this line from the measured intensity, $I(s)$, an approximation of the pure scattering intensity of the homogeneous particles in solution is obtained.^[5, 31]

The compactness of the scattering particle

To monitor the degree of folding of a protein or more general, to gain information on the compactness of a particle in solution, a so-called Kratky plot can be used, i.e. the representation of $s^2 I(s)$ versus s . The scattering profile of a globular particle follows Porod's law ($I(s) \propto s^{-4}$) exhibiting a bell-shaped curve in the Kratky plot. The position of the maximum depends on the radius of gyration of the scattering object. A particle describable by a Gaussian chain shows a plateau at large values of s . This behaviour can also be found for fully unfolded proteins in the configuration of a random coil.^[3, 6, 32]

For an expanded protein structure, $s^2 I(s)$ converges to s^{-2} instead of s^{-4} for rigid particles:

$$\lim_{s \rightarrow \infty} [I(s) s^2] = \frac{2(1 - (s^{-2} R_G^{-2}))}{R_G^2}. \quad (2.30)$$

For a completely unfolded protein with the amino acid chains in a fully elongated conformation, $s^2 I(s)$ also increases initially, but shows a distinct plateau in the central s -region of the plot and finally increases linearly at high values of s as the form factor is now proportional to s^{-1} .^[6]

The molar mass of the particle

If the scattering experiment has been conducted on an absolute scale, the extrapolated scattering intensity at the origin, $I(s=0)$, provides a determination of the molecular mass of the particle:^[3, 5]

$$M = I(0) \cdot \frac{n_e^2}{(1 - \rho_0 \Psi)^2 N_A}. \quad (2.31)$$

The ratio between molecular mass and number of electrons in the particle, n_e , has usually a value close to 1.87 for proteins. ρ_0 is the average electron density of the solvent, Ψ is the ratio of the particle volume to its number of electrons and N_A is Avogadro's number. The intensity $I(0)$, as defined in equations 2.5 and 2.14, is not directly available from the measured scattering curve. However, it can be obtained from the Guinier plot as well as from the pair distance distribution function, $p(r)$, as described by equation 2.10.

2.6 The static structure factor

In all investigations conducted in this thesis, solutions of low concentrations ($< 2\%_{\text{wt}}$) were used, to assure that particle-particle interactions can be neglected. For reasons of completeness the structure factor, accounting for the interaction between the scattering objects in solution, should be introduced briefly in this section. For more details the reader is referred to the literature, e.g. [1, 2, 5, 22, 33–37].

The scattering intensity of non-ideal, non-infinitely diluted solutions with the particle concentration, c , the obtained scattering intensity is not only proportional to the scattering of the single particles, $I(q)$, but given by:^[5]

$$I_{\text{exp}}(c, q) = I(q) \cdot S(c, q) \quad (2.32)$$

The overall scattering intensity is described by two terms. The first term is given by the shape of the isolated particle in solution whereas the second term, $S(c, q)$, the so-called static structure factor, accounts for the attractive or repulsive interaction of particles reflecting the spatial distribution of scattering objects in solution. For an infinite dilution, the structure factor converges to $S(0, q) = 1$. Also in the so-called “theta-state”, at the alternation point between attractive and repulsive interaction, where both forces cancel out, the structure factor becomes unity. Attractive interactions, which often leads to unspecific aggregation in protein solutions, are characterised in the scattering pattern by a strong increase of the scattering intensity at low scattering angles due to the structure factor.^[5] The structure factor, $S(c, q)$, is related to the radial pair distance distribution function, $g(r)$, between the different particles in solution:

$$S(c, q) = 1 + \rho \int_0^{\infty} 4\pi^2 (g(r) - 1) \left(\frac{\sin(rq)}{rq} \right) dr, \quad (2.33)$$

where the particle density in solution is described by ρ .

To calculate the structure factor a simple model from statistical mechanics based on the Ornstein-Zernike (OS) and a proper closure relation, e.g. the “hypernetted chain” (HNC) integral equation, can be used, linking the structure factor and the Fourier transform of the radial pair distance distribution function, $g(r)$, between the different particles in solution to the intermolecular interaction potential.^[5] Instead of the radial pair distance distribution function, $g(r)$, often the total correlation function, $h(r) = g(r) - 1$, is used.

2.7 *Ab initio* particle shape reconstruction

For a long time the interpretation of scattering curves was limited to modelling based on simple geometrical bodies (e.g. spheres, ellipsoids, cylinders, etc.). It was nearly impossible to obtain more detailed information about the particle structure than very general parameters, like the radius of gyration or the averaged diameter. Only the availability of sufficient computer power in the last decades allowed for the development of efficient *ab initio* data interpretation methods, which were based on spherical harmonics in the 1970s,^[38–40] global minimisation algorithms and rigid-body refinement.^[5] A further significant improvement was the introduction of algorithms based on multi-bead models developed in the late 1990s, where the particle shape is approximated by a model built by numerous densely packed, small spheres using the Debye method (q.v. section 2.3.3, page 8).^[13]

For the interpretation of *ab initio* structures, the knowledge of the (partial) atomic structure, e.g. from NMR or crystallography, can be extremely helpful. This *a priori* knowledge can be used to enhance the performance of the *ab initio* calculations, e.g. by imposing restrictions in case of a known symmetry element. In any method knowledge about the particle symmetry reduces the degrees of freedom and therefore the number of independent parameters, thus reducing the calculation time and rendering the final result more reliable.^[5] Additionally, it is often helpful to superimpose *ab initio* structures with atomic structures to reveal differences between crystal structures and the shape of the particle in solution. Missing domains of large proteins can also be modelled easily if only parts of the crystal structure are known. Additionally, it is possible to reconstruct a complex quaternary structure if the structures of the subunits are established.

All modelling algorithms described in this chapter presume that the calculated particle has a homogeneous electron density. A modification of the multi-bead methods allows also the calculation of particles with domains of different electron densities, but the computation time increases dramatically with the number of different electron densities assumed in the model. Usually a model with a homogeneous electron density describes the particle envelope of proteins with sufficient accuracy.

2.7.1 The multipole expansion method

The first effective method of *ab initio* particle shape determination was developed in 1970 by H. Stuhrmann: the multipole expansion or spherical harmonics method.^[38, 39] In this method the particle envelope is constructed using a series of multipole elements, e.g. monopoles, dipoles, quadrupoles, and so on.^[6] However, this algorithm has severe limitations. It can only be applied to simple smooth structures without cavities or complex surface morphology.^[5] An advantage of this method is that it is rather fast and therefore it can quickly provide a first impression of a particle envelope with low resolution. An improved version of this approach, also accounting for the finite width of the particle-solvent interface, was implemented in the shape determination program SASHA by D.I. Svergun.^[41, 42]

Figure 2.2 depicts in the upper part the computed envelope functions of the protein lysozyme by the sum of different multipoles. For comparison, a representation of the highly resolved protein surface is shown beneath it. In the graph, the overall scattering intensity of the protein is plotted as a solid line, whereas the other curves represent the contributions of the different multipoles to the scattering intensity. In the monopole approximation ($L = 0$), the particle is described by a single parameter, the radius of the sphere, R_0 , with the corresponding scattering intensity $I_0(s)$. For all values of $L > 0$ the partial intensity at $s = 0$ equals zero. The contribution of higher harmonics increases with increasing scattering angle. The resolution of the calculated structures is approximately $2\pi R_0 / (L + 1)$ and the number of independent parameters is $(L + 1)^2 - 6$, where six degrees of freedom are subtracted (3 rotational and 3 translational), which do not have any influence on the scattering pattern.^[5]

The major advantage of the spherical harmonics method is that the number of parameters used for the description of the particle shape is comparable to the number of Shannon channels in the experimental data. The Shannon sampling theorem is usually used to describe the information content of solution-scattering data. The scattering curve, $I(s)$, is the Fourier image of the characteristic function, which is equal to zero for intra-particle distances exceeding D_{\max} . The sampling theory now predicts that the continuous function $I(s)$ can be represented by a discrete set of points, the so-called Shannon channels, N_s , given by:^[4, 7]

$$N_s = (q_{\max} - q_{\min}) D_{\max} \pi^{-1}. \quad (2.34)$$

For more details of the the Shannon sampling theorem the reader is advised to the literature [4, 43–46]. The typical number of Shannon channels of a scattering curve is 10 - 15.^[4, 5] The uncertainty in the shape determination of a dataset containing errors depends on the ratio between the number of model parameters, N_P , and the number of Shannon channels, N_S . Shape restoration was found to be practically independent of the initial approximation and stable with respect to random errors when $N_P \approx 1.5N_S$.^[5]

2.7.2 Multi-bead modelling

Another method of calculating *ab initio* structures is the multi-bead approach,^[47] which is based on a complex trial-and-error strategy as well as the Debye method for the systematic determination of structures. Multi-bead modelling relies on the fact that the maximal dimension of the particle, D_{\max} , is readily obtained from the scattering curve and therefore the particle must obviously fit into a spherical volume of this diameter. This spherical volume is then filled with a large number, N_D , of densely packed small spheres (so-called dummy-atoms) of radius $r_0 \ll D_{\max}$. All spheres have an identical electron density. Therefore only the shape of homogeneous particles with a constant electron density can be calculated. Each of these small spheres is defined by its index as belonging to the particle (index = 1) or the solvent (index = 0). The particle shape is now completely described by a string, X , of N_D bits.

Starting from a random configuration of X , the scattering curve of this set of dummy-atoms is calculated and compared to the experimental scattering pattern. By changing the configuration X , the function $f(X) = \chi^2 + \alpha_w P_P(X) G_P(X)$ is minimised. Here, to the normalised discrepancy function χ^2 between experimental and calculated data^[7] a penalty-term is added weighted by the factor $\alpha_w > 0$ to apply external constraints to the solution. The penalty term $P_P(X)$ accounts for the looseness or degree of isolation of each non-solvent dummy-atom and the term $G_P(X)$ is a measure of the connectivity of the overall model. Both penalty terms ensure that the final structure is a compact solution with the smallest possible interfacial structure.^[5, 13] To remove the contribution of internal fluctuations of the particle from

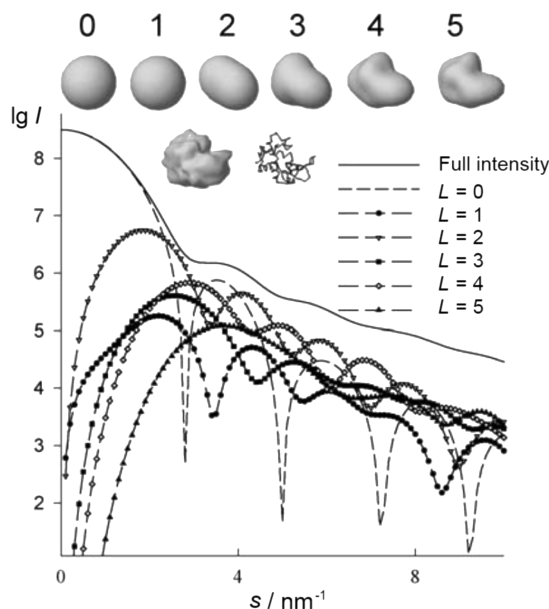


Figure 2.2: Representation of the protein lysozyme by the spherical harmonics method. Top row: surface representation by the sum of different multipole elements. Second row: high resolution protein surface and C_α -trace of lysozyme. Bottom part: Scattering intensity of lysozyme and the contributions from different multipoles.^[5]

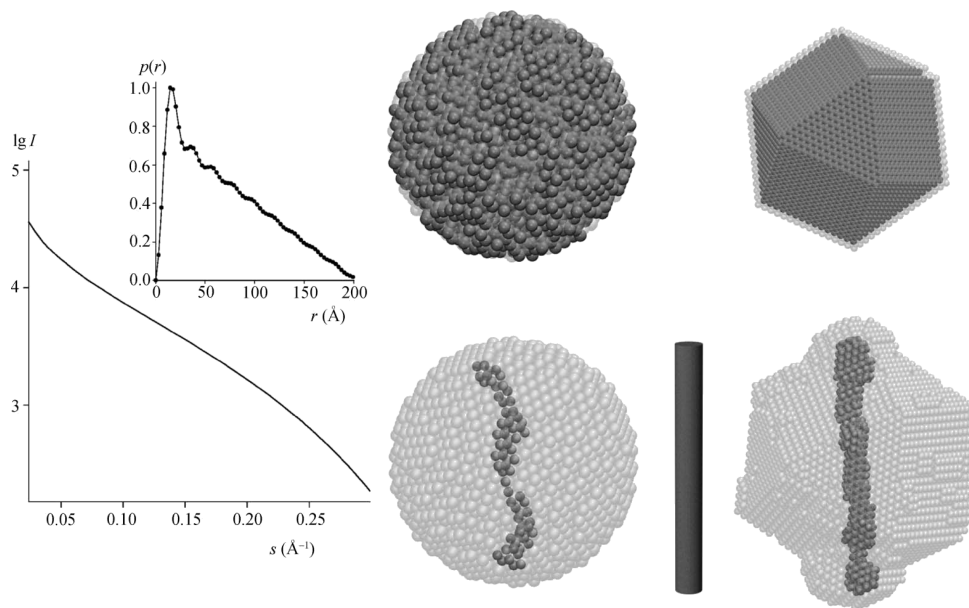


Figure 2.3: Reconstruction of a cylinder (radius: 10 \AA ; height: 200 \AA) using DAMMIN and DAMMIF. Left side: corresponding scattering curves and $p(r)$ -function. Top right: starting configuration of the corresponding program (left DAMMIN and right DAMMIF). Lower right: finally resolved structures. On the left by DAMMIN ($r_0 = 5,3$ \AA , CPU time: 246 min) and on the right by DAMMIF ($r_0 = 3,0$ \AA , CPU time: 8 min).^[49]

the scattering curve (which are undesirable for the determination of the particle envelope), a constant is subtracted from the experimental data. This ensures that the scattering intensity decays as s^{-4} following Porods law for a homogeneous particle (q.v. section 2.28, page 10).^[6]

The minimisation of the $f(X)$ -function is done by a simulated annealing algorithm.^[48] The basic idea of this algorithm is to perform random modifications of the dummy-atom model (DAM) and to evaluate if the new solutions are better than the previous ones. Most of the time the old configuration is replaced by a better new one, but occasionally also configurations are chosen which increase $f(X)$ instead of decreasing it. The probability of accepting a solution, which does not improve the overall structure decreases in the course of the minimisation (the system is “cooled”). Initially, this temperature is high and the changes of X are almost random, whereas towards the end of the optimisation a configuration close to the minimum of the goal function is reached. Both programs written by D.I. Svergun et al. using the multi-bead method, DAMMIN^[13] and the more recent and faster, DAMMIF^[49] (q.v. Figure 2.3), are based on a faster variant of simulated annealing: the simulated quenching.^[50]

In contrast to the multipole-expansion method, which provides an identical solution for every run processing the same input file, bead modelling methods may yield multiple, similar solutions due to factors of randomness in the algorithm. The variation between these solutions can serve as an indicator for the stability of the solution. To reveal the most probable, final structure of a particle, the results of multiple independent runs should be superimposed and averaged.^[5, 6, 13, 51]

The beads in multi-bead models do not represent specific residues or particles, but only define a volume of the scattering particle. The position of the beads in the volume are non-unique and the centres of the beads are situated on an arbitrary chosen grid.^[7] Contrary to the multipole expansion method, the multi-bead approach can also reconstruct complex particle structures without any difficulty; this includes those with internal cavities.^[5]

For an adequate description of a particle structure, the number of dummy-atoms has to be large ($N_D > 10^3$). This number significantly exceeds the number of Shannon channels and therefore, even for a perfectly fitted scattering curve by the model found, uniqueness of this model cannot be meaningfully discussed.^[5]

Currently, the maximal number of beads per model, which can still be calculated on a standard, up-to-date personal computer is around 10000 beads.^[52] Therefore, it is imperative to reduce the size and complexity of huge multi-bead assemblies to overcome the limitations imposed by numerics, computer soft- and hardware. However, a too strong reduction leads to large errors of the model found. The maximal possible reduction of multi-bead models of larger proteins ($M > 10$ kDa) has been investigated comparing the structural parameters (D_{\max} , $p(r)$, R_G) of multi-bead models built by a different number of beads with atomic structures measured by high-resolution crystallography or NMR. These studies revealed that a reduction by a factor of 100 (starting from the initial atomic coordinates) is possible without changing the structural features and predicted molecular properties.^[53]

2.7.3 The dummy-residue method

A completely new *ab initio*-approach for the calculation of protein solution structures from scattering patterns was introduced in 2001 by D.I. Svergun.^[54] The methods described so far are all limited to particles with a homogeneous electron density distribution.

Limiting the new approach to the calculation of protein structures, some constraints can be imposed on the models, leading to a higher resolution of the protein envelopes obtained. This method accounts for the fact that proteins are folded polypeptide chains, where the C_α -atoms of adjacent amino acid residues in the primary sequence are separated by approximately 3.8 Å. A protein can be considered as an assembly of dummy-residues (DR) centred at the C_α -position. To even improve the quality of the results, the algorithm accounts for bound solvent molecules by surrounding the dummy-residues with a layer of solvent molecules representing the first hydration shell. The *ab initio* model is calculated as described before for the multi-bead method by minimising a target function describing the deviation between experimental data and a scattering pattern calculated from the corresponding dummy-residue conformation. An important difference to the multi-bead method is that the dummy-residue method does not use a fixed grid, which means that the dummy-residues can move freely in space only constrained by the constant distance to their two nearest neighbours. Furthermore, the arrangement of the dummy-residues does not have to be compact and is only required to be “chain-compatible”.^[5, 54]

The algorithm as described above is implemented in the program GASBOR by D.I. Svergun et al..^[54] More recently, also a “real-space”-version of GASBOR has been developed, increasing the computational speed by a factor of 5 by fitting the pair distance distribution function, $p(r)$, rather than the scattering curve, $I(q)$.^[55]

For small proteins (< 50 kDa), this algorithm can be even faster than the multipole expansion method. As for the multi-bead modelling, the dummy-residue method also produces a manifold of solutions for one scattering curve, making it necessary to superimpose and average the results of multiple runs. Usually the differences between the various DR models are substantially smaller than those obtained by multi-bead modelling.^[5, 51] An important application of the DR method is the calculation of missing fragments to incomplete high resolution crystal structures of proteins.^[5] In Figure 2.4 the results of *ab initio* calculations obtained by different methods are compared, revealing the best fit of the experimental scattering curve and structure with the highest resolution by the dummy-residue method.

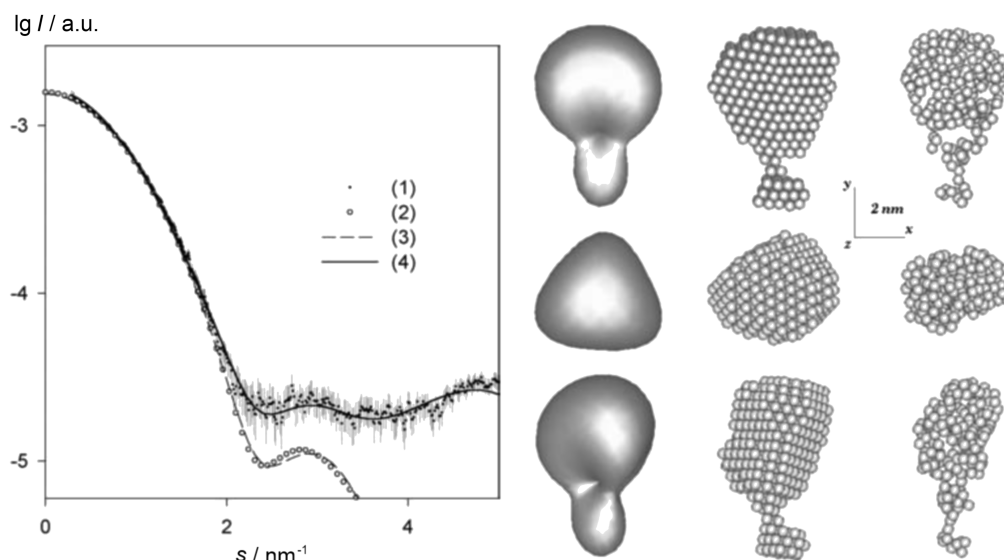


Figure 2.4: Comparison of different *ab initio* methods. Left side: Scattering data of the protein CHB1 (1) and calculated scattering curves from final structures calculated by SASHA (2), DAMMIN (3) and GASBOR (4). Right: Models obtained by multipole expansion (SASHA - left column), multi-bead modelling (DAMMIN - middle column) and the dummy-residue method (GASBOR - right column). The structures in the second and third row are rotated counter-clockwise by 90° around the *x*- and *y*-direction, respectively.^[5]

2.8 Scattering of lipid dispersions

2.8.1 Basics of crystallography

The smallest repetition unit of a crystal, which is only related by translations, is called the unit cell. For a three-dimensional crystal this unit cell is defined by the length of the three axes (*a*, *b* and *c*) and the three angles between those axes (α , β and γ). By crystallographic convention, $a \leq b \leq c$ and $\gamma \leq \pi/2$.^[1] Frequently, when the unit cell contains multiple molecules, internal symmetry exists within the unit cell. If these symmetries apply to the whole lattice, they are crystallographic symmetries and constrain the parameters of the unit cell.^[7]

Mathematically, X-ray diffractions from crystals can be treated as reflection from a plane of angle θ to the incident X-ray beam and therefore the diffraction maxima measured in a scattering experiment are frequently referred to as reflections.^[7] In the crystal, the X-rays are reflected from multiple crystal planes simultaneously, which leads to a path difference between different X-rays. Whenever this path difference corresponds to an integer multiple of the wavelengths of the X-ray, the diffraction undergoes constructive (in-phase) interference and an intensity maximum is experimentally detected. If this condition is not fulfilled, the X-rays interfere destructively (out-of-phase) and no signal is obtained. This requirement is expressed mathematically by the Laue conditions:^[56]

$$\begin{aligned} \vec{a} \cdot \vec{s} &= h, \\ \vec{b} \cdot \vec{s} &= k, \\ \vec{c} \cdot \vec{s} &= l, \end{aligned} \tag{2.35}$$

where \vec{a} , \vec{b} and \vec{c} are the lattice vectors in real space corresponding to the orientations of the unit cell edges, \vec{s} is the scattering vector corresponding to the path difference between incident and scattered secondary wave and h, k, l are the Miller indices. Thus, the planes at which the X-rays are scattered, are defined by the wavelength of the X-rays, the unit cell parameters, and the orientation of the scattering crystal. The observed scattering of a single crystal in reciprocal space is a regular lattice of spots, $\{\vec{q}_{hkl}\}$, defined by the Laue conditions. It is spanned by the three reciprocal lattice vectors \vec{a}^* , \vec{b}^* and \vec{c}^* :

$$\vec{q} \equiv \vec{q}_{hkl} = h\vec{a}^* + k\vec{b}^* + l\vec{c}^*, \quad (2.36)$$

where \vec{a}^* has the properties: $\vec{a}^* \cdot \vec{a} = 2\pi$, $\vec{a}^* \cdot \vec{b} = 0$ and $\vec{a}^* \cdot \vec{c} = 0$. Equivalent relations are valid for \vec{b}^* and \vec{c}^* . Essentially, the Laue conditions state that constructive interference is obtained when the wave vector of the scattering process is identical to the reciprocal lattice vector. This can be graphically represented by an Ewald sphere. In all positions of the reciprocal lattice where the sphere with a radius of q and the centre $(0,0,0)$ coincides with a lattice point, constructive interference is found.^[56, 57]

It is important to notice that only the unit cell's size, shape, and orientation, but not the positions of the atoms in the unit cell define if the diffraction conditions are fulfilled. The atomic species in the unit cell dictates the intensity of the diffracted X-rays.^[7, 58]

The relation between the scattering angle, 2θ , at which the diffraction signal occurs and the distance, d , of periodically occurring distances in the crystal lattice is given by Bragg's law (q.v. section 3.1.2, page 27)

$$n_x \lambda = 2d \sin \theta, \quad (2.37)$$

where n_x is an integer describing the numeric order of the reflection and λ is the wavelength of the X-rays. Bragg's law, existing in real space, is equivalent to the Laue conditions valid in reciprocal space.^[57]

Homogeneous lipid water dispersions can be regarded as powder samples, which are composed of numerous randomly oriented microcrystals. Therefore Bragg's condition is automatically fulfilled and all possible diffraction peaks can be recorded simultaneously.^[59] The width of the signals is correlated to the number of repetition units (i.e. the size of the microcrystals) and the periodicity over large distances (i.e. the degree of congruence of the unit cells – differences may for example be caused by different hydration and therefore slightly different sizes of the unit cells). If a lipid dispersion is lacking any periodicity, only diffuse scattering is observed.^[59]

2.8.2 Lamellar lipid systems

Multilamellar lipid phases (usually denoted by L or P) are built by alternating layers of lipid membranes (bilayers) and water, resulting in a quasi-one-dimensional periodical system, which exhibits small-angle diffraction peaks with the maxima at q_{\max} described by an equation directly derived from Bragg's law:^[59]

$$q_{\max} = \frac{4\pi}{\lambda} \sin \theta = n_x \frac{2\pi}{d}, \quad (2.38)$$

where n_x is the integer numeric order of the reflection and d is the lattice constant of quasi-one-dimensional lattice, which is the sum of the thicknesses of the water layer and the lipid bilayer. Further parameters, which can be directly calculated from the lattice constant of a lamellar phase, are described in section 4.2.2 (page 46).

For lamellar phases from the position q_{\max} and the full width at half maximum (FWHM_{\max}) of the first Bragg peak, the average number of stacked layers, N_{stack} , can roughly be estimated by the equation:^[60]

$$N_{\text{stack}} \approx \frac{q_{\max}}{\text{FWHM}_{\max}}. \quad (2.39)$$

To gain more detailed information about a lipid bilayer system, the scattering curve $I(q) \propto F(q)F^*(q)$ has to be fitted. The form factor, $F(q)$, is the Fourier transform of the electron density profile, $\rho(r)$. This electron density profile across the depth of a bilayer or multilayer lipid system can be modelled by a series of Gaussian functions, each representing a distinct region of the membrane.^[61] An even more sophisticated method was introduced recently by O. Glatter.^[62] Here, the generalised indirect Fourier transform method is used to fit the form factor and the structure factor of multilamellar systems simultaneously. Also the analysis of weakly ordered membrane stacks is possible by fitting a corresponding structure and form factor to the scattering curve.^[63]

2.8.3 Non-lamellar periodic lipid systems

Bragg reflections of the inverse hexagonal lipid mesophase (denoted by H_{\parallel}), which is built by a two-dimensional dense hexagonal packing of water filled channels each surrounded by a monolayer of lipid, occur at positions according to:^[3, 59]

$$s = \frac{2}{\sqrt{3}a} \sqrt{h^2 + k^2 + hk}. \quad (2.40)$$

Here, a is the hexagonal lattice constant, i.e. the distance between the centres of two neighbouring rods and h, k, l are the Miller indices. More details about hexagonal lipid phases can be found in section 4.2.3 (page 47).

In general, Bragg peaks of bicontinuous cubic structures (three-dimensional structures) may be observed according to their lattice constant, a , and the Miller indices, hkl , at:

$$s = \frac{1}{a} \sqrt{h^2 + k^2 + l^2}. \quad (2.41)$$

The combination of Miller indices, hkl , actually leading to diffraction signals, depends on the Bravais lattice type (i.e. primitive (P), body-centred (I), or face-centred (F)) as well as the symmetry elements of the cubic structure.^[3, 59, 64] From equation 2.41 and considering the symmetry elements of the different phases, the Miller indices, hkl , leading to Bragg signals can be calculated for each of the inverse bicontinuous cubic lipid phases. The results for the first 22 potential signal positions are shown in Table 2.1.^[3, 64] From the lattice spacings of these phases, further structural parameters can be calculated for inverse hexagonal as well as cubic phases, as described in section 4.2.3 (page 47) and section 4.2.4 (page 47), respectively.

2.9 Measuring procedure and data treatment

The data treatment procedure depends essentially on the sample system, which is under investigation. The procedure described in the following section is the most complex one, which is used for data of colloidal particles – such as proteins – in solution. For continuous lipid systems (cubic / hexagonal phases,

multi-lamellar vesicles), where only the position of the Bragg reflections as well as the relative peak areas are relevant, the procedure is much simpler. In the majority of those cases a calibration of the q -scale and a rough background correction is sufficient. If the data were measured with a Kratky camera system, an additional desmearing (correction of the instrument broadening) of the data is mandatory to resolve possible Bragg reflexes with low intensity and to correct the peak area.

A number of programs were written during this thesis for the processing of large numbers of SAXS datasets. As an example, the script converting raw synchrotron scattering data to MATLAB structures (Appendix A.2, page a1), the basic structure of the data treatment program (Appendix A.4, page a10) as well as the code of the GUI (graphical user interface) for the manual identification of lipid Bragg peak patterns (Appendix A.3, page a4) are shown. Additionally, in Appendix A.5 (page a14) the GUI and functionality of the largest program written in this thesis – for (semi-) automatic finding and fitting Bragg peaks in scattering pattern and identifying the corresponding (combination) of space groups – is presented.

2.9.1 Data collection

The minimum distance between successive data points, Δq , has to be chosen to be less than D_{\max}/π , where D_{\max} is the longest distance inside the observed particle between two scattering points. If this condition is violated, the information content of the dataset is questionable and no interpretation of the data is possible. Additionally, the smallest s -value should be ideally smaller than $1/(2D_{\max})$.^[4, 65]

Table 2.1: Combinations of Miller indices, hkl , leading to reflections and ratio of the signals of the seven inverse bicontinuous cubic lipid phases as defined in equation 2.41, depending on the symmetry elements inside the crystallographic unit cell.^[3, 64]

$P4_332$ Q^{212}	$Pm3n$ Q^{223}	$Pn3m$ Q^{224}	$Fm3m$ Q^{225}	$Fd3m$ Q^{227}	$Im3m$ Q^{229}	$Ia3d$ Q^{230}	L	ratio
							100	1
110	110	110			110			$\sqrt{2}$
111		111	111	111				$\sqrt{3}$
	200	200	200		200		200	2
210	210							$\sqrt{5}$
211	211	211			211	211		$\sqrt{6}$
220	220	220	220	220	220	220		$\sqrt{8}$
221		221					300	3
310	310	310			310			$\sqrt{10}$
311		311	311	311				$\sqrt{11}$
222	222	222	222	222	222			$\sqrt{12}$
320	320							$\sqrt{13}$
321	321	321			321	321		$\sqrt{14}$
400	400	400	400	400	400	400	400	4
410	410	410						$\sqrt{17}$
411	411	411			411			$\sqrt{18}$
311		311	311	311				$\sqrt{19}$
420	420	420	420		420	420		$\sqrt{20}$
421	421	421						$\sqrt{21}$
332		332			332	332		$\sqrt{22}$

Synchrotron sources

Most of the SAXS experiments in this work were carried out at the high brilliance beamline ID02 at the European Synchrotron Radiation Facility (ESRF) in Grenoble, France.^[66] The X-ray energy was typically between 11 and 17 keV, corresponding to wavelengths of 1.1 Å to 0.73 Å. Two undulators provided a flux of approximately $4 \cdot 10^{13}$ photons s^{-1} and the beam size at the sample was 0.37×0.21 mm². Two-dimensional diffraction images were recorded on an image-intensified charge-coupled device (CCD). The CCD has an active area of 100 mm² (1024×1024 pixels) and a frame rate of about 10 frames per second. A typical sample-detector distance was 1.50 m (distances between 1 and 10 m are possible, covering a q -range of $6 \cdot 10^{-3}$ to 6 nm⁻¹). Usually the sample exposure time – depending on the sample system – was between 0.05 s and 2 s for the complete scattering pattern, which is obtained by azimuthal integration over the whole active detector area.

Either capillaries with a volume of 0.1 ml or PTFE-rings closed by Mylar-foil (inner sample cells of SAXS high pressure cell as described in [67, 68]) with a total volume of 25 μl were used as sample holders.

Kratky camera system

The radiation source of a Kratky camera system is a conventional X-ray tube typically with a copper anode, providing radiation with a wavelength of 1.54 Å, corresponding to an energy of 8.05 keV. The sample is placed into the camera in a small glass capillary with a volume of approximately 100 μl at a distance of 200 mm to the point detector. Prior to the measurement, the air is evacuated from the whole camera system to avoid unnecessary scattering by air molecules. During the measuring process, the detector counts for a given time at a specific height relative to the incident beam and moves to a slightly higher position afterwards. A typical measurement consists of 100-150 steps, each taking a few hundred seconds, resulting in a typical overall time for one scattering pattern of 3-6 h.

2.9.2 Data evaluation and correction

Basic corrections

The calibration of the q -scale is usually done by standard samples with well known and sufficiently large d -spacing, e.g. Ag-behenate ($d = 5.838$ nm), Ag-stearate ($d = 4.868$ nm), dry collagen ($d = 65$ nm) or tripalmitin ($d = 4.06$ nm).^[5, 69, 70]

A number of different methods have been described in the literature to determine the absolute scale of the scattering intensity for X-rays^[71, 72] as well as for neutrons^[73]. Common methods are to use the scattering of pure water as a reference, which can be easily calculated, or the use of a well known standard, e.g. a protein solution with precisely known concentration.

For data measured on a 2D CCD detector, prior to the azimuthal integration, to obtain the scattering pattern, a masking of certain areas of the detector has to be performed to remove contributions of the beamstop (a metal plate blocking the primary beam), spurious effects of the sample container (e.g. Kossel lines from the diamond windows of the high pressure cell^[74, 75]) or shadows from other parts of the equipment.

Desmearing of the raw data

While desmearing of data measured by a Kratky camera system is mandatory due to the large width of the incident X-ray beam, measurements from a synchrotron source do not have to be desmeared. This procedure is necessary in order to obtain an ideal pinhole scattering curve, where the influence of the signal broadening due to the large dimensions of the incident beam are corrected. At a synchrotron source the dimension of the incident beam is nearly point-shaped, resulting in only very little smearing. Most datasets were desmeared by the program GNOM^[20, 21] using an algorithm as described in [4]. This algorithm has been shown to be rather efficient with regard to its computation, but it does not function well on datasets, which are severely truncated in the range of high scattering angles.^[4] Details of desmearing algorithms suitable for colloidal particles in solution can be found for in [4, 76–79]. These algorithms have a number of limitations: in the presence of noise the solutions become sometimes unstable and the calculation fails. Sometimes this is prevented by a smoothing of the data prior to the desmearing procedure, which is intrinsically problematic. Additionally, these algorithms perform rather badly or even fail for (partially) ordered systems, which show Bragg peaks. A number of different algorithms have been developed especially for the correction of ordered samples, as described in [80, 81].

Background correction

The pure contribution of the scattering objects from the measured solution scattering intensity is obtained by subtracting the scattering of the solvent, which has to be measured separately, multiplied by a constant factor accounting for the volume fraction of the solute in the solution, i.e. the relative changes in scattering or absorption cross-sections. Additionally, this procedure removes any non-isotropic contributions in the background scattering, e.g. due to preferential orientation of cell windows or the contribution from the polymer film sealing the sample container.^[5]

Merging of datasets

To obtain an ideal scattering curve over the full q -range, the data of several measurements of the same sample, but different concentrations can be merged. The range of small q -values should be measured with a concentration as low as possible, to minimise the effect of aggregation and particle-particle interaction. At high angles, only an insufficient signal/noise ratio can be achieved by samples of low concentration. Accurate large angle data can be obtained by measuring higher concentrations, increasing the exposure time or decreasing the sample-detector distance. Especially, increasing the concentration, cutting off the low-angle region, which is now affected by the no longer insignificant structure factor, and merging it with the low-concentration measurement yields a nearly perfect overall scattering curve.

2.9.3 Data analysis

Guinier analysis

First of all the data should be plotted in a Guinier-plot (see section 2.4, page 9). A non-linear behaviour in the low-angle region indicates the contribution of a structure factor, aggregation, or polydispersity. If the plot is linear and the particle is not too large, the radius of gyration, R_G , and the forward scattering intensity, $I(0)$, can be obtained. For a series of measurements with different concentrations, c , of the sample an increasing ratio of $I(0)/c$ also indicates multimerisation or aggregation.

Kratky plot

Afterwards, the data should be plotted in a Kratky-plot (see 2.5, page 11) to find out about the compactness of the particle. In case of a protein it can be easily seen if the protein is still folded, partially or even completely unfolded.

Pair distance distribution function

By calculating the $p(r)$ -function, a number of valuable information can be obtained, such as the largest distance inside the particle, D_{\max} , and again, R_G and $I(0)$. The $p(r)$ -function is essential for further *ab initio* calculations and should be calculated with great care. Incorrectly chosen integration limits can have a significant influence on the reliability of the $p(r)$ -function^[4] as well as the quality of the *ab initio* shape reconstruction. If the upper integration limit, D_{\max} , is chosen too small, the scattering data are poorly represented by the resulting $p(r)$ -function, whereas a too large value of D_{\max} will result in much larger values of the derived parameters than the underlying physical features of the scattering particle justify.^[4] A disagreement between the values obtained by the Guinier plot and the values from the $p(r)$ -function usually indicates either incorrect calculation of the $p(r)$ -function or partial aggregation in the sample. Afterwards, the molecular mass, surface area and volume (see section 2.5, page 10) of the particle can be calculated. The calculation of the $p(r)$ -function was usually done using the program GNOM.^[20, 21]

2.9.4 Solution structure modelling

Ab initio shape reconstruction

If the particle in solution is a protein, the number of residues is known and the data extent to reasonably large values of q , the dummy-residue method should be chosen for structure reconstruction. In case of any other particle or lacking information about the protein under investigation, the multi-bead approach is a powerful tool to reveal the particle structure. The multipole expansion method is not recommended and can only be used – at best – for a rough impression of the envelope of very simple particles. After calculating a large number of *ab initio* structures for one particle (at least 16-20), the results of all calculations should be evaluated. If the results are satisfying, the successfully calculated structures should be averaged. *Ab initio* calculations based on the dummy-residue method were carried out using the program GASBOR written by D.I. Svergun et al.^[82] Calculations using the multi-bead method were performed by a user-written MATLAB script utilising the Fortran programs DAMMIF^[49] for the calculation and SUBCOMP^[51] for averaging.

Verification of the *ab initio* structures

Finally, the *ab initio* structures obtained should be compared to atomic structures (by crystallography, NMR), if available. Also the scattering pattern of the *ab initio* particle shape should be calculated and compared to the measured experimental scattering curve. This can be easily done using the program CRY SOL.^[83] Slight deviations are expected, due to the lower resolution of the calculated structure as well as the impact of the averaging process.

CHAPTER 3

Grazing incidence X-ray diffraction and X-ray reflectometry

In the following chapter the basics of X-ray reflectometry (XRR) and grazing incidence X-ray diffraction (GIXD) are introduced. For a more detailed study of these topics, the reader is referred to the literature, especially [58, 84, 85] for GIXD and [57, 71, 84, 86] for XRR.

In Figure 3.1 the scattering geometry and kinematics of the scattering processes of XRR and GIXD are juxtaposed to point out the differences between both methods. By definition, the sample is located in the horizontal xy -plane, normal to the z -direction. Specular X-ray reflectometry is a so-called in-plane method, where all measurements take place in a plane spanned by the incident X-ray beam and the surface normal of the sample ($2\theta = 0$). XRR measurements are performed by varying the angle of incidence (α_i) and keeping the specular condition $\alpha_f = \alpha_i$, where α_f is the angle of the reflected beam. Due to this geometry, XRR probes the vertical structure of the sample, while averaging in lateral xy -direction. Grazing incidence X-ray diffraction, in contrast, is an out-of-plane method. The detector is moved out of the ($2\theta = 0$) plane during the measurement by scanning the angles 2θ and α_f with a constant, very small angle of incidence α_i usually using a position sensitive 2D detector plate (PSD). Here, information about the structure of crystalline domains in the horizontal plane can be gained with high resolution.

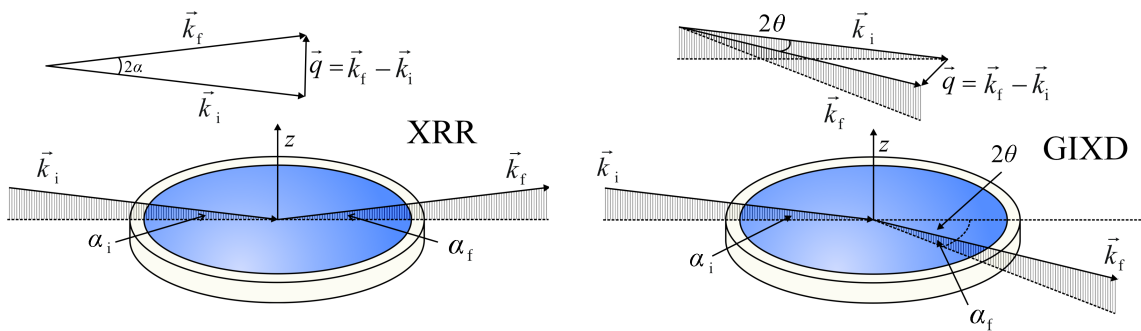


Figure 3.1: Kinematics of the scattering processes at the air-water interface and definitions of the wave vector transfer, \vec{q} , for X-ray reflectometry (XRR – left) and grazing incidence X-ray diffraction (GIXD – right).

3.1 X-ray reflectometry (XRR)

Recent developments in technology have led to an increasing demand on nanostructured surfaces and materials. An established method, suitable for non-destructive and contactless analysis of layer thickness, electron density and interfacial morphology of the materials is X-ray reflectometry. The high surface sensitivity of this method is based on the phenomenon of total external reflection.^[86] This method has several advantages: the system under investigation does not have to be transparent and can be built of several layers each differing in thickness, density and interfacial roughness.^[87, 88] No crystallinity of the sample is required, since the method is based on a density gradient at the interface. Additionally, no complicated sample preparation is required.

3.1.1 Basics of XRR

In the XRR method the reflectivity, $R = I(\alpha_f)/I(\alpha_i)$, is measured as a function of the incident angle, α_i , which is typically smaller than 5° . X-ray reflectometry is an in-plane method, i.e. only the reflected intensity inside the plane defined by the surface normal and the incident beam is considered. This method has the additional condition that the angle of the incident beam, α_i , and the reflected beam relative to the surface, α_f , have to be identical, keeping the so-called specular reflectivity condition ($\alpha_i = \alpha_f$) valid.^[89]

The wave vector transfer, \vec{q} , is small for small angles of incidence, α_i , and therefore the phase, $\vec{q}\vec{r}$, of all factors $\exp(i\vec{q}\vec{r})$ (q.v. equation 2.2 and equation 3.26) is small, too. Thus, the detailed positions of the atoms can be neglected as long as the inter-atomic distances in the sample are much smaller than ($\lambda \sin \alpha_i$) and the sample system is simply described by the corresponding refractive indices.^[86]

For hard X-rays ($\lambda \approx 1 \text{ \AA}$), the refractive index, n , is slightly smaller than unity and given by ^[86, 87, 90]

$$n = 1 - \delta + i\beta = 1 - \frac{\lambda^2 \rho_e r_e}{2\pi} + i \frac{\lambda \mu}{4\pi} = 1 - \frac{N_A \cdot r_e \cdot \lambda^2 \cdot \rho_e \cdot f'}{2 \cdot \pi \cdot M} + i \frac{\lambda \rho_e \mu}{4\pi}, \quad (3.1)$$

where $r_e = 2.82 \cdot 10^{-15} \text{ m}$ is the classical electron radius and ρ_e is the electron density, also often expressed as the scattering length density $\rho = r_e \rho_e$. N_A is Avogadro's number, M the average atomic mass and f' the real part of the average atomic scattering factor. The real part of the refractive index, δ , is typically in the order of 10^{-6} to 10^{-5} in condensed matter and only approximately 10^{-9} in air.^[86, 87] These small numbers result from the relatively weak interaction of X-rays with matter. The imaginary term, β , accounts for absorption, where μ is the linear absorption coefficient. For $\lambda \approx 1 \text{ \AA}$ and sample systems containing no heavy atoms, β is much smaller than δ .^[58, 86, 88]

In general, refraction is described by Snell's law, with the angle of the incident beam, α_i , and the angle of refraction denoted by α_t :

$$n_1 \cos \alpha_i = n_2 \cos \alpha_f. \quad (3.2)$$

n_1 and n_2 are the refractive indices of the upper and lower medium, respectively. The refractive index of air equals one and all other substances have a real part of the refractive index that is smaller than unity. Therefore, below a certain critical angle, α_c , total external reflection occurs. Neglecting absorption ($\mu = 0$), the critical angle, α_c , is proportional to the square root of the electron density, ρ_e , of the material:^[58, 86]

$$\alpha_c = \sqrt{2\delta} = \lambda \sqrt{\frac{r_e \rho_e}{\pi}}. \quad (3.3)$$

In an in-plane reflectivity experiment, the x - and y -components of the scattering vector \vec{q} equal zero. Only the z -component has to be considered. As a consequence, in X-ray reflectometry only information about the laterally averaged vertical electron density profile perpendicular to the interface can be gained, described by [89, 91]

$$q_z = \frac{4\pi}{\lambda} \sin \alpha_i. \quad (3.4)$$

The reflectivity of an ideal flat interface, R_F , where no diffuse scattering is taking place, is given by Fresnel's law [92]

$$R_F = \left| \frac{q_z - q'_z}{q_z + q'_z} \right|^2, \quad (3.5)$$

with $q'^2_z = q_z^2 - q_c^2$. q_c is the critical wave vector transfer at the critical angle α_c . For larger angles ($\alpha_i \gg \alpha_c$), the Fresnel reflectivity, R_F , decays rapidly and approximately with α_i^{-4} (Porods law).^[86] At real interfaces, the measured intensity decreases even faster with α_i , owing to the non-zero roughness of the interface.

3.1.2 Bragg's equation

Bragg reflections occur when X-rays reflected from different lattice planes of crystalline structures interfere constructively. From the q_z -values, where these peaks are observed, the lattice constants, d , of the sample can be calculated using Bragg's law (q.v. section 2.8, page 17).

Constructive interference between two parallel X-ray waves, which are (partially) reflected from parallel lattice planes, can be observed when the relation between their phases is an integer multiple of 2π . This is given when twice the optical path difference, δ_p , of the two X-ray beams equals an integer multiple, n_x , of the wavelength, λ . Using simple trigonometrical functions the relation $\delta_p = 2d \sin \alpha_f$ between optical path difference, δ_p , and the lattice constant, d , can be found. Finally, Bragg's law is obtained:

$$n_x \lambda = 2d \sin \alpha_f. \quad (3.6)$$

From Bragg's law a relation between the position of the maxima in the reflectivity curve, q_{\max} , and the lattice constant, d , of the sample can be found:

$$q_{\max} = \frac{4\pi}{\lambda} \sin \alpha_{f,\max} = n_x \frac{2\pi}{d}. \quad (3.7)$$

3.1.3 Kiessig oscillations

For a sample without any pronounced periodicity perpendicular to the surface, only Kiessig oscillations can be found in the reflectivity curve. These periodic oscillations are due to the constructive or destructive interaction between X-rays reflected at the top surface and the lowest interface of the layer system, depending on the angle of incidence, α_i . Maxima are observed, when the product of the wave vector transfer, q_z , and the overall sample thickness, d_{sample} , equals an integer multiple of 2π .

From the distance of two neighbouring maxima, Δq , the overall thickness of the sample can be estimated by $d_{\text{sample}} \approx 2\pi/\Delta q$.

3.1.4 Parratt's recursive method

From reflectivity curves, the electron density profile of the sample system perpendicular to the surface can be obtained. Therefore, the system can be subdivided either into numerous very thin, uniform layers or into a small number of thicker layers, if the layer structure of the system is known. Then, each layer represents a region of different electron density of the system and the structure profile can be recursively and iteratively calculated from the set of known layers. This method was introduced in 1954 by L. Parratt and therefore is known as Parratt's recursive method. Alternatively to the recursive method a matrix formalism can be used as presented below.^[93]

Each of these layers (indexed by i) is characterised by its electron density, $\rho_{e,i}$, its thickness, d_i , and the roughness of the interface between the two neighbouring layers, $\sigma_{i,i+1}$. By definition, the layer with $i = 0$ is the semi-infinite medium on top (mostly air or water) and the N -th layer is the substrate (e.g. water or Si), which is also assumed to be semi-infinite. Thus, no wave can be reflected from this lowest layer due to absorption.

The wave vector transfer of a medium, q_{medium} , can be calculated in general by^[91]

$$q_{\text{medium}} = \sqrt{q_{i=0}^2 - q_c^2} \approx \sqrt{q_{i=0}^2 - 16\pi\rho_e r_e}. \quad (3.8)$$

The reflectivity coefficient, r_{ij} , (amplitude reflectivity) of the two successive layers, i and $i + 1$, can be calculated from an extension of the Fresnel relation, where the exponential-term is the so-called Debye-Waller factor accounting for the interfacial roughness:^[90]

$$r_{i,i+1} = \frac{q_i - q_{i+1}}{q_i + q_{i+1}} \cdot \exp\left(-\frac{1}{2}q_i q_{i+1} \sigma_{i,i+1}^2\right). \quad (3.9)$$

For a sharp, but rough interface, σ^2 is the root mean square deviation (RMSD) of the height, z_{xy} . The roughness leads to a damping of the reflectivity, due to diffuse scattering of the incident radiation.^[86, 94]

Each layer is now fully specified by a characteristic matrix

$$M_i = \begin{pmatrix} \exp(i\beta_{i-1}) & r_{i-1,i} \cdot \exp(i\beta_{i-1}) \\ r_{i-1,i} \cdot \exp(-i\beta_{i-1}) & \exp(-i\beta_{i-1}) \end{pmatrix}, \quad (3.10)$$

where $\beta = (1/2) n_i q_i d_i$ comprises the refractive index, n_i , and the thickness, d_i , of the layer i .

The reflectivity of a multilayer system is obtained from the product of the matrices of each single layer:^[91]

$$\begin{aligned} M &= \prod_{i=0}^N M_i = \begin{pmatrix} m_{11} & m_{12} \\ m_{21} & m_{22} \end{pmatrix}, \\ R(q) &= \frac{|m_{12}|^2}{|m_{22}|^2}. \end{aligned} \quad (3.11)$$

Using these equations, the reflectivity of a layer system can be calculated iteratively from bottom to top. The Parratt formalism as described in equation 3.9 can only be used if the roughness of each layer is small compared to the corresponding thickness.^[86] Alternatively, an effective density model can be used, constructed from a large number of very thin layers without accounting for roughness, but sustaining continuity.

Based on such layer models, the deviation between the measured reflectivity curve and the calculated curve from the parameters $\rho_{e,i}$, d_i , and $\sigma_{i,i+1}$ can be minimised. Often several mathematical solutions are found fitting the experimental data. A number of these solutions can usually be neglected as physically or logically not appropriate for the sample system studied.

3.1.5 The kinematic approach

In the kinematic approach, the reflectivity curve is given by the Fourier transform of the derivative of the laterally averaged electron density profile perpendicular to the interface. Only single scattering effects are taken into account. Therefore, the scattering amplitude of the incident wave is the same at all points within the sample and only the phase is changing from point to point. This approach is especially useful to describe diffuse scattering and non-Gaussian roughness.^[86, 95]

In the kinematic approach, the reflectivity is calculated by the so-called “master formula for reflectivity”:^[58]

$$R(q_z) = R_F(q_z) \cdot \left| \frac{1}{\rho_\infty} \int_{-\infty}^{\infty} \frac{d\rho(z)}{dz} e^{iq'_z z} dz \right|^2. \quad (3.12)$$

It has to be noted that this formula is based on an approximation, but it is sufficiently accurate for $\alpha_i \gg \alpha_c$. In this formula, the refraction corrected scattering vector $q'_z = 4\pi \sin(\alpha')/\lambda$ is used, where α' is given by $\alpha_i^2 = \alpha_c^2 + (\alpha')^2$.^[58]

3.1.6 X-ray reflectivity data collection and treatment

All XRR experiments were performed at synchrotron radiation sources, i.e. either at the beamline BW1 at HASYLAB (Deutsches Elektronen-Synchrotron DESY, Hamburg, Germany)^[96] or at beamline ID10B at the ESRF (European Synchrotron Radiation Facility, Grenoble, France)^[97]. Details of the beamlines can be found in section 3.2.6, where the measurement procedure of GIXD scans is described.

Typical reflectometry scans were carried out by measuring the scattered intensity as a function of α_i under the specular condition, $\alpha_i = \alpha_f$ (exit angle, α_f). Reflectivity measurements were usually performed in an angular range of $0.5 \alpha_c < \alpha_i < 35 \alpha_c$, with the critical angle of the air-water interface, α_c ($\alpha_c = 0.13^\circ$ at wavelength of 1.3 Å). A typical X-ray reflectivity scan took between 15 and 30 min.

In general, the contribution of diffuse scattering has to be subtracted from the measured data to obtain the so-called “true reflectivity”. Using a 1D detector, diffuse scattering is measured by an offset-scan slightly out of the reflectivity condition by typically 0.05° , depending on the size of the primary beam.^[92] If a multi-channel detector is used, this additional scan is not necessary. Here, the intensity of neighbouring channels to the signal can be subtracted from the peak intensity. Additionally, an illumination correction of the raw data is necessary to correct for the variation of incident photons per surface area due to the changing projection of the X-ray beam on the sample surface during the measurement.

For the data treatment and correction, a number of scripts and programs have been written in MATLAB. The script for the basic data treatment of XRR scans taken at HASYLAB in Hamburg is given in Appendix A.6.1 (page a16). The correction of raw data measured at the ESRF in Grenoble was done with a script presented in Appendix A.6.2 (page a19).

3.1.7 *Excursus: X-rays vs. neutrons*

The theory of neutron reflectometry (NR) and small-angle neutron scattering (SANS) is closely related to the one of X-ray reflectometry (XRR) and small-angle X-ray scattering (SAXS).

The main difference is that neutrons do not scatter at the electron clouds of the sample, but at the atomic nuclei. The scattering length density of X-rays is described by the product of the classical electron radius, r_e , and the electron density of the material, ρ_e . For neutrons, this term is replaced by the product of the coherent scattering length, b , and the density of nuclei, ρ_n , in the material.^[57, 86]

X-rays propagate with the speed of light. Their energy, E , and wavelength, λ , are related by the speed of light, c , and the Planck constant, h :^[27]

$$E = \frac{hc}{\lambda}. \quad (3.13)$$

Typical energies of “soft” X-rays range from 0.12 to 12 keV, corresponding to wavelengths of 100 to 1 Å. X-rays with energies between 12 and 120 keV (with wavelengths of 1 to 0.1 Å) are called “hard” X-rays, due to their ability to penetrate matter more easily.

Neutrons are spin $-\frac{1}{2}$ particles with a magnetic moment of -1.923 nuclear magnetons. Bound to an atomic nucleus neutrons are stable, but free neutrons decay to a proton, an electron and an anti-neutrino within a lifetime of about 900 s.^[27] A neutron can either be described as a particle with a mass of $m = 1.675 \cdot 10^{-27}$ kg or as a wave, which is characterised by its wavelength given by the deBroglie formalism^[27]

$$\lambda = \frac{2\pi}{k} = \frac{h}{vm}, \quad (3.14)$$

where k is the magnitude of the wave vector and v is the velocity of the neutron.

The energy, E , of a neutron is given by:

$$E = \frac{1}{2}mv^2 = \frac{\hbar^2 k^2}{2m} = \frac{h^2}{2m\lambda^2}. \quad (3.15)$$

The energy of a neutron is often classified by a corresponding temperature ($T = E/k_B$). Hot neutrons have temperatures between 1000 and 6000 K (corresponding to wavelengths of 1 - 0.4 Å and energies of 100 - 500 meV), thermal neutrons are found in a temperature range between 60 and 1000 K (wavelengths of 4 - 1 Å and energy of 5 - 100 meV) and cold neutrons, as typically used for scattering experiments, have temperatures of 1 - 120 K, wavelengths of 30 - 3 Å and corresponding energies of 0.1 - 10 meV, which is by a factor of 10^6 smaller than the energy of X-rays typically used for scattering experiments.^[27]

Contrary to X-rays, for neutrons, the scattering length does not only depend on the chemical element, but also on the isotope and the spin-state of the atomic nucleus. For X-rays, the scattering length increases with the number of electrons, whereas for neutrons it varies from element to element in a random manner. Especially for the different hydrogen isotopes this property differs strongly. A special advantage of neutron experiments over X-ray studies arises from this fact. Most measurements are performed in aqueous solutions. The coherent scattering length of water is $-0.56 \cdot 10^{-14}$ cm⁻², whereas fully deuterated water (D₂O, D = ²H) has a completely different coherent scattering length of $6.38 \cdot 10^{-14}$ cm⁻².^[27] Most biological macromolecules under investigation have scattering lengths in between. Only the contrast between the different scattering lengths in the sample system leads to the measured signals. Therefore, the overall scattering length of the solvent can be tuned to an identical scattering length as parts of

the sample system by mixing water (H₂O) and deuterated water (D₂O). This part of the system is now invisible to the neutron beam, thereby enhancing the sensitivity of other parts of the system under investigation.

Another advantage of neutrons is their ability to detect light atoms like hydrogen among much heavier atoms, which is not easily possible by using X-rays. Additionally, the low energy in combination with the high penetration power makes neutrons a very mild probe and investigation of systems sensitive to radiation damage – like proteins in solution – are possible even over long periods of beamtime exposure. On the other hand their weak interaction with matter leads to one of the major disadvantages of this technique. The measurements are very time consuming, i.e. for a single reflectivity or scattering curve the measurements can take several hours. Hence, generally large sample volumes are needed.

3.2 Grazing incidence X-ray diffraction (GIXD)

3.2.1 Basics of GIXD

GIXD scans are performed at a constant incident angle, α_i , which is smaller than the critical angle, α_c , while the diffraction intensity of crystalline domains is detected as a function of the horizontal and vertical angles, $2\theta \neq 0$ and $\alpha_f \geq 0$. As shown in Figure 3.1 (page 25), the wave vectors of the incident and scattered X-rays are denoted by \vec{k}_i and \vec{k}_f , respectively, where $|\vec{k}_i| = |\vec{k}_f| = k = 2\pi/\lambda$. The GIXD scattering process is characterised in reciprocal space by the wave vector transfer $\vec{q} = \vec{k}_f - \vec{k}_i$ (q.v. Figure 3.1), which can be separated into its horizontal and vertical component \vec{q}_{xy} and q_z , respectively.^[58]

From GIXD measurements of quasi two-dimensionally ordered hydrocarbon chains at the air-water interface, the inter-chain characteristic distances, the degree of lattice distortion from the ideal hexagonal grid, the size and height of the crystalline domains, as well as the tilt angle of the chains relative to the surface normal can be determined. Information about disordered domains of the monolayer are not accessible by this technique.^[98]

At total reflection, an evanescent wave travels parallel to the interface in the subphase with an exponentially decreasing intensity with depth. The total penetration depth, Λ , is a function of the incident angle, α_i , and critical angle, α_c :^[98]

$$\Lambda = \frac{\lambda}{4\pi \sin \alpha_c} \sqrt{\frac{\alpha_c^2}{\alpha_c^2 - \alpha_i^2}}. \quad (3.16)$$

For the air-water interface and an incident angle of $0.85 \alpha_c$, the penetration depth into water is, depending on the wavelength, approximately 90 Å, thus enhancing the surface sensitivity and reducing the background scattering from the subphase, which is especially important for GIXD experiments.^[58, 84]

3.2.2 Bragg peaks – two-dimensional crystallography

Molecular films at the air-water interface are generally built by a large number of small quasi two-dimensional crystalline domains, rather than a single crystal. Each domain has a different orientation relative to the incident beam. Therefore, the horizontal components of \vec{q} , q_x and q_y , can only be measured

as their combination $q_{xy} = |\vec{q}_{xy}| = \sqrt{q_x^2 + q_y^2}$. The obtained vertical and horizontal orientations of the scattering vector, q_z and q_{xy} , are given by:^[58, 99, 100]

$$q_z = (2\pi/\lambda) (\sin(\alpha_i) + \sin(\alpha_f)) \approx (2\pi/\lambda) \sin(\alpha_f) . \quad (3.17)$$

$$\begin{aligned} q_{xy} &= (2\pi/\lambda) \sqrt{\cos^2(\alpha_i) + \cos^2(\alpha_f) - 2 \cos(\alpha_i) \cos(\alpha_f) \cos(2\theta_{xy})} \\ &\approx (2\pi/\lambda) \sqrt{1 + \cos^2(\alpha_f) - 2 \cos(\alpha_f) \cos(2\theta_{xy})} \approx (2\pi/\lambda) \sin(2\theta_{xy}) . \end{aligned} \quad (3.18)$$

A crystalline layer at the air-water interface can be regarded as two-dimensional, where the crystalline repeat unit can be described by only two primitive vectors, \vec{a} and \vec{b} , in real space, which are lying in the monolayer plane including the angle γ_D (see Figure 3.2). No periodicity out of the plane exists, therefore the primitive vector in this direction, \vec{c} , is equal to zero. Instead, often the vector spanning diagonally through the unit cell ($\vec{a} + \vec{b}$) is called \vec{c} or $\vec{a} + \vec{b}$. The two-dimensional crystal has to fulfil the Laue conditions, when signals are obtained given by equation 2.36, where $\vec{q} \equiv \vec{q}_{xy} \equiv \vec{q}_{hk}$. Thus, instead of a lattice of points, the diffraction intensity is extended along Bragg rods defined by $\vec{q} = (q_{xy} \cdot q_z)$, where q_{xy} leads to reflections constrained according to Laue's condition, and q_z is unrestricted. The two reciprocal vectors \vec{a}^* and \vec{b}^* are parallel to the surface plane (q.v. section 2.8) and orthogonal with respect to each other. $\vec{a}^* \vec{a} = 2\pi$ and an equivalent relation is valid for \vec{b}^* , thus:^[58]

$$|\vec{a}^*| = \frac{2\pi}{a \sin(\gamma)} \quad \text{and} \quad |\vec{b}^*| = \frac{2\pi}{b \sin(\gamma)} . \quad (3.19)$$

Analogous to the d -spacing in a small-angle scattering experiment (cf. equation 2.38), the repeat distance of the two-dimensional unit cell is given by $d = 2\pi/q_{xy}$. A maximum of three different d -spacings can be obtained experimentally from a two-dimensional primitive unit cell, d_a , d_b and d_c , where a and b denote the magnitude of the lattice vectors of the unit cell and c is the magnitude of the vector between \vec{a} and \vec{b} . With the crystallographic convention $a \leq b \leq c$,^[1] the relationships $d_a \geq d_b \geq d_c$ and $q_a \leq q_b \leq q_c$ can be derived. It has to be noted that all three vectors, \vec{a} , \vec{b} and \vec{c} are located in one plane and are arranged in a triangle as shown in Figure 3.2. Thus, the three vectors are linear dependent. The heights of the triangle spanned by \vec{a} , \vec{b} and \vec{c} correspond to the three lattice spacings, d_a , d_b and d_c . The relation between the d -spacing or the maximum position, $q_{xy, \max}$, with the lattice parameters of the unit cell, a , b and γ , is given by ^[58]

$$d = 2\pi/q_{xy, \max} = [h^2/a^2 + k^2/b^2 - 2(hk/ab) \cos(\gamma)]^{-1/2} \sin \gamma , \quad (3.20)$$

where h and k are the Miller indices of the corresponding peak.

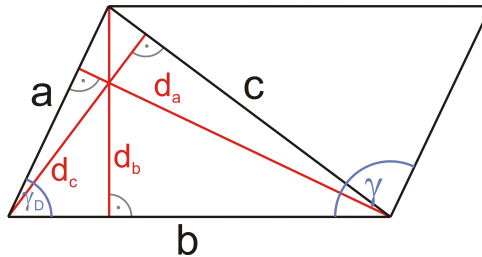


Figure 3.2: Oblique unit cell with lattice vectors (a , b), angles (γ_D , γ) and corresponding lattice spacings (d_a , d_b).

From the experimentally obtained d -spacings, using simple trigonometric relations (q.v. Figure 3.2), the moduli of the lattice vectors, a and b , can be determined:

$$a = \frac{d_b}{\sin \gamma_D}, \quad (3.21)$$

$$b = \frac{d_a}{d_b} a, \quad (3.22)$$

where the angle γ_D is defined as

$$\gamma_D = \arccos \left[\frac{d_b}{2d_a} + \frac{d_a}{2d_b} - \frac{d_a d_b}{2d_c^2} \right]. \quad (3.23)$$

Finally, the angle of the unit cell can be calculated by:

$$\gamma = \arcsin \left(\frac{d_c}{b} \right) + \arcsin \left(\frac{d_c}{a} \right). \quad (3.24)$$

The area of the unit cell can be calculated from $A_{\text{cell}} = a \cdot b \sin(\gamma)$. The observed diffraction intensity of a GIXD experiment is typically plotted as a contour plot of q_{xy} versus q_z . By integration along the q_{xy} - or q_z -axis, Bragg peaks or Bragg rods are observed, respectively.^[58]

3.2.3 Bragg rods

Compared to a single Bragg point of the scattering pattern of a three-dimensional crystal, a Bragg rod contains more information. The diffraction intensity along a Bragg rod is given by:

$$I(h, k, q_z) = |F(h, k, q_z)|^2 \cdot e^{-(q_{hk}^2 u_{\text{hor}} + q_z^2 u_z)} \cdot |T(\alpha_f)|^2. \quad (3.25)$$

The exponential term in equation 3.25 is the so-called vertical Debye-Waller factor, which accounts for internal thermic motion of the molecules as well as capillary waves on the water surface enlarging the roughness of the interface. u_{hor} and u_z are the mean square atomic displacements in the horizontal and vertical direction, respectively. It is evident that a low surface roughness is essential for a high intensity of the Bragg rod, especially in the region of large q_z -values. The factor $|T(\alpha_f)|^2$ equals unity except near the critical angle ($\alpha_f = \alpha_c$), where the sharp Yoneda-Vineyard peak is observed. Here, this effect originates from the interference of X-rays diffracted upwards from the surface with X-rays first diffracted downwards and subsequently reflected upwards again from the interface.^[58, 85, 99, 101]

The experimental diffraction intensity is mainly governed by the structure factor $F(h, k, q_z)$, which is the Fourier transform of the electron density in the unit cell. Alternatively, it can be expressed in terms of the constituent atoms with form factors f_i . It is important to notice that in equation 3.25 only the absolute square of the structure factor appears, owing to the well known phase problem of X-ray crystallography:

$$F(h, k, q_z) = \int_{\vec{r} \in \text{unit cell}} \rho(\vec{r}) e^{i(\vec{q}_{hk}\vec{r} + q_z z)} d^3 \vec{r} = \sum_{j \in \text{unit cell}} f_j e^{i(\vec{q}_{hk}\vec{r}_j + q_z z_j)}. \quad (3.26)$$

Also the orientation of the diffracting particles can be derived from the Bragg rod. Bell-shaped maxima of Bragg rods occur where the plane of maximal structure factor intercepts the rod. In the case of a lipid

monolayer at the air-water interface, only domains of hydrocarbon chains in the all-*trans* conformation lead to diffraction signals, where all lipid chains are straight and parallel with respect to each other, but not necessarily parallel to the surface normal (corresponding to a molecular tilt angle $t \neq 0$). If the tilt angle is zero, the maxima of any Bragg rod are found at the horizon ($q_z = 0 \text{ \AA}^{-1}$).^[58, 84]

3.2.4 The horizontal and vertical coherence lengths

A finite size of the crystalline domains leads to a broadening of the Bragg peaks. When the domains are assumed to be perfectly packed without packing defects, the size of these domains or the vertical coherence length of the two-dimensional crystal, L_{xy} , can be estimated by Scherrer's equation:^[58, 85]

$$L_{xy} \approx 0.9 [2\pi/\text{FWHM}_{\text{intrinsic}}(q_{xy})] . \quad (3.27)$$

The full width at half-maximum $\text{FWHM}_{\text{exp}}(q_{xy})$, observed in the diffraction pattern, has to be corrected by the instrumental resolution $\text{FWHM}_{\text{resol}}(q_{xy})$ to obtain $\text{FWHM}_{\text{intrinsic}}(q_{xy})$:^[58]

$$\text{FWHM}_{\text{intrinsic}}(q_{xy}) = \sqrt{\text{FWHM}_{\text{exp}}(q_{xy})^2 - \text{FWHM}_{\text{resol}}(q_{xy})^2} . \quad (3.28)$$

Analogous to the diameter of crystalline domains on the interfacial plane, L_{xy} , horizontal coherence length of the two-dimensional crystal in z -direction, L_z , can be estimated from the FWHM of the Bragg rod using the equation:^[58]

$$L_z \approx 0.9 [2\pi/\text{FWHM}(q_z)] . \quad (3.29)$$

3.2.5 Plane groups and their GIXD patterns

For three-dimensional crystals, seven different crystal systems and 32 point groups are known. In combination with symmetry elements like glide planes and screw axis, a total number of 14 Bravais lattices and 230 space groups can be constructed. In two-dimensions, this number is reduced to only 17 plane groups and four unit cells, namely oblique ($a \neq b$), square ($a = b$ and $\gamma' = 90^\circ$), hexagonal ($a = b$ and $\gamma = 120^\circ$) and rectangular, which both exists as a primitive ($a > b$ and $\gamma' = 90^\circ$) as well as a centred ($a' > b'$ and $\gamma' = 90^\circ$) cell. a , b , and γ describe hexagonal unit cells, whereas a' , b' , and γ' indicated the rectangular notation of the same unit cells.^[64]

In Figure 3.3, the GIXD patterns of three different, commonly occurring crystalline structures of hydrocarbon chains at the air-water surface are shown. On the left side, the packing is shown, characterised by the lattice parameters of the unit cell (a , b and γ), the tilt angle, t , and the azimuthal angle, ψ . The middle column shows the corresponding Bragg peaks, $I(q_{xy})$, of the packing denoted by their Miller indices $\{hk\}$. In the right column, the Bragg rods, $I(q_z)$, of the structures are shown. Dashed lines represent the intensities from individual reflections as indicated by the Miller indices.

In the top row, showing a hexagonal packing of the chains, the $\{10\}$, $\{01\}$ and $\{1\bar{1}\}$ reflections are degenerated. The Bragg rod obtained from the single diffraction peak has its maximum at $q_z = 0 \text{ \AA}^{-1}$, due to the absence of a molecular tilt ($t = 0^\circ$). When the packing is distorted, e.g. by a tilt angle $t > 0^\circ$ or by packing constraints of the molecules, a centred rectangular or distorted hexagonal packing can be found. Now the peaks are no longer fully degenerated and two peaks can be observed. One comprises two degenerated reflections, $\{10\}$ and $\{01\}$ in case of the hexagonal notation (or $[11]$ and $[1\bar{1}]$ in the

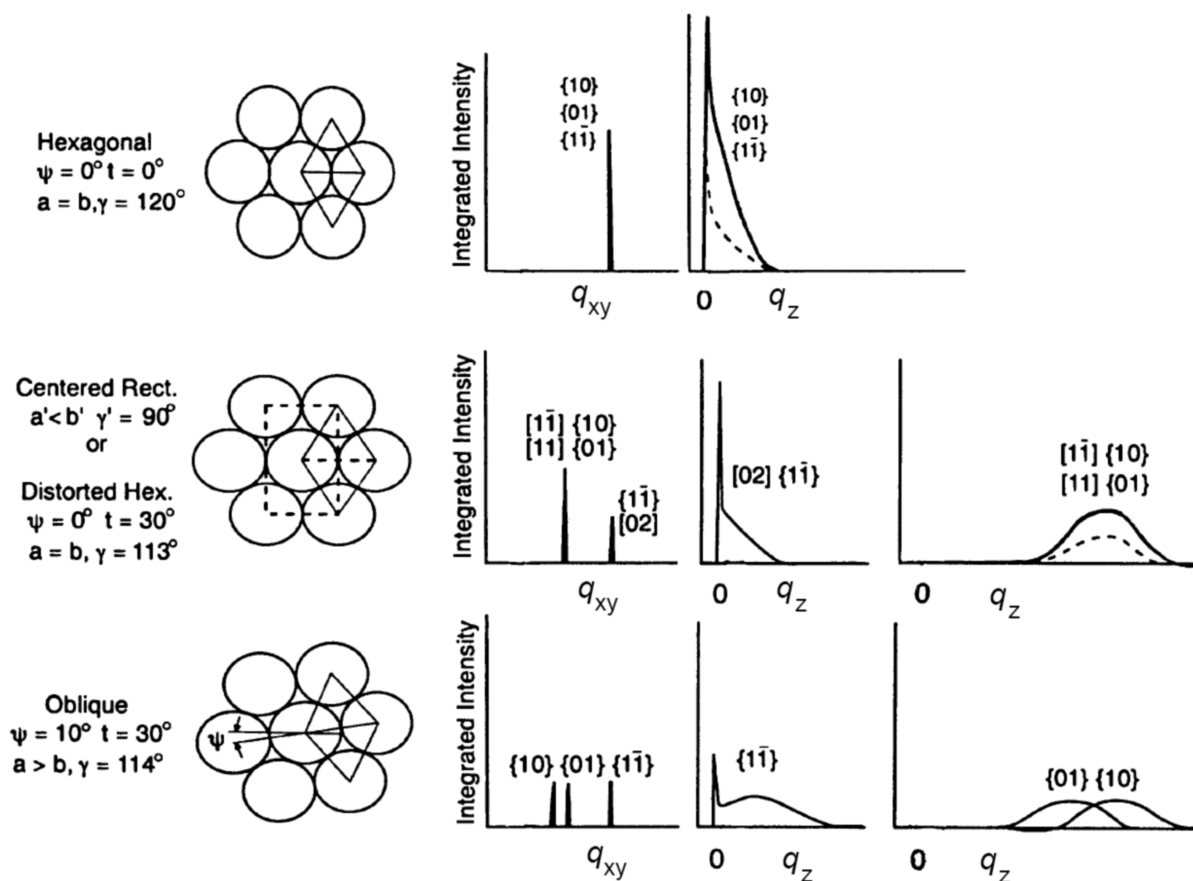


Figure 3.3: Three possible structures of crystalline packed hydrocarbon chains at the air-water interface are presented. In the middle, the obtained Bragg peaks and, on the right, the Bragg rods corresponding to the structures shown on the left are depicted.^[84]

rectangular notation), and the other one is a singlet $\{1\bar{1}\}$ (or correspondingly $[02]$). The Bragg rod of the two degenerated peaks is centred at $q_z > 0 \text{ \AA}^{-1}$, where the positions of the maxima depend on the extent of the molecular tilt. Finally, for an oblique packing, the degeneracy is completely lifted and three distinct Bragg peaks are observed. The position of the Bragg rod maxima are determined here by both the tilt angle and the azimuthal angle.^[84]

3.2.6 Grazing incidence X-ray diffraction data collection and treatment

The X-ray reflectometry as well as the grazing incidence X-ray diffraction experiments were conducted either at the liquid surface diffractometer of beamline BW1 at the synchrotron light source HASYLAB (Deutsches Elektronen-Synchrotron DESY, Hamburg, Germany)^[96] or at the beamline ID10B at the synchrotron light source ESRF (European Synchrotron Radiation Facility, Grenoble, France)^[97]. A monochromatic X-ray wavelength, λ , of $\approx 1.3 \text{ \AA}$ (corresponding to a photon energy, E , of 9.5 keV) was selected by a Be(002) crystal at HASYLAB or by an Si(111) crystal at the ESRF, respectively.

The scattered intensity was measured as a function of the angle between the incident and diffracted beam projected onto the horizontal plane using the Mythen detector, i.e. a noise-free, single-photon counting position sensitive detector consisting of an Si sensor with 1280 strips at HASYLAB or an 150 mm PSD detector (Gabriel) at the ESRF. The detectors have a vertical acceptance of $0 < q_z < 0.8 \text{ \AA}^{-1}$ and a horizontal resolution of $\Delta q_{xy} = 0.0031 \text{ \AA}^{-1}$ at HASYLAB and $\Delta q_{xy} = 0.0051 \text{ \AA}^{-1}$ at the ESRF. In a

typical GIXD scan, the detector is moved in 150 steps in an angular range of $16^\circ < 2\theta < 22^\circ$ counting 10 s per step.

In order to reduce the background scattering from the gas phase, and to avoid possible radiation damage, the air in the sample was replaced by helium during the experiment. To reduce the evaporation of the aqueous subphase, the helium was fully saturated by water vapour.

Reduction of the diffraction data comprises background correction, normalisation and scaling of the data. The basic calculations (q_{xy} , q_z and $I_{\text{corrected}}$) were performed for data measured at the ESRF using MATLAB based software available at the beamline ID10B and for data measured at HASYLAB beamline BW1 using a function written in MATLAB (see Appendix A.7, page a24). Further treatment of the data including normalisation, correction of the background, optionally smoothing, integration to reveal Bragg peaks and Bragg rods as well as plotting the data to maps was done by a MATLAB function as presented in Appendix A.8 (page a26).

CHAPTER 4

Biological macromolecules - proteins and lipids

In this chapter the biomolecules used in this thesis are presented. In the first section general properties of proteins and peptides are summarised and, in particular, Snase A, Gramicidin D, different fusion peptides (VSV, TBEV, HA2, VSV-TMD, L16), MsP1, IAPP, and A β are introduced.

In the second section information about lipids are given: the general phase behaviour, description of different phases like lamellar, inverse hexagonal and inverse bicontinuous cubic phase, calculation of crystallographic unit cell parameters of the different phases, bicellar lipid mixtures and the concept of lipid rafts. Afterwards, a number of lipid classes and substances, which were studied, are introduced: phospholipids, glycolipids, archaeal lipids, monoolein, and different sterols (cholesterol and ergosterol).

Finally, in the third section, a short description of the effect of high hydrostatic pressure on biomolecules is given. For a more detailed view the reader is referred to the literature, especially [14, 102, 103] for proteins and [14, 104–107] for lipids.

4.1 Proteins

4.1.1 General

One of the most important substance classes in biochemistry are the proteins, which are involved in nearly every biological process. Their manifold functions include specific catalysis, selective transport of substances, mechanic support of structures, control over functions like growth and immune defence, and many more.^[102]

Proteins are linear polymeres built by the twenty-two proteinogenic amino acids. Of these, 20 are encoded by the universal genetic code (DNA).^[103] The remaining two, selenocysteine and pyrrolysine, are incorporated into proteins by unique synthetic mechanisms.

All proteinogenic amino acids have the general form HOOC-CHR-NH₂. The amide group is attached to the carbon atom immediately adjacent to the carboxylate group (the α -carbon). The organic substituent, R, can vary widely from a single proton in case of glycine to a complex heterocycle as found in tryptophane. All amino acids found during the translation of proteins in the ribosome are L-amino acids. The other isomer, a D-amino acid, is only rarely found in some proteins, produced by enzymatic posttranslational modifications after translation and translocation to the endoplasmic reticulum. The amino acid sequence is the lowest structural element of proteins and is therefore referred to as primary structure.

After leaving the ribosome, the polypeptide chains fold spontaneously into their native three-dimensional structure. During this process the secondary and tertiary structure is adopted. The secondary structure describes local structural elements built by few amino acids and stabilised by hydrogen bonds. The most common secondary structure elements are α -helices, β -sheets and β -turns. Less ordered domains of the amino acid chain adopt the conformation of a random coil. The formation of secondary structure elements is controlled by the sequence of the amino acids. They are formed minimising the local conformational energy of the corresponding domains in the protein.

The tertiary structure describes the spatial relationship of the secondary structure elements relative to each other. It is stabilised mainly by hydrophobic interaction, i.e. the hydrophobic parts of the structure are oriented to the centre of the protein thus minimising the disfavoured interaction with the aqueous solution surrounding the proteins. Additionally, salt bridges, hydrogen bonds, and disulfide bonds maintain the folded structure of the protein.

Sometimes a protein consists of more than one amino acid chain. The spatial arrangement of more than one folded amino acid to a functional protein is described by the quaternary structure. Typically, these subunits are connected by disulfide bonds, hydrogen bonds as well as ionic, hydrophobic or Van-der-Waals interaction.

Only correctly folded proteins can accomplish their biological functions. Misfolding typically leads to the loss of the protein's activity. When proteins unfold, they usually do not adopt one specific unfolded state, but populate an ensemble of different (partially) disordered random coil structures. There is a third and stable state beside the native and the unfolded conformation: the amyloid fibre. Under certain conditions, proteins can aggregate to stable fibrils rich in β -sheets (q.v. section 4.1.6), which is of special interest due to their role in several severe diseases,^[108–111] including Alzheimer's disease caused by fibrils built by beta amyloid (A β),^[111, 112] diabetes melitus type 2 associated with IAPP (amylin), and Parkinson's disease caused by aggregate structures formed by α -synuclein.^[112]

The (partial) unfolding of proteins can be triggered by many stimuli: low or high temperature, change in pH, high pressure, chemical denaturants, which either are hydrophobic (trifluoroethanol) and interact with the hydrophobic parts of the protein, or are able to form hydrogen bonds (urea) and disturb the hydrogen bonds of the protein destabilising the structure. Hence, a deeper understanding of how proteins maintain their conformational stability and how that stability is affected by mutations and environmental factors such as temperature, pressure, and cosolvents is needed. Mutations that affect the hydrophobic core are particularly pernicious and can significantly change the stability and the conformation of the protein.^[113–117]

The use of pressure to unfold proteins is a unique approach because, in contrast to a temperature increase that simultaneously causes changes in both thermal energy and volume, unfolding induced by high pressure is determined solely by the volume change of the system and is driven predominantly by the disruption of voids and cavities inside the protein.^[118] For this reason, pressure is an excellent denaturant to investigate the effects of amino acid substitutions in the hydrophobic cores of proteins and to examine the compactness of protein structures. A further advantage is that the formation of protein aggregates, which often occurs in temperature-induced unfolding, is suppressed at high pressures.^[119, 120]

Not only the behaviour of proteins in solution is of high biological relevance, but the spontaneous adsorption of proteins at aqueous-solid interfaces also plays an important role in nature, medicine and biotechnology. Examples include the biofouling of material surfaces, the adhesion of mussels, the formation of biofilms on medical implants, the use of protein-biochips in bioanalytics, as well as the binding of antifreeze proteins on ice crystals. The intrinsic interfacial affinity of proteins is subject of intense

research.^[121, 122] So far, protein adsorption has been studied as a function of protein concentration, pH-value, surface chemistry, and temperature. However, very little is known about high pressure effects on protein adsorption and on protein adsorbates at aqueous-solid interfaces. By using pressure as an experimental variable, it is generally possible to gain information about volume and packing effects. In particular, pressure-dependent studies of protein adsorption may yield volume changes upon adsorption, thermodynamic stabilities of adsorbed proteins, and the contribution of hydrophobic interactions to the driving forces of protein adsorption.

4.1.2 SNase variants

Staphylococcal nuclease (SNase) is a rich model system for detailed examination of structural plasticity and structure-energy relations. The wild-type SNase is a small protein with a molecular weight of about 17.5 kDa, containing 149 amino acids and no disulfide bonds. In the crystalline state, 26.2% of the amino acids are located in helices, 24.8% in β -sheets (barrel), 7.4% in extended chains, 24.8% in turns and loops, and finally 8.7% in unordered chains. The residual of 8.1% is uncertain.^[3]

The thermodynamic stability of SNase can be modulated with mutagenesis and has been increased from 5.4 kcal mol⁻¹ for the wild-type protein^[123] to nearly 12 kcal mol⁻¹ for two highly stable variants known as NVIAGA^[124] and Δ +PHS.^[113] The Δ +PHS protein, engineered by a deletion (44 to 49) and five substitutions (V15N, G50F, P117G, H124L, and S128A), is of special interest because it has been shown to tolerate the presence and ionisation of groups buried in its hydrophobic core.^[113–116, 125–128] The majority of variants of Δ +PHS with internal ionisable groups retain a folded structure and cooperative unfolding profiles, even when the internal groups are charged.^[114, 125]

All SNase mutants studied in this thesis are based on the hyperstable Δ +PHS variant. This polypeptide is built by 143 amino acids and has a molecular mass of 16.59 kDa. 25% of the structure are helical and 30% can be found in β -sheets. The structure is identified by the PDB number 3BDC as depicted in Figure 7.7a (page 149).^[125]

Structural, thermodynamic, and kinetic aspects of the unfolding of SNase and many of its variants have been studied previously in great detail.^[113–117, 129–131]

Besides destabilising the native state of a protein, the presence and ionisation of a group buried in the hydrophobic core can trigger changes in conformation and dynamics, and could stabilise partially unfolded excited states in which the internal charged group can interact with water. This is precisely why internal ionisable groups can be useful for mapping the folding free energy landscape of proteins.^[126, 132]

The V66K variant of Δ +PHS was extensively studied. The Lys-66 titrates with a pK_a of 5.7, which is highly depressed relative to the normal pK_a of 10.4 for Lys in water.^[113, 127] This lower pK_a suggests that the interior of SNase is not as good a solvent as water – the charged form of the amino group is destabilised relative to its neutral form.^[127] The crystal structures of V66K variants of SNase are not particularly informative, as they are almost identical to those of the reference protein.^[113, 115, 123] In the structures obtained under conditions of pH where Lys-66 is neutral, the side chain of Lys-66 is buried deeply in the hydrophobic core of the protein, nearly 12 Å from the protein-water interface. In the structure obtained under conditions of pH where Lys-66 is charged, the backbone of the protein is unaffected, but the side chain is disordered.^[115]

The pH-sensitivity of this protein originates primarily from differences in hydration of the Lys residue when it is in water and when it is buried in a hydrophobic pocket, so high hydrostatic pressure can be used to perturb the native and unfolded state and to examine the effects of internal polar and ionisable

groups on conformational stability and dynamics due to changes in the water-inaccessible volume.^[118, 119] The utility of pressure as a thermodynamic variable to study processes affected by electrostatic hydration was already revealed by pressure-jump relaxation studies of variants of SNase with internal ionisable groups.^[131, 133] They showed that the hydration of the transition state ensemble can be affected dramatically by substitution with ionisable groups at positions that are normally part of the main hydrophobic core in the transition state ensemble of the wild-type protein. Although the effects of substitutions of hydrophobic positions with ionisable groups are subtle, the effects on the free-energy landscape can be very significant.^[131, 133]

4.1.3 Gramicidin D

Gramicidin D is a polypeptide consisting of only 15 amino acids, which have alternate L and D chirality. The natural mixture of gramicidin D, produced by *Bacillus brevis*, consists of approximately 80% gramicidin A, 5% gramicidin B and 15% gramicidin C, with tryptophan, phenylalanine, and tyrosine in position 11, respectively.^[134] The amino acid sequence of the peptide is formyl-L-Val¹-D-Gly²-L-Ala³-D-Leu⁴-L-Ala⁵-D-Val⁶-L-Val⁷-D-Val⁸-L-Trp⁹-D-Leu¹⁰-L-Xxx¹¹-D-Leu¹²-L-Trp¹³-D-Leu¹⁴-L-Trp¹⁵-ethanolamine.^[135] All side-chains of the peptide are non-polar. As a consequence, the peptide is able to adopt conformations of β -helices, which would be unacceptable for an all-L-amino acid peptide. The helices can be right- or left-handed, and they can differ in the number of amino acid residues per turn and therefore in the length and diameter.^[136, 137]

Individual molecules can fold into single-stranded helices, which are stabilised by six intramolecular hydrogen bonds, and can associate to helical N-terminus-to-N-terminus dimers – at least in phospholipid bilayers – in which two single-stranded helices are joint, such as the ss $\beta^{6.5}$ helical dimer with 6.5 residues per turn, which has an internal pore diameter of 3-4 Å and a total dimer length of 25 Å.^[134, 138] Also double-stranded helices can be formed in which two strands run either parallel or antiparallel, such as the ds $\beta^{5.6}$ double helix, which has a length of about 32 Å and a maximum diameter of 5 Å.^[139, 140]

All gramicidin forms have β -sheet-like hydrogen bonding patterns, differing in the number of intra- and intermolecular hydrogen bonds. The helical dimers are stabilised by intramolecular hydrogen bonds, whereas the double helical forms contain only intermolecular hydrogen bonds. This high conformational variability allows the gramicidin to adopt easily to changes in the membrane thickness.^[141, 142]

4.1.4 Fusion peptides

Membrane fusion and fission are two important processes in the replication cycle of viruses: access to the interior of host cells (entry) and dissemination of viral progeny after replication (budding).^[143] However, it does not occur spontaneously due to strong hydration, electrostatic and steric repulsive forces between the membranes of the cell and the virus, including a local rupture exposing the hydrophobic interior of the membranes and deformation of the (almost) curvature-free lipid bilayers. Instead, nature uses different highly specialised proteins to induce membrane fusion, such as viral fusion and cellular SNARE proteins. Viral fusion proteins can induce virus-cell fusion leading to infection as well as pathological cell-cell fusion.^[143, 144]

The fusion protein induces different stages during the fusion processes: establishing close contact between viral and cellular membrane, merger of the proximal monolayers via a highly curved stalk/hemi-fusion intermediate and finally formation of fusion pores by merging of the distal lipid monolayers,

Table 4.1: Properties of class I, class II, and class III fusion proteins (adapted from [144]).

	class I	class II	class III
Protein	HA	TBEV	VSV
Orientation with respect to viral membrane	perpendicular	parallel	perpendicular
Major secondary structure	α -helix	β -sheet	α -helix and β -sheet
Oligomeric structure of native fusion protein	trimer	dimer	trimer
Location of fusion peptide in native fusion protein	buried in subunit interface	masked in trimer interface, at tip of extended β -strands	exposed, at tip of extended β -strands
Location of fusion peptide in primary sequence	at or close to the N-terminus	internal	internal
Activated to fusogenic form by	low pH	low pH	low pH

terminating the fusion process.^[144, 145] Viral fusion proteins contain specific segments that are involved in viral membrane fusion: the fusion peptide (FP) and trans-membrane domain (TMD).

During the membrane fusion process each of the two segments fulfils different tasks: first, the fusion peptides insert into the target membrane, leading to a destabilisation of the membrane. This reduces the activation energy needed for the fusion of two membranes – acting as a catalyst in the early stages of membrane fusion.^[146–148] The TMD, attached to the viral membrane, brings both membranes into close proximity, destabilises the lipid bilayer structure in the hemifusion zone and supports the formation of the fusion pore in later stages of the membrane fusion process. This requires the TMD to span both membrane leaflets.^[144, 145, 149]

Based on structural criteria, three different classes of viral membrane fusion proteins could be identified as juxtaposed in Table 4.1, and there are at least four distinct mechanisms to trigger fusion-inducing conformational changes in fusion proteins.^[144] For example, several fusion proteins are activated by low pH, which results in the structural rearrangements necessary for the repositioning of the fusion peptide allowing it to be buried into the target membrane.^[144]

Synthetic fusion peptides are good and fully functional models to study membrane-associated structures and processes in viral fusion.^[146, 150, 151] The general ability of viral fusion peptides to induce membrane fusion suggests that they are actively involved in the fusion process, rather than just acting as an anchoring device for the fusion protein.^[145] But also TMD peptides alone are sufficient to drive fusion of liposomes.

Three different fusion peptides, one trans-membrane domain as well as one control peptide have been studied in this thesis, all of which respond to a low pH as the trigger of the fusion event: an incorporated class I viral FP (HA2, influenza), one viral FP of class II (TBEV, tick-borne encephalitis virus), and finally one FP of class III (VSV, vesicular stomatitis virus). Additionally, the viral TMD (VSV) as well as an artificial peptide with no fusogenic activity (L16) as a control were studied.^[152, 153]

Further details about fusion proteins and membrane fusion can be found in [143, 144, 146–148, 154–157].

4.1.5 MsP1

Growing on lignocellulosic biomasses, the basidiomycetous fungus *Marasmius scorodoni* (“garlic mushroom”) secretes the uncommon peroxidase MsP1 (accession number B0BK71). *M. scorodoni* (strain No.: CBS 137.83) is a small edible fungus, which typically forms fruiting bodies on grass, bark, twigs, and needle duff. Due to its intense garlic-like flavour, it is appreciated as a spice in human nutrition.

MsP1 is built by 513 amino acids and has a molecular weight of about 150 kDa. The function of this extracellular enzyme is the degradation of β -carotenes. It has an isoelectric point of 3.7.

In a previous study, MsP1 has been purified from culture supernatants and cloned from a cDNA library. Size exclusion chromatography and SDS-PAGE analyses suggested a dimeric structure of native MsP1.^[158] Based on the observed amino acid sequence homology of about 48% to the enzymes DyP (Q8WZK8) and TAP (Q8NKF3) from *Thanatephorus cucumeris* and *Termitomyces albuminosus*, respectively, MsP1 was assigned to the group of so-called DyP-type peroxidases.^[159] When cultured submerged in standard nutrition solution, the expression of MsP1 was significantly induced by the addition of lignin.^[160] Representing an essential part of the fungus’ secretome, it may contribute to the modification of lignified biopolymers.^[161] It thus could become an interesting tool for the production of second generation bio-fuels or lignin based polymers in biorefinery approaches. Based on the enzyme’s capability to degrade carotenes and xanthophylls,^[158] further potential industrial applications comprise the bleaching of food products, as well as the formation of norisoprenoid flavor compounds.^[162] A high process stability of the biocatalyst is an essential prerequisite for the implementation of new biotechnological processes.

4.1.6 IAPP, A β , and the small-molecule inhibitor resveratrol

In a biological cell, proteins adopt a functional folded state, which results from highly regulated processes. Upon failure of the quality control of the cell, proteins may suffer from degradation and can form assemblies of unfolded or partially folded monomers or protein fragments, such as ordered cross- β -sheet rich structures, called amyloid fibrils.^[163, 164] Misfolding, aggregation, and fibril formation of proteins such as A β , α -synuclein or islet amyloid polypeptide (IAPP), have severe implications in neurodegenerative diseases like Alzheimer’s and Parkinson’s disease or in affecting peripheral tissues as in the case of type 2 diabetes mellitus (T2DM).^[163–169]

Several studies have shown that lipid-peptide interactions can play a crucial role in amyloid formation of IAPP and A β .^[170–177] For example, the interaction of IAPP with anionic (DOPC/DOPG, molar ratio 7:3)^[173, 174] or model raft membranes (DOPC/DPPC/cholesterol, molar ratio 1:2:1)^[173] and the interaction of A β with negatively charged and neuronal lipid membranes, foster fibrillation.^[175–177]

Islet amyloid polypeptide (IAPP)

In type 2 diabetes mellitus (T2DM) patients, extracellular amyloid plaques are deposited near pancreatic β -cells. Biochemical analysis has shown that these plaques consist mainly of the 37 residue IAPP [KCNTATCATQRLANFLVHSSNFGAILSSTNVGSNTY], which is produced, stored and secreted together with insulin (roughly in a ratio of 1:100 amylin:insulin) by the β -cells in the pancreatic islets of Langerhans. The monomeric form of IAPP is thought to be acting as a regulator of glucose homeostasis.^[170, 178, 179] In its native state, several functions have been associated with IAPP, in particular controlling hyperglycemia by regulating the blood glucose level.^[180]

The mechanism of the fibrillation of IAPP that triggers its conversion from a functional soluble monomer into insoluble amyloid fibrils is still under debate. Several studies have shown that the interaction of IAPP with lipid membranes may induce fibril formation.^[168, 169, 172, 181] It has also been shown that human IAPP (hIAPP) aggregation and fibrillation in the presence of anionic lipid membranes is drastically fostered and occurs via insertion of the N-terminal region of hIAPP, where several cationic residues are located.^[172, 181, 182] In the absence of an anionic lipid membrane, fibrils start to form in solution only if the IAPP concentration is high enough ($> 5 \mu\text{M}$).^[181, 183] Despite recent efforts towards a biophysical characterisation of the different states of aggregation,^[168, 169, 172, 178, 180–182, 184] the lack of structural information still hampers the understanding of its fibrillogenesis.

Amyloid beta ($\text{A}\beta$)

The major component of aggregates in brains of Alzheimer's disease (AD) patients is $\text{A}\beta$, a 40- to 42-residue fragment, containing extracellular (28 residues) and transmembrane parts (12-14 residues) of the 695-residue membrane associated amyloid precursor protein (APP), whose native function is still debated.^[185–188]

Recent clinical studies have pointed to a correlation between T2DM and AD, i.e. patients with T2DM have a higher risk to suffer from AD and vice versa.^[189] Remarkably, both diseases are triggered by amyloidogenic peptides on the molecular level, and the causing peptides IAPP and $\text{A}\beta$ have high similarities with 25 % identical and 50 % similar amino acids.

The $\text{A}\beta$ peptide (Amyloid beta 1-40, [DAEFRHDSGYEVHHQKLVFFAEDVGSNKGAIIGLMVGGVV]) contains six negatively charged residues and three positively charged ones, explaining the preferential interaction of this peptide with charged lipid membranes. It is amphiphilic with a hydrophilic N-terminal region and a hydrophobic C-terminus.

For the formation of $\text{A}\beta$ fibrils, a nucleation-dependent polymerisation mechanism characterised by an initial lag phase has been found *in vitro*.^[190, 191] Fibril formation occurs readily in micelles at concentrations above a critical micelle concentration (cmc), which was determined in the range of 17.5 to 100 μM .^[191–193] Admittedly, the concentrations of free $\text{A}\beta$ found in the cerebral spinal fluid *in vivo* are exceedingly lower (in the subnanomolar range), indicating an alternative fibrillation mechanism.^[194]

Resveratrol

Inhibiting amyloid fibril formation is regarded as a potentially key therapeutic approach towards amyloid-related diseases.^[163, 164] Although the process of inhibition is not fully understood yet, screening of inhibitors turned out to be beneficial.^[183, 195] Polyphenols are a group of compounds, which have been found to act as inhibitors of $\text{A}\beta$, α -synuclein, and prion amyloid formation.^[196] The phenolic compound resveratrol (trans-3,5,4'-trihydroxystilben; chemical structure shown in Figure 8.17c, page 183), which is found to a significant amount in red wine (130-220 μM), effectively inhibits $\text{A}\beta$ (25-35) fibril formation and reduces the secreted and intracellular $\text{A}\beta$ level.^[197] Since IAPP and $\text{A}\beta$ have similar amino acid sequences in the presumable ordered region and exhibit similar secondary structures in the fibrillar state,^[171] it is not surprising that a similar inhibitory effect of resveratrol on IAPP fibril formation has been found recently.^[174]

4.2 Lipids

4.2.1 General

One of the main functions of lipid biomembranes is the separation of the cell's interior from the extracellular space. Important lipid components of eukaryotic membranes are, for example, the zwitterionic phospholipids phosphatidylcholine (PC) and sphingomyelin (SM), and the anionic phospholipids phosphatidylserine (PS) and cardiolipin (CL), and phosphatidic acid (PA). All of these substances have similar cross section areas of the head groups and the hydrocarbon chain regions, leading to the formation of stable lamellar bilayer structures.^[145] In contrast to most other types of cells, Gram-negative bacteria are surrounded by two membranes. In the outer membrane, separating the cell from the periplasm and the intracellular space, lipids are asymmetrically distributed. The inner monolayer of the outer membrane is mainly composed of glycerophospholipids, while the outmost monolayer is largely built up by lipopolysaccharides (LPS).^[198]

Due to the high fluidity of natural membranes they are often described as a two-dimensional fluid. In 1972 S.J. Singer and G. Nicolson developed a first model of such a fluid membrane, called the fluid-mosaic-model. Besides the lipids, it also considers the presence of membrane proteins and further molecules in the lipid bilayer. The degrees of diffusional freedom in a biomembrane are highly anisotropic: all molecules have a high lateral, but nearly no transversal mobility. The lateral diffusion coefficients of lipids are typically in the range of $10^{-12} \text{ m}^2 \text{ s}^{-1}$. In contrast, transverse diffusion from one lipid layer to the opposing one, called "flip-flop", is by a factor of 10^9 less likely to occur compared to lateral diffusion.^[3, 102, 199]

The distribution of lipids in the two monolayers of a cell membrane is asymmetric. This asymmetry persists, because of the low number of naturally occurring flip-flops and the fact that new lipids are only synthesised in the cytosolic side of the endoplasmic reticulum. To ensure a reasonably high number of flip-flops for the regeneration and growth of the other half of the lipid bilayer, special membrane proteins are able to induce flip-flops with a high selectivity, maintaining the asymmetric lipid distribution of the lipid bilayer.

Due to the complexity of natural membranes, often simplified model systems are used to study the behaviour of lipid structures. The basic structural element of biological membranes is a lamellar phospholipid matrix. This lyotropic lipid phase is an organised soft matter system formed by amphiphilic molecules in the presence of water. The reason for the formation of all lipid phases is mainly the hydrophobic effect: the interaction of water with hydrophobic regions of the lipids is entropically disfavoured. Water surrounding hydrophobic molecules is arranged in an ordered clathrate-like structure, where the degrees of freedom of the water molecules are reduced. By forming compact aggregates, the interaction area between water and hydrocarbon chains is minimised and the corresponding entropy loss due to the sorting of the lipid molecules is overcompensated by the release of highly ordered surface water by far.

Lipids dissolved in water exhibit a rich structural polymorphism, depending on the lipid molecular structure and the environmental conditions, such as the water content, ionic strength, temperature and pressure.^[3, 104, 105, 200–203] One of those possible morphologies is the lamellar phospholipid structure, which provides the basic structural element of biological membranes.

Simple, one-component saturated phospholipids bilayers often exhibit two thermotropic lamellar phase transitions, a gel to gel pretransition and a gel to liquid-crystalline main transition at a higher chain-melting temperature, T_m . In the fluid-like L_α -phase (or l_d), the acyl-chains of the lipid molecules are

conformationally disordered containing a certain number of *gauche* conformations, whereas in the gel phase (e.g. $P_{\beta'}$, $L_{\beta'}$ or L_{β} phase), the chains are extended and conformationally ordered.^[200–202] As the average end-to-end distance of disordered hydrocarbon chains in the L_{α} -phase is smaller than the one of ordered (all-trans) chains, the bilayer becomes thinner during the “melting” transition, even though the lipid volume increases. In addition to these thermotropic phase transitions, different pressure-induced phase transformations can also be observed. Upon compression, the lipids adapt to the volume restriction by changing their conformation and packing.^[3, 104, 105]

It is also well known that many biological lipid molecules also form non-lamellar liquid-crystalline phases, such as inverse hexagonal or bicontinuous cubic phases.^[104, 105] Lipids that can adopt non-lamellar phase are present at substantial levels in biological membranes, usually at least 30 %_{mol} of the total lipid contents. It is generally assumed that the non-lamellar lipid structures are also of significant biological relevance, such as for endo- and exocytosis and fat digestion.

The morphology of phases built by a specific lipid depends on the shape of the molecule. This can be expressed by the so-called shape factor or critical packing parameter (CPP) of the lipid,^[204]

$$\gamma = \frac{v_l}{a_0 l}, \quad (4.1)$$

where v_l is the volume of the lipid, l the length of a lipid or the monolayer thickness, and a_0 is the area per lipid at cross section. In case of a shape factor near unity, the formation of non-curved bilayers is most likely. If the shape factor is smaller, type I micelles are formed, where the curvature towards the water is positive and the hydrophobic hydrocarbon chains are inside the aggregates. In cases where the shape factor is significantly larger than one, type II systems, often referred to as inverse structures, form with a negative curvature towards the head groups and water.

The shape factor can be influenced by changing the length or cross sectional area of the corresponding parts of the lipid molecule. The size of the head group depends amongst others on the pH-value, ionic strength of the solution, electronic charge of the head group, temperature and other molecules incorporated into this region of a lipid system. The hydrocarbon chain region can vary with respect to the chain saturation, ratio of *trans* / *gauche* conformers, length of the chain, as well as further hydrophobic molecules integrated into the hydrophobic region of the lipid phase. Additionally, the fluidity of the lipid systems is regulated largely by variations in parameters of the hydrocarbon chain.

It is important to understand not only the physical behaviour of simple one-component systems forming lipid bilayers, but also the behaviour of heterogeneous membranes. This is because it is vital to understand many aspects of the cellular membranes, such as membrane mechanical properties, lateral diffusion of membrane components, and the reaction dynamics of membrane-bound proteins.^[205–207]

In recent years, studies carried out on ternary lipid mixtures combining cholesterol with different saturated and unsaturated phospholipids showed the coexistence of a cholesterol-enriched liquid-ordered (l_o) phase with a cholesterol-depleted liquid-disordered l_d -phase.^[205–207] Compared to the solid-ordered (s_o) gel phases of one-component lipid bilayers, the lipid molecules in the l_o -phase display higher rotational and lateral diffusivities, however the lipid order parameters are relatively large. Additionally, the l_o -phase is nearly as thick as the solid crystalline (s_o) phase, i.e. it contributes to membrane stability and permeability^[208, 209]. Such lipid systems are supposed to mimic distinct liquid-ordered lipid regions, called “rafts”, which seem to be also present in biological cell membranes.

Lipid rafts are small (< 200 nm in natural environments), heterogeneous, sterol- and sphingolipid rich liquid-ordered (l_o) domains, which are floating inside a disordered, liquid (l_d) lipid matrix.^[205, 207, 210, 211]

Increasing evidence suggests that these domains are involved in a number of cellular processes, such as lateral protein organisation and signal transduction, as well as the sorting and transport of lipids and proteins.^[205–207, 212–214] Moreover, lipid raft domains might play an important role in the fibril formation of amyloidogenic peptides.^[215–217] Recently, isolated plasma membranes have been shown to be capable of forming such ordered domains as well, although it has to be considered that raft formation in real cell membranes may not resemble macroscopic phase separation.^[218–220]

Although the static structure and phase behaviour of many lipid systems are now rather well established, a considerable lack of knowledge exists regarding the understanding of the kinetics and mechanisms of lipid phase transformations. Transitions between different lipid phases can be easily induced by changing an external parameter such as temperature or pressure.

4.2.2 Lamellar lipid phases

One-dimensionally periodic (smectic) phases consisting of locally planar, parallel lipid membranes separated by water layers of uniform thickness can be found in multilamellar vesicles (MLVs),^[199] which form spontaneously after dispersing lipids with a cylindrical shape in solution.

Besides MLVs, a number of different vesicles can be formed. A unilamellar vesicle (ULV) is a single, spherical lipid bilayer structure with a typical diameter of about 20 nm up to a few hundred nanometres containing solution in its centre. In a giant unilamellar vesicle (GUV), the topology is unchanged, but the diameter is significantly larger (typically 30 μm).

A number of parameters of a single multilamellar lipid phases in a simple two-component system (lipid+water) can be calculated if the d -spacing is known, which is directly obtainable from the maximum positions of the Bragg reflections according to equation 2.38 (page 18).

The monolayer thickness of the lipid layer, d_1 , can be calculated by:^[204, 221]

$$d_1 = 0.5(d - d_w), \quad (4.2)$$

where d is the lamellar lattice constant and $d_w = \phi_w d$ is the thickness of the water layer between two lamellar bilayers calculated from the water volume fraction ϕ_w .

All lamellar phases are built by lipids with a cylindrical molecular shape (corresponding to a shape factor, γ , of 1). Therefore, the area per lipid at cross section, a_0 , is simply given by the quotient of the lipid molecular volume, v_1 , and the monolayer thickness, d_1 :^[204]

$$a_0 = \frac{v_1}{d_1}. \quad (4.3)$$

The lipid molecular volume, v_1 , can be obtained from its molar mass, M , Avogadro's number, N_A , and its mass density, ρ_1 :

$$v_1 = \frac{M}{N_A \rho_1}. \quad (4.4)$$

From the position $q_{\text{max}1}$ and the full width at half maximum ($FWHM_{\text{max}1}$) of the first Bragg peak, the average number of stacked layers, N_{av} , can roughly be estimated by^[12, 60]

$$N_{\text{av}} \geq q_{\text{max}1} / FWHM_{\text{max}1}. \quad (4.5)$$

4.2.3 Inverse hexagonal lipid phases

Hexagonal phases are built by thin lipid cylinders with a radius of a few nanometres, which are arranged on a two-dimensional hexagonal lattice. When the curvature is negative, i.e. the polar head groups are oriented towards the water filled internal spaces of the cylinders, the structure is called inverse hexagonal phase (H_{\parallel}).^[222, 223]

During the formation of the inverse hexagonal phase some of the lipid chains have to stretch to fill the hydrophobic volume. This stretching has been suspected to cause a free energy barrier for the formation of the H_{\parallel} phase.^[200] The transition from a lamellar phase into an inverse hexagonal phase is fostered by a decreasing in head group ionisation, water content of the system, head group size, hydrocarbon saturation, as well as by an increase in temperature and lipid layer curvature.^[199] In contrast to hexagonal phases where the lipids bend towards the hydrocarbon chains, in inverse hexagonal phases (in a polar solvent) swelling of the lattice causes an increase of the interfacial area per molecule.^[200]

For a single component lipid system several parameters can be directly obtained from the crystallographic lattice constant, a (q.v. equation 2.40, page 19).

The radius of a water channel, r_w , can be calculated from the water volume fraction, ϕ_w :^[204]

$$r_w = a \sqrt{\frac{\sqrt{3}}{2\pi} \phi_w} = \frac{1}{2} d_w. \quad (4.6)$$

The lipid layer thickness, d_l , orthogonal to the cylinder axes, is simply given by^[204]

$$d_l = a - 2 r_w. \quad (4.7)$$

The minimum and maximum lipid lengths can be calculated by^[204]

$$l_{\min} = \frac{1}{2} d_l, \quad (4.8)$$

$$l_{\max} = \frac{a}{\sqrt{3}} - r_w. \quad (4.9)$$

The area per lipid at the lipid water interface is given by^[204]

$$a_0 = \frac{4\pi v_l r_w}{\sqrt{3} a^2 \phi_l}, \quad (4.10)$$

where $\phi_l = 1 - \phi_w$ is the volume fraction of the lipid.

Finally, the shape factor, γ , can be calculated from equation 4.1.

4.2.4 Inverse bicontinuous cubic lipid phases

Inverse bicontinuous cubic lipid phases are three-dimensional networks consisting of a single, continuous lipid bilayer. This bilayer subdivides space into two interpenetrating, but disconnected, water networks with equivalent sub-volumes. Their phase behaviour can be related to the competition between uniform mean interfacial curvature and hydrocarbon chain packing constraints.^[200, 224, 225]

There are three different types of inverse bicontinuous cubic lipid phases. The bilayer midplane, which has a constant zero mean curvature, can be described by a triply periodic minimal surface

Table 4.2: Triply periodic minimal surface (TPMS), corresponding label of cubic phase, and short Hermann-Mauguin symbol for all three basic types of inverse bicontinuous cubic lipid phases.^[64, 224, 225, 228]

periodic minimal surface	cubic phase label	Hermann-Mauguin symbol	equation approximating membrane midplane
Schwarz primitive (P)	Q_{\parallel}^P	$Im3m$	$\cos x \cos y \cos z = 0$
Schoen gyroid (G)	Q_{\parallel}^G	$Ia3d$	$\sin x \cos y + \sin y \cos z + \sin z \cos x = 0$
Schwarz diamond (D)	Q_{\parallel}^D	$Pn3m$	$\sin x \sin y \sin z + \sin x \cos y \cos z + \cos x \sin y \cos z + \cos x \cos y \sin z = 0$

(TPMS).^[225, 226] In Table 4.2 the three different periodic minimal surfaces are assigned to the corresponding crystallographic space groups denoted by their (short) Hermann-Mauguin symbol.^[225, 227]

All three TPMS, Schwarz diamond, Schwarz primitive, and Schoen gyroid, are interrelated by Bonnet transformations, which means, the mean Gaussian curvature at all points on the surface remains unchanged. It has been proposed to describe the dynamic structure of cubic lipid phases by nodal surfaces, which might represent thermal oscillations forming standing waves better.^[227] With increasing temperature the transition from the $Im3m$ to the $Pn3m$ phase can be observed. With increasing water content at constant temperature the phases occur in the sequence $Ia3d \rightarrow Pn3m \rightarrow Im3m$, which is due to the different packing in space, where $Ia3d$ is the most compact and $Im3m$ has the loosest packing. With increasing water content the size of the aqueous channels increases. The free energy minimum decreases in the order $Ia3d \rightarrow Pn3m \rightarrow Im3m$. The enthalpy change during transitions between cubic phases is very small.^[224, 229]

The triply periodic minimal surfaces can be visualised by different methods. The simplest way is using implicit equations as given in Table 4.2. The primitive as well as the gyroid unit cells are described by these equations in the limits ($-\pi \leq x, y, z \leq \pi$) and the limits of the double diamond unit cell are ($-\pi/2 \leq x, y, z \leq \pi/2$). These implicit equations are only approximations of the minimal surfaces. Corrected equations have been calculated with up to 213 trigonometric terms, describing the minimal surface more precisely.^[230]

A much more elegant way to construct these surfaces is by Weierstraß parametrisation.^[231] The parametrisations represent a patch of the surface as the inverse of composite Gauss and stereographic projection mappings on a complex plane. The parametrisations create the structure represented as the inverse of composite Gauss and stereographic projection mappings from a patch of the surface on a complex plane. Using a Gauss map, all points on the surface of the unit cell with parallel normal vectors map to the same point in the complex plane. Therefore only a small patch of the surface can be calculated and not the entire unit cell. A highly precise representation of the overall unit cell can be constructed following the symmetry operations given by the corresponding crystallographic space groups.^[230, 232] These calculations were performed for all three basic unit cells using MATLAB. The results of the parametrisation are stored as Delaunay triangulations, therefore each unit cell is represented by a large number of triangles (> 4000) with high resolution. The results for the Schwarz diamond (space group $Pn3m$) can be found in Figure 4.1. The corresponding graphic for the Schoen gyroid (space group $Ia3d$) is shown

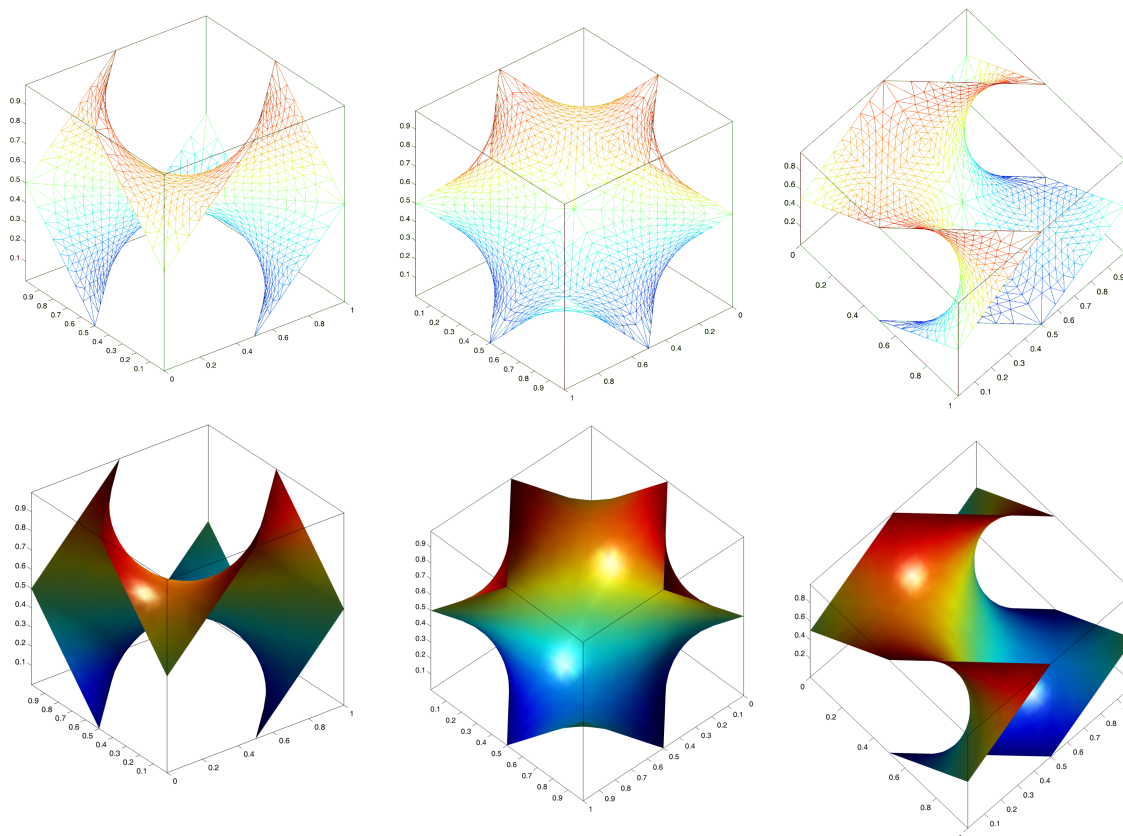


Figure 4.1: The Schwarz diamond (D) triply periodic minimal surface corresponding to the space group $Pn3m$ in different orientations calculated from exact Weierstraß parametrisation using MATLAB. Top row: representation by triangles from a Delaunay triangulation; bottom row: surface representation with interpolated surface shading.

in Figure 6.31 (chapter 6.5, page 113) and the unit cell of a Schwarz primitive (space group $Im3m$) is depicted in Figure 8.7 (chapter 8.2, page 167).

In every unit cell of the $Ia3d$ phase three water channels are coplanarily connected. The $P4_332$ phase has a nearly identical unit cell, only that one water network is replaced by micelles. The unit cell of the $Pn3m$ phase is built by four tetraedrally connected water tubes and the $Fd3m$ phase is the corresponding phase, where again one water network is replaced by micelles. Finally, in the $Im3m$ phase there are six octraedrical arranged water tubes in one unit cell and the $Pm3n$ phase has an identical unit cell except for micelles, which replace a part of the water tubes.^[204]

In Table 4.3 a detailed description of the crystallographic unit cell of all seven experimentally observed cubic phases is given. First the label of the cubic space group is shown, where the superscripted number denotes the number of the corresponding space group. The short as well as the complete Hermann-Mauguin symbols are presented, describing the symmetry space group of the phases. The first letter of these symbols describes the Bravais lattice type. The following letters and numbers describe screw axes and glide planes. Finally, the point symmetry group of each cubic phase is shown.^[56, 64]

A number of parameters can be calculated from the crystallographic lattice constant, a (q.v. equation 2.41, page 19), for a two-component system in a single-phase region.

Table 4.3: Crystallographic space groups, short and complete Hermann-Mauguin symbols of symmetry operations, and point symmetry groups of the seven bicontinuous cubic lipid phases.^[64]

cubic space group	short Hermann-Mauguin symbol	complete Hermann-Mauguin symbol	point symmetry group
Q^{212}	$P4_332$	$P4_332$	43
Q^{223}	$Pm3n$	$P 4_2/m \bar{3} 2/n$	4/m3
Q^{224}	$Pn3m$	$P 4_2/n \bar{3} 2/m$	4/m3
Q^{225}	$Fm3m$	$F 4/m \bar{3} 2/m$	4/m3
Q^{227}	$Fd3m$	$F 4_1/d \bar{3} 2/m$	4/m3
Q^{229}	$Im3m$	$F 4/m \bar{3} 2/m$	4/m3
Q^{230}	$Ia3d$	$I 4_1/a \bar{3} 2/d$	4/m3

Table 4.4: Euler-Poincaré characteristic, χ , and the scaled surface area, A_{S0} , of the different triply periodic minimal surfaces (TPMS).^[68]

cubic phase	TPMS	Euler-Poincaré characteristic χ	scaled surface area A_{S0}
$Pn3m$	D	-2	1.919
$Im3m$	P	-4	2.345
$Ia3d$	G	-8	3.091

The monolayer thickness or lipid chain length, l , can be obtained by solving¹ the equation:^[68, 233]

$$\phi_1 = 2A_{S0} \left(\frac{l}{a} \right) + \frac{4}{3}\pi\chi \left(\frac{l}{a} \right)^3, \quad (4.11)$$

where ϕ_1 is the lipid volume fraction. The Euler-Poincaré characteristic, χ , and the scaled surface area, A_{S0} , of the different triply periodic minimal surfaces are presented in Table 4.4.

The interfacial area integrated over a single monolayer, A_1 , is given by^[204]

$$A_1 = A_{S0}a^2 + 2\pi\chi l^2. \quad (4.12)$$

The number of lipid molecules per unit cell, n_1 , can be calculated from^[204]

$$n_1 = \frac{\phi_1 a^3}{v_1}. \quad (4.13)$$

The area per lipid molecule at the interface, a_0 , can now easily be calculated from the interfacial area of both monolayers, $2A_1$, and the number of lipids in the unit cell, n_1 :^[204]

$$a_0 = \frac{2A_1}{n_1} = 2v_1 \frac{A_{S0}a^2 + 2\pi\chi l^2}{\phi_1 a^3}. \quad (4.14)$$

¹This equation cannot be solved analytically. However a numerical solution is easily obtainable using the MATLAB-functions “fzero” or “fminbnd”.

The radius of a water channel, r_w , based on the minimal surface model is given by^[204]

$$r_w = \sqrt{-\frac{A_{S0}}{2\pi\chi} a - l}. \quad (4.15)$$

Finally, the shape factor, γ , can be calculated:^[204]

$$\gamma = \frac{\phi_1 a^3}{2l(A_{S0} a^2 + 2\pi\chi l^2)}. \quad (4.16)$$

The surface averaged values of mean curvature, $\langle H \rangle$, and Gaussian curvature, $\langle K \rangle$, are given by:^[204]

$$\langle H \rangle = \frac{2\pi\chi l}{a_0} \quad \text{and} \quad \langle K \rangle = \frac{2\pi\chi}{A_{S0} a^2}. \quad (4.17)$$

4.2.5 Bicellar lipid mixtures

Depending on the mixing ratio of its components, the total lipid concentration and the temperature, binary phospholipid mixtures of long-chain lipids, such as DMPC (14:0 PC; 1,2-dimyristoyl-*sn*-glycero-3-phosphocholine) or DPPC (16:0 PC; 1,2-dipalmitoyl-*sn*-glycero-3-phosphocholine), and short-chain lipids, e.g. DHPC (6:0 PC; 1,2-dihexanoyl-*sn*-glycero-3-phosphocholine), show a variety of different morphologies. At low temperatures, a system built by DMPC/DHPC, as studied in this thesis, forms disk-like micelles with the long-chain DMPC preferably residing in the planar bilayer regions and the short-chain DHPC in the highly curved regions at the rim of the aggregates,^[234] hence these mixtures are often referred to as ‘‘bicellar mixtures’’. The lipid composition of these mixtures is typically characterised by the molar ratio of long-to-short-chain lipids, $Q = [\text{DMPC}]/[\text{DHPC}]$, and the total weight percentage of lipid in solution.^[234]

The bicelles in solution at low concentrations have a mostly monodisperse size distribution^[235] with a typical thickness of approximately 5 nm and a radius between 8 and 30 nm, depending on the lipid ratio and the concentration in solution.^[234, 236, 237]

Above temperatures in the range of the main gel-to-fluid transition temperature of pure DMPC, i.e. at around 24 °C, the system transforms into a chiral nematic phase, also referred to as cholesteric phase, formed by flexible worm-like, quasi-cylindrical, elongated micelles with long-range orientational order, but only short-range positional order, which is typical for a nematic phase.^[234, 235, 238] These elongated aggregates have also been described as ribbon-like structures of several hundred nanometres length with high concentrations of DHPC occupying the edges of these structures.^[236, 239] At sufficiently high temperatures, a transition to a lamellar phase is observed, which consists of multilamellar vesicles with pore-like defects in the lamellar sheets. The edges of these defects are lined with DHPC.^[236]

Bicellar mixtures are of particular interest, because the nematic phase at intermediate temperatures can be aligned by a magnetic field, either spontaneously or by doping with lanthanoide ions. Due to this property, such systems have been shown to be ideal to align both hydrophobic as well as hydrophilic macromolecules, like membrane-associated proteins and peptides, in high resolution NMR studies.^[234, 240–243] Proteins embedded in bicelles, which provide a curvature-free membrane-mimicking platform, retain their enzymatic activity in contrast to the loss of activity in most micellar environments.^[244] In general, bicelles present a better alternative to globular micelles as membrane mimetics for investigation of biologically relevant membrane-associated protein structures by NMR.^[240–242] The importance of these systems be-

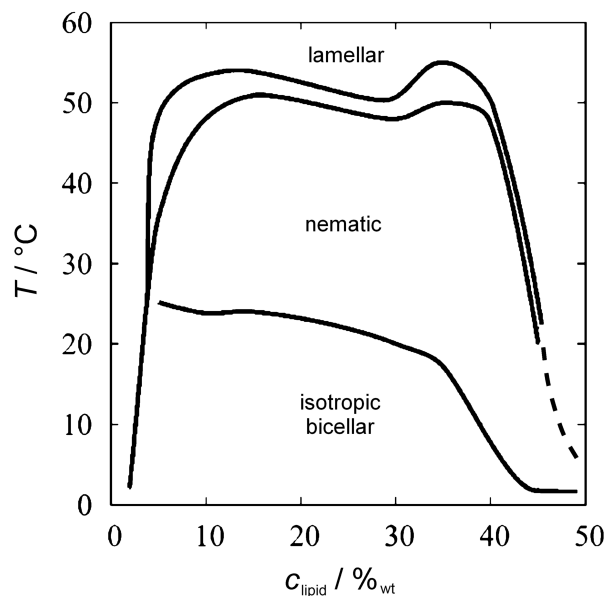


Figure 4.2: Phase diagram of the bicellar mixture DMPC/DHPC (3.2:1 molar ratio) adapted from Harroun et al.^[234] The morphologies were determined by polarised optical microscopy and small-angle neutron scattering measurements. Between the nematic and lamellar phase, a region of phase coexistence has been found.

comes evident taking into account that approximately one third of all known proteins are membrane associated proteins.^[245] The best alignable samples consisting of DMPC / DHPC in the presence of an applied magnetic field were reported in the literature for a molar ratio, Q , of 3.2.^[246]

Figure 4.2 presents the phase diagram of the bicellar mixture DMPC/DHPC (3.2:1 molar ratio) in dependency of the total lipid concentration in aqueous solution.^[234] Although the orientation of the particles in the nematic phase can be influenced, the morphologies formed by bicellar lipid mixtures are independent of the presence of a magnetic field.^[247] Beside their use in biomolecular NMR as magnetically alignable substrate, bicellar mixtures are increasingly used in other applications, such as protein crystallisation^[248] and electrokinetic chromatography.^[249]

4.2.6 Sterols

Cholesterol

Cholesterol (IUPAC: (3 β)-cholest-5-en-3-ol) is a biological important steroid. Besides a certain dietary intake of a few hundred milligram per day, it is mainly produced by the body in the liver, but also in the intestines, adrenal gland and gonad.^[14, 102, 104, 107, 250]

Cholesterol is an amphiphilic molecule with a molar mass of 386.6 g/mol. The chemical structure is depicted in Figure 4.3. It is incorporated into cell membranes of eukaryotes by a hydrogen bond and Van-der-Waals interaction. The cholesterol content can vary between different membrane types and depending on external conditions between 4 % and 50 %. In the membranes of bacteria and mitochondria only very low amounts of cholesterol are found. Plants and fungi contain no cholesterol, but similar steroids, like ergosterol.^[14, 102, 104, 107, 250]

In vitro, the addition of cholesterol to a phospholipid widens the temperature range of the main transition and leads to a drastic reduction of the main transition enthalpy, ΔH_m . Already at a low cholesterol

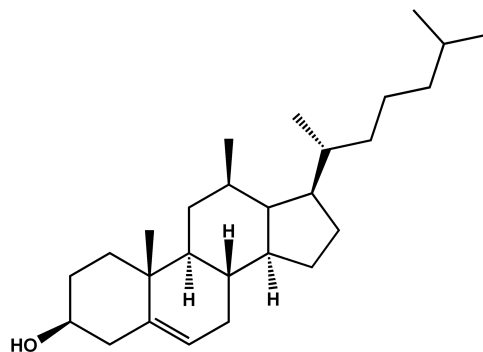


Figure 4.3: Chemical structure of cholesterol (IUPAC: (3 β)-cholest-5-en-3-ol).

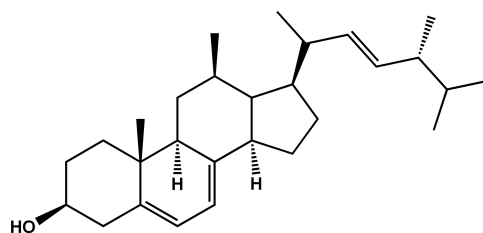


Figure 4.4: Chemical structure of ergosterol (IUPAC: ergosta-5,7,22-trien-3 β -ol).

concentration the pretransition of the phospholipid, between the $P_{\beta'}$ and $L_{\beta'}$ gel phase, can no longer be observed. At cholesterol concentrations of 30-50%_{mol} also the main transition vanishes. This can be easily explained by the different effects of cholesterol on phospholipids in the gel and fluid phase. Below the main transition temperature the presence of cholesterol disrupts the perfect crystalline packing of the lipids in the gel phase, causing conformational disorder and therefore making the membrane more fluid. On the contrary, above the main transition temperature in the fluid phase cholesterol stabilises the hydrocarbon chains of the lipid making the membrane more rigid, similar to the gel phases at lower temperature.^[14, 59, 104, 107]

Ergosterol

Ergosterol (IUPAC: ergosta-5,7,22-trien-3 β -ol, molar mass 396.65 g/mol) is an ubiquitous constituent of yeast and fungal plasma membranes^[251, 252] and essential for the appropriate function of membrane enzymes^[253, 254] as well as for the physical properties of these membranes^[208, 255, 256]. Besides this so-called “bulk-function” which is similar to the function of cholesterol in mammalian cells, ergosterol has also a “sparking-function”, which requires much lower sterol amounts, to initiate fungal growth.^[254, 257] Recently, it was shown that ergosterol, like cholesterol in animals, is able to induce a so-called liquid-ordered (l_o) phase,^[258] which is thought to be crucial for lipid raft formation and membrane protein function.

4.2.7 Phospholipids

Phospholipids are amphiphilic molecules usually built by two long fatty acid hydrocarbon chains (saturated or unsaturated), which are each connected by an ester-bond to a glycerol backbone. A hydrophilic head group is bound to his backbone. Commonly occuring head groups are: phosphatidic acid

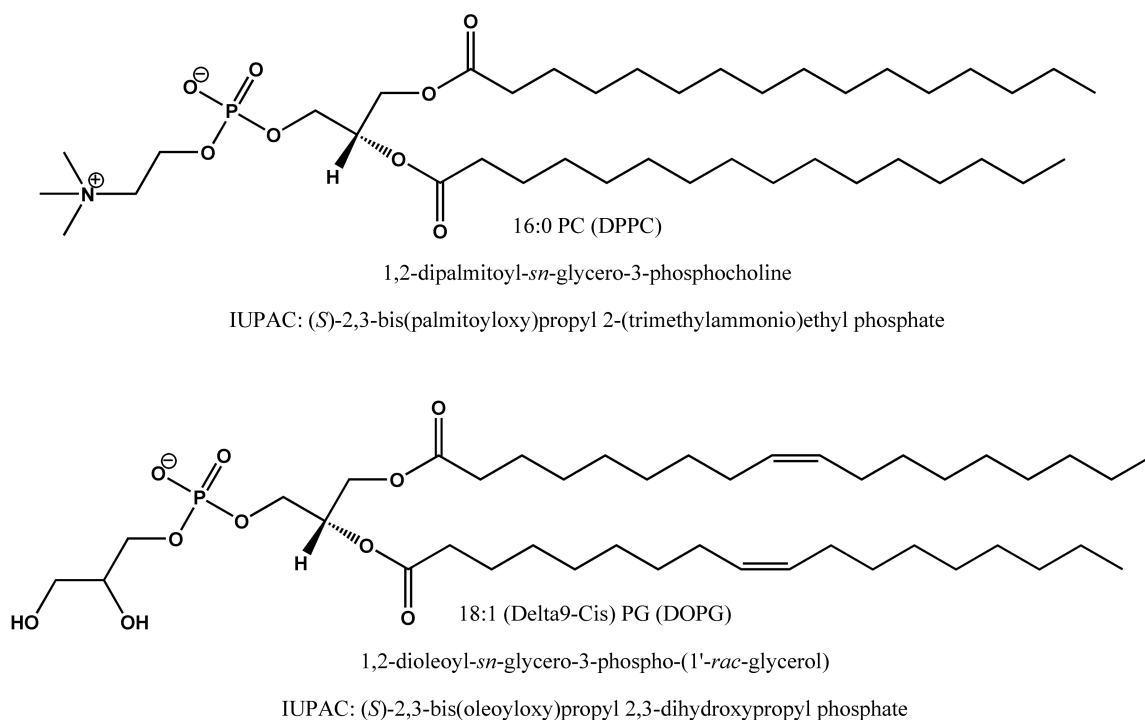


Figure 4.5: Chemical structure of the phospholipids DPPC (top) and DOPG (bottom).

(PA), phosphatidylethanolamine (PE), phosphatidylcholine (PC), phosphatidylglycerol (PG), and phosphatidylserine (PS).

In Figure 4.5 two typical lipids with different hydrocarbon chains and head groups are presented. On top 1,2-dipalmitoyl-*sn*-glycero-3-phosphocholine (DPPC) with two saturated C₁₆ hydrocarbon chains, originating from the palmitic acid, is presented. The head group is the zwitterionic phosphatidylcholine. The second lipid presented in Figure 4.5 is 1,2-dioleoyl-*sn*-glycero-3-phospho-(1'-*rac*-glycerol) (DOPG), which has two $\Delta 9$ - *cis* unsaturated C₁₈ chains and an anionic phosphatidylglycerol (PG) head group.

4.2.8 Monoolein

1-Monoolein (1-(*cis*-9-octadecenoyl)-*rac*-glycerol), as depicted in Figure 4.6, is an amphiphilic molecule with a molar mass of 356.55 g/mol, composed of a hydrocarbon chain attached to a glycerol backbone by an ester bond. Due to the two remaining hydroxyl groups of the glycerol this part of the molecule is hydrophilic and often referred to as head group. In contrast, the unsaturated C₁₈ hydrocarbon chain with a *cis* double bond between position 9 and 10 is highly hydrophobic. Due to this double bond the spatial demand of the hydrocarbon chain is high, leading to a critical packing parameter of this molecule larger than 1. As a consequence, there is the tendency to form type II micelles and structures.^[68, 204]

Monoolein is an important lipid in the fields of drug delivery, emulsion stabilisation or protein crystallisation and has been extensively characterised both as a pure substance and in the presence of fatty acids, proteins and salts.^[68, 204, 225, 259-263] It is also used in food technology to stabilise emulsions since it is non-toxic, biodegradable and biocompatible.^[68, 204]

Monoolein is nearly not soluble in water, but in oil, petrol ether and chloroform. It has a rather low melting point of 36 °C.^[204]

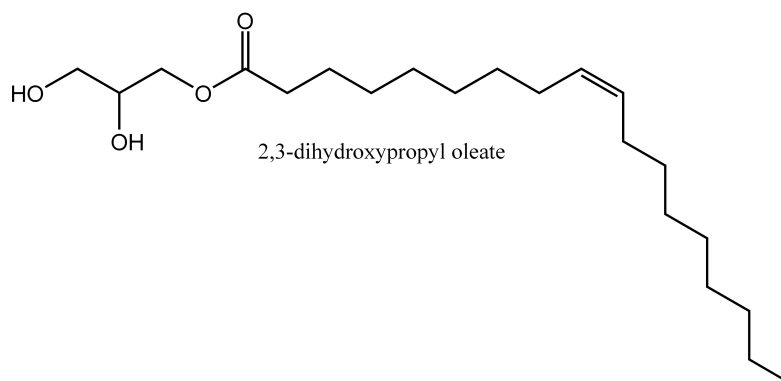


Figure 4.6: Chemical structure of 1-(*cis*-9-octadecenoyl)-*rac*-glycerol (DL- α -monoolein; IUPAC: 2,3-dihydroxypropyl oleate).

Depending on temperature and hydration, different phases can be found in pure monoolein. At high temperatures and high level of hydrations the cubic $Pn3m$ phase is obtained. At intermediate temperatures (20-80 °C, depending on the level of hydration) and in a hydration range between 10 and 40 %_{wt} water content (depending on the temperature) the cubic $Ia3d$ phase is found.^[68, 204] At lower temperature and level of hydration only a lamellar phase is detected. A detailed phase diagram (c_{H_2O} vs. T) as well as further information about monoolein can be found in [204, 264].

4.2.9 Glycolipids

Gram-negative bacteria are surrounded by two membranes in contrast to most other types of cells. In the outer membrane, separating the cell from the periplasm and the intracellular space, lipids are asymmetrically distributed. The inner monolayer of the outer membrane is mainly composed of glycerophospholipids, while the outmost monolayer is largely built by lipopolysaccharides (LPS).^[198]

LPS consist of a vast invariant part, composed of a lipid part called lipid A and a covalently linked core oligosaccharide unit of different length (different rough mutants Re to Ra) carrying several negative charges. The lipid A part possesses four to seven hydrocarbon chains and two negatively charged or phosphorylated N-acetylglucosamines (GlcN). The core oligosaccharide is connected to the lipid A moiety via a 2-keto-3-deoxyoctonoic acid (Kdo) by a 2-6 linkage.^[265, 266] Besides that structural element, another polysaccharide moiety (O-antigen) determining the serotype specificity can be connected to the core oligosaccharide (smooth-form LPS).^[267, 268]

When LPS is released from the outer membrane, for example by the action of immune components or simply by cell division, this can lead to pathophysiological effects including sepsis, septic shock and multi-organ failure.^[269, 270] Therefore, LPS are also known as endotoxins.

The function of LPS in the membrane is to stabilise the structural integrity of bacteria and to act as a protective barrier against chemical attacks,^[271, 272] thus making the bacteria resistant to a variety of host defense factors, such as β -lysine, lysozyme and various leukocyte proteins, which are known to be toxic to Gram-positive bacteria.^[273, 274] Additionally, it has been shown that the outer membrane of Gram-negative bacteria inhibits the diffusion of many antibiotics, such as novobiocin, through the membrane, which are effective against other forms of bacteria.^[268]

Several *in vivo* studies have demonstrated that Gram-negative bacteria are resistant against antimicrobial peptides in the presence of divalent cations.^[275] Moreover, it has been found that divalent, but

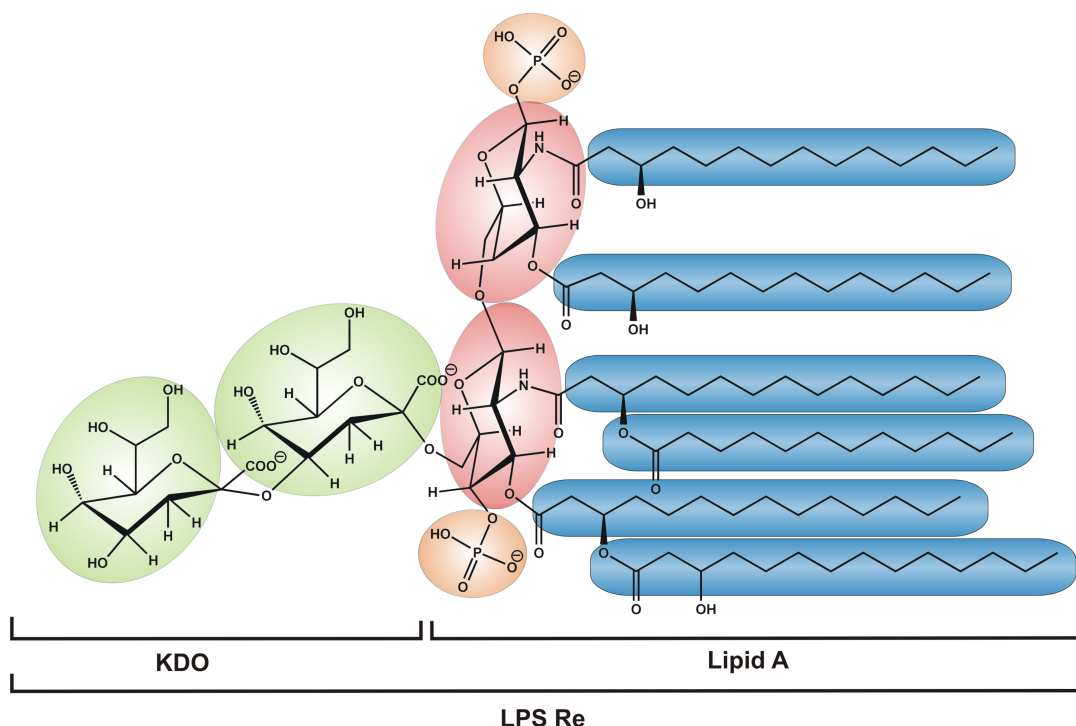


Figure 4.7: Chemical structure of lipopolysaccharide (LPS Re). LPS Re is composed of two domains: 1. a lipid part comprising six hydrocarbon chains (highlighted in blue) and two phosphorylated (orange) N-acetylglucosamine units (red), referred to as “lipid A”, and 2. a moiety containing two 2-keto-3-deoxyoctonic acid (Kdo, green) units.

not monovalent cations lead to LPS aggregation^[268] and cause structural rearrangements in the lipid A region.^[276] Ca^{2+} -ions are essential for the stability of LPS membranes^[277, 278] and most of these ions have been found to interact with the inner core phosphate groups as well as with the inner core of the polysaccharides with an average coordination number of Ca^{2+} of 6.1.^[278]

The deep rough LPS mutant “LPS Re” – as used in studies in this thesis – was extracted from *Salmonella minnesota* strain R595. The deep rough phenotype of LPS appears when bacteria are unable to attach their oligosaccharide core to the lipid A moiety. The molecular structure of LPS Re is shown in Figure 4.7. The N-acetylglucosamines of the lipid A moiety are coloured in red, the hydrocarbon chain region, consisting of six lipid chains, is depicted in blue and Kdo is highlighted in green. As a consequence of the missing oligosaccharide part, deep rough mutants lose almost entirely their resistance to a number of hydrophilic antibiotics, detergents, and lysozyme and they are permeable to steroids.^[272, 279] The LPS Re is the shortest LPS unit required for the survival of the bacteria.^[280]

4.2.10 Archaeal lipids

About 90% of the lipid components in the plasma membrane of the thermoacidophilic archaeon *Sulfolobus Acidocaldarius* are dibiphtanyldiglycerol tetraether lipids,^[281] among which the polar lipid fraction E (PLFE) is one of the main constituents.^[282] PLFE contains a mixture of bipolar tetraether lipids as shown in Figure 4.8 with either a glycerol dialkylcalditol tetraether (GDNT or calditoglycerocaldarchaeol; 90% of total PLFE) or a glycerol dialkylglycerol tetraether (GDGT, or caldarchaeol; 10% of total PLFE) skeleton.^[282–285] Both GDGT and GDNT are bisubstituted in the polar head group regions, thus designated as bipolar tetraether lipids. The nonpolar regions of these lipids consist of a pair of 40-carbon

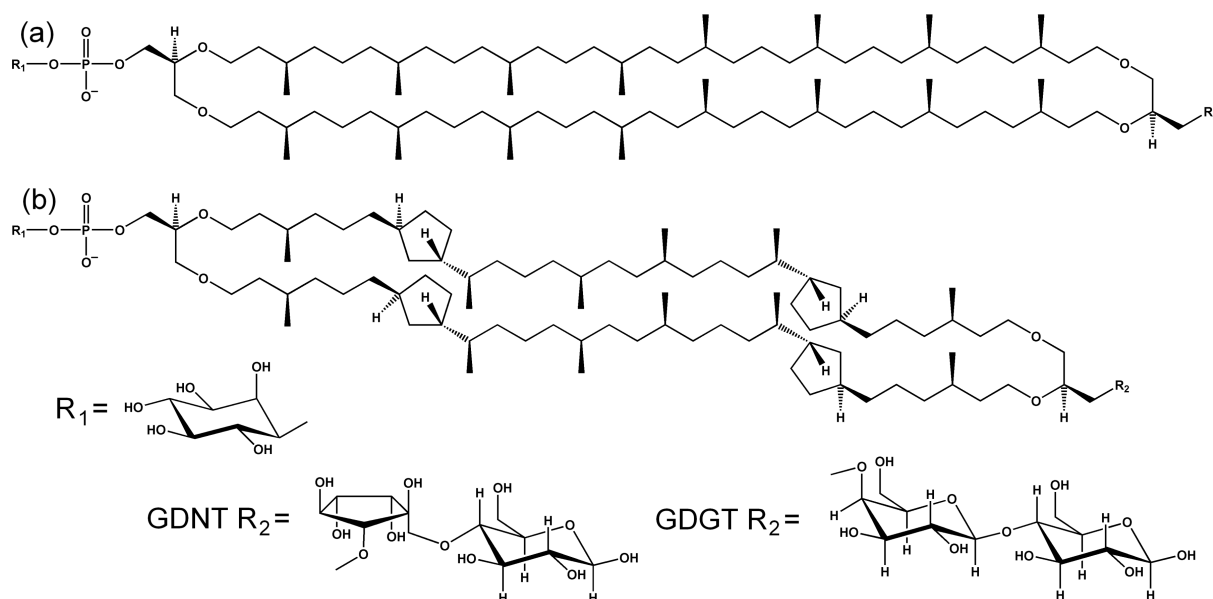


Figure 4.8: Chemical structure of archaeal lipid backbones grown at low temperature (a) and elevated temperature (b). The different head groups of GDNT and GDGT are presented in the bottom row.^[285, 287, 288]

biphytanyl chains, each of which contains up to four cyclopentane rings. The number of the cyclopentane rings in each biphytanyl chain increases with increasing growth temperature.^[286]

In PLFE liposomes, lipids span the entire lamellar structure, forming a monomolecular spanning membrane,^[289] in contrast to the bilayer structure formed by monopolar diester (or diether) phospholipids in mammalian cells. Since PLFE is the major polar lipid component in the plasma membrane of *S. Acidocaldarius*, PLFE liposomes have been used as a model system for studying thermoacidophilic archaeal membranes. PLFE liposomes exhibit high thermal stability and unusually low solute permeability when compared to monopolar diester or diether liposomes (reviewed in Gliozzi et al. [284]). The thermal stability with respect to leakage of dye originally trapped inside PLFE liposomes has been attributed to the negative charges on the membrane surface and to the tight and rigid lipid packing.^[290–292] The low proton permeability in PLFE liposomes has been ascribed to the network of hydrogen bonds between the sugar residues of PLFE exposed at the outer face of the membrane^[291] and to the tight and rigid lipid packing.^[292, 293] Both the dye leakage and proton permeation experiments suggest that membrane packing, in either the hydrocarbon or the polar head group regions or both, is a central issue in understanding PLFE lipid membranes.

To study membrane packing in PLFE liposomes, lateral and rotational diffusions of membrane probes have been examined. The lateral mobility of 1-palmitoyl-2-(10-pyrenyl)-decanoyl-*sn*-glycero-3-phosphatidylcholine (PyrPC) in PLFE liposomes was found to be highly restricted and only became appreciable at temperatures $> 48^\circ\text{C}$.^[294] This indicates a significant structural change near 48°C in the PLFE hydrocarbon core. These studies also suggest that the hydrocarbon region of PLFE liposomes is rigid and tightly packed below 48°C . Above 48°C , the hydrocarbon core of PLFE membranes begins to gain appreciable membrane fluidity, which would be required for the functionality of archaeal membranes.

The polar head group region of PLFE membranes, on the other hand, may still be rigid and tightly packed through the hydrogen-bond network^[295, 296] at elevated temperatures ($> 48^\circ\text{C}$) to maintain a large proton gradient (pH 2-3 outside and pH 6.5 inside the cell) across the membrane at the growth

temperature. This proposition explains why low proton permeability and appreciable membrane fluidity can occur at the same time in thermoacidophiles at high growth temperatures. This point is supported by a spin-label study, which showed that at high temperatures (85 °C) the nonitol (more precisely, calditol) head group of tetraether lipids from the thermoacidophilic archaeon *S. solfataricus* was relatively immobile, whereas the hydrocarbon region possessed some mobility.^[297] Recently, some structural properties of PLFE membranes in bulk solution were revealed by using SAXS^[287] and the thermal phase transitions and volumetric properties were studied by calorimetric methods (DSC, PPC)^[288, 298] and density measurements^[288] in our group.

4.3 Effect of pressure on biomolecules

4.3.1 General

Beside temperature and chemical potential, pressure is a thermodynamic key variable, but due to the technical difficulties of high pressure investigations it is highly underrated and unutilised. Albeit recently a growing number of physical-chemical and biophysical studies of biological systems have been conducted.^[104, 299]

The pressure range used for investigating biomolecules ranges from atmospheric pressure to approximately 10 kbar, where the aqueous solvent is still in its liquid state at ambient temperature. Such pressure changes only intermolecular distances and affects conformations, but is unable to change covalent bond distances or angles. The covalent structure of biomolecules is not perturbed by pressure up to about 20 kbar. High hydrostatic pressure (HHP) acts predominantly on the spatial (secondary, tertiary, quaternary, and supramolecular) structures of biomacromolecules.^[3, 300]

Besides the general physical-chemical interest in using high pressure as a tool for understanding the structure, energetics, phase behaviour and dynamics of biomolecules, it is also of biotechnological and physiological interest, e.g. for understanding the physiology of deep-sea organisms living in cold and high pressure habitats, which exist at pressures up to about 100 MPa.^[300]

The response of all systems to high pressure is governed by Le Châtelier's principle, which states that the application of pressure shifts an equilibrium towards the state of smallest volume and accelerates processes with a smaller volume of the transition state than the ground state.^[59]

Pressure has several advantages over using temperature as the thermodynamic variable of the investigation of a sample system. As pointed out before, pressure is a rather mild perturbing agent. It propagates in the aqueous sample rapidly with the speed of sound, so sample inhomogeneity is only a minor problem and it can be applied bidirectionally, e.g. with increasing and decreasing pressure without any differences in technical difficulty. Additionally, many biomolecules show a fully reversible behaviour of pressure induced conformational and structural changes upon bidirectional variation of the system's pressure. This allows for numerous pressure-cycles with one identical sample either repeating one specific experiment several times to improve the counting statistics of the experiment, or varying the experimental conditions to get a detailed picture of the sample system without any influences of changed sample parameters like hydration, concentration, homogeneity or composition.^[3, 300]

Organisms have to face high hydrostatic pressure in natural habitats like the abyssal plane in the deep sea with an average depth of 3000 metres, resulting in an ambient pressure of 300 bar at 2 °C. The deepest part of the ocean, the Mariana Trench with a depth of 11000 m, even exhibits a pressure of 1100 bar. These enormous pressures are sometimes accompanied with high temperatures, even above

100 °C, at hydrothermal vents (“black-smokers”). The organisms living in these environments have adapted, by changing the basic structure of their lipid membranes, the composition of different lipids and by incorporating further molecules into the bilayer structure ensuring the fluidity of the cell membrane.

Besides the natural occurrence, high hydrostatic pressure is also applied technically to inactivate microorganisms in food, while retaining favourable product properties like texture or flavour,^[301] or for the sterilisation of heat-sensitive pharmaceuticals.^[302, 303] The lethal effects of HHP are caused by the dissociation of macromolecular assemblies like ribosomes or the cytoskeleton and the pressure-induced denaturation of proteins^[209, 304] or by alterations in membrane structure, dynamics and permeability, which lead to the failure of cell homeostasis.^[304, 305] It is generally thought that the latter effects are caused by the transition of the plasma membrane to a solid-like gel phase, accompanied with the ceasing of membrane protein function.^[306, 307]

4.3.2 Pressure effect on lipids

Deep sea organisms have to be able to adapt their lipid membranes to maintain the vital fluid bilayer structure and mechanical properties. This is achieved by altering the lipid composition of the cell membranes, enabling them to cope in an incredibly wide pressure range.^[299]

Upon an increase of the pressure, the equilibrium state of lipid systems is shifted towards configurations of the smallest volume, i.e. the reduction in hydrocarbon chain motion and a corresponding increase in chain ordering, resulting in a reduction of the cross sectional area of the lipid chain region. However, the lipid head groups are much less affected by high pressure than the chains, leading to an increase of the curvature towards the hydrocarbon chain region, i.e. a reduction of the critical packing parameter, γ . For all lamellar and inverse fluid lipid mesophases this means an increase in the crystallographic lattice parameter obtained by diffraction experiments, as long as this effect is not overcompensated by a decrease in the water layer thickness.^[299]

Often, increasing of pressure in a lipid system has a similar effect as decreasing the temperature, i.e. ordering of the lipid arrangement and decreasing the ratio of *gauche* conformeres. However, sometimes phases can be observed upon pressurisation, which are not found at atmospheric pressure as a function of temperature. A typical example is the formation of an additional gel phase, the interdigitated phase L_{β_1} , where the hydrocarbon chains of the opposing lipid monolayers are interpenetrating, as observed in pure DPPC between about 1 kbar and 3 kbar at temperatures above 45 °C.^[3, 203, 308]

More details about the effects of high pressure on lipid systems can be found in a number of excellent reviews, for instance [104, 299, 309, 310].

4.3.3 Pressure effect on proteins

High hydrostatic pressure leads to a unique and gentle thermodynamic perturbation of the native protein structure, due to a decreasing volume of the system upon unfolding.^[311–313] This change of volume comprises the effects of disruption of noncovalent bonds, change in protein hydration, conformational changes, as well as freeing of void volume, which in most cases is the dominant contribution.^[3] In general, high pressure selectively stabilises conformations with smaller specific volumes. Earlier studies on SNase^[129, 131, 133, 314, 315] confirmed that the differences in volume between the various conformational states of proteins arise primarily from variations in their solvent excluded void volumes. Although the interior of proteins is generally quite well packed, this packing is not perfect. Some of this unoccupied

space inside proteins can be filled by water in locally unfolded states or upon complete unfolding.^[118, 119] The molar volume decreases as cavities become hydrated. Therefore, the application of pressure is expected to stabilise the lower volume conformers with higher degree of hydration. In principle, subtle conformational fluctuations that are unnoticed at ambient pressure can be enhanced with high pressure to levels detectable by NMR or FTIR spectroscopy, and SAXS.^[316-319]

Usually, temperature or chemical denaturants are used at atmospheric pressure to investigate the stability and unfolding of proteins. Both methods have significant disadvantages: the temperature changes both the volume and the thermal energy at the same time and the addition of further chemicals poses an intrinsic problem, as these substances interact with the water and are often binding to the protein, which often results in changes of the sample system. Changes of the protein structure caused by high temperature are usually irreversible and often accompanied by aggregation.^[3]

The use of high hydrostatic pressure is advantageous in several respects: the effect of pressure is reversible and no aggregation of the proteins occurs. Instead, a renaturation of proteins is generally observed upon release of the pressure.^[3]

CHAPTER 5

Design and construction of a novel high pressure sample cell for neutron reflectometry

In this chapter the design of a novel high pressure (HP) sample cell for neutron reflectivity (NR) experiments is described, as published in [300]. The cell can be used to study solid-liquid interfaces under pressures up to 2500 bar (250 MPa). The sample interface is based on a thick silicon block with an area of about 14 cm². This area is in contact with the sample solution, which has a volume of only 6 cm³. The sample solution is separated from the pressure transmitting medium (water) by a thin flexible polymer membrane. In addition, the HP cell can be temperature-controlled by a water bath in the range 5-75 °C. By using an aluminium alloy as window material, the assembled HP cell provides a neutron transmission as high as 41 %. The maximum angle of incidence accessible to reflectivity experiments is 7.5°.

The large pressure range and the low required volume of the sample solution make this HP cell highly suitable for studying pressure-induced structural changes of interfacial proteins, supported lipid membranes and, in general, biomolecular systems at soft- and hard-matter interfaces.

5.1 Key design parameters

The high pressure cell for NR studies has been designed to provide a platform for the investigation of a wide variety of sample systems up to 2500 bar in a temperature range between 5 and 75 °C. Key design parameters that had to be taken care of include:

- a strict separation of the sample solution from the metallic cell walls and the pressure transmitting medium to prevent sample contamination,
- a sample volume as small as possible to minimise the required amount of substance,
- an easily accessible and exchangeable sample container inside the high pressure cell,
- corrosion-free materials to ensure a long life time of the setup, which is especially important at HP conditions, where the rate of metal oxidation may significantly be accelerated,
- no need for removing or cleaning of the cell windows upon changing the sample to ensure a constant scattering background of the cell windows.

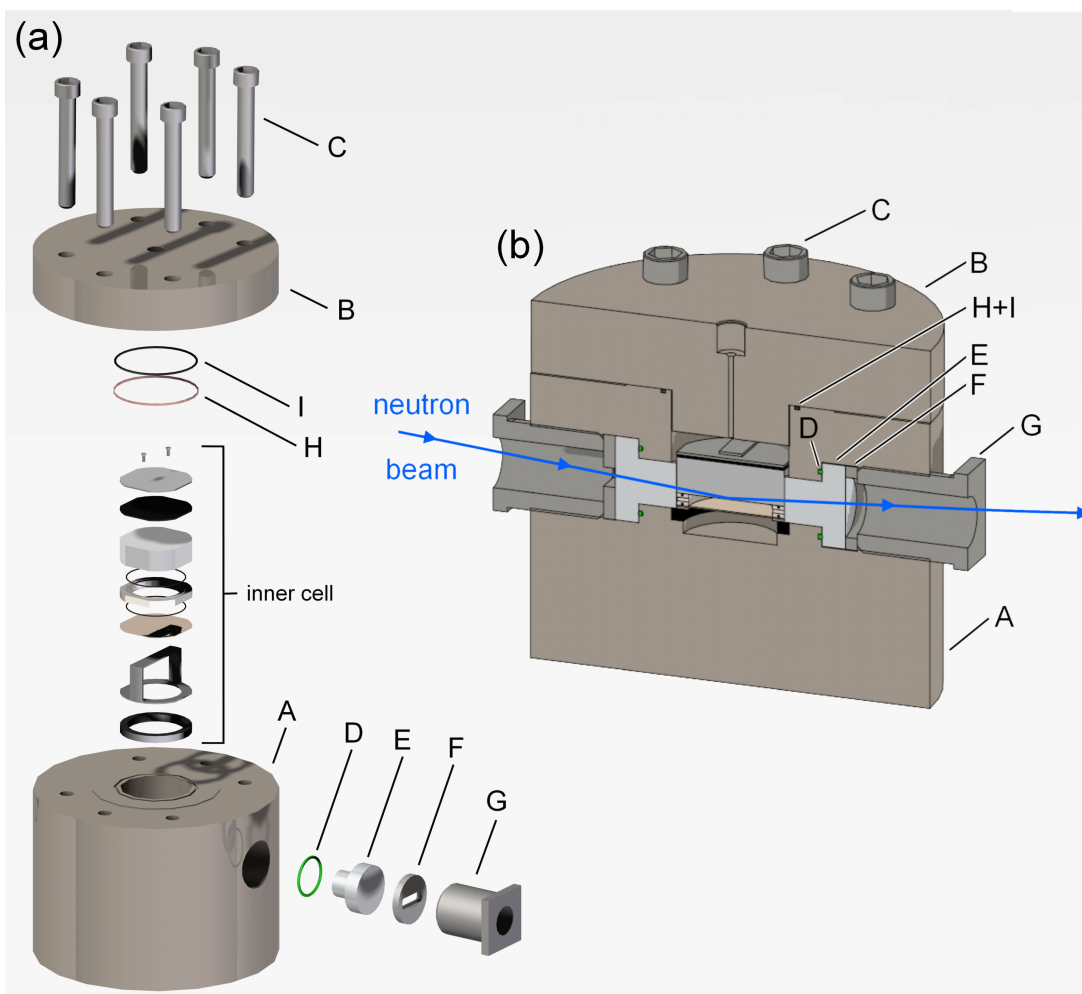


Figure 5.1: (a) Exploded and (b) cross section view of the high pressure neutron reflectometry cell showing the cell body **A**, closure head **B**, closure head screws **C**, cell windows O-ring **D**, cell window **E**, window aperture **F**, window holder screw **G**, closure head O-ring **I**, and copper support ring **H**. The pathway of the neutron beam through the cell is depicted as a blue line in (b).

5.2 Cell design and specifications

The basic design of the cell was realised by hand on scale paper. Afterwards, the draft blueprint was first discussed with PD Dr. C. Czeslik and Prof. R. Winter. Finally, it was adjusted in cooperation with the mechanical workshop at the TU Dortmund University. The engineering drawings were created by me using the Siemens software “Solid Edge”. From these drawings exploded views of the cell could be rendered (Figure 5.1 and Figure 5.2).

5.2.1 Cell body

The cell body, as shown in Figure 5.1 (part A), is based on a cylindrical pressure vessel made from the high-tensile nickel based alloy ALLVAC 718 (UNS N07818), which has an excellent corrosion resistance. The alloy was purchased from Robert Zapp Werkstofftechnik GmbH, Ratingen, Germany. The cell body was fabricated by the mechanical workshop of the Technische Universität Dortmund, Faculty of Chemistry, Dortmund, Germany. The 0.2% offset yield strength, $R_{p0.2}$, defining the stress, which causes a 0.2%

strain of the material, is 11430 bar. The ultimate tensile strength, uts , which is the maximum stress the material can withstand before necking, is 14420 bar at room temperature, and decays to 11390 bar at 649 °C.

Using the simplified model of a thick-walled cylindrical pressure vessel with capped ends operated above 1000 bar, the maximum yield pressure, P_y , of the vessel can be estimated as a function of the offset yield strength, $R_{p0.2}$, of the material and the ratio of the outer and the inner cell diameters, u , by the equation:^[320]

$$P_y = \frac{u^2 - 1}{\sqrt{3}u^2} R_{p0.2}. \quad (5.1)$$

When the wall of the cylinder is infinitely thick ($u \rightarrow \infty$), the maximum yield pressure, P_y , calculated within this simple model is 58 % of the offset yield strength, $R_{p0.2}$. The cell has an outer diameter of 170 mm and an inner diameter of 50 mm, yielding a diameter ratio of $u = 3.4$. For this value, the maximum yield pressure, P_y , is 53 % of the offset yield strength, $R_{p0.2}$. The value of 3.4 was chosen in order to achieve a high maximum pressure of the cell without increasing the cell weight too much. Using equation 5.1, the maximum yield pressure, P_y , of the HP NR cell can be calculated to be 6028 bar. In addition, the theoretical burst pressure, P_b , of a thick-walled cylindrical pressure vessel can be calculated from the Faupel formula:^[320]

$$P_b = \frac{2}{\sqrt{3}} R_{p0.2} \left(2 - \frac{R_{p0.2}}{uts} \right) \ln u. \quad (5.2)$$

For this cell, this equation predicts a burst pressure of 19.5 kbar.

The cell is capped with a closure head, as depicted in Figure 5.1 (part B), which is made of the same alloy as the cell body (ALLVAC 718 - UNS N07818). It is fixed by six M12x80 screws (DIN 912 / ISO 4762) made of quenched and tempered high-tensile steel (grade 12.9) with a minimum fracture force of 103 kN (Figure 5.1, part C).

5.2.2 Cell windows

The cell windows (Figure 5.1, part E), serving as entrance and exit of the incident and reflected neutron beam, are made of the aluminium alloy AlMgSi1 (EN AW - 6082) – an aluminium alloy of particularly high tensile strength – and were also tooled by the mechanical workshop of the faculty. The 0.2 % offset yield strength, $R_{p0.2}$, of the alloy is around 2550 bar and the ultimate tensile strength, uts , is 2950 bar. Exceeding those parameters, the alloy starts to flow continuously without developing cracks. The thermal expansion coefficient of AlMgSi1 is $23.4 \cdot 10^{-6} \text{K}^{-1}$ and is thus significantly higher than the value of $4.5 \cdot 10^{-6} \text{K}^{-1}$ characterising the alloy used for the cell body (ALLVAC 718). This fosters the leak tightness of the assembled windows even at higher temperatures. The high corrosion resistance of the window material ensures a long lifetime of the windows without any degradation that might change the transmissibility.

The windows have a T-shaped profile (Figure 5.1b, part E) with the thinner end (diameter of 19 mm) reaching into the inner cell volume. The thicker end has a diameter of 35 mm, and the thickness of a window, i.e. the path length of the neutron beam through the window, is at least 26 mm. The 1/e-length of AlMgSi1, where the intensity of a neutron beam is attenuated to 1/e (about 0.37), is 71.2 mm at a wavelength of 4.66 Å. A neutron transmission of 68.8 % has been measured for two cell windows aligned

in a row along the neutron beam path (total thickness of 52 mm). This rather low attenuation of the neutron beam by the two cell windows is important for recording neutron reflectivities over several orders of magnitude.

The windows are held in position by hollow screws as shown in Figure 5.1 (part G). Between the entrance window of the cell and its holding screw, a steel aperture is placed to support the window stability and to cut off divergent parts of the neutron beam. A steel ring is used instead at the exit window facing the detector (Figure 5.1, part F).

5.2.3 Sealings

Two different types of seals are used in the cell: cone-to-cone fittings and O-ring seals. The connection of the cell to the high pressure network capillary is achieved by a cone-to-cone coupling using a standard 16 mm HP fitting (NOVA SWISS, Zürich, Switzerland). O-ring seals of different sizes and materials are used for sealing of the cell windows, the closure head of the cell as well as the inner sample cell, separating the pressure medium from the sample liquid. All O-rings were purchased from C. Otto Gehrckens GmbH & Co. KG, Pinneberg, Germany. To seal the contact area between a window and the cell body, Viton700 O-rings (25×2 mm) were used with a shore durometer of 90 shore (Figure 5.1, part D). The inner sample cell is equipped with two P583 / NBR70 O-rings (42×1 mm) as depicted in Figure 5.2 (part c). The cell closure head is sealed by a combination of a Viton580 / FKM80 O-ring (55×2 mm) and a copper support ring (Figure 5.1, parts I and H, respectively). The O-rings of the inner sample cell should be replaced every time the sample fluid is exchanged, and the O-ring of the closure head should be renewed every time the cell is opened; the Viton700 O-rings of the cell windows proved to be tight over several pressure runs.

5.2.4 Inner sample cell

A major objective in the design of the inner sample cell was the minimisation of the required sample solution volume and a clean separation of the sample (interface and solution, typically prepared with D_2O as the solvent) from the pressure transmitting medium, usually H_2O . Moreover, a rapid exchange of the sample (interface and solution) between two experiments should be possible.

All polymer and metal components of the inner sample cell were tooled by the mechanical workshop of the faculty. The silicon wafers used as solid support for the sample interfaces were purchased from Siliciumbearbeitung Andrea Holm, Tann, Germany. They were made of a p-type silicon monocrystal with a (111) surface orientation. The surface side supporting the interface under investigation is polished to show a maximum surface roughness of $6 - 8 \text{ \AA}$.

The inner sample cell is depicted in an exploded view in Figure 5.2a, and the cross section of the assembled inner sample cell is shown in Figure 5.2b. It has a sandwich-type design and is held together by a clamp (Figure 5.2, part a). As drawn in Figure 5.2 from bottom to top, the components are an elastic polymer film (b), a Teflon ring (d) confining the sample liquid, the silicon wafer (f), and a rubber pad (g) to ensure a uniform pressure distribution applied from the clamp screws (i) onto the top steel cover plate (h). The Teflon ring has two small filling holes that can be closed by screws (e).

The elastic polymer film (b) separates the sample liquid from the HP medium, water, and transmits the pressure from the HP medium to the sample liquid. Sealing of the Teflon ring (d) is achieved with O-rings on both sides. The volume of sample liquid in the inner cell is 6 cm^3 . To fill the assembled inner

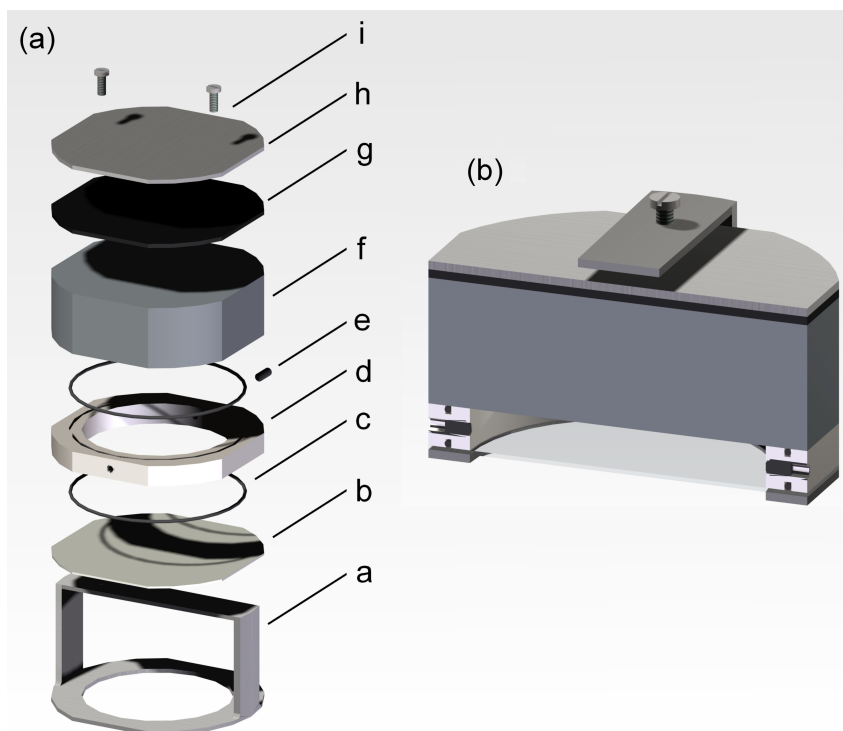


Figure 5.2: (a) Exploded view and (b) cross section view of the inner sample cell showing the clamp **a** holding all components of the inner cell in position, the elastic polymer film **b**, the O-ring **c**, the Teflon sample holder ring **d**, the sample container closure screw **e**, the silicon wafer **f**, the rubber pad **g**, the steel cover plate **h**, and screws **i**.

cell with the sample solution, the two screws (**e**) in the Teflon ring (**d**) are removed and a syringe with the sample solution is connected to one of the screw holes via an appropriate adapter. Then, the syringe is emptied into the inner cell, and the screw holes are closed again without leaving any air bubbles.

By using two identical inner sample cells, a rapid sample exchange can be realised. Samples that require long equilibration times can thus be prepared in advance, while the HP autoclave is still in use with another sample. This is extremely useful considering the limited beam time generally provided at neutron sources. The exchange of two inner sample cells does not require any significant cleaning of the HP cell compartment.

5.2.5 Overall HP experimental setup

To run an experiment, the inner sample cell is inserted into the cell body as depicted in the cross sectional view of the completely assembled cell in Figure 5.1b. The assembled cell is mounted on the beamline table. To adjust the temperature, the whole HP sample cell (HPSC, Figure 5.3) can be inserted into a metal jacket that is connected to a temperature-controlling water bath (not shown). The water is running from the bath through channels in the metal jacket. A temperature sensor (Figure 5.3, part TS1) connected to a temperature display (TD1) is integrated in the cell jacket.

The maximum incident angle of the neutron beam is determined by the length and diameter of the window holder (Figure 5.1, part G) and equals 7.5° for an infinitely thin neutron beam. For typical beam dimensions of 14 mm in width and 1 mm in height, the maximum incident angle is 5.2° , which is fully sufficient to cover a typical q -range of a neutron reflectivity experiment.

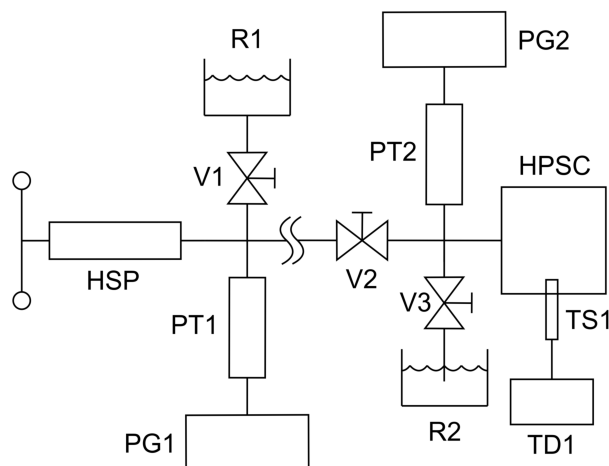


Figure 5.3: Schematic drawing of the high pressure network. The components are: high pressure spindle pump **HSP**, pressure medium reservoirs **R1** and **R2**, hand operated valves **V1**, **V2** and **V3**, pressure transducers **PT1** and **PT2**, pressure gauges **PG1** and **PG2**, high pressure sample cell **HSPC** (q.v. Figure 5.1), temperature sensor **TS1**, and temperature display **TD1**.

The HP NR sample cell is connected to a pressure generating system as schematically pictured in Figure 5.3. All components of the pressure generating system are purchased from NOVA SWISS, Zürich, Switzerland. The HP sample cell (HPSC) is connected to an HP capillary by a cone-to-cone fitting. The pressure generating system can be divided into two sections separated by the valve **V2**: the first section includes components located next to the HP cell, and the second section comprises the hand spindle pump (HSP) located at some distance away from the cell outside the beamline area. The pump is connected to the reservoir **R1** by the valve **V1** to fill the pump with pressure transmitting medium (water). To read the pressure inside this section, the pressure transducer **PT1** and the pressure gauge **PG1** is used. Directly at the cell, pressure transmitting medium can be released into the reservoir **R2** by opening valve **V3**. An additional high pressure transducer (**PT2**) with pressure gauge (**PG2**) is connected to the pressure generating system directly at the HP cell to monitor the pressure inside the cell permanently, even when valve **V2** is closed. The total volume of the pressure transmitting medium inside the whole pressurised system (including the HP cell body) is approximately 30 cm³.

5.2.6 Neutron reflectivity data collection

The neutron reflectivity measurements conducted during this thesis were performed at the Helmholtz-Zentrum Berlin (HZB, Germany) using the instrument V6.^[321] The neutron wavelength selected by a graphite monochromator was 4.66 Å; higher-order wavelengths were suppressed by a Be-filter cooled with liquid nitrogen. The neutrons entered the HP cell and the Si-block inside the cell, were reflected in part at the Si-solution interface, and left the Si-block and the HP cell on the opposite side. Neutron reflectivities were recorded with a fixed incident neutron beam in $\Theta/2\Theta$ geometry using a ³He detector. Raw data were normalised to the number of incoming neutrons hitting the Si-solution interface and were scaled as a function of wave vector transfer. The angle of incidence was typically in the range of 0.0° to 3.0°. In the case of a protein adsorbate sample, the inner sample cell was filled with protein solution and was equilibrated for at least 1 h. In the case of a lipid (spin-)coated Si-wafer, the inner sample cell was filled with pure D₂O. Data treatment comprises correction of footprint effects, calculation of the wave vector

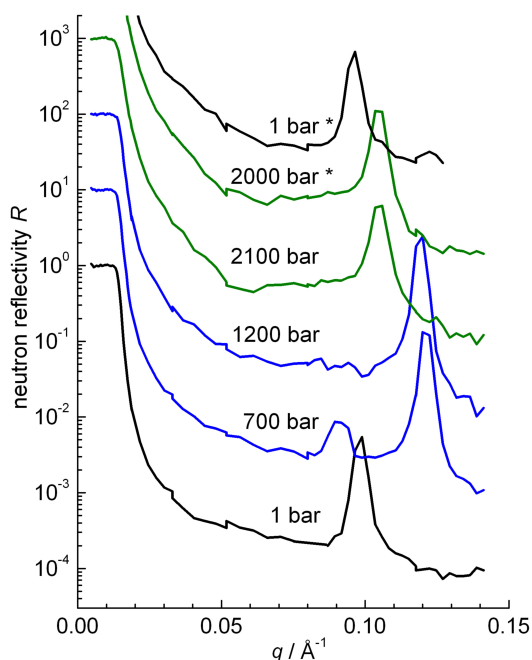


Figure 5.4: Neutron reflectivity curves of an Si / D₂O interface that has been spin-coated with a thin film of the lipid DOPE. Data have been recorded successively from bottom to top (stacked plot – data shifted vertically for better clarity). With increasing pressure, Bragg peaks of the inverse hexagonal phase H_{||} (1 bar), the lamellar fluid phase L_α (700 and 1200 bar), and the lamellar gel phase L_β (2100 and 2000 bar) of adsorbed DOPE are observed. Data were collected at 23 °C except for the top two curves, which were obtained at 16 °C (marked with an asterisk).

transfer and finally fitting the data using the software “Parratt32”, which is based on Parrat’s recursive method (see section 3.1.4, page 28).

5.3 First studies using the high pressure NR sample cell

First studies were conducted to illustrate the performance of the cell and the usefulness of the HP data obtained. The pressure-induced phase transitions between a lamellar and a hexagonal phase of a solid supported DOPE lipid layer as well as the adsorption and pressure dependent denaturation of the protein SNase was investigated.

5.3.1 Pressure-induced phase transitions of lipid films

Figure 5.4 shows neutron reflectivity data of an Si / DOPE / D₂O interface at $T = 23$ °C, as obtained with the new HP NR cell. The sample was prepared by spin-coating of an Si-wafer at 3500 rpm using 80 mg DOPE dissolved in chloroform. The inner sample cell was filled with pure D₂O. At atmospheric pressure, the first Bragg reflection {10} of the H_{||} phase is seen. At 1 bar and 23 °C, the first Bragg reflection can be found at $q = 0.0982$ Å⁻¹, which corresponds to a hexagonal lattice constant of $a = 74$ Å (q.v. equation 2.40, page 19).

The position of Bragg reflections of lamellar phases (L_α and L_β) with one-dimensional periodicity can be calculated from equation 2.38. At 700 bar, the {001} Bragg reflection of the lamellar L_α phase appears. The lamellar repetition unit, corresponding to the lipid bilayer thickness and the interlamellar water layer

around the lipid head groups, is $d = 52 \text{ \AA}$. At 1200 bar, the lamellar repeat unit has increased to 53 \AA . At 2100 bar the phase transition to the lamellar gel phase (L_{β}) can be observed, which displays a larger lamellar repeat unit of $d = 60 \text{ \AA}$. Upon pressure release (and decreasing the temperature to $16 \text{ }^{\circ}\text{C}$), the H_{\parallel} phase is formed again, indicating reversibility of the process. These measurements thus show that lattice constants of lipid mesophases can be determined with high accuracy and reproducibility under high pressure conditions even in NR experiments. The phases found and the lattice constants determined are in good agreement with those obtained for the corresponding bulk solution phases.^[203]

5.3.2 Protein adsorbate at an aqueous-solid interface under high pressures

In this part, neutron reflectivity data of a protein adsorbed at an aqueous-solid interface under high pressure conditions are presented. The protein staphylococcal nuclease (SNase; q.v. section 4.1.2, page 39) was chosen as model protein, since pressure-effects on the folding stability and kinetics have already been determined in bulk solution and are well documented in the literature.^[129, 314, 322] In this study, D_2O was used as the solvent of the protein solution and perdeuterated poly(styrene) (dPS) to cover the surface of a silicon wafer to increase the sensitivity of NR for protein adsorbates dramatically. A thin film of dPS has been deposited on the bare Si wafer by spin-coating. Since D_2O and dPS have almost identical neutron scattering length densities, Kiessig oscillations are observed only when protein molecules adsorb at the D_2O / dPS interface (q.v. section 3.1.7, page 30). However, in the model experiments presented here, 3.9 M urea have been added to the SNase / D_2O solution in order to lower the standard Gibbs energy of unfolding, ΔG° , of SNase.

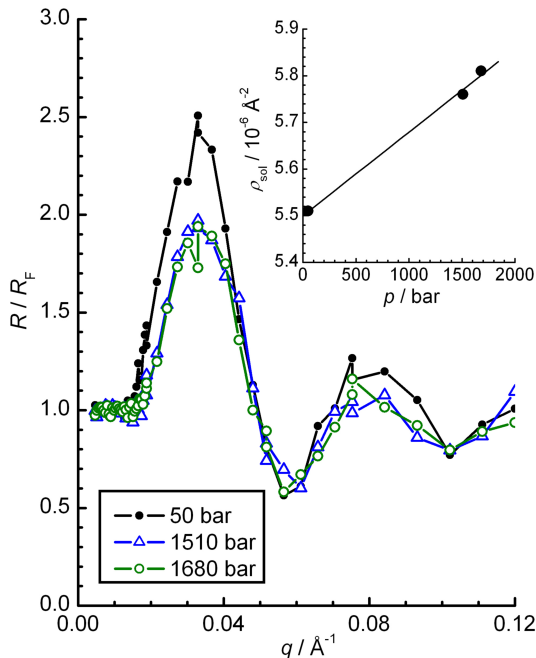


Figure 5.5: Neutron reflectivities of an Si / perdeuterated poly(styrene) / protein adsorbate / protein solution interface at different pressures as indicated in the figure legend. The protein SNase was adsorbed from the aqueous (D_2O) protein solution (0.09 mg ml^{-1} SNase, $\text{pD} = 7.1$, 3.9 M urea). The measured reflectivities, R , are normalised to the corresponding Fresnel reflectivities, R_F , of smooth Si/solution interfaces. In the inset, the resolved scattering length density of the protein solution is plotted as a function of pressure.

In Figure 5.5, neutron reflectivity curves of an Si / dPS / SNase adsorbate / SNase solution interface are plotted for selected pressures as obtained with the new high pressure cell. In order to highlight pressure-induced changes in the data, the measured curves have been normalised to the corresponding Fresnel reflectivities of smooth, uncovered Si / solution interfaces. The amplitude of the reflectivity oscillations is damped under high pressure. Furthermore, the q -value of the critical angle is moving to higher values. The critical q -value depends only on the scattering length densities of the first (solution) and last medium (Si wafer) of an interfacial structure. The scattering length density of the solution, ρ_{solvent} , is plotted in Figure 5.5 in the inset. It is increasing from $5.50 \cdot 10^{-6} \text{ \AA}^{-2}$ at 1 bar to $5.85 \cdot 10^{-6} \text{ \AA}^{-2}$ at 2000 bar. This increase by 6.4 % is consistent with the increase of the mass density of D_2O by 6.8 % in the same pressure interval.^[323] The data clearly show that the signal to noise-ratio obtained with the HP cell is sufficient to probe smallest changes of the neutron reflectivity upon pressurisation from 1 to 1510 bar. The data measured at 1510 and 1680 bar are very similar, as expected, proving a high degree of reproducibility. For a more detailed analysis the data shown in Figure 5.5 have to be modeled to obtain the scattering length density profile of the interface. However, this kind of analysis is beyond the scope of proving the performance of the cell and the usefulness of the HP data obtained.

CHAPTER 6

Investigations of pure lipid systems

In this chapter various studies of pure lipid systems are presented. The first four sections (6.1-6.4) present investigations of phospholipids using small-angle X-ray scattering (SAXS), X-ray reflectometry (XRR) and grazing incidence X-ray diffraction (GIXD). In section 6.5 a comprehensive study of monoolein with a limited hydration of 17%_{wt} is presented including a p, T -phase diagram, exact parameters of all involved phases and detailed information about the phase transition kinetics retrieved from pressure-jump relaxation experiments in combination with time-resolved small-angle X-ray scattering (trSAXS). In the sections 6.6 and 6.7 measurements of monolayers built by archaeal lipids and glycolipids at the air-water interface are presented, respectively. These two classes of lipids differ highly in their chemical structure from phospholipids.

Several different p, T -phase diagrams of the systems in aqueous solution could be established using SAXS and the kinetics of pressure induced phase transitions could be probed by the pressure-jump relaxation technique. In SAXS studies often Fourier transform infrared (FTIR) spectroscopy was additionally performed by coworkers in our group to gain information on the lipid conformation and hydration.

GIXD and XRR were used to investigate Langmuir monolayers of lipids at the air-water interface. GIXD yields valuable information about the lateral crystalline structure, the packing, as well as the lateral and vertical dimensions of crystalline domains in the lipid monolayer. However, disordered domains do not contribute to the GIXD signal. Using XRR the laterally averaged electron density profile of the lipid film can be found with high vertical resolution. The results give detailed insides into the thickness of different layers in the film, the density of these layers as well as the roughness of the interfaces.

6.1 Bicellar lipid mixtures

In this section a study of a bicellar lipid system is presented. Additionally to the synchrotron SAXS experiments, FTIR measurements were performed by S. Uelner, a bachelor student working in our group for three months during his thesis.^[324] All results of this investigation including the FTIR data have been published recently in [12].

6.1.1 Introduction

The phase behaviour of a bicellar mixture built by the long-chain lipid DMPC and the short-chain lipid DHPC has been previously investigated in great detail with respect to its dependence on temperature,

lipid ratio and concentration, as well as the influence of various ions (q.v. section 4.2.5, page 51).^[235, 325] Only little is known about the pressure dependent phase behaviour of this lipid mixture, although it has already been used to conduct high pressure NMR experiments.^[243] Just recently, first data have been published, but only for a limited pressure range.^[104, 326]

In order to reveal the pressure dependent phase behaviour of bicellar lipid mixtures as well as to study the phase transition kinetics between the different phases formed by these systems, high pressure synchrotron SAXS as well as high pressure FTIR spectroscopy measurements were carried out on a DMPC/DHPC mixture with a molar ratio of long-to-short-chain lipids, Q , of 3.2 and a total lipid concentration of 15 %_{wt}. The data allowed the construction of a temperature-pressure phase diagram of the system, which made it possible to study the pressure dependent properties of membrane-associated processes at high pressure conditions; for example the structure, dynamics and function of membrane proteins under high hydrostatic pressure as encountered in deep sea environments.^[327, 328] To additionally reveal the kinetics and mechanisms of the underlying phase transitions, the pressure-jump relaxation technique in combination with time-resolved synchrotron small-angle X-ray scattering (trSAXS) was used.

6.1.2 Materials and methods

Materials

1,2-Dihexanoyl-*sn*-glycero-3-phosphocholine (DHPC) and 1,2-dimyristoyl-*sn*-glycero-3-phosphocholine (DMPC) were purchased as lyophilised powders from Avanti Polar Lipids (Birmingham, AL) and used without further purification. The DMPC/DHPC mixture was prepared from stock chloroform solutions with a molar ratio Q of 3.2. Afterwards, the chloroform was removed via evaporation with dry nitrogen purging. Residual amounts of chloroform were removed by lyophilisation for 24 h. The lipid dispersion was prepared by dissolving the required amount of lipid in ultrapure water for the SAXS and in filtered D₂O for the FTIR spectroscopic measurements, yielding a total concentration of 15 %_{wt}. Subsequently, nine freeze-thaw cycles were conducted to homogenise the sample.

Synchrotron small-angle X-ray scattering

The SAXS experiments were carried out at the high brilliance beamline ID02 at the European Synchrotron Radiation Facility (ESRF, Grenoble, France).^[66] The medium X-ray energy was 16.5 keV, corresponding to a wavelength, λ , of 0.751 Å. The sample-detector distance was 1.56 m, and the sample exposure time was – depending on the phase state of the sample – between 0.05 s and 1 s. The measurements were performed in a home-built high pressure X-ray sample cell that is specified for pressures up to 4000 bar (400 MPa) and temperatures up to 75 °C. Briefly, the cell is made from a stainless steel Ni-Cr-Co alloy of high tensile strength (NIMONIC 90) and equipped with flat diamond windows of 1 mm thickness. Pressure-jumps were achieved in about 5 ms using pneumatic high pressure valves. Further technical details are described by Kraineva et al. [68]. The beamline shutter triggers the electronics controlling the valves to synchronise the pressure-jump and data acquisition.

The plots of the diffraction intensity versus the magnitude of the scattering vector were recorded using MATLAB based software, written by the ESRF staff. For the SAXS measurements, a total of 25 µl of the sample was filled into the high pressure sample cell and pressure-cycled several times between atmospheric pressure and 2.5 kbar for equilibration and homogenisation. The temperature-dependent measurements

at atmospheric pressure were conducted between 6.5 and 61.2 °C (accuracy: ± 0.2 °C) in temperature steps of 3.5 °C. The temperature equilibration time before each measurement was 10 min. The pressure dependent static measurements were performed at 61.2 °C. The maximum pressure applied was 3000 bar. Measurements were performed at steps of 100 bar in the upward and downward direction.

The pressure-jumps were performed by computer-controlled opening of an air operated valve between the high pressure cell and a liquid-reservoir container. With the pressure-jump apparatus used, rapid (< 5 ms) and variable-amplitude pressure-jumps are possible. For the time-resolved pressure-jump experiments, 80 images were taken (30 images every 0.25 s after the pressure-jump, followed by 30 images every 1 s and finally at least 20 images every 5 s).

Lamellar lattice constants, d , were calculated from the low-angle Bragg reflections using Bragg's law (q.v. section 2.8.2, page 18). The kinetics were analysed by comparing the root mean square deviation (RMSD) of each scattering pattern taken during a pressure-jump experiment with the last one of the series. The maximum of the intensity difference was set to 100 %, and the resulting curves were fitted to a multiexponential function to yield the time constants of the kinetic processes.

FTIR spectroscopy

The temperature-dependent measurements were performed¹ between 7 and 80 °C in steps of 1 °C using a Nicolet 5700 FTIR spectrometer. The applied mercury MCT (HgCdTe) detector was cooled with liquid nitrogen. 20 μ l of the sample were filled between CaF₂ windows, which were separated by a 50 μ m thick Mylar spacer. For temperature regulation, the cell was placed in a thermostatised jacket with internal temperature measurement. An external water bath was used for temperature control (accuracy: ± 0.2 °C). The sample chamber was purged constantly with dry air. 256 spectra were accumulated between 4000 and 1100 cm^{-1} to obtain accurate peak positions and to minimise spectral noise (spectral resolution: 2 cm^{-1}). Apodisation was done with a Happ-Genzel function. The temperature equilibration time before spectra recording was 6 min. Peak positions were determined with two significant digits with OMNIC 7.2 spectral processing software.

The pressure dependent measurements were conducted in a Nicolet MAGNA 550 spectrometer at six different temperatures between 20 and 65 °C. As the pressure cell, a P-series diamond anvil cell with type IIa diamonds from High Pressure Diamond Optics (Tucons, USA) was used, and a pressure range up to 10 kbar (1 GPa) was covered. A 50 μ m thick gasket of stainless steel with a 0.45 mm drilling was placed between the two diamonds holding several microliters of the sample. The final volume in the closed cell was approximately 10 nl. Pressure was determined with BaSO₄, which shows a characteristic pressure sensitive symmetric sulfate stretching mode around 983 cm^{-1} that increases almost linearly with pressure (accuracy: 200 bar).^[68] Spectra were recorded from 4000 to 650 cm^{-1} . Temperature control was achieved via an external water bath while the temperature was measured internally with a digital thermometer (accuracy: ± 0.5 °C). All other technical parameters were identical to those used in the temperature-dependent measurements.

The kinetic FTIR spectroscopic experiments were performed using the same spectrometer, which was used for the pressure dependent measurements. To optimise the time-resolution, but still be able to obtain accurate peak positions, only 3 spectra were summed up (spectral resolution: 2 cm^{-1}), yielding an effective time-resolution of 3.5 s/spectrum.

¹All FTIR experiments were planned together with Sebastian Uelner, a Bachelor student in our group. Sebastian performed the actual experiments and the deconvolution of the spectra. Parts of the FTIR data have already been presented in his bachelor thesis.^[324] Here, they are discussed in the context of the scattering data.

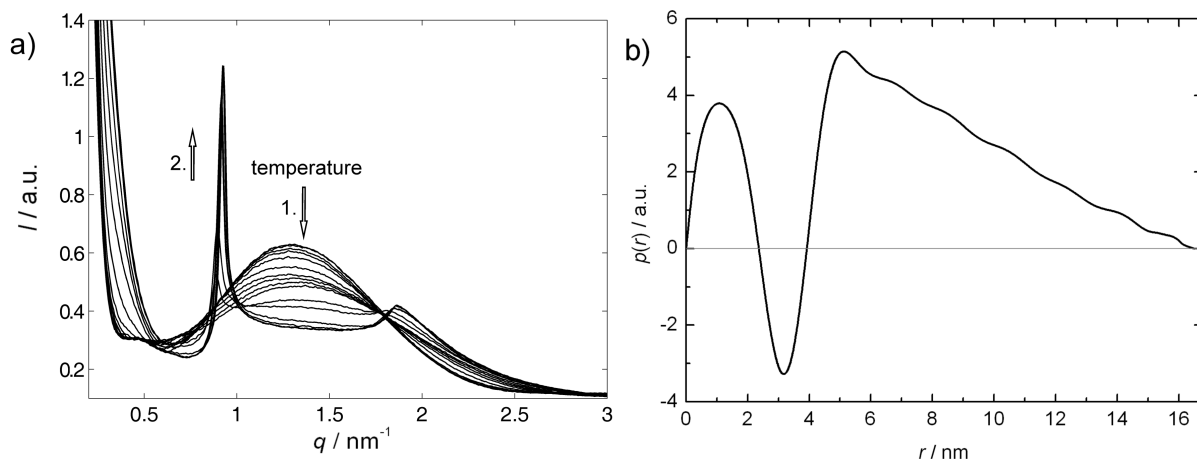


Figure 6.1: a) Small-angle X-ray scattering patterns of the lipid mixture DMPC / DHPC (3.2:1; 15%_{wt} lipid content in pure water) between 6.0 and 61.9 °C at 1 bar. With increasing temperature first the correlation peak at $q \approx 1.35 \text{ nm}^{-1}$ broadens and decreases in intensity during the transition from the bicellar into the nematic phase (arrow 1) and finally the system transforms into the lamellar phase showing two distinct Bragg peaks at high temperatures (arrow 2). b) Pair distance distribution function, $p(r)$, calculated from the scattering curve of the bicellar phase at 9 °C and atmospheric pressure.

6.1.3 Results of the static measurements

Figure 6.1a shows the small-angle X-ray scattering patterns of the system DMPC / DHPC (3.2:1; 15%_{wt} lipid content in water) in a temperature range from 6 to 62 °C at atmospheric pressure. At temperatures up to 15 °C, a broad distinctive correlation peak with a maximum at $q \approx 1.30 \text{ nm}^{-1}$ is observed. Up to this temperature, the system is in the isotropic bicellar phase, consisting of isotropically distributed disk-like micelles without any significant long-range positional or orientational order.^[235] The maximum of the broad correlation peak, which is typical for this bicellar phase,^[60, 237, 329] can be related to an intraparticle separation distance of 4.82 nm, representing essentially the thickness of the lipid bilayer that is mostly built up by DMPC.

Figure 6.1b depicts the pair distance distribution function, $p(r)$, calculated from the scattering intensity, $I(q)$, of the bicellar phase at 9 °C. The maximum size, D_{max} , of the bicelles in solution was determined to 16.5 nm and the radius of gyration was calculated from the $p(r)$ -function to be 5.82 nm. The $p(r)$ -function displays two distinct maxima and a marked minimum with negative values. The first maximum is found at a distance, r , of 1.13 nm, representing the average distance of nearest neighbouring head groups in the closely packed bilayer. The maximum appearing at 5.08 nm can be assigned to the distance between head groups of the opposing monolayer sheets. The dip between 2.3 nm and 4.0 nm with negative values of $p(r)$ is associated with the middle of the lipid bilayer region. The negative values of $p(r)$ can be explained by the difference in the average electron density of the different parts of the bilayer system. While the lipid head groups have a significantly higher electron density than the surrounding solvent, in this case pure water, the hydrocarbon chains of the lipids have a slightly lower electron density. Hence, this difference in the algebraic sign of the electron density contrast to the water can lead to negative values in the pair distance distribution function.^[18] In another study of a bicellar mixture with a nearly identical lipid ratio of $Q = 2.8$, a very similar $p(r)$ -function has been found, but with a slightly smaller maximal size of the particles of $D_{\text{max}} = 11.2 \text{ nm}$.^[237]

Between 15 and 25 °C, a continuous transition to the nematic phase containing elongated flexible worm-like micelles is observed.^[234, 236] In this temperature range, a broadening and a slight shift of

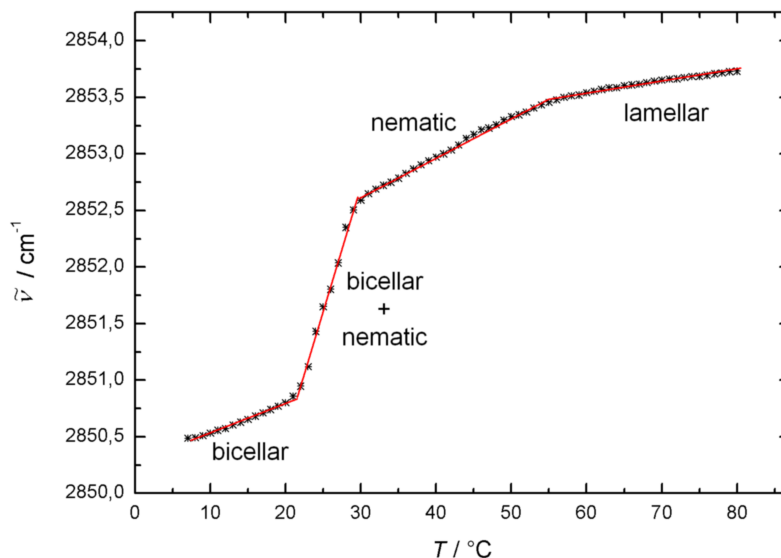


Figure 6.2: Wave number of the symmetrical CH_2 -stretching mode of the bicellar mixture DMPC / DHPC (3.2:1 molar ratio) as a function of temperature. Phase changes are indicated by changes in the slope.^[68]

the correlation peak to approximately $q = 1.38 \text{ nm}^{-1}$ is observed, representing an average distance of 4.55 nm between the lipid head groups in the elongated, quasi-cylindrical micelles.^[238] The absence of any sharp Bragg peaks indicates the absence of long-range positional order also in this phase.

Finally, at temperatures above about 49 °C, Bragg reflections corresponding to stacked lamellar bilayers are emerging, indicating the formation of multilamellar vesicles. These vesicles have been found to consist of lamellar layers containing pore-like defects with high concentration of short-chain DHPC at the rims,^[235] thus allowing diffusion of water into the spaces between the different stacked layers. Up to approximately 57 °C, a two-phase coexisting region of lamellar and nematic phase is observed. The lamellar Bragg reflection at 49 °C appears at $q = 0.885 \text{ nm}^{-1}$, corresponding to a d -spacing of 7.10 nm. With increasing temperature, the lamellar lattice constant, d , shifts to slightly smaller values, reaching 6.87 nm at 62 °C. Please note that the d -spacings comprise the sum of the lipid bilayer thickness and the interlamellar water layer around the lipid head groups ($d = d_{\text{lipid}} + d_{\text{water}}$). The decrease in layer thickness can either be attributed to an increasing number of *gauche*-conformers and kinks in the hydrocarbon chain region or to a thinner water layer between the lamellar sheets. From the position, $q_{\text{max}1}$, and the full width at half maximum, $FWHM_{\text{max}1}$, of the first Bragg peak, the average number of stacked layers, N_{av} , can roughly be estimated using equation 2.39 (page 19).^[60] For a pressure of 3.0 kbar at 62 °C, the average number of ordered stacks in the lamellar phase is at least 30.

Comparing the scattering patterns, $I(q)$, of the system in the bicellar phase at low temperature and low pressure with those taken at high temperature and high pressure, a strong shift of intensity in the low q -region towards smaller q -values is observed, whereas the correlation peak at $q \approx 1.3 \text{ nm}^{-1}$ is barely affected. This shift of intensity can be attributed to a growing size of the bicelles in solution with increasing pressure, whereas the thickness of the bicelle is hardly affected by pressure.

Temperature dependent FTIR spectroscopic measurements of the system DMPC / DHPC (3.2:1; 15 %_{wt} lipid content in D_2O) were performed between 7 and 80 °C in steps of 1 °C. To reveal changes in the hydrocarbon chain region of the lipid, the symmetrical CH_2 -stretching mode at approximately 2850 cm^{-1} was analysed. The position of this band is sensitive to the ratio of *gauche*- and *trans*-conformers in the alkyl chains. Phase changes are indicated by changes in the temperature- or pressure-dependence of the

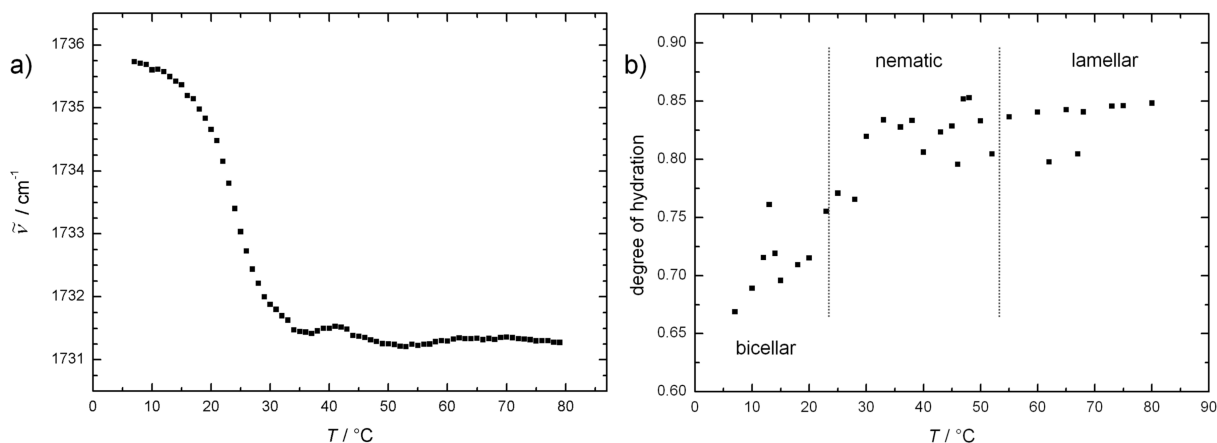


Figure 6.3: a) Temperature dependence of the wave number of the symmetrical carbonyl stretching mode of the bicellar mixture DMPC / DHPC (3.2:1 molar ratio). b) Relative degree of hydration of the lipid head groups as a function of temperature.

slope of this band.^[330, 331] The position of the peak maximum as a function of temperature is shown in Figure 6.2. At low temperatures, a linear increase of the maximum's wave number is observed up to 21 °C, representing the bicellar lipid phase, which is followed by a much steeper and again linear increase up to 30 °C. In this two-phase region, the conversion from the bicellar to the nematic phase takes place. Phase transitions were determined by changes in the slope of $\tilde{\nu}_{\text{CH}_2}(T)$. The kink at about 54 °C can be attributed to the phase transition from the nematic to the lamellar phase. The large increase in the wave number of the symmetrical stretching mode in the two-phase region between the bicellar and nematic phase indicates a drastic decrease of conformational order, i.e. increase of *gauche*-conformers and kinks. In the nematic as well as in the lamellar phase, the order parameter of the acyl chains decreases still slightly with increasing temperature.

Information about the lipid head group region can be gained by investigating the characteristics of the carbonyl stretching mode appearing at around 1730 cm^{-1} .^[330, 331] Figure 6.3a displays the temperature dependence of its peak maximum. Again, at the phase transition from the bicellar to the nematic phase a large wave number shift is observed. Information about the hydration of the lipid head groups can be derived by deconvolution of the carbonyl band. This carbonyl stretching mode consists of at least two subbands, one at 1744 cm^{-1} originating from non-hydrated lipid head groups and another at 1730 cm^{-1} resulting from hydrated head groups.^[330, 331] A third band with a maximum at even lower wave numbers may have to be taken into consideration in cases where multiple hydrated lipid head groups are present. In our case, the carbonyl stretching band could be fitted with high precision by using only the first two carbonyl bands appearing at 1744 and 1730 cm^{-1} , respectively. The intensity ratio of these two bands provides a semi-quantitative measure of the lipid head group hydration^[330] and is depicted in Figure 6.3b. At low temperatures, the hydration level of the lipid head groups in the bicellar phase is around 65 %. In the temperature range of the phase transition into the nematic phase between about 20 and 30 °C, the hydration of the lipids increases steadily by 10 % up to approximately 75 % of its maximum value. At the transition from the nematic to the lamellar phase at 54 °C no significant change in hydration can be observed anymore.

The SAXS patterns of the pressure-dependent measurements at $T = 62^\circ\text{C}$ are plotted in Figure 6.4 for pressures ranging from 1 to 3000 bar (300 MPa). Two phase transitions can be observed with increasing pressure. The lamellar d -spacing of the single lamellar phase increases with increasing pressure from 6.95 nm at atmospheric pressure to a final value of 7.13 nm at 1.0 kbar. In the pressure range from

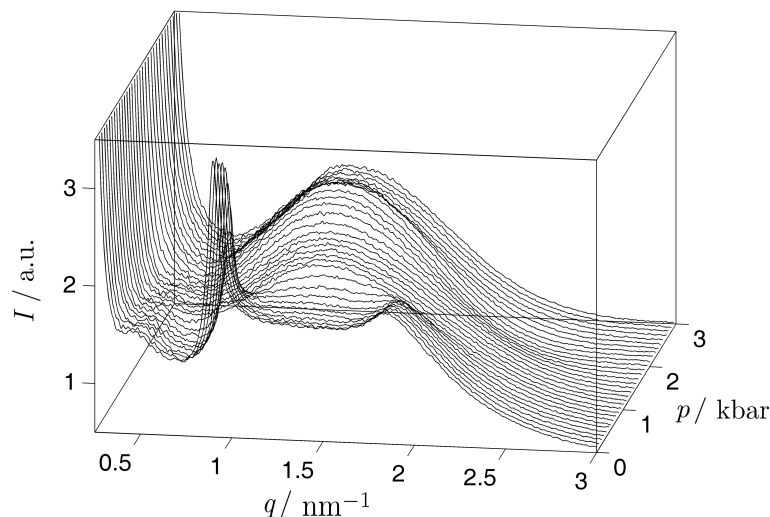


Figure 6.4: Pressure dependence of the small-angle X-ray scattering patterns of the lipid system DMPC/DHPC (3.2:1) at 61.9 °C.

0.5 to 1 kbar, the lamellar phase transforms to the nematic phase, which is indicated by the continuous decrease of the intensity of the Bragg peak and concomitant increase of the broad correlation peak at $q = 1.39 \text{ nm}^{-1}$ (representing the lipid layer thickness of 4.5 nm in the nematic phase). The nematic phase is stable up to 2.2 kbar. At higher pressures, between 2.2 and 2.6 kbar, a two-phase region is observed, which is followed by the pure isotropic bicellar phase at pressures above 2.6 kbar. In this pressure range, the maximum of the broad peak is found at $q = 1.25 \text{ nm}^{-1}$, corresponding to a lipid bilayer thickness of 5.0 nm.

Applying FTIR spectroscopy, the pressure dependent phase transitions of the lipid system were determined by observing the symmetrical CH_2 stretching mode of the lipid acyl chains at six different temperatures between 20 and 65 °C up to 10 kbar. As an example, Figure 6.5 depicts the symmetrical CH_2 stretching band position in a pressure range up to 9 kbar at 35 °C. At atmospheric pressure, the system is in the nematic phase close to the phase transition into the bicellar phase. The wave number of the stretching mode's maximum in the nematic phase appears at 2853.4 cm^{-1} . Between 0.5 and 1.0 kbar, the wave number decreases significantly to 2851.6 cm^{-1} , indicating formation of the two-phase region of the nematic and bicellar phase. Then, up to 5 kbar, the position of this band increases linearly with rising pressure to a value of 2853.5 cm^{-1} due to pressure-induced elastic repulsive interactions between the acyl chains.^[330] Between 5 and 5.5 kbar, a further change in slope is observed, indicating an additional phase transition into a so far unknown high pressure phase of the system. Also in the pressure dependent FTIR measurements at 20, 40, 60 and 65 °C this transition can be found in a region around 5 kbar. Additionally, the splitting of the CH_2 scissoring mode observed around 5.5 kbar, as described later in the text, indicates a distinct phase change in this pressure region.

Using all data from FTIR spectroscopy and SAXS, a p, T -phase diagram of the system could be established, which is displayed in Figure 6.6. In agreement with Gibb's phase rule, between all one-phase regions an area of phase coexistence is found. The phase boundaries of the lamellar-to-nematic as well as the nematic-to-bicellar transition are essentially parallel to each other, having a Clapeyron slope ($dp/dT = \Delta S/\Delta V$) of 14.5 °C/kbar.

The additional high pressure phase that appears above 4 kbar reveals a non-linear phase boundary, indicating a change in sign of ΔS along the phase transition line. The high wave number of the sym-

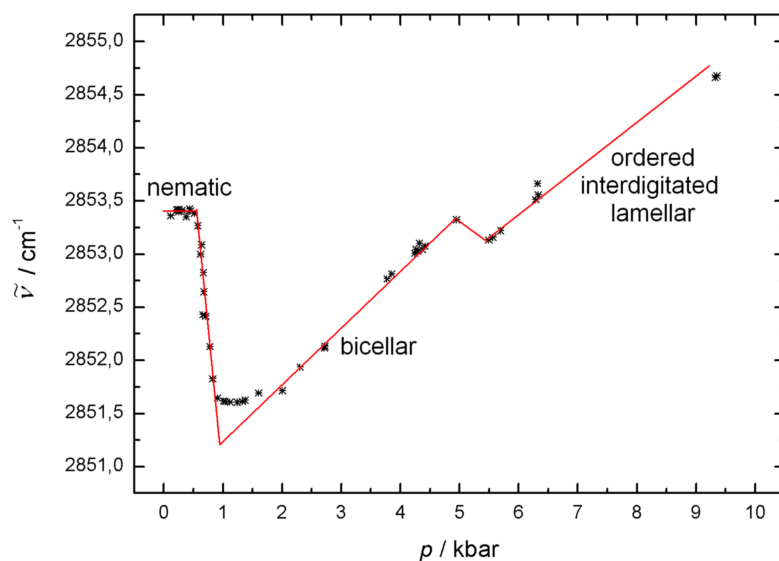


Figure 6.5: Wave number of the symmetrical CH_2 -stretching mode of the bicellar mixture DMPC / DHPC (3.2:1 molar ratio) at 35°C as a function of pressure. Within each lipid phase, the data are fitted with a line.

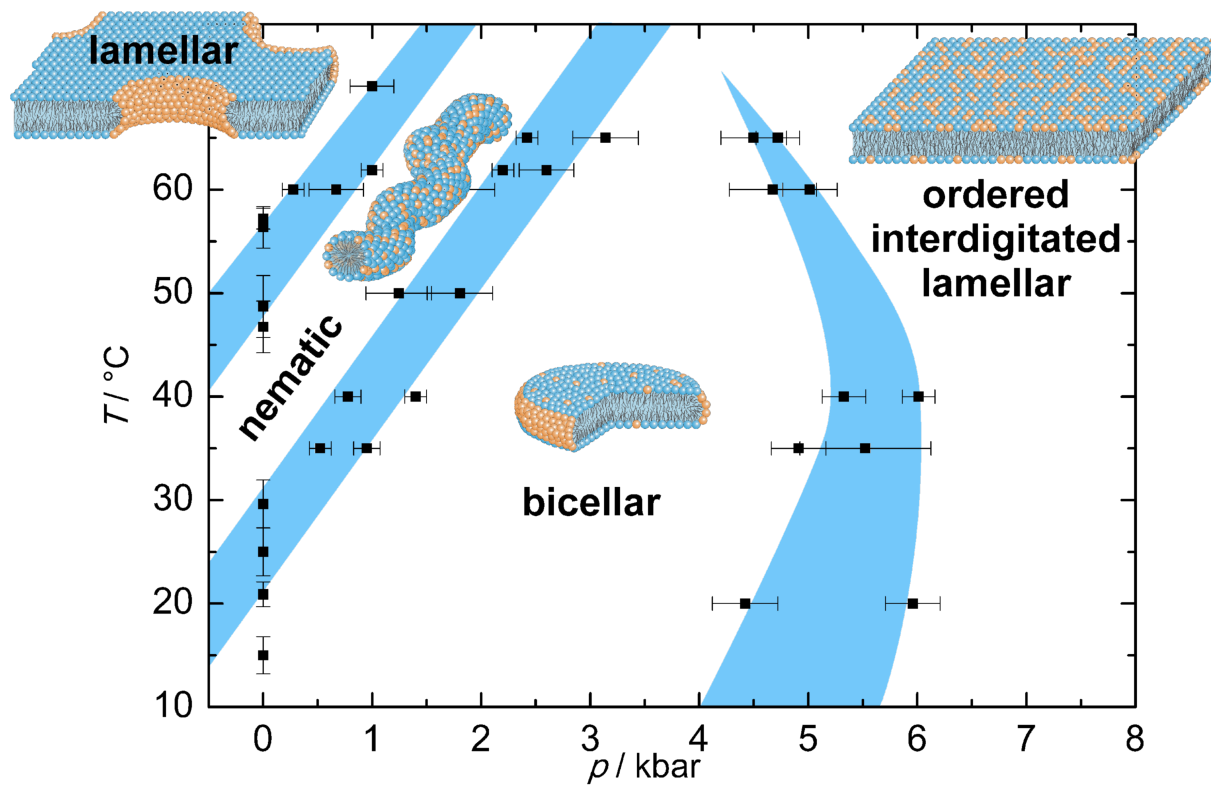


Figure 6.6: p, T -phase diagram of the binary lipid mixture DMPC / DHPC (3.2:1; 15%_{wt} lipid content in water).

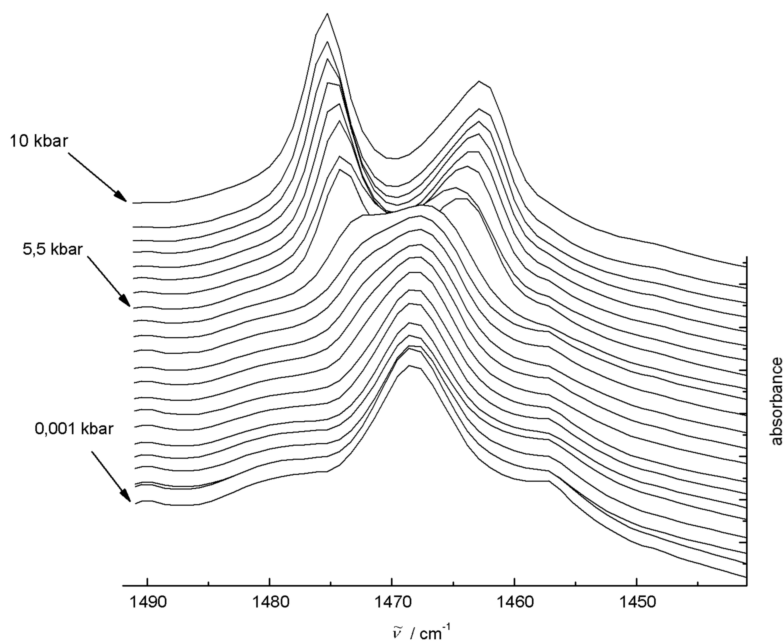


Figure 6.7: CH_2 scissoring mode of the bicellar mixture DMPC / DHPC (3.2:1 molar ratio) at 20°C showing a “correlation field splitting” at elevated pressures.

metrical CH_2 stretching mode of this high pressure phase suggests that the lipids are highly ordered. Additional information can be obtained by examining the CH_2 scissoring mode, which is depicted as a function of pressure at $T = 20^\circ\text{C}$ in Figure 6.7. In the lower pressure range, a single sharp band is detected at 1468 cm^{-1} . At a pressure of 5.5 kbar, this band splits up into two separated bands with maxima appearing at 1462 and 1475 cm^{-1} , respectively. This phenomenon, which is called “correlation field splitting”, is caused by a strong intermolecular coupling of oscillating modes between alkyl chains and can only be observed for a highly ordered membrane with all lipids in the all-*trans* conformation.^[203, 332] Lipid systems with pronounced conformational disorder and high orientational fluctuations do not show a correlation field splitting. High pressures can suppress such fluctuations, leading to a highly ordered gel-like packing of the all-*trans* acyl chains and hence to the correlation field splitting observed here. The correlation field splitting is observed for all temperature-pressure conditions where the phase boundary to this high pressure phase is passed.

The SAXS measurements revealed a continuous increase of the size of the bicelles with increasing pressure up to the phase transition to the new high pressure phase. Generally, an increase in pressure leads to an increase of the chain order parameter and hence length of the acyl chains, thus disfavoring formation of disordered rim regions. Hence, with increasing diameter of the bicelle, the ratio of rim (which is rich in DHPC) and bilayer area of the bicelle decreases with increasing pressure, forcing more and more DHPC molecules into the flat bilayer region. Approximately 24% of the lipids in the system are short-chain DHPC with chains six hydrocarbon units smaller than those of DMPC. Such a drastic mismatch of the hydrocarbon chain length would be energetically highly unfavorable. Hence, a negative ΔV and efficient packing can only be achieved by partial interdigitation of the hydrocarbon chains. In fact, the correlation field splitting observed is typical for a phase transition into a highly ordered interdigitated lipid phase.^[203, 333] Such interdigitated lipid phases with nonlinear phase transition slopes have also been observed for one-component lipid dispersions, such as DPPC.^[104, 203, 333] Different from non-interdigitated lamellar phases, the correlation field bands for interdigitated lipid systems exhibit similar intensities as observed here (q.v. Figure 6.7).^[334]

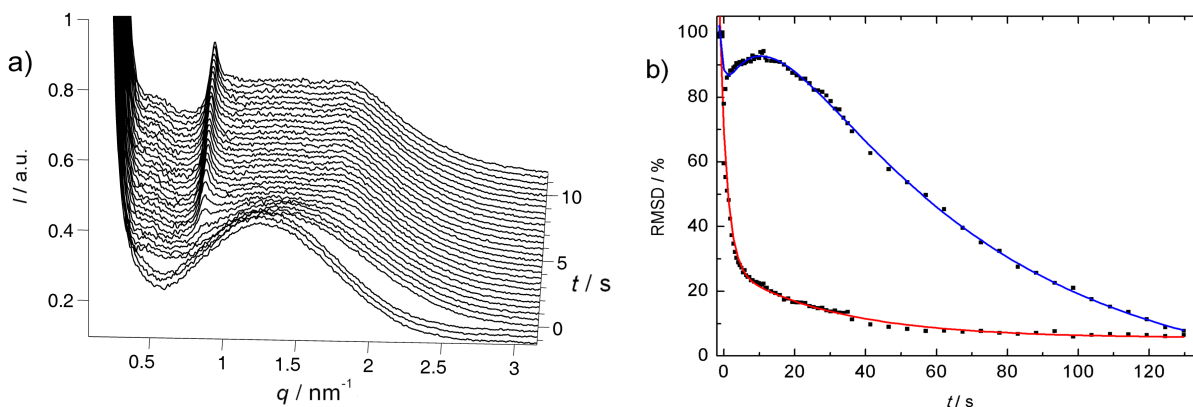


Figure 6.8: a) Diffraction patterns of the lipid mixture DMPC/DHPC (3.2:1) during a pressure-jump from 2.60 to 0.42 kbar (bicellar to lamellar) at $T = 61\text{ }^{\circ}\text{C}$ (raw data; the pressure-jump was triggered at $t = 0\text{ s}$). b) Comparison of the RMSD of the SAXS scattering intensity from the final scattering pattern in the pressurising direction (lamellar to bicellar phase, 0.50 to 2.35 kbar, fit in blue) and in the depressurising direction (bicellar to lamellar phase, 2.60 to 0.42 kbar, fit in red).

By deconvolution of the carbonyl stretching mode, the hydration properties of the head group region can also be determined for the high pressure phases. The head groups in both the high temperature lamellar and the nematic phase are highly hydrated (around 75%). The level of hydration of the bicellar phase is slightly smaller (65%). As expected, the lowest hydration of approximately 50% is found in the highly ordered pressure-induced interdigitated lamellar phase. Within a single-phase region, the hydration properties do not change significantly with changing pressure or temperature.

6.1.4 Results of the pressure-jump induced trSAXS measurements

The bicellar \leftrightarrow lamellar phase transition

The trSAXS patterns of a pressure-jump from the bicellar phase with an initial pressure of 2.60 kbar, passing the nematic phase, to the lamellar phase at 0.42 kbar at a constant temperature of $61\text{ }^{\circ}\text{C}$ are depicted in Figure 6.8a. The p -jump is triggered at $t = 0\text{ s}$. The first three scattering patterns were taken before the pressure-jump and show the typical pattern of a bicellar phase. Within the time-resolution of the experiment (0.25 s), the system transforms to the nematic phase, which is only stable for around 0.75 s. Thereafter, a continuous transition to the lamellar phase is observed, indicated by the emerging lamellar Bragg peak. The signal of the nematic phase has vanished completely 3.5 s after the pressure-jump. Upon disappearance of the nematic phase, the intensity of the lamellar Bragg reflection increases and the peak maximum shifts to slightly higher q -values with time. At $t = 1.25\text{ s}$, the position of the maximum is located at 0.86 nm^{-1} , corresponding to a lamellar d -spacing of 7.34 nm. In the last scattering pattern (taken at $t = 130\text{ s}$), the peak maximum appears at $q = 0.90\text{ nm}^{-1}$ according to $d = 7.02\text{ nm}$. These minor changes in d -spacing with time may be due to water diffusion within the newly arranged perforated multilamellar vesicles.

In Figure 6.8b, the root mean square deviation (RMSD) of each scattering pattern from the final one (taken at $t = 130\text{ s}$) is shown and the fit of the time evolution is presented as a red line. A biexponential function describes the time evolution of the RMSD sufficiently well, thus indicating a two-step mechanism of the overall phase transition. The first step, which is barely resolved, is probably due to the actual structural transition of the lipid system including conformational changes of the lipid chains and short-

range reorientations of the lipid molecules. For this process, a decay constant of only about 2 s was determined by the biexponential fit, whereas the second step of the overall transition has a significantly larger time constant of 31 s. This second stage of the phase transition includes probably the relaxation of the mesophase structure, i.e. macroscopic structural reorganisations as well as water diffusion as a consequence of changing levels of hydration of the lipids in the different phases involved.

The corresponding data of a pressure-jump in the opposite, i.e. pressurisation direction from 0.50 kbar to 2.35 kbar (lamellar to bicellar transition) at a temperature of $T = 61\text{ }^{\circ}\text{C}$ are presented in Figure 6.8b as well (fit in blue). In this case, a reasonable fit could only be realised by using a triexponential function. Directly after the pressure-jump, a fast component with a time constant of less than 1 s was observed. In the scattering pattern obtained directly after the p -jump, the Bragg peak vanished and the typical scattering curve of a bicellar phase could be recorded within 0.5 s. Hence it can be concluded that already in the first step of the transition the multilamellar vesicle structure disappears. An intermediate metastable nematic phase could not be detected during the phase transition, which could be observed in the reverse, depressurising direction where the nematic phase was at least stable for 0.75 s. The first step is followed by a second step with a time constant of 14 s. In this period, no significant changes of the scattering patterns could be observed. The final slow third process with a time constant of 55 s is accompanied by a sharpening of the correlation peak of the scattering pattern as well as a shift to slightly smaller q -values. In this time range, reorganisation of the bicellar structure takes place. The long time-scale of this process can probably be attributed to further hindered diffusion of short-chain DHPC to the rim of the bicelles, which is necessary to obtain the final low free energy equilibrium bicellar structure. At the same time, the inter-sheet distances of lipid head groups become more homogeneous as indicated by the sharpening of the correlation peak.

It has to be noted that the transition from the bicellar to the lamellar phase with an overall time constant of 33 s is much faster than the transition in the opposite direction, i.e. from the lamellar into the bicellar phase, which has an overall time constant of 70 s. The DHPC molecules in the lamellar phase are located at the rim of pore-like defects, which are randomly distributed over the whole lipid bilayer area. The large multilamellar vesicles have to segment into much smaller structures during the transition to the bicellar phase, whereupon the ratio of both lipids has to be approximately identical in all newly formed bicelles. Such significant reorganisation and ordering process is likely the reason for the longer time needed for the formation of the bicellar phase. The transition in the opposite direction is probably faster, because no extensive local ordering of the lipid components is needed here, and the newly built pore-like defects can diffuse freely within the lamellar bilayer plane.

The bicellar \leftrightarrow nematic transition

A pressure-jump from 2.60 to 1.35 kbar at $61\text{ }^{\circ}\text{C}$ has been conducted to study the transition from the bicellar to the nematic phase separately. The scattering patterns reveal a direct and continuous transition. The maximum of the correlation peak is shifted during the transition between the bicellar and the nematic phase to slightly higher q -values and the peak broadens concomitantly. The RMSDs could be fitted to a biexponential function, indicating a two step mechanism. The overall transition is rather fast, represented by time constants of 1.5 s and 16.3 s, respectively.

To also reveal conformational changes during the pressure-jump, FTIR spectroscopic measurements were carried out jumping from the bicellar phase at 4.0 kbar to the nematic phase at 1.2 kbar for $T = 60\text{ }^{\circ}\text{C}$. The positions of the peak maxima of the symmetrical CH_2 stretching mode as a function of time reveal that – as expected – all conformational changes in the lipid hydrocarbon chain region occur

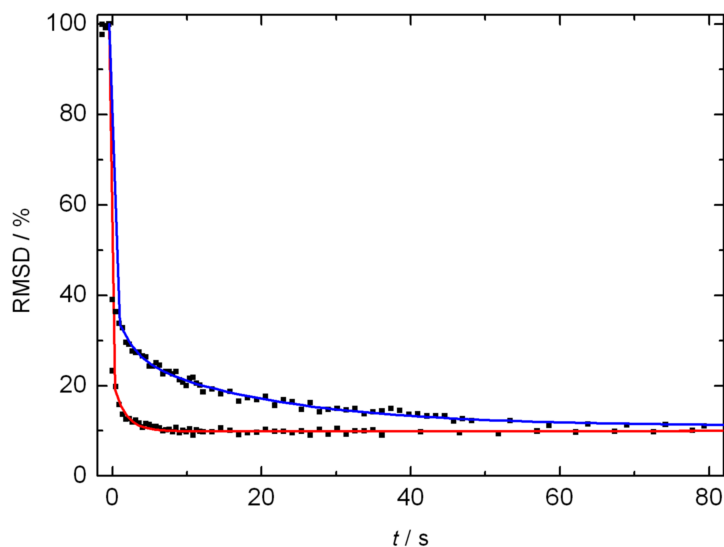


Figure 6.9: RMSDs of the scattering patterns from the final scattering pattern as a function of time after a pressure-jump from 0.55 to 1.35 kbar (lamellar to nematic) of the system DMPC / DHPC (3.2:1) at $T = 61$ °C. Data in pressurising jump direction (0.55 to 1.35 kbar) are presented in red and data in the depressurising direction (1.20 to 0.55 kbar; nematic to lamellar) in blue.

within the time-resolution of FTIR experiment of about 3 s. At the transition, the ordered conformation of the lipid chains in the high pressure bicellar phase gives way to a more disordered state with a higher population of *gauche*-conformers in the low pressure nematic phase. From the observed changes in the carbonyl stretching vibrational region (wave number shift from 1734.4 to 1733.8 cm^{-1}) a concomitant rapid and strong increase of the lipid head group's level of hydration can be deduced. Subsequently, a minor increase of the wave number of this band to 1734.0 cm^{-1} is observed over a period of about 15 s, which is the time range where the structure of the nematic phase still relaxes. During that period also the level of hydration has to adjust, which seems to occur by rather slow water diffusion into the more hydrated nematic phase.

Analysis of the trSAXS data for a pressure-jump into the opposite, i.e. pressurising direction from 1.25 kbar to 2.55 kbar (nematic to bicellar transition), reveals a slower kinetics. The immediate structural change from the nematic to the bicellar phase at the moment of the pressure-jump is followed by a slow shift of the maximum of $I(q)$ as well as a sharpening of the correlation peak. The kinetic data could be fitted using a biexponential function with decay constants of about 1.2 s and 33 s, respectively. Hence, the transition is about a factor of two slower than in the reverse direction.

The nematic \leftrightarrow lamellar transition

To investigate the transition from the lamellar to the nematic phase, a pressure-jump was performed between 0.55 kbar and 1.35 kbar at $T = 61$ °C. Directly after the p -jump, the Bragg peak of the lamellar phase vanishes completely and the transition to the nematic phase is completed within 0.25 s. Figure 6.9 depicts the RMSDs of the scattering patterns from the final one at $t = 80$ s for p -jumps in the pressurising and in the depressurising direction (from 0.55 kbar to 1.35 kbar: lamellar to nematic (red curve), and from 1.2 kbar to 0.55 kbar: nematic to lamellar (blue curve), respectively). The kinetics of the phase transition from the lamellar to the nematic phase is very fast. The fast component of the transition occurs with a time constant of 0.2 s, which is followed by minor structural relaxations and hydrational changes

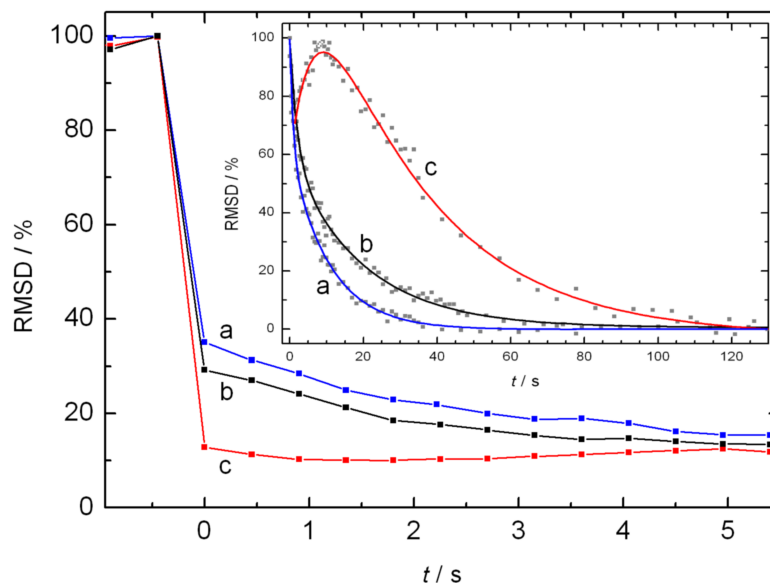


Figure 6.10: RMSDs for the transition from the nematic to the lamellar phase of the system DMPC/DHPC (3.2:1) in the depressurising direction for various p -jump amplitudes: blue curve (a) $\Delta p = 0.325$ kbar; black curve (b) $\Delta p = 0.65$ kbar; red curve (c) $\Delta p = 1.15$ kbar. In the inset only data after the pressure-jump are regarded for the calculation of the RMSDs, highlighting the slow relaxation processes occurring at long time-scales.

with a relaxation time of 1.7 s. Please note that, owing to the large size of the worm-like structures in the nematic phase, additional morphological changes may not be captured by the SAXS technique.

The observed overall kinetics in the opposite, i.e. nematic to lamellar direction, is much slower. For a pressure-jump from 1.20 kbar to 0.55 kbar also a two-step mechanism was found with time constants of 0.2 s and 13.3 s, respectively, i.e. only the second, slower relaxational step is longer.

Finally, the effect of the pressure-jump amplitude on the transition kinetics was explored. Figure 6.10 shows the RMSDs of the first seconds for the transition from the nematic to the lamellar phase for different p -jump amplitudes, all in the pressurising direction at $T = 61$ °C. In the inset data for the slower relaxation process are shown only taking data after the pressure-jump ($t > 0$ s) into account for the calculation of the RMSD. The blue graph (a) represents data for the smallest p -jump amplitude, $\Delta p = 0.32$ kbar (1.00 - 0.68 kbar), the black curve (b) the data for a medium pressure amplitude, $\Delta p = 0.65$ kbar (1.20 - 0.55 kbar), and the red one (c) data for $\Delta p = 1.15$ kbar (1.40 - 0.25 kbar). With increasing p -jump amplitude, the rate of the first rapid process increases, i.e. the time constant decreases from 0.26 s to 0.15 s upon increasing Δp . All scattering patterns display the lamellar Bragg reflection already in the first scattering pattern taken after 0.25 s. Conversely, the rate of the second, slower structural relaxation process decreases with increasing Δp : the overall time constant increases from 7.4 s to 26.8 s for the largest p -jump amplitude.

The rate of the first, rapid structural phase transition step increases with Δp as the change in chemical potential between the different phases, and hence the driving force of the process, increases concomitantly. In terms of volume changes, an increase of the transition rate, k , would be due to a negative activation volume, $\Delta V^\ddagger < 0$, as $k(p) \propto \exp(-p\Delta V^\ddagger/RT)$. The activation volume can generally be interpreted as the difference in volume between the transition state and the volume of the initial state at the same pressure. Hence, ΔV^\ddagger can be thought of as a mechanic (elastic) barrier to transformation, in much the same way as the activation enthalpy ΔH^\ddagger for a reaction is thought of as a thermal energetic barrier to

the reaction. Regarding the slower component that involves regular pore formation within the lamellar bilayer structure as well as water diffusion into or out of the various phase regions (which often represents the kinetic trap of lipid mesophase transitions^[68, 105, 106, 335]), a different scenario is observed. For the large pressure-jump amplitudes, the difference in the level of hydration between phases becomes more pronounced, which may also lead to the slower relaxation times observed.

Interestingly, whereas in the scattering patterns for the p -jumps with low and medium pressure amplitude a sharpening and an increase in the Bragg peak intensity is observed with time, for the p -jump with the highest amplitude, a more complex kinetic behaviour is found: Immediately after the p -jump the typical scattering pattern of a lamellar phase is detected. Within the first 7 s, the intensity of the Bragg reflection decreases slightly and there is a small shift of the peak maximum to smaller q -values. Thereafter, the intensity of the reflection increases, the position of the maximum shifts to higher q -values again, and a significant sharpening of the Bragg peak is observed, indicating a more ordered lamellar packing within the vesicular assembly. This more complex kinetic behaviour might be related to far out-of-equilibrium processes induced by the larger Δp . During the relaxation process in the lamellar phase, formation of pore-like defects and the diffusion of water out of the newly formed vesicles is necessary. To build these pores and allow for efficient water diffusion, the DHPC molecules have first to segregate and arrange. Hampered water flow due to the absence of the pore-like defects in the initial stage directly after the p -jump may lead to the greater disorder and initial swelling of the newly formed multilamellar vesicles, resulting in a decreased intensity of the Bragg reflection and its shift to lower q -values. As soon as these pores are formed, water can rapidly exit the swollen (multilamellar) vesicles, the d -spacing decreases as indicated by the shift of the Bragg peak to larger q -values, and the multilamellar structures become more ordered, leading to the observed sharpening of the Bragg reflections.

6.1.5 Conclusions

By varying the pressure and temperature in the static SAXS and FTIR spectroscopic measurements, valuable structural information about the different phases formed by the system DMPC / DHPC (at molar ratio $Q = 3.2$, lipid concentration 15 %_{wt}) was obtained over a wide range of temperatures and pressures. For the bicellar phase existing at low temperatures up to 15 °C at atmospheric pressure, the SAXS data revealed a bicelle diameter of nearly 16.5 nm with a radius of gyration of 5.82 nm. The distance between the head groups of the opposing layer sheets is 4.82 nm at atmospheric pressure and grows with increasing pressure to 5.03 nm. A distinct minimum in the pair distance distribution function at distances between 2.3 and 4.0 nm confirms the bicellar shape of the aggregates. The FTIR spectroscopy data showed a low population of *gauche*-conformers in the lipid hydrocarbon chain region, revealing a gel-like character of the lipid packing. This results in a rather low level of hydration of the lipid head groups (about 65 % relative to full hydration of the lipid head groups).

The association of the bicelles in the nematic phase occurs at temperatures around the main transition of pure DMPC, i.e. at $T \approx 24$ °C. The spectroscopic data revealed a significantly higher population of *gauche*-conformers and kinks in the lipid chain region, leading to an increased flexibility of the fluid lipid bilayer compared to the essentially rigid all-*trans* conformation in the bicellar phase. This transition is accompanied by an increased hydration (75 %), a larger chain cross-sectional area and a concomitant decrease of the acyl-chain length of DMPC, thus reaching the geometrical requirements needed for the formation of the nematic phase. The decrease in thickness by 0.27 nm can mainly be attributed to the increased disorder of the lipid chains. With increasing pressure, no significant change in the bilayer thickness has been found.

In the bicellar phase, most of the short-chain DHPC molecules are located at the rim of the bicelle, whereas the long-chain DMPC forms the highly ordered lipid bilayers of the bicelle. By building elongated structures in the nematic phase, which are several-fold longer than the bicelles, the rim-to-plane-area ratio decreases significantly. This forces a part of the DHPC into the ordered lamellar planes, thus leading to the transition from flat bicelles to worm-like micelles in the nematic phase. It has been discussed that the release of DHPC from the mixed-lipid aggregates into solution may play an important role in the phase behaviour of bicellar mixtures. Even though the critical micellar concentration (cmc) is rather high with values of 5.2 to 7.2 mg/ml, the fraction of monomeric DHPC in solution would be rather small compared to the overall lipid concentration. Additionally, the cmc is nearly independent of the temperature of the system.^[238] Therefore the phase transition cannot be attributed to the temperature dependent solubility of DHPC in water.^[234, 238]

At high temperatures above 50 °C, a lamellar phase was detected in the SAXS scattering patterns with a lamellar repeat distance, d , of 6.9 nm at atmospheric pressure, which includes the thickness of the lipid bilayer as well as a water layer in the bilayer interspace. The d -spacing increases with increasing pressure, reaching 7.1 nm at $p = 1.0$ kbar. FTIR spectroscopic measurements revealed no drastic differences in the lipid's hydrocarbon chain order and hydration compared to the nematic phase. All phase transitions of this system are fully reversible and no hysteresis could be observed in the static experiments or during the kinetic pressure-jumps.

It has been shown that the fraction of time spent by a DHPC molecule in the DMPC-rich bilayer environment generally increases with increasing temperature.^[326] Such increasing homogeneous mixing of the lipid components induces the growth of the aggregates in the nematic phase, finally leading to a critical bilayer size, where the planar lipid layers spontaneously collapse into vesicles. Our data also show that there are no major changes in the lipid order parameter and level of hydration of the head group region at the phase transition from the nematic to the lamellar phase.

Figure 6.6 depicts the p, T -phase diagram of the bicellar system studied. Interestingly, a new lamellar phase has been found that appears only under high pressure conditions (above 4 kbar) over the whole temperature range covered. The FTIR spectroscopic data indicate an essentially all-*trans* conformation of the lipid hydrocarbon chains and a very low hydration of the lipid head groups (50 %) due to the tight and largely curvature-free packing of the lipid chains in this bilayer phase. The severe hydrophobic mismatch between the DMPC and DHPC molecules, the negative volume change as well as the correlation field splitting of IR bands observed point to an interdigitation of the crystalline hydrocarbon chains in this lamellar phase. So far, pressure-induced interdigitated lamellar phases have only been observed in one-component phospholipid dispersions (e.g. for DPPC, DSPC).^[3, 105, 333, 334] According to the Clapeyron equation, the bicellar-to-interdigitated lamellar phase transition at low temperatures is accompanied by a decrease in conformational entropy, i.e. $\Delta S < 0$ (as ΔV is always < 0). The change in slope at high temperatures must be due to a change in the sign of ΔS . Positive ΔS values could be due to an increase in the mixing entropy at high temperatures, where the molecular disorder becomes increasingly important.

Conversely, the slope of the phase boundaries between the lamellar and nematic as well as between the nematic and bicellar phases of about 14.5 °C/kbar are essentially linear and in good agreement with reported data and within a range that is typically found for transitions between lamellar phases in phospholipid systems.^[3, 11, 104–106, 334–336] With increasing pressure, the line tension at the rim of the pore-like defects in the lamellar phase increases due to the pressure-induced increase in the order parameter and decrease in flexibility of the acyl chains, thus rendering the nematic phase more stable. The same reason holds probably true for the nematic-to-bicellar as well as the bicellar-to-interdigitated

phase transition occurring at higher pressures – no easy adjustment of the lipid lengths (in particular at the rim of the bicelles) is possible anymore, and only minimal ΔV values can be achieved for ordered lamellar structures. The increase in bending energy upon vesicle formation does not seem to play a major role here.

The kinetics of all phase transitions of the system is complex and consists of at least two steps. The first step is likely due to conformational changes of the lipid hydrocarbon chains and short-distance reorientations of the lipid molecules. This step proceeds within the first few seconds of the transitions and is followed by a much slower second stage of the overall phase transition. The second stage includes relaxation of the topology of the mesophase structure as well as water diffusion as a consequence of changes in the hydration level of the lipid head groups in the various phases. Depending on the lipid phases involved, the direction of the pressure-jump and the pressure-jump amplitude, this kinetic trapping lasts for a few seconds up to a maximum of two minutes. Remarkably, the overall kinetics of the phase transitions in the system DMPC / DHPC is fast compared to many lamellar-to-cubic phase transitions and in the same time window as interlamellar phase transitions of more-component phospholipid systems.^[11, 68, 104, 225] This indicates the absence of major free energy barriers as they are often observed for lamellar-to-cubic mesophase transitions.

6.2 Influence of ergosterol on the phase behaviour of DPPC

The study presented in this section was conducted in cooperation with another PhD-student from our group, M. Pühse, who measured Fourier transform infrared (FTIR) spectroscopy. Here, the focus will be on the small-angle X-ray scattering data. Details about the FTIR measurements can be found in the PhD thesis of M. Pühse^[337] or in the paper written about this project, [336]. Additionally, the SAXS data were also part of another investigation, studying composition fluctuations near critical points in the phase diagrams of phospholipid / sterol mixtures mainly by neutron and X-ray small-angle scattering. For details the reader is advised to the corresponding paper, [338].

6.2.1 Introduction

The phase behaviour of the binary lipid mixture 1,2-dipalmitoyl-*sn*-glycero-3-phosphocholine (DPPC) / ergosterol (78:22 molar ratio) was investigated as a function of temperature and pressure using small-angle X-ray scattering (SAXS) and Fourier transform infrared spectroscopy (FTIR). A temperature range of 10 to 70 °C and a pressure range up to 4 kbar by SAXS and 8.5 kbar by FTIR was covered to establish a p, T -phase diagram of this model mixture of a fungal plasma membrane. The results show a liquid-ordered / solid-ordered ($l_o + s_o$) two-phase coexistence region up to 41 °C, followed by a liquid-disordered / liquid-ordered ($l_d + l_o$) coexistence region up to 57.5 °C, giving way to an all-fluid l_d phase at higher temperatures. With increasing pressure, all phase boundaries shift to higher temperatures. The width of the raft-like $l_d + l_o$ two-phase coexistence region is found to be about 2 kbar over the whole temperature range covered. At higher pressures, the transitions to an $l_o + s_o$ two-phase region and, at still higher pressures and low temperatures, an all-ordered s_o phase is detected. Finally, the biological (high pressure-induced upregulation of ergosterol synthesis) and biotechnological (inactivation of fungal microorganisms) relevance of these studies is discussed. The results may be particularly interesting for understanding the function of membrane proteins under external stress conditions, such as high pressure.

The results of this investigation lead to a better understanding of fungal membrane structure and stability under high hydrostatic pressure conditions, as well as to a better understanding of the conditions needed for safe sterilisation of products from fungal contaminations.

6.2.2 Materials and methods

Materials

1,2-dipalmitoyl-*sn*-glycero-3-phosphocholine (DPPC) and ergosterol were purchased from Avanti Polar Lipids (Birmingham, AL) and used without further purification. The DPPC / ergosterol mixture (78:22 molar ratio) was prepared by dissolving the corresponding amounts in chloroform. Afterwards, the chloroform was removed via evaporation with dry nitrogen purging. Residual amounts of chloroform were removed by lyophilisation for 48 h. Lipids were dissolved in 10 mM Tris-buffer (pH 7.2 in H₂O), yielding a 10%_{wt} dispersion, which was homogenised afterwards. Subsequently, eight freeze-thaw cycles were conducted to homogenise the sample, yielding well-hydrated homogeneous multilamellar vesicle dispersions.

Synchrotron small-angle X-ray scattering

The SAXS experiments were performed at the high brilliance beamline ID02 at the European Synchrotron Radiation Facility (ESRF) in Grenoble, France.^[66] The medium X-ray energy was 20.42 keV, corresponding to a wavelength of 0.606 Å. 25 µl of the sample were placed in the high pressure X-ray sample cell, which was equipped with diamond windows. Further technical details are described by Kraineva et al., [68].

Lamellar lattice constants, d , were calculated from the low-angle Bragg reflections. To obtain more precise positions of the wave vector's magnitude, s , the raw data were fitted with an overlay of two Gauss-functions and the resultant peak maxima were used. Reflections of first, second and fourth order showed an acceptable intensity, whereas the reflections of third order did not, hence only the diffraction maxima of $n_x = 1, 2, 4$ were considered in the data analysis.

The temperature-dependent measurements at atmospheric pressure were conducted between 25 and 64 °C (accuracy: ± 1.5 °C). Up to 40 °C, measurements were performed in steps of 5 °C and above this temperature every 1 °C. The temperature equilibration time before each measurement was 5 min. The pressure-dependent measurements were performed at 10, 50, and 60 °C. The maximum pressure applied was 3.0 kbar (accuracy: ± 20 bar). Measurements were performed at steps of 0.1 kbar in the upward and downward direction.

FTIR spectroscopy

Details of the FTIR measurements can be found in the corresponding paper^[336] as well as in section 6.1.2 (page 73) describing the same instruments used for another study.

6.2.3 Results

In Figure 6.11, the small-angle X-ray scattering patterns from 25 to 64 °C at atmospheric pressure are displayed. It can be very clearly seen that up to almost 60 °C, two distinct peaks of two coexisting lamellar phases are found, most easily visible in the higher-order reflections. An inspection of the SAXS patterns

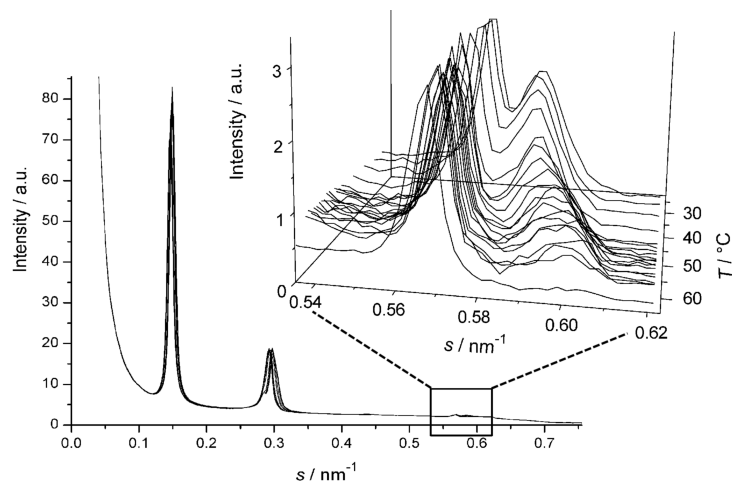


Figure 6.11: Small-angle X-ray scattering patterns of the temperature-dependent measurement of DPPC/ergosterol (22%_{mol}) at atmospheric pressure. The Bragg reflections of $n_x = 4$ are shown as inset, as they provide the best signal separation of the different phases involved. The d -values were calculated using an overlay of two fitted Gauss-functions.

covering the fourth-order Bragg peak clearly reveals the presence of two phases from 25 °C to 58 °C at atmospheric pressure, with peaks located at s -values of about 0.57 nm⁻¹ and 0.59 nm⁻¹, respectively.

The temperature dependence of the corresponding d -spacings as obtained from the well resolved fourth-order diffraction peaks are depicted in Figure 6.12a. The first phase, characterised by the slightly larger d -spacing of about 7.05 nm, exhibits only a minor increase over the whole temperature range studied, i.e. up to 64 °C. Generally, the d -value comprises the sum of the lipid bilayer thickness and the interlamellar water layer thickness. Such a modest increase in d -value could be due to a slight swelling of the interlamellar water layer with rising temperature. The other d -spacing, belonging to the second phase, decreases in a sigmoidal fashion with increasing temperature. At 25 °C, it starts with a value of 6.84 nm and it drops to 6.69 nm at about 58 °C. At higher temperatures, a diffraction peak could not be resolved any more (see inset of Figure 6.11) indicating that this second d -spacing characterises the l_o -phase, which disappears at $T_{\text{crit}} \approx 58$ °C according to the phase diagram by Hsueh et al. [339]. The slightly smaller d -value compared to the one of the l_d -phase could be due to a smaller interlamellar water layer.

Representative results of the pressure dependent measurements of the lamellar d -spacing are shown in Figure 6.13. As in the previous experiments, phase transitions can be obtained from marked changes in the slope of $d(p)$. At 10 °C, only one minor change in the curvature of $d(p)$ may be detected, which appears above 2.6 kbar (Figure 6.13a) and can be assigned to the pressure-induced $l_o + s_o \rightarrow s_o$ transition (a coexistence region of two s_o phases is less probable, as the signal of the phase with higher d -values has almost vanished). The 50 °C experiment (Figure 6.13b) exhibits a phase conversion at 1.1 kbar, where the phase boundary from the $l_o + l_d$ to the $l_o + s_o$ two-phase coexistence region is reached. The increase in d -spacing of the l_o -phase with increasing pressure is probably due to a pressure-induced reduction of *gauche* conformers and kinks in the lipid's hydrocarbon chain region, and the decrease of the $d(p)$ -value in the l_d - and s_o -phases may be due to a compression of the interlamellar water layer with rising pressure. As expected, the pressure dependence of the lattice constant is small and almost linear in an all-ordered lipid state. The pressure dependent SAXS measurements at 60 °C reveal two-phase transformations (Figure 6.13c): At about 0.3 kbar, the $l_d \rightarrow l_d + l_o$ takes place and, according to the Gibbs phase rule, the $l_o + l_o \rightarrow l_o + s_o$ transition at 1.5 kbar. Considering the changes in the d -values, the l_d -phase exhibits a small reduction in lamellar d -spacing of approximately 0.1 nm with rising pressure,

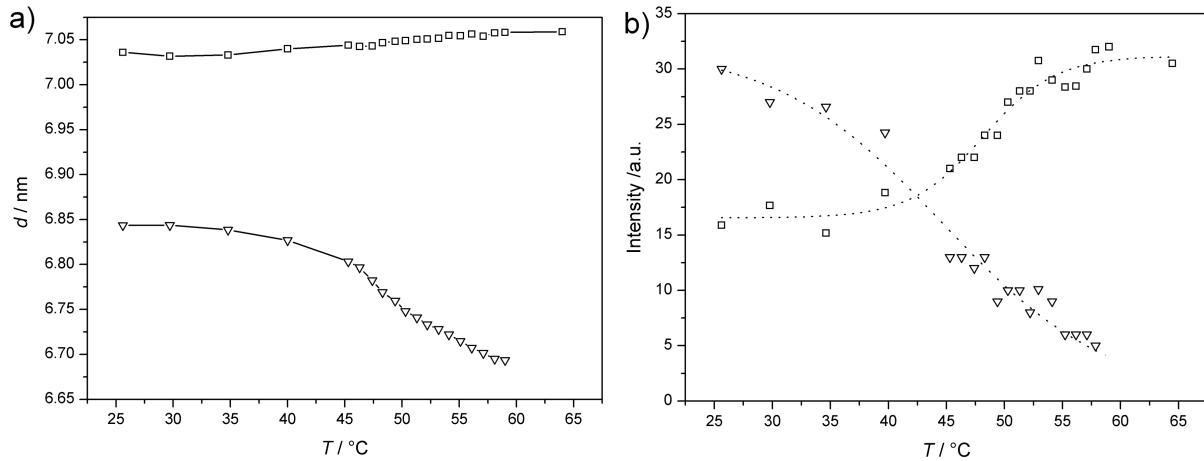


Figure 6.12: Temperature dependence of the lamellar lattice constants d of phase 1 (triangles) and phase 2 (squares) at atmospheric pressure (a) and plot of the integrated peak areas of both phases as a function of temperature (b) of DPPC / ergosterol (22%_{mol}).

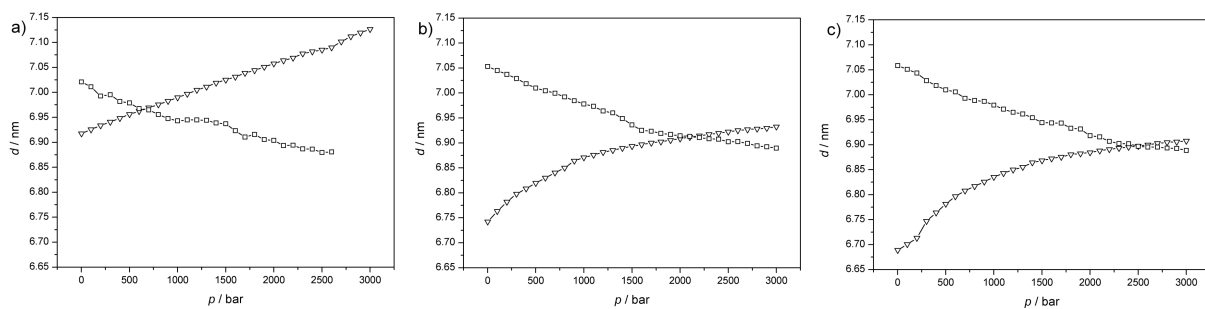


Figure 6.13: Pressure dependence of the lamellar lattice constants, d , of DPPC / ergosterol (22%_{mol}) of phase 1 (triangles) and phase 2 (squares) at three temperatures: 10 °C (a), 50 °C (b) and 60 °C (c).

which, again, is probably due to a pressure-induced reduction in the interlamellar water layer. Similar to the 50 °C measurement, the l_o -phase (with almost vanishing intensities at low pressures) exhibits increasing d -values with increasing pressure. In the s_o -phase, the negative slope of $d(p)$ is rather small and may be attributed to a compression of the interlamellar water layer with rising pressure and / or a slight increase in tilt angle of the acyl-chains.

6.2.4 Conclusions

By combining results of small-angle X-ray scattering (SAXS) and FTIR spectroscopy ², it was possible to construct a p, T -phase diagram of the system DPPC / ergosterol (22 %_{mol}), which is depicted in Figure 6.14. The phase diagram exhibits a series of pressure-induced phase transitions in the temperature-pressure plane covered, i.e. at temperatures ranging from 10 to 70 °C at pressures up to about 8 kbar (0.8 GPa). The $l_d \rightarrow l_d + l_o$ and the $l_d + l_o \rightarrow l_o + s_o$ phase boundaries exhibit a linear slope of about 9 ± 1 °C/kbar, whereas the $l_o + s_o \rightarrow s_o$ transition line seems to be steeper (about 14-20 °C/kbar), and hence those phase transition slopes are of the same order of magnitude as those of the pressure-induced phase transitions of one-component lipid bilayer systems. The fluid to gel ($l_d \rightarrow s_o (P_{\beta'})$) transition in pure DPPC-bilayers however exhibits a steeper slope of about 22 °C/kbar.^[203]

In agreement with the Clausius-Clapeyron equation ($dT/dp = T\Delta V/\Delta H$), this fact could be explained by a more positive transition enthalpy ΔH and / or a smaller volume increase ΔV . It may be assumed that the latter factor plays the dominant role, as the volume changes at the transition are expected to be smaller owing to the fact that part of the fluid phase is replaced by a liquid-ordered (l_o) phase, which has still liquid-like properties. Certainly, due to temperature and pressure dependent ΔV and ΔH values, the transition lines, in particular the one for the $l_d + s_o \rightarrow s_o$ transition, may be curved. Owing to the relatively large error bars for this transition, a linear transition line has been assumed here.

The biologically probably most relevant phase, the $l_d + l_o$ two-phase coexistence region as a very simple model of a raft-like lateral membrane organisation, exhibits a broad temperature range of about 17 °C over the whole pressure range covered. Hence, a temperature decrease of about 20 °C has a similar effect on membrane ordering and lateral organisation as a pressure increase of approximately 2 kbar in the $l_d + l_o$ two-phase coexistence region. Interestingly, in this pressure range, ceasing of membrane protein function in natural membrane environments has been observed for a variety of systems,^[306, 340-345] which might be correlated with the membrane matrix reaching a physiologically unacceptable overall ordered state at these pressures.

From a more biotechnological point of view, these studies could also help to determine the minimal pressure needed for safe inactivation of microorganisms. It is well known that high pressure treatment at low temperatures facilitates sterilisation processes with regard to bacteria and fungi.^[346, 347] It is thought that the transition of the cell membrane to a gel-like ordered phase is, besides other effects like protein denaturation, responsible for microbial inactivation.

6.3 Three-component lipid raft membrane

The study presented in this section was conducted in cooperation with M. Pühse, a PhD student from our group, who performed the Fourier transform infrared (FTIR) spectroscopy measurements, which confirmed and extended the phase diagram found by small-angle X-ray scattering. The complete study

²The FTIR measurements were performed by M. Pühse and are presented in [336].

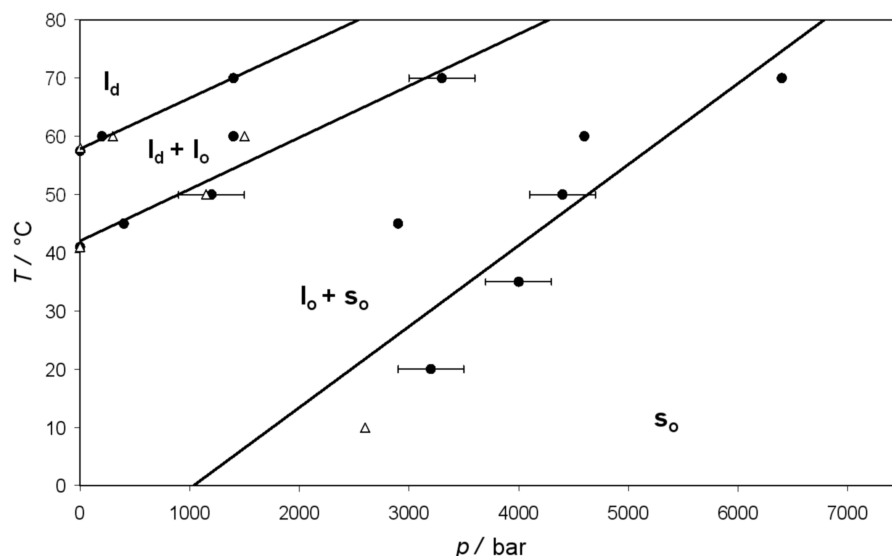


Figure 6.14: Tentative p, T -phase diagram of the binary lipid mixture DPPC / ergosterol (22%_{mol}) in excess water as obtained from the FTIR spectroscopy (circles) and SAXS (triangles) data. Selected error bars are shown, which indicate the uncertainties in the pressure determination.

including the results of the FTIR measurements is published in [11]. The XRR and GIXD measurements were planned and conducted in cooperation with F. Evers (Department of Physics, TU Dortmund University), who fitted the XRR data. The analysis of GIXD data was done by me.

6.3.1 Introduction

By using the pressure-jump relaxation technique in combination with time-resolved synchrotron small-angle X-ray scattering (trSAXS), the kinetics of lipid phase transformations of ternary lipid mixtures serving as model systems of heterogeneous raft-like membranes were investigated. So far, pressure- and temperature-jump relaxation studies have been only performed to study less complex lamellar phase transitions as well as lamellar-to-nonlamellar and intercalic lipid mesophase transitions.^[225, 335, 348–356] The pressure-jump relaxation technique was used, which is often advantageous over the temperature-jump approach; pressure propagates rapidly, so sample homogeneity is less of a problem. Pressure-jumps can be performed bidirectionally, i.e. in the pressurising and depressurising direction, and the amplitude of the pressure-jump can be easily and repeatedly varied to a level of high accuracy.

To this end, the temperature and pressure dependent structure and phase behaviour of a canonical lipid raft model system, the mixture DOPC / DPPC / cholesterol (1:2:1 molar ratio) was first explored, using small-angle X-ray scattering (SAXS) and Fourier transform infrared spectroscopy, covering the pressure range from atmospheric pressure to 2.6 kbar by SAXS and up to 10 kbar by FTIR at temperatures in the range from 7 to 80 °C.

Additionally, a sample of the lipid mixture was spread at the air-water interface on a Langmuir trough. The lipid monolayer was compressed to a film pressure of 30 mN m⁻¹. XRR and GIXD was used to investigate the vertical and lateral structure of the monofilm especially with regard to small crystalline domains floating in a disordered lipid matrix, i.e. lipid rafts.

Finally, the kinetics of inter-lamellar phase transitions of the ternary lipid system in solution was studied by trSAXS involving transitions from the fluid-like (liquid-disordered, l_d) phase to the liquid-ordered

(l_o)/liquid-disordered (l_d) two-phase coexistence region as well as between the two- and three-phase coexistence regions of the system, where also solid-ordered phases (s_o) are involved. The phase transition from the all-fluid l_d -phase to the l_o+l_d two-phase coexistence region turns out to be rather rapid. Phases appear or disappear within the 0.2 s time-resolution of the technique, followed by a slow lattice relaxation process, which, depending on the pressure-jump amplitude, takes several seconds. Contrary to many one-component phospholipid phase transitions, the kinetics of the $l_d \leftrightarrow l_d + l_o$ transition follows a similar time-scale and mechanism of the pressurisation and depressurisation direction. A similar behaviour is observed for the phase transition kinetics of the $s_o + l_o + l_d \leftrightarrow l_o + l_d$ and even for the $s_o + l_o + l_d \leftrightarrow l_d$ transformation, jumping across the l_o+l_d two-phase region. All transitions are fully reversible and no intermediate states are populated. As indicated by the complex relaxation profiles observed, the overall rates seem to reflect the effect of coupling of various dynamical processes through the transformation, involving fast conformational changes in the sub-millisecond time regime and slow relaxation of the lattices growing, probably being largely controlled by the transport and redistribution of water into and in the new phases of the multilamellar vesicle assemblies.

6.3.2 Materials and methods

Materials

1,2-Dipalmitoyl-*sn*-glycero-3-phosphocholine (DPPC) and 1,2-dioleoyl-*sn*-glycero-3-phosphocholine (DOPC) were purchased from Avanti Polar Lipids (Birmingham, AL). Cholesterol (Chol) was acquired from Sigma-Aldrich (Steinheim, Germany). All chemicals were used without further purification. The DOPC/DPPC/Chol (1:2:1 molar ratio) mixture was prepared by dissolving the corresponding amounts of lipid in chloroform. Afterwards, the chloroform was removed via evaporation with dry nitrogen purging. Residual amounts of chloroform were removed by lyophilisation for 24 h. The lipid dispersions were prepared by dissolving the required amounts in the corresponding buffer. Subsequently, six freeze-thaw cycles were conducted to homogenise the sample, yielding well-hydrated homogeneous multilamellar vesicle dispersions.

Synchrotron small-angle X-ray scattering

The SAXS experiments were performed at the high brilliance beamline ID02 at the European Synchrotron Radiation Facility (ESRF, Grenoble, France).^[66] The medium X-ray energy was 16.5 keV, corresponding to a wavelength of 0.751 Å. 2D diffraction images were recorded on an image-intensified CCD detector. The CCD has an active area of (100 mm)² and a frame rate of about 10 frames per second (1024 × 1024 pixels). The sample-detector-distance was 1.50 m and the sample exposure time in the range of 0.1 s. The lipids were dissolved in 10 mM buffer, yielding a 10%_{wt} dispersion, which was homogenised by freeze-thaw cycling. 25 µl of the sample was filled in a high pressure sample cell. The cell was equipped with flat diamond windows of 0.8 mm thickness. Pressure-jumps were achieved in about 5 ms using pneumatic high pressure valves. Further technical details are described by Kraineva et al., [68]. To equilibrate and homogenise the sample, the pressure was varied several times between atmospheric pressure and 2.5 kbar.

Lamellar lattice constants, d , were calculated from the low-angle Bragg reflections using Bragg's equation. To obtain more precise positions of s , the raw data were fitted with an overlay of Gaussian functions and the resultant peak maxima were used. Reflections of first and second order were considered in the data analysis.

The temperature-dependent measurements at atmospheric pressure were conducted between 10.5 and 64.9 °C (accuracy: ± 0.2 °C) in temperature steps of 5 °C. The temperature equilibration time before each measurement was 10 min. The pressure-dependent static experiments were conducted at 61.4 °C. The maximum pressure applied was 2.6 kbar (accuracy: ± 20 bar). Measurements were performed in steps of 0.1 kbar up to 2.0 kbar and after that in steps of 0.2 kbar in the upward and downward direction. The pressure-jumps were performed by a computer-controlled opening of an air operated valve between the high pressure cell and a liquid reservoir container. With the pressure-jump apparatus used, rapid (< 5 ms) and variable amplitude pressure-jumps are possible. To minimise the effect of an adiabatic temperature change in the course of the pressure-jump, the high pressure cell was constructed to hold only a very small volume of the pressurising medium (water). No adiabatic temperature change was detected in these experiments within the accuracy of our temperature measurements. For the time-resolved pressure-jump experiments, 60 images were taken: 20 images every 0.25 s after the pressure-jump, followed by 20 images every 1 s and at least 20 images every 5 s.

Synchrotron X-ray reflectometry and grazing incidence X-ray diffraction

The X-ray reflectometry (XRR) as well as grazing incidence diffraction (GIXD) experiments were conducted at the liquid surface diffractometer of beamline ID10B at the synchrotron light source ESRF (Grenoble, France).^[97] A monochromatic X-ray wavelength, λ , of 1.523 Å (corresponding to a photon energy, E , of 8.14 keV) was selected by a diamond(111) crystal. The lipid mixture dissolved in chloroform was spread on the surface of a Langmuir trough filled with water. This subphase had a temperature of 4.5 °C. The film was compressed to a physiological film pressure of 30 mN m⁻¹.

The monochromatic beam was deflected to an incident angle, α_i , onto the liquid surface. Reflectivity scans were carried out by measuring the scattered intensity as a function of α_i under the specular condition, $\alpha_i = \alpha_f$ (exit angle, α_f), using a 50 mm gas-filled, position-sensitive detector. Reflectivity measurements were performed in an angular range of $0.4 \alpha_c < \alpha_i < 30 \alpha_c$ with the critical angle of total reflection of the air-water interface, $\alpha_c = 0.15^\circ$ at the given wavelength. A typical X-ray reflectometry scan took about 20 min.

In grazing incidence X-ray diffraction (GIXD), the liquid surface was illuminated at a constant incident angle of $0.8 \alpha_c$, i.e. at an angle slightly below the critical angle of the air-water interface. Under this condition, the incident wave is totally reflected, while the refracted wave becomes evanescent, so that a layer of approximately 76 Å beneath the interface is illuminated by X-rays and, thus, surface sensitivity is reached. The scattered intensity was measured as a function of the angle between the incident and diffracted beam projected onto the horizontal plane, 2Θ , using a gas-filled detector (150×10 mm²). The detector had a vertical acceptance of $0 < q_z < 0.8 \text{ \AA}^{-1}$ and a horizontal resolution of $\Delta q_{xy} = 0.0051 \text{ \AA}^{-1}$. In a typical GIXD scan, the detector is moved in 150 steps in an angular range of $14^\circ < 2\Theta < 29^\circ$ (corresponding to $1.01 \text{ \AA}^{-1} < q_{xy} < 2.07 \text{ \AA}^{-1}$) counting 15 s per step.

FTIR spectroscopy

A 10 %_wt lipid dispersion was prepared by dissolving the lipids in 10 mM Bis-Tris- or phosphate-buffer (pH 7.0, in D₂O) and subsequent homogenisation. Bis-Tris-buffer was used for the high pressure measurements and phosphate-buffer for the temperature-dependent measurements, due to the different temperature and pressure sensitivities of the corresponding pK_a-values, respectively.^[357] Further details of

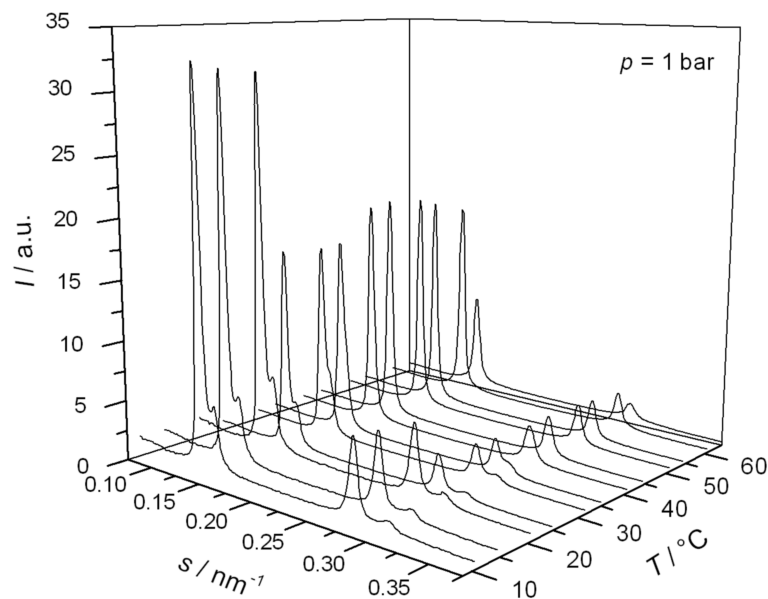


Figure 6.15: Small-angle X-ray scattering patterns of the ternary lipid mixture DOPC / DPPC / Chol (1:2:1 molar ratio) between 10.5 and 64.9 °C at atmospheric pressure.

the FTIR measurements can be found in the literature^[11] as well as in section 6.1.2 (page 73) describing the same instruments used for another study.

6.3.3 Results

Static temperature- and pressure-dependent SAXS measurements

Figure 6.15 displays SAXS patterns of the system DOPC / DPPC / Chol (1:2:1 molar ratio) in the temperature range between 10.5 and 64.9 °C at atmospheric pressure. At high temperatures, the first and second order Bragg-peaks of the fluid-like lamellar (liquid-disordered, l_d) lipid bilayers are visible. Below about 40 °C, the peaks shift to smaller s -values and a second maximum emerges, indicating two coexisting phases, denoted as $l_d + l_o$. By fitting the SAXS data to Gaussian functions, the corresponding lamellar d -spacings can be accurately determined. Below about 30 °C, the scattering pattern changes again, and fitting of the diffraction peaks indicates coexistence of three lamellar phases, which, according to the Gibbs phase rule and to FTIR spectroscopic data (not presented here), may be identified as $l_d + l_o + s_o$.

The lamellar d -spacings of the various phases is displayed in Figure 6.16a as a function of temperature. The corresponding peak-intensities are depicted in Figure 6.16b. Three different regions can be identified. At low temperatures, the solid- and liquid-ordered phases s_o and l_o coexist with the fluid-like l_d -phase. Above 25 ± 2.5 °C, one of the phases (with d -spacings denoted by circles) disappears and the two-phase coexistence region $l_d + l_o$ is reached. At temperatures above 45 ± 2.5 °C, the intensity of the Bragg reflections of the l_o -phase (triangles) vanishes and the high-temperature one-phase region of the liquid-disordered phase l_d with high conformational disorder of its acyl-chains is reached. The d -spacing of the l_d -phase decreases concomitantly and reaches values around 6.7 nm. The drastic decrease of the lattice spacing from 7.13 nm at 10.5 °C to 6.69 nm at 60 °C is probably mainly due to the temperature-induced increase of the conformational disorder of the lipid hydrocarbon chains in the l_d -phase. The d -spacing of the l_o -phase increases modestly from 6.49 nm at 10.5 °C up to 6.64 nm at 35 °C, which could be due

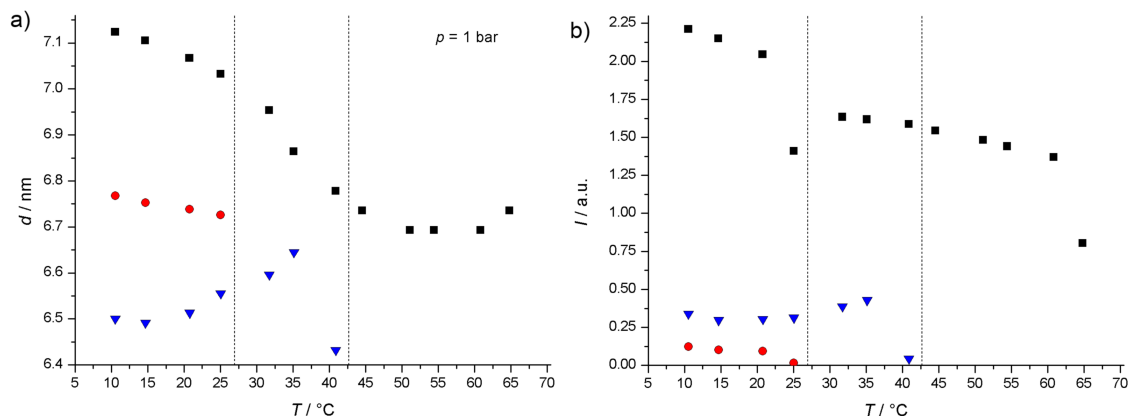


Figure 6.16: Temperature dependence of the lamellar lattice constants, d , of DOPC / DPPC / Chol (1:2:1 molar ratio) in the s_o -phase (red circle), the l_o -phase (blue triangle) and the l_d -phase (black square) at atmospheric pressure (a) and the integrated peak areas of these phases as a function of temperature (b).

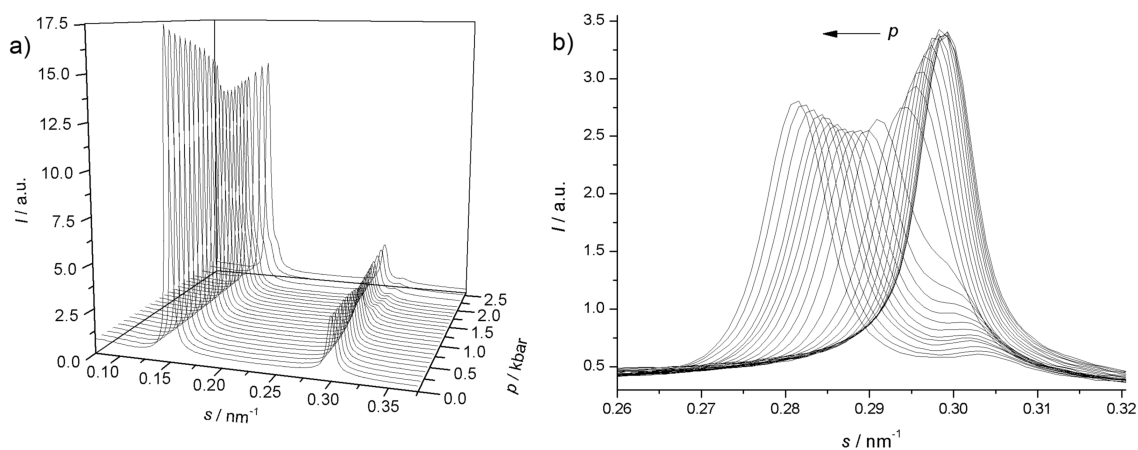


Figure 6.17: (a) Small-angle X-ray scattering patterns of the pressure-dependent measurement on the ternary lipid mixture DOPC / DPPC / Chol (1:2:1) at 60°C . (b) Enlarged view on the second order Bragg reflections ($n_x = 2$).

to a slight swelling of the interlamellar water layer with rising temperature. The slightly smaller d -value compared to the one of the l_d -phase could be due to a smaller interlamellar water layer. As expected, the d -spacing of the s_o -phase does not change significantly with temperature ($d \approx 6.75 \text{ nm}$).

The SAXS data of the pressure-dependent measurements at $T = 61^\circ\text{C}$ are plotted in Figure 6.17a for pressures ranging from 1 bar to 2.5 kbar (250 MPa). As expected, pressure-induced transitions from the one-phase region (l_d) to more-phase regions are detected. This can be more clearly seen in the enlarged s -region (Figure 6.17b) of the second order Bragg reflections. At low pressures, only a single Bragg-peak of the l_d -phase at about 0.299 nm^{-1} is observed. With increasing pressure, this peak shifts to smaller s -values and one (at medium pressures) respectively two (at higher pressures) further peaks or shoulders emerge upon pressurisation.

In Figure 6.18, the d -spacings of the various Bragg reflections are plotted as a function of pressure at $T = 61^\circ\text{C}$. It can be clearly seen that up to 1.0 kbar, only a single-phase region exists, the l_d -phase. Its d -value increases slightly from 6.69 to 6.77 nm with increasing pressure, probably due to a slight pressure-induced increase in the order of the lipid chains.

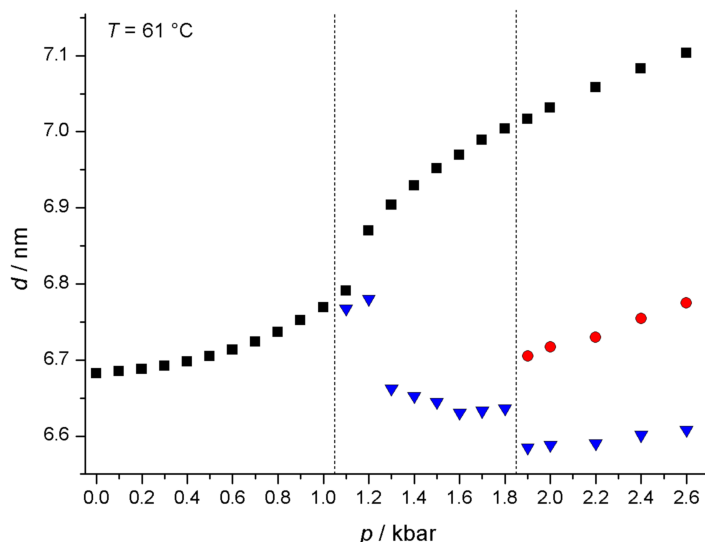


Figure 6.18: Pressure dependence of the lamellar lattice constant of the three phases s_o (red circles), l_o (blue triangles) and l_d (black squares) in the ternary lipid mixture DOPC / DPPC / Chol (1:2:1) at 61 °C.

Above 1.0 kbar, two coexisting phases can be detected, namely $l_d + l_o$. In the pressure range of the $l_d + l_o$ phase coexistence, the thickness of the l_d -phase increases from 6.79 to 7.01 nm, while the d -spacing of the l_o -phase decreases from 6.76 to 6.64 nm.

A second transition to a three-phase coexistence region is found at 1.8 kbar. Here, the diffraction data can only be fitted sufficiently with an overlay of three Gaussian peaks. In this phase region, all lamellar lattice constants increase with rising pressure, probably due to a further pressure-induced reduction of *gauche* isomers and kinks. The d -spacing of the l_d -phase increments from 7.02 to 7.11 nm, the one of the l_o -phase from 6.59 to 6.61 nm, and that of the s_o -phase from 6.71 to 6.78 nm, respectively. Identification of phases is facilitated by following corresponding changes in the Bragg peak intensities (data not shown).

As generally observed for lipid phase transitions, the comparison of the isothermal and the isobaric measurements exhibits adverse effect of temperature and pressure on the phase transitions of the system. For the $l_d \rightarrow l_d + l_o$ -transition, an increase of pressure of 1.0 kbar has the same effect as a decrease of temperature of about 15-19 °C.

Together with the temperature- and pressure-dependent FTIR data (see literature [11]), it is possible to construct a p, T -phase diagram of the DOPC / DPPC / Chol (1:2:1 molar ratio) system, which is presented in Figure 6.19. The phase boundaries observed by the high pressure SAXS measurements are in excellent agreement with those obtained by FTIR spectroscopy.

The $l_d \leftrightarrow l_d + l_o$ and $l_d + l_o \leftrightarrow l_d + l_o + s_o$ phase boundaries exhibit a slope of about 15 and 17 °C/kbar, respectively, whereas the $l_d + l_o + s_o \leftrightarrow l_o + s_o$ and $l_o + s_o \leftrightarrow s_o$ transition lines show both a smaller slope of about 9 °C/kbar. The latter one is significantly smaller than the fluid to gel ($l_d \rightarrow s_o(P_{\beta'})$) transition in pure DPPC-bilayers, which changes at a rate of approximately 22 °C/kbar.^[203] As shown before, the slope of the $l_o + s_o \leftrightarrow s_o$ transition in a DPPC / ergosterol (78:22 %_{mol}) fungal model membrane is 14-20 °C/kbar.^[336]

Recalling the Clausius-Clapeyron equation, $dT/dp = T\Delta V/\Delta H$, it has to be noted that the slope of the p, T -transition curves is given by the relative volume and enthalpy (or entropy, $\Delta S = \Delta H/T$) changes at the transition. Hence, it is likely that the volume increase during the phase transitions is much smaller in our ternary system here, since, with regards to the $l_d + l_o + s_o \rightarrow l_o + s_o$ and $l_o + s_o \rightarrow s_o$

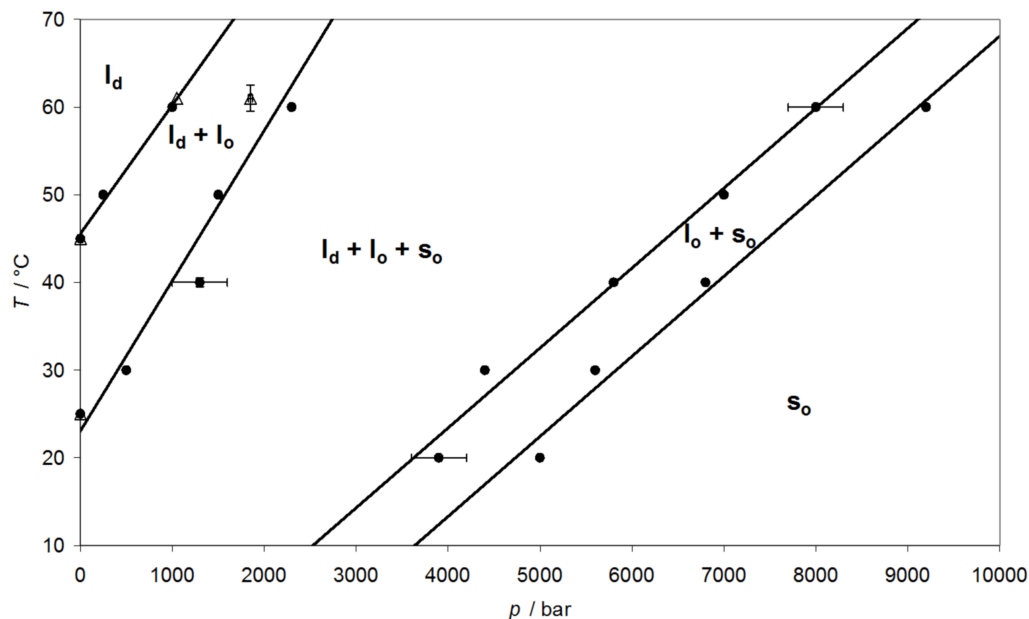


Figure 6.19: p, T -phase diagram of the ternary lipid mixture DOPC / DPPC / Chol (1:2:1 molar ratio) in excess water as obtained from the SAXS and FTIR spectroscopy data. Selected error bars are shown, which indicate the uncertainties in the pressure and temperature determination and phase assignments.

transformations, two of the three participating phases have liquid-ordered or even solid-ordered character and hence exhibit similar physical characteristics, in contrast to the fluid \rightarrow all-ordered ($P_{\beta'}$ gel) phase change in pure DPPC dispersions. In addition, the less steep phase boundaries in the system studied here can also be explained by the presence of the two *cis*-monounsaturated oleic acid chains in DOPC, which impose a kink in the lipid structure generating additional void volume also in the ordered phases and hence reducing the volume difference, ΔV .

The proposed biologically relevant $l_d + l_o$ two-phase region, mimicking raft structures, shows a nearly constant temperature range of about 20 °C over the whole pressure range covered, hence a pressure increase of 1.2 kbar has a similar effect on the membrane properties as a temperature decrease by 20 °C. Interestingly, in this pressure range, the activity of membrane enzymes like the Na^+, K^+ -ATPase starts to decrease dramatically, possibly due to a lateral membrane structure, which becomes too rigid when entering an all-ordered lateral lipid organisation.^[209]

XRR and GIXD measurements at the air-water interface

The lipid raft mixture DOPC / DPPC / Chol was not only investigated in the bulk phase, where it forms multilamellar vesicles, but also as a monolayer at the air-water interface. A small amount of the lipid mixture dissolved in chloroform was spread on a Langmuir trough filled with water and afterwards compressed to a film pressure, π , of 30 mN m^{-1} , mimicking the lateral pressure in a physiological membrane.

In Figure 6.20a a two-dimensional contour plot of the intensity, $I(q_{xy}, q_z)$, along the horizontal (q_{xy}) and vertical (q_z) scattering directions is presented as obtained from a lipid raft monolayer at 10 °C. Three different signals can be found in the GIXD map indicating an oblique packing of the hydrocarbon chains in crystalline lipid domains in the monolayer. The moduli of the lattice vectors in real space, a and b , are 4.561 Å and 4.568 Å, respectively. The angle included by both lattice vectors, \vec{a} and \vec{b} , is 112.8°, which is significantly different from the angle of 120° for an ideal hexagonal packing.

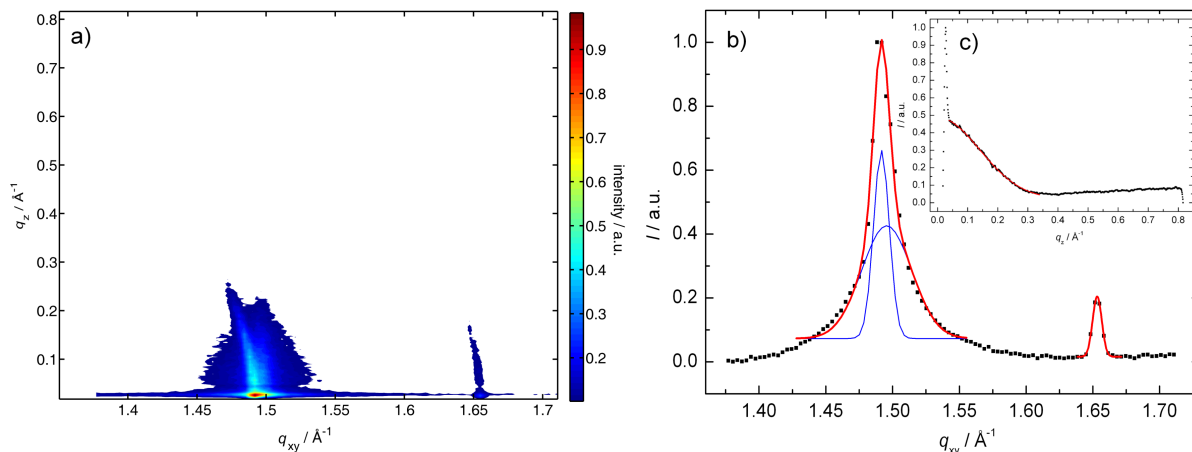


Figure 6.20: a) Two-dimensional contour plot of the intensity, $I(q_{xy}, q_z)$, along the horizontal (q_{xy}) and vertical (q_z) scattering directions as obtained from a lipid raft monolayer (DOPC / DPPC / Chol, molar ratio 1:2:1) at a film pressure of $\pi = 30 \text{ mN m}^{-1}$ at 10°C . b) GIXD pattern, $I(q_{xy})$, obtained by integrating along q_z (solid lines). c) Typical Bragg rod intensity profile, $I(q_z)$, obtained by integrating along the q_{xy} -region of the first Bragg peak. The absence of a peak at $q_z \neq 0$ indicates little or no molecular tilt relative to the surface normal.

In Figure 6.20b the GIXD pattern, $I(q_{xy})$, obtained by integrating along q_z is displayed (squared symbols). The peaks are fitted by Gaussian functions (solid red lines), where the first peak at around $q_{xy} \approx 1.49 \text{ \AA}^{-1}$ is the sum of two overlaying peaks, as indicated by the two blue curves. The area per hydrocarbon chain is 19.19 \AA^2 and the lateral 2D crystalline coherence lengths, L_{xy} , were calculated from the full widths at half maximum of the Gaussian peaks to 100 \AA , 386 \AA and 1006 \AA , respectively. Assuming an ellipsoidal shape of the crystalline domains in the monolayer, the number of molecules in a single crystal domain is in the order of 5000 lipids.

The inset in Figure 6.20b (part c) shows a typical Bragg rod intensity profile, $I(q_z)$, obtained by integrating along the q_{xy} region of the first Bragg peak at $q_{xy} \approx 1.49 \text{ \AA}^{-1}$. The absence of a peak at $q_z \neq 0 \text{ \AA}^{-1}$ indicates little or no molecular tilt of the hydrocarbon chains in the crystalline domains of the monolayer relative to the surface normal. The data can be fitted by (half) a Gaussian function with the maximum at $q_z = 0 \text{ \AA}^{-1}$, depicted by the red line in the inset in Figure 6.20. From the width of this function, the vertical crystalline coherence lengths, L_z , were calculated to be 17.8 and 16.0 \AA , which can be attributed to hydrocarbon chains comprising thirteen carbon atoms in the crystalline domains.

In Figure 6.21a the fitted reflectivity curve (red line) of the lipid raft monolayer on the air-water interface (temperature of subphase = 10°C) compressed to a film pressure of $\pi = 30 \text{ mN m}^{-1}$ is shown. The corresponding electron density profile perpendicular to the monolayer surface is presented in Figure 6.21b. A sufficient fit of the experimental data, using Parratt's recursive method, could only be achieved using a model consisting of three different layers. The values of the electron density, ρ , have been normalised to the electron density of the subphase, $\rho_{\text{H}_2\text{O}}$. Usually, a lipid monolayer at the air-water interface can be represented by two layers; one for the lipid head groups and one for the hydrocarbon chain region. Here, an additional layer had to be introduced between the lipid head groups and the water subphase representing the fraction of the lipid head groups in raft domains, which extend further into the subphase than the ones in the surrounding liquid disordered phase.

In Table 6.1, the detailed parameters of the layer model are given. Each layer is characterised by its thickness, d , surface roughness, σ , and electron density, ρ . The first layer, denoted by an (A) in Figure 6.21b, represents the hydrocarbon chains of the lipid. The electron density is smaller than unity,

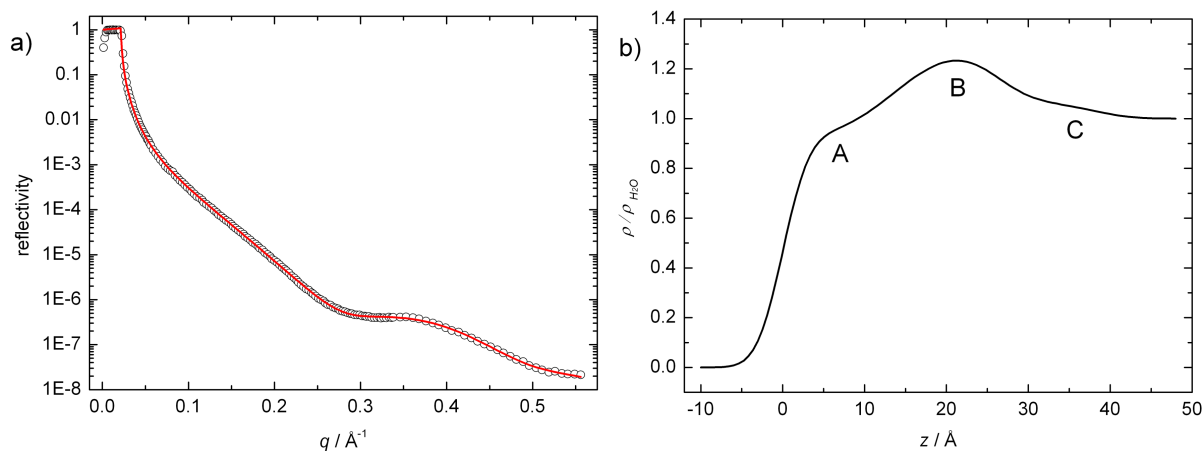


Figure 6.21: a) X-ray reflectivity data of a lipid raft monolayer (DOPC / DPPC / Chol, molar ratio 1:2:1) at a film pressure of $\pi = 30 \text{ mN m}^{-1}$ and a temperature of 10°C on the air-water interface. The fit of the data is depicted by a red line. b) Corresponding electron density profile normalised to water. On the right hand side with a value of 1 the water subphase is reached. The value decreases to 0 representing the air on the left hand side.

Table 6.1: Fitting parameters of the X-ray reflectivity curve of a lipid raft monolayer (DOPC / DPPC / Chol, molar ratio 1:2:1) at the air-water interface: layer thickness, d , roughness, σ , and electron density, ρ , of each layer are listed.

layer name	d [Å]	$\rho/\rho_{\text{H}_2\text{O}}$ []	σ [Å]
air	∞	0.0	–
lipid chains (A)	13.62	0.925	2.52
lipid head group (B)	12.51	1.283	5.50
raft (head group) region (C)	11.96	1.062	3.68
water	∞	1.000	3.64

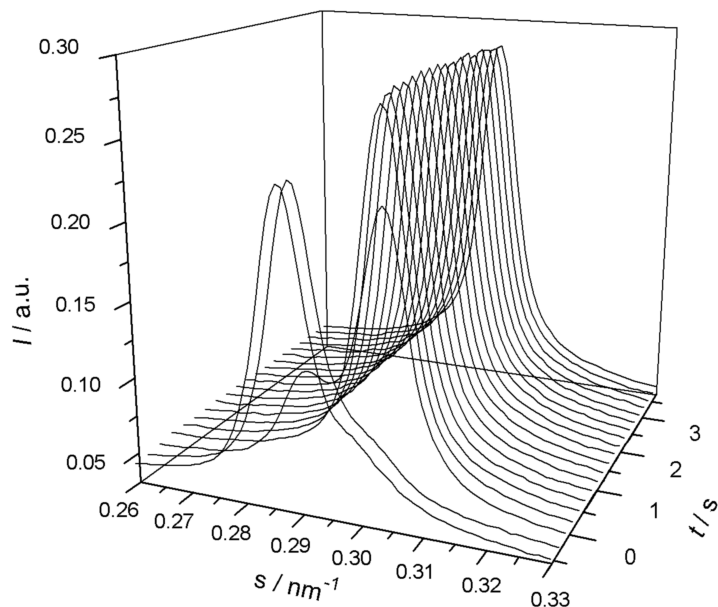


Figure 6.22: Diffraction patterns of the ternary lipid mixture DOPC / DPPC / Chol (1:2:1 molar ratio) during the first 4 s of a pressure-jump from 1.6 kbar to 0.3 kbar at $T = 61\text{ }^{\circ}\text{C}$ (raw data; the pressure-jump was triggered at $t = 0\text{ s}$).

which is typical for this region of a phospholipid monolayer. The second layer, (B) in Figure 6.21b, has a significantly higher electron density than water. This is typical for the head group region of a lipid monolayer. The interfacial roughness, σ , between those two layers is remarkably large with an value of 5.5 \AA , due to the offset between highly ordered, raft domains with extended hydrocarbon chain conformation and the disordered lipid matrix with more *gauche* conformers in the lipids chains.

Finally, a third layer, (C), had to be introduced representing the small fraction of lipid head groups in the ordered raft domains that extend out of the disordered monolayer domains into the water subphase. As the electron density profile measured by XRR is always averaged over the whole illuminated area and the fraction of lipids, which protrude from the monolayer significantly further than the lipids in the disordered domains (represented by the layers A and B), is small. Therefore, the overall electron density of this layer (C, which is mainly built by water and a small fraction of lipid head groups in raft domains) is small compared to the second layer, (B), representing a layer of head groups with little water between the lipids.

Phase transition kinetics $l_d + l_o \leftrightarrow l_d$

The rate at which a phase transition proceeds may be quantified by tracking changes in the amount of both the growing and the disappearing phases. Provided the scattering factor for each phase remains constant, the intensity of the diffraction peaks corresponding to a particular phase may be used as an indication of the amount of the phase. As the observed changes in lattice parameters are small for all phases, the changes in intensity may be assumed to directly reflect changes in phase composition.

As an example, Figure 6.22 shows trSAXS data after a pressure-jump. Here, selected diffraction patterns of the second order reflections are shown for the first 4 s after a pressure-jump from 1.6 to 0.3 kbar at $61\text{ }^{\circ}\text{C}$, hence, according to the phase diagram shown in Figure 6.19, probing the transition from the $l_d + l_o$ two-phase region to the all-fluid l_d phase. Before the pressure-jump, the two overlapping Bragg peaks of

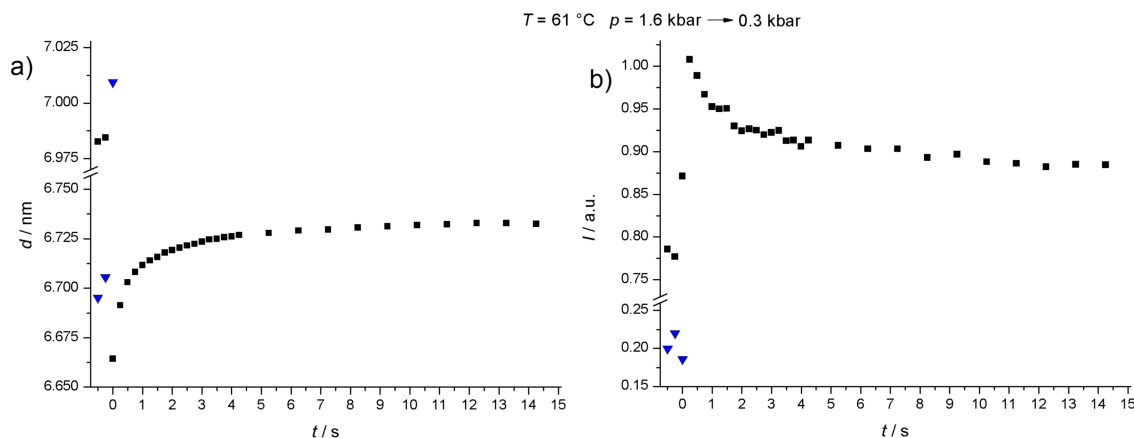


Figure 6.23: Lamellar lattice constants (a) and integrated peak intensities (b) of the ternary lipid mixture DOPC / DPPC / Chol (1:2:1 molar ratio) upon a pressure-jump from 1.6 to 0.3 kbar at 61 °C. For a better presentation of the data, a break in the axis of the ordinate has been introduced in both diagrams. The l_o -phase is represented by blue triangles, the l_d -phase is displayed as black squares.

the two coexisting phases can be clearly identified. Already 0.25 s after the pressure-jump, only a single peak of the l_d -phase is visible. Afterwards, its position changes subsequently slightly with time. These data thus clearly show that the $l_d + l_o \rightarrow l_d$ transition is rather fast, being close to the time-resolution of this method.

The corresponding lamellar lattice constants and the peak intensities as determined by fitting overlapping Gaussian functions to the measured scattering data are shown in Figure 6.23. The l_o -phase (denoted by triangles) has disappeared within the first 0.25 s after the pressure-jump. The d -spacing of the emerging l_d -phase first decreases instantaneously, but then relaxes with time, reaching its equilibrium value of about 6.73 nm largely after about 10 s (to be more precise, 66 % of the final d -value ($t_{66\%}$) of the l_d -phase is reached after 1.5 s, and the corresponding $t_{95\%}$ -value is 24 s). Such slow relaxation process might be due to interlamellar water diffusion, as the head groups in the different phases are differently hydrated. In addition, there might also be a slow temperature relaxation, because the fast pressure-jump might cause a minor decrease of the sample temperature of a few tenths of a degree. The latter effect is less likely, however, indicated by the negligible temperature dependence of the d -spacing in this temperature region as revealed by the equilibrium measurements. Also, the sample cell has been constructed to keep such adiabatic temperature changes upon pressure-jump application as low as possible.^[68]

To investigate the effect of the direction of the phase transition on the kinetics, pressure-jumps were performed from 1.6 to 0.8 kbar and in the reverse direction at the same temperature ($T = 61\text{ °C}$). The corresponding d -spacings and intensities are compared in Figure 6.24 (data in the depressurising direction are represented by hollow symbols, those in the pressurising direction by filled symbols). As expected, for the pressure-jump from the l_d to the $l_d + l_o$ two-phase region, immediately a single-phase region with one Bragg peak (solid squares; l_d) is obtained and after the pressure-jump (at $t = 0$ s), a second phase (solid triangles; l_o) starts to emerge. The inverse behaviour is observed for the jump in depressurising direction. The system starts in a two-phase coexistence region indicated by two different d -spacings and reaches the one-phase l_d -region at 0.8 kbar. The data show the reproducibility of the method and indicate that the pressure-jumps are fully reversible. Moreover, no intermediate states or phases are detectable. The l_d -phase is characterised by d -spacings of 6.98 nm at 1.6 kbar and of 6.78 nm at 0.8 kbar. The d -spacing of the l_o -phase is 6.68 nm and less pressure sensitive. The kinetics is rather fast, with overall transition times of less than 1 s in both directions.

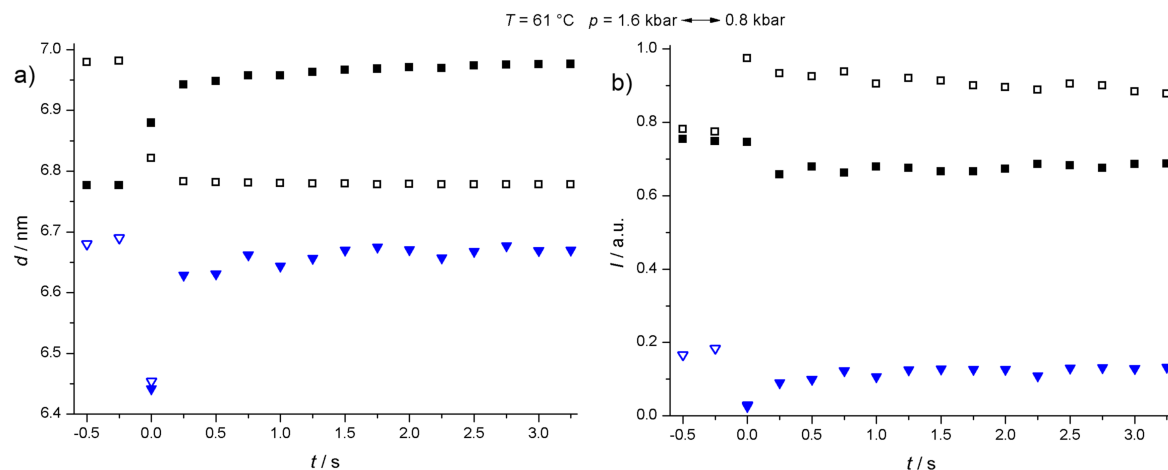


Figure 6.24: Comparison of lamellar lattice constants (a) and intensities (b) of two pressure-jumps in opposing directions between 1.6 kbar and 0.8 kbar at 61 °C. The data of the jump with decreasing pressure are represented with hollow symbols, while the results of the pressure-jump with increasing pressure are shown as solid symbols.

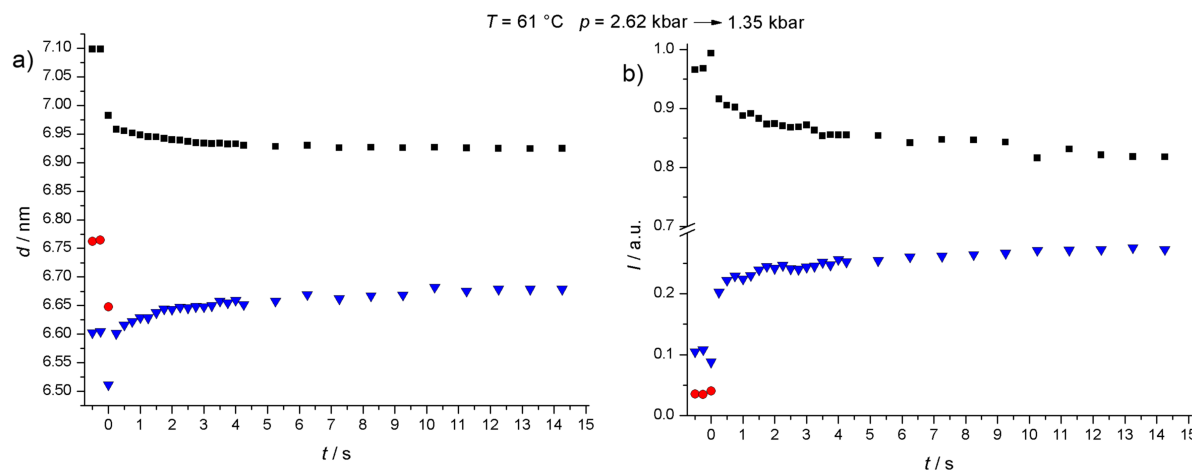


Figure 6.25: Lamellar lattice constants (a) and intensities (b) of a pressure-jump from 2.62 to 1.35 kbar at $T = 61$ °C of the three phases s_o (red circles), l_o (blue triangles) and l_d (black squares).

By comparing the two pressure-jumps from 1.6 kbar down to 0.8 kbar and 0.3 kbar, respectively, the effect of the pressure-jump amplitude on the phase transition kinetics can be studied. Comparison of Figure 6.23 and Figure 6.24 reveals marked differences in the $l_d + l_o \rightarrow l_d$ phase transition kinetics. The smaller pressure-jump amplitude exhibits an about 10-fold faster overall kinetics. The reason might be that for the transition down to 0.3 kbar, the larger pressure difference leads to a 25% larger decrease in d -spacing, which includes larger changes in the thickness of the interlamellar water layer. Hence, longer diffusion times of the water into and out of the multilamellar vesicles might be responsible for the slower lattice relaxation process observed in the case of the larger pressure-jump amplitude.

Phase transition kinetics $l_d + l_o + s_o \leftrightarrow l_d + l_o$

The d -spacings and the integrated intensities of pressure-jump SAXS experiments across the $l_d + l_o + s_o \rightarrow l_d + l_o$ phase boundary are displayed in Figure 6.25. Pressure-jumps were performed starting at a pressure

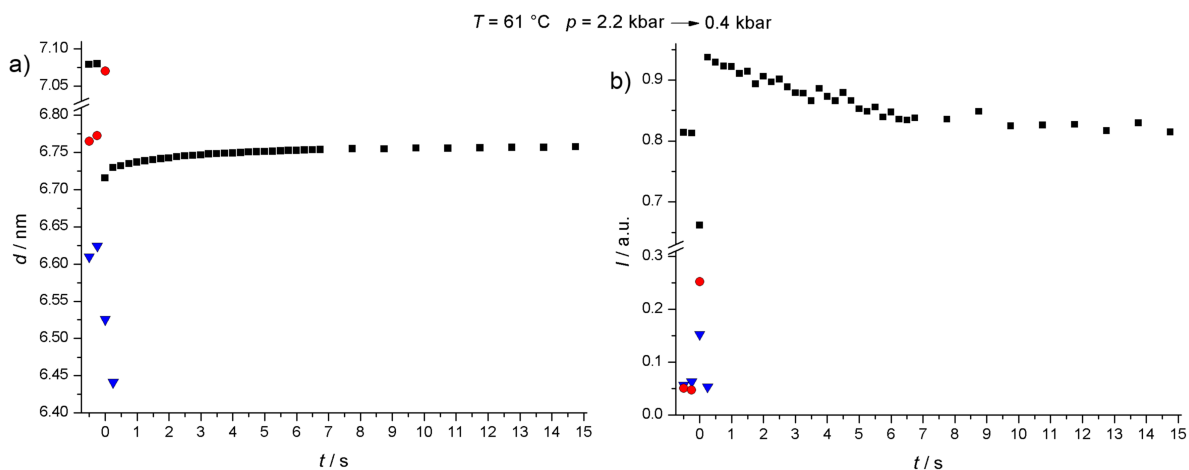


Figure 6.26: Lamellar lattice constants (a) and intensities (b) of the ternary lipid mixture DOPC/DPPC/Chol (1:2:1) upon a pressure-jump from 2.2 to 0.4 kbar at $T = 61\text{ }^{\circ}\text{C}$ (notation of phases: s_o (red circles), l_o (blue triangles), l_d (black squares)).

of 2.62 kbar, i.e. within the $l_d + l_o + s_o$ three-phase coexistence region (q.v. Figure 6.19) jumping down to 1.35 kbar, i.e. into the $l_d + l_o$ two-phase region. At the moment of the pressure-jump at $t = 0$ s, within the time-resolution of the experiment, the s_o -phase (represented by circles) vanishes. The l_d -phase (plotted as squares) has a lattice spacing of 7.10 nm in the pretrigger regime, which decreases with time after the pressure-jump, reaching a final value of about 6.92 nm after about 10 s. The d -spacing of the l_o -phase first decreases from 6.60 to 6.51 nm during the pressure-jump, and then relaxes back to about 6.69 nm. The initial and final d -spacings are in good accordance to the equilibrium values obtained in the isothermal measurements. Hence, again, a slow structural long-term relaxation of a few tens of nm is observed with time. This might be due to a minor temperature relaxation (passive cooling) after the pressure-jump. If present, the relaxation must be very small as it could not be detected by the temperature recording. The results of the isobaric measurements predict that the d -values of the l_o -phase should decrease and that of the l_d -phase should increase with decreasing temperature. The exact opposite is observed after the second data point. Hence, more likely, this rather slow relaxation is due to water diffusional processes between different phases in the multilamellar vesicle than caused by changing temperature.

Phase transition kinetics $l_d + l_o + s_o \leftrightarrow l_d$

Finally, a pressure-jump was performed starting in the $l_d + l_o + s_o$ three-phase coexistence region at 2.2 kbar and ending in the l_d -phase at 0.4 kbar, i.e. involves jumping across the $l_d + l_o$ two-phase region. The corresponding d -spacings and integrated intensities of the phases are displayed in Figure 6.26. At the moment of the pressure-jump ($t = 0$ s) the s_o -phase disappears completely and after 0.5 s the l_o -phase has also vanished. The d -value of the l_d -phase is instantaneously decreasing from 7.08 to 6.71 nm and then relaxes due to a slower process to its equilibrium value of 6.76 nm, which is essentially reached after approximately 10 s (the time $t_{66\%}$ for the l_d -phase is 3.1 s and $t_{95\%}$ is around 60 s). All lamellar lattice constants are in good agreement with the ones obtained in the equilibrium isothermal measurements. Within the time-resolution of the experiment, no intermediate phases, such as the $l_d + l_o$ equilibrium phase, could be detected.

6.3.4 Conclusions

Generally, SAXS measurements of pressure-induced lamellar-to-lamellar, lamellar-to-nonlamellar and inter-cubic lipid mesophase transitions have revealed that the kinetics depends on the topology of the lipid mesophases involved and also on the temperature and the driving force, i.e. the applied pressure-jump amplitude, Δp .^[225, 335, 356] Often multicomponent kinetic behaviour has been observed, with short relaxation times (probably on the nanosecond to microsecond time-scale) in a burst phase referring to the relaxation of the lipid acyl-chain conformation in response to the pressure change, which leads to the changes in the observed lamellar lattice constants right after the pressure-jump. The longer relaxation times measured are probably due to the rate-limiting transport and redistribution of water into the new lipid phase, which has been inferred from lattice relaxation experiments performed in the lipid one-phase regions and from modelling of the data using simple hydrodynamics.^[335] The tortuosity (obstruction) factor of the different structures, especially in cases where non-lamellar (hexagonal and cubic) phases are involved, seem to control these slow-relaxation kinetic components related to water diffusion. Nucleation phenomena and domain size growth of the structures evolving seem to play a minor role. They might play a more important role for jumps in the direct phase transition region, however, where domain relaxation processes are slowed down.^[353, 358]

So far, pressure-jump experiments have been performed essentially on one-component lipid bilayer dispersions, such as the gel-to-fluid ($P_{\beta'} \rightarrow L_{\alpha}$) main transition of fully hydrated DPPC.^[335] In the depressurising direction ($P_{\beta'} \rightarrow L_{\alpha}$) from 410 to 195 bar at $T = 45^{\circ}\text{C}$, the overall transition is relatively slow. Within 1 s after the pressure-jump, the emerging phase has appeared and no intermediate structure seems to occur. The two lattices co-exist only in the first second. The lattice constant of the new phase relaxes slowly, and a constant d -value is reached after about 20 s. At that time, the intensity of the L_{α} phase has reached its plateau value. In the pressurising direction ($L_{\alpha} \rightarrow P_{\beta'}$) from 205 to 360 bar, the transit time is faster; $d(P_{\beta'})$ reaches its plateau value after about 3 s.

In this study, by using the pressure-jump relaxation technique in combination with time-resolved synchrotron X-ray diffraction (trSAXS), the kinetics of lipid phase transformations of a ternary lipid mixture, DOPC / DPPC / cholesterol (1:2:1 molar ratio), serving as model system of heterogeneous raft-like membranes, was investigated. To this end, first the p, T -phase diagram (Figure 6.19) of the model lipid raft mixture was established using small-angle X-ray scattering and Fourier transform infrared spectroscopy. The IR spectral parameters in combination with the scattering patterns from the SAXS measurements were used to detect structural and conformational transformations upon changes of pressure up to 10 kbar and temperature in the range from 5 to 80°C . The lamellar repeat units of the different phases were determined from equilibrium SAXS measurements.

By using X-ray reflectometry (XRR) and grazing incidence X-ray diffraction (GIXD) lipid raft domains could also be found in lipid monolayers at the air-water interface at 10°C . In XRR, the large interfacial roughness between the layers representing the hydrocarbon chain region and the lipid head groups, as well as an additional layer of the small fraction of lipid head groups in the raft domains extending out of the main head group layer into the subphase, hint to the existence of lipid rafts. By measuring GIXD, detailed information of these crystalline areas in the lipid monolayer can be gained. The sharp signals observed by this method prove the existence of extended lipid rafts. Further details of the dimensions of these rafts could be determined. Interestingly, no molecular tilt angle of the hydrocarbon chain axis of the lipids in the monolayer relative to the surface normal could be observed. For pure DPPC at a film pressure, π , of 30 mN m^{-1} a tilt angle of about 32° has been published,^[359] originating from a mismatch of the cross section area of the lipid's head group and hydrocarbon chains. Here, the addition of cholesterol

to the two lipids, DPPC and DOPC, leads to a common packing with approximately equal cross sectional areas of both lipid regions, resulting in no distinctive molecular tilt angle. However, the general packing of molecules is not ideal, as the packing of the lipids is not hexagonal, but oblique, which might result from a non-ideal circular cross sectional area of the single lipid molecules.

The kinetics of inter-lamellar phase transitions of the ternary lipid system was studied involving transitions from the fluid-like, liquid-disordered (l_d) phase to the liquid-ordered (l_o)/liquid-disordered (l_d) two-phase coexistence region as well as between the two- and three-phase coexistence regions, where also a solid-ordered phase (s_o) is involved. To probe the kinetics of the various phase transitions present in the system, pressure-jump induced trSAXS data were recorded. Generally, the appearance or disappearance of Bragg peaks of phases depends on the cooperativity of many molecules being arranged in the lattice, which is detected by this method. Fast conformational changes of individual molecules (typically occurring on the ns to μ s time-scale) and processes involving disordered structures can not be detected. For example, the appearance of two Bragg peaks of the l_o - and l_d -phase, suggests that the system demixes into stacks of l_o - and of l_d -phase. Such a cooperativity might principally affect the phase boundaries and the kinetics. Concerning the phase boundaries, similar phase transition temperatures have been observed in fluorescence microscopic and spectroscopic measurements on unilamellar vesicle (ULV) systems of this mixture. The slow kinetic components might however be slightly affected by multilamellar vesicle (MLV) topologies.

Remarkably, the phase transition from the all-fluid l_d phase to the $l_o + l_d$ two-phase coexistence region turns out to be rather rapid. Phases appear or disappear within the 0.2 s time-resolution of the technique, followed by a slow lattice relaxation process, which, depending on the pressure-jump amplitude, takes several seconds. This slow relaxation process is probably essentially due to interlamellar water diffusion, as the head groups in the different phases are differently hydrated. Contrary to many of the phase transitions of one-component phospholipids dispersions, the kinetics of the $l_d + l_o \leftrightarrow l_d$ transition follows a similar time-scale and mechanism for the pressurisation and depressurisation direction. Furthermore, the data indicate that the structural changes upon the bidirectional pressure-jumps are fully reversible and no intermediate phases are populated. Interestingly, the kinetics of the overall transition is rather fast compared to one-component lamellar and non-lamellar lipid mesophase transitions. A similar behaviour is observed for the phase transition kinetics of the $l_d + l_o + s_o \leftrightarrow l_d + l_o$ transition or even of the $l_d + l_o + s_o \leftrightarrow l_d$ transformation, jumping across the $l_d + l_o$ two-phase region. Within the time-resolution of the experiment, the new phases appear, followed by a slow structural long-term relaxation.

As indicated by the complex relaxation profiles observed, also in this three-component lipid system the overall rate of the transitions seems to reflect the effect of coupling of various dynamical processes through the transformation. Typical rates range from fast conformational changes (probably in the ns to μ s time regime, involving intrinsic molecular relaxation processes of individual molecules or clusters of lipid molecules, which cannot be resolved by the SAXS technique) to the seconds time regime. It seems that water transport (due to head group hydration changes) and changes in the lateral organisation of the lattice are intrinsically linked and can not be easily deconvoluted, at least at this stage. In fact, the changes in lattice spacing are very small and hence may be possible also without invoking translocation of water. Also, the MLV topology can have some effect on the slow kinetic components, in particular with regards to the interlamellar flow of water, which might largely vanish in the case of unilamellar vesicles. Nucleation and domain growth (domain relaxation) may occur on a similar time-scale of milliseconds to seconds, but are probably only important for relaxation processes in the direct neighbourhood of the phase transitions.^[353, 358] Finally, in the multi-component system studied here, the line tension of growing (or disappearing) domain boundaries can be kept small by a lipid sorting mechanism, hence keeping the

activation energies for nucleation and domain growth low. The data presented here thus also suggest that topological changes of heterogeneous natural membrane systems involving such changes in lateral organisation or phase state where raft-like structures are involved, may occur on a similar fast time-scale; for example during membrane fusion, exo- and endocytosis.

6.4 Five-component lipid raft membrane

The results displayed in this section are part of a study conducted in cooperation with F. Evers from the Department of Physics (TU Dortmund University). After the measurements, the raw data were processed using MATLAB routines written by me. The fitting of the XRR data was done by F. Evers. The calculations based on the GIXD measurements were part of my task. All data of this investigation can also be found in a paper and the corresponding supporting information.^[360]

6.4.1 Introduction

Highly ordered lipid domains freely floating in a disordered lipid matrix have repeatedly been found in the past in different lipid mixtures consisting of lipids and cholesterol. These liquid-ordered (l_o) lipid domains are often referred to as "lipid rafts".^[205, 207, 210, 211] Increasing evidence suggests that these domains are essential for a number of cellular processes, such as lateral protein organisation and signalling.^[212] Moreover, lipid raft domains might play an important role in the fibril formation of amyloidogenic peptides.^[215-217]

To investigate such peptide-lipid interactions in detail, simple model lipid systems have to be found with the essential features of natural membranes according to their ability to form lipid rafts. A very simple system, only consisting of DOPC, DPPC and cholesterol, has been introduced in section 6.3. The low number of components of this model system leads to a relatively simple phase behaviour and good manageability.

However, one striking feature of natural cell membranes is not represented by this model system: negative charge. Cell membranes *in vivo* contain a large number of anionic lipids. Therefore, the three-component lipid raft mixture was adapted to account for the negative overall charge of natural membranes. Two lipids with anionic head groups were added to the mixture, 1,2-dioleoyl-*sn*-glycero-3-phospho-(1'-*rac*-glycerol) (DOPG) and 1,2-dipalmitoyl-*sn*-glycero-3-phospho-(1'-*rac*-glycerol) (DPPG). The DOPG with its unsaturated hydrocarbon chains is supposed to stay in the disordered lipid matrix, whereas the saturated DPPG should be integrated into the ordered phase. The existence of such raft-like phase coexistence regions (l_o+l_d) has been proven in our group in various lipid systems, such as multilamellar vesicles and huge unilamellar vesicles, as well as in solid supported bilayers by SAXS, (ATR-)FTIR-spectroscopy, fluorescence and atomic force microscopy.^[11, 216] But so far, no systematic study of complex lipid raft systems has been conducted in a lipid monolayer at the air-water interface.

6.4.2 Materials and methods

Materials and sample preparation

The lipids 1,2-dioleoyl-*sn*-glycero-3-phosphocholine (DOPC), 1,2-dioleoyl-*sn*-glycero-3-phospho-(1'-*rac*-glycerol) (DOPG), 1,2-dipalmitoyl-*sn*-glycero-3-phosphocholine (DPPC) and 1,2-dipalmitoyl-*sn*-glycero-3-phospho-(1'-*rac*-glycerol) (DPPG) were purchased as lyophilised powders from Avanti Polar Lipids (Birmingham, AL). Cholesterol was purchased from Sigma-Aldrich (Steinheim, Germany). All chemicals

were of the highest analytical grade available and used without further purification. Stock solutions (10 mg/ml) of the lipids (DOPC, DOPG, DPPC, DPPG and cholesterol) dissolved in chloroform were prepared, mixed in a molar ratio of 15:10:40:10:25, forming an anionic lipid raft mixture. For the monolayer experiments, the lipid mixture was spread at the air-water interface in a Langmuir trough, which was previously filled with aqueous buffer (10 mM PO_4^{3-} , pH 7.4) and the system was equilibrated for 15 min in order to allow for complete evaporation of the organic solvents. Then, the film was compressed slowly until the desired film pressure was reached. The system was examined by X-ray reflectometry and grazing incidence X-ray diffraction scans at four different lateral film pressures, π , of 10, 20, 30, and 40 mN m^{-1} and two different subphase temperatures, 10 °C and 20 °C.

X-ray reflectometry and grazing incidence X-ray diffraction

The X-ray scattering experiments were conducted at the liquid surface diffractometer of beamline ID10B at the synchrotron light source ESRF (Grenoble, France)^[97] with a wavelength, λ , of 1.52 Å, corresponding to an energy of 8.14 keV. The analysis of surface X-ray scattering data is outlined in detail in chapter 3. X-ray reflectometry (XRR) data are plotted as R/R_F versus q_z , with the reflectivity, R , the Fresnel reflectivity, R_F , and the vertical wave vector transfer, q_z . In a GIXD experiment, the data are depicted as two-dimensional contour plots of the intensity, $I(q_{xy}, q_z)$, and integrated along both directions, q_{xy} and q_z , as Bragg rod and Bragg peak patterns, respectively. Typical GIXD scan parameters are described in section 6.3.2 as well as in section 3.2.6 (page 35).

For the X-ray scattering experiments, the Langmuir trough was placed in a sealed container with Kapton windows transparent to the X-rays and mounted on the diffractometer. All experiments were carried out at subphase temperatures of 10 and 20 °C, respectively. Temperature-control was achieved via thermostated water flowing through the Teflon-clad metal basis of the trough. During the experiments, the container was flushed with helium in order to reduce background scattering from the gas phase and to prevent oxidative damage. Furthermore, radiation damage was reduced by lateral translation of the trough by 0.01 mm after every step during GIXD scans and by 2 mm after each reflectivity scan.

6.4.3 Results

The interfacial structure of the anionic lipid raft monolayer at the air-water interface was characterised by X-ray reflectometry (XRR) and grazing incidence X-ray diffraction (GIXD) measurements. The map of a GIXD measurement taken at a physiological film pressure, π , of 30 mN m^{-1} at 20 °C is presented in Figure 6.27. A single broad peak can be found, representing a monolayer consisting of hexagonally packed lipids in the crystalline domains. In order to analyse the crystallographic unit cell of the packing, the data were integrated along q_z resulting in a Bragg peak profile, $I(q_{xy})$. The single Bragg peak was fitted with a Gaussian function, as depicted in Figure 6.28a. From the position of the peak maximum the lattice dimensions, $a = b$, could be calculated to 5.08 Å in the ordered crystalline-like domains (q.v. Table 6.2). The area per hydrocarbon chain and the lateral 2D crystalline coherence length, L_{xy} , were computed to be 22.4 Å² and 22.2 Å, respectively. Assuming a circular shape of the crystalline-like domains in the monolayer, the average area of these domains is 387 Å², containing approximately nine lipids (each with two hydrocarbon chains).

To calculate the vertical crystalline coherence length, L_z , the data were integrated along the q_{xy} -direction obtaining a typical Bragg rod intensity profile as depicted in Figure 6.28b. From the FWHM of the fitted peak L_z was calculated to be 18.1 Å, which can be attributed to the average length of the

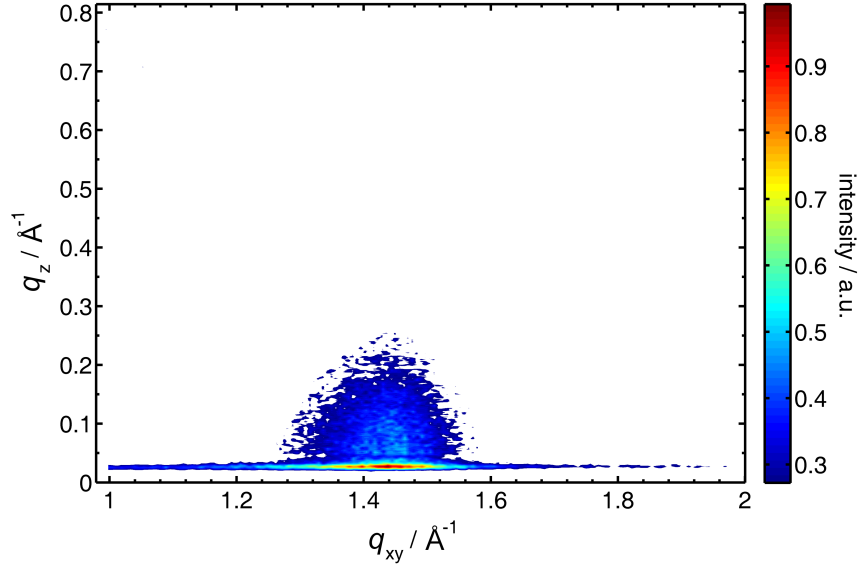


Figure 6.27: Two-dimensional contour plot of the intensity, $I(q_{xy}, q_z)$, along the horizontal (q_{xy}) and vertical (q_z) scattering directions as obtained from an anionic lipid raft monolayer (15 % DOPC, 10 % DOPG, 40 % DPPC, 10 % DPPG and 25 % cholesterol, molar ratio) at a lateral film pressure of $\pi = 30 \text{ mN m}^{-1}$ at 20°C .

Table 6.2: Calculated parameters of grazing incidence X-ray diffraction measurements of different lipid raft monolayers at the air-water interface: lattice vectors in real space, a, b , angle of the 2D unit cell, γ , lateral 2D crystalline domain length, L_{xy} , vertical crystalline domain length, L_z , and area per hydrocarbon chain, A_{chain} , are listed for all samples.

	π [mN m ⁻¹]	T [°C]	a, b [Å]	γ [°]	A_{chain} [Å ²]	L_{xy} [Å]	L_z [Å ²]
neutral raft	30	10	4.557, 4.568	112.8	19.19	99.26, 386.34, 1005.99	17.84, 16.03
anionic raft monolayer	10	20	5.236, 5.236	120.0	25.81	18.30	—
	20	20	5.333, 5.333	120.0	24.63	19.91	17.10
	30	20	5.085, 5.085	120.0	22.39	22.21	18.10
	40	20	5.046, 5.046	120.0	22.05	24.08	17.10
	30	10	5.053, 5.053	120.0	22.11	29.88	17.02
	40	10	5.016, 5.016	120.0	21.79	31.98	18.06

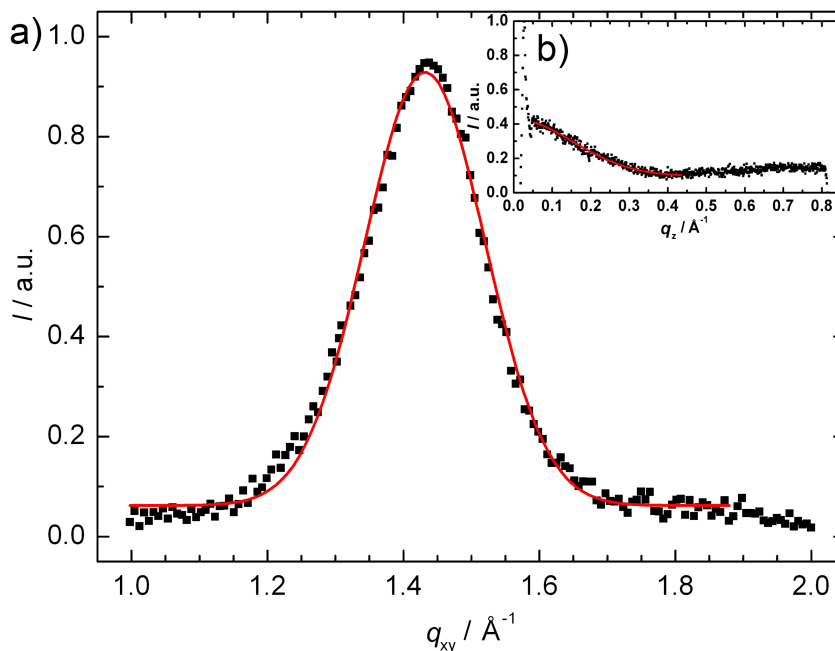


Figure 6.28: (a) GIXD pattern, $I(q_{xy})$, obtained by integrating along q_z of a lipid raft monolayer (15% DOPC, 10% DOPG, 40% DPPC, 10% DPPG and 25% cholesterol, molar ratio). The peak was fitted by a Gaussian function (solid line). (b) Typical Bragg rod intensity profile, $I(q_z)$, obtained by integrating along the q_{xy} -region of the Bragg peak. The absence of a peak at $q_z \neq 0$ indicates no molecular tilt.

hydrocarbon chains in the crystalline-like domains. The Bragg rod profile did not show any peak with a maximum at $q_z \neq 0$, indicating that the hydrocarbon chains are not tilted relative to the surface normal. These small, crystalline-like (ordered) domains, which are probably rich in DPPC, are floating within a disordered, fluid-like lipid matrix consisting of a higher concentration of disordered lipids (DOPC).

GIXD measurements were also taken at other film pressures between 10 and 40 mN m^{-1} at 20 °C subphase temperature. At all pressures a hexagonal packing of the lipids was observed as well. In Figure 6.29 the GIXD pattern, $I(q_{xy})$, of an anionic lipid raft monolayer at 20 °C obtained by integrating along q_z is depicted as a function of the film pressure, π . The intensity of the Bragg peaks is not normalised, showing the increasing intensity of the signal with increasing film pressure – at $\pi = 10 \text{ mN m}^{-1}$ (green), 20 mN m^{-1} (blue), 30 mN m^{-1} (red), and 40 mN m^{-1} (black) – and concomitantly increasing order of the crystalline packing. During the increase of the film pressure from 10 to 40 mN m^{-1} the modulus of the lattice vectors decrease by 8%, the area per hydrocarbon chain went concomitantly down by 17%, and at the same time the lateral crystalline domain length, L_{xy} , increased by 24%, indicating a compression of the crystalline unit cell and an ordering of the film leading to larger crystalline domains with increasing film pressure (q.v. Table 6.2). Between 20 and 40 mN m^{-1} the vertical crystalline domain length, L_z , remained nearly undisturbed as expected for domains built by lipids with their hydrocarbon chains in the *all-trans* conformation.

GIXD measurements were also taken for a lower temperature of 10 °C at a film pressure of 30 mN m^{-1} . The parameters of the unit cell remain nearly unaffected by the decrease in temperature. The only difference found is an increase in the lateral dimension of the crystalline domains by 35%. As expected, at low temperature the crystalline domains on the lipid monolayer are larger, due to the lower thermal fluctuations in the lipid film and the higher number of ordered lipids in the system. At 10 °C, each crystalline domain contains 16 lipid molecules on average.

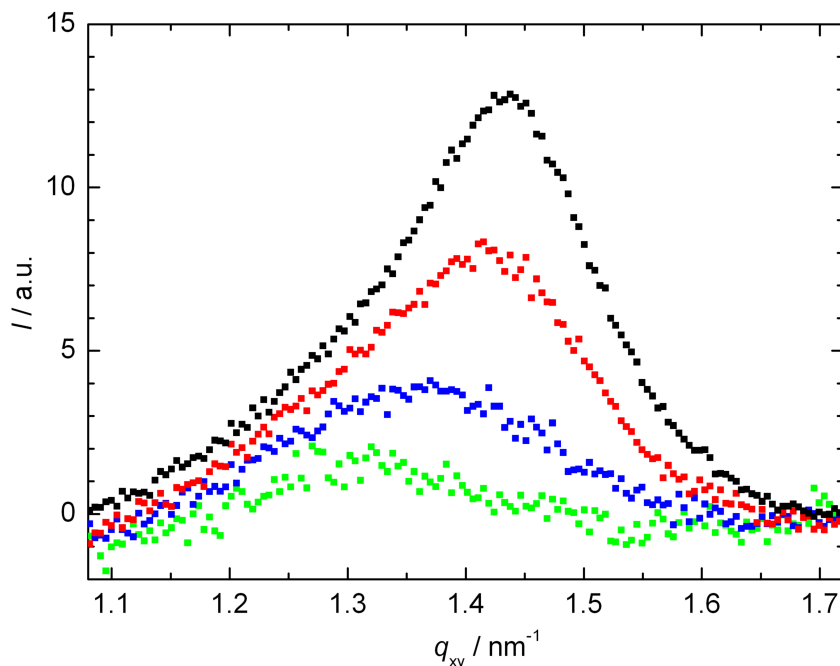


Figure 6.29: GIXD pattern, $I(q_{xy})$, obtained by integrating along q_z of an anionic lipid raft monolayer (15% DOPC, 10% DOPG, 40% DPPC, 10% DPPG and 25% cholesterol, molar ratio) at 20 °C as a function of the film pressure, π . The intensities of the Bragg peaks are not normalised. Measurements were taken – as presented from bottom to top – at $\pi = 10 \text{ mN m}^{-1}$ (green), 20 mN m^{-1} (blue), 30 mN m^{-1} (red), and 40 mN m^{-1} (black).

Hence, the GIXD data unambiguously demonstrate the presence of lipid raft domains in this negatively charged lipid monolayer over a wide temperature range. Such ordered raft-like domains have previously also been found in giant unilamellar vesicles (GUVs) as well as solid supported bilayers of the same lipid mixture presented here.^[216]

In the XRR scans, typical parameters of a lipid monofilm at the air-water interface were detected. A two-layer model described the experimental data sufficiently well – one representing the hydrophilic lipid head groups and the other the lipid’s hydrocarbon chain region.

6.4.4 Conclusions

A complex anionic lipid raft monolayer consisting of four different lipids, two of them negatively charged, and cholesterol (15% DOPC, 10% DOPG, 40% DPPC, 10% DPPG and 25% cholesterol, molar ratio) has been investigated by XRR and GIXD at the air-water interface as a function of film pressure and subphase temperature. Both phases, the liquid disordered lipid matrix as well as the ordered lipid raft domains, contain most likely anionic lipids. Thus, this lipid mixture is one of the best model systems of natural membranes so far, representing the anionic features as well as the raft characteristic of these membranes reasonable well. Although the system has been studied in bulk solution (MLVs by FTIR, DSC, PPC and GUVs by fluorescence microscopy) as well as solid supported (by AFM) and the existence of rafts could be clearly proven,^[216] so far no investigation has been conducted on corresponding monolayers at the air-water interface. In the previous study the l_o/l_d two-phase coexistence region has been observed in a temperature range from about 30 °C to 55 °C at atmospheric pressure. The size of the raft domains, as obtained by AFM, was in the range of a few micrometres.

In this study, lipid rafts were obtained in such a complex lipid mixture at the air-water interface for the first time. The phase behaviour was significantly different from the one found for lipid bilayers in a previous study.^[216] A two-phase region in the monolayer containing lipid rafts was observed at 10 °C as well as at 20 °C. The diameter of the raft domains was always in the range of 20 nm, thus at least by a factor of 100 smaller than the ones found in a solid supported bilayer by AFM. Both can be easily explained by the high lateral mobility of the lipids at the air-water interface. This high dynamics impedes the formation of larger crystalline raft domains and leads concomitantly to an increased disorder in the lipid conformation, shifting the phase behaviour observed in lipid bilayers^[216] towards lower temperatures.

6.5 Monoolein under limited hydration conditions

The data presented in this section are part of a cooperation project (q.v. section 8.2, page 158) with Dr. K. Weise, who is a post-doctoral student in our group. She planned the experiments and did the sample preparation. The experiments were conducted together at the ESRF, beamline ID02, in several experimental runs over a period of 1.5 years. Using different MATLAB scripts, I performed data corrections, processing of the raw data to obtain lattice spacings and integrated peak intensities of all identified phases, as well as the construction of the p, T -phase diagram and calculation of further parameters of the pure phases at selected points in the phase diagram.

6.5.1 Introduction

Monoolein is a simple lipid used in numerous studies in the past. The phase behaviour as a function of water content, temperature and pressure is well established.^[204] Under limited hydration conditions it shows a transition between a lamellar and cubic phase in the intermediate temperature range. In the past, monoolein has been extensively characterised both as a pure substance and in the presence of fatty acids, proteins and salts^[68, 204, 225, 259–263] to reveal the influence of these substances on the phase behaviour of the lipid system and on the phase transition kinetics. Here, the phase behaviour of monoolein at a limited hydration of 17%_{wt} water content has been studied in a temperature range of 5–80 °C and up to pressures of 4 kbar by small-angle X-ray scattering. A p, T -phase diagram was established and from the lattice constants detailed structural parameters of the pure phases were calculated. Finally, a series of pressure-jumps was conducted to study the phase transition kinetics of lamellar-cubic phase transitions.

6.5.2 Materials and methods

Materials

1-Oleoyl-*rac*-glycerol (monoolein, MO) was purchased as lyophilised powder of the highest analytical grade available from Sigma-Aldrich (Steinheim, Germany) and used without further purification. All experiments were conducted at a constant level of limited hydration of 17%_{wt} water. To prepare the sample, monoolein was molten and a corresponding amount of aqueous Tris-buffer solution was added. The sample container was sealed and kept closed until the start of the experiment. 30 freeze-thaw cycles were conducted to homogenise the sample. Additionally, prior to the experiment each sample was pressure-cycled between 40 and 150 times at 60 °C until a 2D scattering pattern was obtained showing rings resulting from a large number of microcrystals in the sample instead of spots, originating from a few large crystals.

Synchrotron small-angle X-ray scattering

The SAXS experiments were carried out at the high brilliance beamline ID02 at the European Synchrotron Radiation Facility (ESRF) in Grenoble (France)^[66] and at the SWING beamline^[361] of the synchrotron source Soleil (Giv sur Yvette, France). The medium X-ray energy of all experiments was approximately 12.5 keV, corresponding to a wavelength, λ , of 0.99 Å. A typical sample exposure time was – depending on the phase state of the sample – between 0.05 s and 2 s.

The measurements were performed in a high pressure sample cell, which is specified for pressures up to 4.0 kbar (400 MPa). Briefly, the cell is made from a stainless steel Ni-Cr-Co alloy of high tensile strength (NIMONIC 90) and equipped with flat diamond windows of 0.7 mm thickness. Pressure-jumps were achieved in about 5 ms using pneumatic high pressure valves. Further technical details were described by Kraineva et al., [68]. The beamline shutter triggered the electronics controlling the valves synchronising the pressure-jump and data acquisition.

For the SAXS measurements, a total of 25 μl of the sample was filled into the high pressure sample cell and pressure-cycled for equilibration and homogenisation. The equilibration time before each temperature-dependent measurements at atmospheric pressure was 10 min. The maximum pressure applied was 4.0 kbar (accuracy: 20 bar). Measurements were usually performed in steps of 100 bar. The pressure-jumps were triggered by computer-controlled opening of an air operated valve between the high pressure cell and a liquid-reservoir container. For the time-resolved pressure-jump experiments, typically 93 images were taken (3 images before the pressure-jump was triggered, 30 images every 0.25 s after the pressure-jump, followed by 30 images every 1 s and finally 30 images every 3 s).

The phases were identified and the lattice constants (d, a) were calculated from the position of the Bragg reflections. The intensity of the phases was calculated by summing up the integrated intensities of all peaks assignable to the corresponding phase using a program written in MATLAB.

6.5.3 Results and discussion

Static measurements

In Figure 6.30 the SAXS patterns of monoolein (17%_{wt} water content) at 60 °C between atmospheric pressure and 2 kbar are shown. At low pressure, the scattering patterns of the cubic $Ia3d$ phase can be found. Around 1.25 kbar the transition to a lamellar phase is observed. The first and second order peak of this phase, which are indexed by the miller indices $\{100\}$ and $\{200\}$, respectively, can be clearly identified.

The first eight reflections of the cubic $Ia3d$ phase (q.v. Table 2.1, page 20) are well resolved in the scattering patterns. The peaks can be denoted by their Miller indices – from small to large q -values – as $\{211\}$, $\{220\}$, $\{321\}$, $\{400\}$, $\{420\}$, $\{332\}$, $\{422\}$, and $\{431\}$, respectively. To give an impression of the geometry of the corresponding crystallographic unit cell, the bilayer midplane of this phase represented by a Schoen gyroid (G) triply periodic minimal surface is depicted in Figure 6.31 calculated from exact Weierstraß parametrisation using MATLAB. The top row depicts a representation by triangles from a Delaunay triangulation and the bottom row shows a surface representation with interpolated surface shading.

By fitting Gaussian functions to all peaks in the scattering patterns, the lattice constant as well as the overall peak intensity of each phase can be obtained. The lattice constants of the cubic phase, a , and the lamellar phase, d , can be calculated from equations 2.41 and 2.38, respectively.

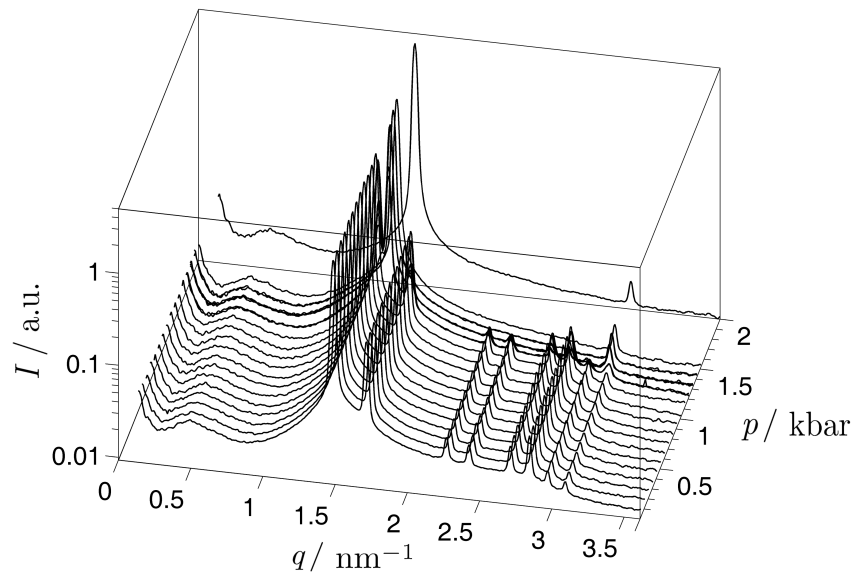


Figure 6.30: SAXS scattering patterns of monoolein (17 %_{wt} water content) at 60 °C between atmospheric pressure and 2.0 kbar. At 1.25 kbar, the transition from the cubic $Ia3d$ to a lamellar phase can be observed.

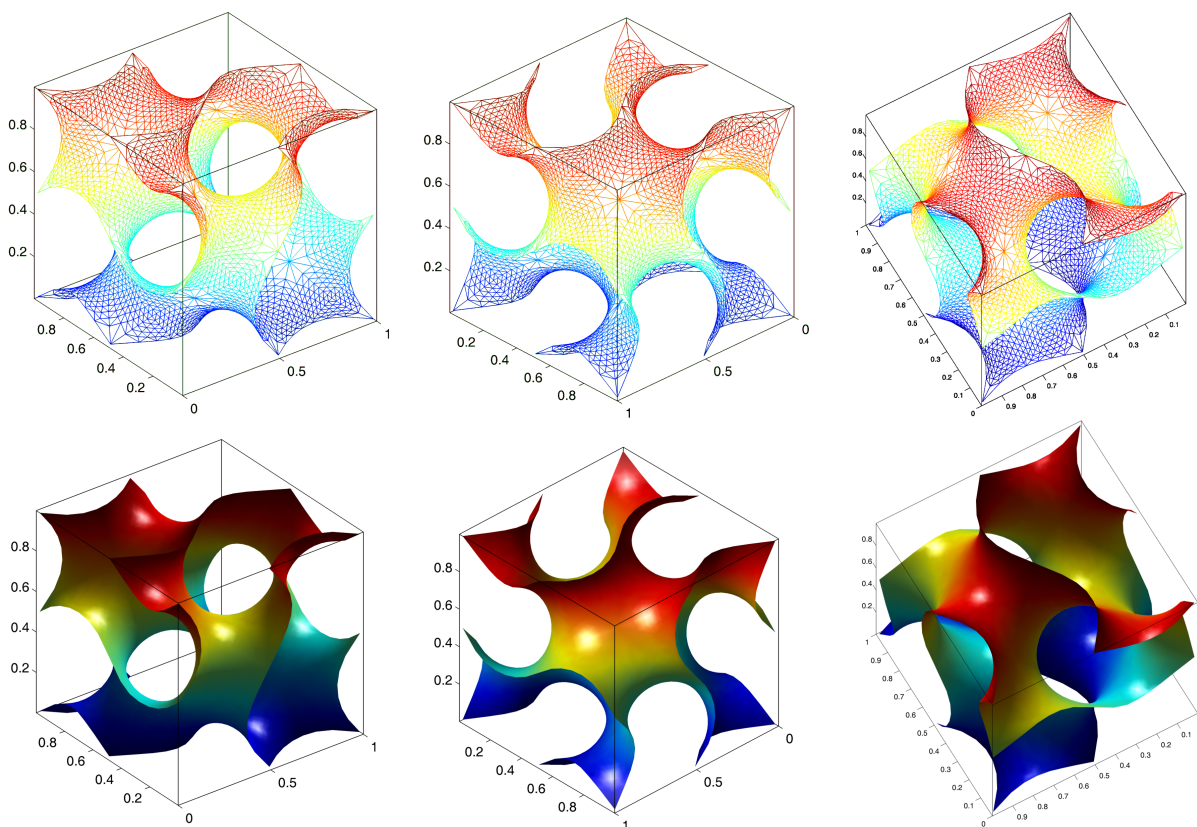


Figure 6.31: The Schoen gyroid (G) triply periodic minimal surface corresponding to the space group $Ia3d$ in different orientations calculated from exact Weierstraß parametrisation using MATLAB. Top row: representation by triangles from a Delaunay triangulation; bottom row: surface representation with interpolated surface shading.

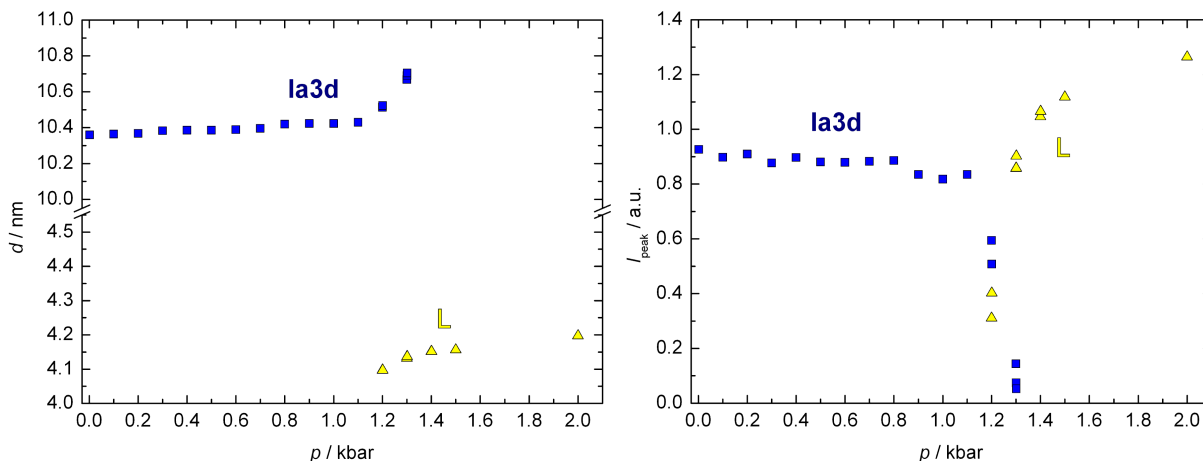


Figure 6.32: Lattice constant, a , and integrated peak intensity, I_{peak} , of monoolein (17%wt water) at 60 °C between atmospheric pressure and 2 kbar. At 1.25 kbar a transition from the cubic $Ia3d$ (blue squares) to a lamellar phase (yellow triangles) can be observed.

As an example, the lattice constants and integrated peak intensities found at 60 °C are presented in Figure 6.32 in a pressure range between atmospheric pressure and 2.0 kbar. Initially only one phase, the cubic $Ia3d$ phase, can be found. Up to 1.1 kbar the peaks in this single-phase region have a constant intensity and the lattice spacing increases only slightly from 10.36 nm at atmospheric pressure to 10.43 nm at 1.1 kbar. Thereafter, a two-phase coexistence region can be found between 1.15 and 1.35 kbar. Here, the intensity of the cubic phase decreases and the intensity of the emerging lamellar phase increases concomitantly. At higher pressures again a single-phase region can be observed with a lamellar lattice constant of 4.15 nm at 1.4 kbar, which increases to 4.20 nm at 2.0 kbar.

From numerous additional pressure dependent measurements at different temperatures – approximately 770 in total – as well as temperature dependent measurements at atmospheric pressure, a p, T -phase diagram could be constructed as presented in Figure 6.33. At high temperatures and low pressures the pure cubic $Ia3d$ phase can be found (blue area). In the middle of the phase diagram a fluid lamellar phase, denoted by L_{α} , is obtained. Finally, at high pressures and low temperatures a crystalline lamellar L_c phase exists. Between all pure phases a region of phase coexistence can be found according to Gibb’s phase rule. The different colours of data points represent the different samples measured at various experimental runs conducted during this project. The transition from the pure cubic to the lamellar-cubic coexistence region is depicted by a square, the transition from the coexistence region into the pure fluid lamellar phase by a dot, the boundaries found between the pure fluid lamellar to the lamellar-lamellar phase is denoted by a triangle, and finally the transition from this coexistence region to the pure crystalline lamellar phase by a star.

A number of structural parameters of simple two-component systems (lipid and water) in their single-phase regions can be calculated. All samples had a water content of 17%wt. Taking into account the mass densities of water (0.9970 g/ml) and monoolein (0.942 g/ml) at 25 °C, the volume fraction of water, ϕ_w , can be calculated to 0.162. Accordingly, the lipid volume fraction, ϕ_l , is 0.838. The lipid molecular volume can be calculated from the mass density and the molar mass of monoolein (356.6 g/mol) to 0.6285 nm³. Finally, the critical packing parameter, γ , which is independent of the lattice spacing and therefore identical for all samples in the $Ia3d$ phase, can be calculated to 1.4383 using equation 4.16.

For the cubic $Ia3d$ phase, the lipid chain length, l , the interfacial area integrated over a single monolayer, A_1 , the number of lipid molecules per unit cell, n_1 , the area per lipid molecule at the interface, a_0 , the

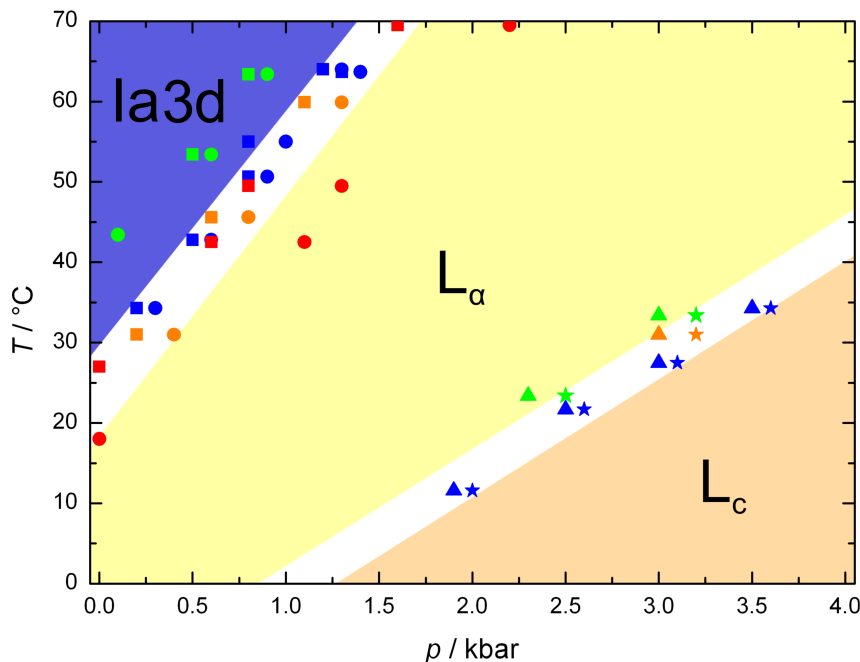


Figure 6.33: p, T -phase diagram of pure monoolein (17 %_{wt} water content). Regions of pure phases are depicted in colours and phase coexistence regions are in white. The different colours of data points represent the different samples measured at various experimental runs conducted during this project.

radius of a water channel, r_w , as well as the surface averaged values of mean curvature, $\langle H \rangle$, and Gaussian curvature, $\langle K \rangle$, can be calculated according to equations 4.11 - 4.15 and 4.17. The resulting parameters for different temperatures and pressures are given in Table 6.3. All data are in excellent agreement with data found in the literature for monoolein with a similar level of hydration (20 %_{wt}).^[68]

Increasing the pressure from atmospheric pressure to 1.0 kbar at 64.0 °C leads only to minor changes in the parameters of the cubic $Ia3d$ unit cell. The lattice spacing, a , and the lipid chain length, l , increase slightly from 10.39 nm to 10.46 nm and 1.623 nm to 1.634 nm, respectively. The radius of the water channels rises from 0.954 nm to 0.960 nm. As a consequence, the size of the unit cell increases and a larger interfacial area integrated over a single monolayer (from 201.3 nm² to 204.0 nm²) as well as a higher number of lipid molecules per unit cell (from 1495 to 1526) can be observed. The area per lipid molecule at the interface remains basically the same, indicating no significant lateral compression in the monolayer with increasing pressure in the system.

Table 6.3: Parameters of the cubic $Ia3d$ unit cell of pure monoolein (17%_{wt} hydration) as a function of pressure, p , and temperature, T : the lattice constant, a , the lipid chain length, l , the interfacial area integrated over a single monolayer, A_1 , the number of lipid molecules per unit cell, n_1 , the area per lipid molecule at the interface, a_0 , the radius of a water channel, r_w , and the surface averaged values of the mean curvature, $\langle H \rangle$, and Gaussian curvature, $\langle K \rangle$.

T [°C]	p [kbar]	a [nm]	l [nm]	A_1 [nm ²]	n_1 []	a_0 [nm ²]	r_w [nm]	$\langle H \rangle$ [nm ⁻¹]	$\langle K \rangle$ [nm ⁻²]
64.0	0.001	10.39	1.623	201.3	1495	0.269	0.954	-302.9	-0.151
64.0	1.0	10.46	1.634	204.0	1526	0.267	0.960	-307.0	-0.149
34.3	0.001	11.00	1.718	225.6	1774	0.254	1.010	-339.5	-0.134

Table 6.4: Parameters of lamellar phases calculated for pure monoolein (17%_{wt} hydration) as a function of temperature, T , and pressure, p : the lattice constant, d , the lipid chain length, l , area per lipid at cross section, a_0 , and the thickness of a water channel, d_w .

phase	T [°C]	p [kbar]	d [nm]	l [nm]	A_l [nm ²]	d_w [nm]
L _α	64.0	1.4	4.18	1.767	0.359	0.678
L _α	64.0	3.5	4.31	1.822	0.348	0.699
L _α	34.4	0.5	4.42	1.868	0.339	0.717
L _α	34.4	3.0	4.53	1.915	0.331	0.734
L _α	11.6	0.001	4.55	1.923	0.330	0.738
L _α	11.6	1.5	4.63	1.957	0.324	0.751
L _c	34.3	4.0	4.37	1.847	0.343	0.708
L _c	11.6	2.0	4.40	1.860	0.341	0.713
L _c	11.6	3.6	4.35	1.839	0.345	0.705

Decreasing the temperature from 64.0 °C to 34.3 °C at atmospheric pressure leads to a strong increase of the cubic lattice spacing from 10.39 nm to 11.00 nm and a rise in the lipid chain length from 1.623 nm to 1.718 nm. Also, the radius of the water channel increases from 0.954 nm at 64.0 °C to 1.010 nm at 34.3 °C. The larger dimensions of the unit cell at the lower temperature, caused by the grown water channel radius as well as lipid chain length, result in an increased interfacial area integrated over a single monolayer of 225.6 nm² (201.3 nm² at 64.0 °C) and more lipids inside a unit cell (1774 at 34.3 °C compared to 1495 at 64.0 °C). The area per lipid molecule at the interface decreases with decreasing temperature, probably due to lower thermal fluctuations, which impede a tight lateral packing of lipids at elevated temperatures. The small thermal fluctuations in combination with a higher conformational order of the lipids (which causes an elongation of the molecules) lead to a smaller critical packing parameter, lower curvature of the membrane, and a larger lattice constants of the cubic $Ia3d$ phase at low temperatures.

Also for the lamellar single-phase regions, L_α and L_c, several structural parameters can be calculated: the lipid chain length, l , area per lipid at cross section, a_0 , and the thickness of a water channel, d_w . The values found for pure lamellar phases of monoolein with a hydration level of 17%_{wt} at different temperatures and pressures are shown in Table 6.4.

The d -spacing of the L_α-phase increases with increasing pressure at 64 °C. Both the lipid thickness as well as the thickness of the water layer between two lamellar sheets, contribute to the obtained d -spacing. By increasing the pressure from 1.4 kbar to 3.5 kbar at 64 °C, the d -spacing increases from 4.18 nm to 4.31 nm, which comprises a thickening of the lipid chain length, l , from 1.767 to 1.822 nm and a rise of the water channel from 0.678 to 0.699 nm. The increase of the chain length is probably due to a more extended conformation of the lipid hydrocarbon chains and decreasing ratio of *gauche* conformers with increasing pressure. The sum of the two effects equals the change in d -spacing, suggesting no significant contribution of the lipid head groups. The cross sectional area per lipid, a_0 , decreases slightly from 0.359 to 0.348 nm² upon compression of the lipid membrane, owing to the higher conformational order of the hydrocarbon chains. A very similar behaviour was found with increasing pressure at 34.4 °C and 11.6 °C in the L_α-phase.

Decreasing the temperature from 64 °C (at 3.5 kbar) to 34.4 °C at 3.0 kbar, the d -spacing of the L_α-phase increases from 4.31 nm to 4.53 nm. This increase results from a thickening of the lipid chain length (from 1.822 to 1.915 nm) as well as a growing thickness of the water channel (from 0.699 to 0.734 nm).

As expected, the cross sectional area per lipid, a_0 , decreases from 0.348 to 0.331 nm². Whereas the larger d -spacing can be contributed to a more ordered and extended conformation of the lipids, the decrease in the cross sectional area is probably due to the lower thermal fluctuations, and slowed dynamics and lateral lipid diffusion in the membrane. Similar temperature dependent effects were also obtained for other pressures.

As expected, the effects of temperature and pressure on the L_c-phase are significantly smaller. The main reason is probably that the hydrocarbon chains of the lipids in the L_c-phase are already in the all-*trans* conformation, arranged in a highly ordered, crystalline packing. The degrees of freedom in this phase are very small. With increasing pressure from 2.0 to 3.6 kbar at 11.6 °C a slight decrease in the d -spacing from 4.40 to 4.35 nm can be observed. This behaviour is contrary to the one observed in the L_α-phase, where an increasing pressure led always to an increase in the d -spacing due to a higher conformational order. In the L_c-phase, an increase in the conformational order is not possible – the system is already completely ordered at low pressure. Therefore pressure is expected to lead to a small compression of the molecules and the water layer between the lamellar sheets only. In fact, slightly decreasing values of the lipid chain length and the thickness of the water layer, as well as a slightly increasing cross sectional area per lipid are observed.

Decreasing the temperature from 34.3 °C at 4.0 kbar to 11.6 °C at 3.6 kbar leads only to an insignificant reduction of the d -spacing from 4.37 to 4.35 nm. The lipid hydrocarbon chain length decreases concomitantly from 1.847 to 1.839 nm and the thickness of the water layer as well as the area per lipid at cross section do not change in the range of error. This very slight decrease in the d -spacing originates from the lower thermal fluctuations and therefore closer packing of the lipids at lower temperature.

The small alternations in the L_c-phase with varying temperature and pressure indicate that most of the changes in the L_α-phase originate from adjustments in the conformational order and consequential rearrangements in lateral packing. The effect of the compression of the molecules, i.e. compression and changes in the angle of chemical bonds, plays only a minor role for pressures up to 4.0 kbar.

Kinetic pressure-jump experiments

Nine pressure-jumps were conducted at different temperatures and with various pressure-jump amplitudes, yielding about 840 scattering patterns. The kinetics of the phase transition was evaluated by observing the lattice constants and integrated peak intensities of all phases as a function of time. The rate at which a phase transition proceeds may be quantified by tracking changes in the amount of both the growing and the disappearing phases. Provided the scattering factor for each phase remains constant, the intensity of the diffraction peaks corresponding to a particular phase may be used as an indication of the amount of the phase. As the observed changes in lattice parameters are relatively small for all phases, the changes in intensity may be assumed to directly reflect changes in phase composition.

Figure 6.34 shows the scattering patterns of monoolein (17%_{wt} water content) for the first 19 s after a pressure-jump from 1.0 kbar to 2.0 kbar at 63.7 °C. The first three scattering patterns are taken before the jump was triggered at $t = 0$ s, showing the first eight peaks of a pure *Ia3d* phase, as expected at this temperature and pressure (q.v. Figure 6.33). Already at $t = 0$ s a small shoulder emerges between the first two cubic peaks, denoted by their Miller indices as the {211} and {220} reflection, respectively. The new peak, identified as the {100} reflection of an emerging lamellar phase, increases in intensity with time without barely changing its peak position. The second order of the lamellar reflection, i.e. the {200} peak, does not allow to monitor the growth of this phase, because the position of this peak is

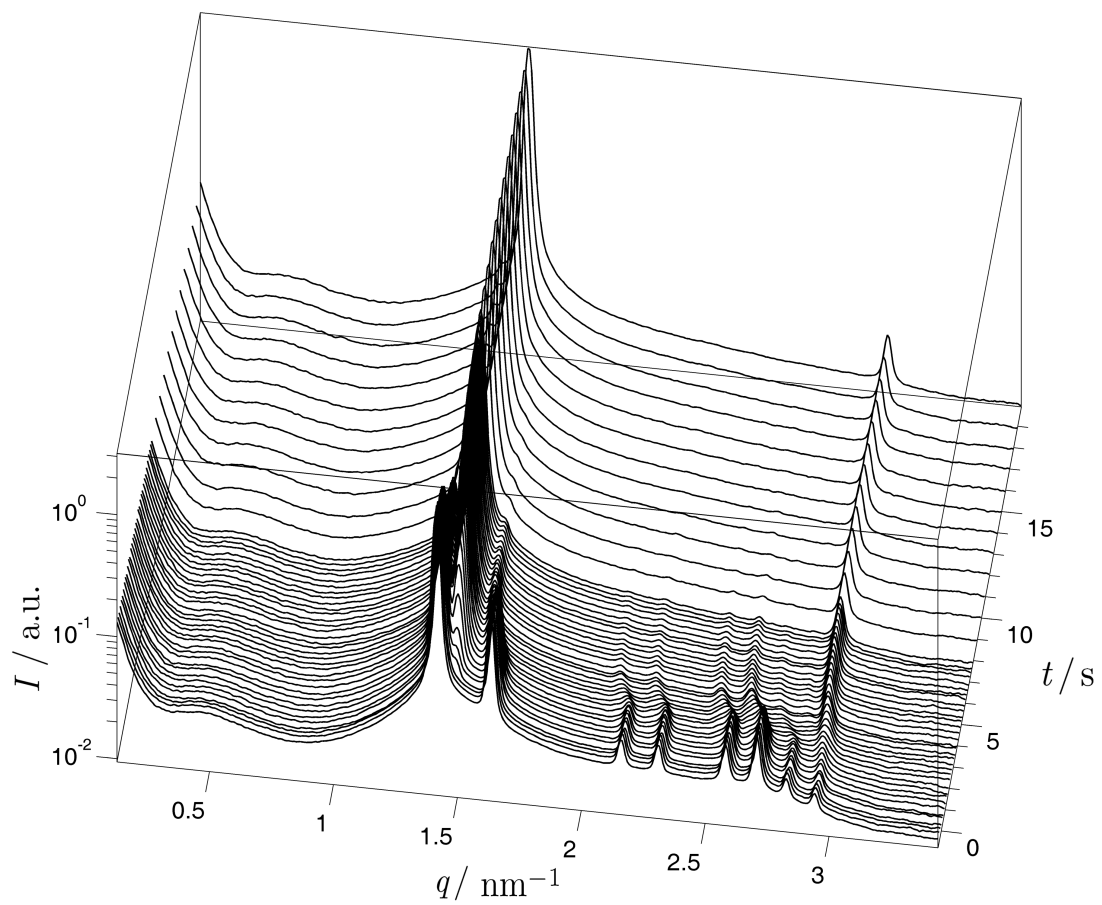


Figure 6.34: Scattering patterns after a pressure-jump of monoolein from 1.0 kbar to 2.0 kbar at 63.7°C , jumping from the cubic $Ia3d$ into the fluid lamellar L_α -phase.

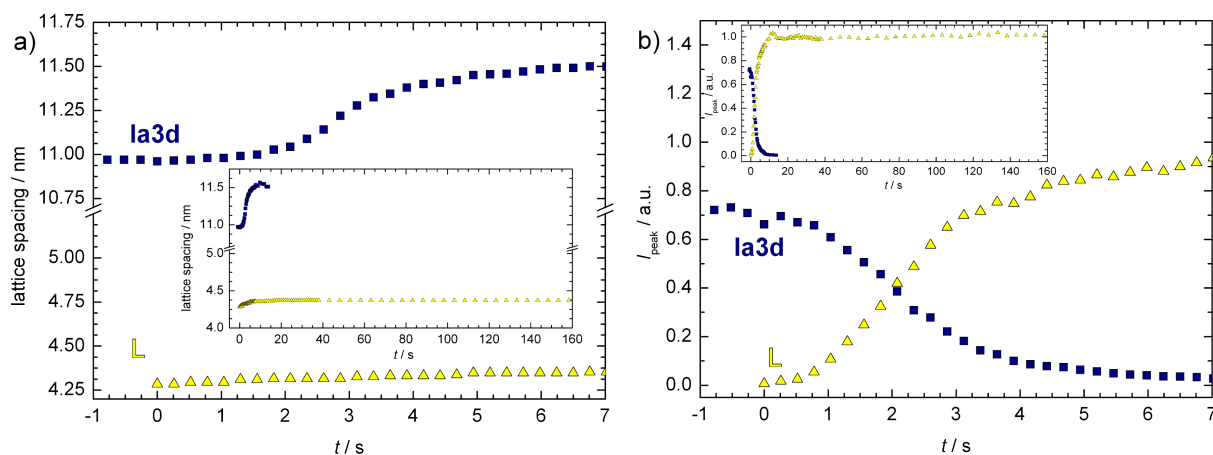


Figure 6.35: Structural parameters of a pressure-jump of monoolein (17%_{wt} water content) from 1.0 kbar to 2.0 kbar at 63.7°C. Lattice constants (a) and integrated peak intensities (b) of all phases as a function of time for the first 7 s after the pressure-jump are shown. The insets show the same data on a much larger time-scale, up to 160 s.

nearly identical with the position of the eighth peak of the *Ia3d* phase, the {431} reflection, resulting in a seamless transition between cubic and lamellar reflections at this position.

To obtain more detailed information, all peaks were fitted and the lattice spacings as well as the integrated peak intensities of all phases were plotted as a function of time. In Figure 6.35a, the observed lattice constants of a pressure-jump from 1.0 kbar to 2.0 kbar at 63.7°C, corresponding to the scattering patterns shown in Figure 6.34, are presented. The appendent integrated peak intensities are depicted in Figure 6.35b. Here, a continuous transition from the cubic *Ia3d* phase to a lamellar phase can be found. The lamellar phase emerges already at the moment of the pressure-jump ($t = 0$ s). Afterwards, a long coexistence of both phases is found over approximately 15 s, with increasing intensity of the lamellar phase and concomitantly decreasing intensity of the cubic phase.

The d -spacing of the lamellar phase increases only slightly from 4.28 nm at $t = 0$ s to a final value of 4.37 nm at $t = 160$ s. A more complex behaviour is observed for the lattice spacing of the *Ia3d* phase. Barely no changes of the initial value of 10.97 nm at $t = -0.78$ s are found in the first 1.5 s. Interestingly, the change in pressure due to the p -jump has nearly no effect on the d -spacing or peak intensity of this phase, indicating a kinetic trapping. Afterwards, a sigmoidal increase within 3.5 s to a value of 11.45 nm at $t = 4.9$ s, followed by a small linear increase to a final value of 11.51 nm at $t = 13.8$ s, is observed. The intensity of the cubic *Ia3d* phase has already nearly vanished at $t \approx 5$ s.

The lattice constants and peaks intensities as a function of time calculated from a pressure-jump in the opposing pressurising direction with a nearly identical pressure amplitude (2.0 kbar to 0.95 kbar) at the same temperature of 63.7°C are shown in Figure 6.36. It is obvious that this transition from the lamellar to the cubic *Ia3d* phase is much faster than the transition in the reverse direction. The lamellar phase vanishes completely within 0.26 s after the pressure-jump. The full intensity of the cubic signal is reached already at $t = 0.78$ s (see Figure 6.36b). The lattice constant of the *Ia3d* phase decreases afterwards slightly from 11.08 nm at $t = 0.26$ s to 10.95 nm at $t = 160$ s.

Other pressure-jumps were conducted at 63.7°C in both pressurising directions with a higher pressure-jump amplitude, Δp , of 2.10 kbar (data not shown). As found before, the transition from the lamellar to the cubic phase is much faster with an overall transition time of 1.6 s than the transition in the reverse direction from cubic to lamellar phase with an overall transition time of 4.7 s. Interestingly, the lamellar

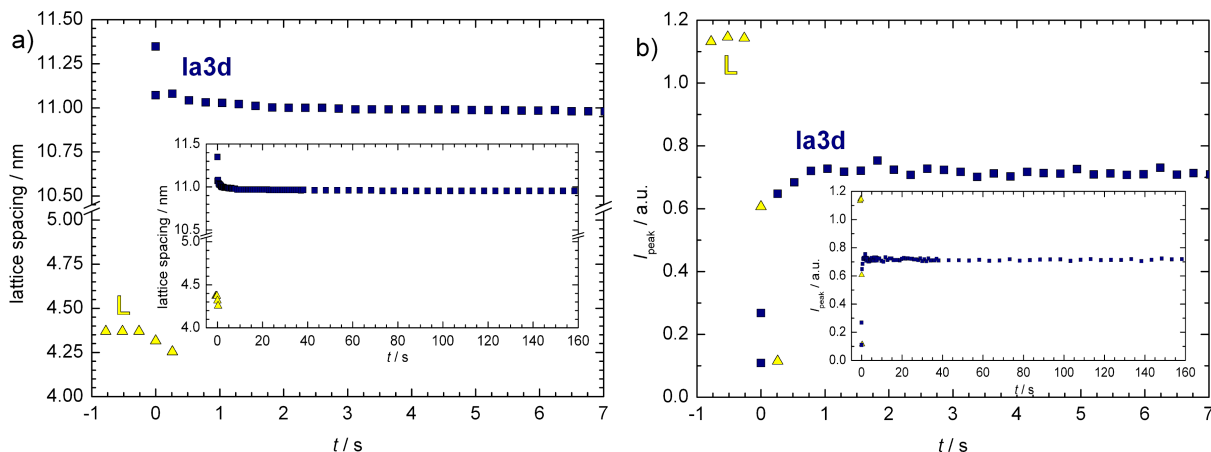


Figure 6.36: Pressure-jump of monoolein (17%_{wt} water content) from 2.00 kbar to 0.95 kbar at 63.7 °C. Lattice constants (a) and integrated peak intensities (b) of all phases as a function of time for the first 7 s after the pressure-jump. The insets show the same data on a much larger time-scale up to 160 s.

to cubic transition is faster with a small pressure-jump amplitude (0.78 s at $\Delta p = 1.05$ kbar compared to 1.6 s at $\Delta p = 2.10$ kbar), whereas the cubic to lamellar transition is faster for the large pressure-jump amplitude (15 s at $\Delta p = 1.05$ kbar compared to 4.7 s at $\Delta p = 2.10$ kbar). A larger pressure-jump amplitude is equivalent to a larger amount of (mechanical) energy transferred into the system, but also leads to a stronger disruption of the phases. The slower transition from lamellar to cubic with a higher pressure-jump amplitude indicates that already with the small pressure-jump amplitude enough energy was available for the phase transition. A larger pressure-jump amplitude leads just to a stronger disruption of the system resulting in a longer relaxation time. For the pressure-jump into the lamellar phase an opposite behaviour can be observed. The larger jump amplitude, providing more energy, leads to a faster transition. The transition to the lamellar (fluid) phase is very fast.

Another set of pressure-jumps with an amplitude, Δp , of about 1 kbar was conducted at 50.1 °C. Compared to the pressure-jump at 63.7 °C with the same pressure-amplitude, very similar overall transition times in both pressure-jump directions have been found. At 50 °C, the transition from lamellar to cubic phase is finished after approximately 1 s, and the transition in the opposite direction takes 14.5 s – compared to 0.78 s and 15 s at 63.7 °C. It can be concluded that the temperature has only a minor influence on the transition rate between lamellar and cubic phase, whereas the pressure-jump amplitude has a strong effect on the kinetics of the phase transition observed here.

6.5.4 Conclusions

Pure monoolein at a limited hydration level of 17%_{wt} has been studied. A detailed knowledge of the system's phase behaviour was gained. The observed phase transition from the lamellar to the cubic *Ia3d* phase found at about 30 °C at atmospheric pressure is in good agreement with the published temperature, hydration-phase diagram found in the literature.^[264]

It can be concluded that monoolein at this hydration level is highly suitable for the study of lamellar-cubic phase transition and the influence of different additives (e.g. fusion peptides, which are known to induce cubic phases) on this transition, as presented in section 8.2.

The system can also be used to study lamellar-cubic phase transition kinetics with overall transition times of a few seconds up to a minute.

6.6 Archaeal lipids

The results shown in this section were measured in cooperation with F. Evers (Department of Physics, TU Dortmund University). The experiments were planned and conducted together at the ESRF in Grenoble (France). The correction of the raw data (integration of the detector raw data, background- and illumination-correction, etc.) to obtain the corrected intensities, $I(q)$ and $I(q_{xy}, q_z)$, was done using MATLAB scripts written by me. The fitting of the XRR data was performed by F. Evers and the calculations based on the GIXD results were my task. Finally, the results were discussed together. The results of this study are published in [362].

6.6.1 Introduction

Langmuir monolayer films of three different bipolar tetraether lipids (PLFE, “archaeal lipids”) at the air-water interface were prepared, and the dependence of the surface pressure on the structure and packing properties of the PLFE monolayer were analysed in a temperature range between 10 °C and 50 °C by X-ray reflectometry (XRR) and grazing incidence X-ray diffraction (GIXD). The measurements were conducted on an aqueous subphase at a pH value of 2.2, mimicking the environmental conditions surrounding thermoacidophilic archaeon cells. The experiments were performed with PLFE lipid mixtures isolated from cells grown at 68 °C, 76 °C, and 81 °C.

A total monolayer thickness of approximately 30 Å was found for all monolayers, hinting at a U-shape conformation of the molecules with both head groups in contact with the interface. The monolayer thickness increased with rising film pressure and decreased with increasing temperature. At 10 °C and 20 °C large, highly crystalline domains were observed by GIXD, whereas at higher temperatures no distinctive crystallinity could be found. For lipids grown at higher temperatures a slightly more rigid behaviour of the lipid chains could be observed. A variation in the pH of the subphase changed the response of disordered regions of the monolayer to the film pressure significantly, whereas only a small effect on highly ordered domains could be found.

6.6.2 Materials and methods

Materials

The dibiphtanyldiglycerol tetraether lipids (PLFE, chemical structure displayed in Figure 4.8, page 57) were extracted from the plasma membrane of the thermoacidophilic archaeon *Sulfolobus Acidocaldarius*, grown at 68 °C, 76 °C, and 81 °C. Chloroform, methanol, and hydrochloric acid were purchased from Sigma (Taufkirchen, Germany) and used without further purification. Aqueous solutions were prepared using water filtered through a Milli-Q purification system. The pH of the aqueous subphase was adjusted to 2.2 using hydrochloric acid. PLFE was dissolved in a mixture of chloroform, methanol and water (75:19:5 vol) and spread on the aqueous subphase.

X-ray reflectometry and grazing incidence X-ray diffraction

Archaeal lipid stock solutions were spread at the air-water interface on a Langmuir trough. Lipid films were examined at various lateral film pressures, π , between 10 and 40 mN m⁻¹ and different subphase temperatures ranging from 10 °C to 50 °C.

The X-ray scattering experiments were conducted at the liquid surface diffractometer of beamline ID10B at the synchrotron light source ESRF (Grenoble, France).^[97] For these experiments, the Langmuir trough was mounted on the diffractometer. The analysis of surface X-ray scattering data is outlined in detail in chapter 3. X-ray reflectivity (XRR) data are plotted as R/R_F versus q_z , with the reflectivity, R , the Fresnel reflectivity, R_F , and the vertical wave vector transfer, q_z . In a GIXD experiment, the momentum transfer has a horizontal and vertical component, q_{xy} and q_z (q.v. section 3.2.2). Integration along those directions yields Bragg rod and Bragg peak patterns, respectively.

6.6.3 Results and discussion

Vertical structure of PLFE monolayers as a function of surface pressure

X-ray scattering data of PLFE monolayers spread on subphases at different temperatures and pH-values as a function of lateral film pressure are presented. Figure 6.37 shows X-ray reflectivity data and inferred electron density profiles of PLFE monolayers, grown at 68 °C, at varying lateral film pressure and different subphase temperatures. All X-ray reflectivity data of pure PLFE monolayers could be adequately described by a two-layer model, accounting for a PLFE lipid head group and lipid chain region, respectively. Thus, from the analysis of XRR measurements³, variations in lateral surface pressure and subphase temperature can be related to changes in the vertical structure of PLFE monolayers.

For PLFE (grown at 68 °C) at a subphase temperature of 10 °C (Figure 6.37 top row), increasing film pressure results in a successively rising total monolayer thickness (from 30.2 Å at $\pi = 10 \text{ mN m}^{-1}$ to 32.8 Å at $\pi = 30 \text{ mN m}^{-1}$), which can be ascribed to an increasing thickness of the head group region (from 5.6 Å to 9.2 Å). The electron density of the head group region decreases slightly and concomitantly the electron density of the lipid chains increases at higher film pressures. However, at a subphase temperature of 50 °C (Figure 6.37 bottom row), changes of the monolayer thickness with increasing film pressure are not as pronounced as at low temperature. Increasing film pressure from $\pi = 10 \text{ mN m}^{-1}$ to $\pi = 20 \text{ mN m}^{-1}$ leads to an enhanced electron density of the head group and an increase in thickness of the hydrocarbon region. Between $\pi = 20 \text{ mN m}^{-1}$ and $\pi = 30 \text{ mN m}^{-1}$ the electron density profile (EDP) does not vary drastically.

PLFE monolayers composed of lipids grown at 76 °C and 81 °C show a different response to increased film pressure at low and elevated subphase temperatures, respectively.^[362] In these cases, the variations of the total monolayer thickness are more pronounced at a subphase temperature of 50 °C than at 10 °C. The strongest effects of the subphase temperature on the total monolayer thickness are observed at a PLFE monolayer grown at 81 °C, where the overall thickness changes between 10 mN m^{-1} and 30 mN m^{-1} by only 0.8 Å at 10 °C and by 3.4 Å at 50 °C. For both PLFE grown at 76 °C and 81 °C, both the head group as well as the hydrocarbon chain region thicknesses increase with increasing lateral film pressure.

Influence of subphase temperature on the vertical structure of PLFE monolayers

Figure 6.38 highlights the effect of varying subphase temperatures on the electron density profile of PLFE monolayers at different film pressures. Again, lipid monolayers composed of PLFE grown at different temperatures show slightly different responses to variations of the subphase temperature, T_{sub} . However, two general trends become visible: the total monolayer thickness increases with rising film pressure and decreases with rising subphase temperature. For monolayers composed of PLFE grown at

³All XRR data were fitted by F. Evers using LSFIT.

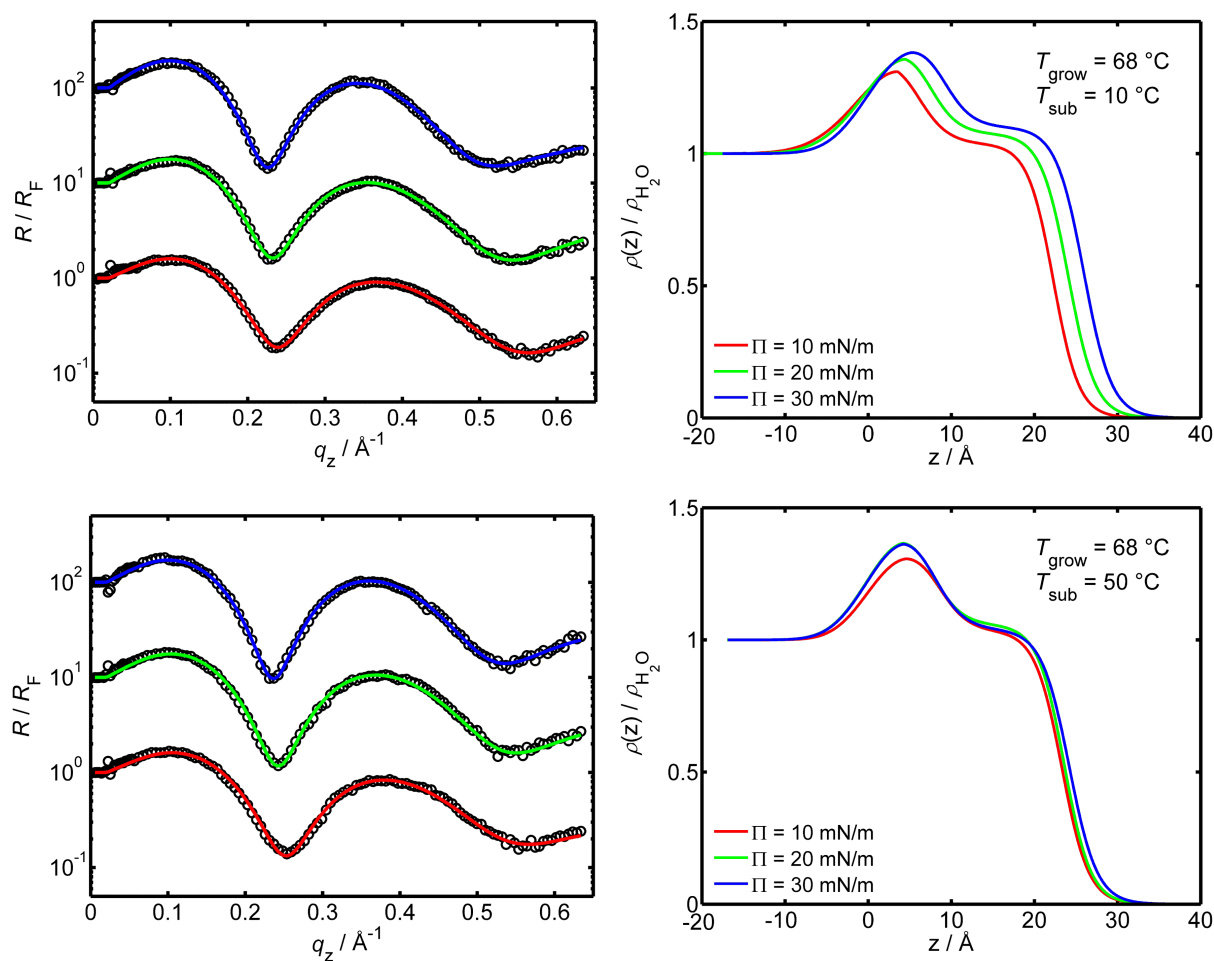


Figure 6.37: (Left) X-ray reflectometry data (symbols) obtained from archaeal lipid monolayers (PLFE grown at 68°C) at the air-water interface, presented together with the best fits (solid lines) normalised to the Fresnel reflectivity, R_F . For clarity, the reflectivity curves are shifted along the ordinate with increasing film pressure. (Right) Normalised electron density profiles as retrieved from the fits on the left-hand side. PLFE monolayers were spread on subphases at different subphase temperatures of 10°C (top) and 50°C (bottom).

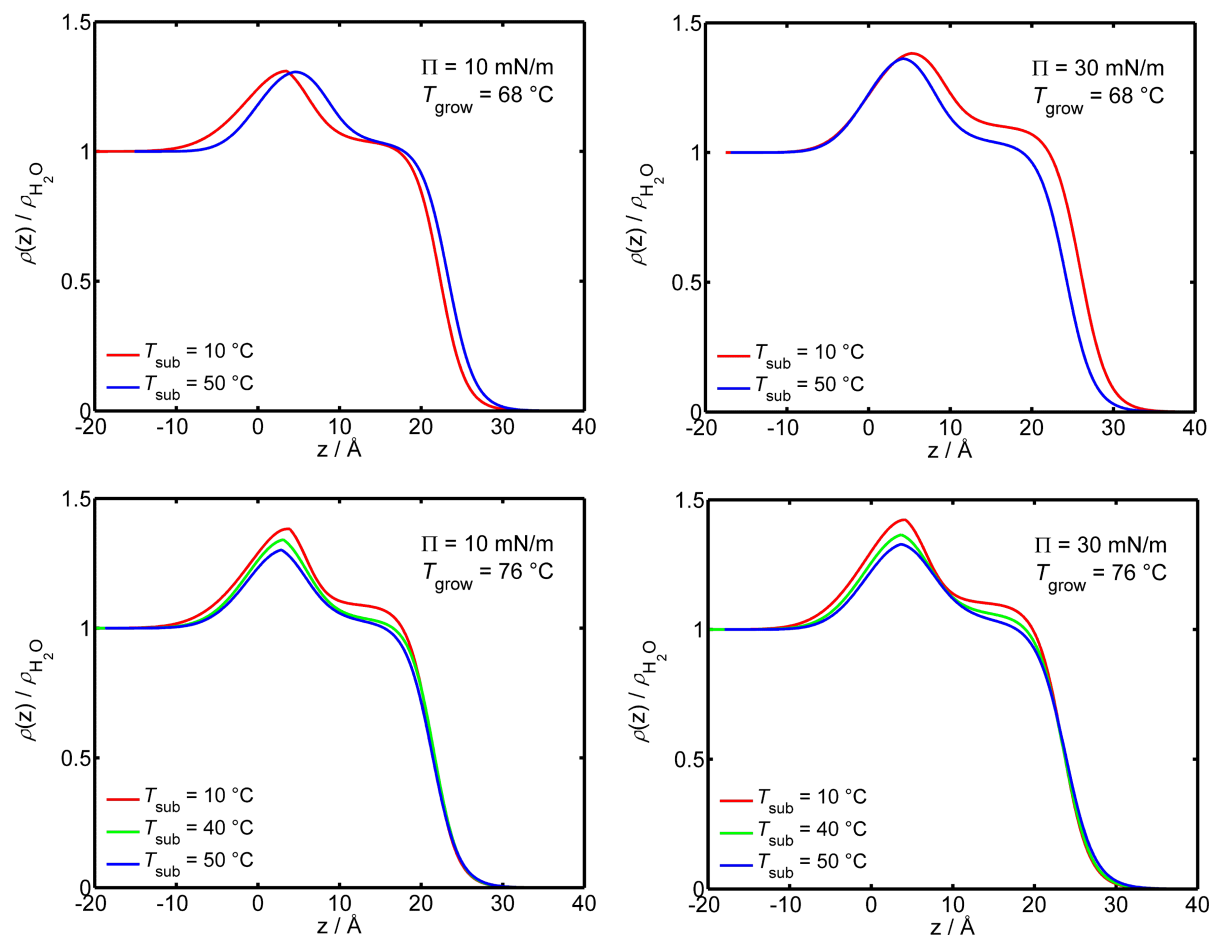


Figure 6.38: Influence of subphase temperature on the PLFE monolayer structure at different surface pressures (left: 10 mN m^{-1} , right: 30 mN m^{-1}) for PLFE grown at 68°C (top row) and 76°C (bottom row).

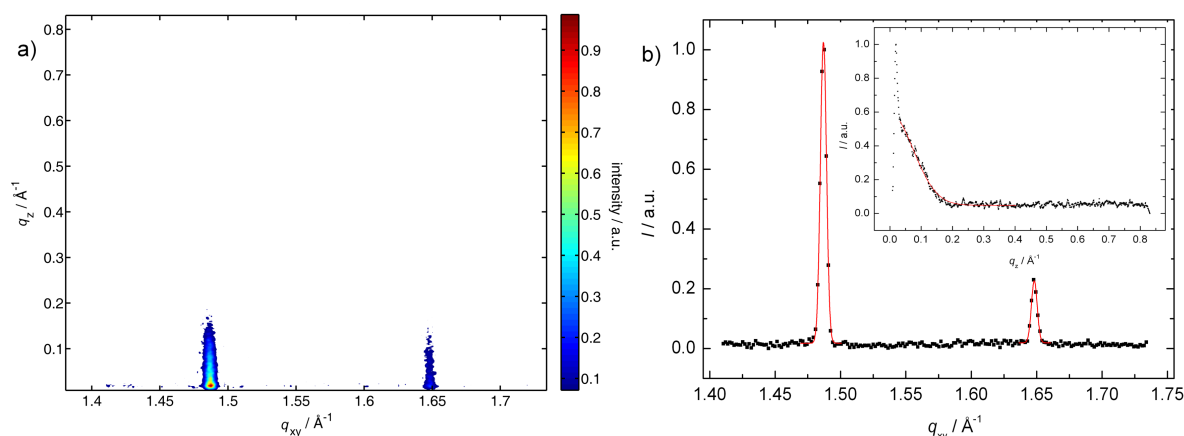


Figure 6.39: a) Two-dimensional contour plot of the intensity, $I(q_{xy}, q_z)$, along the horizontal (q_{xy}) and vertical (q_z) scattering directions as obtained from an archaeal lipid monolayer (grown at 81°C) at a film pressure of $\pi = 30 \text{ mN m}^{-1}$. b) GIXD pattern $I(q_{xy})$ obtained by integrating along q_z for an archaeal lipid monolayer (grown at 81°C ; squared symbols). Peaks were fitted by Gaussian functions (solid lines). (Inset) Typical Bragg rod intensity profile, $I(q_z)$, obtained by integrating along the q_{xy} -region of the first Bragg peak. The absence of a peak at $q_z \neq 0$ indicates little or no molecular tilt.

68°C , changing subphase temperature from 10°C to 50°C at a low film pressure of $\pi = 10 \text{ mN m}^{-1}$ mainly alters the organisation of the lipid head groups. In particular, the thickness of the tail region decreases by 2 \AA , while the thickness of the head group region increases by 3 \AA . At an elevated surface pressure of $\pi = 30 \text{ mN m}^{-1}$, the decrease of total monolayer thickness (2 \AA) with rising subphase temperature is pronounced. Moreover, this high lateral film pressure, the electron density and the thickness of the head group as well as those of the chain region are diminished. For lipid monolayers composed of PLFE grown at 76°C both at a low film pressure of $\pi = 10 \text{ mN m}^{-1}$ and at a high film pressure of $\pi = 30 \text{ mN m}^{-1}$, increasing T_{sub} from 10°C over 40°C to 50°C successively decreases the electron density of both the head group and the chain region, while the thickness changes are not that striking. For example, at $\pi = 30 \text{ mN m}^{-1}$, the total monolayer thickness drops from 31.4 \AA over 31.2 \AA to 31.0 \AA with increasing temperature.

Effect of growth temperature on the vertical structure of PLFE monolayers

In all cases, monolayers composed of PLFE grown at 76°C and at 81°C , respectively, show rather similar structure upon different external stresses. However, films composed of PLFE grown at 68°C exhibit an enlarged total monolayer thickness (by 1 \AA) at low subphase temperature and high film pressure as well as at elevated subphase temperature and low film pressure.

Lateral structure of PLFE monolayers as revealed by grazing incidence X-ray diffraction

A typical GIXD map, $I(q_{xy}, q_z)$, as obtained from an archaeal lipid monolayer (growth temperature 81°C) at the air-water interface with a lateral film pressure of $\pi = 30 \text{ mN m}^{-1}$ and a subphase temperature of 10°C , is shown in Figure 6.39a. Two distinct peaks are observed, indicating the existence of highly ordered domains in the monolayer with a distorted hexagonal packing. In all GIXD measurements, two peaks were found suggesting an identical structure of the crystalline unit cell for all samples studied. All fit parameters of the unit cells are presented in Table 6.5 in detail.

Table 6.5: Calculated parameters of grazing incidence diffraction measurements of different archaeal lipid monolayers at the air-water interface: Lattice vectors in real space, $a = b, c$, angle included by lattice vectors, γ , lateral 2D crystalline domain length, L_{xy} , vertical crystalline domain length, L_z , and area per hydrocarbon chain, A_{chain} , are listed for all samples.

T_{growth} [°C]	pH []	T_{sub} [°C]	π [mN m ⁻¹]	a, c [Å]	γ [°]	L_{xy} [Å]	L_z [Å]	A_{chain} [Å ²]
76	2.2	10	30	4.580, 5.077	112.7	1650, 1320	30.3, 31.2	19.35
68	2.2	10	30	4.581, 5.081	112.6	2200, 1700	30.9, 28.9	19.37
81	2.2	10	30	4.581, 5.081	112.6	2200, 1860	30.3, 30.9	19.37
76	2.2	20	30	4.581, 5.081	112.5	1800, 1510	26.0, 26.4	19.37
76	6.5	20	10	4.531, 5.102	111.5	760, 400	25.1, —	19.10
76	6.5	20	30	4.582, 5.064	112.9	1620, 880	26.2, 26.6	19.33
76	6.5	20	10	4.569, 5.056	112.8	1310, —	26.8, —	19.24
76	6.5	20	20	4.571, 5.061	112.8	1190, 760	28.2, —	19.27
76	6.5	20	30	4.574, 5.062	112.8	1050, 730	28.0, —	19.28
76	6.5	20	40	4.577, 5.060	112.9	920, 720	28.6, —	19.30

In Figure 6.39b, the GIXD pattern, $I(q_{xy})$, obtained by integrating along the q_z -direction for an archaeal lipid monolayer (grown at 81 °C) at a lateral film pressure of $\pi = 30 \text{ mN m}^{-1}$ is presented in squared symbols. The peaks of the distorted hexagonal packing can be denoted by their indices - from left to right - $\{10, 01\}$ and $\{1\bar{1}\}$. All peaks were fitted by Gaussian functions in order to locate the positions of the peak maxima as well as to determine their full widths at half maximum (FWHM). The two lattice constants were calculated from the maximum positions of the peaks to $a = b \approx 4.58 \text{ Å}$ and $c \approx 5.08 \text{ Å}$. The angle of the unit cell, γ , was approximately 112.6° , which is slightly smaller than the expected value of 120° for an ideal hexagonal packing. The occupied area per hydrocarbon chain, A_{chain} , was directly calculated from the lattice parameters to $19.4 \text{ Å}^2/\text{chain}$.

From the full widths at half maximum of the Bragg peaks, the lateral crystalline domain lengths, L_{xy} , was calculated. For the $\{10, 01\}$ peak at about $q_{xy} = 1.49 \text{ Å}^{-1}$ and the $\{1\bar{1}\}$ peak at about $q_{xy} = 1.65 \text{ Å}^{-1}$, values in the order of 2200 Å and 1860 Å were obtained, respectively. These values represent huge areas of high crystallinity on the monolayer at a lateral film pressure of $\pi = 30 \text{ mN m}^{-1}$ and a subphase temperature of 10°C .

In Figure 6.39c, a typical Bragg rod intensity profile, $I(q_z)$, obtained by integrating along the q_{xy} -region of the $\{10, 01\}$ Bragg peak is depicted. The maximum at $q_z = 0$ is the so-called Vineyard-Yoneda peak,^[99] which arises from the interference between X-rays diffracted up into the Bragg rod and X-rays diffracted down and then reflected up by the interface. The absence of a peak at $q_z \neq 0$ indicates negligible or no molecular tilt of the hydrocarbon chains relative to the surface normal. The vertical crystalline domain lengths, L_z , was obtained from the full width at half maximum of the Bragg rods. For the two rods corresponding to both Bragg peaks, vertical domain length of 30.3 Å and 30.9 Å were found, respectively.

Archaeal lipids grown at different temperatures (68°C , 76°C , and 81°C) were spread at the air-water interface at 10°C and compressed to a lateral film pressure of $\pi = 30 \text{ mN m}^{-1}$. According to the GIXD data, no significant differences in the lattice parameters and dimensions of crystalline domains were found between the different growth conditions.

GIXD signals were only obtained at subphase temperatures of 10°C and 20°C . No crystalline domains could be found at higher temperatures, probably due to the higher thermal fluctuations and temperature

induced disorder of the lipids hydrocarbon region. The lattice parameters of an archaeal lipid monolayer with a lateral film pressure of $\pi = 30 \text{ mN m}^{-1}$ at a subphase temperature of 20°C show only insignificant variations to the parameters observed at 10°C . However, the dimension of the crystalline domains decreases with increasing temperature by about 20% in lateral direction (L_{xy}) and by approximately 15%, from 30 \AA to 26 \AA , in vertical direction (L_z).

Effect of subphase pH-value on PLFE monolayer structure

So far, the focus was on PLFE monolayers at the air-water interface with a pH value of 2.2, mimicking the environment of thermoacidophilic archaeon cells. Furthermore, PLFE monolayers on subphases with a pH value of 6.5, which is the pH value inside archaeal cells, have been studied as well. At this pH value, PLFE monolayers exhibit different behaviour responding to increasing lateral film pressure in the XRR experiments: while, at a pH value of 2.2, increasing π leads to continuously rising monolayer thickness, at pH 6.5, the largest thickness can be found at low film pressures. At mediate π the monolayer thickness decreases and rises slightly at high values of π again. Moreover, these changes can be related to a growing thickness of the chains (4 \AA) and decreasing thickness of the head groups (4 \AA) upon increasing film pressure.

In the GIXD experiments no significant influence of the subphase pH on the unit cell parameters can be found. The lateral crystalline domain length decreases by about 10% with increasing pH value from 2.2 to 6.5. With increasing lateral film pressure, the archaeal lipid monolayer (growth temperature of 76°C) on a subphase with a pH of 6.5 at 20°C becomes more ordered. The lateral crystalline domain lengths increase between 10 mN m^{-1} and 30 mN m^{-1} from approximately 760 \AA to 1620 \AA . The height of the crystalline domains increases concomitantly slightly by about 5%. Interestingly, the area per hydrocarbon chain also increases with increasing lateral film pressure from $19.1 \text{ \AA}^2/\text{chain}$ at 10 mN m^{-1} to 19.3 \AA^2 at 30 mN m^{-1} . At the same time, the angle of the unit cell, γ , increases briefly from 111.5° to 112.9° .

6.6.4 Conclusions

The behaviour of an archaeal lipid monolayer at the air-water interface has been studied as a function of subphase temperature, subphase pH, film pressure, and growth temperature. From the overall thickness of the film of approximately 30 \AA it could be concluded that the lipids adopt a U-shape conformation with both head groups in contact with the interface. This behaviour has been observed before;^[363, 364] in another study first coexistence of upright standing and U-shape conformation was found, but afterwards a relaxation within 12 h into a pure U-shape conformation was reported.^[364] Here, no sign of any upright standing lipids could be found.

Even though the lipids are not in the same conformation as in a cell membrane of an archaeon bacterium, the results obtained here lead to a better understanding of the thermal stability and the packing properties of archaeal lipids, especially in terms of the lipid head groups. Very little response of lipids in crystalline domains in the monolayer was detected upon changes of the lateral film pressure. At low pH of 2.2 the crystalline domains found were much larger than at pH 6.5 at the same temperature. This indicates a more fluid behaviour of the archaeal cell membrane in the inner side of the cell, where the pH is much higher, than on the outside, where the pH of the environment is highly acidic. Thus, this membrane is separating the cell properly at the outside and at the same time shows a certain fluidity in the inside, allowing for vital membrane associated processes.

In addition to their biological function, owing to their high temperature stability, archaeal lipids are also widely discussed for pharmacological applications. The knowledge gained here can help in designing archaeal bipolar tetraether lipid layers or coatings for technological applications such as crystallisation of membrane-bound proteins, immuno-assays, vaccines or drug delivery.

6.7 Glycolipids

The results presented in this section are part of a cooperation project with the Department of Physics (TU Dortmund University, Germany) and the Forschungszentrum Borstel (Borstel, Germany). The glycolipid, LPS Re, used in this project was extracted and purified by J. Howe from the group of Prof. Dr. K. Brandenburg at the Forschungszentrum Borstel. The experiments were conducted together with F. Evers from the Department of Physics, who also fitted the XRR data. The evaluation of GIXD scans was done by me. All results of this study are published in [365].

6.7.1 Introduction

Gram-negative bacteria are surrounded by two membranes in contrast to most other types of cells. In the outer membrane, separating the cell from the periplasm and the intracellular space, lipids are asymmetrically distributed. The inner monolayer of the outer membrane is mainly composed of glycerophospholipids, while the outmost monolayer is largely built by lipopolysaccharides (LPS).^[198] More details about glycolipids and specially LPS can be found in section 4.2.9 (page 55).

It has been shown that Ca^{2+} -ions are essential for the stability of LPS membranes^[277, 278] and most of these ions have been found to interact with the inner core phosphate groups as well as with the inner core of the polysaccharides with an average coordination number of Ca^{2+} of 6.1.^[278] But also Na^{+} -ions are present in biological systems in high concentrations. Owing to the lack of quantitative data on the effect of ions on the structural properties of LPS, the influence of different ions on Langmuir-type monolayers composed of LPS Re spread on subphases containing monovalent (Na^{+}) and divalent (Ca^{2+}) ions as well as mixtures thereof has been investigated. The Langmuir-type experiments allow additional tuning of the lateral pressure profile, which can vary from one membrane type to another.

The vertical and lateral structure as well as the packing properties of these LPS monolayers were analysed by synchrotron X-ray reflectometry (XRR) and grazing incidence X-ray diffraction (GIXD), thus revealing a detailed, molecular-scale picture of the structural changes in the LPS layer caused by specific or non-specific glycolipid-ion interactions.

6.7.2 Materials and methods

Materials

The deep rough mutant lipopolysaccharide (LPS Re) was extracted from *Salmonella minnesota* strain R595 provided by Prof. K. Brandenburg.^[280] Salts (NaCl , CaCl_2) and phosphate buffer ($\text{H}_2\text{PO}_4^- / \text{HPO}_4^{2-}$) were purchased from Sigma (Taufkirchen, Germany) and used without further purification. Aqueous solutions were prepared using water filtered through a Milli-Q purification system, yielding a specific electrical resistivity of $> 18 \text{ M}\Omega\cdot\text{cm}$. Four different subphases were prepared: (i) a 10 mM phosphate buffer solution at a pH of 7, (ii) 100 mM NaCl in 10 mM phosphate buffer solution, (iii) a 50 mM CaCl_2

solution, and (iv) a 50 mM CaCl₂ and 100 mM NaCl solution. LPS Re was dissolved in a mixture of chloroform and methanol (9:1 vol) and spread on the aqueous subphases of different ion content.

Surface pressure-area isotherms

A Langmuir trough made from Teflon (Riegler & Kirstein, Potsdam, Germany) with a volume of 240 ml (as sketched in [174]) was used and equipped with a Wilhelmy plate sensor for measuring the lateral surface pressure, π , and a single moveable Teflon barrier, allowing for compression of the monolayers by changing the surface area.

X-ray reflectometry and grazing incidence X-ray diffraction

The LPS Re stock solution was spread at the air-subphase interface, and the system was equilibrated for 15 min in order to allow for complete evaporation of the organic solvents. Then, the films were compressed at a rate of compression of $5 \text{ \AA}^2 \text{ molecule}^{-1} \text{ min}^{-1}$ until the desired film pressure was reached. The systems were examined by X-ray reflectometry and grazing incidence X-ray diffraction at four different lateral film pressures, π , of 10, 20, 30, and 40 mN m⁻¹.

For the X-ray scattering experiments performed at the liquid surface diffractometer of beamline BW1 at HASYLAB (DESY, Hamburg, Germany),^[96] the Langmuir trough was placed in a sealed container with Kapton windows transparent to the X-rays and mounted on the diffractometer. All experiments were carried out at a temperature of 10 °C (± 2 °C) in order to minimise lateral diffusion and thermal fluctuations in the monolayer at the air-water interface. Temperature-control was achieved via thermostated water flowing through the Teflon-clad metal basis of the trough. During the experiments, the container was flushed with helium in order to reduce background scattering from the gas phase and to prevent oxidative damage. Furthermore, radiation damage was reduced by lateral translation of the trough by 0.01 mm after every step during GIXD scans and by 2 mm after each XRR scan.

6.7.3 Results and discussion

Pressure-area isotherms

Lateral pressure-area isotherms, $\pi(A_{\text{mol}})$, of LPS monolayers spread on subphases of various ion content at 10 °C are shown in Figure 6.40. For LPS on a pure buffer solution (black line), the onset of the isotherm can be found at $370 \text{ \AA}^2/\text{molecule}$, corresponding to an area per molecule, A_{mol} that is controlled by the interaction of neighbouring lipopolysaccharides. The lowest value of $315 \text{ \AA}^2/\text{molecule}$ is found for the monolayer on a 50 mM CaCl₂ solution (blue line). Intermediate values with $345 \text{ \AA}^2/\text{molecule}$ and $325 \text{ \AA}^2/\text{molecule}$ were recorded for the 100 mM NaCl (red line) and the sample containing both salts, i.e. 100 mM NaCl and 50 mM CaCl₂ (green line), respectively.

At a film pressure of 30 mN m^{-1} - the lateral pressure typically found in biological membrane systems - the LPS molecules occupy nearly an identical area of $120 \text{ \AA}^2/\text{molecule}$ for all four ionic solutions. Despite similar A_{mol} values, the LPS films differ in their lateral compressibilities $\chi = -(1/A)(\partial A/\partial \pi)$ calculated from the isotherms at 30 mN m^{-1} . The smallest compressibility of $2.26 \cdot 10^{-2} \text{ m mN}^{-1}$ is found for the sample containing the divalent salt, 50 mM CaCl₂. The largest χ -value of $2.90 \cdot 10^{-2} \text{ m mN}^{-1}$ is observed with 100 mM NaCl in the subphase. The corresponding values for the pure buffer solution and the sample containing 100 mM NaCl as well as 50 mM CaCl₂ are $2.45 \cdot 10^{-2} \text{ m mN}^{-1}$ and $2.53 \cdot 10^{-2} \text{ m mN}^{-1}$, respectively.

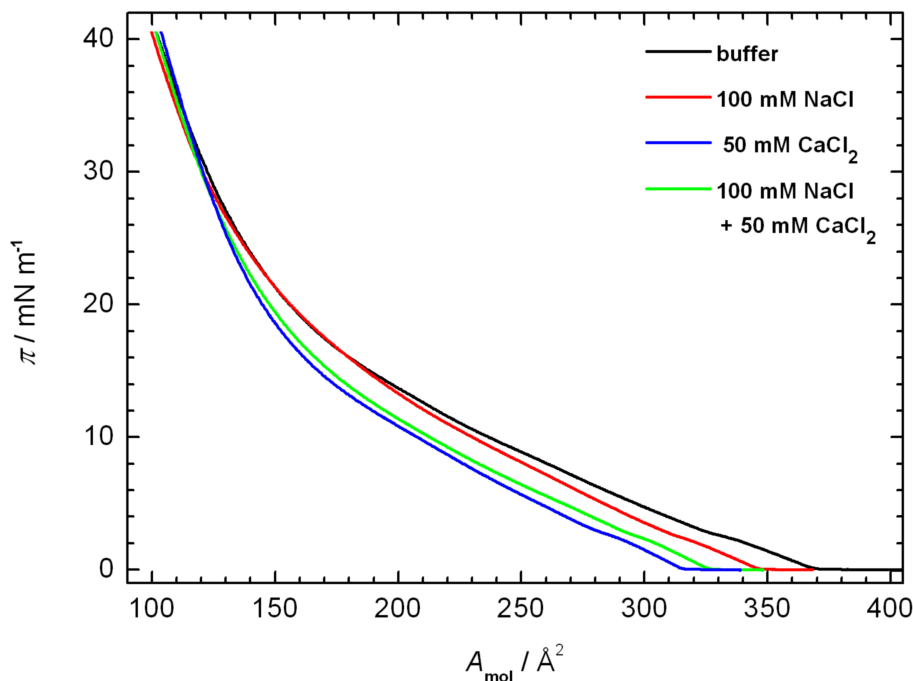


Figure 6.40: Compression isotherms (lateral film pressure, π , as a function of area per molecule, A_{mol}) of LPS monolayers spread on subphases of various ion content: pure buffer solution (black line), 100 mM NaCl (red line), 50 mM CaCl_2 (blue), 100 mM NaCl and 50 mM CaCl_2 (green).

A distinct change of the slope of all isotherms is visible at around $150 \text{ \AA}^2/\text{molecule}$. This is probably the point where the LPS molecules are finally oriented upright standing and more or less densely arranged on the surface. Further decreasing the area per molecule leads only to a compression of the single molecules, resulting in a much higher film pressure and lower lateral compressibility of the film due to increased intermolecular interactions.

Analysis of the pressure-area isotherms reveals different scenarios for monovalent and divalent salts. The data suggest an unspecific charge screening of the anionic LPS film by the Na^+ -ions and a specific interaction with Ca^{2+} -ions leading to a more rigid packing (lower χ -value) of the LPS molecules. For the LPS monolayer in pure buffer solution, the highest onset value of the surface pressure-area isotherms of all four subphases was observed, probably due to the strong repulsive electrostatic interactions of the equally charged LPS molecules. For the sample containing Na^+ -ions in the subphase, efficient screening of the negative charges (the Debye screening length decreases to 3 nm in 100 mM NaCl) results in lower onset values of the monolayer isotherms. The lowest onset and at the same time the smallest compressibility at 30 mN m^{-1} was found for the monolayer on a solution rich in Ca^{2+} -ions, which can be explained by a condensation of the LPS molecules in the presence of Ca^{2+} -ions, in agreement with literature data.^[98] The low compressibility of this sample can be explained by an efficient cross-linking of the condensed LPS molecules by divalent Ca^{2+} -ions, facilitated by Ca^{2+} bridging the negatively charged saccharide units, which might be accompanied by dehydration effects.

The presence of both salts leads to intermediate onset values caused by the interplay of the unspecific charge screening effect of the Na^+ -ions and the compacting effect of the Ca^{2+} -ions. Here, the cross-linking effect is reduced as compared to the sample with solely Ca^{2+} -ions in the subphase, leading to smaller interconnected domains (supported by the GIXD measurements, see below) and, hence lower compressibility values as compared to the lipid sample on a pure NaCl-solution.

Table 6.6: Fitting parameters of the X-ray reflectivity curves obtained from LPS monolayers at the air-water interface as a function of lateral film pressure, π : Layer thickness, d , roughness, σ , and electron density, ρ , of each layer are listed.

	π [mN m ⁻¹]	σ_{air} [Å]	$\rho_{\text{head}}/\rho_{\text{ref}}$	σ_{head} [Å]	d_{head} [Å]	$\rho_{\text{tail}}/\rho_{\text{ref}}$	σ_{tail} [Å]	d_{tail} [Å]	d_{total} [Å]
Na ⁺	10	4.0	1.338	2.2	9.5	1.057	4.3	13.5	31.3
	20	3.0	1.264	2.4	12.1	1.005	4.4	13.8	33.3
	30	3.7	1.279	3.4	13.3	0.973	4.8	14.7	36.5
	40	3.6	1.279	3.9	12.7	0.963	4.8	15.8	36.9
Ca ²⁺	10	3.2	1.266	2.0	13.3	1.039	4.2	13.6	34.3
	20	2.9	1.269	2.2	13.2	0.995	4.3	14.3	34.7
	30	2.3	1.247	2.6	13.0	0.939	4.4	15.6	35.3
	40	2.3	1.269	3.0	12.5	0.975	4.6	15.9	35.3
Na ⁺ + Ca ²⁺	10	3.8	1.246	2.2	10.5	1.060	4.3	13.5	32.1
	20	2.5	1.244	2.5	13.1	0.967	4.4	14.5	34.5
	30	2.1	1.240	2.5	13.1	0.949	4.4	15.5	35.1
	40	2.7	1.233	1.4	13.4	1.003	5.5	15.9	37.5

Specular synchrotron X-ray reflectometry

The X-ray reflectometry data, normalised to the Fresnel reflectivity, R_{F} , obtained from LPS monolayers at the air-water interface are presented together with their best fits (solid lines) on the left-hand side of Figure 6.41.⁴ On the right hand-side, the normalised electron density profiles (EDPs) are depicted, which were retrieved from the refinement of the XRR data. For all three subphases studied, the effect of increasing film pressure is already clearly visible in the primary reflectivity data. In general, the minimum of the oscillation shifts to lower q_z -values with increasing film pressure, hinting at a thickening of the LPS films, while the first oscillation of the reflectivity curves becomes more pronounced.

More detailed information on the vertical LPS film structure can be inferred from the EDPs, which display the vertical electron density of the LPS monolayer at the air-water interface (normalised to the electron density of water) as a function of distance from the water surface, z . On the left-hand side of the EDP diagrams, the subphase can be found at negative values of z , with the electron density $\rho(z) = \rho_{\text{H}_2\text{O}}$, followed by the polysaccharide region of the LPS film exhibiting a significantly higher electron density. At a distance, z , of approximately 15 Å, the hydrocarbon chain region of lipid A sets in with an electron density similar to that of water. Finally, at a distance, z , of around 28-30 Å, $\rho(z)$ decays slowly to a value of zero representing the roughness between the hydrocarbon chains and the air. Detailed values characterising the various layers of the LPS film in terms of thickness, roughness and electron density can be found in Table 6.6.

The electron density profiles of the LPS monolayer on the 100 mM NaCl solution (Figure 6.41(i)) show a continuous increase of the monolayer thickness with increasing film pressure. Between 10 mN m⁻¹ and 20 mN m⁻¹, this increase of about 4 Å is mainly caused by the polysaccharide head group region of LPS, whereas, for higher lateral pressures, the thickness of this region is almost constant, and the further marked thickness increase of the LPS layer only takes place in the lipid A region. The change of the electron density profile at lower film pressures indicates a distinct change in the packing of the LPS

⁴The reflectivity data were fitted by F. Evers using LSFIT.

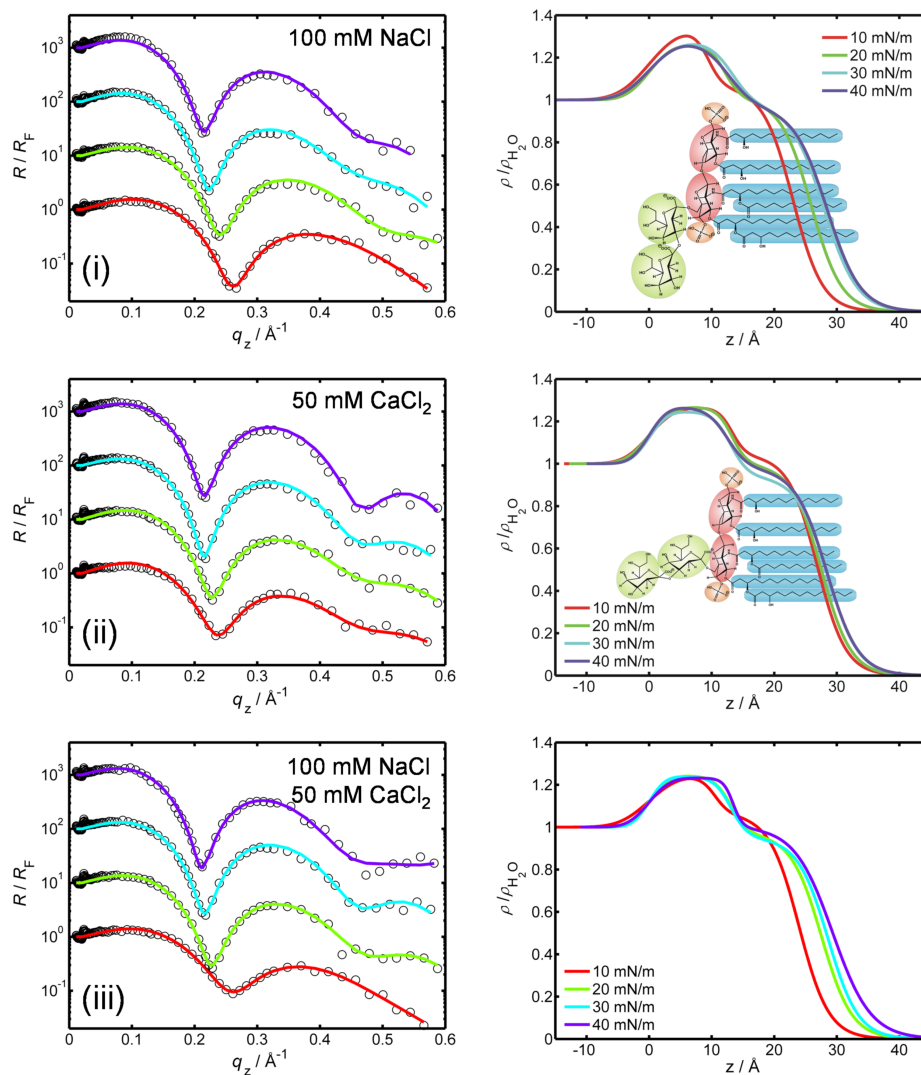


Figure 6.41: Left side: X-ray reflectivity data (symbols) obtained from LPS monolayers at the air-water interface, presented together with the best fits (solid lines) normalised to the Fresnel reflectivity, R_F . LPS monolayers were spread on subphases comprising (i) 100 mM NaCl, (ii) 50 mM CaCl_2 , and (iii) 100 mM NaCl and 50 mM CaCl_2 , and analysed as a function of lateral film pressure. For clarity, the reflectivity curves are shifted along the y -axis with increasing film pressure. On the right: Normalised electron density profiles as retrieved from the fits on the left-hand side. In the EDPs of (i) and (ii), the tentative molecular structures of LPS at low surface pressures are overlaid.

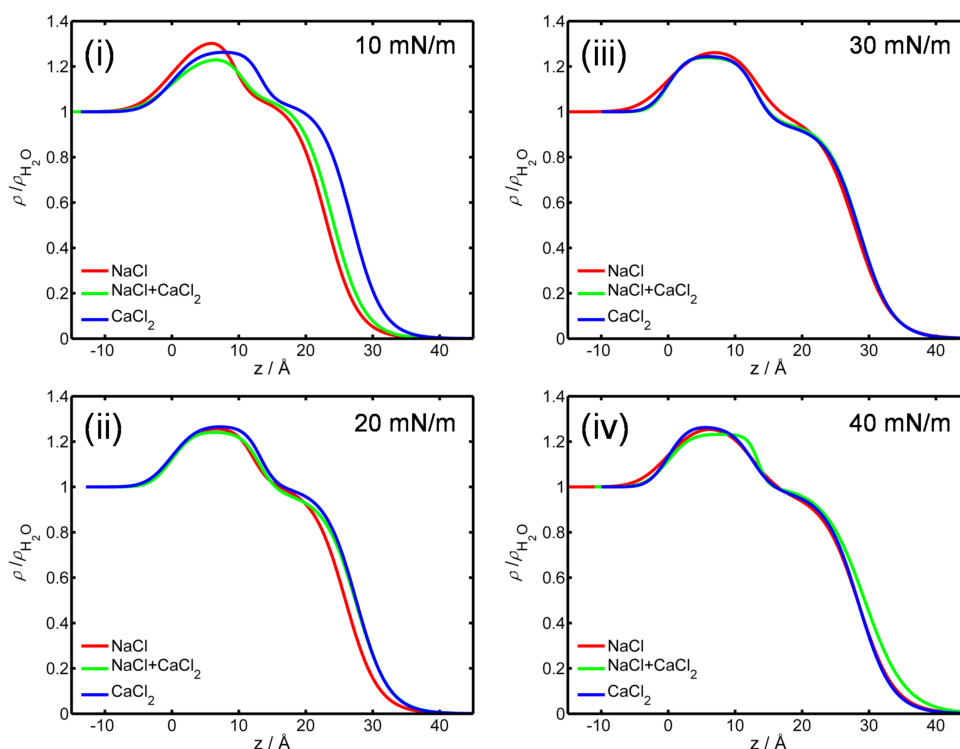


Figure 6.42: Electron density profiles of LPS on three different aqueous subphases, containing 100 mM NaCl (red), 50 mM CaCl₂ (blue), or 100 mM NaCl and 50 mM CaCl₂ (green), at different lateral film pressures, (i) 10 mN m⁻¹, (ii) 20 mN m⁻¹, (iii) 30 mN m⁻¹, and (iv) 40 mN m⁻¹.

molecules concomitant with a stretching of the polysaccharide region. The influence of increasing film pressure on the LPS monolayer on the 50 mM CaCl₂ solution (Figure 6.41(ii)) is significantly smaller. The small increase in layer thickness originates, to a similar degree, from both the polysaccharide and the lipid A region of LPS. Interestingly, the distinct plateau of the polysaccharide layer in the EDP demonstrates that this region of the monolayer is highly ordered with only minor roughness at all film pressures, even at 10 mN m⁻¹.

The effect of both kinds of ions, 100 mM NaCl and 50 mM CaCl₂, on the monolayer structure can be seen in Figure 6.41(iii) and Figure 6.42, where the electron density profiles of LPS on three different aqueous subphases at different lateral film pressures are depicted. In this case, between film pressures of 10 and 20 mN m⁻¹ a significant structural change in the polysaccharide region is observed, which is similar to that of the sample on 100 mM NaCl. Further increase of the film pressure leads only to a minor thickness increase of the structure.

At 10 mN m⁻¹, the LPS sample on the subphase containing only Na⁺-ions shows a significantly higher electron density in the polysaccharide region than at higher film pressures and, at the same time, a small layer thickness of the polysaccharide region (q.v. Figure 4.7a, page 56). Such compact arrangement is probably only possible due to the charge screening effect of the Na⁺-ions. Upon increase of surface pressure, the sugar residues bend away toward the normal of the surface layer as depicted in Figure 4.7b (page 56). The electron density of the polysaccharide region is 5% lower in the bent conformation, whereas the thickness has increased by approximately 3 Å due to reorientation of the Kdo-region of the LPS molecule. A similar molecular conformation seems to be present in the absence of screening Na⁺-ions and for all LPS monolayers at higher film pressures.

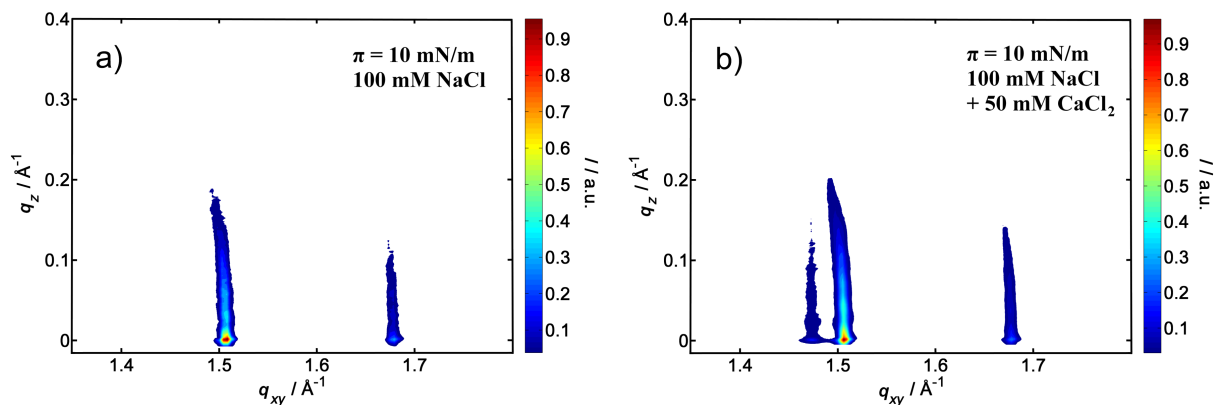


Figure 6.43: Two-dimensional contour plots of the intensity, $I(q_{xy}, q_z)$, along the horizontal (q_{xy}) and vertical (q_z) scattering directions as obtained from a LPS monolayer at a lateral film pressure of $\pi = 10 \text{ mN m}^{-1}$ on a subphase containing only Na^+ -ions (a) and Na^+ - and Ca^{2+} -ions (b).

In the monolayer on a subphase containing Ca^{2+} -ions as well as Na^+ -ions, the cross-linking effect of the Ca^{2+} -ions can still be observed, indicated by the distinct polysaccharide head group region and minor changes in the overall monolayer thickness with increasing film pressure. Only at low film pressures of 10 mN m^{-1} , is the charge screening effect of the Na^+ -ions still dominant, leading to a reduction of the thickness of the polysaccharide head group region.

Grazing incidence X-ray diffraction

A representative contour plot of the intensity, $I(q_{xy}, q_z)$, along horizontal (q_{xy}) and vertical (q_z) scattering directions as obtained from LPS monolayers at a lateral film pressure of $\pi = 10 \text{ mN m}^{-1}$ on a subphase containing 100 mM NaCl is shown in Figure 6.43a. The splitting into two signals indicates a distorted hexagonal packing of the LPS hydrocarbon chains with Miller indices $\{10, 01\}$ for the first peak and $\{1\bar{1}\}$ for the second one.^[84, 85] In Figure 6.43b, the corresponding data of the LPS monolayer on a subphase containing Na^+ - and Ca^{2+} -ions is depicted. Here, an additional peak is visible, indicating an oblique packing of the hydrocarbon chain region of the LPS. These peaks can be indexed by the Miller indices $\{10\}$, $\{01\}$ and $\{1\bar{1}\}$.^[84, 85]

In Figure 6.44, the intensity, $I(q_{xy})$, integrated along q_z (GIXD Bragg peak pattern) is shown for the various systems. All peaks were fitted by Gaussian functions in order to locate the position of the peak maxima as well as to determine their full widths at half maximum (FWHM). From the positions of the peak maxima, the repeat distances of the lattice (d -spacings) could be calculated. The FWHM of the 2D Bragg peaks hold direct information about the coherence length L_{xy} of ordered domains. In almost all measurements, three 2D Bragg peaks were detected, indicating an oblique packing of the hydrocarbon chains. Exceptions are the samples without Ca^{2+} -ions, which exhibit two peaks at low film pressures ($\pi = 10 \text{ mN m}^{-1}$), corresponding to a more symmetrical, distorted hexagonal packing of the lipid chains ($a = b = 4.50 \text{ \AA}$, $\gamma = 122^\circ$).

Inspection of the $\{10\}$ Bragg peak at $q_{xy} \approx 1.48 \text{ \AA}^{-1}$ in Figure 6.44 reveals the general tendency that high film pressures favour an oblique packing of the lipid chains, i.e. high lateral pressures restrict symmetric ordering of the LPS chains leading to an increase of the intensity of the $\{10\}$ peak. In the case of oblique packing, the two lattice vectors are of different lengths and $\gamma \approx 111.5^\circ$. All data calculated from the GIXD measurements are listed in Table 6.7. The oblique unit cell has lattice constants of $a \approx 4.48 \text{ \AA}$ and $b \approx 4.58 \text{ \AA}$ at $\pi = 10 \text{ mN m}^{-1}$.

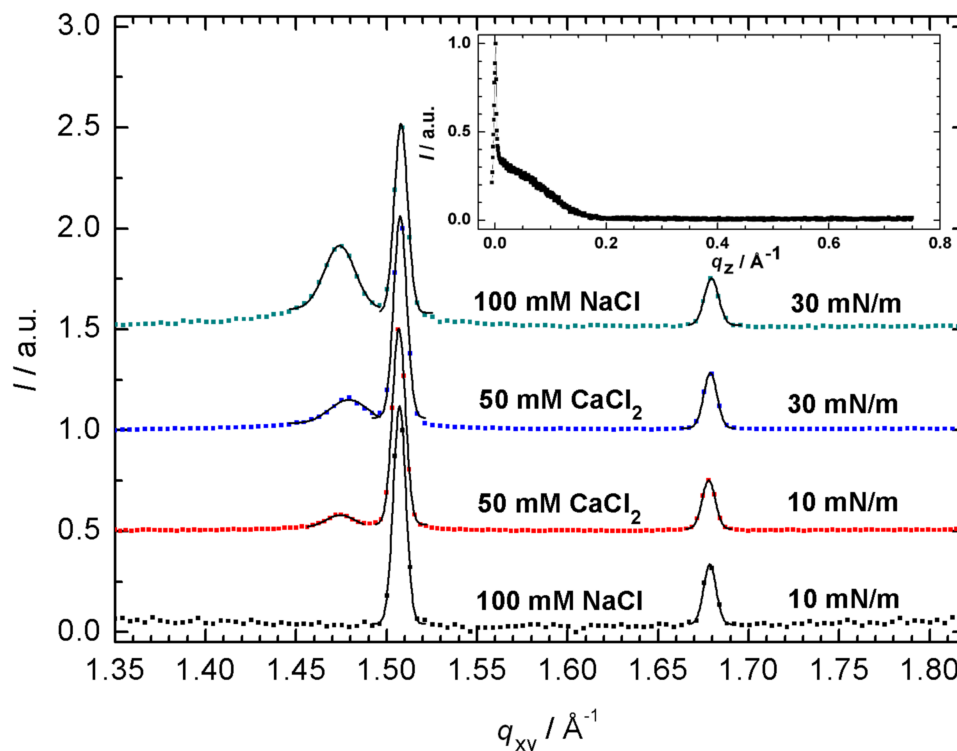


Figure 6.44: GIXD pattern, $I(q_{xy})$, obtained by integrating along q_z for different LPS monolayers (squared symbols). Peaks were fitted by Gaussian functions (solid lines). For clarity, data are shifted vertically. (Inset) Typical Bragg rod intensity profile, $I(q_z)$, obtained by integrating along the q_{xy} -region of the Bragg peak. The absence of a peak at $q_z \neq 0$ indicates little or no molecular tilt.

Table 6.7: Calculated parameters of grazing incidence diffraction measurements obtained from LPS monolayers at the air-water interface as a function of film pressure π : Lattice vectors in real space, a, b , angle of the unit cell, γ , lateral 2D crystalline coherence length, L_{xy} , area per hydrocarbon chain, A_{chain} , and area per molecule, A_{mol} , are listed for all samples.

	π [mN m ⁻¹]	a, b [Å]	γ [°]	L_{xy} [Å]	A_{chain} [Å ²]	A_{mol} [Å ²]
buffer	10	4.50, 4.50	112.3	—, 707.8, 752.1	18.8	112.5
	20	4.47, 4.60	111.3	294.2, 738.4, 714.6	19.1	114.8
	30	4.48, 4.58	111.5	233.2, 681.3, 628.2	19.1	114.5
	40	4.47, 4.60	111.3	201.5, 736.5, 713.5	19.1	114.8
Na ⁺	10	4.51, 4.51	112.3	—, 749.2, 741.7	18.8	112.7
	20	4.48, 4.58	111.4	396.9, 730.4, 711.6	19.1	114.6
	30	4.48, 4.58	111.5	374.9, 704.0, 652.8	19.1	114.5
	40	4.47, 4.58	111.4	260.8, 679.6, 674.4	19.1	114.5
Ca ²⁺	10	4.48, 4.57	111.5	268.1, 723.3, 688.4	19.1	114.5
	20	4.48, 4.58	111.5	228.7, 717.4, 734.5	19.1	114.6
	30	4.48, 4.57	111.6	216.5, 694.7, 697.5	19.0	114.3
	40	4.48, 4.56	111.6	163.7, 641.8, 644.9	19.0	114.1
Na ⁺ + Ca ²⁺	10	4.48, 4.58	111.5	293.3, 714.5, 700.3	19.1	114.6
	20	4.48, 4.57	111.5	344.6, 696.6, 685.7	19.1	114.4
	30	4.48, 4.57	111.6	279.5, 684.0, 677.0	19.0	114.3
	40	4.48, 4.57	111.6	185.8, 660.1, 637.2	19.0	114.1

The occupied area per hydrocarbon chain, A_{chain} , can be directly calculated from the lattice parameters. Values of $18.8 \text{ \AA}^2/\text{chain}$ in the distorted hexagonal packing and $19.1 \text{ \AA}^2/\text{chain}$ for the oblique packing can be determined. From these data, the area per LPS molecule, each having six hydrocarbon chains, can be calculated to be 115 \AA^2 . This value is in good agreement with the value found in the Langmuir isotherms at $\pi = 30 \text{ mN m}^{-1}$ (Figure 6.40) and is comparable with a value of 129 \AA^2 for LPS Re reported in the literature^[98] as well as values between 110 and 125 \AA^2 for other lipopolysaccharides depending on the length of the saccharide side group.^[366]

The inset in Figure 6.44 depicts a typical Bragg rod intensity profile, $I(q_z)$, obtained at the q_{xy} -position of the $\{01\}$ Bragg peak. The maximum at $q_z = 0$ is the so-called Vineyard-Yoneda peak,^[99] which arises from the interference between X-rays diffracted up into the Bragg rod and X-rays diffracted down and then reflected up by the interface. The absence of a further peak at $q_z \neq 0$ indicates negligible or no molecular tilt of the hydrocarbon chains to the surface normal.

The coherence lengths L_{xy} of ordered domains in all samples were calculated from the full width at half maximum of each Bragg peak. The coherence lengths calculated from the $\{10\}$ reflection at $q_{xy} \approx 1.48 \text{ \AA}^{-1}$ are shown in Figure 6.45 in dependency of film pressure and ionic composition of the subphase. Large coherence lengths ranging from 150 to 300 \AA and opposite effects of Na^+ - and Ca^{2+} -ions on the coherence length are found. Addition of Na^+ -ions leads to an increase of L_{xy} and hence the size of highly ordered domains in the monolayer. Probably owing to the effective screening of the negative charges of the LPS molecules (3.5 per molecule on average – 4 negative phosphates and carboxylates and one non-stoichiometric positive charged amino-arabinose), a tight packing of LPS molecules over large areas of the lipid monolayer is facilitated. Conversely, Ca^{2+} -ions reduce the possibility of the LPS molecules to build larger ordered domains. Remarkably, a decrease of the coherence length and hence long-range ordering is observed with increasing film pressure for all systems. Obviously, a highly ordered packing of the hydrocarbon chains over a large area in the monolayer is hampered by packing defects under these conditions of increased lateral pressures.

The coherence length L_{xy} calculated from the $\{01\}$ and $\{1\bar{1}\}$ signals (see Table 6.7) are in a range of 650 to 750 \AA with slightly decreasing values with increasing film pressure for all samples, similar to the scenario observed for the $\{10\}$ signal. From these data and the modulus of the lattice vectors, the number of molecules in a crystalline domain can be estimated. In an ellipsoidal ordered domain with average coherence lengths of 700 \AA and 300 \AA for the main axes, approximately 1400 LPS molecules can be found. The vertical coherence length, L_z , for the LPS monolayer of 13 \AA corresponds, as expected, to a fully stretched C_{12} hydrocarbon chain.

The LPS data can be compared with corresponding GIXD data on phospholipid systems, such as 1,2-dipalmitoyl-*sn*-glycero-3-phosphocholine (DPPC) monolayers at the water-air interface at room temperature.^[359] At all film pressures, the area per hydrocarbon chain of the phospholipid is much larger than the areas found for the LPS in this study. For example, at 10 mN m^{-1} , the area per chain of DPPC is 150 % larger than the one found for LPS, and decreases drastically with film pressure. Furthermore, the acyl chains in the DPPC monolayer exhibit a tilt angle relative to the surface normal, which decreases from 36° at 15 mN m^{-1} to 27° at 45 mN m^{-1} .^[359] For the LPS, no significant change of the area per chain is observed and the tilt angle determined is zero. This suggests that the lateral compressibility of the phospholipid DPPC is governed by the lipid head group area, which is larger than its chain cross sectional area. This results in a marked tilt of the hydrocarbon chains and the changes of the chain cross sectional area mainly originate from the compression of the head group region. Conversely, for LPS, the lateral structure and compressibility seems to be controlled by the six hydrocarbon chains.

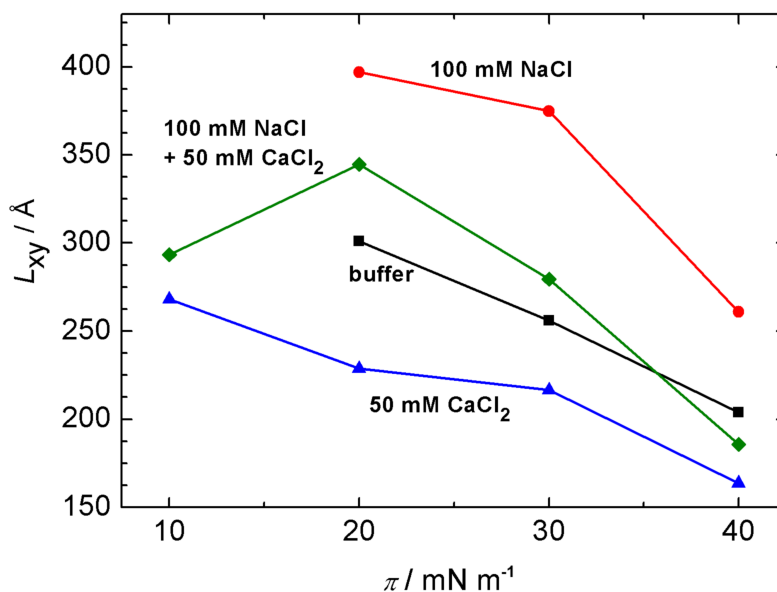


Figure 6.45: Coherence length, L_{xy} , calculated from the $\{10\}$ peak as a function of the lateral film pressure, π , of LPS spread on four different subphases: buffer (black squares), 100 mM NaCl (red circles), 50 mM CaCl₂ (blue triangles), and 100 mM NaCl + 50 mM CaCl₂ (green diamond). For the samples containing no Ca²⁺-ions, the coherence length at $\pi = 10 \text{ mN m}^{-1}$ could not be calculated due to the absence of a splitting of the $\{10, 01\}$ signal in these measurements. The error of the coherence length is estimated to be $\pm 25 \text{ Å}$.

6.7.4 Conclusions

One of the most intriguing issues in membrane biology and biophysics today is their lateral organisation. Still very little is known about the structure and lateral organisation of membranes built from lipopolysaccharides and how their conformation is modulated by the ionic strength at the lipid interface. By combining synchrotron X-ray reflectometry (XRR) and grazing incidence X-ray diffraction (GIXD) the influence of mono- and divalent ions on the structure and lateral organisation of lipopolysaccharide monolayers spread at the air-water interface could be revealed. Specular X-ray reflectivity measurements are sensitive to the electron density distribution along the surface normal, the in-plane packing properties and correlation length scales of the ordered (diffraction) properties of the monolayer film are provided by GIXD. Together, XRR and GIXD techniques provide a means to measure the structure of self-organising molecularly thick films in bulk water with unprecedented resolution.^[101, 176, 367]

Based on this studies, new modes of lipopolysaccharide packing could be revealed upon changing the ionic valency and strength of the aqueous subphase. In general, the results indicate that Na⁺-ions interact unspecifically with LPS molecules based on their ability to screen the negative charges of the LPS molecules, whereas Ca²⁺-ions interact specifically by cross-linking adjacent molecules in the monolayer. At low lateral pressures, Na⁺-ions present in the subphase lead to a LPS monolayer structure ordered over large areas with high compressibility, nearly hexagonal packing of the hydrocarbon chains and high density in the LPS head group region. At higher film pressures, the LPS monolayer becomes more rigid and results in a less perfect, oblique packing of the LPS hydrocarbon chains as well as a smaller lateral size of highly ordered domains on the monolayer. Furthermore, associated with the increased surface pressure, a conformational change of the head group occurs, leading to a thickening of the entire LPS monolayer structure. Generally, negligible or no molecular tilt of the hydrocarbon chains to the surface normal has been detected in all phases.

The effect of Ca^{2+} -ions in the subphase is to increase the rigidity of the LPS monolayer leading to an oblique packing of the hydrocarbon chains already at low lateral pressures. As a consequence, the lateral compressibility of the LPS monolayer is much lower compared to the LPS monolayer on a subphase containing Na^+ -ions. In the presence of Ca^{2+} -ions, an increase of the film pressure has only a minor effect on the conformational properties of the LPS molecules. Intermolecular Ca^{2+} / lipid phosphate and Ca^{2+} / sugar carboxylate interactions lead to an upright orientation of the sugar molecules and cross-linking of the LPS molecules on the subphase containing the divalent Ca^{2+} -ions. Therefore, they exhibit just minor conformational and orientational changes with increasing lateral pressure. The only distinct effect is a decrease of the lateral size of ordered domains in the monolayer caused by an increased packing stress at higher film pressures.

In the presence of both, Na^+ - as well as Ca^{2+} -ions in the subphase, the screening effect of Na^+ is predominant at low film pressures, whereas at higher film pressures, the structure and lateral organisation of LPS molecules is governed by the influence of Ca^{2+} -ions. In other words, the unspecific charge screening effect of the Na^+ -ions on the conformation of the sugar moiety becomes less dominant at increased film pressures of magnitude relevant for biological membranes, probably by partial replacement of Na^+ in the inner core region by Ca^{2+} and subsequent formation of Ca^{2+} -ion bridges to negatively charged saccharide / head group moieties.

CHAPTER 7

Investigations of proteins in solution

Small-angle X-ray scattering provides a unique opportunity to investigate proteins in their physiological environment – an aqueous solution – with high spatial resolution, contrary to other high-resolution techniques like cryo-TEM or protein crystallography, where usually crystals of the sample are used or extensive sample manipulations are needed prior to the measurements. An additional advantage of measurements in aqueous solutions is the high number of experimental parameters of the system. Temperature and pressure are accessible in a large range and numerous co-solvents can be used to modify the properties of the solution or to control the interaction of the protein with the solvent.

In this section of the thesis, two different studies are presented using these unique features of small-angle X-ray scattering. In the first, the structure of different SNase variants are studied in solution as a function of temperature, pressure, and solution pH-value using several *ab initio* shape reconstruction techniques. In the second study, the temperature and pressure dependence of the stability and function of the protein MsP1, an uncommon peroxidase from the basidiomycetous fungus *Marasmius scorodonius*, was investigated.

7.1 *Ab initio* shape reconstruction of Staphylococcal nuclease variants in solution

The study presented in this section was conducted in cooperation with M. Schroer from the Department of Physics and the synchrotron light source DELTA at TU Dortmund University. Additionally, scientists at the College of Pharmaceutical Science at Ritsumeikan University (Shiga, Japan), the High Pressure Research Center at Kinki University (Wakayama, Japan), the Department of Biophysics at the John Hopkins University (Baltimore, MD, USA), and the Centre de Biochimie Structurale at the Université de Montpellier (Montpellier, France) were involved in the study, providing the different protein variants and performing complementary experiments, e.g. NMR and fluorescence spectroscopy. The SAXS measurements were performed by M. Schroer (Department of Physics, TU Dortmund University) at different synchrotron light sources (ESRF, DELTA, DESY). After correction of the raw data, he calculated the pair distance distribution function, which were the basis for my *ab initio* calculations. The complete results of the studies, including the *ab initio* structures, are published in [368, 369].

7.1.1 Introduction

A structural interpretation of the thermodynamic stability of proteins requires an understanding of the structural properties of the unfolded state. Also ionisation of internal groups in proteins can trigger conformational change. Despite the knowledge that these processes are the structural basis of most biological energy transduction, they are only poorly understood. A set of variants of a stabilised variant of staphylococcal nuclease (Δ +PHS) with the Val-66, which is located in the hydrophobic core, replaced by Ala, Tyr, Lys or Arg was used to examine how changes in the volume and polarity of an internal microcavity affect the native conformation and the pressure sensitivity of the structures. Δ +PHS differs from wild-type SNase by a set of substitutions (P117G, H124L, S128A, G50F, and V51N) and one deletion (Δ 44-49).^[131, 368, 369]

Small-angle X-ray scattering at atmospheric and high hydrostatic pressure was used to examine the effects of temperature, pressure and pH on the radii of gyration and structure of the folded state and the unfolded state ensembles of staphylococcal nuclease. The unfolded state ensembles, achieved for these proteins with high pressure, were more compact than those achieved at high temperature. Substitutions at the hydrophobic core detectably altered the conformation of the protein, even in the folded state. The introduction of a charged residue, such as Arg, inside the hydrophobic interior of the protein could dramatically alter the structural properties, even those of the unfolded state. The data suggest that a charge at an internal position can interfere with the formation of transient hydrophobic clusters in the unfolded state. The radius of gyration of the unfolded state ensemble approaches the value for a statistical random coil only at high temperatures.^[368, 369]

NMR spectroscopy at atmospheric pressure showed previously that the neutral Lys-66 in Δ +PHS/V66K affects slow conformational fluctuations globally, whereas the effects of the charged form are localised to the region immediately surrounding position 66. *Ab initio* models from SAXS data suggest that when Lys-66 is charged, the protein expands, which is consistent with results from NMR spectroscopy. The application of moderate pressures (< 2 kbar) at pH values above the pK_a , where Lys-66 is normally neutral at atmospheric pressure, left most of the structure unperturbed, but produced significant non-linear changes in chemical shifts in the helix where Lys-66 is located. Above 2 kbar pressure at these pH values, the protein with Lys-66 unfolded cooperatively adopting a relatively compact, albeit random structure according to Kratky analysis of the SAXS data. In contrast, at low pH, below the pK_a of Lys-66 (4.5), and high pressure the unfolded state of the Δ +PHS/V66K variant is more expanded than that of the reference protein.^[368, 369]

7.1.2 Materials and methods

Protein preparation

The stabilised Δ +PHS variant and the other mutants of SNase, Δ +PHS/V66K, Δ +PHS/V66A, Δ +PHS/V66R, and Δ +PHS/V66Y, were prepared as described in the literature.^[116, 370] After purification, the proteins were dialysed against 1 M KCl, then against water before lyophilisation.

SAXS sample preparation and measurements

To avoid pressure-induced changes of solution pH, 25 mM Tris buffer was used in the pH range of 6–7.^[357] At pH 4.5 the proteins were dissolved in a 15 mM sodium acetate buffer solution instead. For the pressure dependent measurements of the variants V66A, V66Y, and V66R, bis-Tris buffer (50 mM) was used at

pH 5.5.^[357] All buffers were prepared with deionised water¹. The protein concentration in the solutions was 3.5–5.0 mg ml⁻¹. At this concentration, the solution is diluted enough so that the single scattering approximation is still valid.^[37]

The SAXS experiments were performed at beamline BL9 of DELTA (TU Dortmund, Germany)^[371], at beamline BW4 of HASYLAB (DESY, Hamburg, Germany)^[372], and at beamline ID02 of the ESRF (Grenoble, France).^[66] To perform high pressure SAXS experiments on the protein solutions, a special sample cell with two flat diamond windows (thickness 1 mm) was used.^[67, 68] A pressure range up to 3 kbar was covered in the experiments. At BW4 ($\lambda = 1.3808 \text{ \AA}$), using the Pilatus 300 K detector, a q -range of 0.2 to 2.8 nm⁻¹ was covered. The exposure time was 20 min. At BL9, using a MAR345 image plate detector, the exposure time was similar. A wavelength of $\lambda = 1.239 \text{ \AA}$ allowed covering a q -range of 0.3 to 3.5 nm⁻¹. At ID02, different sample-detector distances were used to cover a q -range of 0.1 to 4.5 nm⁻¹ (at $\lambda = 0.995 \text{ \AA}$).

SAXS data analysis

After retrieving the pair distance distribution functions, $p(r)$, from the corrected raw data, which were calculated by M. Schroer, 16 independent *ab initio* calculations of each protein were started using the program DAMMIF based on the multi-bead method. The resulting 16 *ab initio* structures were aligned using DAMAVER to build the “most probable” model for each protein. The crystal structures of the Δ +PHS (3BDC)^[125] was fit into the *ab initio* model using the same program. Additionally, *ab initio* structures were calculated using the multipole expansion method (SASSHA) and the dummy-residue approach (GASBOR). Using the multipole expansion method, no multiple calculations and subsequential averaging of the structures were necessary. The structures displayed in the figures, which were calculated by the dummy-residue method, are also not averaged, but for each particle several *ab initio* structures were calculated and compared to ensure correctness of the displayed model. For the visualisation of the resulting structures the VMD viewer, developed by the Theoretical and Computational Biophysics Group at the University of Illinois, was used.^[373] The rendering of the structures was done with the Tachyon ray-tracer.^[374, 375]

7.1.3 Results

First, the small-angle X-ray scattering (SAXS) of Δ +PHS and its V66K variant^[319, 376] was measured at atmospheric pressure to probe the global structural consequences of the V66K substitution and of the ionisation of Lys-66. Whereas at pH values above 5.7, the Δ +PHS protein and its V66K variant exhibited a similar radius of gyration, R_G , (16.9 ± 0.4 and $16.6 \pm 0.8 \text{ \AA}$, respectively) and nearly identical pair distribution functions, at pH 4.5, where Lys-66 is charged, the V66K variant exhibited a significantly broader pair-distance distribution function and a larger R_G ($18.1 \pm 0.5 \text{ \AA}$) (see Table 7.1). The Δ +PHS also showed some expansion at pH 4.5 ($17.6 \pm 0.3 \text{ \AA}$). The Kratky plots, regardless of variant or pH, were all very similar, although not identical, with a strong maximum consistent with structured, globular proteins.

Ab initio modelling of the SAXS data for Δ +PHS and its V66K variant at atmospheric pressure and pH 6.0 was performed.^[49] The most probable model from among 16 separate calculations for the Δ +PHS protein calculated using DAMMIF revealed a generally globular structure, with a circular indentation (Figure 7.1). Superposition of the crystal coordinates of the Δ +PHS structure (PDB accession code

¹The sample preparations as well as the SAXS measurements were performed by M. Schroer.

Table 7.1: Radii of gyration, R_G , of different SNase variants calculated from SAXS measurements.

SNase variant	experimental conditions	R_G [Å]
Δ +PHS	1 bar, pH 7.0, 30 °C	16.9 ± 0.4
Δ +PHS	1 bar, pH 4.5, 30 °C	17.6 ± 0.3
Δ +PHS/V66K	1 bar, pH 6.0, 30 °C	16.6 ± 0.8
Δ +PHS/V66K	1 bar, pH 4.5, 30 °C	18.1 ± 0.5
Δ +PHS/V66K	3 kbar, pH 6.0, 30 °C	19.8 ± 2.0
Δ +PHS/V66K	1 kbar, pH 4.5, 30 °C	22.8 ± 0.7
Δ +PHS/V66K	2 kbar, pH 4.5, 30 °C	32.5 ± 2.0
Δ +PHS/V66K	3 kbar, pH 4.5, 30 °C	30.2 ± 2.0
Δ +PHS/V66A	1 bar, pH 5.5, 34 °C	16.8 ± 0.4
Δ +PHS/V66Y	1 bar, pH 5.5, 34 °C	17.7 ± 0.3
Δ +PHS/V66R	1 bar, pH 5.5, 25 °C	18.9 ± 0.5
Δ +PHS/V66R	1 bar, pH 5.5, 34 °C	24.2 ± 0.5

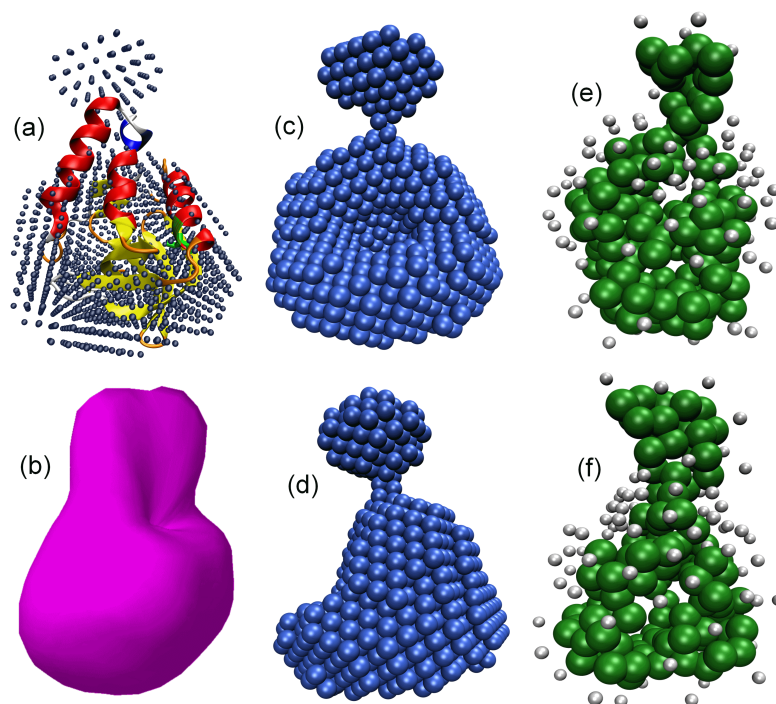


Figure 7.1: *Ab initio* structures of Δ +PHS at pH 7.0, ambient pressure and temperature. (a) Crystal structure of Δ +PHS (3BDC)^[125] modelled into the *ab initio* multi bead model. (b) *Ab initio* model computed using the multipole expansion method ($L = 8$). (c) and (d) show structures calculated by multi-bead modelling. (e) and (f) display representations of the protein shape using the dummy-residue method (each green bead represents one amino acid and the smaller white spheres indicate water of the closest hydration layer). The structures (d) and (f) are turned by 90° relative to the corresponding models (c and e) in the first row.

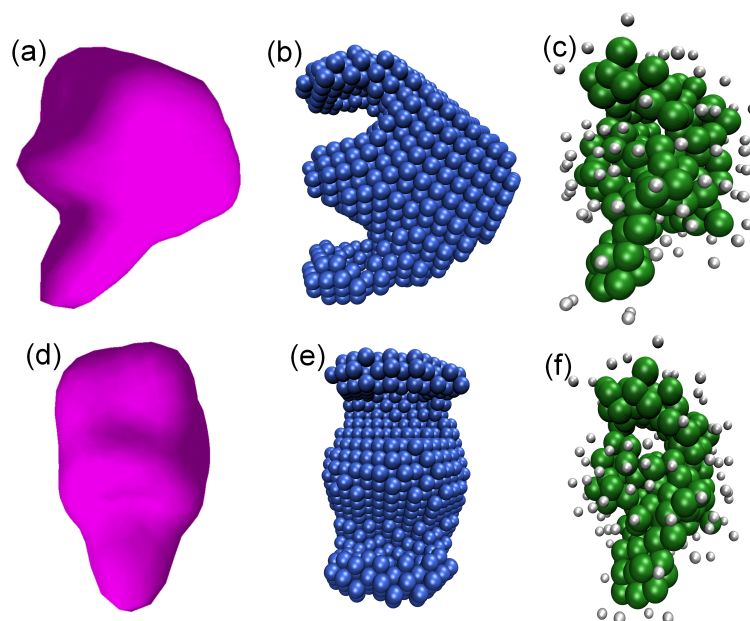


Figure 7.2: *Ab initio* structures of Δ +PHS V66K at pH 6.0, ambient temperature and pressure. The structures are calculated – from left to right column – by multipole expansion, multi-bead modelling and the dummy-residue method, respectively. The models in the second row are turned by 90° to the right relative to the structures depicted in the first row.

3BDC)^[125] with the *ab initio* model yielded the best fit for the orientation shown in Figure 7.1a, with helix-3 bearing tryptophan 140 (among the last residues that are usually resolved in crystal structures of SNase variants) placed just below a protrusion calculated by DAMMIF. The particle envelope calculated by the multipole expansion (Figure 7.1b) fails to resolve the protrusion in the upper part of the structure as well as the cavity in the centre of the particle, which are known limitations of this method. The structures derived from the dummy-residue method (Figure 7.1e,f) are especially well suited to provide an impression of the local density of amino acids in the structure. Here, the cavity in the inner of the protein is well resolved.

Comparison of a scattering curve calculated from the crystal structure with experimentally obtained data revealed a significant deviation between the two, whereas the one calculated from the DAMMIF *ab initio* model describes the experimental results very well. Therefore, it is likely that the protrusion in the *ab initio* model corresponds to the manifestation in the DAMMIF calculation of experimental scattering from the disordered C-terminal residues 141–149, although a contribution from the disordered N-terminal residues 1–7 cannot be excluded. It has to be noted that such *ab initio* modelling, while appropriate for stable globular structures, does not yield reliable envelopes for dynamically disordered regions, and that therefore, this protrusion in the model should not be interpreted as a precise structural envelope.

Despite the similarity in their R_G values, the *ab initio* model for the Δ +PHS/V66K variant (Figure 7.2) appears quite different from the one of the Δ +PHS reference protein (Figure 7.1). In particular, the *ab initio* modelling of the Δ +PHS/V66K variant produced two extensions that, as in the case of the single protrusion calculated for the reference protein, may also arise from disordered regions, which are more likely to find in the Δ +PHS/V66K protein than in the reference protein (Δ +PHS). At pH 6.0, close to the pK_a of 5.7 of Lys-66, the SAXS data might be representing the superposition of multiple conformations. A slow dynamic disordering of helix 1 is supported by H/D exchange data measured by NMR,^[368] which revealed substantial increases in the helix 1 exchange rates for Δ +PHS/V66K compared

to the Δ +PHS reference protein, supporting the results from the *ab initio* calculations. As seen before, the structures calculated by multipole expansion (Figure 7.2a,d) are less resolved, although they show the basic features present in the other particle models. The model calculated by the dummy-residue method shows still a distinct cavity in the centre of the structure (Figure 7.2c,f).

The *ab initio* model of the V66K variant at pH 4.5, as depicted in Figure 7.3g-i, shows a more elongated structure compared to the particle shape at pH 6.0, suggesting that under conditions where Lys-66 is charged, the protein populates a state in which a part or all of helix-1 is separated from the core of the structure. This is consistent with the NMR results, which show even faster H/D exchange, the loss of the resonances for residues 62–66 and the broadening of resonances in the ^1H - ^{15}N HSQC spectra of the protein when Lys-66 is charged.^[368]

The effect of pressure on the global structure of the reference Δ +PHS protein (Figure 7.4) and its V66K variant (Figure 7.3 and, in detail, Figure 7.5 and 7.6) was also characterised by SAXS. *Ab initio* modelling of the reference protein Δ +PHS (Figure 7.4) revealed in all methods used only a very little change in shape up to 3 kbar. The small differences observed might only be due to the lower resolution of the high pressure *ab initio* models caused by the lower electron density contrast between protein and water at high pressure. The structures obtained from the dummy-residue method seem to be slightly more compact at high pressure.

In contrast, a major change in conformation of the Δ +PHS/V66K variant was observed by SAXS as a function of pressure (Figure 7.5 and 7.6). The pair distance distribution function, $p(r)$, of this variant at pH 6.0 is broadened and the radius of gyration, R_G , increased from $16.6 \pm 0.4 \text{ \AA}$ at atmospheric pressure to $19.8 \pm 2.0 \text{ \AA}$ at 3 kbar (Table 7.1), indicating expansion of the chain relative to the native state. However, this value for the R_G of the pressure-unfolded Δ +PHS/V66K variant is much smaller than the value of 35 \AA obtained previously for the high pressure unfolding of the true wild-type form of SNase under similar conditions (pH 5.5).^[314] Hence, even with the V66K substitution, the pressure unfolded state of the Δ +PHS variant remained much less expanded than that of the wild-type protein. The Kratky plot obtained from the scattering data on the V66K variant at 3 kbar and at pH 6.0 exhibited a small maximum reflecting some residual globular structure in this unfolded state.

Ab initio modelling of the scattering curves of Δ +PHS/V66K at pH 6.0 and a pressure of 3 kbar, as presented in Figure 7.5, was consistent with a significantly expanded structure relative to atmospheric pressure. Furthermore, the SAXS data show that ionisation of Lys-66 (at pH 4.5) shifted the unfolding transition to lower pressure (see Figure 7.6), which was complete at 2 kbar, as observed previously by fluorescence.^[131] The radius of gyration at pH 4.5 and 2 kbar of about 32 \AA was close to the value of 35 \AA ^[314] observed for pressure-denatured wild-type SNase. Yet it was not as large as for chemically denatured wild-type SNase ($R_G = 37.2 \pm 1.2 \text{ \AA}$)^[377] or for the temperature denatured WT protein ($R_G = 45 \pm 2 \text{ \AA}$).^[314] Kratky plots of the high pressure SAXS profiles (2 and 3 kbar) at pH 4.5 showed no maximum, indicating that under these conditions the protein behaved like a random polymer. Likewise, the *ab initio* model depicted in Figure 7.6 was consistent with a highly expanded chain. Because Lys-66 in the Δ +PHS/V66K variant is charged in the unfolded state at pH 6.0 as well as at pH 4.5, the observed expansion of the pressure unfolded state at low pH must arise from general destabilisation of residual interactions caused by increased electrostatic repulsion in the unfolded state as carboxylic groups begin to become uncharged.

The scattering signals of Δ +PHS/V66A, Δ +PHS/V66Y, and Δ +PHS/V66R were measured at atmospheric pressure and a temperature of 34°C . The maximum dimension, D_{max} , of Δ +PHS/V66Y, calculated from the pair-distance distribution function, is slightly larger than that of Δ +PHS/V66A

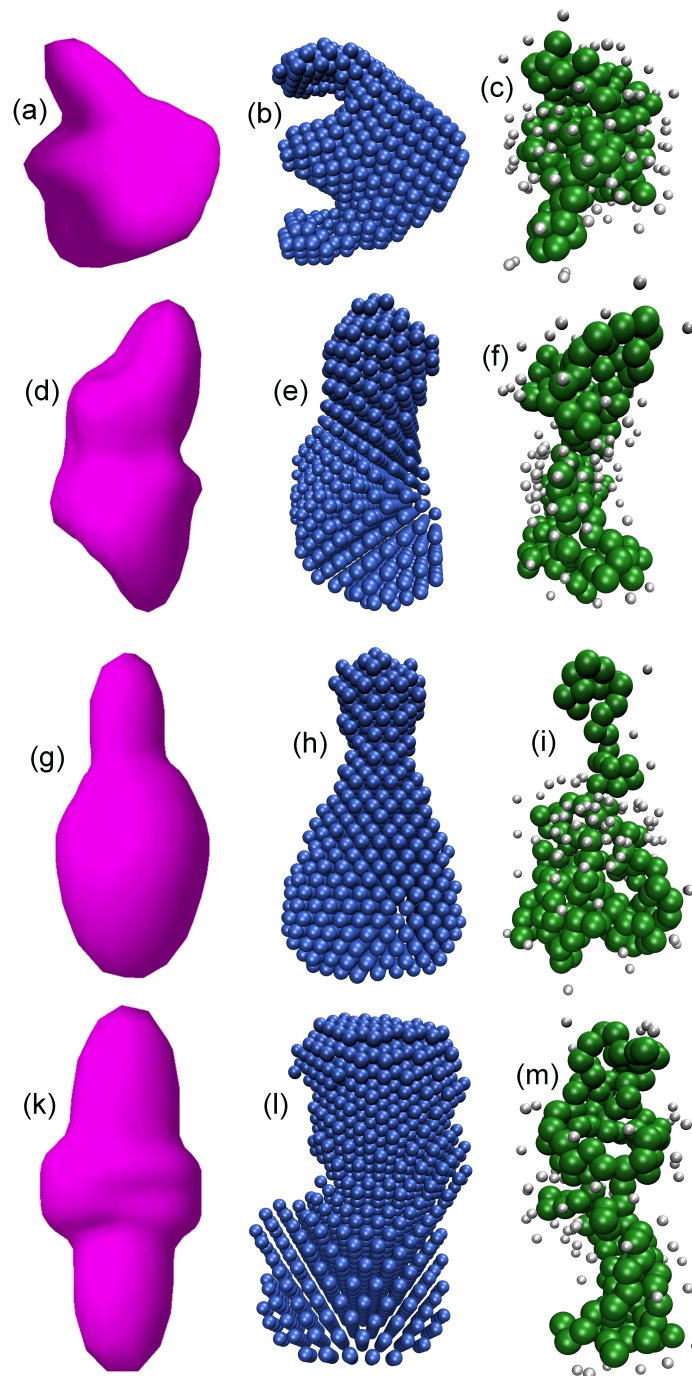


Figure 7.3: *Ab initio* structures of Δ +PHS/V66K at ambient temperature. The structures are calculated – from left to right column – by multipole expansion, multi-bead modelling and the dummy-residue method, respectively. The upper two rows depict structures of the proteins at pH 6.0 and the lower two rows at pH 4.5. The first and the third row show particles at atmospheric pressure, whereas the second and fourth row depict high pressure models – at 3 kbar and 1 kbar, respectively.

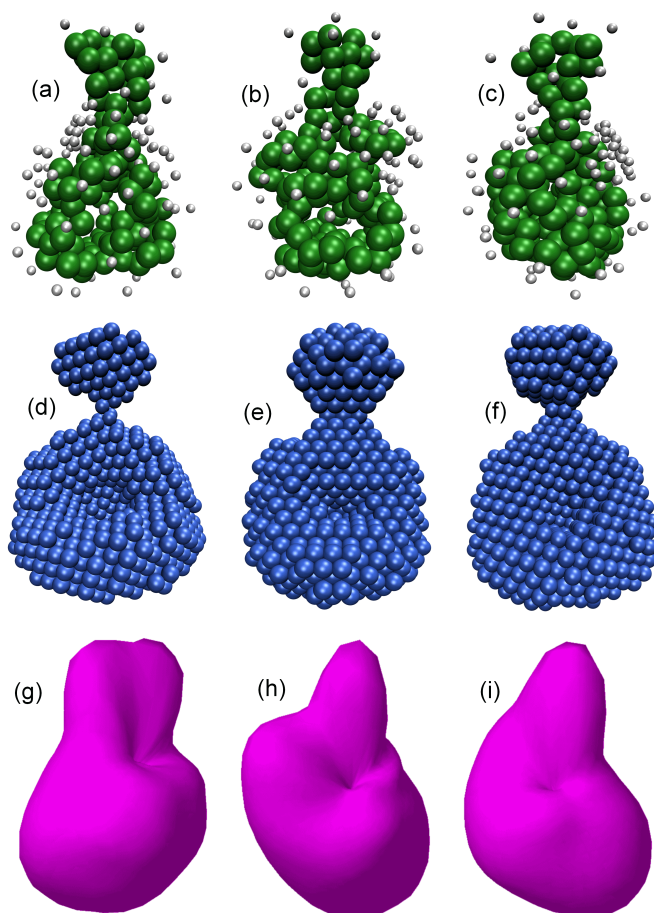


Figure 7.4: *Ab initio* structures of Δ +PHS at pH 7.0 and ambient temperature calculated at different pressures (1 bar - left column; 2 kbar - middle; 3 kbar - right column). The models in the top row are calculated using the dummy-residue method, structures in the middle row are computed using multi-bead modelling, and the models in the bottom row are based on multipole expansion.

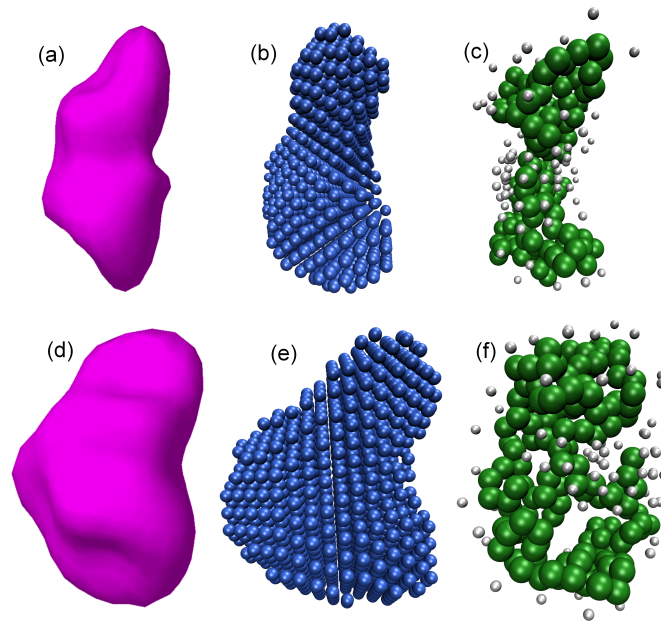


Figure 7.5: *Ab initio* structures of Δ +PHS/V66K at pH 6.0, ambient temperature and high hydrostatic pressure of 3 kbar. The structures were calculated – from left to right column – by multipole expansion, multi-bead modelling and the dummy-residue method, respectively. The second row depicts the structures presented in the first row turned to the right by 90° .

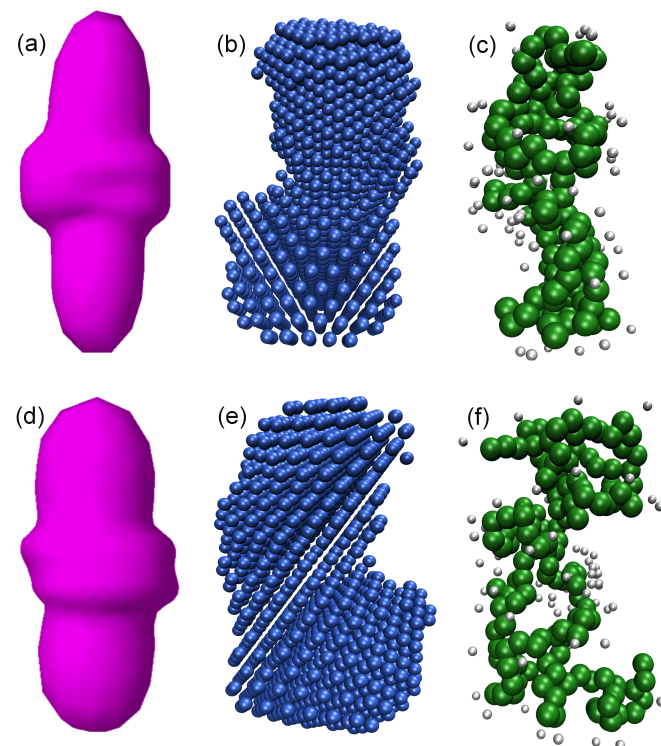


Figure 7.6: *Ab initio* structures of Δ +PHS/V66K at pH 4.5, ambient temperature and high pressure of 1 kbar. The structures were calculated – from left to right column – by multipole expansion, multi-bead modelling and the dummy-residue method, respectively. The second row depicts the same particles as presented in the first row turned by 90° to the right.

($52 \pm 0.5 \text{ \AA}$ compared to $49 \pm 0.5 \text{ \AA}$). The R_G -values of these two proteins confirm this result (q.v. Table 7.1). In contrast, Δ +PHS/V66R appears to be denatured at this temperature, indicated by the large R_G and D_{\max} of $24.2 \pm 0.5 \text{ \AA}$ and $85 \pm 1.0 \text{ \AA}$, respectively. It should be noted that V66A and V66Y differ in the radius of gyration by about 1 \AA , and whereas the volume of the Tyr buried inside a protein was found to be 197.1 \AA^3 , the volume of Ala is only 90.1 \AA^3 .^[378] The side chains of both residues are in a microcavity inside the protein.^[379] Thus, it appears that because of the Tyr's larger volume, insertion of this residue into the cavity leads to a widening of the cavity and consequently to a small, but still well detectable increase of the volume of the folded protein.

The large D_{\max} - and R_G -values of Δ +PHS/V66R point to an already partially unfolded conformation of this variant at 34°C . In contrast, at a temperature of 25°C , where the protein is still folded, the R_G of this variant is $18.9 \pm 0.5 \text{ \AA}$, which is still larger than the R_G of Δ +PHS/V66A and of Δ +PHS/V66Y. This behaviour is caused by the Arg at position 66, which has a large and ionisable side chain. In contrast to Lys-66, Asp-66, and Glu-66, which titrated with highly shifted pK_a -values,^[113, 114, 127, 380] the pK_a of Arg-66 appears to be quite normal.^[381] This probably reflects some form of dislocation of the side chain from the hydrophobic core that allows the guanidinium moiety to make contact with bulk water. The increase of R_G by $6\text{--}7 \text{ \AA}$ relative to the Δ +PHS/V66A and Δ +PHS/V66Y variants may be attributed to the structural reorganisation that is expected to occur upon relaxation of the structure in the local neighbourhood of Arg-66. Crystallographic studies and computer simulations showing that the first β -strand of the β -barrel is disrupted in the Δ +PHS/V66R variant are consistent with the large R_G measured by SAXS for this variant.^[381, 382]

The resulting models of the *ab initio* calculations obtained from SAXS measurements are shown in Figure 7.7 together with the ribbon representation of the crystallographic structure of Δ +PHS (3BDC)^[125]. The structures for the Δ +PHS/V66A and Δ +PHS/V66Y variants have a largely globular body with a smaller cone-shaped feature on top. A comparison of these two models with the crystallographic structure of Δ +PHS suggests that this feature could be due to the disordered C-terminal residues 141–149. The model for Δ +PHS/V66R obtained by the *ab initio* calculations is much more extended, reflecting that this variant is largely unfolded. Of interest, the main differences between the model of Δ +PHS/V66R and those of the other variants are in the larger part where the mutation should be present. As found before, the structures calculated by multipole expansion give only a rough impression of the particle envelope with low resolution. The models derived from the dummy-residue method represent the packing and ternary structure of the protein particularly well.

7.1.4 Discussion and conclusions

Previous studies of the Δ +PHS protein and its V66K variant with NMR spectroscopy have shown that the response of the protein to the ionisation of Lys-66 is limited and localised to the vicinity of the lysine's side chain.^[126] Because structural and dynamic consequences of the presence and ionisation of the internal Lys-66 are affected by the volume differences between Lys and the amino acids used for substitution (e.g. Val), and by the differences in hydration of Lys in water and Lys inside the protein, the application of high-hydrostatic pressure was expected to shed light on the structural determinants of the properties of the internal Lys-66 and the response of the protein to the presence of a charged group inside its hydrophobic core.

Interestingly, the SAXS data revealed that the pressure-unfolded form of the protein is significantly more compact than that of wild-type SNase under comparable conditions of high pressure, pH and temperature,^[131] despite the fact that the calculated volume changes and tryptophan fluorescence prop-

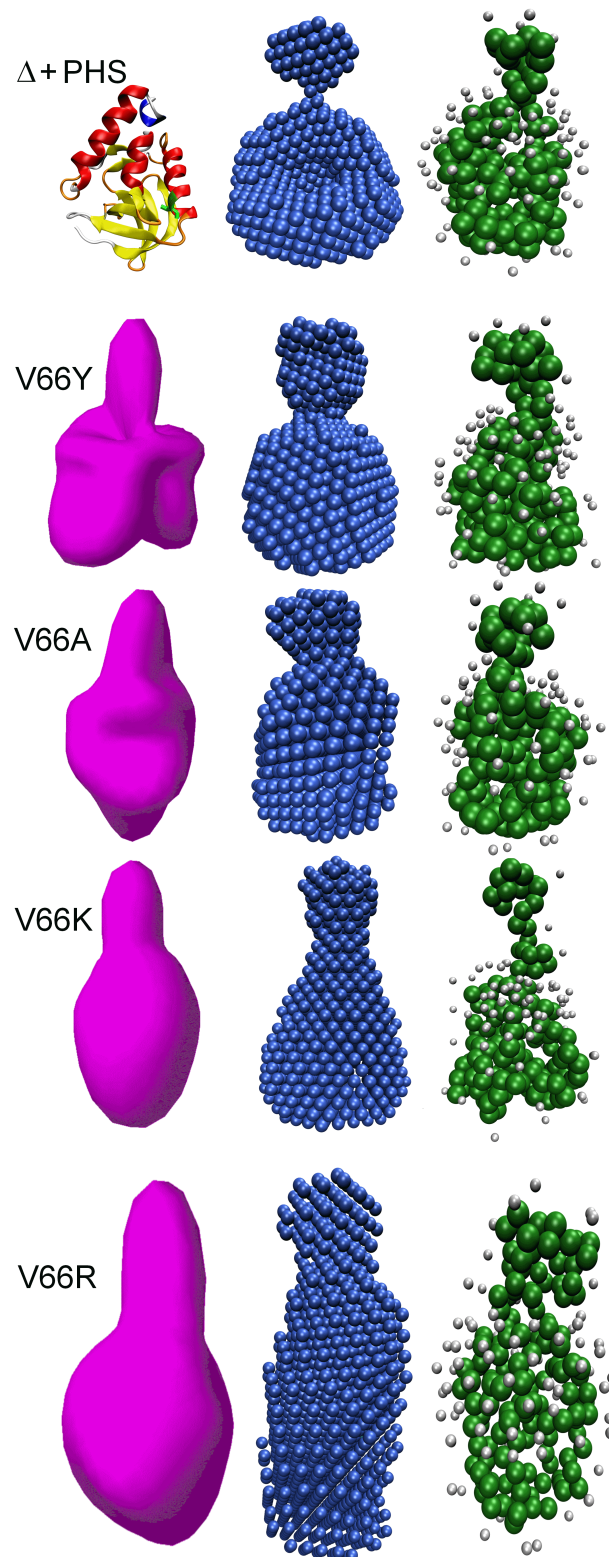


Figure 7.7: *Ab initio* structures of different Δ +PHS mutants at ambient pressure and temperature. The first column shows models calculated by multipole expansion except for the first row, where the crystal structure of Δ +PHS (3BDC)^[125] is depicted. The structures in the middle and right column are computed using multi-bead modelling and the dummy-residue method, respectively. The first row shows Δ +PHS without further mutations and all other proteins have the Val-66 exchanged by – from top to bottom – tyrosine, alanine, lysine and arginine.

erties are nearly identical. The more condensed chain at high pressure for the unfolded state of the Δ +PHS/V66K variant could arise from residual stabilising interactions in the hydrophobic core that are inherent to the Δ +PHS reference protein (as compared with the true wild-type form of SNase). The differences in compactness between the unfolded states of the variants of SNase reported here and previously^[129, 314] may be less apparent using chemical denaturants because the physical basis for chemical denaturation involves interaction of the denaturant with the polypeptide chain. Hence, denaturants, unlike pressure, intrinsically favour expanded structures. In contrast, pressure acts simply to reduce volume, and hence, residual interactions that do not contribute to volume effects are often preserved at high pressure.^[322, 383–385] Apparently, further disruption of the core in the case of wild-type SNase compared with the compact denatured state populated by the Δ +PHS/V66K protein is not associated with a further decrease in volume. The differences observed in chain compaction in the pressure unfolded ensemble for the V66K variant compared with wild-type SNase suggests that pressure may reveal intrinsic sequence dependent characteristics of the unfolded state that are obscured using harsher, chemical perturbation.

The detailed examination of the structural and dynamic consequences of the presence and ionisation of groups in the protein's hydrophobic core has revealed that the response of the protein can be rather subtle. The comparison of site-specific structural and dynamic information obtained from NMR^[368] with the global information about protein shape and chain condensation available from SAXS has confirmed that there is a change which is localised to the region in the vicinity of Lys-66, but surprisingly, most of the protein remains intact after the ionisation of the internal group. By using both changes in hydrostatic pressure and pH to perturb the system, it was possible to examine the effect of the substitution on the local malleability of the structure, as well as the surprising robustness of the folded ensemble. These important observations confirm that the apparent dielectric constant needed to reproduce the pK_a of Lys-66 with continuum electrostatics methods is high because the subtle, dynamic structural reorganisation coupled with the ionisation of the internal Lys needs to be accounted for implicitly in the dielectric constant.^[114, 115, 127]

When the internal cavity in the hydrophobic core of SNase was occupied with Tyr-66, a small increase in the size of the folded protein relative to the case with Ala-66 was detected at atmospheric pressure. Presumably, this effect is related to the larger volume of the aromatic side chain of tyrosine. An even larger R_G was found with Arg-66, reflecting marked structural changes that were detectable even at ambient temperature and pressure, and probably originated from the reorganisation required to accommodate a large and charged side chain in the hydrophobic interior of the protein.

The application of high hydrostatic pressure made it possible to identify differential stabilities for the variants under conditions of constant thermal energy. In the case of the Δ +PHS/V66Y variant, no changes were detectable in the pressure range studied, whereas the Δ +PHS/V66A variant showed a slight increase with rising pressure ($\Delta R_G \approx 3 \text{ \AA}$ up to 4 kbar). In contrast, the variant with Δ +PHS/V66R unfolded continuously up to 2 kbar upon pressurisation, where an R_G -value of 31.7 \AA was reached. This protein at high pressure did not adopt a random-coil like state. In contrast, its temperature-unfolded state reached an R_G of about 37 \AA , which is compatible with the random coil.

7.2 Peroxidase MsP1

The results shown in this section are part of a cooperation project with the group of Prof. Dr. H. Zorn (Institute of Food Chemistry and Food Biotechnology, Giessen, Germany). Fluorescence- and Fourier transform infrared spectroscopic measurements, as well as the investigations by differential scanning calorimetry were performed by M. Puehse^[337] and Y. Ma from our group. Enzyme production and purification, protein quantification, and the enzyme assays were done by R.T. Szweida working in Prof. Dr. Zorn's group in Giessen. Here, the focus is mainly on the SAXS measurements conducted by me. The complete study including all results is published in [386].

7.2.1 Introduction

The temperature and pressure dependent stability and function of MsP1, an uncommon peroxidase from the basidiomycetous fungus *Marasmius scorodonius*, was investigated. To this end, a series of biophysical techniques (DSC, fluorescence and FTIR spectroscopy, small-angle X-ray scattering) were combined with enzymatic studies of the enzyme. The dimeric MsP1 turned out to be not only rather thermostable, but also highly resistant to pressure, i.e. up to temperatures of about 65 °C and pressures as high as 8 - 10 kbar at ambient temperatures.

Remarkably, the activity of MsP1 increased by a factor of two until ~500 bar. At about 2 kbar, the enzymatic activity was still as high as under atmospheric pressure conditions. As revealed by the fluorescence and SAXS data, the increased activity of MsP1 at pressures around 500 bar may result from slight structural changes, which might stabilise the transition state of the enzymatic reaction. Owing to this marked high pressure stability of MsP1, it may represent a valuable tool for industrial high pressure applications.

7.2.2 Materials and methods

Enzyme production and purification

The *Marasmius scorodonius* strain (CBS 137.86) was obtained from the Dutch "Centraalbureau voor Schimmelcultures", Baarn. Enzyme production and purification were performed as described previously in the literature [158].

Small-angle X-ray scattering (SAXS)

The SAXS experiments were performed at the high brilliance beamline ID2 at the European Synchrotron Radiation Facility (ESRF)^[66] in Grenoble, France. The medium X-ray energy was 12.46 keV, corresponding to a wavelength, λ , of 0.995 Å. The lyophilised protein buffer mixture (Bis-Tris; pH 5.8) was dissolved in 100 μ l H₂O, yielding a 1.9 % (w/v) solution. 20 μ l of the sample were placed in a high pressure sample cell.^[67, 68] The cell was equipped with Kapton polymer windows. Plots of the diffraction intensity versus reciprocal spacings were recorded using MATLAB based software, written by the ESRF staff. The pressure dependent measurements were performed at 30 °C and the maximal pressure applied was 3 kbar (accuracy: \pm 20 bar). Measurements were performed at steps of 100 bar in the upward and downward direction. Additional measurements under the same conditions were taken with a pure buffer sample for background correction.

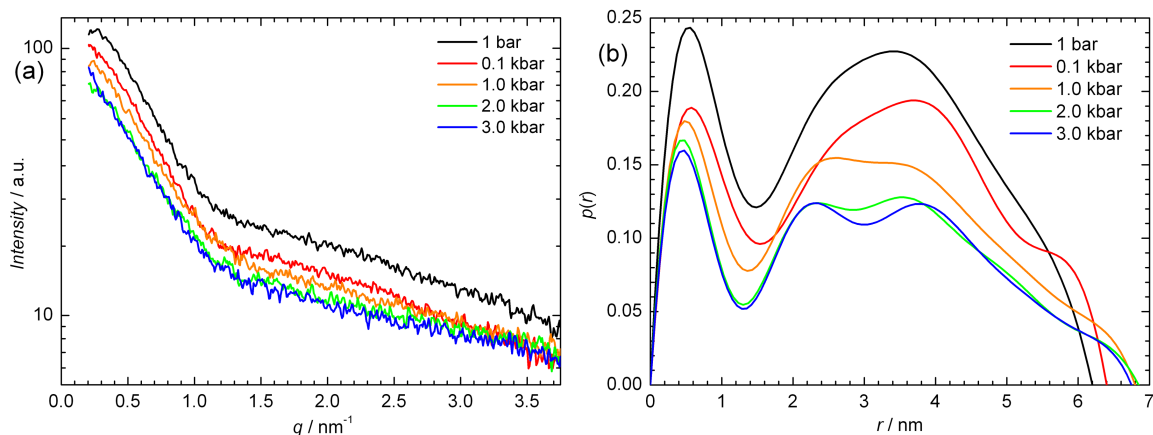


Figure 7.8: SAXS scattering patterns (a) and pair-distance distribution functions of the protein MsP1 at selected pressures ($T = 30 \text{ }^\circ\text{C}$).

Temperature dependent SAXS measurements were conducted with a Kratky-camera (Model KKK, Anton Paar, Graz, Austria) in our laboratory at TU Dortmund University. The X-ray energy was 8.05 keV ($\lambda = 0.154 \text{ \AA}$). After dissolving the lyophilised protein-buffer mixture (phosphate buffer; pH 6.0) in 100 μl water, yielding a 1.5 % (w/v) protein solution, measurements were executed at 30, 60, and 70 $^\circ\text{C}$. Temperature control was achieved via an external water bath ($\Delta T = \pm 1.5 \text{ }^\circ\text{C}$).

7.2.3 Results

To reveal details of small pressure-induced conformational changes of the protein in the lower pressure regime previously found by FTIR spectroscopy,^[386] small-angle X-ray scattering measurements were performed as a function of pressure up to 3 kbar. Figure 7.8a shows the small-angle X-ray scattering intensity as a function of momentum transfer, $I(q)$, for pressures from 1 bar to 3 kbar at $T = 30 \text{ }^\circ\text{C}$. The shape of the SAXS curve with a breakpoint in the slope of $I(q)$ at about 1.2 nm^{-1} is typical for dimeric protein structures.^[387] Interestingly, upon pressurisation, changes occur only in the intermediate momentum transfer region between 1.25 and 3 nm^{-1} , indicating only minor medium-range-order changes of the protein conformation in this pressure range. Besides, with increasing pressure only a decrease in scattering intensity is observed, which is due to a decrease of the electron density contrast between the protein and the surrounding water upon pressurisation. The radius of gyration, R_G , was determined from the Guinier-plots ($\ln I$ versus q^2) in the low- q regime as well as from the pair-distance distribution function.^[314] Within the accuracy of the measurements, a constant R_G -value of $2.41 \pm 0.05 \text{ nm}$ was found up to pressures of 3 kbar.

For further data analysis, the measured $I(q)$ data were subjected to indirect Fourier transformation using the program GNOM, which calculates the distance distribution function, $p(r)$, for monodisperse systems from the one-dimensional scattering curves. Interestingly, $p(r)$, as presented in Figure 7.8b, exhibits two maxima with a minimum around 1.5 nm, again indicating the presence of a dimeric structure. The first maximum at an r -value of about 0.5 nm represents distances with high electron densities, which are basically not changing with pressure. However, with increasing pressure, a minimum is emerging at intermediate distances of $\sim 3 \text{ nm}$, which might be due to a decreasing electron density in the connection region of the two monomeric parts of the protein. The change of $p(r)$ between 2 and 5 nm thus originates from a pressure-induced small tertiary structural change in the pressure range starting below 1 kbar.

After all, no dissociation and no significant unfolding or major changes in tertiary structure can be deduced from the analysis of the pressure dependent SAXS measurements up to 3 kbar.

The Guinier-plots of the temperature dependent measurements at atmospheric pressure exhibit an R_G -value of approximately 2.4 nm at 30 °C as well as 60 °C. At 70 °C, this value first drops to about 1.2 nm and subsequently increases drastically due to aggregation of the protein (data not shown as the R_G of such a large polydisperse aggregate cannot be determined). This clearly indicates a temperature-induced dissociation of the MsP1 dimer into monomers, which manifests itself in a decrease of the enzyme activity as observed above 60 °C, as well as in the aggregation of the protein as revealed by the DSC and FTIR spectroscopic data.^[386] Hence, the catalytic activity of the enzyme seems to be restricted to the integrity of the dimeric structure.

7.2.4 Discussion and conclusions

Compared to other members of the DyP-type enzyme family, MsP1 exhibits a remarkably high temperature optimum and a good thermostability. For the peroxidase DyP from *T. cucumeris* (formerly denominated as *Geotrichum candidum*), which is capable of decolorising various synthetic dyes, an optimal temperature of 30 °C has been described.^[388] Lignolytic enzymes like manganese peroxidases, laccases, and members of the DyP family represent interesting tools for the low-energy and low-cost alternatives for industrial processes in which lignin modification is of importance, such as paper and pulp processing and processes for valorisation of agricultural residues. The polymeric carbohydrates of agricultural residues, cellulose and hemicellulose are typically hydrolysed by carbohydrases up to temperatures of 50 °C. More recent developments of cellulases active beyond 50 °C is of interest, since reactions are energetically more favourable at higher temperatures and they give additional benefits in processes, such as a decrease of viscosity.^[389, 390] Thus, simultaneous delignification and saccharification at higher temperatures requires thermostable delignifying enzymes.

Remarkably, the activity of MsP1 increases until about 500 bar, before it starts to decrease again. Conversely, various enzymes are markedly inactivated upon high pressure treatment of about 2 kbar. Activity losses of 20 and 50 % have been reported for soy lipoxygenase and horseradish peroxidase, respectively, after 15 min exposure to a hydrostatic pressure of 2 kbar at 55 °C. Total inactivation of the lipoxygenase was observed at 5.7 kbar.^[391] On the other hand, some proteins are stabilised at high pressure. Up to 4 kbar were required to maintain a carboxypeptidase from the archaeobacterium *Sulfolobus solfataricus* in its active state at higher temperatures,^[392] and L-galactosidases from *E. coli* and *Aspergillus oryzae* were stabilised in the range of 2-3 kbar at 50 and 65 °C, respectively.^[393] The pressure level causing full dissociation of the MsP1 dimer could not be revealed in the present study. Other oligomeric enzymes such as glyceraldehyde-3-phosphate dehydrogenase, lactate dehydrogenase, and malate dehydrogenase were found to reversibly dissociate and re-associate upon application and release of hydrostatic pressure up to 2 kbar.^[393]

The increased activity of MsP1 at pressures around 500 bar may result from slight structural changes stabilising the transition state of the enzymatic reaction. Generally, high pressure may influence enzyme-catalyzed reactions either by enzyme conformational changes, or by modification of the reaction mechanism.^[394] In fact, high pressure has been used to enhance the activity or selectivity of a number of enzymes, paving the way for new applications. Most of the applications have been reported from the food processing industry, especially from dairy and juice production.^[395] For example, the reduction of bitterness in citrus juices correlates directly with the concentration of naringin. The enzyme naringinase hydrolyses naringin to the tasteless naringenin, and the activity of the enzyme was shown to increase

3-fold under high pressure conditions (1.6 kbar).^[396] The use of microbial transglutaminase (MTG) under hydrostatic pressure of up to 6 kbar allowed for the cross-linking of proteins, which could not be affected by MTG at atmospheric pressure.^[397] However, at higher pressures the tertiary structure of the native enzyme was impaired, and α -helical secondary structures were unfolded.^[398]

No significant changes in the secondary structure of MsP1 occurred up to 10 kbar. Minor changes – possibly a slight pressure-induced swelling, indicating the onset of the unfolding reaction – occur only above about 8 kbar up to 10 kbar. Regarding this remarkable high pressure stability of MsP1, it may represent a valuable tool for industrial high pressure applications. Delignification of agricultural residues represents an interesting target. The common pretreatment of lignocellulosic substrates prior to carbohydrate hydrolysis and fermentation to ethanol is performed by steam explosion,^[399, 400] dilute acid,^[401, 402] or an organosolv process.^[403] However, these procedures come along with the formation of toxic by-products, which impede the downstream enzymatic hydrolysis and the fermentative conversion of the released sugars into ethanol.^[401, 404–408] An entirely enzymatic delignification process may overcome these obstacles.

CHAPTER 8

Investigations of lipid-peptide interactions

In this chapter different studies are presented, investigating the interaction of various lipid systems with peptides or proteins. The importance of these investigations becomes evident, taking into account that approximately one third of all known proteins are membrane associated proteins.^[245] In the first section, the interaction of the ion channel peptide gramicidin D with an archaeal lipid (PLFE) monolayer at the air-water interface, using X-ray reflectometry and grazing incidence X-ray diffraction, is presented. In the section 8.2, the effect of different fusion peptides on the static phase behaviour as well as the phase transition kinetics, studied by synchrotron small-angle X-ray scattering, is discussed. Finally, in the third section three studies are summarised, investigating the interaction of amyloidogenic peptides, i.e. IAPP and A β , with different phospholipid raft films as well as glycolipids at the air-water interface.

8.1 Interaction of gramicidin D with archaeal lipids

The investigation presented in this section was conducted in cooperation with F. Evers (Department of Physics, TU Dortmund University). The experiments were planned and performed together at the ESRF (Grenoble, France). The correction of the raw data (integration of the detector raw data, background- and illumination-correction, etc.), to obtain the corrected intensities, $I(q)$ and $I(q_{xy}, q_z)$, was done using MATLAB scripts written by me. The XRR data were fitted by F. Evers using the software LSFIT and the calculations based on the GIXD results were performed by me using different MATLAB scripts. The results were discussed together and finally published in [362].

8.1.1 Introduction

A comprehensive study of archaeal lipid (PLFE) monolayers at the air-water interface by XRR and GIXD is presented in section 6.6 (page 121ff.). As a next step, the interaction of the ion channel peptide gramicidin D with an archaeal lipid monolayer (grown at 76 °C) was investigated as a function of surface pressure with a subphase pH of 6.5, mimicking the conditions inside thermoacidophilic archaeon cells. The main objective of this study was not only to learn about the interaction of polypeptides (which usually insert into lipid membranes) with the monolayer, but also to test the quality of a PLFE monolayer as a model system for a natural plasma membrane of thermoacidophilic archaeon organisms.

The addition of gramicidin D to an archaeal lipid monolayer led to a more disordered state of the lipid film observed by XRR, especially at low surface pressures. At elevated surface pressures a thickening of

the lipid chain region could be observed, indicating the presence of gramicidin D mainly in this area of the monolayer. In GIXD no major changes could be found except for a decreasing size of crystalline domains, indicating that gramicidin D interacts mainly with the disordered areas of the monolayer. The monolayer system was not suitable to investigate the peptide-lipid interaction occurring in biological systems due to the U-shaped conformation of the lipid even at a high film pressure of 40 mN m^{-1} .

8.1.2 Materials and methods

Materials

The dibiphytanyldiglycerol tetraether lipids (PLFE) were extracted from the plasma membrane of the thermoacidophilic archaeon *Sulfolobus Acidocaldarius*, grown at 76°C . Chloroform, methanol and gramicidin D from *Bacillus Aneurinolyticus* were purchased from Sigma (Taufkirchen, Germany) and used without further purification. Aqueous solutions were prepared using water filtered through a Milli-Q purification system, yielding a specific electrical resistivity of $> 18 \text{ M}\Omega\text{ cm}$. PLFE was dissolved in a mixture of chloroform, methanol, and water (75:19:5 vol) and 2%_{wt} gramicidin D was added into the lipid solution prior to spreading at the air-water interface. The gramicidin D / PLFE interactions were studied at a subphase pH value of 6.5.

X-ray reflectometry and grazing incidence X-ray diffraction

The archaeal lipid / gramicidin D stock solutions were spread at the air-water interface on a Langmuir trough. Monolayer films were examined at various lateral film pressures, π , between 10 and 40 mN m^{-1} at a subphase temperature of 20°C .

The X-ray scattering experiments were conducted at the liquid surface diffractometer of beamline ID10B at the synchrotron light source ESRF (European Synchrotron Radiation Facility, Grenoble, France).^[97] For the experiments, the Langmuir trough was mounted on the diffractometer. The analysis of surface X-ray scattering data is outlined in detail in chapter 3. X-ray reflectometry (XRR) data are plotted as R/R_F versus q_z , with the reflectivity, R , the Fresnel reflectivity, R_F , and the vertical wave vector transfer, q_z . In a GIXD experiment, the momentum transfer has a horizontal and vertical component, q_{xy} and q_z (q.v. section 3.2.2). Integration along these directions yields Bragg rod and Bragg peak patterns, respectively.

8.1.3 Results and discussion

Figure 8.1 shows X-ray reflectometry data and electron density profiles of PLFE monolayers (grown at 76°C) spread on subphases with a pH value of 6.5 and a temperature of 20°C as well as data of the interaction of PLFE with 2%_{wt} gramicidin D on the same subphase. Remarkably, when both gramicidin D and PLFE are present at the interface, a less ordered, more heterogeneous monolayer structure can be found at low film pressures compared to lipid films built by pure PLFE. Such structures were adequately described by a single-layer model (cyan curve in Figure 8.1a) because of the absence of pronounced Kiessig oscillations, which are characteristic of well-defined lipid films. In the presence of gramicidin D, the total monolayer thickness rises with increasing film pressure. Comparing the film structures in the presence and absence of gramicidin D at high film pressures reveals that the addition of gramicidin D leads to an increase of the electron density of the chain region, while the electron density of the head group is slightly decreased (Figure 8.1b).

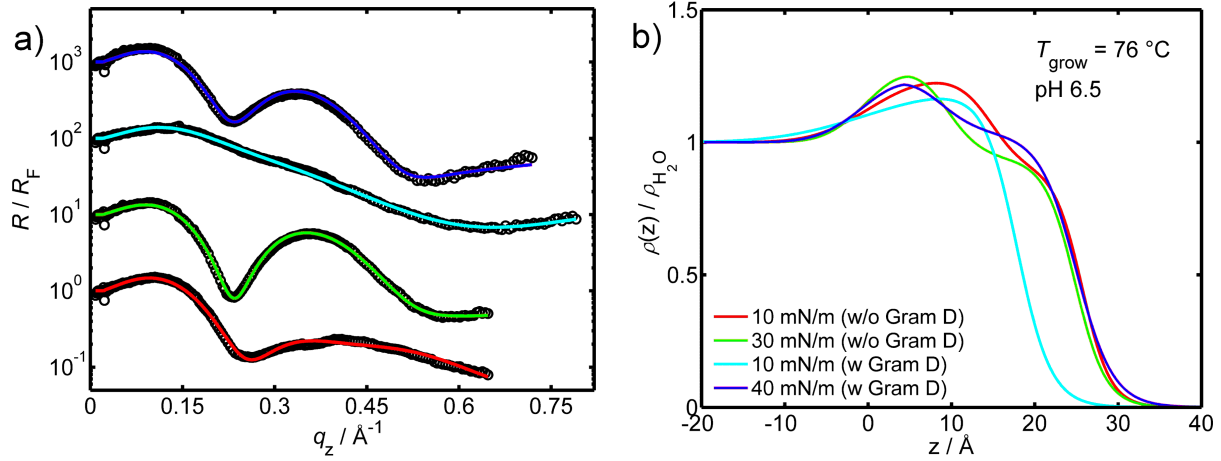


Figure 8.1: a) X-ray reflectometry data (symbols) obtained from archaeal lipid monolayers containing 2%_{wt} gramicidin D at the air-water interface, presented together with the best fits (solid lines) normalised to the Fresnel reflectivity, R_F . For clarity, the reflectivity curves are shifted along the ordinate with increasing film pressure. b) Normalised electron density profiles as retrieved from the fits on the left-hand side. PLFE monolayers with and without gramicidin D were prepared at different film pressures and a constant subphase temperature of 20 °C.

Table 8.1: Calculated parameters of grazing incidence diffraction measurements of an archaeal lipid (grown at 76 °C) monolayer containing 2%_{wt} gramicidin D at the air-water interface: lattice vectors in real space, $a = b, c$, angle included by lattice vectors, γ , lateral 2D crystalline domain length, L_{xy} , vertical crystalline domain length, L_z , and area per hydrocarbon chain, A_{chain} , are listed for all samples.

sample	pH	T_{sub} [°C]	π [mN m ⁻¹]	a, c [Å]	γ [°]	L_{xy} [Å]	L_z [Å]	A_{chain} [Å ²]
PLFE	6.5	20	10	4.531, 5.102	111.5	760, 400	25.1, —	19.10
PLFE	6.5	20	30	4.582, 5.064	112.9	1620, 880	26.2, 26.6	19.33
PLFE + gram D	6.5	20	10	4.569, 5.056	112.8	1310, —	26.8, —	19.24
PLFE + gram D	6.5	20	20	4.571, 5.061	112.8	1190, 760	28.2, —	19.27
PLFE + gram D	6.5	20	30	4.574, 5.062	112.8	1050, 730	28.0, —	19.28
PLFE + gram D	6.5	20	40	4.577, 5.060	112.9	920, 720	28.6, —	19.30

The addition of 2%_{wt} gramicidin D into the archaeal lipid (growth temperature of 76 °C) monolayer at the air-water interface (pH 6.5) at 20 °C and a lateral film pressure of 30 mN m⁻¹ leads to no significant changes in the unit cell parameters and vertical dimensions of crystalline domains observed by GIXD (q.v. Table 8.1). This indicates that the interaction of the gramicidin D with the lipid occurs mainly in the disordered areas of the monolayer. The lateral length of these highly ordered domains decreases to about 50% compared to samples without gramicidin D at 30 mN m⁻¹.

The archaeal lipid monolayer containing 2%_{wt} gramicidin D has been investigated at 20 °C for four different film pressures (10, 20, 30, 40 mN m⁻¹) by GIXD. Only minor changes in the unit cell parameters could be observed, as for example a slight increase of the area per lipid chain by 1% with increasing film pressure. However, there is a strong change in the dimensions of the crystalline domains with growing lateral film pressure. The lateral domain size decreases linearly by approximately 40% between 10 mN m⁻¹ and 40 mN m⁻¹ to about 920 Å.

According to the XRR data, the addition of gramicidin D leads to a more heterogeneous, disordered state at low film pressures. At higher film pressures, the presence of gramicidin D induces a slightly

higher overall thickness of the monolayer compared to the measurement without gramicidin D. The main difference between pure archaeal lipids and a system containing gramicidin D is an increasing electron density of the lipid chain region and concomitantly decreasing electron density of the head group region with increasing film pressure in the presence of gramicidin D. This indicates the incorporation of gramicidin D solely into the hydrophobic region of the monolayer. In GIXD, no major changes in the unit cell parameters can be found. The lateral length of crystalline domains decreases to 50 % after the addition of gramicidin D at 30 mN m^{-1} . Also, for samples containing gramicidin D, a decreasing lateral domain size with increasing film pressure can be observed. This might indicate the presence of gramicidin D in the disordered areas of the monolayer. With increasing film pressure, gramicidin D is pressed into previously highly ordered domains and increases the disorder leading to smaller lateral crystalline domain lengths.

8.1.4 Conclusions

Only an unspecific interaction of gramicidin D with the archaeal lipid monolayer could be found. The lipid film at the air-water interface can be subdivided into two layers due to the U-shape conformation (q.v. section 6.6, page 121). Directly in contact with the water interface is the highly hydrophilic layer consisting of the lipid head groups. Conterminous with this region of the lipid monolayer, a layer built by the lipid's hydrophobic hydrocarbon chains can be found extending into the air. GIXD results indicated that the interaction of gramicidin D occurs mainly in disordered regions of the monolayer, where the flexibility and mobility of molecules is much higher. XRR showed a strong interaction of gramicidin D exclusively with the hydrophobic layer of the lipid film. This indicates that the peptide is preferentially inserted into this layer without extending into the hydrophilic regions of the monolayer. No evidence can be found of a favoured orientation of the gramicidin D main axis parallel to the monolayer normal, as previously found for phospholipid bilayers in solution, although the length of the gramicidin D helical dimer would fit the overall length of the PLFE lipid film at the air-water interface rather well.^[138–140]

To conclude, it was neither possible to create a PLFE monolayer at the air-water interface with a “physiological” orientation as present in the plasma membrane of thermoacidophilic archaeon organisms, nor could gramicidin D be inserted in such a “non-ideally” aligned membrane specifically with an orientation spanning the whole membrane, as obtained in nature in phospholipid membranes. Only a non-specific integration of the hydrophobic polypeptide into the hydrocarbon chain region of disordered regions in the PLFE monolayer could be found.

8.2 Interaction of monoolein with fusion peptides

The study presented in this section was conducted in cooperation with Dr. K. Weise, a post-doctoral student in our group at TU Dortmund University. She planned the experiments and prepared all samples. The experiments were performed together at the synchrotron light sources ESRF (Grenoble, France) and Soleil (Giv-Sur-Yvette, France). Two new PhD-students in our lab, S. Grobelny and M. Erlkamp, attended the last two synchrotron SAXS experiments at the ESRF. The data correction and processing to obtain the lattice constants, peak intensities, as well as the detailed parameters of the unit cells of all phases was done by me. From these data, p, T -phase diagrams could be constructed. Finally, the interpretation of the results, as presented in this thesis, was done by me. The results of the whole study will be published soon.

Before the interaction of monoolein with different fusion peptides was studied, the phase behaviour and phase transition kinetics of pure monoolein at a constant limited hydration of 17 %_{wt} water content were investigated. The results of this investigation are presented in section 6.5 (page 111ff.).

8.2.1 Introduction

Although membrane fusion is essential for many biological processes, it does not occur spontaneously due to strong hydration, electrostatic and steric repulsive forces between the membranes. Instead, nature uses different highly specialised proteins to induce membrane fusion, such as viral fusion and cellular SNARE proteins. Viral fusion proteins contain specific segments, which are involved in viral membrane fusion: the fusion peptide (FP) and trans-membrane domain (TMD).

Each of the two segments fulfils different tasks: the fusion peptides insert first into the target membrane, leading to a destabilisation of the membrane and reducing the activation energy needed for the fusion of two membranes, i.e. it acts as a catalyst in the early stages of membrane fusion.^[146–148] The function of the TMD is the further destabilisation of the membrane as well as supporting the formation of fusion pores in later stages of the membrane fusion process. This requires the TMD to span both membrane leaflets.^[149] Synthetic fusion peptides are good models for studying membrane-associated structures and processes in viral fusion.^[146, 150, 151] Even TMD peptides alone are sufficient to drive fusion of liposomes. Further details can be found in section 4.1.4 (page 40ff.).

In the present study, time-resolved small-angle X-ray scattering (trSAXS) experiments were carried out to evaluate the effect of membrane fusion promoting domains on the fluid lamellar to inverse bicontinuous cubic phase transition (L_α to Q_{II}) of monoolein, which serves as a well established model system for studying the final steps of the fusion process of bilayer membranes. Fusion peptides from different viral fusion protein classes were studied to evaluate the influence of distinct conformational properties of the peptides on the modulation of membrane curvature and on the structural changes occurring during the various stages of the membrane fusion process.

Three different fusion peptides, a trans-membrane domain as well as one control peptide have been studied. The fusion peptides used for this investigation were an incorporated class I viral FP (HA2, influenza), one viral FP of class II (TBEV, tick-borne encephalitis virus), and finally one FP of class III (VSV, vesicular stomatitis virus). Additionally, the viral TMD (VSV) as well as an artificial peptide with no fusion activity (L16) were studied.^[152, 153]

8.2.2 Materials and methods

Materials

The preparation of the samples was performed as described in the study of pure monoolein in section 6.5.2 (page 111). Additionally, 2 %_{wt} of the fusion peptide was added to the molten monoolein during the preparation process. The fusion peptides (HA2, VSV, TBEV) and the trans-membrane domain (TMD) were synthesised and purified at the Deutsches Krebsforschungszentrum (DKFZ, Heidelberg, Germany) and the HPLC purified control peptide (L16) was purchased from the Peptide Specialty Laboratories (PSL, Heidelberg, Germany).

Synchrotron small-angle X-ray scattering data

The SAXS experiments were carried out at the high brilliance beamline ID02^[66] of the European Synchrotron Radiation Facility (ESRF, Grenoble, France) and at the SWING beamline^[361] at the synchrotron light source Soleil (Giv sur Yvette, France). The medium X-ray energy of all experiments was approximately 12.5 keV, corresponding to a wavelength, λ , of about 1.0 Å. A typical sample exposure time was – depending on the phase state of the sample – between 0.05 s and 2 s. Since the quality of the data taken at beamline ID02 (ESRF) outclasses the data obtained at the SWING beamline (Soleil) by far, only data from experiments at the ESRF are presented. All measurements performed at Soleil were, at least, once reproduced at the ESRF. For further experimental details see section 6.5.2 (page 112), where the experiments conducted on pure monoolein are presented, as a part of this study.

Evaluation of the scattering data

After correction of the raw data using MATLAB scripts, all peaks of each scattering pattern were fitted by a Gaussian function. From the positions of the maxima, the different space groups occurring in the samples could be identified. The lattice constants were calculated from the positions of all peaks of one phase. The sum of all peak areas of a specific phase yielded the overall integrated peak intensity.

For each p, T -phase diagram, numerous series of measurements at constant temperatures were conducted in a pressure range between atmospheric pressure and 3-4 kbar (usually in steps of 0.1 kbar adding up to an average of 35 measurements per series). The resulting number of data points (one per measurement) in the phase diagrams of the different samples is presented in Table 8.2. In the plots of the phase diagrams only the points are presented where a phase transition occurred. All points showing no changes in the phase behaviour are not plotted for purposes of clarity.

In the pressure-jump experiments usually 3 measurements were performed before the pressure-jump was triggered, then 30 SAXS patterns were taken every 0.15 s, followed by another series of 30 measurements every 1 s and finally 30 patterns were taken every 3-5 s, depending on the expected phase transition kinetics of the sample system. Pressure-jumps of each sample were conducted at different temperatures, with varying pressure-jump amplitudes and individually chosen initial and final pressures. An overview of all jumps performed in this study is given in Table 8.2.

In lamellar phases, usually the first 2-3 peaks could be obtained. For cubic phases at least 8 peaks could be identified in most of the scattering patterns. In the scattering patterns of a hexagonal phase at least the first 3 peaks were clearly visible. Due to frequently occurring phase coexistence, on average each scattering pattern showed 10 Bragg peaks. The total number of fitted peaks for this project can be estimated to be approximately 85000.

8.2.3 Results and discussion

The influence of different fusion peptides on the phase behaviour of monoolein with a limited hydration level of 17%_{wt}, as studied in section 6.5 (page 111ff.), was investigated. As mentioned before, numerous pressure dependent series of scattering experiments were conducted. As an example, the detailed evaluation of two of these series is presented. Both show a very different behaviour compared to pure monoolein. The first sample containing 2%_{wt} of the fusion peptide TBEV at 5.7 °C forming an inverse hexagonal phase and the other sample containing 2%_{wt} of the trans-membrane domain TMD at 24.3 °C showing the coexistence of the cubic $Ia3d$ and $Pn3m$ phase.

Table 8.2: Estimated numbers of measurements taken from monoolein samples containing different fusion peptides. On average in a pressure dependent series 35 scattering patterns were taken (temperature dependent measurements can be neglected) and the typical number of trSAXS patterns of one kinetic pressure-jump experiment was 93. Each static measurement led to one data point in the corresponding p, T -phase diagram.

sample system	static series	static measurements	pressure-jumps	kinetic measurements
MO	22	770	9	840
MO + L16	15	520	8	740
MO + HA2	22	770	21	1950
MO + VSV	18	630	5	470
MO + TMD	7	250	2	190
MO + TBEV	12	430	9	840
total:	96	3370	54	5030

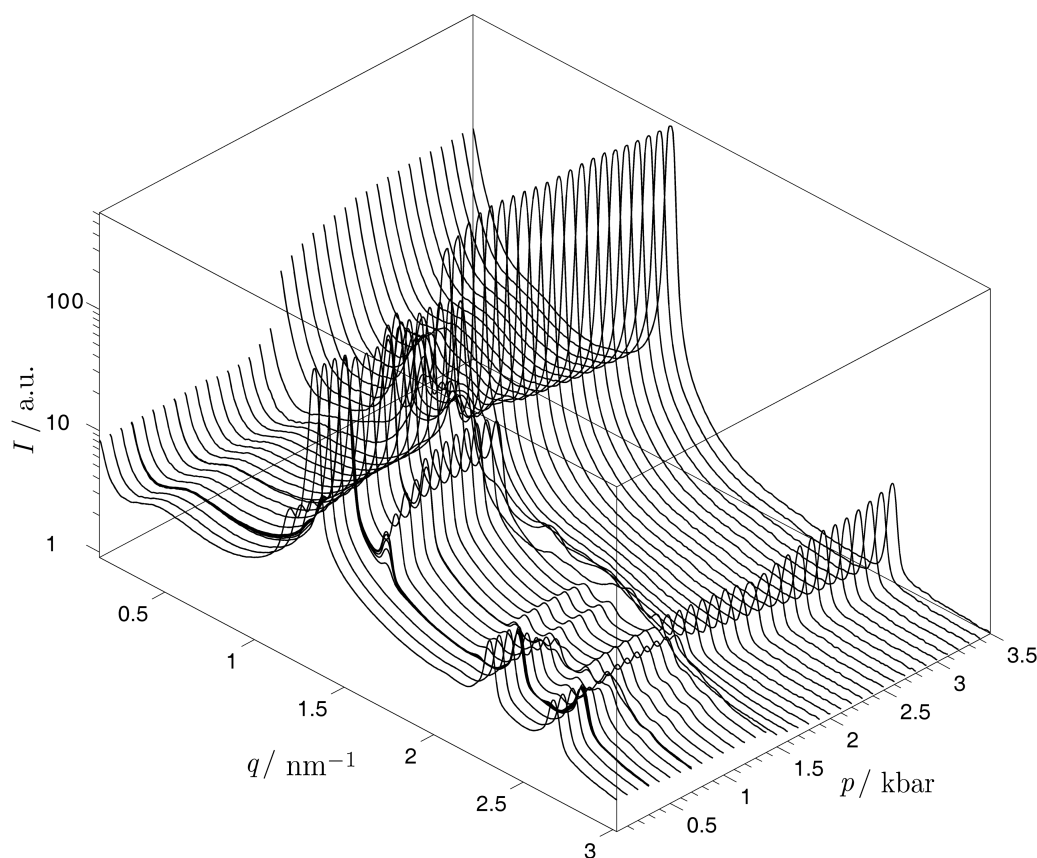


Figure 8.2: Scattering patterns of monoolein (17%_{wt} water content) containing the fusion peptide TBEV (2%_{wt}) as a function of pressure at 5.7°C.

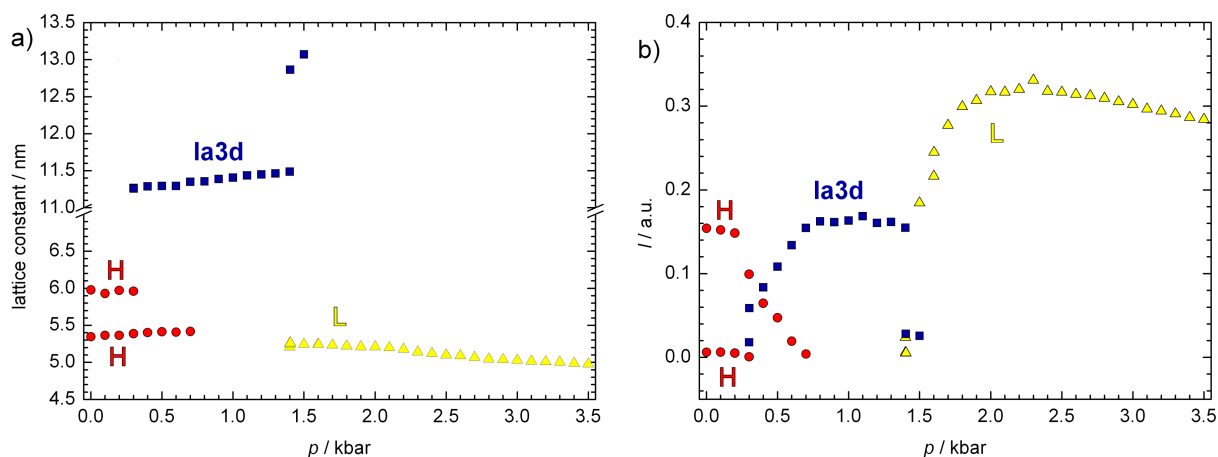


Figure 8.3: Lattice constants (a) and integrated peak intensities (b) of monoolein containing the fusion peptide TBEV as a function of pressure at 5.7 °C.

The scattering patterns of monoolein (17%_{wt} water content) containing the fusion peptide TBEV are depicted in Figure 8.2 as a function of pressure at 5.7 °C. Already in the scattering patterns several different phases can be identified. At low pressure, three distinct peaks can be found assignable to an inverse hexagonal phase. The small shoulder at low q -values indicates a second hexagonal phase with similar lattice spacing and much lower intensity. At intermediate pressures the typical scattering pattern of a cubic $Ia3d$ phase can be found. Finally, at high pressure only two peaks are observed with high intensity, which originate from a lamellar phase. This behaviour is much more complex than the one found for pure monoolein at the same level of hydration and temperature. Below 1.5 kbar a disordered lamellar (L_α) phase was detected. At higher pressures an ordered lamellar (L_c) could be found (q.v. section 6.5.3, page 112ff. and figure 8.6a, page 165).

All peaks found in the scattering patterns of monoolein (17%_{wt} water content) containing the fusion peptide TBEV were fitted to identify the corresponding phases. The lattice constants as a function of pressure are presented in Figure 8.3a. The corresponding integrated peak intensities of the phases are shown in Figure 8.3b. As already observed in the scattering patterns, at low pressure two inverse hexagonal phases (red circles in Figure 8.3) are present. The intensity of the inverse hexagonal phase with the lower lattice constant, a , of 5.34 nm at atmospheric pressure is significantly higher than the other one with an a -value of 5.98 nm. At a pressure of 0.3 kbar a cubic $Ia3d$ phase starts to emerge with an initial lattice spacing of 11.27 nm (blue squares in Figure 8.3). Simultaneously the low-intensity inverse hexagonal phase vanishes. It can be suspected that the two inverse hexagonal phases comprise a different content of fusion peptide. The one with the higher lattice constant and much lower intensity is probably richer in fusion peptide, which might impair the formation of a defect- and stress-free inverse hexagonal lattice. The moment a cubic phase forms, the fusion peptide can be incorporated into this new phase and the stressed inverse hexagonal phase dissolves.

Up to 0.7 kbar the coexistence of one inverse hexagonal phase and the cubic $Ia3d$ phase can be found. The lattice spacing of the inverse hexagonal phase is nearly uninfluenced by the increasing pressure – only a slight increase from 5.34 nm at atmospheric pressure to 5.40 nm at 0.7 kbar can be observed. Between 0.7 kbar and 1.4 kbar an $Ia3d$ single-phase region is observed, where the lattice constant increases slightly from 11.33 nm to 11.52 nm. Between 1.4 kbar and 1.5 kbar the cubic phase vanishes and a lamellar phase emerges (yellow triangles in Figure 8.3). The d -spacing of the lamellar phase decreases with increasing pressure from 5.25 nm at 1.4 kbar to 4.98 nm at 3.5 kbar, indicating a fluid lamellar phase (L_α).

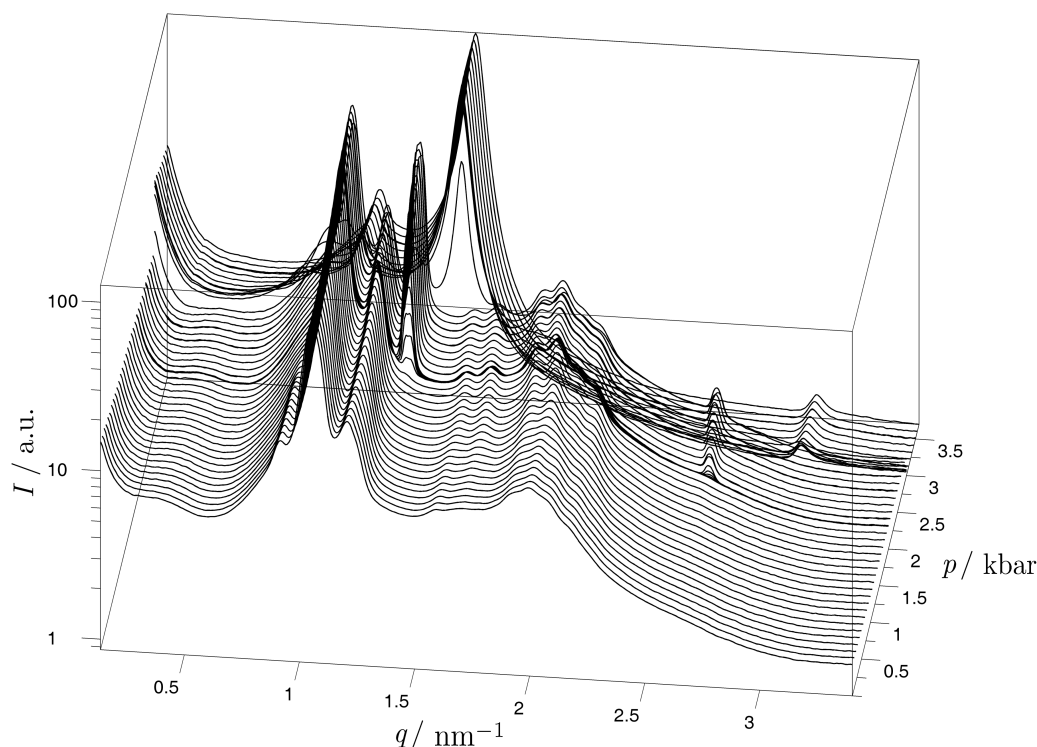


Figure 8.4: Scattering patterns of monoolein containing 2%_{wt} of the fusion peptide TMD as a function of pressure at 24.3 °C.

As a second example of the evaluation of the static experiments, the scattering patterns of monoolein (17%_{wt} water content) containing 2%_{wt} of the trans-membrane domain TMD are presented as a function of pressure at 24.3 °C in Figure 8.4. Two-phase transitions can be found around 2 and 3 kbar, respectively.

Also here, all Bragg peaks were fitted, phases identified, the corresponding lattice constants calculated, and the integrated peak intensities of each phase determined. The results of these calculations are depicted in Figure 8.5. At low pressures a cubic two-phase region (*Ia3d* and *Pn3m*) can be found. Graphical representations of the lipid layer midplane in the crystalline unit cells are depicted in Figure 6.31 (page 113) and Figure 4.1 (page 49), respectively. The lattice spacings of both cubic phases, *Ia3d* and *Pn3m*, do barely deviate with increasing pressure from their initial values of 14.74 nm and 9.67 nm, respectively. The *Pn3m* phase vanishes around 1.1 kbar and a cubic *Ia3d* single-phase region is observed up to a pressure of 2.0 kbar, where a single lamellar phase emerges with a lamellar lattice constant, d , of 4.76 nm. Both phases coexist up to 3.0 kbar. The lattice constant of the cubic *Ia3d* phase increases between 1.1 kbar and 3.0 kbar from 14.71 nm to 15.40 nm. Also the d -spacing of the lamellar phase increases slightly with rising pressure to a value of 4.85 nm at 3.0 kbar, indicating a fluid lamellar phase (L_α).

At 3.0 kbar the cubic *Ia3d* phase vanishes and concomitantly the system segregates into two new lamellar phases both with a significantly different lattice constant, one higher and one lower as the one of the lamellar phase found in the coexistence region with the cubic *Ia3d* phase. The lattice constants of both lamellar high pressure phases decrease slightly with increasing pressure indicating crystalline lamellar phases (L_c). One of the lamellar phases has a d -spacing of 4.26 nm. This is about 0.5 nm lower than the one found in the fluid lamellar phase at lower pressure, which is not an unusual difference of the lattice constant between liquid disordered and crystalline lamellar phases. The other lamellar phase found at high pressure has a significantly higher lattice spacing of 6.07 nm at 3.0 kbar, which decreases

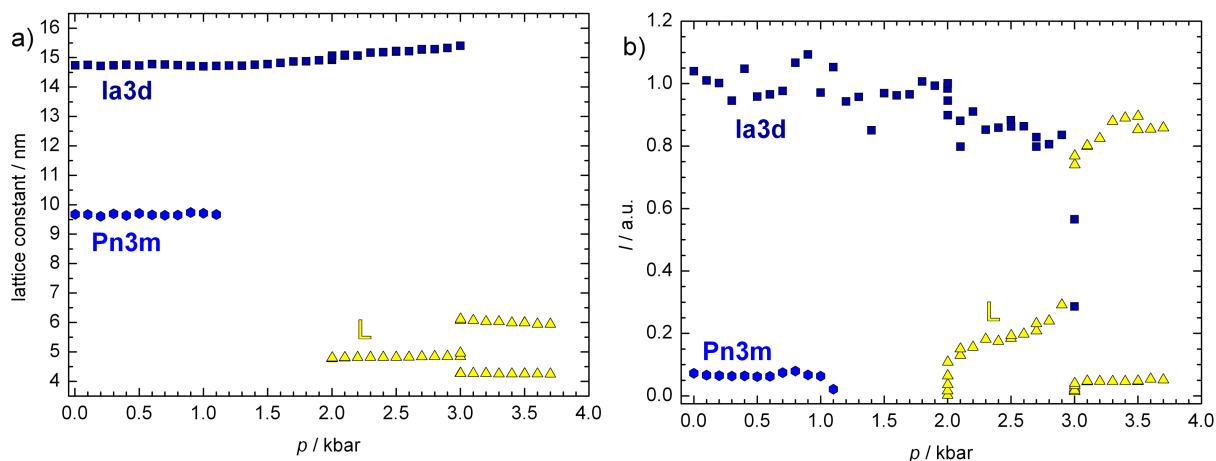


Figure 8.5: Lattice constants (a) and integrated peak intensities (b) of monoolein containing the fusion peptide TMD as a function of pressure at 24.3 °C.

to 5.95 nm at 3.7 kbar. The splitting into two lamellar phases and the high lattice constant of one of both phases can probably be explained again by a demixing of the monoolein system. The d -spacing of 4.26 nm of one of the lamellar phases is even slightly smaller than the corresponding value of pure monoolein of 4.35 nm at the same pressure. This indicates that most of the fusion peptide can be found in the second lamellar phase with the larger lattice constant, but much lower peak intensity. This low peak intensity can either originate from a low proportion of lipids in this phase or from a non-ideal stacking of lipid bilayers in this phase due to packing-constraints caused by the peptide.

Evaluating all pressure dependent experiments for each of the five peptides under investigation, the corresponding p, T -phase diagrams could be constructed, as depicted in Figure 8.6. All systems had a limited hydration of 17%_{wt} water content and contained 2%_{wt} of the corresponding peptide. For comparison, also the phase diagram of pure monoolein is presented as established in section 6.5 (page 111ff.). Regions of pure phases are depicted in different colours, each representing a certain phase. Boundaries between different areas of phase coexistence are depicted as dashed grey lines. In cases where it might not be obvious which phases are involved in these regions or where it enhances the clarity of the phase diagram, also the regions between pure phases are labelled. All other regions between pure phases are the expected two-phase regions consisting of the neighbouring single phases.

The p, T -phase diagram of monoolein containing 2%_{wt} of the control peptide L16 (Figure 8.6b) is identical to the one of pure monoolein (Figure 8.6a) within the experimental error. This proves that the sole addition of a peptide with an identical number of amino acids as the active fusion peptides under investigation has nearly no influence on the static phase behaviour of the model lipid system. It can easily accommodate inside the water channels of the monoolein mesophases. Any change in the phase behaviour of the other samples can therefore be attributed to the corresponding peptide and its specific interaction with the lipid membrane.

In Figure 8.6c the phase diagram of monoolein containing 2%_{wt} of the fusion peptide HA2 is presented. It looks very similar to the one found for pure monoolein, but all phase transitions are shifted towards lower temperature by about 5 °C. The slope of the cubic $Ia3d$ to fluid lamellar (L_α) phase boundary in the system containing HA2 of about 32.5 °C/kbar is slightly higher than the value of approximately 28 °C/kbar for pure monoolein. The slope of the fluid lamellar (L_α) to crystalline lamellar (L_c) transition line of around 15 °C/kbar is nearly identical to the one of pure monoolein with a value of 14.5 °C/kbar.

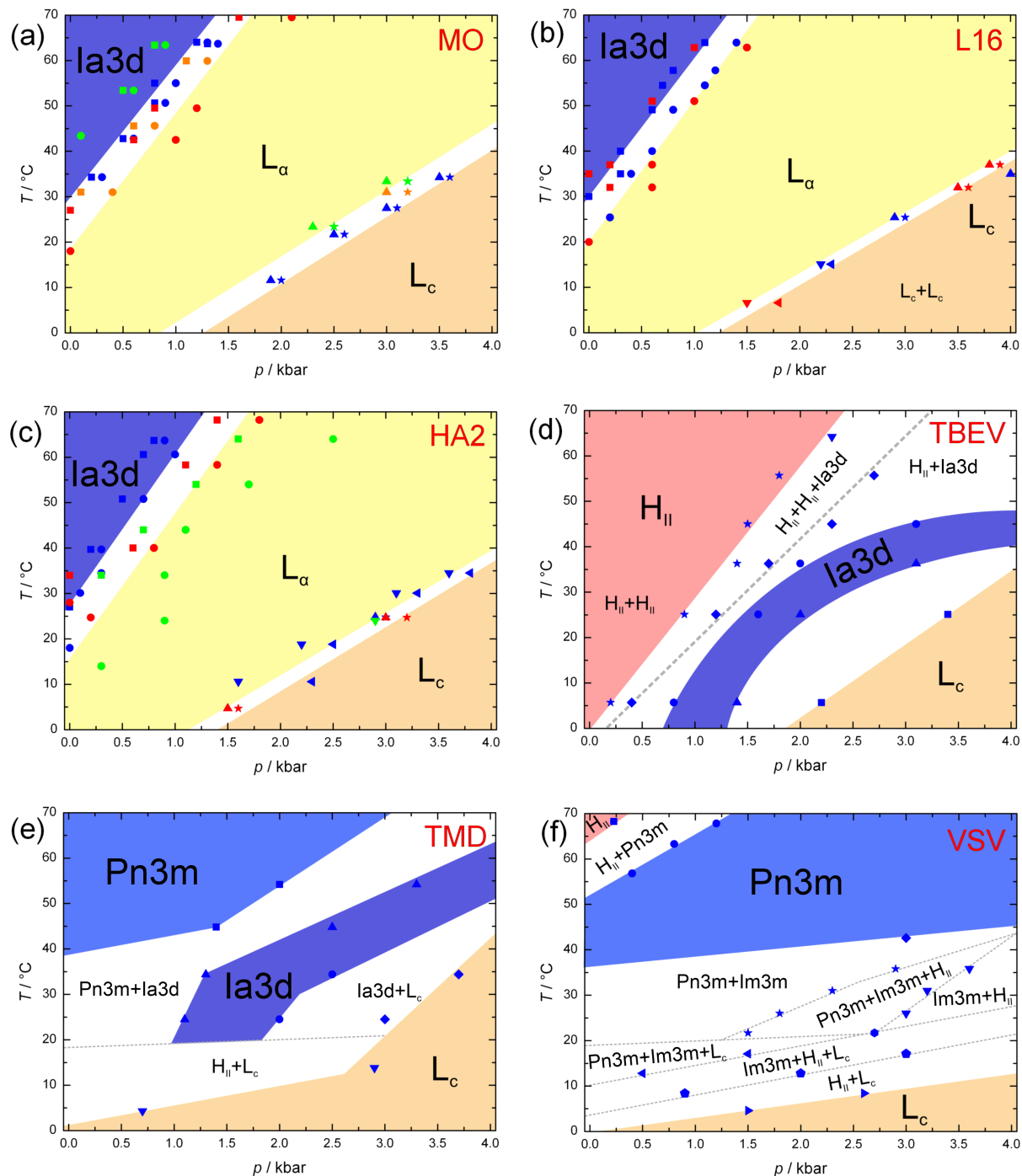


Figure 8.6: p, T -phase diagrams of monoolein without (a) and with 2%_{wt} of different fusion peptides: b) control peptide L16; c) HA2; d) TBEV; e) TMD; f) VSV. Regions of pure phases are depicted in colours and phase coexistence regions are white. The different colours of data points represent the different samples measured at various experimental runs conducted during this project.

Compared to HA2, the fusion peptide TBEV has a huge effect on the phase behaviour of monoolein as revealed by the phase diagram depicted in Figure 8.6d. The only common feature with the phase diagram of the pure monoolein dispersion is the crystalline lamellar phase at low temperature and high pressure. In the intermediate region of the phase diagram a pure cubic region is found, which seems to have a non-linear phase boundary. At low pressure and elevated temperatures a wide-stretched area of an inverse hexagonal phase is found. More precisely, in this area – especially at low temperature – two coexisting inverse hexagonal phases is found; one of each has a significantly higher intensity than the other, as already mentioned before in the discussion of the pressure dependent series of scattering patterns taken at 5.7 °C (q.v. Figure 8.2). It is obvious that the presence of small amounts of TBEV induce a significant increase in curvature in the lipid system leading to the extended area of the inverse hexagonal phase in the phase diagram.

In Figure 8.6e the phase diagram of monoolein containing 2%_{wt} of the trans-membrane domain (TMD) is depicted. As a common feature with all other phase diagrams also here a crystalline lamellar region has been detected at high pressure and low temperature. Similar to the phase diagram of the system containing TBEV, also a cubic *Ia3d* phase is found in the middle of the phase diagram, but no sign of this cubic phase could be found at temperatures lower than 20 °C. Instead, a lamellar phase coexisting with an inverse hexagonal phase is observed at low temperature. This is unusual, since highly curved phases like the inverse hexagonal phase appear usually only at elevated temperatures and not in coexistence with the phase with the lowest curvature of all – a lamellar phase. The existence of the inverse hexagonal phase at this low temperature can be explained by a demixing of the system. The lamellar phase contains probably (almost) no peptide, as revealed by the nearly identical *d*-spacing of this phase with the lamellar phase in pure monoolein under similar experimental conditions. The peptide to lipid ratio in the inverse hexagonal phase is consequently much larger than the average 2%_{wt}, leading to the extreme curvature of these domains in the system. At high temperature and low pressure a cubic *Pn3m* phase is obtained. This is highly unexpected, as the curvature of the *Pn3m* phase is lower than the one of the *Ia3d* phase and generally the curvature of cubic systems increases with increasing temperature. Here, the direct opposite is the case. The less curved *Pn3m* phase is found at higher temperatures than the higher curved *Ia3d* phase. Finally, the phase diagram of monoolein containing the fusion peptide VSV is presented in Figure 8.6f. At high temperature and low pressure an inverse hexagonal phase could just be found. With decreasing temperature first the cubic *Pn3m* and then the less curved cubic *Im3m* phase is formed. The *Im3m* phase is only obtained in the phase diagram of monoolein containing VSV. In Figure 8.7 the Schwarz primitive (P) triply periodic minimal surface, corresponding to the space group *Im3m*, is presented calculated from exact Weierstraß parametrisation using MATLAB. In the left graphic the lipid bilayer midplane is represented by triangles from a Delaunay triangulation and the right graphic shows the same structures with interpolated surface shading. At low temperature and high pressure a crystalline lamellar phase was detected in the sample containing 2%_{wt} VSV. As observed before in the phase diagram of the system containing TMD, an inverse hexagonal phase could be identified at low temperature coexisting with cubic and lamellar phases. However, according to the integrated peak intensity, either the fraction of the inverse hexagonal phase in the system is always much smaller than the one of all other phases or this phase has a very low periodic order. This might be explained once again by a (partial) segregation of the system at low temperatures during the formation of a crystalline lamellar phase.

For the simple two-component lipid + water systems, a number of structural parameters can be calculated. Neglecting the fusion peptide content of 2%_{wt}, these calculations can be performed as already presented for pure monoolein (17%_{wt} water content) in section 6.5.3 (page 114ff.).

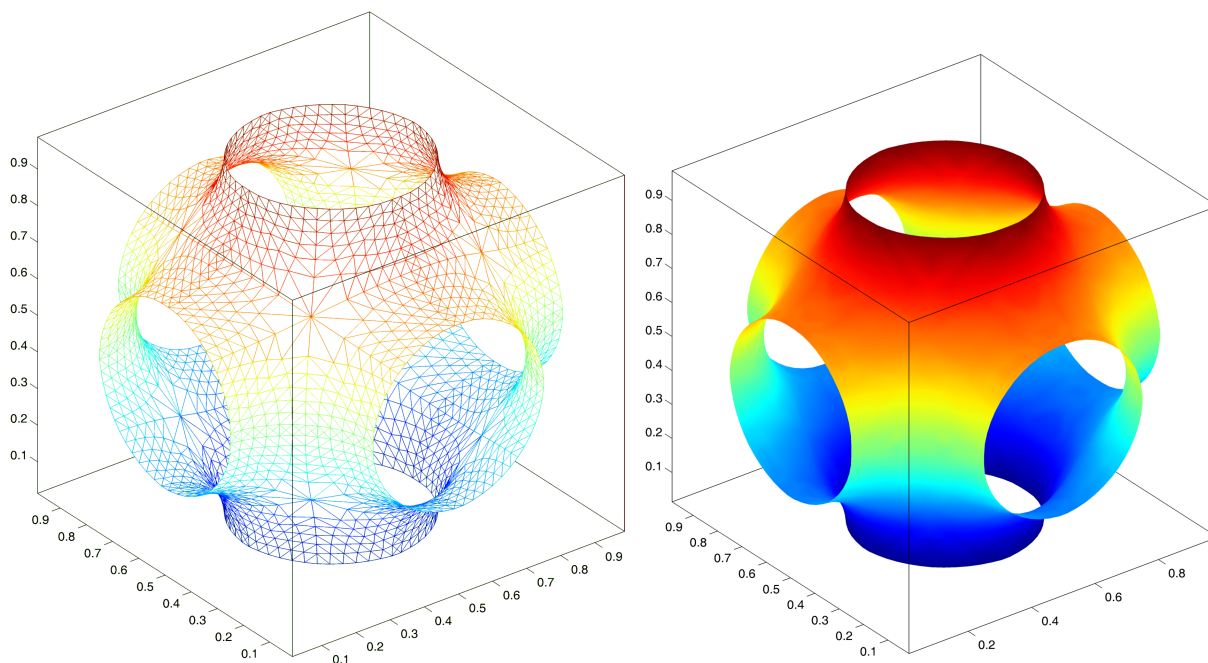


Figure 8.7: The Schwarz primitive (P) triply periodic minimal surface, corresponding to the space group $Im\bar{3}m$, calculated from exact Weierstraß parametrisation using MATLAB. Left: representation by triangles from a Delaunay triangulation; right: surface representation with interpolated surface shading.

For the lamellar single-phase regions, L_α and L_c , the following structural parameters can be calculated: the lipid chain length, l , area per lipid at cross section, a_0 , and the thickness of a water channel, d_w . Values found for lamellar phases of monoolein including 2%_{wt} of different peptides with a limited hydration of 17%_{wt} water at selected temperatures and pressures are presented in Table 8.3. Corresponding parameters of pure monoolein are shown in Table 6.4 (page 116).

Only few values displayed in Table 8.3 which attract the attention will be discussed here. Generally, in the fluid lamellar (L_α) phase an increasing d -spacing is observed with increasing pressure and decreasing temperature mainly due to a decreasing ratio of *gauche* conformeres in the lipid's hydrocarbon chains. On the contrary, in the crystalline lamellar (L_c) phase a decrease in the d -spacing is observed with increasing pressure and decreasing temperature. This originates mainly from the compression and lower thermal fluctuations of the inter-sheet water layer, since a major contribution of the lipid chain order or compression of the lipid headgroup can be neglected – all acyl chains are already in the all-*trans* conformation in this phase.

The lattice constants of lamellar phases and therefore all other resulting parameters are very similar in the samples containing 2%_{wt} of the peptides HA2 and L16 to the ones found for pure monoolein. All d -values are in a range 4.0- 4.6 nm. The d -spacings of samples containing the viral sequences VSV and TMD are slightly larger covering a range of 4.3- 4.9 nm. The lattice spacing of the crystalline lamellar phase found in monoolein containing TBEV is outstandingly large with values between 5.0- 5.3 nm. The spatial requirements of the peptides seem to increase in the order $L16 < HA2 < VSV < TMD \ll TBEV$.

For the cubic phases also several parameters can be calculated according to equation 4.11 - 4.15 and 4.17: the lipid chain length, l , the interfacial area integrated over a single monolayer, A_1 , the number of lipid molecules per unit cell, n_1 , the area per lipid molecule at the interface, a_0 , the radius of a water channel, r_w , as well as the surface averaged values of mean curvature, $\langle H \rangle$, and Gaussian curvature,

Table 8.3: Parameters of lamellar phases of monoolein (17%_{wt} hydration) including 2%_{wt} of different fusion peptides as a function of temperature, T , and pressure, p : the lattice constant, d , the lipid chain length, l , area per lipid at cross section, a_0 , and the thickness of a water channel, d_w .

peptide	phase	T [°C]	p [kbar]	d [nm]	l [nm]	a_0 [nm ²]	d_w [nm]
L16	L $_{\alpha}$	63.9	1.4	4.09	1.729	0.367	0.663
L16	L $_{\alpha}$	63.9	3.5	4.25	1.797	0.353	0.689
L16	L $_{\alpha}$	63.9	4.0	4.27	1.805	0.351	0.692
L16	L $_{\alpha}$	35.0	0.5	4.27	1.805	0.351	0.692
L16	L $_{\alpha}$	35.0	3.0	4.44	1.877	0.338	0.720
L16	L $_{\alpha}$	15.1	0.001	4.40	1.860	0.341	0.713
L16	L $_{\alpha}$	15.1	1.5	4.52	1.911	0.332	0.733
L16	L $_c$	25.4	4.0	4.48	1.894	0.335	0.726
L16	L $_c$	15.1	2.5	4.40	1.860	0.341	0.713
L16	L $_c$	15.1	4.0	4.36	1.843	0.344	0.707
HA2	L $_{\alpha}$	63.7	1.4	4.01	1.695	0.374	0.695
HA2	L $_{\alpha}$	63.7	3.5	4.18	1.767	0.359	0.678
HA2	L $_{\alpha}$	34.5	0.5	4.26	1.801	0.352	0.691
HA2	L $_{\alpha}$	34.5	3.0	4.41	1.864	0.340	0.715
HA2	L $_{\alpha}$	10.6	0.001	4.37	1.847	0.343	0.709
HA2	L $_{\alpha}$	10.6	1.5	4.48	1.894	0.335	0.726
HA2	L $_c$	34.5	4.0	4.50	1.902	0.333	0.730
HA2	L $_c$	10.6	2.5	4.54	1.919	0.330	0.736
HA2	L $_c$	10.6	3.6	4.50	1.902	0.333	0.730
HA2	L $_c$	10.6	4.0	4.50	1.902	0.333	0.730
TMD	L $_c$	34.0	3.7	4.25	1.797	0.353	0.689
TMD	L $_c$	14.0	3.5	4.80	2.029	0.313	0.778
TMD	L $_c$	4.0	1.0	4.89	2.067	0.307	0.793
TMD	L $_c$	4.0	3.5	4.81	2.033	0.312	0.780
VSV	L $_c$	5.0	1.5	4.88	2.063	0.307	0.791
VSV	L $_c$	5.0	3.5	4.81	2.033	0.312	0.780
VSV	L $_c$	8.0	3.5	4.83	2.042	0.311	0.783
TBEV	L $_c$	25.0	3.5	5.27	2.228	0.285	0.854
TBEV	L $_c$	6.0	2.5	5.10	2.156	0.294	0.827
TBEV	L $_c$	6.0	3.5	4.98	2.105	0.301	0.807

Table 8.4: Unit cell parameters of cubic phases in the system monoolein (17%_{wt} hydration) including 2%_{wt} of different fusion peptides as a function of temperature, T , and pressure, p : the lattice constant, a , the lipid chain length, l , the interfacial area integrated over a single monolayer, A_1 , the number of lipid molecules per unit cell, n_1 , the area per lipid molecule at the interface, a_0 , the radius of a water channel, r_w , and the surface averaged values of mean curvature, $\langle H \rangle$, and Gaussian curvature, $\langle K \rangle$.

peptide	phase	T [°C]	p [kbar]	a [nm]	l [nm]	A_1 [nm ²]	n_1 []	a_0 [nm ²]	r_w [nm]	$\langle H \rangle$ [nm ⁻¹]	$\langle K \rangle$ [nm ⁻²]
L16	<i>Ia3d</i>	63.9	0.001	10.14	1.584	191.7	1390	0.276	0.931	-288.5	-0.158
L16	<i>Ia3d</i>	63.9	1.0	10.22	1.596	194.8	1423	0.274	0.938	-293.1	-0.156
L16	<i>Ia3d</i>	35.0	0.001	10.55	1.648	207.6	1565	0.265	0.968	-312.3	-0.146
HA2	<i>Ia3d</i>	63.7	0.001	9.86	1.540	181.3	1278	0.284	0.905	-272.8	-0.167
HA2	<i>Ia3d</i>	63.7	0.7	9.91	1.548	183.1	1298	0.282	0.910	-275.6	-0.166
HA2	<i>Ia3d</i>	34.5	0.001	10.47	1.635	204.4	1530	0.267	0.961	-307.6	-0.148
TMD	<i>Pn3m</i>	54.0	0.001	8.21	2.086	74.6	738	0.202	1.122	-129.6	-0.097
TMD	<i>Pn3m</i>	54.0	1.5	9.22	2.343	94.1	1045	0.180	1.260	-163.4	-0.077
TMD	<i>Pn3m</i>	45.0	0.001	8.71	2.213	84.0	881	0.191	1.190	-145.8	-0.086
TMD	<i>Ia3d</i>	54.0	3.5	15.10	2.358	425.2	4590	0.185	1.386	-639.8	-0.071
TMD	<i>Ia3d</i>	34.0	1.5	14.27	2.229	379.7	3874	0.196	1.310	-571.4	-0.080
TMD	<i>Ia3d</i>	34.0	2.5	14.47	2.260	390.5	4039	0.193	1.328	-587.5	-0.078
VSV	<i>Pn3m</i>	63.0	1.0	8.22	2.089	74.8	740	0.202	1.123	-129.9	-0.097
VSV	<i>Pn3m</i>	63.0	3.5	9.58	2.435	101.6	1172	0.173	1.309	-176.4	-0.071
VSV	<i>Pn3m</i>	48.0	0.001	8.07	2.051	72.1	701	0.206	1.103	-125.2	-0.101
VSV	<i>Pn3m</i>	48.0	3.5	10.20	2.592	115.2	1415	0.163	1.394	-200.0	-0.063
VSV	<i>Pn3m</i>	43.0	0.001	8.34	2.119	77.0	773	0.199	1.140	-133.7	-0.094
VSV	<i>Pn3m</i>	43.0	2.5	10.12	2.572	113.4	1382	0.164	1.383	-169.9	-0.064
TBEV	<i>Ia3d</i>	45.0	3.5	11.84	1.849	261.4	2213	0.236	1.087	-393.4	-0.116
TBEV	<i>Ia3d</i>	25.0	1.7	11.28	1.762	237.3	1913	0.248	1.035	-357.0	-0.128
TBEV	<i>Ia3d</i>	6.0	0.8	11.35	1.773	240.2	1949	0.247	1.042	-361.5	-0.126
TBEV	<i>Ia3d</i>	6.0	1.3	11.46	1.790	244.9	2006	0.244	1.052	-368.5	-0.124

$\langle K \rangle$. The resulting parameters for different temperatures and pressures are displayed in Table 8.4. The corresponding parameters of the cubic *Ia3d* phase of pure monoolein can be found in Table 6.3 on page 115.

For all cubic phases the lattice spacing generally increased with increasing pressure and decreasing temperature. In pure monoolein only the cubic *Ia3d* phase was found. In all samples containing fusion peptides, except the sample with VSV, also an *Ia3d* single-phase region could be detected. In the lattice constants of this phase another interesting trend can be found. The values for samples containing L16 and HA2 of 10.55 nm and 10.47 nm at atmospheric pressure and 35 °C, respectively, are slightly smaller than the one found for pure monoolein of 11.00 nm under the same conditions. This indicates that these peptides increase the curvature of the lipid phase resulting in a smaller unit cell. In contrast, the lattice spacings of the cubic *Ia3d* phase in samples containing TBEV and TMD are in the ranges of 11.4-11.8 nm and 14.3-15.1 nm, respectively, which is significantly larger than the lattice constant found for pure monoolein. Here, the presence of the peptides seems to increase the size of the unit cells and therefore the membrane curvature is decreased.

Finally, the parameters of the inverse hexagonal phases found in samples containing VSV and TBEV are displayed in Table 8.5: the lattice constant, a , the radius of a water channel, r_w , the lipid layer

Table 8.5: Parameters of the hexagonal unit cell of monoolein (17%_{wt} hydration) including 2%_{wt} of different fusion peptides as a function of pressure and temperature: the lattice constant, a , the radius of a water channel, r_w , the lipid layer thickness, d_l , the minimum and maximum lipid lengths, l_{\min} and l_{\max} , and the area per lipid at the lipid water interface, a_0 . Two different lattice constants, a , at the same temperature and pressure originate from phase coexistence of two inverse hexagonal phase.

phase	T [°C]	p [kbar]	a [nm]	d_l [nm]	a_0 [nm ²]	r_w [nm]	l_{\min} [nm]	l_{\max} [nm]	H [nm ⁻¹]
VSV	67.8	0.001	5.69	3.284	0.202	1.203	1.642	2.082	0.429
TBEV	56.0	0.001	4.90	2.828	0.235	1.036	1.414	1.793	0.498
TBEV	56.0	0.001	5.82	3.359	0.198	1.230	1.680	2.130	0.419
TBEV	56.0	2.0	5.90	3.405	0.195	1.247	1.703	2.159	0.414
TBEV	56.0	2.0	5.10	2.944	0.226	1.078	1.472	2.156	0.478
TBEV	45.0	0.001	5.24	3.024	0.220	1.108	1.512	1.918	0.466
TBEV	45.0	0.001	5.50	3.175	0.209	1.163	1.587	2.013	0.444
TBEV	45.0	1.5	5.36	3.094	0.215	1.133	1.547	1.961	0.455
TBEV	45.0	1.5	5.61	3.238	0.205	1.186	1.619	2.372	0.435
TBEV	25.0	0.001	5.28	3.047	0.218	1.116	1.524	1.932	0.462
TBEV	25.0	0.001	5.82	3.359	0.198	1.230	1.680	2.130	0.419
TBEV	25.0	0.7	5.34	3.082	0.215	1.129	1.541	1.954	0.457
TBEV	25.0	0.7	5.81	3.353	0.198	1.228	1.677	2.126	0.420
TBEV	6.0	0.001	5.34	3.082	0.215	1.129	1.541	1.954	0.457
TBEV	6.0	0.001	5.98	3.451	0.192	1.264	1.726	2.188	0.408

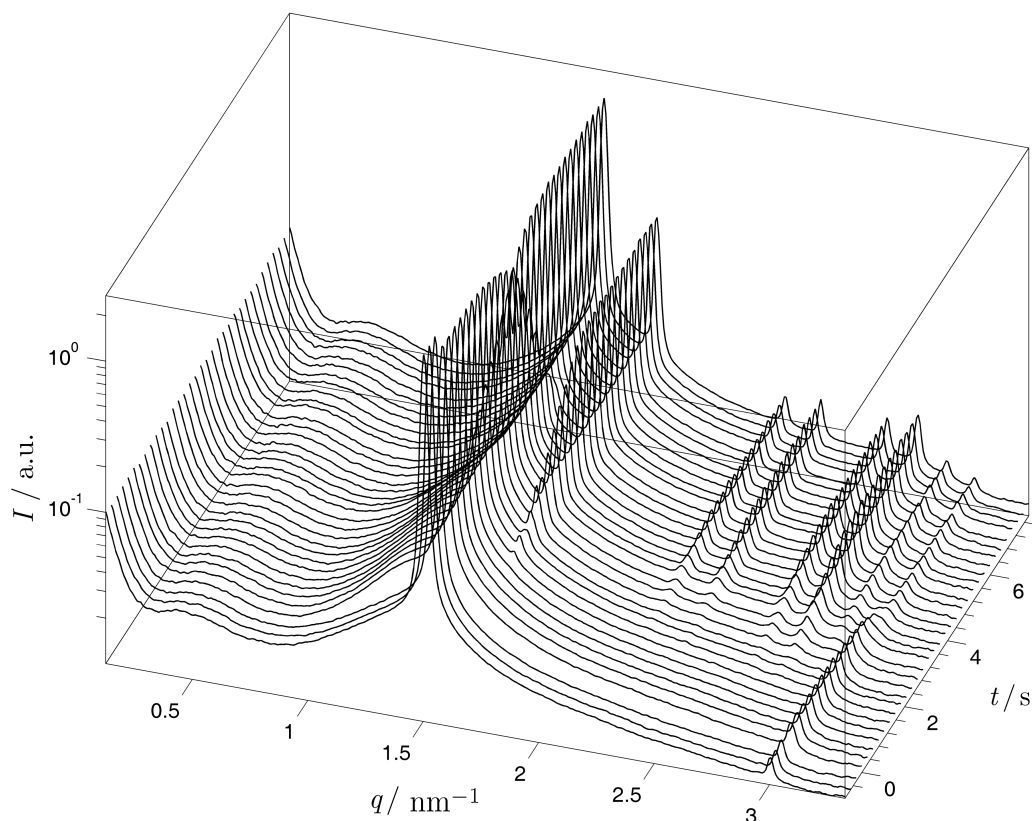


Figure 8.8: Scattering patterns of monoolein and 2%_{wt} L16 after a pressure-jump (at $t = 0$ s) from 2.0 kbar to 0.9 kbar at 64.0 °C from the fluid lamellar L_α into the cubic $Ia3d$ phase.

thickness, d_l , the minimum and maximum lipid lengths, l_{\min} and l_{\max} , and the area per lipid at the lipid water interface, a_0 . Two different lattice constants, a , at the same temperature and pressure originate from phase coexistence of two inverse hexagonal phase under the corresponding conditions. As a general trend, the lattice spacing of the inverse hexagonal phase increases with increasing pressure and decreasing temperature.

Kinetic pressure-jump experiments

Over 50 pressure-jumps have been performed during this study. But only the jumps of the systems containing L16 or HA2 can be directly compared to the jumps performed on pure monoolein, since only those samples show the same phase transitions as pure monoolein in a similar pressure- and temperature-range.

The rate at which a phase transition proceeds may be quantified by tracking changes in the amount of both the growing and the disappearing phases. Provided the scattering factor for each phase remains constant, the intensity of the diffraction peaks corresponding to a particular phase may be used as an indication of the amount of the phase. As long as the observed changes in lattice parameters are small for all phases, the changes in intensity may be assumed to directly reflect changes in phase composition.

In Figure 8.8 the scattering patterns of the system monoolein (17%_{wt} water content) containing 2%_{wt} of the non-fusogenic control peptide L16 after a pressure-jump from 2.0 kbar to 0.9 kbar at 64.0 °C are displayed. Before the pressure-jump ($t < 0$ s) the pattern of a pure lamellar phase is observed, as expected from the static p, T -phase diagram. At the moment the jump is triggered, the intensity of the

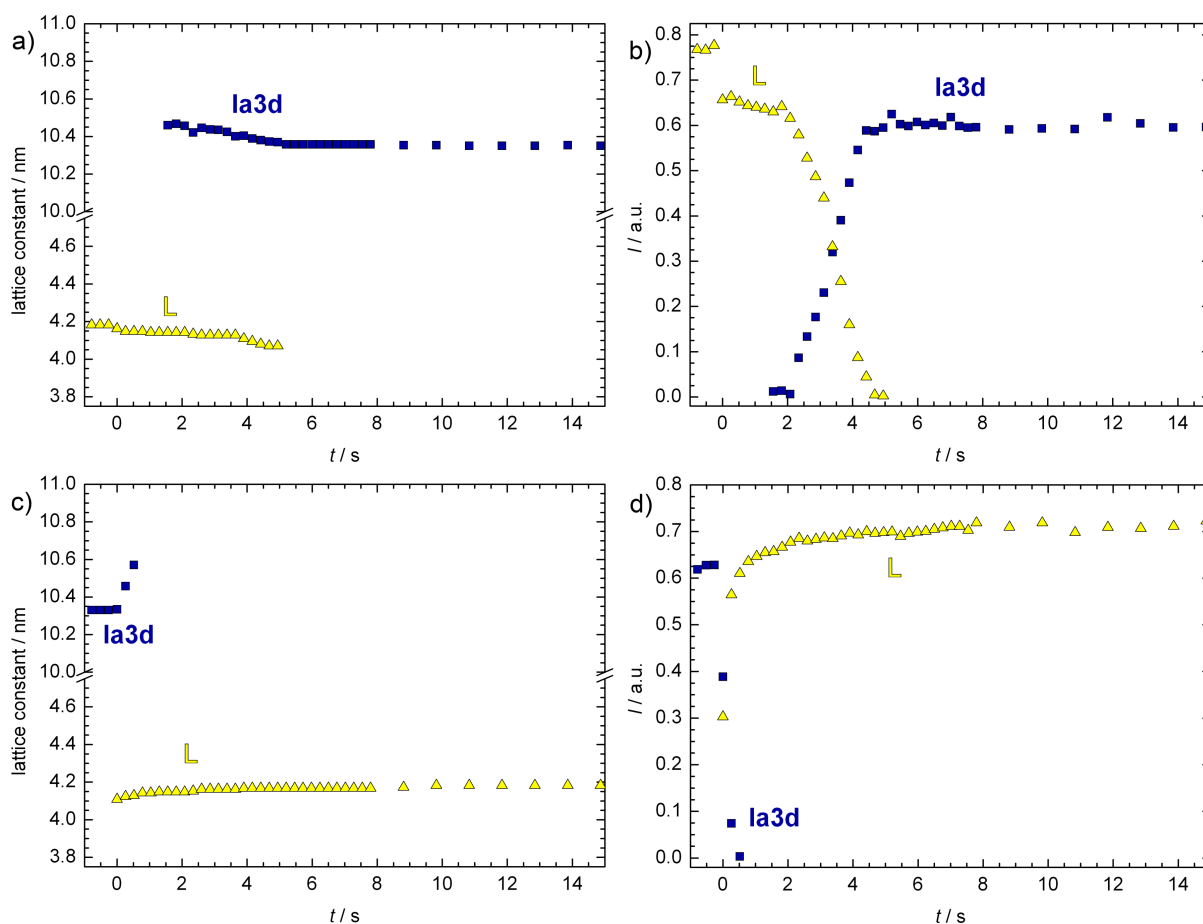


Figure 8.9: Lattice constants and phase intensities of monoolein including 2%_{wt} control peptide (L16) after pressure-jumps at 63.7 °C. Lattice constants (a) and integrated peak intensities (b) of all phases as a function of time for the first 15 s after the pressure-jump from 2.0 kbar to 0.9 kbar as well as lattice constants (c) and phase intensities (d) recorded after a jump in the opposite pressurising direction from 1.0 kbar to 2.0 kbar.

fluid lamellar phase changes, but the d -spacing remains almost constant for more than 2 s. Afterwards a continuous transition into a pure cubic $Ia3d$ phase is observed. The first eight Bragg peaks of this phase are well resolved in the scattering patterns.

In Figure 8.9a the lattice constants of all phases found during this pressure-jump are presented as a function of time for the first 15 s after the jump was triggered at $t = 0$ s. In Figure 8.9b the corresponding integrated peak intensities of the phases involved are plotted. As already observed in the scattering patterns directly after the pressure-jump, only the peak intensity of the lamellar phase decreases slightly due to the changed electron density contrast upon pressurisation. After 2 s the cubic $Ia3d$ phase emerges slowly and concomitantly the intensity of the lamellar phase decreases, vanishing completely after 5 s. The d -spacing of the fluid lamellar phase decreases slightly from 4.18 nm at $t = -0.78$ s to a final value of 4.07 nm at $t = 4.9$ s. The first lattice constant detected of the cubic phase, where this phase has already an intensity significantly higher than zero, is 10.46 nm at $t = 2.1$ s. The lattice constant of the cubic $Ia3d$ phase reaches its final value of 10.35 nm about 9 s after the pressure-jump.

The corresponding pressure-jump of pure monoolein is presented in Figure 6.36 (page 120). A comparison of both jumps reveals a severe effect of the presence of 2%_{wt} L16 in the system. For pure monoolein the transition was almost instantaneous – the lamellar phase had vanished after 0.26 s and the maximal

intensity of the emerging cubic *Ia3d* phase was reached after approximately 1 s. Thus, it can be concluded that the lamellar to cubic *Ia3d* transition is slowed down significantly by 2%_{wt} L16 in the system. Directly after the pressure-jump, the system is trapped in the lamellar phase for about 2 s. Both may be explained by the slowed lipid diffusion in the presence of the highly hydrophobic peptide, which stabilises the hydrophobic interactions in the lipid phases. Therefore a higher activation energy is needed to induce the necessary changes in this region of the membrane to form a curved cubic phase.

In Figure 8.9c the lattice constants of a pressure-jump in the opposite pressurising direction from 1.0 kbar to 2.0 kbar of monoolein containing 2%_{wt} L16 are presented. In Figure 8.9d the corresponding peak intensities are shown. The kinetics of this jump in the pressurising direction is much faster. Already 0.26 s after the pressure-jump the cubic *Ia3d* phase completely vanished. The first signal of the fluid lamellar phase is obtained in the first scattering pattern taken after the pressure-jump. The full intensity of the lamellar phase is reached after approximately 8 s after the jump. In the same interval the *d*-spacing of the lamellar phase increases slightly from 4.11 nm at $t = 0$ s to 4.18 nm at $t = 10$ s.

Compared to the corresponding pressure-jump of pure monoolein, as depicted in Figure 6.35 (page 119), the kinetics of the jump (*Ia3d* → L) in the system containing L16 is much faster. In the pure monoolein sample a continuous transition over about 15 s is observed. The addition of L16 accelerates this transition drastically. This might indicate that L16 supports the transition into the lamellar phase as well as stabilises the lamellar phase. In the equilibrium state, represented by the p, T -phase diagrams, no difference between pure monoolein and the system containing 2%_{wt} L16 could be found.

After the effect of a peptide (which does not influence the static phase behaviour) on the phase transition kinetics of monoolein has been studied, the data should be compared to the influence of the active fusion peptide HA2. In Figure 8.10a,b the lattice constants and integrated peak intensities of all phases for the first 20 s after a pressure-jump from 1.6 kbar to 0.7 kbar are plotted as a function of time. The pressure-jump amplitude as well as the temperature are almost identical to those of the experiment investigating L16. Contrary to the system containing L16, a very fast transition from the lamellar phase into the cubic *Ia3d* phase was found. The lamellar phase vanished within the first 0.25 s after the pressure-jump was triggered without showing any signs of a kinetic trapping as previously observed for the sample containing L16. The full intensity of the cubic *Ia3d* phase is reached already 0.5 s after the pressure-jump occurred. Also, the lattice constant of the cubic phase does not change significantly after this time. It can be concluded that the presence of HA2 increases the rate of the transition from the lamellar to the cubic *Ia3d* phase by about one order of magnitude.

Also, the behaviour observed after a pressure-jump in the opposite pressurising direction in the system containing HA2 is completely different compared to the sample system with L16. In Figure 8.10c,d the lattice constants and peak intensities of a pressure-jump from 0.7 kbar to 1.7 kbar of monoolein containing 2%_{wt} HA2 are depicted. In the system containing L16 a very fast transition within 0.5 s from the cubic *Ia3d* into the lamellar phase was observed, followed by a relaxation of the newly formed lamellar phase. Here, in the sample containing the active fusion peptide HA2, a very slow transition from the cubic *Ia3d* into the lamellar phase is found. An initial kinetic trapping of the vanishing cubic phase is not observed. Directly after the pressure-jump, the intensity of the cubic phases decreases and the intensity of the lamellar phase increases; both processes showing sigmoidal characteristics. After approximately 15 s the cubic *Ia3d* phase has vanished and the lamellar phase has reached its full intensity. The *d*-spacing of the lamellar phase increases slightly with time, from 4.09 nm at $t = 1.0$ s to the final value of 4.15 nm reached 10 s after the jump was triggered. The lattice constant of the cubic phase changes in a sigmoidal manner, from 10.37 nm before the pressure-jump continuously – even at the moment of the jump – to a final value of 10.77 nm, which is reached about 6.5 s after the pressure-jump.

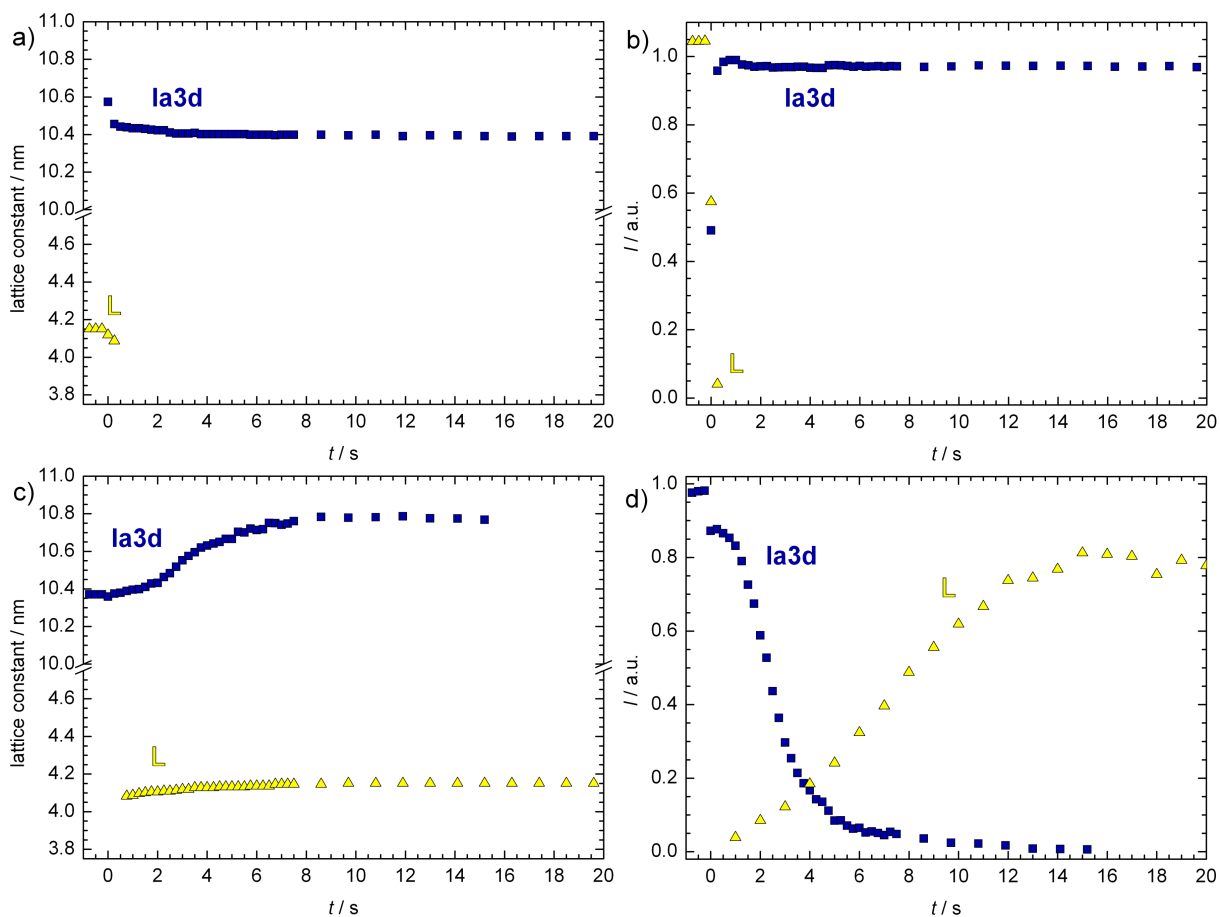


Figure 8.10: Lattice constants and phase intensities of pressure-jumps at 58.2 °C of monoolein including 2%_{wt} fusion peptide (HA2). Lattice constants (a) and integrated peak intensities (b) of all phases as a function of time for the first 20 s after the pressure-jump from 1.6 kbar to 0.7 kbar as well as lattice constants (c) and phase intensities (d) of a jump in the opposite pressurising direction from 0.7 kbar to 1.7 kbar.

From the pressure-jump experiments it becomes obvious that the peptide HA2 favours the formation of a cubic *Ia3d* phase and hampers the transformation from this phase into the lamellar phase, in complete contradiction to the behaviour observed in the system containing the control peptide L16.

In Figure 8.11 the lattice constants and phase intensities of pressure-jumps in the pressurising direction with different pressure-jump amplitudes of monoolein containing 2%_{wt} HA2 at 48.7°C are displayed. In parts a and b, the data of a pressure-jump from 0.6 kbar to 1.3 kbar ($\Delta p = 0.7$ kbar) are displayed and in parts c and d the jump is conducted between atmospheric pressure and 1.8 kbar ($\Delta p = 1.8$ kbar). For both jumps, a transition from the cubic *Ia3d* phase into the lamellar phase is observed. The lattice constant of the cubic phase increases after the pressure-jump and the *d*-spacing of the emerging lamellar phase rises slightly to its final value. For both jumps, a sigmoidal decay of the intensity of the cubic phase is observed and concomitantly the intensity of the lamellar phase increases. Regarding the jump with the smaller pressure-jump amplitude of 0.7 kbar (Figure 8.11b), the intensity of the cubic *Ia3d* phase decreases within approximately 5 s and the lamellar phase reaches its full intensity at the same time. Interestingly, for the pressure-jump with the much larger pressure amplitude of 1.8 kbar (Figure 8.11d), a completely different kinetics is observed. The intensity of the cubic *Ia3d* phase decays much faster (within 1.5 s), but the relaxation of the lamellar phase after the pressure-jump takes significantly longer.

The rate of the first, rapid transition from the cubic into the lamellar phase increases with Δp as the change in chemical potential between the different phases, and hence the driving force of the process, increases concomitantly. In terms of volume changes, an increase of the transition rate, k , would be due to a negative activation volume, $\Delta V^\ddagger < 0$, as $k(p) \propto \exp(-p\Delta V^\ddagger/RT)$. The activation volume can generally be interpreted as the difference in volume between the transition state and the volume of the initial state at the same pressure. Hence, ΔV^\ddagger can be thought of as a mechanic (elastic) barrier to transformation, in much the same way as the activation enthalpy ΔH^\ddagger for a reaction is thought of as a thermal energetic barrier to the reaction. On the other hand, the large pressure-jump amplitude leads to a much further out-of-equilibrium state, which may result in a longer relaxation time of the emerged lamellar phase. This relaxation comprises lipid diffusion and ordering in the lamellar plane as well as water diffusion into the newly built multilamellar vesicles.

Comparing the kinetics displayed in Figure 8.11 at 48.7°C with the jump in the same pressurising direction at a higher temperature of 58.2°C, as depicted in Figure 8.10c,d, the effect of temperature on the kinetics can be studied. The pressure-jump amplitude of the jump at higher temperature is 1.0 kbar, thus in the middle between the amplitudes of the jumps taken at lower temperature (of 0.7 kbar and 1.8 kbar). It is remarkable that the kinetics of the jump at higher temperature is much slower with an overall transition time of approximately 15 s than the jumps at lower temperature. Mainly, the ordering of the emerging lamellar phase takes significantly longer, but also the cubic *Ia3d* phase vanishes a bit slower at higher temperature. The retarded formation and ordering of the emerging lamellar phase at higher temperature might be explained by the larger thermal fluctuations hindering a fast and cooperative reorganisation of the lipid phases and a higher disorder of the lipid chains favouring curved phases like the cubic *Ia3d* phase.

In Figure 8.12, again data of pressure-jumps in the system monoolein including 2%_{wt} of the fusion peptide HA2 with different pressure-jump amplitudes are displayed, this time in the depressurising direction. In Figure 8.12a,b the lattice constants and intensities of a pressure-jump between 1.3 kbar and 0.5 kbar ($\Delta p = 0.7$ kbar) are shown. In parts c and d, the data of a jump from 1.8 kbar to atmospheric pressure ($\Delta p = 1.8$ kbar) are displayed. In both jumps, the *d*-spacing of the lamellar phase decreases before the phase vanishes and the lattice constant of the emerging cubic *Ia3d* phase subsides from its first appearance to a level of equilibrium after a few seconds. As observed before in the pressure-jump in the

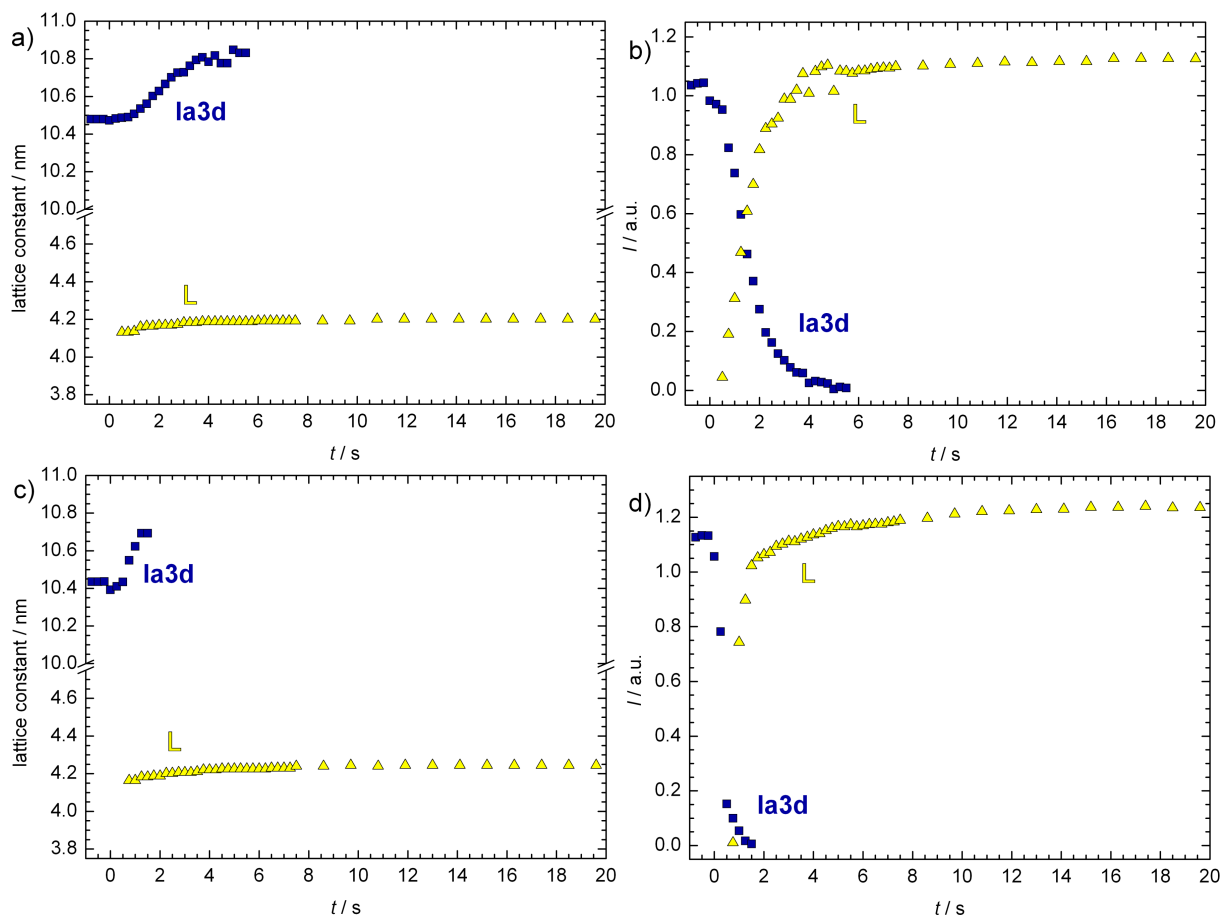


Figure 8.11: Lattice constants and phase intensities of pressure-jumps at 48.7 °C of monoolein including 2 %_{wt} fusion peptide (HA2). Lattice constants (a) and integrated peak intensities (b) of all phases as a function of time for the first 20 s after the pressure-jump from 0.6 kbar to 1.3 kbar. Lattice constants (c) and phase intensities (d) of a jump with a larger pressure-jump amplitude from 1 bar to 1.8 kbar.

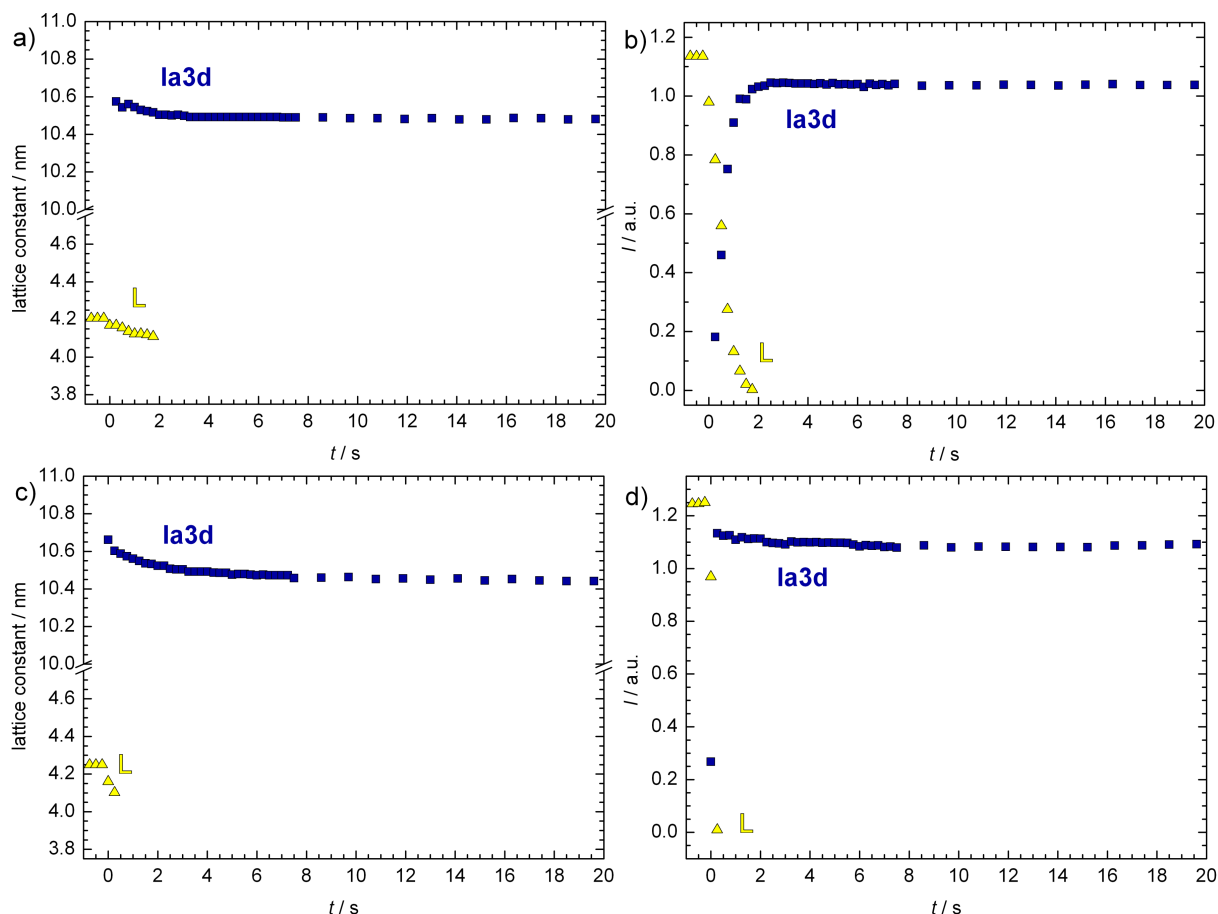


Figure 8.12: Lattice constants and phase intensities of pressure-jumps at 48.7 °C of monoolein including 2%_{wt} fusion peptide (HA2). Lattice constants (a) and integrated peak intensities (b) of all phases as a function of time for the first 20 s after the pressure-jump from 1.3 kbar to 0.5 kbar. Lattice constants (c) and phase intensities (d) of a jump with a larger pressure-jump amplitude from 1.8 kbar to 1 bar.

opposite pressurising direction, the actual transition is faster in the jump with the higher pressure-jump amplitude due to the larger activation energy provided here, but the relaxation of the emerging phase takes much longer for the larger pressure-jump amplitude.

Comparing Figure 8.12, showing data taken at 48.7 °C, with the pressure-jump also in depressurising direction at a higher temperature of 58.2 °C (Figure 8.10a,b) no significant influence of the temperature on the kinetics of the pressure-jumps from the lamellar into the cubic *Ia3d* phase can be found, which all are rather fast.

Also, for all other monoolein samples containing fusion peptides numerous pressure-jumps were conducted. In all cases the phase transitions were completed within 30 s after the pressure-jump. In no case could a distinctive, long-lasting kinetic trapping of any phase be found. Due to the highly different phase diagrams of the peptides TBEV, VSV, and the trans-membrane domain TMD, a comparison with the kinetic data of the peptides HA2, L16 or the pure lipid system monoolein as well as among each other cannot lead to meaningful results.

As an example of one of these datasets, the scattering patterns of a pressure-jump of monoolein containing 2%_{wt} TBEV from atmospheric pressure to 2.4 kbar at 4.8 °C are depicted in Figure 8.13, jumping from the inverse hexagonal into an ordered lamellar phase. The initial scattering patterns are characteristic for a single inverse hexagonal phase showing the first three intense peaks. The final scattering

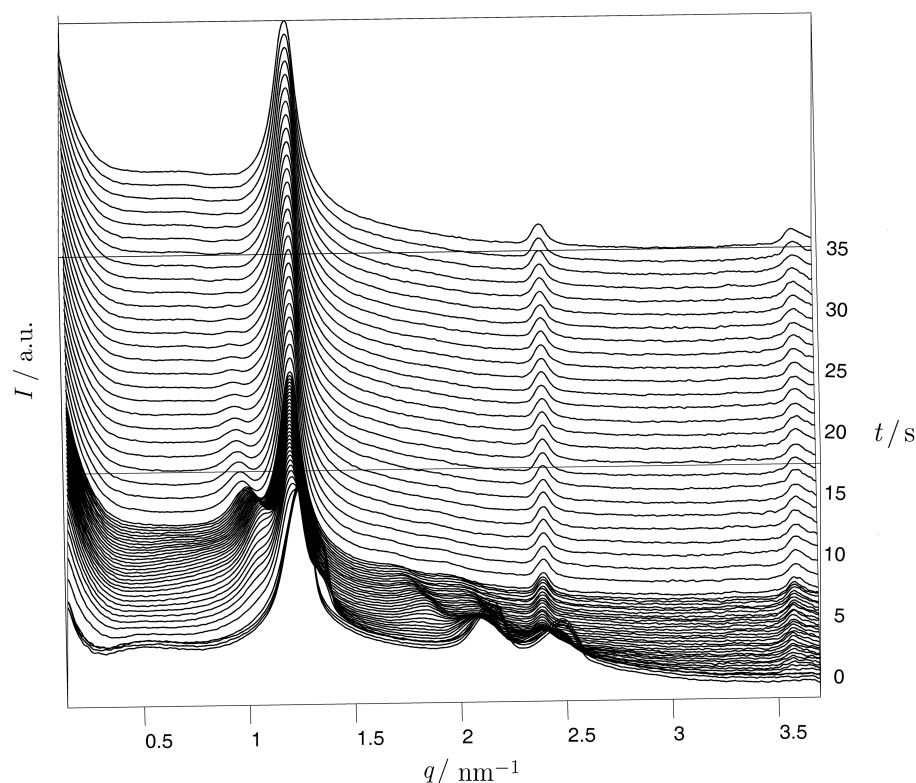


Figure 8.13: Scattering patterns of a pressure-jump of monoolein and 2%_{wt} TBEV from 1 bar to 2.4 kbar at 4.8 °C, jumping from the inverse hexagonal into the lamellar phase.

patterns present clearly the first three equidistant peaks of a lamellar phase. During the transition a number of additional peaks can be obtained, indicating the appearance of intermediate phases.

In Figure 8.14 the lattice constants and phase intensities of all phases are shown as a function of time for the first 30 s after the pressure-jump. A significantly more complex behaviour is observed compared to the previously discussed pressure-jumps. Besides the vanishing inverse hexagonal phase and the emerging lamellar phase another inverse hexagonal phase is involved in the phase transition process. Right after the pressure-jump, the intensity of the hexagonal phase decreases and the lattice constant increases from 5.87 nm before the pressure-jump to 6.09 nm at $t = 1.75$ s. At the moment of the pressure-jump ($t = 0$ s) a lamellar phase emerges and shortly afterwards a second inverse hexagonal phase can be observed. The initial d -spacing of the lamellar phase of 5.27 nm barely changes over time to a final value of 5.22 nm. The intensity of the lamellar phase increases rapidly within 2 s to a plateau, where it only increases very slightly until all inverse hexagonal phases disappear around 8-10 s after the pressure-jump was triggered. Afterwards, the intensity of the lamellar phase increases again more rapidly to its final value after about $t = 16$ s. The initial inverse hexagonal phase vanishes within 2 s after the pressure-jump. The intensity of the second inverse hexagonal phase, emerging shortly after the jump, increases for about 3.5 s and at the same time the lattice constant of this phase decreases from 7.34 nm at $t = 0.5$ s to 6.85 nm at $t = 3.25$ s. Afterwards, the intensity of this phase decreases until it disappears approximately 9 s after the jump was triggered. The lattice spacing increases again during this process to a final value of 7.61 nm.

The second inverse hexagonal phase might appear due to a segregation process during the phase transition. Initially the system is homogeneous – showing just a single inverse hexagonal phase. After the pressure-jump, a lamellar phase appears, which remains imperfectly ordered until all inverse hexagonal phases are gone. Interestingly, the d -spacing of the lamellar phase barely changes with time and is, with

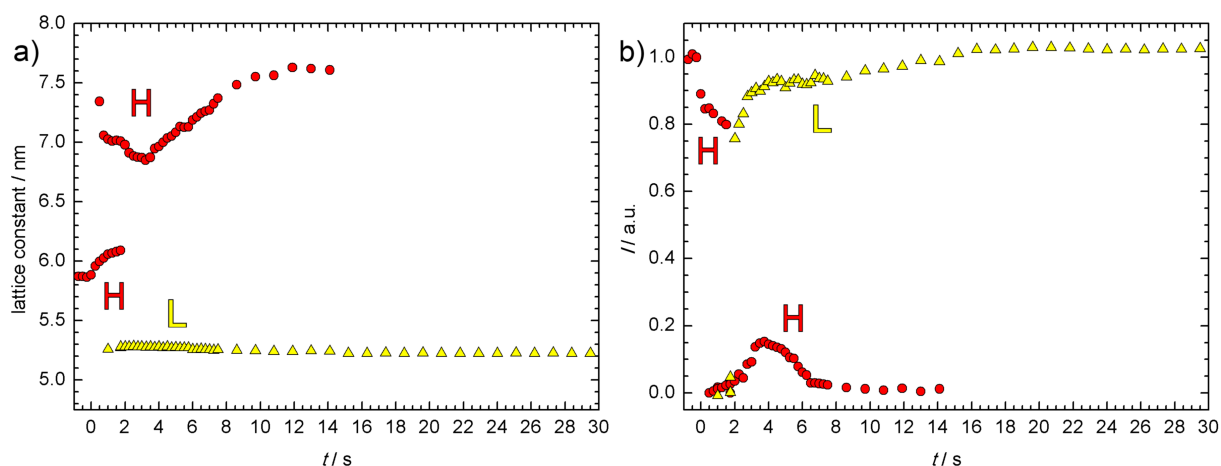


Figure 8.14: Lattice constants (a) and phase intensities (b) of all phases as a function of time for the first 30 s after a pressure-jump from atmospheric pressure to 2.4 kbar at 4.8 °C of monoolein including 2%_{wt} fusion peptide (TBEV).

a value of 5.3 nm, significantly larger than the d -spacing of pure monoolein of 4.3-4.4 nm under the same experimental conditions. This might indicate that the TBEV is embedded into the lamellar phase directly after the pressure-jump and no significant changes in the fusion peptide content of this phase occur with time. The second inverse hexagonal phase appearing after the pressure-jump has a significantly higher lattice spacing than the previously observed one, indicating that this phase might contain nearly no fusion peptide at all. Probably, the TBEV diffuses out of the inverse hexagonal phase into the emerging lamellar phase right after the pressure-jump, leaving a metastable inverse hexagonal phase in the system consisting mainly of pure monoolein. The larger lattice spacing with decreased fusion peptide content can be explained by the membrane curvature inducing effect of TBEV. About 4 s after the jump this phase starts disappearing and the order of the lamellar phase increases.

8.2.4 Conclusions

The effect of three different fusion peptides (HA2, VSV and TBEV), one trans-membrane domain (TMD VSV), as well as one non-fusogenic control peptide (L16) on the phase behaviour and phase transition kinetics of monoolein (at limited hydration of 17%_{wt}) has been investigated.

The p, T -phase diagram obtained for the control peptide L16 was identical to the one of pure monoolein within the margin of error. From the pressure-jumps experiments it could be concluded that L16 actually favours the lamellar phase instead of inducing cubic phases, as expected of an active fusion peptide. The results prove that the mere presence of 2%_{wt} of a peptide does not change the static equilibrium phase behaviour as well as does not induce or favour cubic phases during the transition between lamellar and cubic phases in the monoolein system.

Also, the p, T -phase diagram of the fusion peptide HA2 was almost identical to the one of pure monoolein, except for a shift of all transitions to a slightly lower temperature (by about 5 °C). This indicates a minor tendency of HA2 to induce the lamellar to cubic phase transition. In the pressure-jump experiments the kinetics of a transition from the lamellar phase into the cubic $Ia3d$ phase was found to be much faster in the system containing 2%_{wt} of the fusion peptide compared to the same transition of pure monoolein.

Whereas in samples of pure monoolein and the ones containing L16 or HA2 only the cubic $Ia3d$ phase was found, in samples containing the fusion peptide VSV or the trans-membrane domain a region of $Pn3m$ was also detected. The cubic $Im3m$ phase was observed in a sample including VSV. Finally, an inverse hexagonal phase was detected in samples containing VSV and TBEV.

The p, T -phase diagrams of TBEV, VSV and TMD display a phase behaviour which is completely different from the one of pure monoolein. The lamellar regions at low temperature and elevated pressure in these phase diagrams was severely shifted to lower temperatures and higher pressures, showing the pronounced capability of these peptides to induce non-lamellar phases.

Not only could the p, T -phase diagrams of monoolein containing 2%_{wt} of different fusion peptides be established, but detailed structural parameters of single-phase regions were also calculated and the phase transition kinetics between different phases in the system were studied extensively, revealing an accelerating and promoting effect of the fusion peptides on the lamellar to cubic phase transitions.

8.3 Further studies of lipid-peptide interactions

In this section further investigations of lipid-peptide interactions are briefly described. For full details the reader is referred to the corresponding publications, [174, 409, 410].

8.3.1 Interaction of IAPP with resveratrol at an anionic lipid raft monolayer

Introduction

The islet amyloid polypeptide (IAPP) or amylin is a pancreatic hormone and crucially involved in the pathogenesis of type-II diabetes melitus (T2DM). Aggregation and amyloid formation of IAPP is considered as the primary culprit for pancreatic β -cell loss in T2DM patients. In this study, first X-ray reflectometry (XRR) measurements on IAPP at lipid interfaces have been carried out, providing a molecular level characterisation of the first steps of the lipid-induced fibrillation process of IAPP, which is initiated by lipid-induced nucleation, oligomerisation, followed by detachment of larger IAPP aggregate structures from the lipid membrane, and terminated by the formation of mature fibrils in the bulk solution. Moreover, it was shown that the polyphenolic red-wine compound resveratrol is able to inhibit IAPP aggregation also in the presence of aggregation-fostering negatively charged lipid interfaces, revealing its potential as a drug candidate for T2DM.

The adsorption process of IAPP at lipid interfaces in the absence and presence of negatively charged lipids has also been studied by complementary ATR-FTIR spectroscopic measurements conducted by D. Sellin, a PhD student in our group. The morphological properties of early IAPP oligomers were followed by atomic force microscopy (AFM), which was performed by Dr. Weise, a post-doctoral student in our group at TU Dortmund University.

In this section only the results based on X-ray reflectometry are presented. The measurements were planned, conducted and evaluated in cooperation with F. Evers (Department of Physics, TU Dortmund University). The complete results of the study are published in [174].

Materials and methods

Human IAPP was obtained from Calbiochem (Darmstadt, Germany). NaH_2PO_4 , Na_2HPO_4 , resveratrol and 2,2,2-trifluoroethanol (TFE) were purchased from Sigma-Aldrich (Steinheim, Germany). 1,2-dioleoyl-*sn*-glycero-3-phosphocholine (DOPC) and 1,2-dioleoyl-*sn*-glycero-3-[phospho-*rac*-(1-glycerol)] (DOPG) were ordered from Avanti Polar Lipids (Alabaster, AL, USA). D_2O and chloroform were obtained from Merck (Darmstadt, Germany). All reagents were of the highest analytical grade available and used without further purification.

hIAPP was initially dissolved in 1 ml TFE, a procedure that dissolves any preformed fibrils. 500 μl of this solution was dried at the inner side of a round bottom flask using a gentle stream of nitrogen. Then, a phosphate buffer solution (10 mM, pH 7.0) was added to obtain an IAPP sample solution with a concentration of 1 μM . For the samples including resveratrol, the inhibitor was dissolved in the buffer yielding a resveratrol:IAPP molar ratio of 1.5. All IAPP solutions were used immediately after preparation. The lipids in a ratio DOPC/DOPG of 7:3 were dissolved in chloroform and spread on the air-water interface afterwards.

The X-ray reflectometry measurements were performed at the liquid surface diffractometer of beamline BW1 at HASYLAB (DESY, Hamburg, Germany).^[96] All experiments were carried out at 22 °C. The samples were illuminated with an X-ray beam with a wavelength, λ , of 1.3 Å, corresponding to a photon energy, E , of 9.5 keV. One reflectometry scan took 35 min, reaching a maximum wave vector transfer, q_z , of 0.7 Å⁻¹, and covers a dynamic range of 10 orders of magnitude. The starting point of an experiment ($t = 0$ h) is defined as the moment when the sample system is prepared on the Langmuir through in which the XRR measurements were performed and the used substances could interact for the first time.

Results and discussion

The X-ray reflectivity data of the DOPC / DOPG lipid film in the presence of IAPP (Figure 8.15a) reveal marked IAPP-induced changes in the intermediate time range. Inspection of the time-evolution of the electron density profiles (Figure 8.15b) shows that right after preparation of the 1 μM IAPP solution, a film thickness of 22 Å is observed, which is consistent with the thickness of the pure lipid film. Thereafter, $\rho(z)$ of the head group and lipid chain region changes, indicating insertion of IAPP into the lipid's upper chain region, where the aggregation process via oligomerisation is initiated, which is followed by an increase of $\rho(z)$ in the tail region. Integration of the electron density for $-10 \text{ \AA} < z < 30 \text{ \AA}$ indicates that the size of the IAPP oligomers is restricted to 20 Å. After 3 h, the maximal IAPP particle size observed by XRR is roughly 13 Å.

For comparison, the interaction of IAPP with a neutral, zwitterionic DOPC lipid monolayer was also studied. The reflectivity measurements reveal that the structure of the DOPC lipid layer is not significantly affected in the presence of IAPP. This can be attributed to the absence of an electrostatically driven interaction between the positively charged IAPP and the lipid interface, in agreement with recent IRRAS spectroscopic studies.^[181] This clearly shows that the initial association of IAPP with lipid membranes is mainly driven by electrostatic interactions.^[181, 184]

Finally, the interaction of resveratrol with the lipid monolayer has been examined in the absence and presence of IAPP. The corresponding electron density profiles $\rho(z)$ are displayed in Figure 8.16. For the lipid / resveratrol system, initially an intact lipid film is observed, which is not perturbed by the small molecule. Subsequently, changes of $\rho(z)$ in the lipid head group and chain region are detected, indicating

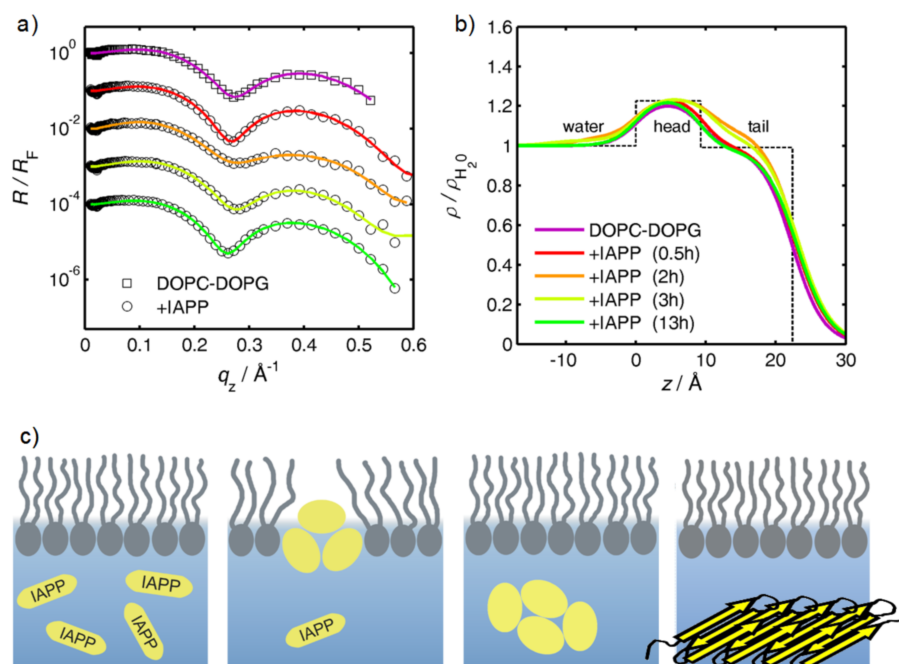


Figure 8.15: Association of IAPP with a negatively charged DOPC / DOPG lipid film at the air-water interface. (a) Normalised XRR data (dotted) and refinement (solid lines) at different times (vertically shifted for better visibility by one order of magnitude). (b) Corresponding normalised electron density profiles. (c) Schematic illustration of the time-evolution of the lipid-induced IAPP aggregation process: IAPP in bulk solvent, adsorption, and oligomerisation at the anionic lipid interface, detachment of larger aggregate structures, and fibril formation (yellow arrows: cross β -sheet arrangement of fibrils) at IAPP concentrations $> 5 \mu\text{M}$.

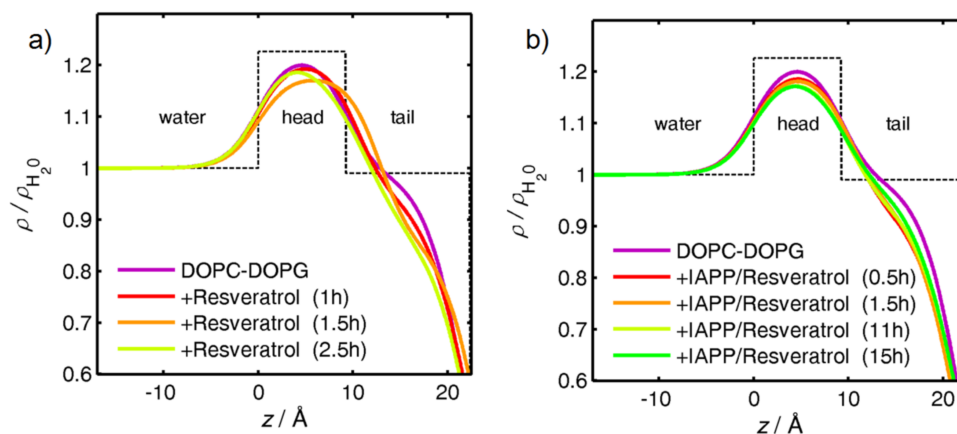


Figure 8.16: (a) Normalised electron density profiles of the negatively charged DOPC / DOPG monolayer in the presence of resveratrol at different times (time evolution: resveratrol dissolved in the bulk solvent, adsorption to the lipid head group area, partial penetration into the upper chain region). (b) Time evolution of the electron density profile of the lipid film in the presence of 1 μM resveratrol and IAPP.

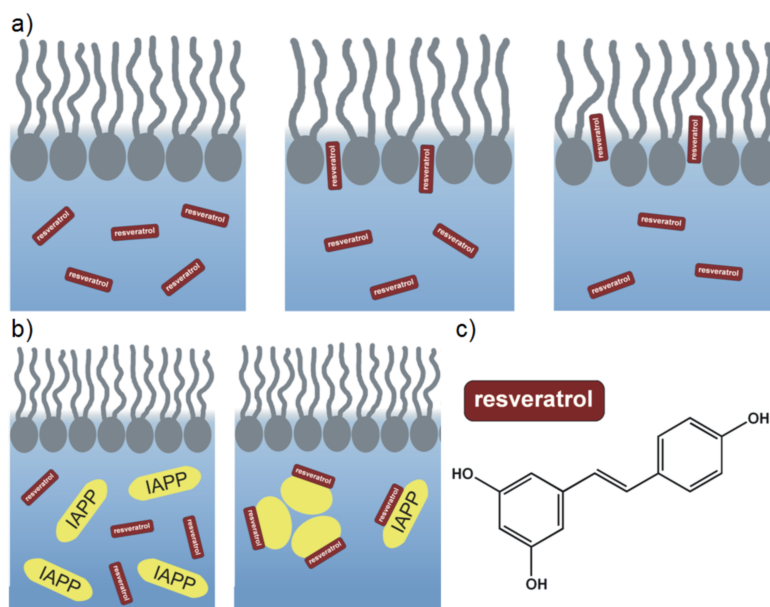


Figure 8.17: Schematic illustration of (a) how resveratrol perturbs the lipid monolayer structure and (b) of the inhibitory effect of resveratrol on IAPP fibrillation. (c) Chemical structure of resveratrol.

a decrease of lipid chain packing by migration of resveratrol in the upper chain region passing the lipid head group area (see Figure 8.17a).

Figures 8.16b and 8.17b reveal the corresponding effect upon addition of IAPP. Different from the pure IAPP / lipid system (Figure 8.15b), no aggregation of IAPP is observed at the lipid interface and no marked adsorption of resveratrol at the lipid interface is detected any more. Hence, it may be concluded that resveratrol and IAPP interact essentially in the bulk solution, so that the N-terminus of IAPP is masked in a way that interaction with the aggregation-fostering membrane and consequently, amyloid formation does not occur.

In the presence of IAPP no effect of resveratrol on the lipid layer can be observed. It can be concluded that the interaction with IAPP is much stronger and preferred to the interaction with the lipid membrane. That can be easily explained by the fact that there is a strong hydrophobic interaction of the mostly hydrophobic resveratrol with the peptide and barely any interaction with the hydrophilic head group region of the lipid layer, which first have to be penetrated by the resveratrol to access the preferred hydrophobic chain region of the membrane.

Conclusions

To conclude, first XRR studies on IAPP at lipid interfaces have been carried out, providing a molecular picture of the time-dependent scenario occurring upon aggregation of IAPP at anionic lipid interfaces. The lipid interface essentially serves only as nucleation side for IAPP aggregation. After growth of larger structures, the protein aggregates are released to the bulk, where at IAPP concentrations higher than $5 \mu\text{M}$, growth of large fibrils takes place. Moreover, the polyphenolic red-wine compound resveratrol is able to inhibit IAPP aggregation also in the presence of aggregation-fostering negatively charged lipid interfaces. Inhibition takes place during the very early stages of the fibrillogenesis and is efficient already at stoichiometric concentrations of resveratrol and IAPP.

8.3.2 Cross-interaction of A β and IAPP with an anionic raft monolayer

Introduction

The interaction of IAPP and A β with a complex heterogeneous model membrane system comprising 15 % DOPC, 10 % DOPG, 40 % DPPC, 10 % DPPG, and 25 % cholesterol was studied, to be able to address effects of lateral heterogeneity as well as charge effects upon peptide-membrane interaction. This novel model membrane system combines anionic and raft features, and yields further insights into differences and similarities of IAPP and A β aggregation in the presence of fibrillation-fostering membranes. Furthermore, the cross interaction of IAPP and A β in the presence of this membrane was analyzed in order to figure out at which aggregation state the interaction between IAPP and A β takes place and what kind of aggregation product is formed.

In order to obtain a detailed molecular scale picture of the membrane-mediated aggregation process, both X-ray diffraction and infrared spectroscopic techniques were applied. X-ray reflectometry (XRR) and grazing incidence X-ray diffraction (GIXD) were used to investigate the interaction of the peptides with a lipid monolayer at the air-water interface and to monitor time-dependent changes in the vertical and lateral structure as well as in the packing properties of the monolayer. The lipid monolayer was compressed to a physiological lateral film pressure of 30 mN m⁻¹. Using XRR, information about the laterally averaged layer structure, thickness and electron density of the different layers could be gained. By using GIXD, detailed information about the regions of high crystallinity in the disordered lipid monolayer, so-called rafts, were obtained.

Changes in the secondary structure of IAPP and A β upon fibrillation at a solid supported bilayer of the anionic raft mixture were determined by attenuated total reflection Fourier transform infrared (ATR-FTIR) spectroscopy. These measurements were performed by J. Seeliger, a PhD student in our group. Additionally to the ATR-FTIR measurements, the secondary structure of the peptides at the air-water interface was investigated by infrared reflection absorption spectroscopy (IRRAS) measurements, which were conducted in our lab at TU Dortmund University by S. Kapoor. The complete study is published in [409]. Here, the focus will be mainly on the XRR and GIXD measurements, which were conducted in cooperation with F. Evers (Department of Physics, TU Dortmund University).

As expected, both peptides formed larger oligomers and finally amyloid fibrils in the presence of an anionic lipid raft system with time. The aggregation of IAPP occurred significantly faster than the aggregation of A β . In the presence of both peptides in solution, the rate of aggregation was slowed down compared to the interaction of pure IAPP with the anionic lipid raft membrane. The secondary structure and the behaviour of both peptides in solution during the interaction with the lipid membrane suggests a dominant effect of the IAPP on the oligomer and fibril structure as well as aggregation mechanism in the presence of both peptides. The governing effect of the IAPP on the aggregation behaviour of A β was corroborated by studying the interaction of an equimolar mixture of IAPP-GI, a mimic of the non-amyloidogenic IAPP conformation, and A β , where no aggregation could be observed at all.

Materials and methods

The lipids 1,2-dioleoyl-*sn*-glycero-3-phosphocholine (DOPC), 1,2-dioleoyl-*sn*-glycero-3-phospho-(1'-*rac*-glycerol) (DOPG), 1,2-dipalmitoyl-*sn*-glycero-3-phosphocholine (DPPC) and 1,2-dipalmitoyl-*sn*-glycero-3-phospho-(1'-*rac*-glycerol) (DPPG) were purchased as lyophilised powders from Avanti Polar Lipids (Birmingham, AL). IAPP (human Amylin) was obtained from Calbiochem (Darmstadt, Germany). A β

(Amyloid β (1-40)) was obtained from Bachem (Bubendorf, BL, Switzerland). Moreover, A β as well as IAPP-GI [IAPP-[(N-Me)G24, (N-Me)I26]] were synthesised by the group of Prof. A. Kapurniotu.^[166] Cholesterol, NaH₂PO₄, Na₂HPO₄, 1,1,1,3,3,3-hexafluoroisopropanol (HFIP) were purchased from Sigma-Aldrich (Steinheim, Germany). All chemicals used were of the highest analytical grade available and used without further purification.

Stock solutions (10 mg/ml) of the lipids (DOPC, DOPG, DPPC, DPPG and cholesterol) dissolved in chloroform were prepared and mixed in a molar ratio of 15:10:40:10:25. Afterwards, the lipid mixture was spread at the air-water interface in a Langmuir trough, which was previously filled with aqueous buffer / peptide solution (10 mM PO₄³⁻, pH 7.4). Then, the film was compressed to an initial surface pressure of 30 mN m⁻¹, mimicking the lateral pressure of biological membranes. Afterwards, the surface area was kept constant, and the temporal evolution of the surface pressure was recorded. In all measurements, the temperature of the subphase was maintained at 20 ± 0.5 °C. Peptide solutions were prepared by dissolving IAPP and A β in hexafluoroisopropanol (HFIP), respectively, yielding a concentration of 0.5 mg/ml for each peptide. Thus, any preformed fibrils of IAPP and A β were dissolved. The required amount of IAPP or A β was dried using a gentle stream of nitrogen. A phosphate buffer solution was added to obtain a peptide sample solution. In this way, three different sample solutions were prepared with final concentrations of 500 nM for pure IAPP, 250 nM for pure A β , and each 250 nM in the solution containing both peptides.

The X-ray scattering experiments were conducted at the liquid surface diffractometer of beamline ID10B at the synchrotron light source ESRF (European Synchrotron Radiation Facility, Grenoble, France).^[97] A monochromatic X-ray wavelength, λ , of 1.523 Å (corresponding to a photon energy, E , of 8.14 keV) was selected by a diamond (111) crystal. Radiation damage was reduced by lateral translation of the trough by 0.01 mm after every step during GIXD scans and by 2 mm after each reflectometry scan.

Reflectometry scans were carried out by measuring the scattered intensity as a function of the incident angle, α_i , under the specular condition, $\alpha_i = \alpha_f$ (exit angle, α_f), using a 50 mm gas filled, position-sensitive detector. Reflectivity measurements were performed in an angular range of $0.4 \alpha_c < \alpha_i < 30 \alpha_c$ with the critical angle of total reflection of the air-water interface, α_c ($\alpha_c = 0.15^\circ$ at the given wavelength). In grazing incidence X-ray diffraction (GIXD), the liquid surface was illuminated at a constant incident angle of $0.8 \alpha_c$, i.e. at an angle slightly below the critical angle of the air-water interface. The scattered intensity was measured using a gas-filled detector (150 × 10 mm²). The detector had a vertical acceptance of $0 < q_z < 0.8 \text{ \AA}^{-1}$ and a horizontal resolution of $\Delta q_{xy} = 0.0051 \text{ \AA}^{-1}$. In a typical GIXD scan, the detector is moved in 200 steps in an angular range of 12° to 28° (corresponding to $0.86 \text{ \AA}^{-1} < q_{xy} < 2.0 \text{ \AA}^{-1}$) counting 15 s per step.

Results

The interfacial structure of the anionic lipid raft monolayer at the air-water interface was characterised by X-ray reflectometry and grazing incidence X-ray diffraction measurements. The results are shown in section 6.4.3 (page 107ff.). In Figure 8.18 the Bragg peak profile of the anionic lipid raft membrane is depicted in grey symbols, showing a single broad peak, corresponding to small crystalline domains of hexagonally packed lipids.

After spreading the lipids on a 500 nM IAPP solution of pH 7.4, the formed anionic lipid raft monolayer was compressed to a lateral film pressure of 30 mN m⁻¹. Then, while the area available for the lipid film was kept constant, the time-dependent evolution of the lateral film pressure, $\pi(t)$, was monitored (Figure 8.19, black symbols). Within the first 3 h, the film pressure has a nearly constant value of

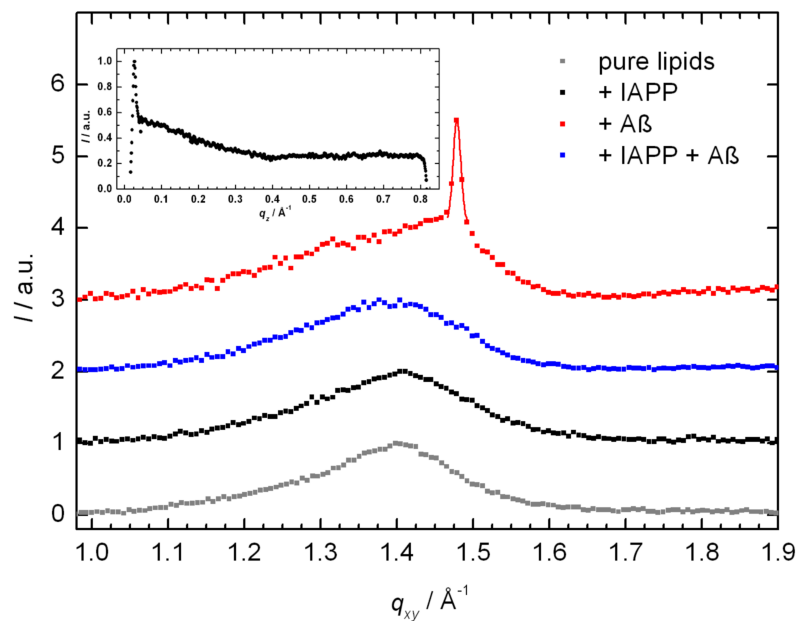


Figure 8.18: GIXD patterns, $I(q_{xy})$, of an anionic lipid raft monolayer on different peptide subphases. For clarity, data are shifted vertically. Inset: typical Bragg rod intensity profile, $I(q_z)$ (here for the sample containing 250 nM A β); the absence of a peak at $q_z \neq 0$ indicates little or no molecular tilt of the lipid tails.

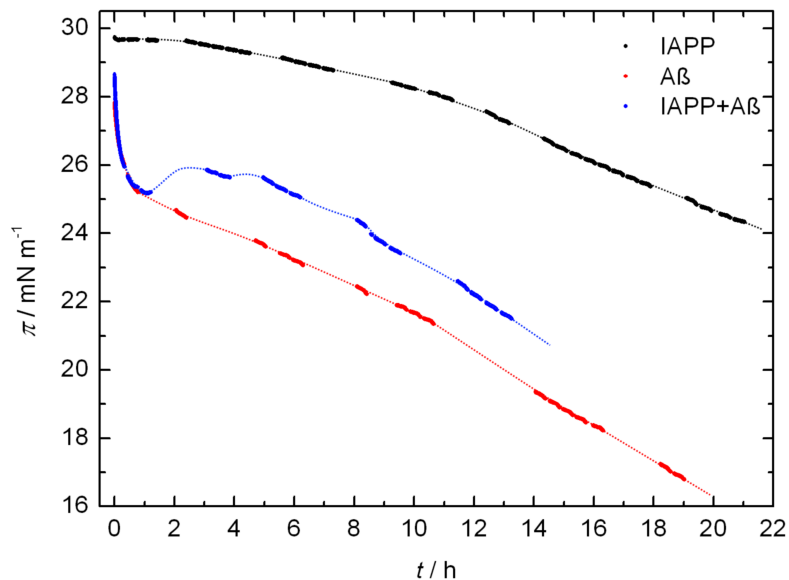


Figure 8.19: Lateral film pressure, π , as a function of time, t , of an anionic lipid raft monolayer spread on subphases containing different peptides: 500 nM IAPP (black symbols), 250 nM A β (red symbols), and IAPP / A β (250 nM each, blue symbols).

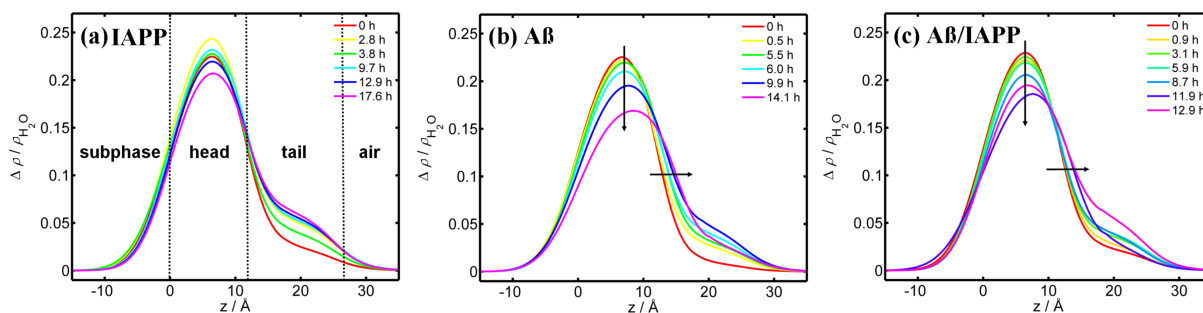


Figure 8.20: Time evolution of the normalised electron density profiles for the interaction of IAPP (a), A β (b), and both A β and IAPP (c) with anionic lipid raft monolayers. The temporal evolution is indicated by the arrows.

29.6 mN m⁻¹. Then, π decreases linearly to a value of 28 mN m⁻¹ after 11 h, followed by a steeper decrease ending at a final film pressure of 24.3 mN m⁻¹ after 21 h.

Figure 8.20 shows the temporal evolution of the normalised electron density profiles (EDPs) obtained by fitting the XRR data.¹ The data clearly reveal changes in the interfacial structure of the lipid film upon interaction with the aggregation-prone peptide. These time-dependent changes reflect the temporal evolution of the lateral surface pressure profile depicted in Figure 8.19. Within the first 3 h, IAPP penetrates the lipid head group (at about $0 < z < 12$ Å), thereby increasing the electron density in this area. In a second step, changes are observed in the hydrocarbon chain region (at about $z > 12$ Å) of the lipid film, namely a continuous increase of the electron density, which can be ascribed to IAPP penetration, oligomer formation and growth in the upper chain region. The volume occupied by IAPP in the lipid head group region decreases concomitantly. Beyond 11 h, the electron density of the head group decreases, hinting at a reorganisation of IAPP aggregates or a detaching from the lipid monolayer. A similar scenario has been proposed for the interaction of IAPP with anionic model membranes (DOPC:DOPG, 7:3) recently, as presented in section 8.3.1.^[174]

The first GIXD data in the presence of IAPP, taken 1.8 h after starting the experiment (Figure 8.18, black squares), is almost identical to the one of the pure lipid raft monolayer. The crystalline-like domains of the monolayer also show a hexagonal packing with a lattice vector, $a = b$, of 5.20 Å, a lateral 2D coherence length, L_{xy} , of 22.2 Å and a vertical coherence length, L_z , of 16.8 Å. Again, no significant tilt angle of the lipid hydrocarbon chains relative to the surface normal was observed. Additional GIXD measurements were performed at selected time points of the experiment. However, no significant changes of the GIXD patterns were recorded. Hence, the results of the GIXD measurements suggest that IAPP does not interact with the ordered domains of the heterogeneous lipid monolayer.

The time-dependent behaviour of the lateral film pressure for a lipid raft monolayer spread on a 250 nM A β solution of pH 7.4 is presented in Figure 8.19 (red squares). Immediately after starting the experiment, a rapid decay of the film pressure can be observed, from 30 mN m⁻¹ to 25.3 mN m⁻¹ within the first hour. Thereafter, the film pressure decreases only slowly to 21.4 mN m⁻¹ after 10.5 h. Finally, a steeper, nearly linear decrease of the film pressure to 16.8 mN m⁻¹ after 20 h is observed.

In analogy to the interaction of IAPP with the lipid raft monolayer, the temporal evolution of the anionic raft monolayer in the presence of A β - as observed by X-ray reflectometry - also reflects the variations of the surface pressure (Figures 8.20b). With time, the electron density of the lipids head group region decreases, first slowly, than more rapidly. This decrease is more pronounced compared to the IAPP case.

¹The fitting of the XRR data was performed by F. Evers using LSFIT.

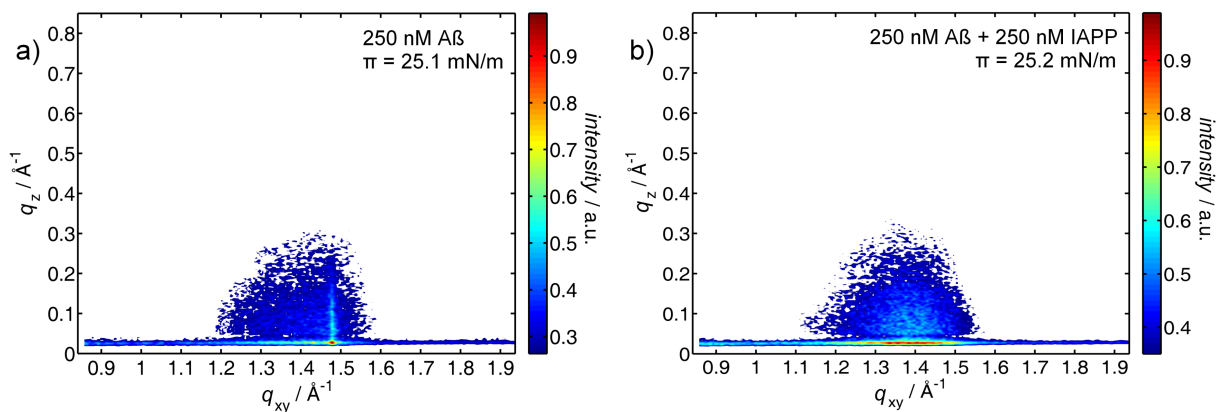


Figure 8.21: Two-dimensional contour plots of the intensity, $I(q_{xy}, q_z)$, along the horizontal (q_{xy}) and vertical (q_z) scattering directions as obtained from an anionic lipid raft monolayer (15% DOPC, 10% DOPG, 40% DPPC, 10% DPPG and 25% cholesterol, molar ratio) in the presence of 250 nM A β (a) and a mixture of IAPP / A β (b) at a lateral film pressure of $\pi \approx 25 \text{ mN m}^{-1}$ at 20 °C.

The width of the head group region and the intensity in the upper chain region increases concomitantly. The strongly decreasing electron density in the head group region points to a more disordered state of the lipids with a looser lipid packing as compared to the monolayer observed without peptide. Such strong disordering effect has also not been observed upon insertion of IAPP (Figure 8.20a).

GIXD measurements were also performed at selected time points during the interaction of the lipid raft monolayer with a 250 nM A β solution. The two-dimensional contour plot of the intensity, $I(q_{xy}, q_z)$, is presented in Figure 8.21a and the integrated intensity along q_z at a lateral film pressure of 25.1 mN m^{-1} at 20 °C is presented in Figure 8.18 (red squares). Remarkably, two signals are observed: a broad peak with a maximum at approximately $q_{xy} = 1.39 \text{ \AA}^{-1}$ and a sharp peak at $q_{xy} = 1.48 \text{ \AA}^{-1}$. The first, broad signal can easily be assigned to hexagonally packed crystalline domains of the lipid monolayer. As compared to the lipid monolayer in the absence of A β , only little differences can be found in the parameters retrieved from the analysis of the GIXD data. Hence, these ordered domains resemble those of the pure lipid layer. The second, sharp peak represents another hexagonally packed structure with a lattice spacing, $a = b$, of 4.91 \AA and a lateral 2D coherence length, L_{xy} , of 327 \AA . The lattice vector is significantly larger than the typical distance of parallel β -sheets in peptide aggregates of 4.76 \AA . Hence, the peak can only be ascribed to another ordered lipid domain. Also the large coherence length indicates that this signal originates from the lipid monolayer and not from the small amount of peptide in the system. Furthermore, the almost identical vertical coherence length, L_z , of both highly ordered domains in the system of 17.3 \AA shows that both signals represent the hydrocarbon chain region of the lipid monolayer. Hence, the incorporation of A β leads to a major reorganisation process of the lateral structure of the lipid monolayer. Upon addition of A β , formation of much larger, highly ordered domains is induced. These newly formed domains seem to coexist with the previously observed much smaller crystalline domains of the pure lipid system.

For the small crystalline-like domains represented by the broad peak at $q_{xy} = 1.39 \text{ \AA}^{-1}$, a small and continuous increase of the lattice vectors of 2% and a gain of the size of the lateral coherence length L_{xy} of 28% is found until the end of the experiment. For the peptide-induced sharp peak at $q_{xy} = 1.48 \text{ \AA}^{-1}$, no significant change in the lattice vectors can be observed, but the lateral coherence length, L_{xy} , decreases remarkably over time (by 63%). This decrease can be easily explained by the decreasing lateral film pressure as depicted in Figure 8.19 (red squares), which obstructs large crystalline domains in the monolayer. The vertical coherence length of both crystalline domains remains constant

during the whole experiment. The Bragg rod intensity profile, $I(q_z)$, obtained by integrating along the q_{xy} region of the Bragg peak region reveals no peak at $q_z \neq 0$, indicating little or no molecular tilt of both ordered domains in the system.

Figure 8.19 shows the lateral film pressure of the anionic lipid raft monolayer spread on an IAPP / A β (250 nM each) solution as a function of time (blue symbols). At first, a strong decrease in film pressure is observed, from 30 mN m⁻¹ to 25.2 mN m⁻¹ within the first hour. This behaviour is very similar to the one found for the pure A β solution. Subsequently, the lateral film pressure increases again over 3 h to a maximal value of 25.9 mN m⁻¹. Thereafter, a decay of the film pressure is detected, which can be divided into two linear regions. In the first region, π decays slightly to 25.0 mN m⁻¹ at 7 h after the start of the experiment, and in the second region, π decreases even faster to 21.5 mN m⁻¹ at the end of the experiment. Comparing these data with the film pressure data of the single peptide solutions, it can be noticed that the data for the IAPP / A β mixture are almost completely governed by A β in the first hour, and both peptides seem to contribute equally to the overall development of the lateral film pressure afterwards.

In the presence of both IAPP and A β , the electron density profiles (Figure 8.20c) indicate a combination of the processes observed for pure IAPP and A β . Referring to the X-ray reflectometry data, the effect of A β is dominating, i.e. a continuous decrease of the head group's electron density with time and an increasing layer thickness of the head group related to oligomer formation. However, the presence of both peptides delays the membrane-induced oligomerisation process, as indicated by the retarded increase of the electron density in the lipid chain region. The decreasing electron density in the lipid head group area can again be interpreted by an increased disorder of the packing of lipid molecules in the monolayer.

The two-dimensional contour plots of the intensity, $I(q_{xy}, q_z)$, measured by GIXD of a lipid monolayer on a subphase containing both 250 nM IAPP and 250 nM A β at a film pressure of 25.2 mN m⁻¹ at 20 °C is presented in Figure 8.21b. The corresponding peak intensity integrated along q_z is shown in Figure 8.18 (blue symbols). In this case, only one broad peak has been found, indicating a hexagonal packing of the lipid monolayer. Only minor changes could be observed with time. The lattice vectors increase over the entire time period of 13 h by approximately 2%, and the vertical coherence length decreases by 13%. The less perfect packing can be related to the strong decrease in lateral film pressure over time.

Discussion and conclusions

In this study, the aggregate formation of A β and IAPP (each peptide separately) as well as the cross-amyloid interaction (in an equimolar mixture of both peptides) in the presence of a heterogeneous anionic lipid raft membrane was investigated. All experiments were conducted both on an anionic lipid raft monolayer at the air-water interface by XRR, GIXD and IRRAS, mimicking the outer leaflet of biological membranes and ensuring for a high lateral mobility of the lipids in the monolayer, and on a solid-supported anionic lipid raft bilayer membrane by ATR-FTIR, mimicking the inner and outer leaflet of natural membranes. This lipid mixture has been chosen because it is able to address effects of lateral heterogeneity (coexisting liquid ordered and disordered domains) as well as charge effects upon peptide-membrane interaction, since both peptides, IAPP and A β , have shown a larger propensity to aggregate and fibrillate in the presence of anionic membranes.^[171, 172, 174–176, 411] In this study, using X-ray reflectometry and grazing incidence X-ray diffraction measurements, it was possible to show that formation of raft-like ordered domains not only appears in bilayers of this lipid mixture, but also in the corresponding monolayer system.

Generally, the presence of anionic and lipid raft membranes accelerates the aggregation and fibrillation process of both peptides and leads to a marked disintegration of the lipid bilayer into peptide-lipid aggregates, which is thought to be important for explaining the cytotoxicity of these amyloidogenic peptides.^[412, 413] Lowering of the local solvent dielectric permittivity at the lipid interface facilitates the formation of peptide-peptide hydrogen bonds in the β -sheet aggregate, and the reduction of the dimensionality from three in the bulk solvent to two on the membrane interface introduces spatial restrictions that foster the fibrillation process.^[411] The latter two effects seem to play a significant role in the formation of α -helical intermediate structures as well.^[411] The aggregation and fibrillation reaction of A β and IAPP, observed in the presence of the lipid monolayers or lipid bilayer membranes, can be subdivided into several processes. At first, the monomeric peptide inserts into the lipid film, followed by the growth of small oligomers, which remain stable for several hours. Finally, larger aggregate structures (such as small fibrils as detected by AFM^[217]) form and grow in size with time. For the interaction of IAPP with a negatively charged monolayer (DOPC / DOPG, molar ratio 7:3) at the air-water interface, a detachment of the oligomers from the monolayer after a certain time has been observed before.^[174] The XRR results (cf. Figure 8.20) suggest that IAPP inserts into the head group region of the anionic lipid raft monolayer during the first 3 h of the experiment, leading to an increased electron density in the head group region. Thereafter, IAPP oligomers grow inside the head group and upper chain region, resulting in a slight decrease of the lateral film pressure over time (Figure 8.19). During this period, the vertical EDP of the monolayer does not change significantly, indicating only lateral movement of the components inside the lipid film. Finally, after 11 h, the larger oligomeric aggregate structures start detaching from the lipid monolayer, which is indicated by the decreasing electron density of the head group region. The GIXD measurements reveal that the lateral domain organisation of the lipid monolayer remains essentially intact, indicating that IAPP does not interact with the ordered raft domains of the lipid monolayer; rather, IAPP preferentially inserts into the disordered regions of the lipid monolayer, which is rich in DOPG and DOPC.

The aggregation process of A β observed at anionic raft membranes is completely different from the behaviour of IAPP. In contrast to the scenario found for IAPP, a more complex aggregation process is observed by ATR-FTIR in the case of A β (data published in [409]). Interestingly, the XRR as well as the GIXD data reveal a strong reorganisation of the lipid film and weakened lipid packing of the monolayer at the air-water interface in the presence of A β , i.e. the structural integrity of the membrane is simultaneously compromised. This process is also reflected in the rapid decrease of the lateral film pressure of the lipid monolayer within the first hour of the experiment. The GIXD data reveal the formation of additional ordered raft-like domains induced by A β insertion. At the beginning of the insertion process of A β , an increase in the thickness of the head group region, accompanied by a decrease in the electron density of this part of the lipid monolayer, has been found by XRR, indicating lipid reorganisation and oligomerisation of the A β in the monolayer. At the same time, only a slow decrease of the lateral film pressure is observed. Finally, after 10.5 h, the decrease of the lateral film pressure speeds up and the thickness of the lipids head group increases further, indicating an increasing rate of oligomer growth in the lipid monolayer. At this point, the lateral coherence length of the newly formed ordered domains has decreased by 63%, indicating that with time fewer lipids are recruited in such domains, which can be explained by the decreasing number of A β molecules entering the lipid layer and hence inducing such domains.

Finally, the interaction of A β with IAPP in the presence of the anionic lipid raft mixture has been investigated. In the GIXD experiments, only a single broad peak assignable to lipid raft domains is found. A second peak representing new peptide-induced ordered lipid domains, as observed for pure A β , has not

been detected, indicating that the scenario observed for pure A β being capable of recruiting lipids to form new domains, does not take place in the presence of IAPP in solution. Obviously, the cross-interaction of IAPP and A β occurs already in an very early oligomeric state.

To conclude, a distinct interaction of both peptides with the anionic lipid raft monolayer was observed, including the incooperation of peptides into the monolayer and growth of oligomers inside the lipid film. The cross-interaction of both peptides led to an early interaction of both peptides, but no inhibition of the aggregation process, although compared to the aggregation of pure IAPP the kinetic of this process was slowed down.

8.3.3 Interaction of IAPP with glycolipids

Synchrotron X-ray reflectometry was used to investigate the interaction of IAPP with a lipopolysaccharide (LPS) extracted from *Salmonella minnesota* strain R595. The deep rough mutant LPS Re, which was used for this study, is composed of a lipid moiety called lipid A, build by six hydrocarbon chains and two phosphorylated N-acetylglucosamines (GlcN), as well as two 2-keto-3-deoxyoctonic (KDO) acid units connected by a 2-6 linkage to the lipid A. Each LPS molecule carries 3.5 negative net charges. For more details see section 4.2.9 (page 55) .

A monolayer of LPS Re was spread on a 1 μ M solution of IAPP (10 mM phosphate buffer, pH 7.0), using a Langmuir trough and immediately compressed to a film pressure, π , of 30 mN m⁻¹ mimicking the physiological conditions of the outer membrane of gram-negative bacteria. Inspection of the time evolution of the measured reflectivities revealed no significant changes of the LPS monolayer on the water-air interface within 10 h, indicating the absence of any strong interaction of IAPP with the negatively charged LPS film. This behaviour could be explained by a compact configuration of the LPS molecules in the monolayer, where the negatively charged phosphate groups of the lipid A region are not exposed to the subphase and the partially negatively charges KDO subunits are not fully accessible to the bulk solution containing the IAPP. Therefore, the repulsive interaction of the highly hydrophilic KDO units and the hydrophobic IAPP could outweigh the attractive electrostatic interaction of IAPP and the partially accessible negative charges of the LPS.

CHAPTER 9

Summary & Zusammenfassung

9.1 Summary

In this thesis various studies of biomolecules like proteins, lipids and mixtures thereof, using X-ray and neutron diffraction techniques are presented. High pressure small-angle X-ray scattering (SAXS) was commonly used to establish p, T -phase diagrams of various sample systems in bulk solution, as well as the combination of time-resolved SAXS with the pressure-jump relaxation technique to study the phase transition kinetics of biologically relevant systems. Furthermore, X-ray reflectometry (XRR) and grazing incidence X-ray diffraction (GIXD) proved to be excellent tools to investigate corresponding molecular monolayers at the air-water interface.

First of all, the design of a novel high pressure cell for neutron reflectivity experiments up to pressures of 2.5 kbar (250 MPa) in a temperature range between 5 °C and 75 °C has been described. The large accessible pressure range and the low required volume of the sample solution make this high pressure cell highly suitable for studying pressure-induced structural changes of interfacial proteins, supported lipid membranes and in general, biomolecular systems that are only available in small quantities.

Studies on two different protein systems were conducted by high pressure SAXS:

- the effect of high pressure and solution pH on the structure of a highly stable staphylococcal nuclease (SNase) variant, Δ +PHS. Additionally, the Val-66, which is located in the hydrophobic core, was replaced by Ala, Tyr, Lys, or Arg to examine how changes in the volume and polarity of an internal microcavity affect the native conformation and the stability of the structures. The particle envelopes were obtained from different *ab initio* methods, i.e. spherical harmonics, the dummy-residue method, as well as the multi-bead approach.
- the temperature and pressure dependent stability of the dimeric protein MsP1, which turned out to be not only rather thermostable, but also highly resistant to pressure, i.e. up to temperatures of about 65 °C and pressures as high as 3 kbar at ambient temperatures in the SAXS measurements.

The p, T -phase diagrams of diverse lipid systems have been established in a typical temperature range of 5 °C to 75 °C for pressures up to 4 kbar and the phase transition kinetics and underlying mechanisms have been studied by trSAXS:

- a mixture of the long-chain lipid DMPC and the short-chain lipid DHPC forming flat, cylindrical micelles, so-called bicelles, at low temperature and low pressure; elongated worm-like micelles in

the intermediate temperature- and pressure-range, as well as a lamellar phase built by perforated multilamellar vesicles at high temperature and pressure. Finally, at pressures larger than about 5 kbar a so far unknown, lamellar, ordered, interdigitated phase was found.

- pure monoolein at a limited hydration level of 17 %_{wt} showing at very low temperature and high pressure an ordered and at low temperature a disordered lamellar phase, and finally at elevated temperatures a bicontinuous cubic *Ia3d* phase.
- monoolein samples containing different fusion peptides (HA2, VSV, TBEV) and a trans-membrane domain (TMD VSV), all influencing the phase behaviour and phase transition kinetics of the monoolein, as well as a control peptide (L16), which had nearly no influence on the lipid system. The results yield valuable information on the effect of fusion peptides on the bending constants of membranes.
- the phospholipid DPPC containing 22 %_{mol} of the fungal steroid ergosterol, as a model system for a heterogeneous fungal plasma membrane.
- and finally a heterogeneous lipid raft mixture composed of the lipids DOPC and DPPC as well as cholesterol in a molar ratio of 1:2:1, showing an extended region of liquid ordered domains in a liquid disordered matrix (lipid rafts) in the physiological temperature range between 20 °C and 45 °C.

Finally, a number of pure lipid monolayer studies as well as the interaction studies of peptides with lipid monolayers at the air-water interface have been carried out by XRR and GIXD:

- a lipid raft mixture (DOPC, DPPC, cholesterol; molar ratio 1:2:1), as previously studied by SAXS in the subphase, also revealing its heterogeneous raft characteristics in the lipid monolayer.
- an even more complex anionic model membrane system comprising 15 % DOPC, 10 % DOPG, 40 % DPPC, 10 % DPPG, and 25 % cholesterol showing a strong lateral heterogeneity (with coexisting liquid disordered and ordered domains).
- monolayers of the deep rough mutant lipopolysaccharide (LPS Re) as a model of the outmost monolayer in the cell membrane of gram-negative bacteria and the influence of monovalent (Na^+) as well as divalent (Ca^{2+}) cations on the structure and behaviour of these lipid monolayers.
- monolayers of archaeal lipids (PLFE) as a function of film pressure, subphase pH, temperature, and growth temperature of the lipids, which adopt in all cases a U-shape conformation with both head groups of each lipid in contact with the subphase.
- the interaction of the ion channel peptide gramicidin D with an archaeal lipid monolayer, revealing only an unspecific interaction of the peptide with the lipid film.
- and finally, the interaction of different peptides, known to form amyloid fibrils (IAPP and $\text{A}\beta$), with anionic lipid films fostering the aggregation of the peptides, as well as the inhibition of the fibril formation of IAPP by the red-wine component and small molecule inhibitor resveratrol.

9.2 Zusammenfassung

Im Rahmen dieser Doktorarbeit wurden zahlreiche Studien an verschiedenen Biomolekülen, wie zum Beispiel Proteinen, Lipiden und Mischungen beider Substanzklassen, mit Hilfe von Röntgen- und Neutronenstreutechniken untersucht. Die Methode der Röntgenkleinwinkelstreuung (SAXS) wurde wiederholt genutzt, um p, T -Phasendiagramme verschiedener Probensysteme zu bestimmen. Zeitaufgelöste Röntgenkleinwinkelstreuung (trSAXS) in Kombination mit der Drucksprung-Relaxationsmethode ermöglichte es die Kinetik von Phasenübergängen in biologisch relevanten Systemen zu untersuchen. Weiterhin wurden die Techniken der Röntgenreflektometrie (XRR) und der Röntgendiffraktion unter streifendem Einfallswinkel (GIXD) genutzt, um entsprechende molekulare Monofilme an der Luft-Wasser-Grenzfläche zu untersuchen.

Zu allererst wurde die Entwicklung einer neuartigen Hochdruck-Neutronenreflektometrie-Probenzelle, ausgelegt für Drücke bis zu 2.5 kbar (250 MPa) in einem Temperaturbereich von 5 °C bis 75 °C, beschrieben. Der hohe Maximaldruck in Kombination mit dem vergleichsweise kleinen Volumen benötigter Probenlösung macht diese Hochdruckzelle hochgeeignet zur Untersuchung von druckinduzierten Strukturänderungen von an Grenzflächen adsorbierten Proteinen, Lipidmembranen und allgemeiner, von biomolekularen Systemen, die nur in geringen Mengen zur Verfügung stehen.

An zwei verschiedenen Protein-Systemen wurden Studien mittels Hochdruck-Röntgenkleinwinkelstreuung durchgeführt:

- der Effekt von Hochdruck und dem pH-Wert der Lösung auf die Struktur der hochstabilen Staphylokokken Nukleasen-Variante, Δ +PHS. Zusätzlich wurde die Aminosäure Val-66, die sich im hydrophoben Kern des Proteins befindet, durch jeweils eine der Aminosäuren Ala, Tyr, Lys oder Arg ersetzt, um zu erforschen, wie Veränderungen des Volumens und der Polarität im Inneren des Proteins die native Konformation und die Stabilität des Proteins beeinflussen. Die äußere Partikelform wurden mittels verschiedener *ab initio*-Methoden berechnet.
- der Effekt von Temperatur und Druck auf die Stabilität des dimeren Proteins MsP1, welches sich nicht nur als sehr temperaturstabil bis zu Temperaturen von 65 °C, sondern auch als sehr druckbelastbar erwies – weit über den in der Hochdruck-Kleinwinkelstreuung angewendeten Maximaldruck von 3 kbar hinaus.

p, T -Phasendiagramme verschiedenster Probensysteme wurden ermittelt – typischerweise in einem Temperaturbereich zwischen 5 °C und 75 °C sowie für Drücke bis zu 4 kbar. Des Weiteren wurden häufig die jeweiligen Phasenübergangskinetiken sowie die zugrunde liegenden Mechanismen der Phasenübergänge mittels zeitaufgelöster Kleinwinkelstreuung bestimmt:

- eine Mischung aus dem lang-kettigen Lipid DMPC und dem kurz-kettigen Lipid DHPC, welche im Bereich geringer Temperaturen und Drücke zylinderförmige Mizellen, sogenannte Bizellen, bildet. Im mittleren Temperatur und Druckbereich zeigt es ausgedehnte, röhrenartige Mizellen und schließlich bei hohen Temperaturen wird eine lamellare Phase gebildet, die aus perforierten, multilamellaren Vesikeln besteht. Zusätzlich konnte im Bereich hoher Drücke über 5 kbar eine bislang unbekannte, geordnete, lamellare Phase gefunden werden, bei der die Lipidketten der gegenüberliegenden Lipidmonoschichten ineinander verschränkt vorliegen.
- pures Monoolein mit einem Hydratisierungsgrad von 17 %_{wt}, welches bei sehr niedrigen Temperaturen und hohen Drücken eine geordnete lamellare Phase ausbildet, bei etwas erhöhten Temperaturen

in eine ungeordnete lamellare Phase übergeht und schließlich bei hohen Temperaturen eine bikontinuierliche kubische $Ia3d$ Phase zeigt.

- verschieden Monoolein-Proben, die jeweils 2%_w eines der drei Fusionspeptide (HA2, VSV, TBEV) oder der Transmembran-Domäne (TMD VSV) enthielten, was jeweils das Phasenverhalten und die Phasenübergangskinetik des Lipidsystems deutlich beeinflusste. Zusätzlich wurde der Effekt eines Kontrollpeptides (L16) untersucht, das nahezu keinen Einfluss auf das Phasenverhalten von Monoolein zeigte. Die Ergebnisse bieten wertvolle Informationen über den Effekt von Fusionspeptiden auf die Biegsamkeit und Elastizität von Membranen.
- eine Mischung des Phospholipides DPPC mit 22%_{mol} des Pilzsteroids Ergosterol als ein Modellsystem für eine heterogene Pilz-Plasmamembran.
- und schließlich eine heterogene Lipid-Raftmischung, bestehend aus den Lipiden DOPC und DPPC sowie dem Steroid Cholesterol im molaren Verhältnis 1:2:1, welches eine ausgedehnte Phasenregion von flüssig-geordneten Domänen, sogenannten "Rafts" in einer flüssig-ungeordneten Lipidmatrix im physiologisch wichtigen Temperaturbereich zwischen 20 °C und 45 °C zeigte.

Zuletzt wurden noch eine Reihe von reinen Lipidmonofilmen sowie die Wechselwirkung von Peptiden mit Lipidmonofilmen an der Luft-Wasser-Grenzfläche mittels XRR und GIXD untersucht:

- die Lipid-Raft-Mischung (DOPC, DPPC, cholesterol; molares Verhältnis 1:2:1), die zuvor in der Subphase in Form multilamellarer Vesikel mittels SAXS untersucht worden war, zeigte ebenfalls ihre heterogene Raft-Charakteristik im Lipidmonofilm.
- ein noch deutlich komplexeres, anionisches Modellmembran-System bestehend aus 15% DOPC, 10% DOPG, 40% DPPC, 10% DPPG und 25% Cholesterol, das ebenfalls eine starke laterale Heterogenität aufwies (Koexistenz von flüssig-geordneten und ungeordneten Filmbereichen).
- Monofilme des stark verkürzten Lipopolysaccharids LPS Re, ein Modellsystem für die äußerste Monoschicht einer Zellmembran von gram-negativen Bakterien, und den Einfluss von sowohl einwertigen (Na^+) als auch zweiwertigen (Ca^{2+}) Kationen auf die Struktur und das Verhalten dieser Lipidfilme.
- Monofilme aus Archaealipiden (PLFE) als Funktion des Filmdruckes, des Lösungs-pHs, der Temperatur und der Wachstumstemperatur der Lipide, die in allen Fällen eine U-förmige Konfiguration mit beiden Kopfgruppen des Lipids im Kontakt mit der Wassergrenzfläche einnehmen.
- eine Mischung des Ionenkanal-Peptides Gramizidin D mit einem Archaealipid-Monofilm, welches keine spezifischen Wechselwirkungen mit dem Lipidmonofilm zeigte.
- und zuletzt die Wechselwirkung verschiedener Peptide, welche bekannt sind Amyloid-Fibrillen auszubilden (IAPP und $\text{A}\beta$) mit anionischen Lipidmonofilmen, welche diese Form der Peptid-Aggregation unterstützen und beschleunigen. Außerdem wurde die Unterdrückung der Fibrillbildung durch den niedermolekularen Rotweininhaltsstoff Resveratrol untersucht.

Bibliography

- [1] A. Guinier and G. Fournet. *Small-Angle Scattering of X-Rays*. John Wiley & Sons, Inc., 1955.
- [2] O. Glatter and O. Kratky. *Small Angle X-ray Scattering*. Academic Press, London, New York, 1982.
- [3] R. Winter and R. Koehling. Static and time-resolved synchrotron small-angle X-ray scattering studies of lyotropic lipid mesophases, model biomembranes and proteins in solution. *Journal of Physics Condensed Matter*, 16:327 – 352, 2004.
- [4] P.B. Moore. Small-Angle Scattering. Information Content and Error Analysis. *J. Appl. Crystallogr.*, 13:168 – 175, 1980.
- [5] M.H.J. Koch, P. Vachette, and D.I. Svergun. Small angle scattering: a view on the properties, structure and structural changes of biological macromolecules in solution. *Q. Rev. Biophys.*, 36:147 – 227, 2003.
- [6] E. Dainese, A. Sabatucci, and I. Cozzani. Small Angle X-Ray Scattering: A Powerful Tool to Analyze Protein Conformation in Solution. *Curr. Org. Chem.*, 9:1781 – 1800, 2005.
- [7] C.D. Putnam, M. Hammel, G.L. Hura, and J.A. Tainer. X-ray solution scattering (SAXS) combined with crystallography and computation: defining accurate macromolecular structures, conformations and assemblies in solution. *Q. Rev. Biophys.*, 40:191 – 285, 2007.
- [8] B.H. He. *TWO-DIMENSIONAL X-RAY DIFFRACTION*. John Wiley & Sons, Inc., Hoboken, New Jersey, 1954.
- [9] N. Stribeck. *X-Ray Scattering of Soft Matter*. Springer-Verlag Berlin Heidelberg, 2007.
- [10] L.A. Feigin and D.I. Svergun. *Structure Analysis by Small-Angle X-Ray and Neutron Scattering*. Plenum Press, 1987.
- [11] C. Jeworrek, M. Pühse, and R. Winter. X-ray Kinematography of Phase Transformations of Three-Component Lipid Mixtures: A Time-Resolved Synchrotron X-ray Scattering Study Using the Pressure-Jump Relaxation Technique. *Langmuir*, 24:11851 – 11859, 2008.
- [12] C. Jeworrek, S. Uelner, and R. Winter. Phase behavior and kinetics of pressure-jump induced phase transitions of bicellar lipid mixtures. *Soft Matter*, 7:2709 – 2719, 2011.
- [13] D.I. Svergun. Restoring Low Resolution Structure of Biological Macromolecules from Solution Scattering Using Simulated Annealing. *Biophys. J.*, 76:2879 – 2886, 1999.
- [14] R. Winter and F. Noll. *Methoden der biophysikalischen Chemie*. B.G. Teubner, Stuttgart, 1. edition, 1998.
- [15] G. Damaschun and H.-V. Pürschel. Röntgen-Kleinwinkelstreuung von isotropen Proben ohne Fernordnung. I. Allgemeine Theorie. *Acta Crystallogr.*, A27:193 – 197, 1971.
- [16] P. Vachette and D. Svergun. *Structure and Dynamics of Biomolecules.*, chapter Small-angle X-ray scattering by solutions of biological macromolecules., pages 199 – 237. Oxford University Press, 2002.

- [17] O. Glatter. Determination of Particle-Size Distribution Functions from Small-Angle Scattering Data by Means of the Indirect Transformation Method. *J. Appl. Crystallogr.*, 13:7 – 11, 1980.
- [18] O. Glatter. The Interpretation of Real-Space Information from Small-Angle Scattering Experiments. *J. Appl. Crystallogr.*, 12:166 – 175, 1979.
- [19] O. Glatter. A new method for the evaluation of small-angle scattering data. *J. Appl. Crystallogr.*, 10: 415–421, 1977.
- [20] D.I. Svergun. Determination of the regularization parameter in indirect-transform methods using perceptual criteria. *J. Appl. Crystallogr.*, 25:495 – 503, 1992.
- [21] A.V. Semenyuk and D.I. Svergun. GNOM - a program package for small-angle scattering data processing. *J. Appl. Crystallogr.*, 24:537 – 540, 1991.
- [22] J.S. Pedersen. Analysis of small-angle scattering data from colloids and polymer solutions: modeling and least-squares fitting. *Adv. Colloid Interface Sci.*, 70:171 – 210, 1997.
- [23] M. Nakano, M. Fukuda, T. Kudo, M. Miyazaki, Y. Wada, N. Matsuzaki, H. Endo, and T. Handa. Static and Dynamic Properties of Phospholipid Bilayer Nanodiscs. *J. Am. Chem. Soc.*, 131:8308 – 8312, 2009.
- [24] I. Pilz, O. Glatter, and O. Kratky. Small-Angle X-Ray Scattering. *Methods Enzymol.*, 61:148 – 249, 1979.
- [25] A. Guinier. La diffraction des rayons X aux très petits angles: application à l'étude de phénomènes ultra-microscopiques. *Annales de Physique*, 12:161 – 237, 1939.
- [26] I.N. Bronstein and K.A. Semendjaev. *Taschenbuch der Mathematik*. G. Grosche and V. Ziegler and D. Ziegler, 1987.
- [27] M. Engel, T. Spehr, and B. Stühn. Small-Angle X-Ray and Neutron Scattering. *Bunsen-Magazin*, 13:4 – 15, 2011.
- [28] G. Porod. Die Kleinwinkelstreuung von dichtgepackten kolloiden Systemen. *Kolloid. Z.*, 124:83 – 114, 1951.
- [29] P. Mittelbach and G. Porod. Zur Röntgenkleinwinkelstreuung kolloider Systemen. *Kolloid. Z.*, 202:40 – 49, 1964.
- [30] A. Bergmann, G. Fritz, and O. Glatter. Solving the generalized indirect Fourier transform (GIFT) by Boltzmann simplex simulated annealing (BSSA). *J. Appl. Crystallogr.*, 33:1212 – 1216, 2000.
- [31] S. Ciccariello, J. Goodisman, and H. Brumberger. On the Porod Law. *J. Appl. Crystallogr.*, 21:117 – 128, 1988.
- [32] P. Debye. Molecular-weight Determination by Light Scattering. *J. Phy. Colloid Chem.*, 51:18 – 32, 1947.
- [33] M. Malfois, F. Bonnete, L. Belloni, and A. Tardieu. A model of attractive interactions to account for fluid–fluid phase separation of protein solutions. *J. Chem. Phys.*, 105:3290 – 3300, 1996.
- [34] M.J. Grimson. Small-angle Scattering from Colloidal Dispersions. *J. Chem. Soc., Faraday Trans. 2*, 79:817 – 832, 1983.
- [35] A. Tardieu, A. Le Verge, M. Malfois, F. Bonnete, S. Finet, M. Ries-Kautt, and L. Belloni. Proteins in solution: from X-ray scattering intensities to interaction potentials. *J. Crys. Growth*, 196:193 – 203, 1999.
- [36] V.K. Kelkar, J. Narayanan, and C. Manohar. Structure Factor for Colloidal Dispersions. Use of Exact Potentials in Random Phase Approximation. *Langmuir*, 8:2210 – 2214, 1992.
- [37] N. Javid, K. Vogtt, C. Krwka, M. Tolan, and R. Winter. Protein-Protein Interactions in Complex Cosolvent Solutions. *ChemPhysChem*, 8:679 – 689, 2007.

- [38] H.B. Stuhrmann. Interpretation of small-angle scattering functions of diluted solutions and gases. A representation of the structures related to a one-particle-scattering function. *Acta Crystallogr.*, 26:297 – 306, 1970.
- [39] H.B. Stuhrmann. Ein neues Verfahren zur Bestimmung der Oberflächenform und der inneren Struktur von gelösten globularen Proteinen aus Roentgenkleinwinkelstreuungsmessungen. *Zeitschrift für Physikalische Chemie (Neue Folge)*, 72:177 – 198, 1970.
- [40] S.C. Harrison. Structure of tomato bushy stunt virus. The spherical averaged electron density. *J. Membr. Biol.*, 42:457 – 483, 1969.
- [41] D.I. Svergun. Restoring three-dimensional structure of biopolymers from solution scattering. *J. Appl. Crystallogr.*, 30:792 – 797, 1997.
- [42] D.I. Svergun, V.V. Volkov, M.B. Kozin, and H.B. Stuhrmann. New Developments in Direct Shape Determination from Small-Angle Scattering. 2. Uniqueness. *Acta Crystallogr.*, A52:419 – 426, 1996.
- [43] H.D. Lüke. The Origins of the Sampling Theorem. *IEEE Communications Magazine*, 37:106 – 108, 1999.
- [44] C.E. Shannon. Communication in the Presence of Noise. *IEEE*, 86:447 – 457, 1998.
- [45] R.J. Marks II. *Introduction to Shannon Sampling and Interpolation Theory*. Springer-Verlag, New York, 1991.
- [46] R.J. Marks II, editor. *Advanced topics in Shannon sampling and interpolation theory*. Springer-Verlag, New York, 1993.
- [47] P. Chacon, F. Moran, J.F. Diaz, E. Pantos, and J.M. Andreu. Low-resolution structures of proteins in solution retrieved from X-ray scattering with a genetic algorithm. *Biophys. J.*, 74:2760 – 2775, 1998.
- [48] S. Kirkpatrick, C.D. Gelatt, and M.P. Vecchi. Optimization by simulated annealing. *Science*, 220:671 – 680, 1983.
- [49] D. Franke and D.I. Svergun. DAMMIF, a program for rapid ab-initio shape determination in small-angle scattering. *J. Appl. Crystallogr.*, 42:342 – 346, 2009.
- [50] L. Ingber. Simulated annealing: practise versus theory. *Mathematics and Computer Modelling*, 18:29 – 57, 1993.
- [51] M.B. Kozin and D.I. Svergun. Automated matching of high- and low-resolution structural models. *J. Appl. Crystallogr.*, 34:33 – 41, 2001.
- [52] P. Zipper, H. Durchschlag, and A. Krebs. *Modelling of biopolymers*. Royal Society of Chemistry, Cambridge, 2005.
- [53] P. Zipper and H. Durchschlag. Modeling Complex Biological Macromolecules: Reduction of Multibead Models. *J. Biol. Phys.*, 33:523 – 539, 2007.
- [54] D.I. Svergun, M.V. Petoukhov, and M.H.J. Koch. Determination of domain structure of proteins from X-ray solution scattering. *Biophys. J. Appl. Crystallogr.*, 80:2946 – 2953, 2001.
- [55] M.V. Petoukhov and D.I. Svergun. New methods for domain structure determination of proteins from solution scattering data. *J. Appl. Crystallogr.*, 36:540 – 544, 2003.
- [56] S. Haussühl. *Kristallstrukturbestimmung*. Verlag Chemie, Weinheim, 1979.
- [57] J. Als-Nielsen and D. McMorrow. *Elements of Modern X-Ray Physics*. Wiley, New York, 2001.

- [58] T.R. Jensen and K. Kjaer. *Novel methods to study interfacial layers.*, chapter Structural properties and interactions of thin films at the air-liquid interface explored by synchrotron X-ray scattering., pages 205 – 254. Elsevier Science: Amsterdam, 2001.
- [59] R. Winter. Synchrotron X-ray and neutron small-angle scattering of lyotropic lipid mesophases, model biomembranes and proteins in solution at high pressure. *Biochim. Biophys. Acta*, 1595:160 – 184, 2002.
- [60] J. Bolze, T. Fujisawa, T. Nagao, K. Norisada, H. Saito, and A. Naito. Small angle X-ray scattering and ^{31}P NMR studies on the phase behavior of phospholipid bilayered mixed micelles. *Chemical Physical Letters*, 329:215 – 220, 2000.
- [61] M.R. Brzustowicz and A.T. Brunger. X-ray scattering from unilamellar lipid vesicles. *J. Appl. Crystallogr.*, 38:126–131, 2005.
- [62] T. Frühwirth, G. Fritz, N. Freiberger, and O. Glatter. Structure and order in lamellar phases determined by small-angle scattering. *J. Appl. Crystallogr.*, 37:703 – 710, 2004.
- [63] G. Pabst, R. Koschuch, B. Pozo-Navas, M. Rappolt, K. Lohner, and P. Laggnier. Structural analysis of weakly ordered membrane stacks. *J. Appl. Crystallogr.*, 36:1378 – 1388, 2003.
- [64] S. Haussühl. *Kristallgeometrie*. VCH, Weinheim, 1977.
- [65] G. Damaschun, J.J. Müller, and H.-V. Pürschel. Über die Mess-Strategie bei der Untersuchung der Röntgenkleinwinkelstreuung von verdünnten monodispersen Lösungen von Makromolekülen. *Monatsh. Chem.*, 99:2343 – 2348, 1968.
- [66] T. Narayanan, O. Diat, and P. Bösecke. SAXS and USAXS on the high brilliance beamline at the ESRF. *Nuclear Instruments and Methodes in Physics Research A*, 467 - 468:1005 – 1009, 2001.
- [67] J. Woenckhaus, Köhling R., P. Thiyagarajan, S. Finet, and R. Winter. High pressure-jump apparatus for kinetic studies of protein folding recations using the small-angle synchrotron X-ray scattering technique. *Rev. Sci. Instrum.*, 71:3895 – 3899, 2000.
- [68] J. Kraineva, R.A. Narayanan, E. Kondrashkina, P. Thiyagarajan, and R. Winter. Kinetics of Lamellar-to-Cubic and Intercubic Phase Transitions of Pure and Cytochrome c Containing Monoolein Dispersions Monitored by Time-Resolved Small-Angle X-ray Diffraction. *Langmuir*, 21:3559 – 3571, 2005.
- [69] T.C. Huang, H. Toraya, T.N. Blanton, and Y. Wu. X-ray Powder Diffraction Analysis of Silver Behenate, a Possible Low-Angle Diffraction Standard. *J. Appl. Crystallogr.*, 26:180 – 184, 1993.
- [70] J.S. Lamb, S. Cornaby, K. Andresen, L. Kwok, H.Y. Park, X. Qiu, D.-M. Smilgies, D.H. Bilderback, and L. Pollack. Focusing capillary optics for use in solution small-angle X-ray scattering. *J. Appl. Crystallogr.*, 40:193 – 195, 2007.
- [71] T.P. Russel. An absolute intensity standard for small-angle X-ray scattering measured with position sensitive detectors. *J. Appl. Crystallogr.*, 16:473 – 478, 1983.
- [72] D. Orthaber, A. Bergmann, and O. Glatter. SAXS experiments on absolute scale with Kratky systems using water as a secondary standard. *J. Appl. Crystallogr.*, 33:218 – 225, 2000.
- [73] G.D. Wignall and F.S. Bates. Absolute calibration of small-angle neutron scattering data. *J. Appl. Crystallogr.*, 20:28 – 40, 1987.
- [74] M. Okada and H. Iwasaki. X-ray diamond anvil cell and Pseudo-Kossel line pattern. *physica status solidi (a)*, 58:623 – 628, 1980.
- [75] A. Shiryaev, K. Dembo, Y. Klyuev, A. Naletovb, and B. Feigelson. Small-angle X-ray scattering of extended defects in diamonds. *J. Appl. Crystallogr.*, 36:420 – 424, 2003.

- [76] J. Soler. A Numerical Slit-Hight Correction in Small-Angle Scattering without Spherical Symmetry. *J. Appl. Crystallogr.*, 10:444 – 449, 1977.
- [77] J. Mazur and A.M. Wims. A Formal Solution for Slit Corrections in Small-Angle X-Ray Scattering. *Journal of Research of the National Bureau of Standards - A. Physics and Chemistry and Physics of Lipids*, 70A: 467 – 471, 1966.
- [78] J. Schelten and R.W. Hendricks. Recent Developments in X-ray and Neutron Small-Angle Scattering Instrumentation and Data Analysis. *J. Appl. Crystallogr.*, 11:297 – 324, 1978.
- [79] M. Deutsch. The Primitive Function for Slit-Hight Desmearing in SAXS. *J. Appl. Crystallogr.*, 20:179 – 181, 1987.
- [80] M. Soliman, B.-J. Jungnickel, and E. Meister. Stable Desmearing of Slit-Collimated SAXS Patterns by Adequate Numerical Conditioning. *Acta Crystallogr.*, A54:675 – 681, 1998.
- [81] O. Glatter and K. Gruber. Indirect Transformation in Reciprocal Space: Desmearing of Small-Angle Scattering Data from Partially Ordered Systems. *J. Appl. Crystallogr.*, 26:512 – 518, 1993.
- [82] D.I. Svergun, M.V. Petoukhov, and M.H.J. Koch. Determination of Domain Structure of Proteins from X-Ray Solution Scattering. *Biophys. J.*, 80:2946 – 2953, 2001.
- [83] D.I. Svergun, C. Barberato, and M.H.J. Koch. Crysol - a Program to Evaluate X-ray Solution Scattering of Biological Macromolecules from Atomic Coordinates. *J. Appl. Crystallogr.*, 28:768 – 773, 1995.
- [84] J. Als-Nielsen, D. Jacquemain, K. Kjaer, F. Leveiller, M. Lahav, and L. Leiserowitz. Principles and applications of grazing incidence X-ray and neutron scattering from ordered molecular monolayer at the air-water interface. *Physics Reports*, 246:251 – 313, 1994.
- [85] D. Jacquemain, S.G. Wolf, F. Leveiller, M. Deutsch, K. Kjaer, J. Als-Nielsen, M. Lahav, and L. Leiserowitz. Zweidimensionale Kristallographie an amphiphilen Molekülen an der Luft-Wasser-Grenzfläche. *Angew. Chem.*, 104:134 – 158, 1992.
- [86] M. Tolan and W. Press. X-ray and neutron reflectivity. *Z. Kristallogr.*, 213:319 – 336, 1998.
- [87] O. Brunkahl. *Introduction to X-ray Reflectometry (XRR)*. Institute of Inorganic Chemistry, Frankfurt, j.-w.-goethe university edition, 2007.
- [88] M. Krumrey, M. Hoffmann, and M. Kolbe. Schichtdickenbestimmung mit Röntgenreflektometrie. *Sonderdruck aus PTB-Mitteilungen*, 115 Heft 3:38 – 40, 2005.
- [89] M. Paulus. *Röntgenstreuung an Flüssigkeits-Gas Grenzflächen*. PhD thesis, Universität Dortmund, FB Physik, 2006.
- [90] D.K.G. de Boer, A.J.G. Leenaers, and W.W. von den Hoogenhof. Glancing-Incidence X-Ray Analysis of Thin-Layered Materials: a Review. *X-Ray Spectrometry*, 24:91 – 102, 1995.
- [91] C. Czeslik. *Neutronenreflektometrie.*, 2006.
- [92] T. Salditt, C. Li, A. Spaar, and U. Mennicke. X-ray reflectivity of solid-supported, multilamellar membranes. *Eur. Phys. J. E*, 7:105 – 116, 2002.
- [93] L.G. Parratt. Surface Studies of Solids by Total Reflection of X-rays. *Phys. Rev.*, 95:359 – 369, 1954.
- [94] A. Biermanns. *Röntgenreflektometrie zur Untersuchung von Oberflächen und dünnen Schichtsystemen*. Technical report, Universität Siegen, Festkörperphysik, 2007.
- [95] S.K. Sinha, E.B. Sirota, S. Garoff, and H.B. Stanley. X-ray and neutron scattering from rough surfaces. *Phys. Rev. B*, 38:2297 – 2311, 1988.

- [96] R. Frahm, J. Weigelt, G. Meyer, and G. Materlik. X-ray undulator beamline BW1 at DORIS III. *Rev. Sci. Instrum.*, 66:1677 – 1680, 1995.
- [97] D.-M. Smilgies, N. Boudet, B. Struth, and O. Konovalov. Troika II: a versatile beamline for the study of liquid and solid interfaces. *J. Syn. Radiation*, 12:329 – 339, 2005.
- [98] R.G. Oliveira, E. Schneck, B.E. Quinn, O.V. Konovalov, C. Brandenburg, T. Gutschmann, T. Gill, C.B. Hanna, D.A. Pink, and M. Tanaka. Crucial roles of charged saccharide moieties in survival of gram negative bacteria against protamine revealed by combination of grazing incidence X-ray structural characterization and Monte Carlo simulations. *Phys. Rev. E*, 81:041901, 2010.
- [99] G.H. Vineyard. Grazing-incidence diffraction and the distorted-wave approximation for the study of surfaces. *Phys. Rev. B*, 26:4146 – 4159, 1982.
- [100] K. Kjaer. Some simple ideas on X-ray reflection and grazing incidence diffraction from thin surfactant films. *Physica B*, 198:100 – 109, 1994.
- [101] F. Leveiller, D. Jacquemain, L. Leiserowitz, K. Kjaer, and J. Als-Nielsen. Toward a Determination at Near Atomic Resolution of Two-Dimensional Crystal Structures of Amphiphilic Molecules on the Water Surface. A Study Based on Grazing Incidence Synchrotron X-ray Diffraction and Lattice Energy Calculations. *J. Phys. Chem.*, 96:10380 – 10389, 1992.
- [102] L. Stryer. *Biochemie*. Spektrum Akademischer Verlag, Heidelberg, Berlin, Oxford, 2. korr. nachdruck edition, 1994.
- [103] T.E. Creighton. *Proteins*. W. H. Freeman and Company, New York, 1. auflage edition, 1984.
- [104] R. Winter and C. Jeworrek. Effect of pressure on membranes. *Soft Matter*, 5:3157 – 3173, 2009.
- [105] R. Winter and C. Czeslik. Pressure effects on the structure of lyotropic lipid mesophases and model biomembrane systems. *Z. Kristallogr.*, 215:454 – 474, 2000.
- [106] R. Winter, J. Erbes, R.H. Templer, J.M. Seddon, A. Syrykh, N.A. Warrender, and G. Rapp. Inverse Bicontinuous Cubic Phases in Fatty Acid/Phosphatidylcholine Mixtures. The Effects of Pressure and Lipid Composition. *Phys. Chem. Chem. Phys.*, 1:887 – 893, 1999.
- [107] R. Winter. Struktur und Dynamik von Modell-Biomembranen. *Chemie in unserer Zeit*, 24 (2):71 – 81, 1990.
- [108] C.M. Dobson. Principles of protein folding, misfolding and aggregation. *Seminars in Cell & Developmental Biology*, 15:3 – 16, 2004.
- [109] V.N. Uversky and A.L. Fink. Conformational constraints for amyloid fibrillation: the importance of being unfolded. *Biochim. Biophys. Acta*, 1698:131 – 153, 2004.
- [110] T.R. Jahn and S.E. Radford. The yin and yang of protein folding. *FEBS J.*, 272:5962 – 5970, 2005.
- [111] D.J. Selkoe. Folding proteins in fatal ways. *Nature*, 426:900 – 904, 2003.
- [112] G.B. Irvine, O.M. El-Agnaf, G.M. Shankar, and D.M. Walsh. Protein aggregation in the brain: the molecular basis for Alzheimer’s and Parkinson’s diseases. *Molecular medicine*, 14:451 – 464, 2008.
- [113] B.E. García-Moreno, J.J. Dwyer, A.G. Gittis, E.E. Lattman, D.S. Spencer, and W.E. Stites. Experimental measurement of the effective dielectric in the hydrophobic core of a protein. *Biophys. Chem.*, 64:211 – 224, 1997.
- [114] D.A. Karp, A.G. Gittis, M.R. Stahley, C.A. Fitch, W.E. Stites, and E.B. Garcia-Moreno. High apparent dielectric constant inside a protein reflects structural reorganization coupled to the ionization of an internal Asp. *Biophys. J.*, 92:2041 – 2053, 2007.

- [115] D.A. Karp, M.R. Stahley, and E.B. Garcia-Moreno. Conformational consequences of ionization of Lys, Asp, and Glu buried at position 66 in staphylococcal nuclease. *Biochemistry*, 49:4138 – 4146, 2010.
- [116] D.G. Isom, B.R. Cannon, C.A. Castaneda, A. Robinson, and B. Garcia-Moreno. High tolerance for ionizable residues in the hydrophobic interior of proteins. *Proc. Natl. Acad. Sci. U. S. A.*, 105:17784 – 17788, 2008.
- [117] D.G. Isom, C.A. Castañeda, B.R. Cannon, P.D. Velu, and E.B. García-Moreno. Charges in the hydrophobic interior of a protein. *Proc. Natl. Acad. Sci. U. S. A.*, 107:16096 – 16100, 2010.
- [118] C.A. Royer. Revisiting volume changes in pressure-induced protein unfolding. *Biochim. Biophys. Acta*, 1595:201 – 209, 2002.
- [119] J.L. Silva, D. Foguel, and C.A. Royer. Pressure provides new insights into protein folding, dynamics and structure. *Trends Biochem. Sci.*, 26:612 – 618, 2001.
- [120] S. Perrett and J.M. Zhou. Expanding the pressure technique: insights into protein folding from combined use of pressure and chemical denaturants. *Biochim. Biophys. Acta*, 1595:210 – 223, 2002.
- [121] C. Czeslik. Factors Ruling Protein Adsorption. *Z. Phys. Chem.*, 218:771 – 801, 2004.
- [122] J.J. Gray. The interaction of proteins with solid surfaces. *Curr. Opin. Struct. Biol.*, 14:110 – 115, 2004.
- [123] W.E. Stites, A.G. Gittis, E.E. Lattman, and D. Shortle. In a staphylococcal nuclease mutant the side-chain of a lysine replacing valine 66 is fully buried in the hydrophobic core. *J. Mol. Biol.*, 221:7 – 14, 1991.
- [124] K.L. Baran, M.S. Chimenti, J.L. Schlessman, C.A. Fitch, K.J. Herbst, and B.E. Garcia-Moreno. Electrostatic effects in a network of polar and ionizable groups in staphylococcal nuclease. *J. Mol. Biol.*, 379:1045 – 1062, 2008.
- [125] C.A. Castaneda, C.A. Fitch, A. Majumdar, V. Khangulov, J.L. Schlessman, and B.E. Garcia-Moreno. Molecular determinants of the pK_a values of Asp and Glu residues in staphylococcal nuclease. *Proteins*, 77: 570 – 588, 2009.
- [126] M.S. Chimenti, C.A. Castaneda, A. Majumdar, and B. Garcia-Moreno. Structural origins of high apparent dielectric constants experienced by ionizable groups in the hydrophobic core of a protein. *J. Mol. Biol.*, 405:361 – 377, 2011.
- [127] C.A. Fitch, D.A. Karp, K.K. Lee, W.E. Stites, E.E. Lattman, and E.B. Garcia-Moreno. Experimental pK(a) values of buried residues: analysis with continuum methods and role of water penetration. *Biophys. J.*, 82:3289 – 3304, 2002.
- [128] Y. Takayama, C.A. Castaneda, M. Chimenti, E.B. Garcia-Moreno, and J. Iwahara. Direct evidence for deprotonation of a lysine side chain buried in the hydrophobic core of a protein. *J. Am. Chem. Soc.*, 130: 6714 – 6715, 2008.
- [129] G. Panick, G.J.A. Vidugiris, R. Malessa, G. Rapp, R. Winter, and C.A. Royer. Exploring the temperature-pressure phase diagram of staphylococcal nuclease. *Biochemistry*, 38:4157 – 4164, 1999.
- [130] R. Ravindra and R. Winter. On the temperature—pressure free-energy landscape of proteins. *ChemPhys-Chem.*, 4:359 – 365, 2003.
- [131] L. Brun, D.G. Isom, P. Velu, B. Garcia-Moreno, and C.A. Royer. Hydration of the folding transition state ensemble of a protein. *Biochemistry*, 45:3473 – 3480, 2006.
- [132] Z. Zheng and T.R. Sosnick. Protein vivisection reveals elusive intermediates in folding. *J. Mol. Biol.*, 397: 777 – 788, 2010.

- [133] L. Mitra, K. Hata, R. Kono, A. Maeno, D. Isom, J.B. Rouget, R. Winter, K. Akasaka, B. Garcia-Moreno, and C.A. Royer. V(i)-value analysis: a pressure-based method for mapping the folding transition state ensemble of proteins. *J. Am. Chem. Soc.*, 129:14108 – 14109, 2007.
- [134] L. Becucci, A. Santucci, and R. Guidelli. Gramicidin conducting dimers in lipid bilayers are stabilized by single-file ionic flux along them. *J. Phys. Chem. B*, 111:9814 – 9820, 2007.
- [135] J. Eisenblätter and R. Winter. Pressure effects on the structure and phase behavior of DMPC-gramicidin lipid bilayers: a synchrotron SAXS and ^2H -NMR spectroscopy study. *Biophys. J.*, 90:956 – 966, 2006.
- [136] B.A. Wallace. Gramicidin channels and pores. *Annu. Rev. Biophys. Chem.*, 19:127 – 157, 1990.
- [137] B.A. Wallace. Recent Advances in the High Resolution Structures of Bacterial Channels: Gramicidin A. *J. Struct. Biol.*, 121:123 – 141, 1998.
- [138] R.R. Ketchum, B. Roux, and T.A. Cross. High-resolution polypeptide structure in a lamellar phase lipid environment from solid state NMR derived orientational constraints. *Structure*, 5:1655 – 1669, 1997.
- [139] D.A. Langs. Three-dimensional structure at 0.86 Å of the uncomplexed form of the transmembrane ion channel peptide gramicidin A. *Science*, 241:188 – 191, 1988.
- [140] B.M. Burkhardt, R.M. Gassman, D.A. Langs, W.A. Pangborn, and W.L. Duax. Heterodimer formation and crystal nucleation of gramicidin D. *Biophys. J.*, 75:2135 – 2146, 1998.
- [141] J. Eisenblätter and R. Winter. Pressure effects on the structure and phase behavior of phospholipid-gramicidin bilayers. *Defects and diffusion forum vols.*, 208 - 209:35 – 46, 2002.
- [142] J. Eisenblätter and R. Winter. Pressure effects on the structure and phase behavior of phospholipid-polypeptide bilayers - a synchrotron small angle X-ray scattering and ^2H -NMR spectroscopy study on DPPC-gramicidin lipid bilayers. *Z. Phys. Chem.*, 219:1321 – 1345, 2005.
- [143] M. Lorizate, N. Haurte, A. Saez-Cirion, and J.L. Nieva. Interfacial pre-transmembrane domains in viral proteins promoting membrane fusion and fission. *Biochim. Biophys. Acta*, 1778:1624 – 1639, 2008.
- [144] J.M. White, S.E. Delos, M. Brecher, and K. Schornberg. Structure and mechanism of viral membrane fusion proteins: multiple variations on a common theme. *Crit. Rev. Biochem. Mol. Biol.*, 43:189 – 219, 2008.
- [145] G. Basanez. Membrane fusion: the process and its energy suppliers. *Cell. Mol. Life Sci.*, 59:1478 – 1490, 2002.
- [146] J.L. Nieva and A. Agirre. Are fusion peptides a good model to study viral cell fusion? *Biochim. Biophys. Acta*, 1614:104 – 115, 2003.
- [147] R.M. Epand. Fusion peptides and the mechanism of viral fusion. *Biochim. Biophys. Acta*, 1614:116 – 121, 2003.
- [148] S.G. Peisajovich and Y. Shai. Viral fusion proteins: multiple regions contribute to membrane fusion. *Biochim. Biophys. Acta*, 1614:122 – 129, 2003.
- [149] B. Schroth-Diez, K. Ludwig, B. Baljinyam, C. Kozerski, Q. Huang, and A. Herrmann. The Role of the Transmembrane and of the Intraviral Domain of Glycoproteins in Membrane Fusion of Enveloped Viruses. *Biosci. Rep.*, 20:571 – 595, 2000.
- [150] I. Martin and J.M. Ruysschaert. Common properties of fusion peptides from diverse systems. *Biosci. Rep.*, 20:483 – 500, 2000.
- [151] L.K. Tamm and X. Han. Viral fusion peptides: a tool set to disrupt and connect biological membranes. *Biosci. Rep.*, 20:501 – 518, 2000.

- [152] K. Weise and J. Reed. Fusion Peptides and Transmembrane Domains of Fusion Proteins are Characterized by Different but Specific Structural Properties. *ChemBioChem.*, 9:934 – 943, 2008.
- [153] M.W. Hofmann, K. Weise, J. Ollesch, P. Agrawal, H. Stalz, W. Stelzer, F. Hulsbergen, H. de Groot, K. Gerwert, J. Reed, and D. Langosch. De novo design of conformationally flexible transmembrane peptides driving membrane fusion. *Proc. Natl. Acad. Sci. U. S. A.*, 101:14776 – 14781, 2004.
- [154] L.J. Earp, S.E. Delos, H.E. Park, and J.M. White. The many mechanisms of viral membrane fusion proteins. *Curr. Top. Microbiol. Immunol.*, 285:25 – 66, 2005.
- [155] S.C. Harrison. Mechanism of membrane fusion by viral envelope proteins. *Adv. Virus Res.*, 64:231 – 261, 2005.
- [156] M. Kielian and F.A. Rey. Virus membrane-fusion proteins: more than one way to make a hairpin. *Nat. Rev. Microbiol.*, 4:67 – 76, 2006.
- [157] W. Weissenhorn, A. Hinz, and Y. Gaudin. Virus membrane fusion. *FEBS Lett.*, 581:2150 – 2155, 2007.
- [158] M. Scheibner, B. Hülsdau, K. Zelena, M. Nimtz, L. de Boer, R.G. Berger, and H. Zorn. Novel peroxidases of *Marasmius scorodoni* degrade β -carotene. *Appl. Microbiol. Biotechnol.*, 27:1241 – 1250, 2008.
- [159] V. Faraco, A. Piscitelli, G. Sannia, and P. Giardina. Identification of a new member of the dye-decolorizing peroxidase family from *Pleurotus ostreatus*. *World J. Microbiol. Biotechnol.*, 23:889 – 893, 2007.
- [160] B. Hülsdau. *Oxidativer Abbau von Carotinoiden durch Pilzenzyme*. PhD thesis, Gottfried Wilhelm Leibniz Universität, Hannover, 2007.
- [161] H. Bouws, A. Wattenberg, and H. Zorn. Fungal secretomes—nature’s toolbox for white biotechnology. *Appl. Microbiol. Biotechnol.*, 80:381 – 388, 2008.
- [162] H. Zorn, S. Langhoff, M. Scheibner, M. Nimtz, and R.G. Berger. A Peroxidase from *Lepista irina* cleaves β -carotene to flavour compounds. *Biol. Chem.*, 384:1049 – 1056, 2003.
- [163] F. Chiti and C.M. Dobson. Protein Misfolding, Functional Amyloid, and Human Disease. *Annu. Rev. Biochem.*, 75:333 – 366, 2006.
- [164] F.E. Cohen and J.W. Kelly. Therapeutic approaches to protein-misfolding diseases. *Nature*, 426:905 – 909, 2003.
- [165] C. Ege, J. Majewski, G. Wu, K. Kjaer, and K.Y.C. Lee. Templating Effect of Lipid Membranes on Alzheimer’s Amyloid β Peptide. *ChemPhysChem*, 6:226 – 229, 2005.
- [166] L.M. Yan, A. Velkova, M. Tatarek-Nossol, E. Andreetto, and A. Kapurniotu. Designed IAPP Mimic Blocks Ab Cytotoxic Self-Assembly: Cross-Suppression of Amyloid Toxicity of A β and IAPP Suggests a Molecular Link between Alzheimer’s Disease and Type 2 Diabetes. *Angew. Chem., Int. Ed.*, 46:1246 – 1252, 2007.
- [167] A. Velkova, M. Tatarek-Nossol, E. Andreetto, and A. Kapurniotu. Exploiting Cross-Amyloid Interactions to Inhibit Protein Aggregation but not Function: Nanomolar Affinity Inhibition of Insulin Aggregation by an IAPP mimic. *Angew. Chem., Int. Ed.*, 47:7114 – 7118, 2008.
- [168] E. Sparr, M.F.M. Engel, D.V. Sakharov, M. Sprong, J. Jacobs, B. de Kruijff, J.W.M. Höppener, and J.A. Killian. Islet amyloid polypeptide-induced membrane leakage involves uptake of lipids by forming amyloid fibers. *FEBS Lett.*, 577:117 – 120, 2004.
- [169] M.F.M. Engel, L. Khemtémourian, C.C. Kleijer, H.J.D. Meeldijk, J. Jacobs, A.J. Verkleij, B. de Kruijff, J.A. Killian, and J.W.M. Höppener. Membrane damage by human islet amyloid polypeptide through fibril growth at the membrane. *Proc. Natl. Acad. Sci. U. S. A.*, 105:6033 – 6038, 2008.

- [170] M.F.M. Engel. Membrane permeabilization by Islet Amyloid Polypeptide. *Chem. Phys. Lipids*, 160:1 – 10, 2009.
- [171] S.A. Jayasinghe and R. Langen. Lipid Membranes Modulate the Structure of Islet Amyloid Polypeptide. *Biochemistry*, 44:12113 – 12119, 2005.
- [172] M.F.M. Engel, H. Yigittop, R.C. Elgersma, D.T.S. Rijkers, R.M.J. Liskamp, B. de Kruijff, J.W.M. Höppener, and J.A. Killian. Islet amyloid polypeptide inserts into phospholipid monolayers as monomer. *J. Mol. Biol.*, 356:783 – 789, 2006.
- [173] S. Jha, D. Sellin, R. Seidel, and R. Winter. Amyloidogenic propensities and conformational properties of ProIAPP and IAPP in the presence of lipid bilayer membranes. *J. Mol. Biol.*, 389:907 – 920, 2009.
- [174] F. Evers, C. Jeworrek, S. Tiemeyer, K. Weise, D. Sellin, M. Paulus, B. Struth, M. Tolan, and R. Winter. Elucidating the Mechanism of Lipid Membrane-Induced IAPP Fibrillogenesis and Its Inhibition by the Red Wine Compound Resveratrol: A Synchrotron X-ray Reflectivity Study. *J. Am. Chem. Soc.*, 131:9516 – 9521, 2009.
- [175] P.T. Wong, J.A. Schauerte, K.C. Wisser, H. Ding, E.L. Lee, D.G. Steel, and A. Gafni. Amyloid- β membrane binding and permeabilization are distinct processes influenced separately by membrane charge and fluidity. *J. Mol. Biol.*, 386:81 – 96, 2009.
- [176] E.Y. Chi, C. Ege, A. Winans, J. Majewski, G. Wu, K. Kjaer, and K.Y.C. Lee. Lipid membrane templates the ordering and induces the fibrillogenesis of Alzheimer's disease amyloid- β peptide. *Proteins*, 72:1 – 24, 2008.
- [177] C. Aisenbrey, T. Borowik, R. Byström, M. Bokvist, F. Lindström, H. Misiak, M.A. Sani, and G. Gröbner. How is protein aggregation in amyloidogenic diseases modulated by biological membranes? *Eur. Biophys. J.*, 37:247 – 255, 2008.
- [178] P. Westermark, C. Wernstedt, E. Wilander, D.W. Hayden, T.D. O'Brien, and K.H. Johnson. Amyloid fibrils in human insulinoma and islets of Langerhans of the diabetic cat are derived from a neuropeptide-like protein also present in normal islet cells. *Proc. Natl. Acad. Sci. U. S. A.*, 84:3881 – 3885, 1987.
- [179] G.J. Cooper, A.C. Willis, A. Clark, R.C. Turner, R.B. Sim, and K.B. Reid. Purification and characterization of a peptide from amyloid-rich pancreases of type 2 diabetic patients. *Proc. Natl. Acad. Sci. U. S. A.*, 84:8628 – 8632, 1987.
- [180] L. Marzban, K. Park, and C.B. Verchere. Islet amyloid polypeptide and type 2 diabetes. *Exp. Gerontol.*, 38:347 – 351, 2003.
- [181] D.H.J. Lopes, A. Meister, A. Gohlke, A. Hauser, A. Blume, and R. Winter. Mechanism of Islet Amyloid Polypeptide Fibrillation at Lipid Interfaces Studied by Infrared Reflection Absorption Spectroscopy. *Biophys. J.*, 93:3132 – 3141, 2007.
- [182] J.A. Williamson and A.D. Miranker. Direct detection of transient α -helical states in islet amyloid polypeptide. *Protein Sci.*, 16:110 – 117, 2007.
- [183] R. Mishra, B. Bulic, D. Sellin, S. Jha, H. Waldmann, and R. Winter. Small Molecule Inhibitors of Islet Amyloid Polypeptide Fibril Formation. *Angew. Chem., Int. Ed.*, 47:4679 – 4682, 2008.
- [184] C. Jeworrek, O. Hollmann, R. Steitz, R. Winter, and C. Czeslik. Interaction of IAPP and Insulin with Model Interfaces Studied Using Neutron Reflectometry. *Biophys. J.*, 96:1115 – 1123, 2009.
- [185] G.G. Glenner and C.W. Wong. Alzheimer's disease: initial report of the purification and characterization of a novel cerebrovascular amyloid protein. *Biochem. Biophys. Res. Commun.*, 120:885 – 890, 1984.

- [186] E.G. Zinser, T. Hartmann, and M.O.W. Grimm. Amyloid beta-protein and lipid metabolism [Review]. *Biochim. Biophys. Acta, Biomembr.*, 1768:1991 – 2001, 2007.
- [187] J. Kang, H.G. Lemaire, A. Unterbeck, J.M. Salbaum, C.L. Masters, K.H. Grzeschik, G. Multhaup, K. Beyreuther, and B. Müller-Hill. The precursor of Alzheimer's disease amyloid A4 protein resembles a cell-surface receptor. *Nature*, 325:733 – 736, 1987.
- [188] G. Brezesinski, E. Maltseva, and H. Möhwald. Adsorption of Amyloid β (1-40) Peptide at Liquid Interfaces. *Z. Phys. Chem.*, 221:95 – 111, 2007.
- [189] M.R. Nicolls. The clinical and biological relationship between type II diabetes mellitus and Alzheimer's disease. *Curr. Alzheimer Res.*, 1:47 – 54, 2004.
- [190] Y. Fezoui and D.B. Teplow. Kinetic studies of amyloid β -protein fibril assembly - differential effects of α -helix stabilization. *J. Biol. Chem.*, 277:36948 – 36954, 2002.
- [191] A. Lomakin, D.S. Chung, G.B. Benedek, D.A. Kirschner, and D.B. Teplow. On the nucleation and growth of amyloid β protein fibrils: detection of nuclei and quantitation of rate constants. *Proc. Natl. Acad. Sci. U. S. A.*, 93:1125 – 1129, 1996.
- [192] R. Sabate and J. Estelrich. Evidence of the existence of micelles in the fibrillogenesis of β -amyloid peptide. *J. Phys. Chem. B*, 109:11027 – 11032, 2005.
- [193] B. Soreghan, J. Kosmoski, and C. Glabe. Surfactant properties of Alzheimer's A β peptides and the mechanism of amyloid aggregation. *J. Biol. Chem.*, 269:28551 – 28554, 1994.
- [194] P. Seubert, C. Vigo-Pelfrey, F. Esch, M. Lee, H. Dovey, D. Davis, S. Sinha, M. Schiossmacher, J. Whaley, C. Swindlehurst, R. McCormack, R. Wolfert, D. Selkoe, I. Lieberburg, and D. Schenk. Isolation and quantification of soluble Alzheimer's bold β -peptide from biological fluids. *Nature*, 359:325 – 327, 1992.
- [195] B. Bulic, M. Pickhardt, I. Khlistunova, J. Biernat, E.M. Mandelkow, E. Mandelkow, and H. Waldmann. Rhodanine-based Tau Aggregation Inhibitors in Cell Models of Tauopathy. *Angew. Chem., Int. Ed.*, 46: 9215 – 9219, 2007.
- [196] Y. Porat, A. Abramowitz, and E. Gazit. Inhibition of Amyloid Fibril Formation by Polyphenols: Structural Similarity and Aromatic Interactions as a Common Inhibition Mechanism. *Chem. Biol. Drug Des.*, 67:27 – 37, 2006.
- [197] P. Marambaud, H. Zhao, and P. Davies. Resveratrol Promotes Clearance of Alzheimer's Disease Amyloid- β Peptides. *J. Biol. Chem.*, 280:37377 – 37382, 2005.
- [198] C.R.H. Raetz. Biochemistry of endotoxins. *Annu. Rev. Biochem.*, 59:129 – 170, 1990.
- [199] S.M. Gruner, P.R. Hope, and C.P.S. Tilcock. Lipid polymorphism: the molecular basis of nonbilayer phases. *Annu. Rev. Biophys. Chem.*, 14:211 – 238, 1985.
- [200] J.M. Seddon. Structure of the inversed hexagonal phase, and non-lamellar phase transitions of lipids. *Biochim. Biophys. Acta, Biomembr.*, 1031:1 – 69, 1990.
- [201] G. Cevc, editor. *Phospholipids Handbook*. Marcel Dekker: New York, 1993.
- [202] R. Lipowski and E. Sackmann, editors. *Structure and Dynamics of Membranes*. Elsevier Science: Amsterdam, 1995.
- [203] C. Czeslik, O. Reis, R. Winter, and G. Rapp. Effect of high pressure on the structure of dipalmitoylphosphatidylcholine bilayer membranes: a synchrotron-X-ray diffraction and FT-IR spectroscopy study using the diamond anvil technique. *Chem. Phys. Lipids*, 91:135 – 144, 1998.

- [204] C.V. Kulkarni, W. Wachter, G. Iglesias-Salto, S. Engelskirchen, and S. Ahualli. Monoolein: a magic lipid? *Phys. Chem. Chem. Phys.*, 13:3004 – 3021, 2011.
- [205] K. Simons and W.L. Vaz. Model systems, lipid rafts, and cell membranes. *Annu. Rev. Biophys. Biomol. Struct.*, 33:269 – 295, 2004.
- [206] R.G.W. Anderson and K. Jacobson. A Role for Lipid Shells in Targeting Proteins to Caveolae, Rafts, and Other Lipid Domains. *Science*, 296:1821 – 1825, 2002.
- [207] M. Edidin. The State of Lipid Rafts: From Model Membranes to Cells. *Annu. Rev. Biophys. Biomol. Struct.*, 32:257 – 283, 2003.
- [208] O.G. Mouritsen and M.J. Zuckermann. What’s so special about cholesterol? *Lipids*, 39:1101 – 1113, 2004.
- [209] R. Winter, D. Lopes, S. Grudzielanek, and K. Vogtt. Towards an Understanding of the Temperature / Pressure Configurational and Free-Energy Landscape of Biomolecules. *J. Non-Equilib. Thermodyn.*, 32:41 – 97, 2007.
- [210] K. Simons and E. Ikonen. Functional raft membranes in cell membranes. *Nature*, 387:569 – 572, 1997.
- [211] C. Dietrich, L.A. Bagatolli, Z.N. Volovyk, N.L. Thompson, M. Levi, K. Jacobson, and E. Gratton. Lipid rafts reconstituted in model membranes. *Biophys. J.*, 80:1417 – 1428, 2001.
- [212] D.A. Brown and E. London. Functions of lipid rafts in biological membranes. *Annu. Rev. Cell Dev. Biol.*, 14:111 – 136, 1998.
- [213] S. Janosch, C. Nicolini, B. Ludolph, C. Peters, M. Völkert, T.L. Hazlet, E. Gratton, H. Waldmann, and R. Winter. Partitioning of Dual-lipidated Peptides into Membrane Microdomains - Lipid Sorting vs. Peptide Aggregation. *J. Am. Chem. Soc.*, 126:7496 – 7503, 2004.
- [214] C. Nicolini, J. Baranski, S. Schlummer, J. Palomo, M. Lumbierres-Burgues, M. Kahms, J. Kuhlmann, S. Sanchez, E. Gratton, H. Waldmann, and R. Winter. Visualizing Association of N-Ras in Lipid Microdomains: Influence of Domain Structure and Interfacial Adsorption. *J. Am. Chem. Soc.*, 128:192 – 201, 2006.
- [215] K. Simons and R. Ehehalt. Cholesterol, lipid rafts, and disease. *J. Clin. Invest.*, 110:597 – 603, 2002.
- [216] S. Kapoor, A. Werkmüller, C. Denter, Y. Zhai, J. Markgraf, K. Weise, N. Opitz, and R. Winter. Temperature-Pressure Phase Diagram of a Heterogeneous Anionic Model Biomembrane System: Results from a Combined Calorimetry, Spectroscopy and Microscopy Study. *Biochim. Biophys. Acta, Biomembr.*, 1808:1187 – 1195, 2011.
- [217] K. Weise, D. Radovan, A. Gohke, N. Opitz, and R. Winter. Interaction of hIAPP with Model Raft Membranes and Pancreatic β -cells: Cytotoxicity of hIAPP Oligomers. *ChemBioChem*, 11:1280 – 1290, 2010.
- [218] T. Baumgart, A. Hammond, P. Sengupta, S. Hess, D. Holowka, B. Baird, and W.W. Webb. Large-Scale Fluid/Fluid Phase Separation of Proteins and Lipids in Giant Plasma Membrane Vesicles. *Proc. Natl. Acad. Sci. U. S. A.*, 104:3165 – 3170, 2007.
- [219] D. Lingwood, J. Ries, P. Schuille, and K. Simons. Plasma membranes are poised for activation of raft phase coalescence at physiological temperature. *Proc. Natl. Acad. Sci. U. S. A.*, 105:10005 – 10010, 2008.
- [220] H.J. Risselada and S.J. Marrink. The molecular face of lipid rafts in model membranes. *Proc. Natl. Acad. Sci. U. S. A.*, 105:17367 – 17372, 2008.
- [221] S.C. Costigan, P.J. Booth, and R.H. Templer. Estimations of lipid bilayer geometry in fluid lamellar phases. *Biochim. Biophys. Acta*, 1468:41 – 54, 2000.

- [222] G. Tresset. The multiple faces of self-assembled lipidic systems. *PMC Biophysics*, 2::3, 2009.
- [223] C.V. Kulkarni, T.-Y. Tang, A. Seddon, J.M. Seddon, O. Ces, and R.H. Templer. Engineering bicontinuous cubic structures at the nanoscale - the role of chain splay. *Soft Matter*, 6:3191 – 3194, 2010.
- [224] R. Templer. Thermodynamic and theoretical aspects of cubic mesophases in nature and biological amphiphiles. *Curr. Opin. Colloid Interface Sci.*, 3:255 – 263, 1998.
- [225] C.E. Conn, O. Ces, A.M. Squires, X. Mulet, R. Winter, S.M. Finet, R.H. Templer, and J.M. Seddon. A Pressure-Jump Time-Resolved X-ray Diffraction Study of Cubic-Cubic Transition Kinetics in Monoolein. *Langmuir*, 24:2331–2340, 2008.
- [226] E.A. Lord and A.L. Mackay. Periodic minimal surfaces of cubic symmetry. *Current Science*, 85:346 – 362, 2003.
- [227] K. Larsson. Aqueous dispersions of cubic lipid-water phases. *Curr. Opin. Colloid Interface Sci.*, 5:64 – 69, 2000.
- [228] K. Larsson and F. Tiberg. Periodic minimal surface structures in bicontinuous lipid-water phases and nanoparticles. *Curr. Opin. Colloid Interface Sci.*, 9:365 – 369, 2005.
- [229] D. Yang, B. Armitage, and S.R. Marder. Cubic Liquid-Crystalline Nanoparticles. *Angew. Chem., Int. Ed.*, 43:4402 – 4409, 2004.
- [230] J.D. Enlow. *Mathematical Modelling of Surfactant Liquid Crystal X-ray Diffraction*. PhD thesis, University of Otago, Dunedin, New Zealand, 2002.
- [231] K. Weierstraß. Über die Flächen deren mittlere Krümmung überall gleich null ist. *Monatsber. Berliner Akad.*, 3:312 – 625, 1866.
- [232] J.D. Enlow, R.L. Enlow, K.M. McGrath, and M.W. Tate. Modeling liquid crystal bilayer structures with minimal surfaces. *J. Phys. Chem.*, 120:1981 – 1989, 2004.
- [233] D.P. Siegel. Fourth-Order Curvature Energy Model for the Stability of Bicontinuous Inverted Cubic Phases in Amphiphile-Water Systems. *Langmuir*, 26:8673 – 8683, 2010.
- [234] T.A. Harroun, M. Koslowsky, M.-P. Nieh, C.-F. de Lannoy, V.A. Raghunathan, and J. Katsaras. Comprehensive Examination of Mesophases Formed by DMPC and DHPC Mixtures. *Langmuir*, 21:5356 – 5361, 2005.
- [235] J. Katsaras, T.A. Harroun, J. Pencer, and M.-P. Nieh. "Bicellar" lipid mixtures as used in biochemical and biophysical studies. *Naturwissenschaften*, 92:355 – 366, 2005.
- [236] M.-P. Nieh, V.A. Raghunathan, C.J. Glinka, T.A. Harroun, G. Papst, and J. Katsaras. Magnetically Alignable Phase of Phospholipid "Bicelle" Mixtures Is a Chiral Nematic Made Up of Wormlike Micelles. *Langmuir*, 20:7893 – 7897, 2004.
- [237] M. Kozak, M. Kempka, K. Szpotkowski, and S. Jurga. NMR in soft materials: A study of DMPC/DHPC bicellar system. *J. Non-Cryst. Solids*, 353:4246 – 4251, 2007.
- [238] L. van Dam, G. Karlsson, and K. Edwards. Direct observation and characterization of DMPC/DHPC aggregates under conditions relevant for biological solution NMR. *Biochim. Biophys. Acta*, 1664:241 – 255, 2004.
- [239] L. van Dam, G. Karlsson, and K. Edwards. Morphology of Magnetically Aligning DMPC/DHPC Aggregates - Perforated Sheets, Not Disks. *Langmuir*, 22:3280 – 3285, 2006.

- [240] J.A. Whiles, R. Deems, R.R. Vold, and E.A. Dennis. Bicelles in structure-function studies of membrane-associated proteins. *Bioorg. Chem.*, 30:431 – 442, 2002.
- [241] C.R. Sanders and K. Oxenoid. Customizing model membranes and samples for NMR spectroscopic studies of complex membrane proteins. *Biochim. Biophys. Acta*, 1508:129 – 145, 2000.
- [242] R.R. Vold, R.S. Prosser, and A.J. Deese. Isotropic solutions of phospholipid bicelles: A new membrane mimetic for high-resolution NMR studies of polypeptides. *J. Biomol. NMR*, 9:329 – 335, 1997.
- [243] E. Brunner, M.R. Arnold, W. Kremer, and H.R. Kalbitzer. Pressure-stability of phospholipid bicelles: measurement of residual dipolar couplings under extreme conditions. *J. Biomol. NMR*, 21:173 – 176, 2001.
- [244] C.R. Sanders and G.C. Landis. Facile Acquisition and Assignment of Oriented Sample NMR Spectra for Bilayer Surface-Associated Proteins. *J. Am. Chem. Soc.*, 116:6470 – 6471, 1994.
- [245] A. Goffeau. Life with 482-genes. *Science*, 270:445 – 446, 1995.
- [246] J. Struppe, J.A. Whiles, and R.R. Vold. Acidic phospholipid bicelles: a versatile model membrane system. *Biophys. J.*, 78:281 – 289, 2000.
- [247] J. Katsaras, R.L. Donaberger, I.P. Swainson, D.C. Tennant, Z. Tun, R.R. Vold, and R.S. Prosser. Rarely Observed Phase Transitions in a Novel Lyotropic Liquid Crystal System. *Phys. Rev. Lett.*, 78:899 – 902, 1997.
- [248] S. Faham and J.U. Bowie. Bicelle crystallization: a new method for crystallizing membrane proteins yields a monomeric bacteriorhodopsin structure. *J. Mol. Biol.*, 316:1 – 6, 2002.
- [249] L.A. Holland and A.M. Leigh. Bilayered phospholipid micelles and capillary electrophoresis: A new additive for electrokinetic chromatography. *Electrophoresis*, 24:2935 – 2939, 2003.
- [250] T. Kreuzig. *Kurzlehrbuch Biochemie*. Urban & Fischer, München, Jena, 11. auflage edition, 2002.
- [251] R.P. Longley, A.H. Rose, and B.A. Knights. Composition of the protoplast membrane from *Saccharomyces cerevisiae*. *Biochem. J.*, 108:401 – 412, 1968.
- [252] G. Tuller, T. Nemeč, C. Hrastnik, and G. Daum. Lipid composition of subcellular membranes of an FY1679-derived haploid yeast wild-type strain grown on different carbon sources. *Yeast*, 15:1555 – 1564, 1999.
- [253] F. Bracher. Angriffspunkt Ergosterolbiosynthese. Wirkstoffe und Wirkprinzipien. *Pharm. Unserer Zeit*, 32: 118 – 123, 2003.
- [254] I.S. Mysiakina and N.S. Funtikova. The role of sterols in morphogenetic processes and dimorphism in fungi. *Mikrobiologiya*, 76:1 – 13, 2007.
- [255] J.A. Urbina, S. Pekerar, H.B. Le, J. Patterson, B. Montez, and E. Oldfield. Molecular order and dynamics of phosphatidylcholine bilayer membranes in the presence of cholesterol, ergosterol and lanosterol: a comparative study using ^2H -, ^{13}C - and ^{31}P -NMR spectroscopy. *Biochim. Biophys. Acta*, 1238:163 – 176, 1995.
- [256] X. Xu, R. Bittman, G. Duportail, D. Heissler, C. Vilcheze, and E. London. Effect of the structure of natural sterols and sphingolipids on the formation of ordered sphingolipid/sterol domains (rafts). Comparison of cholesterol to plant, fungal, and disease-associated sterols and comparison of sphingomyelin, cerebroside, and ceramide. *J. Biol. Chem.*, 276:33540 – 33546, 2001.
- [257] R.J. Rodriguez, C. Low, C.D. Bottema, and L.W. Parks. Multiple functions for sterols in *Saccharomyces cerevisiae*. *Biochim. Biophys. Acta*, 837:336 – 343, 1985.

- [258] Y.W. Hsueh, K. Gilbert, C. Trandum, M. Zuckermann, and J. Thewalt. The effect of ergosterol on dipalmitoylphosphatidylcholine bilayers: a deuterium NMR and calorimetric study. *Biophys. J.*, 88:1799 – 1808, 2005.
- [259] P. Mariani, F. Rustichelli, and L. Saturni. Stabilization of the monoolein $Pn3m$ cubic structure on trehalose glasses. *Eur. Biophys. J.*, 28:294 – 301, 1999.
- [260] M. Pisani, S. Bernstor, C. Ferrero, and P. Mariani. Pressure induced cubic-to-cubic phase transition in monoolein hydrated system. *J. Phys. Chem. B*, 105:3109 – 3119, 2001.
- [261] H. Takahishi, A. Matsuo, and I. Hatta. Effects of salt on the lamellar and bicontinuous cubic phases of fully hydrated monoacylglycerol. *Phys. Chem. Chem. Phys.*, 4:2365 – 2370, 2002.
- [262] A. Angelova, M. Ollivon, A. Campitelli, and C. Bourgaux. Detailed Structure of Diamond-Type Lipid Cubic Nanoparticles. *Langmuir*, 19:6928 – 6935, 2003.
- [263] J. Lendermann and R. Winter. Interaction of Cytochrome c with Cubic Monoolein Mesophases under Limited Hydration Conditions: The Effects of Concentration, Temperature and Pressure. *Phys. Chem. Chem. Phys.*, 5:1440 – 1450, 2003.
- [264] H. Qui and M. Caffrey. The phase diagram of the monoolein/water system: metastability and equilibrium aspects. *Biomaterials*, 21:223 – 234, 2000.
- [265] E.T. Rietschel, T. Kirikae, F.U. Schade, U. Mamat, G. Schmidt, H. Loppnow, A.J. Ulmer, U. Zähringer, U. Seydel, F. Di Padova, M. Schreier, and H. Brade. Bacterial endotoxin: molecular relationships of structure to activity and function. *FASEB J.*, 8:217 – 225, 1994.
- [266] K. Brandenburg, J. Andrä, M. Müller, M.H.J. Koch, and P. Garidel. Physicochemical properties of bacterial glycopolymers. *Carbohydr. Res.*, 338:2477 – 2489, 2003.
- [267] H. Nikaido and T. Nakae. Review: The outer membrane of Gram-negative bacteria. *Adv. Microb. Physiol.*, 20:163 – 250, 1979.
- [268] S. Snyder, D. Kim, and T.J. McIntosh. Lipopolysaccharide Bilayer Structure: Effect of Chemotype, Core Mutations, Divalent Cations, and Temperature. *Biochemistry*, 38:10758 – 10767, 1999.
- [269] R. Stone. Search for sepsis drugs goes on despite past failures. *Science*, 264:365 – 367, 1994.
- [270] U. Seydel, A.J. Ulmer, S. Uhlig, and E.T. Rietschel. *Membrane Structure in Disease and Drug Therapy*. Marcel Dekker: New York, Basel, 2000.
- [271] H. Nikaido and M. Vaara. Molecular basis of bacterial outer membrane permeability. *Microbiol. Rev.*, 49:1 – 32, 1985.
- [272] H. Nikaido. Prevention of drug access to bacterial targets: permeability barriers and active efflux. *Science*, 264:382 – 388, 1994.
- [273] D.M. Donaldson, R. Roberts, H.S. Larsen, and J.G. Tew. Interrelationship between serum beta-lysin, lysozyme and the antibody complement system in killing of *Escherichia coli*. *Infect. Immun.*, 40:657 – 666, 1974.
- [274] J. Patterson-Delafield, R.J. Martinez, and R.I. Lehrer. Microbicidal cationic proteins in rabbit alveolar macrophages: a potential host defense mechanism. *Infect. Immun.*, 30:180 – 192, 1980.
- [275] L.T. Truelstrup-Hansen, J.W. Austin, and T.A. Gill. Antibacterial effect of protamine in combination with EDTA and refrigeration. *Int. J. Food Microbiol.*, 66:149 – 161, 2001.

- [276] K. Brandenburg, M.H.J. Koch, and U. Seydel. Phase diagram of lipid A from *Salmonella minnesota* and *Escherichia coli* rough mutant lipopolysaccharide. *J. Struct. Biol.*, 105:11 – 21, 1990.
- [277] L.P. Kotra, D. Golemi, N.A. Amro, G.Y. Liu, and S. Mobashery. Lipopolysaccharide Assembly on the Surface of *Escherichia coli*. *J. Am. Chem. Soc.*, 121:8707 – 8711, 1999.
- [278] R.M. Shroll and T.P. Straatsma. Molecular structure of the outer bacterial membrane of *Pseudomonas aeruginosa* via classical simulation. *Biopolymers*, 65:395 – 407, 2002.
- [279] R.J. Roantree, T.T. Kuo, and D.G. MacPhee. The Effect of Defined Lipopolysaccharide Core Defects upon Antibiotic Resistances of *Salmonella typhimurium*. *J. Gen. Microbiol.*, 103:223 – 234, 1977.
- [280] K. Brandenburg and U. Seydel. Physical aspects of structure and function of membranes made from lipopolysaccharides and free lipid A. *Biochim. Biophys. Acta*, 775:225 – 238, 1984.
- [281] T.A. Langworthy and J.L. Pond. *Thermophiles: General, Molecular, and Applied Microbiology*. John Wiley & Sons, New York, 1986.
- [282] S.-L. Lo and E.L. Chang. Purification and characterization of a liposomal-forming tetraether lipid fraction. *Biochem. Biophys. Res. Commun.*, 167:238 – 243, 1990.
- [283] A. Sugai, R. Sakuma, I. Fukuda, N. Kurosawa, Y.H. Itoh, K. Kon, S. Ando, and T. Itoh. The structure of the core polyol of the ether lipids from *Sulfolobus acidocaldarius*. *Lipids*, 30:339 – 344, 1995.
- [284] A. Gliozzi, A. Relini, and P.L.-G. Chong. Structure and permeability properties of biomimetic membranes of bolaform archaeal tetraether lipids (review). *J. Membr. Sci.*, 206:673 – 679, 2002.
- [285] P.L.-G. Chong. *Thermophiles : biology and technology at high temperatures.*, chapter Physical Properties of Membranes Composed of Tetraether Archaeal Lipids., pages 73 – 96. CRC Press, 2008.
- [286] M. De Rosa, B. Esposito, A. Gambacorta, B. Nicholas, and J.D. Bu'lock. Effects of temperature on ether lipid composition of *Caldariella acidophila*. *Phytochemistry*, 19:827 – 831, 1980.
- [287] P.L.-G. Chong, M. Zein, T.K. Khan, and R. Winter. Structure and conformation of bipolar tetraether lipid membranes derived from thermoacidophilic archaeon *sulfolobus acidocaldarius* as revealed by small-angle X-ray scattering and high pressure FT-IR spectroscopy. *J. Phys. Chem. B*, 107:8694 – 8700, 2003.
- [288] P.L.-G. Chong, M. Sulc, and R. Winter. Compressibilities and volume fluctuations of archaeal tetraether liposomes. *Biophys. J.*, 99:3319 – 3326, 2010.
- [289] M.G.L. Elferink, J.G. de Wit, R. Demel, A.J.M. Driessen, and W.N. Konings. Functional reconstitution of membrane proteins in monolayer liposomes from bipolar lipids of *Sulfolobus acidocaldarius*. *J. Biol. Chem.*, 267:1375 – 1381, 1992.
- [290] E.L. Chang. Unusual thermal stability of liposomes made from bipolar tetraether lipids. *Biochem. Biophys. Res. Commun.*, 202:673 – 679, 1994.
- [291] M.G.L. Elferink, J.G. de Wit, A.J.M. Driessen, and W.N. Konings. Stability and proton-permeability of liposomes composed of archaeal tetraether lipids. *Biochim. Biophys. Acta*, 1193:247 – 254, 1994.
- [292] H. Komatsu and P.L.-G. Chong. Low Permeability of Liposomal Membranes Composed of Bipolar Tetraether Lipids from Thermoacidophilic Archaeobacterium *Sulfolobus acidocaldarius*. *Biochemistry*, 37:107 – 115, 1998.
- [293] T. Baba, H. Minamikawa, H. Masakatsu, and T. Handa. Hydration and molecular motions in synthetic phytanyl-chained glycolipid vesicle membranes. *Biophys. J.*, 81:3377 – 3386, 2001.

- [294] Y.L. Kao, E.L. Chang, and P.L.-G. Chong. Unusual pressure dependence of the lateral motions of pyrene-labeled phosphatidylcholine in bipolar lipid vesicles. *Biochem. Biophys. Res. Commun.*, 188:1241 – 1246, 1992.
- [295] M.G.L. Elferink, J.G. de Wit, A.J.M. Driessen, and W.N. Konings. Energy-transducing properties of primary proton pumps reconstituted into archaeal bipolar lipid vesicles. *Eur. J. Biochem.*, 214:917 – 925, 1993.
- [296] I. Vilalta, A. Gliozzi, and M. Prats. Interfacial air/water proton conduction from long distances by *Sulfolobus solfataricus* archaeal bolaform lipids. *Eur. J. Biochem.*, 240:181 – 185, 1996.
- [297] S. Bruno, S. Cannistraro, A. Gliozzi, M. De Rosa, and A. Gambacorta. A spin label ESR and saturation transfer-ESR study of archaeobacteria bipolar lipids. *Eur. Biophys. J.*, 13:67 – 76, 1985.
- [298] P.L.-G. Chong, R. Ravindra, M. Khurana, V. English, and R. Winter. Pressure Perturbation and Differential Scanning Calorimetric Studies of Bipolar Tetraether Liposomes Derived from the Thermoacidophilic Archaeon *Sulfolobus acidocaldarius*. *Biophys. J.*, 89:1841 – 1849, 2005.
- [299] N.J. Brooks, O. Ces, R.H. Templer, and J.M. Seddon. Pressure effects on lipid membrane structure and dynamics. *Chem. Phys. Lipids*, 164:89 – 98, 2011.
- [300] C. Jeworrek, R. Steitz, C. Czeslik, and R. Winter. High pressure cell for neutron reflectivity measurements up to 2500 bar. *Rev. Sci. Instrum.*, 82:25106, 2011.
- [301] A.M. Matsner, B. Krebbers, R.W. van den Berg, and P.V. Bartels. Advantages of high pressure sterilization on quality of food products. *Trends Food Sci. Technol.*, 75:79 – 85, 2004.
- [302] Y. Rigaldie, A. Largeteau, G. Lemagnen, F. Ibalot, P. Pardon, G. Demazeau, and L. Grislain. Effects of high hydrostatic pressure on several sensitive therapeutic molecules and a soft nanodispersed drug delivery system. *Pharm. Res.*, 20:2036 – 2040, 2003.
- [303] Y. Rigaldie, A. Largeteau, G. Lemagnen, L. Grislain, and G. Demazeau. *Advances in High Pressure Bioscience and Biotechnology II.*, chapter Decontamination and sterilization of sensitive drugs using high hydrostatic pressure (HHP)., pages 315 – 319. Springer, Berlin, Heidelberg, NewYork, 2002.
- [304] R.F. Vogel, M.A. Ehrmann, M.G. Gaenzle, C. Kato, M. Korakli, C.H. Scheyhing, A. Molina-Gutierrez, H.M. Ulmer, and R. Winter. *Advances in High Pressure Bioscience and Biotechnology II.*, chapter High pressure response of lactic acid bacteria., pages 249 – 254. Springer, Berlin, Heidelberg, New York, 2002.
- [305] A. Molina-Gutierrez, V. Stippl, A. Delgado, M.G. Gaenzle, and R.F. Vogel. In situ determination of the intracellular pH of *Lactococcus lactis* and *Lactobacillus plantarum* during pressure treatment. *Appl. Environ. Microbiol.*, 68:4399 – 4406, 2002.
- [306] H.M. Ulmer, H. Herberhold, S. Fahsel, M.G. Gänzle, R. Winter, and R.F. Vogel. Effects of pressure-induced membrane phase transitions on inactivation of HorA, an ATP-dependent multidrug resistance transporter, in *Lactobacillus plantarum*. *Appl. Environ. Microbiol.*, 68:1088 – 1095, 2002.
- [307] L. Beney and P. Gervais. Influence of the fluidity of the membrane on the response of microorganisms to environmental stresses. *Appl. Microbiol. Biotechnol.*, 57:34 – 42, 2001.
- [308] D. Worcester and B. Hammoufa. Interdigitated Hydrocarbon Chains in C₂₀ and C₂₂ Phosphatidylcholines Induced by Hydrostatic Pressure. *Physica B*, 241:1175 – 1177, 1997.
- [309] R. Winter. Effects of hydrostatic pressure on lipid and surfactant phases. *Curr. Opin. Colloid Interface Sci.*, 6:303 – 312, 2001.

- [310] R. Winter and W. Dzwolak. Exploring the temperature-pressure configurational landscape of biomolecules: from lipid membranes to proteins. *Philos. Trans. R. Soc. A*, 363:537 – 562, 2005.
- [311] K. Heremans and L. Smeller. Protein Structure and Dynamics at High Pressure. *Biochim. Biophys. Acta*, 1386:353 – 370, 1998.
- [312] V.V. Mozhaev, N. Bec, and C. Balny. Pressure effects on enzyme reactions in mainly organic media: α -Chymotrypsin in reversed micelles of Aerosol OT in octane. *Biochem. Mol. Biol. Int.*, 34:191 – 199, 1994.
- [313] J. Jonas, L. Ballard, and D. Nash. High-resolution, high-pressure NMR studies of proteins. *Biophys. J.*, 75: 445 – 452, 1998.
- [314] G. Panick, R. Malessa, R. Winter, G. Rapp, K.J. Frye, and C.A. Royer. Structural characterization of the pressure-denatured state and unfolding/refolding kinetics of staphylococcal nuclease by synchrotron small-angle X-ray scattering and Fourier-transform infrared spectroscopy. *J. Mol. Biol.*, 275:389 – 402, 1998.
- [315] J. Woenckhaus, R. Kohling, P. Thiyagarajan, K.C. Littrell, S. Seifert, C.A. Royer, and R. Winter. Pressure-jump small-angle X-ray scattering detected kinetics of staphylococcal nuclease folding. *Biophys. J.*, 80:1518 – 1523, 2001.
- [316] K. Akasaka and H. Li. Low-lying excited states of proteins revealed from nonlinear pressure shifts in ^1H and ^{15}N NMR. *Biochemistry*, 40:8665 – 8671, 2001.
- [317] K. Akasaka. Highly fluctuating protein structures revealed by variable-pressure nuclear magnetic resonance. *Biochemistry*, 42:10875 – 10885, 2003.
- [318] K. Akasaka. Probing conformational fluctuation of proteins by pressure perturbation. *Chem. Rev.*, 106: 1814 – 1835, 2006.
- [319] M. Kataoka, I. Nishii, T. Fujisawa, T. Ueki, F. Tokunaga, and Y. Goto. Structural characterization of the molten globule and native states of apomyoglobin by solution X-ray scattering. *J. Mol. Biol.*, 249:215 – 228, 1995.
- [320] T. Christopher, B.S.V. Rama Sarma, P.K. Govindan Potti, B. Nageswara Rao, and K. Sankarnarayanamsamy. A comparative study on failure pressure estimations of unflawed cylindrical vessels. *Int. J. Pressure Vessels and Piping*, 79:53 – 66, 2002.
- [321] 2011. URL http://www.helmholtz-berlin.de/media/media/grossgeraete/nutzerdienst/neutronen/instrumente/inst/bensc_v6.pdf.
- [322] J.-B. Rouget, M.A. Schroer, C. Jeworrek, M. Pühse, J.L. Saladana, Y. Bessin, M. Tolan, D. Barrick, R. Winter, and C.A. Royer. Unique Features of the Folding Landscape of a Repeat Protein Revealed by Pressure Perturbation. *Biophys. J.*, 98:2712 – 2721, 2010.
- [323] J. Jonas, T. DeFries, and D.J. Wilbur. Molecular motions in compressed liquid water. *J. Chem. Phys.*, 65: 582 – 588, 1976.
- [324] S. Uelner. FTIR-spektroskopische Untersuchung der p,T-Phasendiagramme bicellarer Lipidmischungen., 2009.
- [325] M.N. Triba, D.E. Warschawski, and P.F. Devaux. Reinvestigation by phosphorus NMR of lipid distribution in bicelles. *Biophys. J.*, 88:1887 – 1901, 2005.
- [326] M.N. Uddin and M.R. Morrow. Bicellar Mixture Phase Behavior Examined by Variable-Pressure Deuterium NMR and Ambient Pressure DSC. *Langmuir*, 26:12104 – 12111, 2010.

- [327] I. Daniel, P. Oger, and R. Winter. Origins of life and biochemistry under high-pressure conditions. *Chem. Soc. Rev.*, 35:858 – 875, 2006.
- [328] R. Winter. *High-Pressure Crystallography. From Fundamental Phenomena to Technological Applications.*, chapter Exploring the Energy and Conformational Landscape of Biomolecules Under Extreme Conditions., page 573. Springer, Dordrecht, 2010.
- [329] P. Laggner, J.D. Gotto, and J.D. Morrisett. Structure of the dimyristoylphosphatidylcholine vesicle and the complex formed by its interaction with apolipoprotein C-III: X-ray small angle scattering studies. *Biochemistry*, 18:164 – 171, 1979.
- [330] O. Reis, R. Winter, and T.W. Zerda. The Effect of High External Pressure on DPPC-Cholesterol Multilamellar Vesicles – A Pressure-Tuning Fourier-transform Infrared Spectroscopy Study. *Biochim. Biophys. Acta, Biomembr.*, 1279:5 – 16, 1996.
- [331] C. Czeslik, R. Winter, G. Rapp, and K. Bartels. Temperature and Pressure Dependent Phase Behaviour of the Monoacylglycerides Monoolein and Monoelaidin. *Biophys. J.*, 68:1423 – 1429, 1995.
- [332] P.T.T. Wong. Pressure-induced correlation field splitting of vibrational modes: structural and dynamic properties in lipid bilayers and biomembranes. *Biophys. J.*, 66:1505 – 1514, 1994.
- [333] M. Auger, H.C. Jarrell, I.C.P. Smith, D.J. Siminovitch, H.H. Mantsch, and P.P.T. Wong. What factors control hepatic triacylglycerol accumulation in alcohol abuse? *Biochemistry*, 27:6086 – 6093, 1988.
- [334] P.T.T. Wong. *High Pressure Chemistry, Biochemistry and Materials Science.*, chapter High pressure vibrational spectroscopic studies of aqueous biological systems: from model systems to intact tissues., pages 511 – 543. Kluwer Academic Publishers, Dordrecht, 1993.
- [335] J. Erbes, A. Gabke, G. Rapp, and R. Winter. Kinetics of phase transformations between lyotropic lipid mesophases of different topology: a time-resolved synchrotron X-ray diffraction study using the pressure-jump relaxation technique. *Phys. Chem. Chem. Phys.*, 2:151 – 162, 2000.
- [336] M. Pühse, C. Jeworrek, and R. Winter. The temperature–pressure phase diagram of a DPPC–ergosterol fungal model membrane - a SAXS and FT-IR spectroscopy study. *Chem. Phys. Lipids*, 152:57 – 63, 2008.
- [337] M. Pühse. *Auswirkung hoher hydrostatischer Drücke auf Modelllipidmembranen, Proteine und proteinmimetische Polymere.* PhD thesis, TU Dortmund University, 2009.
- [338] R. Krivanek, C. Jeworrek, C. Czeslik, and R. Winter. Composition Fluctuations in Phospholipid-Sterol Vesicles - a Small-angle Neutron Scattering Study. *Z. Phys. Chem.*, 222:1679 – 1692, 2008.
- [339] Y.W. Hsueh, K. Gilbert, C. Trandum, M. Zuckermann, and J. Thewalt. The effect of ergosterol on dipalmitoylphosphatidylcholine bilayers: A deuterium NMR and calorimetric study. *Biophys. J.*, 88:1799 – 1808, 2005.
- [340] P.L. Chong, P.A. Fortes, and D.M. Jameson. Mechanisms of inhibition of (Na,K)-ATPase by hydrostatic pressure studied with fluorescent probes. *J. Biol. Chem.*, 260:14484 – 14490, 1985.
- [341] S. Janosch, E. Kinne-Saffran, R.K.H. Kinne, and R. Winter. *Advances in High Pressure Bioscience and Biotechnology II*, chapter Inhibition of Na⁺, K⁺-ATPase by hydrostatic pressure., pages 215 – 219. Springer-Verlag, Heidelberg, 2003.
- [342] S. Scarlata. Determination of the activation volume of PLC β by G- β - γ -subunits through the use of high hydrostatic pressure. *Biophys. J.*, 88:2867 – 2874, 2005.

- [343] C. Nicolini, J. Kraineva, M. Khurana, N. Periasamy, S.S. Funari, and R. Winter. Temperature and pressure effects on structural and conformational properties of POPC/SM/cholesterol model raft mixtures – a FT-IR, SAXS, DSC, PPC and Laurdan fluorescence spectroscopy study. *Biochim. Biophys. Acta*, 1758:248 – 258, 2006.
- [344] C. Nicolini, A. Celli, E. Gratton, and R. Winter. Pressure Tuning of the Morphology of Heterogeneous Lipid Vesicles: A Two-Photon-Excitation Fluorescence Microscopy Study. *Biophys. J.*, 91:2936 – 2942, 2006.
- [345] E. Powalska, S. Janosch, E. Kinne-Saffran, R.K.H. Kinne, C.F.L. Fontes, J.A. Mignaco, and R. Winter. Fluorescence Spectroscopic Studies of Pressure Effects on Na^+ , K^+ -ATPase Reconstituted into Phospholipid Bilayers and Model Raft Mixtures. *Biochemistry*, 46:1672 – 1683, 2007.
- [346] J.-M. Perrier-Cornet, S. Tapin, and P. Gervais. *Advances in high pressure bioscience and biotechnology II.*, chapter High pressure inactivation of yeast and spheroplasts at subzero temperatures., pages 389 – 393. Springer, Berlin, Heidelberg, New York, 2002.
- [347] J.-M. Perrier-Cornet, S. Tapin, S. Gaeta, and P. Gervais. High-pressure inactivation of *Saccharomyces cerevisiae* and *Lactobacillus plantarum* at subzero temperatures. *J. Biotechnol.*, 115:405 – 412, 2005.
- [348] A. Blume and M. Hillmann. Dimyristoyl Phosphatidic Acid/Cholesterol Bilayers. Thermodynamic Properties and Kinetics of the Phase Transition as Studied by the Pressure Jump Relaxation Technique. *Eur. Biophys. J.*, 13:343 – 353, 1986.
- [349] A. Genz, J.F. Holzwarth, and T.Y. Tsong. The influence of cholesterol on the main phase transition of unilamellar dipalmytoylphosphatidylcholine vesicles. A differential scanning calorimetry and iodine laser T-jump study. *Biophys. J.*, 50:1043 – 1051, 1986.
- [350] M. Caffrey, R.L. Magin, B. Hummel, and J. Zhang. Kinetics of the lamellar and hexagonal phase transitions in phosphatidyl-ethanolamine: A time-resolved X-ray diffraction study using a microwave-induced temperature-jump. *Biophys. J.*, 58:21 – 29, 1990.
- [351] O. Reis and R. Winter. Pressure and Temperature Effects on Conformational and Hydrational Properties of Lamellar and Bicontinuous Cubic Phases of the Fully Hydrated Monoacylglyceride Monoelaidin - A Fourier Transform-Infrared Spectroscopy Study Using the Diamond Anvil Technique. *Langmuir*, 14:2903 – 2909, 1998.
- [352] G. Pabst, M. Rappolt, H. Amenitsch, S. Bernstorff, and P. Laggner. X-ray kinematography of temperature-jump relaxation probes the elastic properties of fluid bilayers. *Langmuir*, 16:8994 – 9001, 2000.
- [353] P. Grabitz, V.P. Ivanova, and T. Heimburg. Relaxation kinetics of lipid membranes and its relation to the heat capacity. *Biophys. J.*, 82:299 – 309, 2002.
- [354] K. Boehm, J. Guddorf, and H.-J. Hinz. Application of pressure-modulated differential scanning calorimetry to the determination of relaxation kinetics of multilamellar lipid vesicles. *Biophys. Chem.*, 126:218 – 227, 2007.
- [355] M. Schiewek, M. Krumova, G. Hempel, and A. Blume. Pressure jump relaxation setup with IR detection and millisecond time resolution. *Rev. Sci. Instrum.*, 78:045101, 2007.
- [356] C.E. Conn, O. Ces, X. Mulet, S. Finet, R. Winter, J.M. Seddon, and R.H. Templer. Dynamics of Structural Transformations between Lamellar and Inverse Bicontinuous Cubic Lyotropic Phases. *Phys. Rev. Lett.*, 96:108102, 2006.
- [357] R.C. Neumann, W. Kauzmann, and A. Zipp. Pressure dependence of weak acid ionization in aqueous buffers. *J. Phys. Chem.*, 77:2687 – 2691, 1973.

- [358] M.I. Kanehisa and T.Y. Tsong. Cluster model of lipid phase transitions with application to passive permeation of molecules and structure relaxations in lipid bilayers. *J. Am. Chem. Soc.*, 100:424 – 432, 1978.
- [359] A. Aroti, E. Leontidis, B. Maltseva, and G. Brezesinski. Effect of Hofmeister Anions on DPPC Langmuir Monolayers at the Air-Water Interface. *J. Phys. Chem. B*, 108:15238 – 15245, 2004.
- [360] F. Evers, C. Jeworrek, K. Weise, M. Tolan, and R. Winter. Detection of lipid raft domains in Langmuir monolayers of complex lipid composition. *in preparation*, 2011.
- [361] G. David and J. Perez. Combined sampler robot and high-performance liquid chromatography: a fully automated system for biological small-angle X-ray scattering experiments at the Synchrotron SOLEIL SWING beamline. *J. Appl. Crystallogr.*, 42:892 – 900, 2009.
- [362] C. Jeworrek, F. Evers, M. Erkkamp, S. Grobelny, M. Tolan, P.L.-G. Chong, and R. Winter. Structure and phase behavior of archaeal lipid monolayers. *submitted to Langmuir*, 2011.
- [363] A. Gliozzi, A. Relini, R. Rolandi, S. Dante, and A. Gambacorta. Organization of bipolar lipids in monolayers at the air-water interface. *Thin solid films*, 242:208 – 212, 1994.
- [364] U. Balowsky, U. Rothe, E. Antonopoulos, T. Martini, L. Henkel, and H.-J. Freisleben. Monomolecular organization of the main tetraether lipid from *Thermoplasma acidophilum* at the water-air interface. *Chem. Phys. Lipids*, 105:31 – 42, 2000.
- [365] C. Jeworrek, F. Evers, J. Höwe, K. Brandenburg, M. Tolan, and R. Winter. Effects of Specific versus Non-Specific Ionic Interactions on the Structure and Lateral Organization of Lipopolysaccharides. *Biophys. J.*, 100:2169 – 2177, 2011.
- [366] K. Brandenburg and A. Wiese. Endotoxins: relationships between structure, function, and activity. *Curr. Top. Med. Chem.*, 4:1127–1146, 2004.
- [367] C.A. Helm, P. Tippmann-Krayer, H. Möhwald, J. Als-Nielsen, and K. Kjaer. Phases of phosphatidylethanolamine monolayers studied by synchrotron X-ray scattering. *Biophys. J.*, 60:1457 – 1476, 1991.
- [368] R. Kitahara, K. Hata, A. Maeno, K. Akasaka, M.S. Chimenti, B. Garcia-Moreno, M.A. Schroer, C. Jeworrek, M. Tolan, R. Winter, J. Roche, C. Roumestand, K.M. de Guillen, and C.A. Royer. Structural plasticity of staphylococcal nuclease probed by perturbation with pressure and pH. *Proteins - Structure Function and Bioinformatics*, 79:1293 – 1305, 2011.
- [369] M.A. Schroer, M. Paulus, C. Jeworrek, C. Krywka, S. Schmacke, Y. Zhai, D.C.F. Wieland, C.J. Sahle, M. Chimenti, C.A. Royer, B. Garcia-Moreno, M. Tolan, and R. Winter. High-Pressure SAXS Study of Folded and Unfolded Ensembles of Proteins. *Biophys. J.*, 99:3430 – 3437, 2010.
- [370] D. Shortle and A.K. Meeker. Mutant forms of staphylococcal nuclease with altered patterns of guanidine hydrochloride and urea denaturation. *Proteins*, 1:81 – 89, 1986.
- [371] C. Krywka, C. Sternemann, M. Paulus, N. Javid, R. Winter, A. Al-Sawalmih, S. Yi, D. Raabe, and M. Tolan. The small-angle and wide-angle X-ray scattering set-up at beamline BL9 of DELTA. *J. Synchrotron Rad.*, 14:244 – 251, 2007.
- [372] S.V. Roth, R. Dohrmann, M. Dommach, M. Kuhlmann, I. Kroger, R. Gehrke, H. Walter, C. Schroer, B. Lengeler, and P. Mueller-Buschbaum. Small-angle options of the upgraded ultrasmall-angle X-ray scattering beamline BW4 at HASYLAB. *Rev. Sci. Instrum.*, 77:085106, 2006.
- [373] 2011. URL <http://www.ks.uiuc.edu/Research/vmd/>.
- [374] J.E. Stone. *An Efficient Library for Parallel Ray Tracing and Animation*. PhD thesis, University of Missouri - Rolla, 1998.

- [375] 2011. URL <http://jedi.ks.uiuc.edu/~johns/raytracer/papers/tachyon.pdf>.
- [376] D.I. Svergun and M.H.J. Koch. Small-angle scattering studies of biological macromolecules in solution. *Rep. Prog. Phys.*, -:1735 – 1782, 2003.
- [377] J.E. Kohn, I.S. Millett, J. Jacob, B. Zagrovic, T.M. Dillon, N. Cingel, R.S. Dothager, S. Seifert, P. Thiagarajan, T.R. Sosnick, M.Z. Hasan, V.S. Pande, I. Ruczinski, S. Doniach, and K.W. Plaxco. Random-coil behavior and the dimensions of chemically unfolded proteins. *Proc. Natl. Acad. Sci. U. S. A.*, 101(34):12491 – 12496, 2004.
- [378] Y. Harpaz, M. Gerstein, and C. Chothia. Volume changes on protein folding. *Structure*, 2:641 – 649, 1994.
- [379] J.L. Schlessman, C. Abe, C.A. Gittis, D.A. Karp, M.A. Dolan, and B.E. Garcia-Moreno. Crystallographic study of hydration of an internal cavity in engineered proteins with buried polar or ionizable groups. *Biophys. J.*, 36:3208 – 3216, 2008.
- [380] J.J. Dwyer, A.G. Gittis, D.A. Karp, E.E. Lattman, D.S. Spencer, W.E. Stites, and B.E. García-Moreno. High apparent dielectric constants in the interior of a protein reflect water penetration. *Biophys. J.*, 79:1610 – 1620, 2000.
- [381] D.A. Karp. *Structural and energetic consequences of the ionization of internal groups in staphylococcal nuclease*. PhD thesis, Johns Hopkins University, Baltimore, MD, 2007.
- [382] A. Damjanovic, X. Wu, B.E. García-Moreno, and B.R. Brooks. Backbone relaxation coupled to the ionization of internal groups in proteins: a self-guided Langevin dynamics study. *Biophys. J.*, 95:4091 – 4101, 2008.
- [383] Y. Kobashigawa, M. Sakurai, and K. Nitta. Effect of hydrostatic pressure on unfolding of α -lactalbumin: volumetric equivalence of the molten globule and unfolded state. *Protein Sci.*, 8:2765 – 2772, 1999.
- [384] X. Peng, J. Jonas, and J.L. Silva. Molten-globule conformation of Arc repressor monomers determined by high-pressure ^1H NMR spectroscopy. *Proc. Natl. Acad. Sci. U. S. A.*, 90:1776 – 1780, 1993.
- [385] K. Ruan, R. Lange, N. Bec, and C. Balny. A stable partly denatured state of trypsin induced by high hydrostatic pressure. *Biochem. Biophys. Res. Commun.*, 239:150 – 154, 1997.
- [386] M. Pühse, R.T. Szweda, Y. Ma, C. Jeworrek, R. Winter, and H. Zorn. *Marasmius scorodoni* extracellular dimeric peroxidase — Exploring its temperature and pressure stability. *Biochim. Biophys. Acta*, 1794:1091 – 1098, 2009.
- [387] D.I. Svergun, V.V. Volkov, M.B. Kozin, H.B. Stuhmann, C. Barberato, and M.H.J. Koch. Shape determination from solution scattering of biopolymers. *J. Appl. Crystallogr.*, 30:798 – 802, 1997.
- [388] S.J. Kim and M. Shoda. Purification and characterization of a novel peroxidase from *Geotrichum candidum* Dec 1 involved in decolorization of dyes. *Appl. Environ. Microbiol.*, 65:1029 – 1035, 1999.
- [389] R. Kumar, S. Singh, and O.V. Singh. Bioconversion of lignocellulosic biomass: biochemical and molecular perspectives. *J. Ind. Microbiol. Biotechnol.*, 35:377 – 391, 2008.
- [390] L. Viikari, M. Alapuranen, T. Puranen, J. Vehmaanperä, and M. Siika-Aho. Thermostable enzymes in lignocellulose hydrolysis. *Adv. Biochem. Eng. Biotechnol.*, 108:121 – 145, 2007.
- [391] W. Tedjo, M.N. Eshtiaghi, and D. Knorr. Impact of supercritical carbon dioxide and high pressure on lipoxygenase and peroxidase activity. *J. Food Sci.*, 65:1284 – 1287, 2000.
- [392] N. Bec, A. Villa, P. Tortora, V.V. Mozhaev, C. Balny, and R. Lange. Enhanced stability of carboxypeptidase from *Sulfolobus solfataricus* at high pressure. *Biotechnol. Lett.*, 18:483 – 488, 1996.

- [393] B.B. Boonyaratanakornkit, C.B. Park, and D.S. Clark. Pressure effects on intra- and intermolecular interactions. *Biochim. Biophys. Acta*, 1595:235 – 249, 2002.
- [394] D.B. Northrop. Effects of high pressure on enzymatic activity. *Biochim. Biophys. Acta*, 1595:71 – 79, 2002.
- [395] G.K. Kouassi, R.C. Ananteswaran, S.J. Knabel, and J.D. Floros. Effect of high pressure processing on activity and structure of alkaline phosphatase and lactate dehydrogenase in buffer and milk. *J. Agric. Food Chem.*, 55:9520 – 9529, 2007.
- [396] L. Ferreira, C. Afonso, H. Vila-Real, A. Alfaia, and M.H.L. Ribeiro. Evaluation of the effect of high pressure on naringin hydrolysis in grapefruit juice with naringinase immobilised in calcium alginate beads. *Food Technol. Biotechnol.*, 46:145 – 150, 2008.
- [397] S. Lauber, I. Krause, H. Klostermeyer, and T. Henle. Microbial transglutaminase crosslinks β -casein and β -lactoglobulin to heterologous oligomers under high pressure. *Eur. Food Res. Technol.*, 216:15 – 17, 2003.
- [398] O. Mendez, H. Rawel, U. Schwarzenbolz, and T. Henle. Structural changes of microbial transglutaminase during thermal and high-pressure treatment. *J. Agric. Food Chem.*, 54:1716 – 1721, 2006.
- [399] M. Galbe and G. Zacchi. Pretreatment of lignocellulosic materials for efficient bioethanol production. *Adv. Biochem. Eng. Biotechnol.*, 109:41 – 65, 2007.
- [400] R.P. Chandra, R. Bura, W.E. Mabee, A. Berlin, X. Pan, and J.N. Saddler. Substrate pretreatment: the key to effective enzymatic hydrolysis of lignocellulosics? *Adv. Biochem. Eng. Biotechnol.*, 108:67 – 93, 2007.
- [401] X.B. Lu, Y.M. Zhang, J. Yang, and Y. Liang. Enzymatic hydrolysis of corn stover after pretreatment with dilute sulfuric acid. *Chem. Eng. Technol.*, 30:938 – 944, 2007.
- [402] Y.Y. Lee, P. Iyer, and R.W. Torget. Dilute-acid hydrolysis of lignocellulosic biomass. *Adv. Biochem. Eng. Biotechnol.*, 65:93 – 115, 1999.
- [403] F. Sun and H. Chen. Organosolv pretreatment by crude glycerol from oleochemicals industry for enzymatic hydrolysis of wheat straw. *Bioresour. Technol.*, 99:5474 – 5479, 2008.
- [404] M. Cantarella, L. Cantarella, A. Gallifuoco, A. Spera, and F. Alfani. Effect of inhibitors released during steam-explosion treatment of poplar wood on subsequent enzymatic hydrolysis and SSF. *Biotechnol. Prog.*, 20:200 – 206, 2004.
- [405] J.P. Delgenes, R. Moletta, and J.M. Navarro. Effects of lignocellulose degradation products on ethanol fermentations of glucose and xylose by *Saccharomyces cerevisiae*, *Zymomonas mobilis*, *Pichia stipitis*, and *Candida shehatae*. *Enzyme Microb. Technol.*, 19:220 – 225, 1996.
- [406] S.I. Mussatto, M. Fernandes, A.M.F. Milagres, and C. Roberto. Effect of hemicellulose and lignin on enzymatic hydrolysis of cellulose from brewer's spent grain. *Enzyme Microb. Technol.*, 43:124 – 129, 2008.
- [407] E. Ruiz, C. Cara, P. Manzanares, M. Ballesteros, and E. Castro. Evaluation of steam explosion pre-treatment for enzymatic hydrolysis of sunflower stalks. *Enzyme Microb. Technol.*, 42:160 – 166, 2007.
- [408] S. Ando, I. Arai, K. Kiyoto, and S. Hanai. Identification of aromatic monomers in steamexploded poplar and their influences on ethanol fermentation by *Saccharomyces cerevisiae*. *J. Ferment. Technol.*, 64:567 – 570, 1989.
- [409] J. Seeliger, F. Evers, C. Jeworrek, S. Kapoor, M. Tolan, A. Kapurniotu, and R. Winter. Cross-amyloid interaction of A β and IAPP at anionic lipid raft membranes. *submitted to J. Am. Chem. Soc.*, 2011.
- [410] K. Weise, R. Mishra, S. Jah, D. Sellin, D. Radovan, A. Gohlke, C. Jeworrek, J. Seeliger, S. Möbitz, and R. Winter. *Lipids and Cellular Membranes in Amyloid Diseases.*, chapter 4. Interaction of hIAPP and Its Precursors with Model and Biological Membranes., pages 92 – 120. Wiley-VCH, 2011.

-
- [411] S.M. Butterfield and H.A. Lashuel. Amyloidogenic Protein–Membrane Interactions: Mechanistic Insight from Model Systems. *Angew. Chem., Int. Ed.*, 49:5628 – 5654, 2010.
- [412] D. Sellin, L.M. Yan, A. Kapurniotu, and R. Winter. Suppression of IAPP fibrillation at Anionic Lipid Membranes via IAPP-derived Amyloid Inhibitors and Insulin. *Biophys. Chem.*, 150:73 – 79, 2010.
- [413] D. Radovan, N. Opitz, and R. Winter. Fluorescence Microscopy Studies on Islet Amyloid Polypeptide Fibrillation at Heterogeneous and Cellular Membrane Interfaces and its Inhibition by Resveratrol. *FEBS Lett.*, 583:1439 – 1445, 2009.
- [414] 2011. URL <http://www.mathworks.co.uk/products/matlab/description1.html>.

APPENDIX A

MATLAB code examples

A.1 Introduction

Nearly all programming during this thesis was done using MATLAB. MATLAB[®], developed by MathWorks and short for “MATrix LABORatory”, is a high-level (fourth generation) technical computing language and interactive environment for algorithm development, data analysis and visualisation, and numeric computation. Using MATLAB technical computing problems can usually be solved faster than using traditional programming languages, such as C, C++, and Fortran.^[414]

During this thesis numerous scripts, functions and sub-functions have been written. All codes written by me are organised by the prefix of the corresponding file name (see Table A.1). In this part of the appendix several programs are introduced to illustrate the general programming style, which should help to understand all written code.

Table A.1: Prefixes of different user-programmed MATLAB files and description of their function.

file prefix	description
cjf_	function file expecting input parameters as defined in the function file and corresponding short documentation
cjs_	script file without parameter input
cji_	information file storing structures containing parameters or information – cannot be executed
cjgui_	files containing code of a GUI (graphical user interface)
cjp_	file containing parts of a function – not documented code usually called by another function file
cjibf_	code of “in-built functions” is usually saved within other function files – rarely found in separate files and not intended for calling from the command line

A.2 Splitting of spec-files from synchrotron sources

Data of all measurements at a synchrotron SAXS beamline, like the high brilliance beamline ID02 at the ESRF, are often saved in one large ASCII file (up to several GB in size) with the file extension “spec”. After a typical experimental run of three days this ASCII-file has at least 2.5 million lines. To split this file into smaller parts, a script has been written, which separates all data of one measurement and saves it as a binary file containing a single MATLAB structure. Those files then can be easily imported into other user written software (e.g., see section A.4). Here, a MATLAB function is presented to demonstrate the code of a typical data import routine.

```

1 function [] = cjf_split_spec_to_m()
2 %CJS_SPLIT_SPEC_TO_M Converts ESRF_spec-file to structure and exports to *.mat-files
3 %   -> INPUT: ESRF SAXS .spec-file
4 %   -> OUTPUT: Single ~.mat-file / measurement containing one structure "data"
5 % by Christoph Jeworrek, 2009 - 2011, last change 25.04.2010
6 clear all %clear complete variable space
7
8 rawdata(1).splitter_version = '1.1.08'; %program version
9 max_length_no=4; %maximal digits of number of measurement (up to 99 files = 2, 999 = 3, etc.)
10 filepath='D:\Promotion\Messaufenthalte'; %standard import path
11
12 disp(' '), disp(['==> Programm started - version ' rawdata(1).splitter_version])
13 disp('=====') %command line output
14 disp(datestr(now)), disp(' ')
15
16 %Initial sequences in file for parameters:
17 ip_tablez='#UESRF_ID2_SAXS_TABLEZ'; %table height
18 ip_sary='#UESRF_ID2_SAXS_SARY'; %angle of cell
19 ip_info='#UDmoInfo'; %beamline info
20 ip_Tnn='#UHS32V14'; %time not normalized
21 ip_masch_exp='#UHS32V01'; %exposure time saved by maschine (factor 10 to small)
22 ip_proposal='#UProposalInfo'; %proposal info
23 ip_detector='#UDetectorInfo'; %used detector
24 ip_lambda='#UWaveLength'; %wave length of radiation
25 ip_SD_dist='#USampleDistance'; %sample-detector distance
26 ip_t_exp='#UExposureTime'; %real exposure time
27
28 %Get name and location of import file
29 [filename,pathname1] = uigetfile('*.spec','Choose a file to import', filepath);
30 if filename == 0
31     errordlg('Data file not found','file error');
32     return
33 end
34 disp(['=> start importing files from "' pathname1 '\' filename]), disp(' ')
35
36 %Import of data from file
37 [fid,msg] = fopen(fullfile(pathname1, filename),'r'); %open file
38 if fid == -1;
39     error(msg);
40 end
41 ifound=0; %number of found scans
42 line=fgetl(fid); %reads first line
43 while (ischar(line) && ~feof(fid)); %reading file "line-by-line" and searching for parameters
44     if length(line)>5; %line contains information
45         if strcmp(line(1:2),'#S'); %first line of a scan
46             ifound=ifound+1;
47             rawdata(ifound).splitter_version=rawdata(1).splitter_version;
48             scanno=sscanf(line(3:length(line)),'%g');
49             ckscan = textscan(line, '%*s %*n %s %s',1);
50             rawdata(ifound).no=scanno(1); %#ok<*AGROW> %number of scan
51             disp(['-> reading scan No. ' num2str(scanno(1))])
52             rawdata(ifound).aq_date=ckscan{1};
53             rawdata(ifound).name=ckscan{2};
54             line=fgetl(fid);
55             elseif length(line)>= length(ip_tablez) && strcmp(line(1:length(ip_tablez)), ip_tablez)
56                 rawdata(ifound).tablez=str2double(line(length(ip_tablez)+2:end));
57                 line=fgetl(fid);
58             elseif length(line)>= length(ip_sary) && strcmp(line(1:length(ip_sary)), ip_sary)
59                 rawdata(ifound).sary=str2double(line(length(ip_sary)+2:end));
60                 line=fgetl(fid);
61             elseif length(line)>= length(ip_info) && strcmp(line(1:length(ip_info)), ip_info)
62                 rawdata(ifound).info=line(length(ip_info)+2:end);
63                 line=fgetl(fid);
64             elseif length(line)>= length(ip_Tnn) && strcmp(line(1:length(ip_Tnn)), ip_Tnn)
65                 T_temp=line(length(ip_Tnn)+2:end);
66                 line=fgetl(fid);
67             elseif length(line)>= length(ip_masch_exp) &&...
68                 strcmp(line(1:length(ip_masch_exp)), ip_masch_exp)
69                 exp_temp=line(length(ip_masch_exp)+2:end);
70                 line=fgetl(fid);
71                 rawdata(ifound).T=str2double(T_temp)./str2double(exp_temp);
72             elseif length(line)>= length(ip_proposal) &&...

```

```

73     strcmp(line(1:length(ip_proposal)), ip_proposal)
74     rawdata(ifound).proposal=line(length(ip_proposal)+2:end);
75     line=fgetl(fid);
76     elseif length(line)>= length(ip_detector) &&...
77         strcmp(line(1:length(ip_detector)), ip_detector)
78         rawdata(ifound).detector=line(length(ip_detector)+2:end);
79         line=fgetl(fid);
80     elseif length(line)>= length(ip_lambda) && strcmp(line(1:length(ip_lambda)), ip_lambda)
81         rawdata(ifound).wavelength=line(length(ip_lambda)+2:end);
82         line=fgetl(fid);
83     elseif length(line)>= length(ip_SD_dist) && strcmp(line(1:length(ip_SD_dist)), ip_SD_dist)
84         rawdata(ifound).sample_detector_distance=line(length(ip_SD_dist)+2:end);
85         line=fgetl(fid);
86     elseif length(line)>= length(ip_t_exp) && strcmp(line(1:length(ip_t_exp)), ip_t_exp)
87         rawdata(ifound).t_exp=line(length(ip_t_exp)+2:length(ip_t_exp)+...
88             find(line(length(ip_t_exp)+1:end) == 's', '1', 'first'));
89         line=fgetl(fid);
90     elseif strcmp(line(1:2), '#L') %start of actual SAXS data
91         rawdata(ifound).raw_legend=line(4:end);
92         rawdata(ifound).raw=[];
93         while (ischar(line) && ~strcmp(line(1:2), '#S')); %line-by-line reading of SAXS data
94             line=fgetl(fid);
95             line=[line ' '];
96             [numdata,n]=sscanf(line, '%g');
97             if n > 0;
98                 numdata=numdata';
99                 rawdata(ifound).raw=[rawdata(ifound).raw;numdata];
100             end
101             if feof(fid);
102                 break
103             end
104         end
105     else
106         line=fgetl(fid);
107     end
108 else
109     line=fgetl(fid);
110 end
111 end
112 fclose(fid);
113
114 %Exclude intensity values of -10 at beginning and end of dataset (
115 for i= 1:length(rawdata)
116     first_data_pos=find(rawdata(i).raw(:,end)~= -10, 1, 'first');
117     last_data_pos=find(rawdata(i).raw(:,end)~= -10, 1, 'last');
118     rawdata(i).I=rawdata(i).raw(first_data_pos:last_data_pos,end);
119     rawdata(i).q=rawdata(i).raw(first_data_pos:last_data_pos,2);
120 end
121
122 %Creating export directory
123 projectname=cjf_generate_unique_foldername(pathname1, [filename(1:end-5) '_splitted']);
124 mkdir(fullfile(pathname1,projectname));
125 disp(' '), disp(['=> start saving splitted files to: ' cd])
126
127 %Complete missing data and export data
128 for i=1:length(rawdata)
129     data=rawdata(i); %#ok<NASGU>
130     if isempty(rawdata(i).proposal) %proposal number not in file
131         inpt_no=inputdlg({'Enter proposal number (for output filename):'},...
132             'Proposal number',1,{'sc0000'});
133         part1=cell2mat(inpt_no);
134     else
135         part1=rawdata(i).proposal;
136     end
137     if length(num2str(rawdata(i).no)) < max_length_no %add zeros to scan numbers (e.g., 1 -> 01)
138         nullen=num2str(zeros(1,max_length_no-length(num2str(rawdata(i).no))));
139         save_number=[nullen(1,nullen=='0') num2str(rawdata(i).no)];
140     else
141         save_number = num2str(rawdata(i).no);
142     end
143     savename=[part1 '_scan_' save_number '.mat'];
144     save(fullfile(pathname1,projectname,savename), 'data'); %saves complete structure

```

```

145 %save(savename, '-struct', 'data'); %saves all fields of structure as single variable
146 disp(['-> scan No ' num2str(rawdata(i).no) ' saved to file "' savename '"'])
147 clear data
148 end
149
150 disp(' '), disp('-----'), disp('=> DONE!!!')
151 end

```

A.3 GUI: manual identification of space groups from Bragg peaks

A program has been written with a graphical user interface (GUI) to identify different crystallographic space groups from SAXS Bragg peak patterns. First a screen shot of the GUI is presented and afterwards the corresponding MATLAB code is shown.

A.3.1 Graphical user interface (GUI)

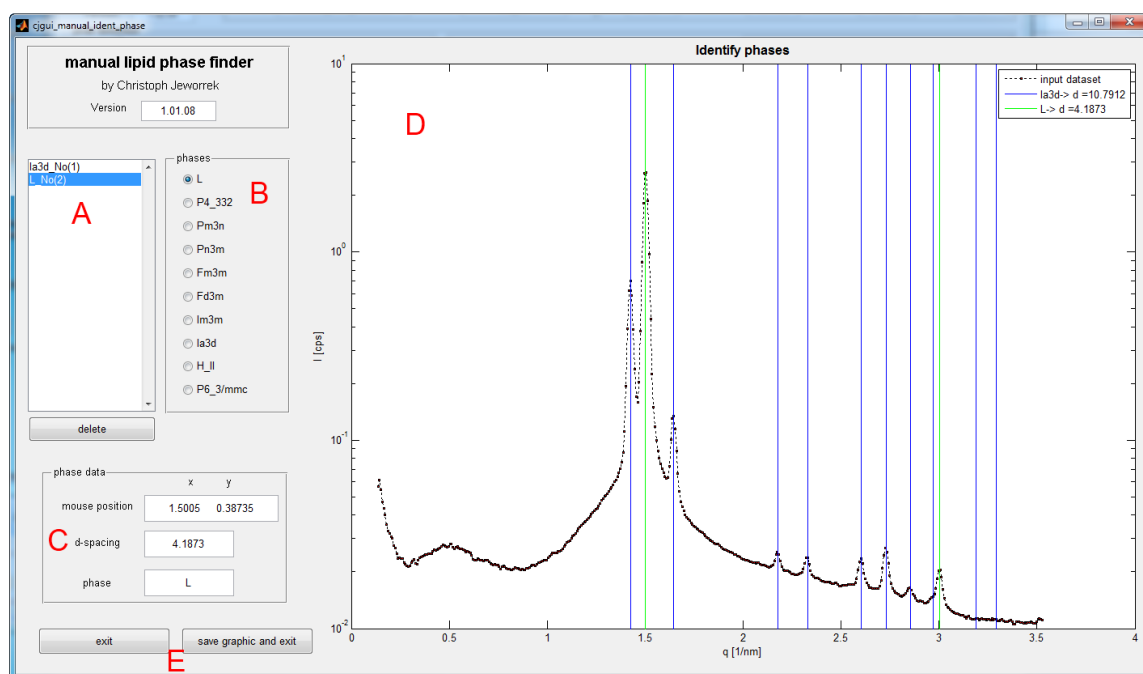


Figure A.1: Graphical user interface (GUI) of a program to identify different crystallographic space groups from SAXS Bragg peak patterns.

The GUI of the program is depicted in Figure A.1. In part D the imported scattering curve is plotted. To evaluate the positions of a potential phase, first in panel B one of the phases is selected by clicking on the corresponding radio button. In the screen shot the lamellar (L) phase is active. Afterwards, the mouse is moved into the graphic window D. By pressing the left mouse button down, lines appear at positions of the expected reflections, where the position of the mouse is always the first Bragg signal. By moving the mouse (with pressed button) the lines can be shifted to the desired position. Upon release of the mouse button inside the graphic window D the found phase is saved and added to the list A. At the same time in panel C information of the phase are visible. If the mouse button is released outside graphic D, the chosen phase is dismissed.

In the screen shot two phases have been identified: an *Ia3d* phase and a lamellar phase. The lamellar phase has been selected in list A. Therefore, the corresponding parameters are shown in panel C and the corresponding Bragg reflex positions are highlighted in graphic D (green lines). A selected phase can be deleted with the "delete"-button, which removes the phase from the list and the reflex positions from the

graphic D. After all peaks are identified the program can be closed with the buttons E (including the option of saving graphic D). The names of the found phases as well as the corresponding crystallographic d -spacings and found reflexes are written into a single output structure containing the fields (.pos; .d; .name).

A.3.2 Programming code

The programming code corresponding to the GUI shown in Figure A.1 is presented here. It is a typical and relatively short example of the code of a GUI program. To execute the code another file is needed – the .fig file, which defines the positions of the different elements (buttons, panels, graphic windows, etc.) relative to the window frame.

```

1 function varargout = cjgui_manual_ident_phase(varargin)
2 % CJGUI_MANUAL_IDENT_PHASE M-file for cjgui_manual_ident_phase.fig
3 % - INPUT: two columns of numerical data. 1) xdata=q; 2)ydata=I;
4 %           3) standard save folder & 4) standard save name both as string
5 % - OUTPUT: structure with fields:
6 %   .name = name of found phase
7 %   .d = d-spacing of phase in units of 1/q
8 %   .pos = ratio of peak positions according to d-spacing
9 %
10 % Last Modified by GUIDE v2.5 14-Dec-2010 10:43:21
11 %by Christoph Jeworrek, 2010, last change 22.12.2010
12
13 %Initialization code
14 gui_Singleton = 1;
15 gui_State = struct('gui_Name',      mfilename, ...
16   'gui_Singleton',  gui_Singleton, ...
17   'gui_OpeningFcn', @cjgui_manual_ident_phase_OpeningFcn, ...
18   'gui_OutputFcn',  @cjgui_manual_ident_phase_OutputFcn, ...
19   'gui_LayoutFcn',  [], ...
20   'gui_Callback',   []);
21 if nargin && ischar(varargin{1})
22     gui_State.gui_Callback = str2func(varargin{1});
23 end
24
25 if nargin
26     [varargout{1:nargout}] = gui_mainfcn(gui_State, varargin{:});
27 else
28     gui_mainfcn(gui_State, varargin{:});
29 end
30
31 %Execution before GUI becomes visible
32 function cjgui_manual_ident_phase_OpeningFcn(hObject, eventdata, handles, varargin)
33 global version theory_phases phase_string actual_phase std_path std_savename...
34 xdata legend_dat found_result %global variables in GUI
35 clear h_legend
36 version='1.01.08';
37
38 varargin_num=nargin-3; %handling of variable input
39 if varargin_num < 2
40     error('not enough input arguments!');
41 else
42     xdata=cell2mat(varargin(1));
43     ydata=cell2mat(varargin(2));
44 end
45 if varargin_num < 3, std_path = pwd; else std_path=cell2mat(varargin(3)); end
46 if varargin_num < 4, std_savename = 'Manual_ident_phases_result.png';
47 else std_savename=cell2mat(varargin(4)); end
48
49 handles.output = hObject;
50
51 %set initial parameters of GUI elements
52 set(handles.figure1,'WindowButtonDownFcn',{@cjibf_mouse_down, handles});
53 set(handles.figure1,'WindowButtonUpFcn', {@cjibf_mouse_up, handles});
54 set(handles.edit_version,'String',version);
55 set(handles.uipanel_phases,'SelectionChangeFcn',@uipanel_phases_SelectionChangeFcn);
56 set(handles.listbox_found_phases,'Max',1);

```

```

57 set(handles.listbox_found_phases,'Min',0);
58
59 cjibf_plot_data(handles, xdata, ydata) %plot imported data
60
61 %load theoretical data of different lipid phases
62 theory_phases = cji_lamellar_phase();
63 tmp_phases = cji_cubic_phases();
64 for i=1:length(tmp_phases)
65     theory_phases(length(theory_phases)+1)=tmp_phases(i);
66 end
67 tmp_phases = cji_hexagonal_phases();
68 for i=1:length(tmp_phases)
69     theory_phases(length(theory_phases)+1)=tmp_phases(i);
70 end
71 phase_string={};
72 for i = 1:length(theory_phases)
73     phase_string=cat(1,phase_string,{theory_phases(i).space_group});
74 end
75
76 actual_phase=1;
77 set(handles.edit_phase,'String',cell2mat(phase_string(actual_phase)))
78 legend_dat={'input dataset'};
79 found_result={};
80
81 guidata(hObject, handles);
82 uiwait(handles.figure1);
83
84 % GUI output after execution
85 function varargout = cjgui_manual_ident_phase_OutputFcn(hObject, eventdata, handles)
86 global found_result
87 if exist('found_result','var') && ~isempty(found_result)
88     phase_struc(size(found_result,1)) = struct('pos', [], 'd', [], 'name', []);
89     for n = 1:size(found_result,1)
90         phase_struc(n).pos=cell2mat(found_result(n,5));
91         phase_struc(n).d=cell2mat(found_result(n,2));
92         phase_struc(n).name=cell2mat(found_result(n,1));
93     end
94     varargout{1} = phase_struc;
95 else
96     varargout{1} = 0;
97 end
98 close %LAST LINE OF GUI
99
100 %===== BUTTONS =====
101
102 function pushbutton_exit_Callback(hObject, eventdata, handles)
103 uiresume(handles.figure1);
104
105 function pushbutton_exit_and_save_Callback(hObject, eventdata, handles)
106 cjibf_save_graphic(hObject, eventdata, handles)
107 uiresume(handles.figure1);
108
109 function pushbutton_delete_phase_Callback(hObject, eventdata, handles)
110 global found_result
111 selected = get(handles.listbox_found_phases,'Value');
112 string = get(handles.listbox_found_phases,'String');
113 target_tag=string(selected,1);
114 target_handle = findobj(handles.axes1,'Tag',target_tag);
115 if ~isempty(target_handle), delete(target_handle); end
116 set(handles.listbox_found_phases,'Value',1)
117 new_string=string(~strcmp(string,target_tag),:);
118 set(handles.listbox_found_phases,'String',new_string)
119 found_result(strcmp(found_result(:,4),target_tag,:)=[]);
120 old_legend_string=get(findobj(get(handles.figure1,'Children'),'Tag','legend'),'String');
121 new_string={old_legend_string(1,~strcmp(old_legend_string,old_legend_string(1,selected+1)))};
122 set(findobj(get(handles.figure1,'Children'),'Tag','legend'),'String',new_string)
123 guidata(hObject, handles);
124
125 %===== EDITS =====
126
127 function edit_version_Callback(hObject, eventdata, handles)
128 global version

```

```

129 set(handles.edit_version, 'String', version);
130
131 function edit_version_CreateFcn(hObject, eventdata, handles)
132 if ispc && isequal(get(hObject, 'BackgroundColor'), get(0, 'defaultUicontrolBackgroundColor'))
133     set(hObject, 'BackgroundColor', 'white');
134 end
135
136 function edit_phase_Callback(hObject, eventdata, handles)
137 global actual_phase phase_string
138 set(handles.edit_phase, 'String', cell2mat(phase_string(actual_phase)));
139
140 function edit_phase_CreateFcn(hObject, eventdata, handles)
141 if ispc && isequal(get(hObject, 'BackgroundColor'), get(0, 'defaultUicontrolBackgroundColor'))
142     set(hObject, 'BackgroundColor', 'white');
143 end
144
145 function edit_mouse_pos_Callback(hObject, eventdata, handles)
146 set(handles.edit_mouse_pos, 'string', '');
147
148 function edit_mouse_pos_CreateFcn(hObject, eventdata, handles)
149 if ispc && isequal(get(hObject, 'BackgroundColor'), get(0, 'defaultUicontrolBackgroundColor'))
150     set(hObject, 'BackgroundColor', 'white');
151 end
152
153 function edit_d_spacing_Callback(hObject, eventdata, handles)
154
155
156 function edit_d_spacing_CreateFcn(hObject, eventdata, handles)
157 if ispc && isequal(get(hObject, 'BackgroundColor'), get(0, 'defaultUicontrolBackgroundColor'))
158     set(hObject, 'BackgroundColor', 'white');
159 end
160
161 %===== RADIO BUTTON =====
162 function uipanel_phases_SelectionChangeFcn(hObject, eventdata)
163 global actual_phase phase_string
164 handles = guidata(hObject);
165 switch get(eventdata.NewValue, 'Tag')
166     case 'radiobutton_L'
167         actual_phase=1;
168     case 'radiobutton_P4_332'
169         actual_phase=2;
170     case 'radiobutton_Pm3n'
171         actual_phase=3;
172     case 'radiobutton_Pn3m'
173         actual_phase=4;
174     case 'radiobutton_Fm3m'
175         actual_phase=5;
176     case 'radiobutton_Fd3m'
177         actual_phase=6;
178     case 'radiobutton_Im3m'
179         actual_phase=7;
180     case 'radiobutton_Ia3d'
181         actual_phase=8;
182     case 'radiobutton_H_II'
183         actual_phase=9;
184     case 'radiobutton_x_phase'
185         actual_phase=10;
186 end
187 set(handles.edit_phase, 'String', cell2mat(phase_string(actual_phase)));
188 set(handles.edit_d_spacing, 'String', '');
189 set(handles.edit_mouse_pos, 'String', '');
190 guidata(hObject, handles);
191 %===== LISTBOX =====
192
193 function listbox_found_phases_Callback(hObject, eventdata, handles)
194 global found_result
195 selected = get(handles.listbox_found_phases, 'Value');
196 string = get(handles.listbox_found_phases, 'String');
197 target_tag=string{selected,1};
198 cjibf_highlight_phase(hObject, eventdata, handles, target_tag)
199 result_row=strcmp(found_result(:,4), target_tag);
200 set(handles.edit_phase, 'String', cell2mat(found_result(result_row,1)));

```

```

201 set(handles.edit_d_spacing, 'String', num2str(cell2mat(found_result(result_row,2))));
202 guidata(hObject, handles);
203
204 function listbox_found_phases_CreateFcn(hObject, eventdata, handles)
205 if ispc && isequal(get(hObject, 'BackgroundColor'), get(0, 'defaultUiControlBackgroundColor'))
206     set(hObject, 'BackgroundColor', 'white');
207 end
208
209 %===== CJIBF =====
210
211 function cjibf_highlight_phase(hObject,eventdata,handles, target_tag)
212 %highlights chosen phase in green
213 old_target_handle = findobj(handles.axes1, 'Color', 'g');
214 if ~isempty(old_target_handle)
215     for n = 1:length(old_target_handle) % n=n+1
216         set(old_target_handle(n), 'Color', 'b')
217     end
218 end
219 target_handle = findobj(handles.axes1, 'Tag', target_tag);
220 child_handle=get(target_handle, 'Children');
221 if ~isempty(child_handle)
222     for n = 1:length(child_handle) % n=n+1
223         set(child_handle(n), 'Color', 'g')
224     end
225 end
226 guidata(hObject, handles);
227
228 function cjibf_get_currentpoint_in_axes(hObject,eventdata,handles)
229 %gets current position of mouse in GUI
230 global mouse_pos inside
231 handles = guidata(hObject);
232 ylim=get(handles.axes1, 'Ylim');
233 xlim=get(handles.axes1, 'Xlim');
234 mouse_pos = get(handles.axes1, 'CurrentPoint');
235 fig_pos=get(handles.figure1, 'Position');
236 if (mouse_pos(1,1)>= xlim(1) && mouse_pos(1,1) <= xlim(2)) && (mouse_pos(1,2)>=...
237     ylim(1) && mouse_pos(1,2) <= ylim(2))
238     legend_handle=findobj(get(handles.figure1, 'Children'), 'Tag', 'legend');
239     if isempty(legend_handle)
240         set(handles.edit_mouse_pos, 'string', num2str([mouse_pos(1,1) mouse_pos(1,2)]));
241         inside=1;
242     else
243         leg_pos=get(legend_handle, 'OuterPosition');
244         mouse_pos_rel = get(handles.figure1, 'CurrentPoint');
245         mouse_pos_abs = [mouse_pos_rel(1)+fig_pos(1) mouse_pos_rel(2)+fig_pos(2)];
246         leg_pos_abs=[leg_pos(1)*fig_pos(3)+fig_pos(1) ... left side
247             (leg_pos(1)+leg_pos(3))*fig_pos(3)+fig_pos(1) ... right side
248             leg_pos(2)*fig_pos(4)+fig_pos(2) ... lower side
249             (leg_pos(2)+leg_pos(4))*fig_pos(4)+fig_pos(2)... upper side
250         ];
251         if (mouse_pos_abs(1) > leg_pos_abs(1) && mouse_pos_abs(1) < leg_pos_abs(2)) ...
252             && (mouse_pos_abs(2) > leg_pos_abs(3) && mouse_pos_abs(2) < leg_pos_abs(4))
253             inside=0;
254         else
255             set(handles.edit_mouse_pos, 'string', num2str([mouse_pos(1,1) mouse_pos(1,2)]));
256             inside=1;
257         end
258     end
259 else
260     inside=0;
261 end
262 guidata(hObject, handles);
263
264 function cjibf_set_d_spacing(hObject,eventdata,handles)
265 %set d-spacing value in corresponding edit-box
266 global mouse_pos d_spacing xdata
267 ylim=get(handles.axes1, 'Ylim');
268 if (mouse_pos(1,1)>= xdata(1,1) && mouse_pos(1,1) <= xdata(end,1)) && (mouse_pos(1,2)>=...
269     ylim(1) && mouse_pos(1,2) <= ylim(2))
270     set(handles.edit_d_spacing, 'String', num2str(d_spacing));
271 end
272 guidata(hObject, handles);

```



```

273
274 function cjibf_mouse_down(hObject,eventdata,handles)
275 %action when mouse button1 is pressed down
276 global inside
277 cjibf_get_currentpoint_in_axes(hObject,eventdata,handles);
278 if inside==1
279     cjibf_calc_d_spacing
280     cjibf_set_d_spacing(hObject,eventdata,handles)
281     cjibf_plot_lines(hObject,eventdata,handles)
282     set(handles.figure1, 'WindowButtonMotionFcn', {@cjibf_mouse_move,handles});
283 end
284 guidata(hObject, handles);
285
286 function cjibf_mouse_move(hObject,eventdata,handles)
287 %action during mouse movement (only when button is pressed)
288 cjibf_get_currentpoint_in_axes(hObject,eventdata,handles);
289 cjibf_move_lines(hObject,eventdata,handles)
290 guidata(hObject, handles);
291
292 function cjibf_mouse_up(hObject,eventdata,handles)
293 %action when mouse button1 is released
294 global lines_temp
295 cjibf_get_currentpoint_in_axes(hObject,eventdata,handles);
296 set(handles.figure1, 'WindowButtonMotionFcn', '');
297 if exist('lines_temp','var') && ~isempty(lines_temp)
298     cjibf_keep_or_delete_lines(hObject,eventdata,handles)
299 end
300 guidata(hObject, handles);
301
302 function cjibf_plot_data(handles, xdata, ydata)
303 %(re-)plotting of data
304 semilogy(handles.axes1,xdata, ydata, 'sk', 'LineWidth',0.5, 'MarkerSize',2,...
305     'MarkerFaceColor','r', 'MarkerEdgeColor','k');
306 xlabel(handles.axes1,{'q [1/nm]'})
307 ylabel(handles.axes1,{'I [cps]'})
308 title(handles.axes1,{'Identify phases'}, 'LineWidth',3, 'FontWeight', 'bold', 'FontSize',12)
309
310 function cjibf_calc_d_spacing
311 %calculation of crystallographic d-spacing
312 global d_spacing actual_phase theory_phases mouse_pos peak_max_pos
313 d_spacing=2.*pi*theory_phases(actual_phase).peak_pos_ratio(1)./mouse_pos(1,1);
314 peak_max_pos=(2.*pi.*theory_phases(actual_phase).peak_pos_ratio./d_spacing)';
315
316
317 function cjibf_move_lines(hObject,eventdata,handles)
318 %calculation of line movement according to expected phase positions
319 global peak_max_pos xdata lines_temp
320 cjibf_calc_d_spacing
321 cjibf_set_d_spacing(hObject,eventdata,handles)
322 plot_pos=peak_max_pos(peak_max_pos<=max(xdata));
323 if length(lines_temp)==size(plot_pos,1) && ~isempty(plot_pos) && plot_pos(1) >= ...
324     xdata(1,1) && plot_pos(1) <= xdata(end,1)
325     for i = 1:size(plot_pos,1) % i=i+1
326         set(lines_temp(i), 'XData', [plot_pos(i) plot_pos(i)])
327         set(lines_temp(i), 'YData', get(lines_temp(1), 'YData'))
328     end
329 elseif exist('lines_temp','var') && ~isempty(lines_temp) && ~isempty(plot_pos) && ...
330     plot_pos(1) >= xdata(1,1) && plot_pos(1) <= xdata(end,1)
331     delete(lines_temp)
332     cjibf_plot_lines(hObject,eventdata,handles)
333 end
334 hold(handles.axes1, 'off')
335
336 function cjibf_plot_lines(hObject,eventdata,handles)
337 %plotting of lines according to expected phase positions
338 global peak_max_pos xdata lines_temp
339 plot_pos=peak_max_pos(peak_max_pos<=max(xdata));
340 ylim=get(handles.axes1, 'Ylim');
341 ypos=[ylim(1) ylim(2)];
342 newpos=[plot_pos plot_pos]';
343 hold(handles.axes1, 'on')
344 lines_temp=plot(handles.axes1, newpos, ypos, '-r');

```

```

345 hold(handles.axes1,'off')
346 guidata(hObject, handles);
347
348 function cjibf_keep_or_delete_lines(hObject,eventdata,handles)
349 %decide if lines after moving and releasing mouse are kept
350 global theory_phases actual_phase d_spacing legend_dat lines_temp inside ...
351     peak_max_pos xdata found_result h_legend
352 cjibf_get_currentpoint_in_axes(hObject,eventdata,handles);
353 if exist('lines_temp','var') && sum(ishandle(lines_temp))==size(lines_temp,1),...
354     delete(lines_temp); end
355 if inside == 1
356     plot_pos=peak_max_pos(peak_max_pos<=max(xdata));
357     ylim=get(handles.axes1,'Ylim');
358     ypos=[ylim(1) ylim(2)];
359     newpos=[plot_pos plot_pos]';
360     tag=[theory_phases(actual_phase).space_group '_No(' num2str(size(found_result,1)+1) ')'];
361     AGroup = hggroup('Tag',tag);
362     set(AGroup,'Parent',handles.axes1)
363     hold(handles.axes1,'on')
364     plot(handles.axes1,newpos,ypos,'-b','Parent',AGroup);
365     hold(handles.axes1,'off')
366     set(get(AGroup,'Annotation'),'LegendInformation','IconDisplayStyle','on');
367     legend_dat(length(legend_dat)+1,1)=[theory_phases(actual_phase).space_group ...
368         '-> d = ' num2str(d_spacing)];
369     h_legend=legend(legend_dat);
370     found_result(size(found_result,1)+1,:)=theory_phases(actual_phase).space_group, ...
371         d_spacing, actual_phase, tag, plot_pos);
372     string_temp=get(handles.listbox_found_phases,'String');
373     if isempty(string_temp), string_temp={string_temp}; end
374     string_temp(size(found_result,1),:)=tag;
375     set(handles.listbox_found_phases,'String',string_temp)
376     set(handles.listbox_found_phases,'Value',size(found_result,1))
377     cjibf_highlight_phase(hObject,eventdata,handles,tag)
378 end
379 guidata(hObject, handles);
380
381 function cjibf_save_graphic(hObject, eventdata, handles)
382 %save plotted graphic when exiting GUI
383 global std_path std_savename
384 axes_units = get(handles.axes1,'Units');
385 newFig = figure;
386 axesObject2 = copyobj(handles.axes1,newFig);
387 set(axesObject2,'Units',axes_units);
388 set(axesObject2,'Position',[0.1 0.1 0.85 0.85]);
389 set(newFig,'Units',axes_units);
390 set(newFig,'Position',[1.05 1.1 0.9 0.80]); %opens "outside" the monitor
391 print(['-f' num2str(newFig)],'-dpng','-r300',fullfile(std_path, std_savename))
392 close(newFig)

```

A.4 Advanced processing of SAXS data - main routine

The main routine of this program package several all sub-functions during the execution. The purpose of the program is the processing of SAXS measurements series, like in static pressure dependent SAXS series or trSAXS pressure jump experiments. This includes basic correction of the data (correction of q -scale based on a reference measurement as well as cutting of the maximal q -scale to exclude instrument shadows), 2D and 3D plotting of the raw data, and finally evaluation of the data based on the automatic detection of Bragg peaks followed by the determination of the underlying crystallographic unit cells. Alternatively or additionally, also an evaluation of the data based on the Porod invariant or the RMSDs of each measurement of the series from the last dataset is possible. Finally, the result is exported as ASCII files and plotted into several graphics.

```

1 %CJS_START_AKP Script calls all needed subfunctions for SAXS Automatic Kinetics Processing
2 % based on Porod invariant / RMSDs or Braggs law
3 % by Christoph Jeworrek, 2009–2011, contact: christoph.jeworrek@tu-dortmund.de
4 % last change 19/04/2011
5

```

```

6 clear all; close all;
7 prog_vers = '01.04.18'; %version number of program
8 pathname0=pwd; %path where program is started
9 just_plot=0; % control to stop execution after 3D plot
10 stand_imp_path='C:\Promotion\Messaufenthalte';
11 stand_para_file=[]; %path and file of standard parameters of GUI/script - find_peak_and_phase
12 correction_factor_q=1.016687; %correction factor of q-scale from AgBehenate measurement
13 manual_search=2; %parameter determines output level of "peak_find" and "phase_find"
14
15 head={['=> Programm started - version ' prog_vers];'-----';datestr(now);' '};
16 for i=1:length(head)
17     disp(cell2mat(head(i,:)))
18 end
19 [log1, importfolder, data] = cjf_import_data(stand_imp_path);
20 projectname=[importfolder(1,find(importfolder(1,1:end-1)=='\,1,'last')+1:end) '_results'];
21 projectpath = uigetdir(importfolder,['Choose folder to save results! Subfolder "' ...
22     projectname " will be automatically created"]);
23 [projectname] = cjf_generate_unique_foldername(projectpath, projectname);
24 mkdir(projectpath, projectname);
25 savepath=fullfile(projectpath, projectname);
26 try
27     clc
28     diary(fullfile(savepath, [projectname '.log']))
29     for i=1:length(head) %save head to diary
30         disp(cell2mat(head(i,:)))
31     end; clear head
32     disp(['-> Export folder created: "' projectname " in: ' projectpath])
33     disp(['-> Writing data from screen into "' [projectname '.log'] "''])
34     disp(' ')
35     disp('-----')
36     disp(' ')
37     for i=1:length(log1) %save log1 to diary
38         disp(cell2mat(log1(i,1)))
39     end; clear log1
40     disp(' ')
41     disp('-----')
42     disp(' ')
43
44     bgcor = questdlg('Do you want to subtract a background dataset?',...
45         'Background correction?','Yes','No','No');
46     if strcmp(bgcor,'Yes')
47         disp('=> importing and subtracting background file...')
48
49         [filename_BG, pathname_BG] =uigetfile({'*.mat'; '*.dat'; '*..*'},...
50             'Select background-file for import...',stand_imp_path);
51         disp(['-> importing background file from: ' pathname_BG])
52         [~, ~, data_BG] = cjf_import_data([pathname_BG filename_BG]); disp(' ')
53         data_xbg=data_BG.q; data_ybg=data_BG.I;
54         for i=1:length(data)
55             data_x=data(i).q; data_y=data(i).I;
56             [data_ycorr] = cjf_background_correction(data_x, data_y, data_xbg, data_ybg);
57         end
58         disp(' '); disp('-----'); disp(' ')
59     end; clear bgcor
60
61     disp('=> reading data of p,t or T...')
62     static_or_dynamic =questdlg('Data from static (p or T) or dynamic (t) dataset?',...
63         'Static or dynamic?','static','dynamic','static');
64     disp(['-> evaluation mode for ' static_or_dynamic ' data chosen'])
65     again='yes';
66     while strcmp(again,'yes')
67         switch static_or_dynamic
68             case 'static'
69                 [data, var] = cjf_enter_puT_static(data);
70                 jump_after_no=0;
71             case 'dynamic'
72                 [data, var, jump_after_no] = cjf_enter_put_kinetic(data);
73         end
74         again = questdlg('Have you entered data of p/t/T again?',...
75             'Run subroutine again?','yes','no','no');
76     end
77     disp(' '); disp('-----'); disp(' '); clear again

```

```

78
79 %correction q-values
80 disp('=> Correction of q-scale started...')
81 disp(['-> correction factor: ' num2str(correction_factor_q)])
82 for i=1:length(data)
83     data(i).q=data(i).q.*correction_factor_q;
84 end
85 disp(' '); disp('_____'); disp(' ')
86
87 %[data] = cjf_cor_I_exposure_t(data); %correction of different exposure times
88
89 disp('=> Cutting end of dataset...')
90 [data] = cjf_cut_off_data(data); %cut end of dataset (due to shadows of instrument)
91 disp(' '); disp('_____'); disp(' ')
92
93 %2D plotting of data
94 disp('=> 2D plotting of I(q)...')
95 cjf_plot_2D(data, var, savepath, 2, 0);
96 disp(' '); disp('_____'); disp(' ')
97
98 %3D plotting of data
99 disp(['=> 3D plotting of I(q,' var ')...'])
100 [X, Y, Z] = cjf_prepare_plot3_structure(data, var); %Preparing matrices for 3D plotting
101 cjf_plot3_SAXS(X,Y,Z, var) %cjf_plot3_SAXS_new(X,Y,Z, var) <- for publications
102 save_p = questdlg('Do you want to save the 3D plot?','Save graphic?','Yes','No','Yes');
103 if strcmp(save_p, 'Yes')
104     [~, first]=fileparts(data(1).file); [~, last]=fileparts(data(end).file);
105     filename1 = ['3D-plot_' first '-' last '.png'];
106     print('-dpng', fullfile(savepath, filename1),'-r300')
107     disp(['3D plot exported to "' filename1 '"'])
108 end
109 close; clear save_p first last
110 disp(' '); disp('_____'); disp(' ')
111
112 if just_plot==1
113     disp('=> Saving MatLab variables of plots...')
114     matlab_filename=cjf_generate_unique_filename(savepath, 'matlab_data_just_plot.mat');
115     save(fullfile(savepath, matlab_filename),'-mat')
116     disp(['-> Matlab variables saved to "' matlab_filename '"'])
117     disp(' '); disp('_____'); disp(' ')
118     disp(' ')
119     disp(datestr(now))
120     disp('Short execution DONE!')
121     disp(' ')
122     diary off
123     return
124 end
125
126 %Dimensionality
127 dim_sw = questdlg('Do you want to evaluate the dimensionality D of the dataset?',...
128     'Evaluate dimensionality?','Yes','No','Yes');
129 if strcmp(dim_sw,'Yes')
130     disp('=> Calculation of the dimensionality of all dataset...')
131     [data] = cjf_find_Dimensionality_SAXS(data, var, savepath, 2);
132     disp(' '); disp('_____'); disp(' ')
133 end; clear dim_sw
134
135 %Choose mode of further evaluation
136 text={'Further data evaluation based on Porod invariant or Braggs law?'; ' '; ...
137     '"Bragg-mode" for all data showing Bragg reflexions (based on fitting of those peaks)';...
138     '"Porod-mode" for data showing no Bragg reflexions (based on Porod invariant / RMSDs)'};
139 eval_mode = questdlg(text,'data evaluation mode...','Porod','Bragg','Both','Bragg');
140 clear text
141
142 %===== Evaluation based on Bragg reflexions =====
143 if strcmp(eval_mode,'Bragg') || strcmp(eval_mode,'Both')
144     disp('=> Data evaluation based on Braggs law:')
145     disp('=> finding peak positions and corresponding phases...')
146     disp(['-> outputfolder is ' savepath])
147     phase_mat={};
148     old_peak_mat=[]; old_phase_mat=[]; %essential for i=1
149     GUI_mode = questdlg('Choose mode of GUI execution for first run','GUI-mode',...

```

```

150     'script mode', 'GUI mode', 'GUI mode');
151 manual_search_fp=1; %cjf_find_peak should be executed here with a value of 1!
152 for i=1:length(data)
153     disp(' ')
154     disp(['-----==== processing file No ' num2str(i) ' - ' data(i).file ' ====='])
155     disp(' ')
156     [~,savename_part1]=fileparts(data(i).file);
157     if strcmp(GUI_mode, 'GUI mode')
158         parafile=[]; %path and filename of input parameterfile
159         [data(i), maxima, phase_mat2, stand_para, output_file]=process_lipid1(data(i), ...
160             parafile, old_peak_mat, savepath, savename_part1, old_phase_mat);
161         maxima_mat=maxima.maxima;
162     else
163         if ~isempty(stand_para_file) && i == 1
164             stand_para=load(stand_para_file);
165         elseif i == 1
166             stand_para=cji_stand_para_peak_and_phase_find;
167         end
168         [maxima_struct(i)] = cjf_find_peak_new(data(i).q, data(i).I, manual_search, ...
169             savepath, [savename_part1 '_overview_find_peaks.png'], data(i).file, old_peak_mat, ...
170             stand_para); %#ok<SAGROW> %automatic, non-GUI execution
171         maxima_mat=maxima_struct(i).maxima;
172         [phase_mat2] = cjf_find_phases_new(maxima_mat, data(i).q, data(i).I, ...
173             [stand_para.d_min, stand_para.d_max], stand_para.max_phases, manual_search, ...
174             savepath, [savename_part1 '_overview_find_phases.png'], data(i).file, ...
175             old_phase_mat); %automatic, non-GUI execution
176     end
177     switch var
178     case 'p'
179         phase_mat2(:,4)={data(i).p};
180     case 'T'
181         phase_mat2(:,4)={data(i).T};
182     case 't'
183         phase_mat2(:,4)={data(i).t};
184     end
185     [maxima_mat, area_sum] = cjf_find_peak_areas(maxima_mat, phase_mat2, ...
186         data(i).q, data(i).I);
187     for n=1:length(area_sum) % n=n+1
188         phase_mat2(n,5)={area_sum(n).rough_A};
189         phase_mat2(n,6)={area_sum(n).fit_A_corrected};
190     end; clear n
191     phase_mat=cat(1, phase_mat, phase_mat2);
192     old_peak_mat=maxima_mat;
193     old_phase_mat=phase_mat2;
194     if i == 1
195         GUI_mode = questdlg('Choose mode of GUI execution for all further datasets', ...
196             'GUI-mode', 'script mode', 'GUI mode', 'GUI mode');
197     end
198 end; clear savename_part1 phase_mat2 maxima_mat maxima_struct old_peak_mat ...
199     old_phase_mat area_sum i graout_name
200
201 [~, first]=fileparts(data(1).file); [~, last]=fileparts(data(end).file);
202 graout_name=[first '-' last '.png'];
203 [split_phases] = cjf_plot_result_akp(phase_mat, var, savepath, graout_name);
204 disp(['-> exporting files to ' savepath])
205 cjf_export_ASCII_AKP_bragg(savepath, phase_mat, split_phases, data)
206 disp(' '); disp('-----'); disp(' ')
207 end; clear first last
208
209 %===== Evaluation based on Porod invariant / RMSDs =====
210
211 if strcmp(eval_mode, 'Porod') || strcmp(eval_mode, 'Both')
212     text={'Further calculations based on Porod invariant Q or integral intensity?'; ' '; ...
213         ' Running both modes is highly recommended to reveal full kinetic behaviour of sample!'};
214     calc_mode = questdlg(text, 'data evaluation mode...', 'Porod invariant', ...
215         'Integral deviations', 'Both', 'Both'); clear text
216
217 if strcmp(calc_mode, 'Porod invariant') || strcmp(calc_mode, 'Both')
218     disp('=> Data evaluation based on Porod invariant:')
219     [kinetics_all_Porod, kinetics_after_Porod, data, boundary] = ...
220         cjf_evaluate_kinetics(data, var, jump_after_no, savepath, 'pi', []);
221     cjf_export_kin_data(kinetics_all_Porod, var, savepath, 'data_Porod_all')

```

```

222     if strcmp(var,'t')
223         cjf_export_kin_data(kinetics_after_Porod, var, savepath, 'data_Porod_after')
224     end
225     disp(' '); disp('-----'); disp(' ')
226 end
227 if strcmp(calc_mode,'Integral deviations')
228     disp('=> Data evaluation based on Integral deviations:')
229     [kinetics_all_integral_deviations, kinetics_after_integral_deviations, data,...
230      boundary] = cjf_evaluate_kinetics(data, var, jump_after_no, savepath, 'id', []);
231 elseif strcmp(calc_mode,'Both')
232     disp('=> Data evaluation based on Integral deviations:')
233     [kinetics_all_integral_deviations, kinetics_after_integral_deviations, data,...
234      boundary] = cjf_evaluate_kinetics(data, var, jump_after_no, savepath, 'id', boundary);
235 end
236 if strcmp(calc_mode,'Integral deviations') || strcmp(calc_mode,'Both')
237     cjf_export_kin_data(kinetics_all_integral_deviations, var, savepath, 'data_IntDev_all')
238     if strcmp(var,'t')
239         cjf_export_kin_data(kinetics_after_integral_deviations, var,...
240             savepath, 'data_IntDev_after')
241     end
242 end
243 disp(' '); disp('-----'); disp(' ')
244 end
245
246 %save all variables to matlab file
247 disp('=> Saving MatLab variables...')
248 matlab_filename=cjf_generate_unique_filename(savepath, 'matlab_data_all.mat');
249 save(fullfile(savepath, matlab_filename),'-mat')
250 disp(['-> Matlab variables saved to "' matlab_filename '"'])
251 disp(' '); disp('-----'); disp(' ')
252 disp(' '), disp(datestr(now)), disp('DONE!'), disp(' ')
253 diary off
254 catch error_s2
255     cd(pathname0);
256     errordlg('A critical and unexpected error occurred.','Critical error');
257     disp(' '), disp('=====')
258     disp('====> A critical and unexpected error occurred. Program has been terminated!')
259     disp('-----'), disp('Error details:')
260     disp(error_s2.message), disp(error_s2.identifier), disp(error_s2.cause), disp(' ')
261     for z=1:length(error_s2.stack)
262         disp(error_s2.stack(z).file), disp(error_s2.stack(z).name)
263         disp(num2str(error_s2.stack(z).line)), disp(' ')
264     end
265     if ~exist('crash_report','dir')
266         mkdir('crash_report');
267     end
268     [crash_report_name] = cjf_generate_unique_filename(cd, ...
269         ['Detailed crash conditions ' datestr(date) '.mat']);
270     save(fullfile(pathname0, 'crash_report', crash_report_name)); %saving workspace into file
271     disp(['=> crash conditions saved to "' pathname0 '\crash_report" file: ' crash_report_name])
272     diary off
273 end
274 close all

```

A.5 GUI of a program identifying space groups automatically from Bragg patterns

A program has been written with a graphical user interface (GUI) to first automatically find Bragg peaks in a SAXS pattern and afterwards identify autonomously the corresponding crystallographic space groups. If the program fails, the user can switch to the GUI described in section A.3 to identify the space groups manually. In a series of measurements each scattering pattern is processed separately.

Figure A.2 depicts a screen shot of the GUI. In panel A the parameters of the scan are displayed: file name, file information, scan number, temperature, pressure, and time after the pressure jump for kinetic data. The parameters can be edited by setting a new value in the corresponding box.

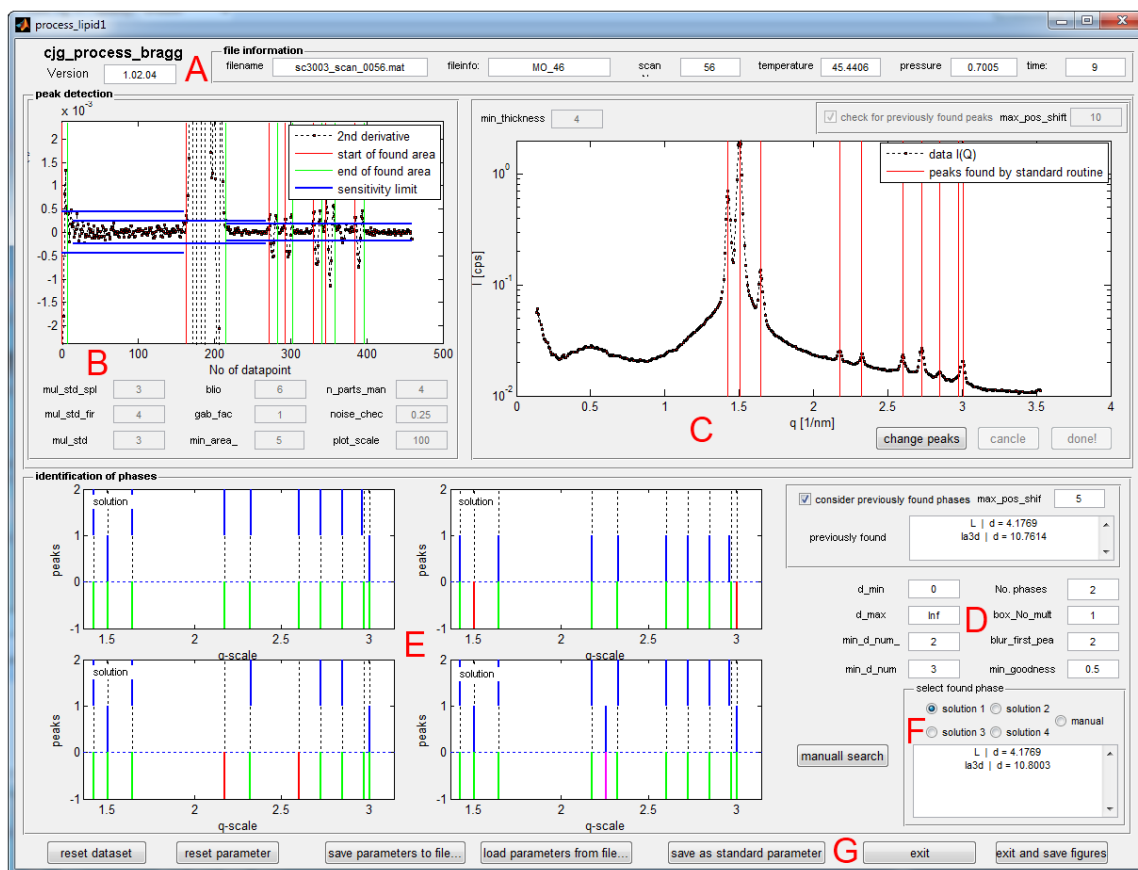


Figure A.2: GUI of a program identifying space groups automatically from Bragg peak patterns.

The parameters regulating the automatic detection of the Bragg peak positions are placed in panel B. The graph in this panel displays the second derivative of the experimental data as well as the boundaries, where peaks are suspected. The second part of the peak detection is performed directly afterwards.

In panel C the peak maxima found are displayed and can then manually be edited using the button “change peaks” and clicking into the graphic window (right click removes closest found peak and left click adds a new peak position). In the upper right of this panel there is a smaller panel giving the opportunity to include the result of the previous scan of the series into the detection process (inactive in the screen shot), which improves the performance in smeared or noisy scattering patterns.

In the lower part of the GUI the automatic detection of crystallographic space groups corresponding to the Bragg peak pattern is performed. The performance can be optimised by changing the parameters in part D. Again, there is an option to include information of the phases found in the previous Bragg peak pattern of a series to improve the success rate of the program. This is especially important for patterns containing more than two coexisting phases or systems containing a lamellar phase, where only the first Bragg reflection is visible.

The four most likely combinations of space groups corresponding to the scattering pattern are displayed in the figures in part E. The vertical dotted black lines indicate positions where a peak was found. In the upper part of each graphic the blue lines indicate the positions of reflections of the corresponding phase. In the lowest column the success of each solution is represented. A green line represents a match of theoretical and found peak positions. A red line indicates an experimentally found peak, which is not represented by the chosen phases. Finally, a pink line represents a theoretical peak of the space groups, which is not present in the scattering pattern.

In panel F each of the four solutions represented by the graphics in part E can be selected. The name(s) and crystallographic spacing(s) of the phase(s) in the solution are displayed. Additionally, a manual selection of the space groups is possible. In this case the GUI described in section A.3 opens.

The results of the process are saved and all data are written into an output structure when the “exit”-button (part G) is pressed. Additional buttons in this part enable the user to reset the GUI, reset parameters, save and load parameters as well as save the figures of the GUI.

Changing any parameter during the execution leads to an instant re-evaluation of all subsequent steps of the process. The evaluation speed decreases exponentially with the number of possible phases (part D, top right hand side parameter). It is highly recommended to chose values smaller than 4 and to use in all other cases the manual detection.

A.6 XRR raw data processing

A.6.1 Data measured at beamline BW1 at HasyLab, Hamburg

For technical reasons a reflectivity curve at HasyLab is measured with two different detectors – one counting the first part of the reflectivity curve, where the intensity is very high. The second part of the curve with much lower intensity is measured by another detector. The script merges both parts (including a correction for intensity differences between both detectors), calculates the magnitude of the wave vector transfer, q , and the reflectivity, R . If desired the reflectivity is re-normalised. Finally, the data are exported into one ASCII file per scan in the correct format for the fitting programs, Parratt32 or LSFIT.

```

1 %Script reads data from a XRR dat file (HasyLab BW1)
2 %Subscans are merged automatically (and I is corrected by a constant factor)
3 %Script exports every measurement as separate number.dat file, with
4 % number = number of first scan of measurement; detailed info in scanlist.txt
5 %Program writes two new arrays: "output" containing the processed data and scanlist
6 %written by Christoph Jeworrek, 2009–2011, contact: christoph.jeworrek@tu-dortmund.de
7 % last change 09/09/2010
8
9 clear all
10 prog_version='1.02.06';
11 Q_max_exp=0.6; %maximal Q value which is exported to file
12 export_extention='dat'; %File extention for export files
13 stand_imp_path='C:\Users\C.Jeworrek\Desktop\test_hasyLab\XRR'; %Standard input folder
14 ffm = 1; %Automatic correction of intensity while merging by constant factor? 1 = yes; 0 = no
15 renorm = 1; %Renormalization after merging parts? 1 = yes; 0 = no
16 exec_com = 'piba'; %exec command which starts reflectivity measurement
17 check_com = 'saux'; %command for alignment scans like table hight
18 gid_com = 'mytw'; %command for GID scan
19 Q_col_name = 'Q'; %name of column containing Q values in input files
20 R_col_name = 'REFL'; %name of column containing R values in input files
21
22 importpath = uigetdir(stand_imp_path,'Choose a folder for import');%select import directory
23
24 %create array of all filenames in folder
25 all_filenames_temp = dir(fullfile(importpath,'*.dat'));
26 sz_fn=size(all_filenames_temp,1);
27 for NZ=1:sz_fn
28     all_filenames{NZ,1} = all_filenames_temp(NZ,1).name;
29 end
30 scanlist=all_filenames; %write names to output file
31
32 %Import of data from file
33 data(sz_fn).raw=[];data(sz_fn).name=[];data(sz_fn).com_type=[];data(sz_fn).column_def=[];
34 for no_runs=1:sz_fn
35     filename = all_filenames{no_runs,1};
36     disp(['loading ' filename])
37     [fid,msg] = fopen(fullfile(importpath, filename),'r');
38     if fid == -1, error(msg), end
39     data(no_runs).name=filename;
40     line=fgetl(fid); % Reads the first line
41     while (ischar(line) && ~feof(fid))
42         while (ischar(line))
43             line=fgetl(fid); % Read new line
44             line=[line ' '];

```



```

45     if strcmp(line(1:4), '#cmd')
46         data(no_runs).com_type = strread(line(5:end), '%s', 'delimiter', ' ');
47     end
48     if strcmp(line(1:4), '#fip')
49         data(no_runs).column_def=strread(line(5:end), '%s', 'delimiter', ' ');
50     end
51     [numdata,n]=sscanf(line, '%g');
52     if n > 0;
53         data(no_runs).raw=[data(no_runs).raw;numdata'];
54     end
55     if feof(fid);
56         break
57     end
58 end
59 end
60 fclose(fid);
61 end
62 disp('=> file import finished'), disp(' ')
63
64 %Finding reflectivity measurements in the scans
65 ifound=1;
66 for i=1:length(data)
67     if strcmp(exec_com, data(i).com_type, 'exact')
68         tomerge(ifound).dat=data(i).raw;
69         tomerge(ifound).name=data(i).name;
70         tomerge(ifound).column_def=data(i).column_def;
71         tomerge(ifound).pos_in_data=i;
72         ifound=ifound+1;
73         scanlist(i,2)={'XRR-scan'};
74     elseif strcmp(check_com, data(i).com_type(1), 'exact')
75         scantype=cell2mat(data(i).com_type(2));
76         scanlist(i,2)={scantype(1:end-1) '-scan'};
77     elseif strcmp(gid_com, data(i).com_type(1))
78         scanlist(i,2)={'GID-scan'};
79     else
80         scanlist(i,2)={'unidentified scan'};
81     end
82 end
83 disp(' '), disp(['=> ' num2str(ifound-1) ' files containing reflectivity data found...'])
84
85 %Merging of subscans and writing output-filename into scanlist
86 no_parts = 1; outno=1; abbruch=0;
87 Q_pos=strmatch(Q_col_name, tomerge(1).column_def, 'exact');
88 R_pos=strmatch(R_col_name, tomerge(1).column_def, 'exact');
89 if (isempty(Q_pos) || isempty(R_pos))
90     disp('First datafile corrupt!!! Columns of R and Q could not be found!')
91     abbruch=1;
92 end
93 dataset(:,1)=tomerge(1).dat(:,Q_pos); %first Q
94 dataset(:,2)=tomerge(1).dat(:,R_pos); %first intensity
95 exp_filenames(1,1)={tomerge(1).name(1:3) tomerge(1).name(end-6:end-4)};
96 scanlist{tomerge(1).pos_in_data,3}=['Exported to: ' cell2mat(exp_filenames(1,1)) '.dat'];
97
98 if abbruch==0;
99     for N=2:length(tomerge)
100         Q_pos=strmatch(Q_col_name, tomerge(N).column_def, 'exact');
101         R_pos=strmatch(R_col_name, tomerge(N).column_def, 'exact');
102         if dataset(end-5,1) < tomerge(N).dat(1,Q_pos) %if part II of a scan
103             sds=size(dataset);
104             cut_off=find(tomerge(N).dat(:,Q_pos) < dataset(end,1));
105             srs=size(tomerge(N).dat);
106             if ffm == 1 %searches for factor of intensity for merging
107                 RG1=robustfit(dataset(end-4:end,1),...
108                     log10(dataset(end-4:end,2))); %Linear regression last 5 datapoints of first dataset
109                 RG2=robustfit(tomerge(N).dat((cut_off(end,1)+1):(cut_off(end,1)+5),Q_pos),...
110                     log10(tomerge(N).dat((cut_off(end,1)+1):...
111                         (cut_off(end,1)+5),R_pos))); %Linear regression first 5 data points of new dataset
112                 mid_RG1=RG1(1)+RG1(2).*(dataset(end,1)+(tomerge(N).dat(cut_off(end,1)+1,Q_pos)-...
113                     dataset(end,1))./2)); %function value exactly between both datasets
114                 mid_RG2=RG2(1)+RG2(2).*(dataset(end,1)+(tomerge(N).dat(cut_off(end,1)+1,Q_pos)-...
115                     dataset(end,1))./2)); %function value exactly between both datasets
116                 MF = (10.^mid_RG1)./(10.^mid_RG2);

```

```

117     else
118         MF = 1;
119     end
120     dataset((sds(1,1)+1):(sds(1,1)+srs(1,1)-(cut_off(end,1))),1)=...
121         tomerge(N).dat((cut_off(end,1)+1):end,Q_pos);
122     dataset((sds(1,1)+1):(sds(1,1)+srs(1,1)-(cut_off(end,1))),2)=...
123         tomerge(N).dat((cut_off(end,1)+1):end,R_pos).*MF;
124     no_parts = no_parts+1;
125     if ffm == 0
126         scanlist{tomerge(N).pos_in_data,3}='merged to previous file';
127     elseif ffm == 1
128         scanlist{tomerge(N).pos_in_data,3}=...
129             ['merged to previous file + I corrected by factor ' num2str(MF)];
130     end
131     else %if new scan
132         output(outno).XRR(:,1)=dataset(:,1);
133         output(outno).XRR(:,2)=dataset(:,2);
134         outno=outno+1;
135         no_parts = 1;
136         clear dataset
137         dataset(:,1)=tomerge(N).dat(:,Q_pos);
138         dataset(:,2)=tomerge(N).dat(:,R_pos);
139         exp_filenames(end+1,1)={ [tomerge(N).name(1:3) tomerge(N).name(end-6:end-4)]};
140         scanlist{tomerge(N).pos_in_data,3}=['Exported to: ' cell2mat(exp_filenames(end,1))...
141             '.' export_extention];
142     end
143 end
144 output(outno).XRR(:,1)=dataset(:,1);
145 output(outno).XRR(:,2)=dataset(:,2);
146 end
147
148 % (Re-)Normalisation of Reflectivity and writing LOG_R into output
149 for N=1:outno
150     maxpos = find(output(N).XRR(:,2)==max(output(N).XRR(:,2)),1,'first');
151     output(N).XRR(:,3)=output(N).XRR(:,2)./output(N).XRR(maxpos,2);
152     output(N).column_def={'Q' 'R_unnormalised' 'R_normalised' 'log(R_unnormalised)' ...
153         'log(R_normalised)'};
154     pospos=find(output(N).XRR(:,3)>0); %Search for values >= 0
155     output(N).XRR(pospos,4)=log10(output(N).XRR(pospos,2));
156     output(N).XRR(pospos,5)=log10(output(N).XRR(pospos,3));
157 end
158
159 %Export data to file
160 foldername='data_Hasylab_processed';
161 [foldername] = cjf_generate_unique_foldername(importpath, foldername);
162 mkdir(importpath, foldername);
163 scanlist2=scanlist';
164 diary(fullfile(importpath, foldername, 'scanlist.txt'));
165 disp(['==> Programm version ' prog_version])
166 disp('_____'), disp(datestr(now)), disp(' ')
167 disp(['files imported @ ' importpath ' :']); disp(' ');
168 disp_scanlist=sprintf('%s\t%s\t%s\n',scanlist2{:})
169 disp('by Christoph Jeworrek 2009-2011');
170 diary off
171
172 mkdir(fullfile(importpath, foldername), 'R(q)');
173 mkdir(fullfile(importpath, foldername), 'LOG_R(q)');
174 for N=1:outno
175     export_filename=[cell2mat(exp_filenames(N,1)) '.' export_extention];
176     clear content content2
177     pospos=find(output(N).XRR(:,1)<Q_max_exp);
178     pospos2=find(output(N).XRR(:,3)>=0);
179     if output(N).XRR(end,1)>Q_max_exp
180         pospos_ovz=find(pospos2>=Q_lim(1,1)); pospos2=pospos2(1:pospos_ovz(1,1)-1,1);
181     end
182     Q_lim=find(output(N).XRR(:,1)>Q_max_exp);
183     if renorm==1
184         normpos=3;
185     else
186         normpos=2;
187     end
188     content(:,1:3)=[output(N).XRR(pospos,1), output(N).XRR(pospos,normpos), 0];

```

```

189 content2(:,1:3)=[output(N).XRR(pospos,1), output(N).XRR(pospos,normpos+2), 0];
190 save(fullfile(importpath, foldername, 'R(q)', export_filename), 'content', '-ascii', '-tabs')
191 save(fullfile(importpath, foldername, 'LOG_R(q)', export_filename), 'content2', '-ascii', '-tabs')
192 end
193
194 clear content N NZ Q_pos R_pos abbruch all_filenames all_filenames_temp col_def...
195 cut_off data dataset empty export_extention export_filename fid filename line...
196 maxpos msg n no_parts no_runs numdata outno pospos sds Q_col_name...
197 srs stand_imp_path ans Q_lim Q_max_exp pospos_ovz MF ffm mid_RG1...
198 mid_RG2 RG1 RG2 i tomerge scantype ifound exec_com check_com R_col_name
199
200 save(fullfile(importpath, foldername, 'Matlab_variables.mat'), 'output', ...
201 'scanlist', 'importpath', 'prog_version');
202 disp(' '); disp('=> DONE! :-)')

```

A.6.2 Data measured at beamline ID10B at the ESRF

X-ray reflectivity data are measured with a PSD 2D detector at the beamline ID10B at the ESRF (Grenoble, France). This has the advantage that no separate scan for the correction of the diffuse background scattering is necessary.

All data of an experimental run are recorded in a single detector file. The script presented here reads this file, integrates the main detector channels, corrects the influence of the variation in the incident X-ray intensity and of background noise, the effect of different attenuators, plots the raw data of each scan, calculated the q -values, merges several sub-scans to a complete reflectivity curve, normalises the intensity and finally exports the data as a single ASCII files per measurement in a format, which is suitable for the fitting programs Parratt32 and LSFIT.

```

1 % Script reads data from a XRR detector file (ESRF ID10B)
2 % Data are converted to normalised R(Q) in [1/unit of wavelength]
3 % Subscans are merged automatically
4 % Script exports every measurement as separate number.dat file, with
5 % number = number of first scan of measurement; detailed info in scanlist.txt
6 % Program writes three new arrays: "output" containing the processed data, "data" containing
7 % part of the processed raw data and scanlist
8 % => Structure of data: .autoint:automatically integrated data by beamline
9 % software, for column definition see input file / .nr: datasetno. from
10 % inputfile / .type: measurement type / .maxpos: channel with maximal
11 % intensity / .I_int: col1-integrated I, col2-integrated bg, col3-corrected
12 % integrated I
13 % by Christoph Jeworrek, 2009–2011, christoph.jeworrek@tu-dortmund.de – last change 13/01/2010
14 clear all; close all; clc
15
16 %Parameters
17 prog_version = '1.2.06'; %program version
18 export_extention = 'dat'; %file extention of ASCII export file
19 scanlist={'number' 'type' 'axis' 'status'}; %initialisation of array
20 filepath='C:\Promotion\Messaufenthalte'; %Standard import path
21 correct_scans={'a2scan'; 'a3scan'}; %dcan types to take into account
22 mu_motor_name='mu'; %name of scanned motor in case of mu-scan
23 mu_name='mu'; %name of column containing mu data (incident angle)
24 monitor_name='Monitor'; %name of column containing monitor counts data
25 curratt_name='curratt'; %name of column containing current state of attenuator data
26 export_foldername='data_processed';
27 abs_thickness = 108; %Thickness of absorber Al plate in [um]
28 default_wavelength='1.56';
29 default_absorber='81.68';
30
31 %Find file to read
32 pathname0 = pwd; filename=0;
33 while filename==0
34     [filename,pathname1] = uigetfile('*.','Choose a detector file to import', filepath);
35 end
36 cd(pathname1);
37 kennung=find(filename=='.',1,'last');
38 if isempty(kennung)
39     diaryname=['logfile_' filename '.txt'];

```

```

40     foldername=filename;
41 else
42     diaryname=['logfile_' filename(1:kennung(1,end)-1) '.txt'];
43     foldername=[filename(1:kennung(1,end)-1) '_' filename(kennung(1,end)+1:end)];
44 end
45 if ~exist(export_foldername,'dir')
46     mkdir(export_foldername);
47 end
48 cd(export_foldername);
49 [foldername] = cjf_generate_unique_foldername(pwd, foldername);
50 mkdir(foldername);
51 cd(foldername);
52
53 %Get attenuation length and wave length of experiment from user
54 inppar=[];
55 while isempty(inppar)
56     prompt={'Enter the wavelength in [' char(197) ']:'},...
57           'Enter attenuation length in [\mum]:'};
58     name='Input parameters';
59     defaultanswer={default_wavelength,default_absorber};
60     options.Resize='on';
61     options.WindowStyle='normal';
62     options.Interpreter='tex';
63     inppar=inputdlg(prompt,name,1,defaultanswer,options);
64     if ~isempty(inppar)
65         att_length =str2double(inppar(2,1)) ; %attenuation length of A1
66         lambda = str2double(inppar(1,1)); %wave lenght in [AA]
67     end
68 end
69 clear inppar; pause(.5)
70
71 diary(diaryname)
72 disp(' '), disp(['==> Programm started - version ' prog_version])
73 disp('_____'), disp(datestr(now)), disp(' ')
74 disp(['=> Export folder is: " ' pathname1 export_foldername '\ ' foldername '\ "')
75 disp(['=> Writing data from screen into " ' diaryname "'']), disp(' ')
76 disp(['=> Start reading data from file: " ' filename "'']), cd(pathname1); disp(' ')
77
78 %Import of data from file
79 [fid,msg] = fopen(filename,'r');
80 if fid == -1
81     error(msg);
82 end
83 ifound=0; % Counter for found scans
84 line=fgetl(fid); % Reads the first line
85 while (ischar(line) && ~feof(fid)); %read line-by-line
86     if length(line)>3;
87         if strcmp(line(1:2), '#S');
88             iscan=sscanf(line(3:length(line)),'%g'); % Scan number
89             ckscan = textscan(line, '%*s %*n %s %s',1); %find scan type and first motor
90             scanlist{(end+1),1}=iscan; scanlist{(end),2}=...
91                 ckscan{1}; scanlist{(end),3}=ckscan{2};
92             if sum(strcmp(ckscan{1}, correct_scans),1)>0 && strcmp(ckscan{2},mu_motor_name)
93                 disp(['-> Reading and processing scan no. ' num2str(iscan)])
94                 ifound=ifound+1; % Add scan counter
95                 data(ifound).autoint=[]; % Initialize data variable
96                 line(1:2)='##';
97                 data(ifound).nr=iscan; data(ifound).type=[ckscan{1} ckscan{2}];
98                 ptfound=0;
99                 while (~strcmp(line(1:2), '#L'))
100                     line=fgetl(fid);
101                 end
102                 data(ifound).autoheader=strread(line(4:end), '%s' , 'delimiter', ' ');
103                 line=fgetl(fid);
104                 line=[line ' ']; %#ok<AGROW>
105                 numdata=sscanf(line, '%g');
106                 data(ifound).autoint=[data(ifound).autoint; numdata'];
107                 while (ischar(line) && ~strcmp(line(1:2), '#S')); % Empty or scan end
108                     if length(line)>3
109                         if (strcmp(line(end-2), '\') && ~strcmp(line(1), '#'))
110                             line=fgetl(fid);
111                             line=[line ' '];

```

```

112         numdata=sscanf(line,'%g');
113         data(ifound).d4i(ptfound).scan=[data(ifound).d4i(ptfound).scan;numdata'];
114     elseif (~strcmp(line(end-2),'\') && ~strcmp(line(1),'#'))
115         line=fgetl(fid);
116         line=[line ' '];
117         if strcmp(line(1:2),'@A')
118             line(1:3)=[];
119             ptfound=ptfound+1;
120             data(ifound).d4i(ptfound).scan=[];
121             numdata=sscanf(line,'%g');
122             data(ifound).d4i(ptfound).scan=[data(ifound).d4i(ptfound).scan;numdata'];
123         elseif ~strcmp(line,' ')
124             numdata=sscanf(line,'%g');
125             data(ifound).autoint=[data(ifound).autoint;numdata'];
126         end
127     else
128         line=fgetl(fid);
129         line=[line ' '];
130     end
131     else
132         line=fgetl(fid);
133     end
134     if feof(fid);
135         break
136     end
137     end
138     else
139         line=fgetl(fid);
140     end
141     else
142         line=fgetl(fid);
143     end
144     else
145         line=fgetl(fid);
146     end
147 end
148 fclose(fid);
149 disp(' '), disp(['-> ' num2str(ifound) ' datasets found in "' filename '"']), disp(' ')
150 clear ans ckscan fid ifound iscan kennung line msg numdata ptfound
151
152 % plot of detector rawdata
153 plot_var=0; %VAR: which kind of plot is used; possible values [0,1]
154 cd(export_foldername); cd(foldername);
155 mkdir('detector_raw_images'); cd('detector_raw_images')
156 disp('=> Plotting detector raw data...'), disp([' writing files to: "' cd '"']), disp(' ')
157 for i=1:length(data)
158     plotdata=[];
159     for k=1:length(data(i).d4i)
160         plotdata=cat(2, plotdata, mean(data(i).d4i(k).scan,2));
161     end
162     if plot_var==1
163         colormap pink
164         [~, c]=contourf(plotdata,length(plotdata)./2);
165         set(get(c,'Children'),'LineStyle','none')
166         set(gca,'PlotBoxAspectRatio',[1 1 1])
167         colorbar
168         if ~isempty(find(mean(plotdata,2)>1,1,'first')) &&...
169             ~isempty(find(mean(plotdata,2)>1,1,'last'))
170             ylim([find(mean(plotdata,2)>1,1,'first') find(mean(plotdata,2)>1,1,'last')]);
171         end
172         xlabel('number of datapoint'); ylabel('number of channel');
173         title('detector raw data - only non-zero rows shown');
174     else
175         subplot(5,1,1:3)
176         imagesc(plotdata)
177         colorbar
178         title('detector raw data');
179         ylabel('number of channel');
180         subplot(5,1,4:5)
181         imagesc(plotdata)
182         colorbar
183         if ~isempty(find(mean(plotdata,2)>1,1,'first')) &&...

```

```

184     ~isempty(find(mean(plotdata,2)>1,1,'last'))
185     ylim([find(mean(plotdata,2)>1,1,'first') find(mean(plotdata,2)>1,1,'last')]);
186     end
187     xlabel('number of datapoint'); ylabel('number of channel');
188     end
189     print('-dpng', ['detector_raw_' num2str(data(i).nr)])
190     close
191     disp(['-> writing "detector_raw_' num2str(data(i).nr) '.png" to file...'])
192 end
193 cd ..
194 disp(' Done!'), disp(' ')
195 clear plot_var
196
197 disp('=> Start integration of data...'), disp(' ')
198 disp('No | mean(max_pos) | std(max_pos) | No(signal_channels)')
199 halfwidth_fac=0.5; %VAR: hight of peak to search for "half width"
200 for j=1:length(data)
201     for i=1:length(data(j).d4i) %finding max-channel position and half-width of "peak"
202         data(j).d4i(i).mean=mean(data(j).d4i(i).scan,2); %mean value over all detector channels
203         data(j).d4i(i).maxpos_det=find(max(data(j).d4i(i).mean)==...
204         data(j).d4i(i).mean,1,'first'); %maximal of mean data
205         higher_pos=find(data(j).d4i(i).mean >= data(j).d4i(i).mean(data(j).d4i(i).maxpos_det)...
206         .*halfwidth_fac); %find position of values higher than "halfwidth_fac"
207         data(j).d4i(i).startpos=higher_pos(1,1)-...
208         (data(j).d4i(i).maxpos_det-higher_pos(1,1))-1; %find start-index of peak region
209         data(j).d4i(i).endpos=higher_pos(end,1)+...
210         (higher_pos(end,1)-data(j).d4i(i).maxpos_det)+1; %find end-index of peak region
211         data(j).int_hlp(i,1)=data(j).d4i(i).maxpos_det;
212         data(j).int_hlp(i,2)=data(j).d4i(i).startpos;
213         data(j).int_hlp(i,3)=data(j).d4i(i).endpos;
214     end
215     data(j).int_hlp(end+2,1:3)=mean(data(j).int_hlp,1);
216     data(j).int_hlp(end+1,1:3)=std(data(j).int_hlp(1:end-2,:),1);
217     av_maxpos(j,1)=round(data(j).int_hlp(end-1,1));
218     av_startpos(j,1)=round(data(j).int_hlp(end-1,2));
219     av_endpos(j,1)=round(data(j).int_hlp(end-1,3));
220     disp([num2str(data(j).nr) ' | ' num2str(data(j).int_hlp(end-1,1))...
221     ' | ' num2str(data(j).int_hlp(end,1))...
222     ' | ' num2str(av_endpos(j,1)-av_startpos(j,1)+1)])
223 end
224 avav_maxpos = round(cjfp_eval_hist(av_maxpos));
225 avav_startpos = round(cjfp_eval_hist(av_startpos));
226 avav_endpos = round(cjfp_eval_hist(av_endpos));
227 disp(' '), disp(['-> Averaged parameters used for all datasets:'])
228 disp([num2str(avav_maxpos) ' | ' num2str(avav_startpos) ' | ' num2str(avav_endpos)])
229 disp(' ')
230 for j=1:length(data)
231     for i=1:length(data(j).d4i)
232         data(j).I_int(i,1)=mean(data(j).d4i(i).mean(avav_startpos:avav_endpos,1)); %intensity
233         mean_left=mean(data(j).d4i(i).mean((avav_startpos-...
234         (avav_maxpos-avav_startpos)-1):avav_startpos,1));
235         mean_right=mean(data(j).d4i(i).mean(avav_endpos:(avav_endpos+...
236         (avav_endpos-avav_maxpos)+1),1));
237         data(j).I_int(i,2)=(mean_left+mean_right)/2; %intensity of background (diffuse scattering)
238         data(j).I_int(i,3)=data(j).I_int(i,1)-data(j).I_int(i,2); %background corrected intensity
239     end
240 end
241 clear av_endpos av_startpos av_maxpos c halfwidth_fac higher_pos i j k mean_left...
242     mean_right hist_a hist_b avav_endpos avav_startpos avav_maxpos
243
244 %Correction of intensity - monitor correction and absorber jumps + Calculation of Q [A^-1]
245 disp('=> Start correction of intensity...')
246 disp(['-> Thickness of absorber plates for absorber correction is ' ...
247     num2str(abs_thickness) '*10^-6 m'])
248 disp(['-> Intensity corrected with Monitor counts'])
249 disp(['-> Theta angle converted to Q [A^-1]'])
250 disp(' ')
251 for i=1:length(data)
252     if ~isempty(data(i).I_int)
253         data(i).Q=4.*pi.*sind(data(i).autoint(:,strmatch(mu_name, data(i).autoheader)))./lambda;
254         if data(i).autoint(:,strmatch(curratt_name, data(i).autoheader))> 13
255             error('WARNING: Found too high attenuator value!')

```

```

256     elseif data(i).autoint(:,strmatch(curratt_name, data(i).autoheader)) < 0
257         error('WARNING: Found too low attenuator value!')
258     end
259     data_corr_temp = data(i).I_int(:,3).*exp((abs_thickness.*...
260         data(i).autoint(:,strmatch(curratt_name, data(i).autoheader))./att_length);
261     data(i).I_int_corr = data_corr_temp ./ data(i).autoint(:,strmatch(monitor_name,...
262         data(i).autoheader));
263     scanlist((find(cell2mat(scanlist(2:end,1))==data(i).nr)+1),4)={'scan processed'};
264 else
265     data(i).Q=0; data(i).I_int_corr=0;
266     scanlist((find(cell2mat(scanlist(2:end,1))==data(i).nr)+1),4)={'empty scan'};
267 end
268 end
269 clear data_corr_temp i
270
271 %Merging of subscans
272 disp('=> Start merging subscans...')
273 no_parts = 1; N=2; outno=1;
274 dataset(:,2)=data(1).I_int_corr(:,1); %first intensity
275 dataset(:,1)=data(1).Q(:,1); %first Q
276 dataset(no_parts,3)=data(1).nr(1,1); %first No
277 while N <= length(data)
278     if dataset(end,1) == data(N).Q(1,1) %Only working if last Q of part1 == first Q of part2
279         sds=length(dataset); srs=length(data(N).I_int_corr);
280         dataset((sds+1):(sds+srs-1),1)=data(N).Q(2:end,1);
281         dataset((sds+1):(sds+srs-1),2)=data(N).I_int_corr(2:end,1);
282         no_parts = no_parts+1;
283         dataset(no_parts,3)=data(N).nr(1,1);
284         message=[cell2mat(scanlist((find(cell2mat(scanlist(2:end,1))==data(N).nr)+1),4))...
285             ' and merged'];
286         scanlist((find(cell2mat(scanlist(2:end,1))==data(N).nr)+1),4)={message};
287     else
288         output(outno).XRR(:,1)=dataset(:,1);
289         output(outno).XRR(:,2)=dataset(:,2);
290         output(outno).no(:,1)=dataset(1:no_parts,3);
291         outno=outno+1;
292         no_parts = 1;
293         clear dataset
294         dataset(:,2)=data(N).I_int_corr(:,1);
295         dataset(:,1)=data(N).Q(:,1);
296         dataset(no_parts,3)=data(N).nr(1,1);
297     end
298     N=N+1;
299 end
300 output(outno).XRR(:,1)=dataset(:,1);
301 output(outno).XRR(:,2)=dataset(:,2);
302 output(outno).no(:,1)=dataset(1:no_parts,3);
303 disp([num2str(outno) ' measurements found after merging of subscans'])
304 disp(' ')
305 clear N dataset message sds srs no_parts
306
307 %Normalisation of intensity
308 disp('=> Start calculation of reflectivity')
309 for N = 1:outno
310     if ~isempty(find(output(N).XRR(:,2)==inf, 1)) %check for infinite elements in I and set to 0
311         output(N).XRR(output(N).XRR(:,2)==inf,2)=0;
312         disp(['Infinite number values found in file no. ' num2str(output(N).no(1,1))...
313             '! All infinite values set to 0!!!'])
314     end
315     over95pos = output(N).XRR(:,2)>0.95*output(N).XRR(find(output(N).XRR(:,2)==...
316         max(output(N).XRR(:,2)),1,'first'),2); %find position of values > 0.95*I_max
317     output(N).XRR(:,3)=output(N).XRR(:,2)./mean(output(N).XRR(over95pos,2));
318     output(N).XRR((output(N).XRR(:,3)>1),3)=1;
319 end
320 disp('=> Intensity successfully normalized'), disp(' ')
321 clear over95pos N
322
323 %Export data to files
324 disp('=> Start exporting files...')
325 diary off
326 scanlistname=['scanlist_' foldername '.txt'];
327 diary(scanlistname);

```

```

328 disp(scanlist); disp(' ');
329 for N=1:outno
330     disp(['-> Measurement ' num2str(N) ':'])
331     disp(output(N).no); disp(' ');
332 end
333 disp(' '); disp('by Christoph Jeworrek 2009–2011');
334 diary off; clc
335 diary(diaryname)
336 disp(['-> List of processed files saved as "' scanlistname '" into folder "' foldername '"'])
337 disp(' '), disp(['-> Writing data files...'])
338 for N=1:outno
339     export_filename=[num2str(output(N).no(1,1)) '.' export_extention];
340     clear content
341     content=[output(N).XRR(2:end,1) output(N).XRR(2:end,3)];
342     save(export_filename, 'content', '-ascii', '-tabs')
343     disp(export_filename)
344 end
345 disp(' '), disp(['=> Saving Matlab variables into "Matlab_variables.mat"'])
346 clear N ans content filepath
347 variablesavename=['Matlab_variables_' foldername '.mat'];
348 save(variablesavename)
349 disp(' '), cd(pathname0); disp(['==> Processing of file "' filename '" done!'])
350 disp(datestr(now)), disp(' ')
351 diary off

```

A.7 Converting GIXD raw data to MATLAB structures

Whereas GIXD data measured at the ESRF beamline ID10B are already provided as GIXD maps, where several calculations and corrections are made using a MATLAB program written by the beamline staff, for the processing of data measured at the beamline BW1 at HasyLab such a program was not available. Therefore, a function was written importing the detector raw data (each step of the scanning process results here in a separate file). Afterwards, q_{xy} and q_z are calculated, the intensity is normalised, and finally the data are written into a MATLAB file almost identical to the one provided by the program at the ESRF. This makes it possible to use one single program (as presented in section A.8) for the further processing of the data independently if they have been measured at the ESRF or HasyLab.

```

1 function [ ] = cjf_convert_GID_HasyLab_to_ESRF( )
2 %CJF_CONVERT_GID_HASYLAB_TO_ESRF reads and converts HasyLab-BW1-GID files and exports
3 % it compatible to import format of cjf_plot_gid
4 % by Christoph Jeworrek, 2010–2011, christoph.jeworrek@tu-dortmund.de – last change 13/10/2010
5
6 prog_version = '1.00.10'; %program version
7 start_path='C:\Dokumente und Einstellungen\Christoph'; %standard import path
8 para_extention='.dat'; %file extention of parameter files to import
9 lambda=1.305; %wavelength of x-rays in Å
10 alpha_crit=0.13; %critical angle of water–air–interface at given wavelength
11 alpha_i=0.85.*alpha_crit; %incident angle in degree
12 chan_deg=135.5; %channels/degree
13 central_channel=40; %position of central channel @ alpha_i && alpha_PSD_arm
14
15 %Command line output
16 disp(' '), disp(['==> Programm started – version ' prog_version])
17 disp('=====')
18 disp(datestr(now)), disp(' ')
19
20 directory_name=0;
21 while directory_name==0 %search for directory including all GIXD scan raw data
22     directory_name = uigetdir(start_path,'Select import path!');
23 end
24 filename_imp=cjf_get_filenames(directory_name, 'empty');
25
26 disp(['=> importing files from ' directory_name]), disp(' ') %command line...
27
28 num_scan=1; %read rawdata files – one by one
29 full_name=cell2mat(filename_imp(1,1));
30 scans(num_scan).name=full_name(1,1:end-4);

```



```

31 data=load(fullfile(directory_name, full_name));
32 disp([' loading file: ' scans(num_scan).name])
33 scans(num_scan).channels=data(:,1);
34 scans(num_scan).I=data(:,2);
35 if size(filename_imp,1)>1
36     for i=2:size(filename_imp,1)
37         full_name=cell2mat(filename_imp(i,1));
38         data=load(fullfile(directory_name, full_name));
39         if strcmp(full_name(1,1:end-4),scans(num_scan).name)
40             scans(num_scan).I=horzcat(scans(num_scan).I,data(:,2));
41         else
42             num_scan=num_scan+1;
43             scans(num_scan).name=full_name(1,1:end-4);
44             disp([' loading file: ' scans(num_scan).name])
45             scans(num_scan).channels=data(:,1);
46             scans(num_scan).I=data(:,2);
47         end
48     end
49 end
50 disp(' '), disp(['-> number of loaded files: ' num2str(num_scan)]), disp(' ');
51
52 for i=1:num_scan %read parameters from scan files
53     importfilename=[scans(i).name para_extention];
54     disp(['loading parameter from: ' importfilename])
55     [fid,msg] = fopen(fullfile(directory_name,importfilename),'r');
56     if fid == -1 %if file could not be opened
57         scans(i).parameter_file='file not found';
58         error(msg)
59     else
60         scans(i).parameter_file=importfilename;
61         line=fgetl(fid); % reads the first line
62         stop_reading=0;
63         while (ischar(line) && ~feof(fid) && stop_reading==0)
64             line=fgetl(fid); % Read new line
65             line=[line ' '];
66             if strcmp(line(1:4),'#cmd')
67                 header_data = strread(line(5:end),'%s','delimiter',' ',' ');
68                 scans(i).scan_command=header_data;
69                 start_angle=cell2mat(header_data(1));
70                 start_angle=str2double(start_angle(6:end));
71                 end_angle=str2double(cell2mat(header_data(2)));
72                 steps=str2double(cell2mat(header_data(3)));
73                 scans(i).zweiTL=start_angle:(end_angle-start_angle)/(steps-1):end_angle;
74                 stop_reading=1;
75             end
76         end
77         fclose(fid);
78     end
79 end, disp(' ')
80
81 for i=1:size(scans,2) %calculation of q_z and q_xy
82     scans(i).alpha_f=((scans(i).channels-central_channel)./chan_deg)+alpha_i;
83     scans(i).q_z=-1.*cjf_Qz_GID(alpha_i, scans(i).alpha_f, lambda);
84     for k=1:size(scans(i).zweiTL,2) % k=k+1 %calculation of q_xy
85         scans(i).q_xy(:,k)=cjf_Qxy_GID(scans(i).zweiTL(1,k), scans(i).alpha_f, lambda);
86     end
87 end
88
89 for i=1:size(scans,2) %normalisation of intensity
90     scans(i).I_norm=(scans(i).I-min(min(scans(i).I)))/max(max(scans(i).I));
91 end
92
93 [exportfolder] = cjf_generate_unique_foldername(... %create export directory
94     directory_name, fullfile(directory_name, 'matlab_GIDs'));
95 mkdir(exportfolder)
96 disp(['=> exporting files to "' exportfolder]), disp(' ')
97
98 for i=1:size(scans,2) %converting into correct format and export Matlab data
99     export_filename=cjf_generate_unique_filename(exportfolder,[scans(i).name '.mat']);
100     %exp_struct=scans(i); %export hole structure
101     exp_struct.PSDNorm=scans(i).I_norm';
102     exp_struct.Qy=scans(i).q_xy';

```

```

103     exp_struct.Qz= repmat(scans(i).q_z', size(scans(i).q_xy', 1), 1);
104     disp(['    exporting: ' export_filename])
105     save(fullfile(exportfolder, export_filename), 'exp_struct', '-mat')
106     clear exp_struct
107 end
108
109 disp(' '), disp('-----===== DONE ====='), disp(datestr(now)), disp(' ')
110 end

```

A.8 Advanced processing of GIXD data

The program presented here is designed to import GIXD raw maps (a single file or several at once for batch processing) as provided by the beamline ID10B at the ESRF or calculated by the program shown in section A.7 from data measured at beamline BW1 at HasyLab.

The function of this program includes import of the data, check for data inconsistency, cutting of “zero intensity channels” at the beginning and end of the map, (re-)normalisation of the intensity, as well as integration of the data to obtain Bragg rod and Bragg peak profiles. The integration boundaries can be chosen automatically or manually.

From the Bragg peak profiles a straight line is subtracted to account for background effects. Data of Bragg rod and Bragg peak profiles are exported to ASCII files.

For ideal graphical representation of the GIXD maps, first a plane is subtracted from the data correcting systematic shifts in the background. Optionally, the data can be smoothed. Finally, the program provides two graphics showing up to four sub-plots: one showing raw data, GIXD maps and a Bragg peak pattern. The other depicting the Bragg peak pattern including the integration boundaries for the Bragg rods as well as up to three Bragg rod graphics.

```

1 function [ ] = cjf_plot_gid(path, cut, sm, strt, norm, fft, man_lim)
2 %CJF_PLOT_GID Summary of this function goes here
3 %   -> INPUT: path: if empty -> path for import is requested + single file
4 %   can be imported. if path is given -> import all *.mat files from path
5 %   || cut [0/1]: activate / deactivate automatic cutoff of 0-data ||
6 %   hpf: ['off']=no highpass filtering; ['1D']=highpass filtering Qz-values;
7 %   ['2D']=highpass filtering of both axes || lpf: ['off']=no lowpass
8 %   filtering; ['1D']=lowpass filtering Qxy-values; ['2D']=lowpass
9 %   filtering of both axes || sm [0/1]: activate / deactivate
10 %   automatic smoothing of data || strt [0/1]: activate / deactivate
11 %   automatic correction of systematic slope of background || norm [0/1]:
12 %   activate / deactivate automatic normalisation of intensity values
13 %   (max=1, min=0) || fft [0/1]: activate / deactivate automatic 2D FFT
14 %   filter (ATTENTION: highly experimental) || man_lim [0/1]: activate /
15 %   deactivate manual selection of integration limit along Q_z, e.g. as
16 %   needed if several unit cells are coexisting || imported files have to be
17 %   build by "MatSpecGUI" from ESRF ID10B or by "cjf_convert_GID_HasyLab_to_ESRF"
18 %   and contain only a single structure with fields (.PSDNorm, .Qy, .Qz)
19 %   Routine processed every step in new matrix -> slow, but "manual" retreatment
20 %   of data possible!
21 % by Christoph Jeworrek, 2010-2011, christoph.jeworrek@tu-dortmund.de - last change 10/05/2011
22
23 %Set values to input parameters if undefined or empty
24 if ~exist('cut','var') || isempty(cut), cut=1; end
25 if ~exist('sm','var') || isempty(sm), sm=1; end
26 if ~exist('strt','var') || isempty(strt), strt=1; end
27 if ~exist('norm','var') || isempty(norm), norm=1; end
28 if ~exist('fft','var') || isempty(fft), fft=0; end
29 if ~exist('man_lim','var') || isempty(man_lim), man_lim=1; end
30 if ~exist('path','var') || isempty(path)
31     questfile=1; filepath='C:\Users\Promorpheus\Desktop\test_space'; %pwd;
32 else
33     questfile=0; filepath=path;
34 end
35
36 prog_version = '5.00.06'; %program version
37 cutoff_per=0.7; %VAR: min percentage of mean intensity for cutoff of "dead" channels

```

```

38 % at the beginning and end of dataset
39 num_std=2.5; %VAR: multiple of standard deviation for lower plot level
40 no_lv=50; %VAR: number of levels in "regular-level-plot"
41 scrsz = get(0,'ScreenSize'); %reads screensize
42 plot_size=[scrsz(1)+20 scrsz(2)+50 scrsz(3)-40 scrsz(4)-150]; %VAR: size of plot on monitor
43
44 %Command line output
45 disp(' '), disp(['==> Programm started - version ' prog_version])
46 disp('=====')
47 disp(datestr(now)), disp(' ')
48
49 %Get file name(s) and location of input file(s)
50 if questfile==1
51     filename=0;
52     while filename==0
53         [filename,filepath] = uigetfile('*.mat','Choose a file to import', filepath);
54     end
55     filename_imp={filename}; %to enter the for-loop with only one file
56     if filename == 0
57         errordlg('Data file not found','file error');
58         return
59     end
60     disp(['=> file imported: ' fullfile(filepath, filename)], disp(' '))
61 else
62     filename_imp=cjf_get_filenames(filepath, '*.mat');
63 end
64
65 for fileno=1:length(filename_imp(:,1)) %for each input file...
66     filename=cell2mat(filename_imp(fileno));
67     if questfile==0, disp(['-----=> processing file: ' filename ' <=====']), end
68     struc_name=who('-file',fullfile(filepath, filename)); %read name of input structure
69     imp_struct=load(fullfile(filepath, filename),cell2mat(struc_name)); %load .mat
70     inPSDNorm=eval(['imp_struct.' cell2mat(struc_name) '.PSDNorm']); %intensity raw data
71     inQy=eval(['imp_struct.' cell2mat(struc_name) '.Qy']); %import Q_xy data
72     inQz=eval(['imp_struct.' cell2mat(struc_name) '.Qz']); %import Q_z data
73     [~, save_name_part1]=fileparts(filename); clear filename fileno imp_struct struc_name
74
75 %Check if import data format is consistent (may be problematic for aborted scans)
76 if sum(size(inQy)~=size(inQz))>0 || sum(size(inQy)~=size(inPSDNorm))>0
77     error('=> ERROR: sizes of imported data not identical!!! Evaluation of dataset aborted!')
78 end
79
80 if cut==1 %Cutoff of "low-intensity-lines" at beginning and end of the map - I(Q_xy,Q_z)
81     avIall=mean(mean(inPSDNorm));
82     linecontrol(1,size(inPSDNorm,2))=0; % find problematic lines
83     for i=1:size(inPSDNorm,2)
84         if sum(inPSDNorm(:,i)~=0)==0
85             linecontrol(1,i)=1;% 1=only containing zeros
86         elseif mean(inPSDNorm(:,i)) < avIall*cutoff_per
87             linecontrol(1,i)=2; % 2=average intensity of line much lower than average of dataset
88         end
89     end
90     halfpos=floor(length(linecontrol)./2);
91     firstpos=find(linecontrol(:,1:halfpos)~=0,1,'last')+1; %first correct line in map
92     if isempty(firstpos) || firstpos==halfpos+1
93         firstpos=1;
94         disp('=> WARNING: no first cutoff position found!')
95     end
96     lastpos=find(linecontrol(:,halfpos:end)~=0,1,'first')-1+halfpos; %last correct line in map
97     if isempty(lastpos) || lastpos==halfpos
98         lastpos=size(inPSDNorm,2);
99         disp('=> WARNING: no last cutoff position found!')
100    end
101    Qz=inQz(:,firstpos:lastpos); %corrected Q_z matrix
102    PSDNorm=inPSDNorm(:,firstpos:lastpos); %corrected intensity matrix
103 else
104     Qz=inQz;
105     PSDNorm=inPSDNorm;
106 end; clear avIall halfpos i linecontrol
107
108 per_lim=0.015; %VAR: percent of maximal deviation allowed in Q_xy for "integration"
109 def_Qy=abs(1-(inQy(floor(length(inQy(:,1))./2),:)./inQy(floor(length(inQy(:,1))./2),1)));

```

```

110 near_lin_no=find(def_Qy>=def_Qy(1,firstpos)+max(def_Qy).*per_lim,1,'first');
111 clear plotdata def_Qy per_lim
112
113 if man_lim==1 %limit Q_xz range of integration manually
114     fig_temp=figure('Position',plot_size, 'color','w'); %open plot
115     plotvec=mean(mean(PSDNorm))+num_std*mean(std(PSDNorm)):. . .
116         (max(max(PSDNorm))-mean(mean(PSDNorm))+num_std*mean(std(PSDNorm)))/(no_lv-1):. . .
117         max(max(PSDNorm));
118     plotvec=horzcat(plotvec,max(max(PSDNorm)));
119     figure(fig_temp)
120     contour(inQy(:,firstpos:lastpos),Qz,PSDNorm,plotvec,'-k') %plot data
121     title('Click on lower and upper limit of Q_z')
122     xlabel(['Q_{xy} / ' char(197) '^^{-1}']); ylabel(['Q_z / ' char(197) '^{-1}']);
123     [~,y2] = ginput(2); %get user limits by manual input
124     close(fig_temp)
125     if y2(1,1)<y2(2,1) %check if user chose lower or higher limit first
126         man_start=y2(1,1); man_end=y2(2,1);
127     else
128         man_start=y2(2,1); man_end=y2(1,1);
129     end
130     man_pos_start=find(abs(Qz(1,:)-man_start)==min(abs(Qz(1,:)-man_start)),1,'first');
131     man_pos_end=find(abs(Qz(1,:)-man_end)==min(abs(Qz(1,:)-man_end)),1,'first');
132 end; clear y2
133
134 if norm==1 %normalise all intensity data (min = 0, max = 1)
135     normdata=mean(inPSDNorm(:,firstpos:near_lin_no),2)-. . .
136         min(mean(inPSDNorm(:,firstpos:near_lin_no),2));
137     normdata2=mean(inPSDNorm(:,firstpos:lastpos),2)-. . .
138         min(mean(inPSDNorm(:,firstpos:lastpos),2));
139     normdata=normdata./max(normdata);
140     normdata2=normdata2./max(normdata2);
141     plotdata(:,1:2)=[inQy(:,firstpos) normdata];
142     plotdata_full(:,1:2)=[inQy(:,firstpos) normdata2];
143     if man_lim==1
144         normdata_man=mean(inPSDNorm(:,man_pos_start:man_pos_end),2)-. . .
145             min(mean(inPSDNorm(:,man_pos_start:man_pos_end),2));
146         normdata_man=normdata_man./max(normdata_man);
147         plotdata_man(:,1:2)=[inQy(:,firstpos) normdata_man];
148     end
149 else
150     plotdata(:,1:2)=[inQy(:,firstpos) mean(inPSDNorm(:,firstpos:near_lin_no),2)];
151     plotdata_full(:,1:2)=[inQy(:,firstpos) mean(inPSDNorm(:,firstpos:lastpos),2)];
152     if man_lim==1
153         plotdata_man(:,1:2)=[inQy(:,firstpos) mean(inPSDNorm(:,man_pos_start:man_pos_end),2)];
154     end
155 end; clear near_lin_no normdata
156
157 if size(plotdata,1)>5 %subtract straight line from Bragg peak profile
158     [y_fit, ~] = cjf_lower_envelope_1D(plotdata(:,1),plotdata(:,2), 0);
159     plotdata_flat=[plotdata(:,1) (plotdata(:,2)-y_fit)];
160 else
161     plotdata_flat=plotdata;
162     y_fit=zeros(size(plotdata,1),1);
163 end
164
165 if man_lim==1 && size(plotdata_man,1)>5 %subtract straight line from Bragg peak profile
166     [y_fit2, ~] = cjf_lower_envelope_1D(plotdata_man(:,1),plotdata_man(:,2), 0);
167     plotdata_man_flat=[plotdata_man(:,1) (plotdata_man(:,2)-y_fit2)];
168 end
169
170 if man_lim==1 && norm==1 %renormalise straightened Bragg peak profile
171     norm2=plotdata_flat(:,2)-min(plotdata_flat(:,2));
172     plotdata_flat=[plotdata_flat(:,1) norm2./max(norm2)];
173     norm6=plotdata_man_flat(:,2)-min(plotdata_man_flat(:,2));
174     plotdata_man_flat=[plotdata_man_flat(:,1) norm6./max(norm6)];
175 elseif norm==1
176     norm2=plotdata_flat(:,2)-min(plotdata_flat(:,2));
177     plotdata_flat=[plotdata_flat(:,1) norm2./max(norm2)];
178 end; clear norm2 norm6
179
180 fig1=figure('Position',plot_size, 'color','w');
181 subplot(2,2,4); %plot Bragg peak profile to graphic

```

```

182 plot(plotdata(:,1),plotdata(:,2),'-sk','MarkerSize',2)
183 hold on
184 plot(plotdata(:,1),y_fit,':r','LineWidth',2)
185 plot(plotdata_flat(:,1),plotdata_flat(:,2),'-ob','MarkerSize',2)
186 plot(plotdata_full(:,1),plotdata_full(:,2),'-g')
187 if man_lim==1
188     plot(plotdata_man(:,1),plotdata_man(:,2),'-c')
189     plot(plotdata_man_flat(:,1),plotdata_man_flat(:,2),'-or','MarkerSize',2)
190     legend({'data_{raw}','line_{background}','data_{corrected}','data_{overall-int}',...
191           'data_{man-int}','data_{man-int-flat}'})
192 else
193     legend({'data_{raw}','line_{background}','data_{corrected}','data_{overall-int}'})
194 end
195 hold off
196 xlabel(['Q_{xy} / ' char(197) '^-\^1']); ylabel('integrated intensity / a.u. ');
197 if norm==1
198     title('Integrated and normalised raw data');
199     ylim([-0.02 1.02]);
200 else
201     title('Integrated raw data');
202 end
203
204 %Export ASCII data of integrated PSDNorm(Q_xy) = Bragg peak profiles
205 plotdata=double(plotdata);
206 plotdata(:,3)=double(plotdata_flat(:,2));
207 plotdata(:,4)=double(plotdata_full(:,2));
208 if man_lim==1
209     plotdata(:,5)=double(plotdata_man(:,2));
210     plotdata(:,6)=double(plotdata_man_flat(:,2));
211 end
212 temp_savename=cjff_generate_unique_filename(filepath,[save_name_part1 '_int_Qxy.dat']);
213 save(fullfile(filepath,temp_savename),'plotdata','-ASCII','-tabs');
214 clear temp_savename
215
216 figure(fig1)
217 subplot(2,2,1); %plot GIXD map of imported unprocessed raw data
218 [~,c]=contourf(inQy,inQz,inPSDNorm);
219 xlabel(['Q_{xy} / ' char(197) '^-\^1']); ylabel(['Q_z / ' char(197) '^-\^1']);
220 h=colorbar;
221 title('Uncut raw data')
222 set(get(h,'ylabel'),'String','intensity / a.u.','Rotation',270,...
223     'VerticalAlignment','Bottom')
224 set(get(c,'Children'),'LineStyle','none')
225 clear inPSDNorm
226
227 if sm==1 %smoothing of map-data
228     for n=1:length(PSDNorm(:,1))
229         PSDNorm(n,:)=smooth(PSDNorm(n,:));
230     end
231 end; clear ft2_PSD
232
233 if strt==1 %subtract plain, uncurved area from map for background effect correction
234     PSDNorm=cjff_lower_envelope_2D(inQy(:,firstpos:lastpos), Qz, PSDNorm);
235 end
236 clear linecorr_m linecorr_y0 linepar_Qz n sm_PSD w_state linepar_Qz_corr
237
238 if fft==1 %apply FFT filter (not recommended - highly experimental!)
239     PSDNorm=cjff_pass_filter_2D(PSDNorm, 0.04, 'lp');
240 end
241
242 for in = 1:(1 + man_lim) % processing of Bragg rods with possibility of manual limits
243     if in==1 %set up parameters for particular run
244         pd_col=3; %column of integrated data in "plotdata"
245         min_int_lim=1; max_int_lim=size(PSDNorm,2);
246         out_name=save_name_part1;
247         tfp=firstpos;
248         tlp=lastpos;
249     elseif in > 1
250         pd_col=6;
251         min_int_lim=man_pos_start;
252         max_int_lim=man_pos_end;
253         tlp=firstpos+man_pos_end;

```

```

254     tfp=firstpos+man_pos_start;
255     out_name=[save_name_part1 '_man'];
256 end
257
258 peak_num_ok=0;
259 while peak_num_ok==0
260     stand_para=cji_stand_para_peak_and_phase_find; %load standard parameters
261     stand_para.min_thickness=2;
262     [maxima_struct] = cjf_find_peak_new(plotdata(:,1),... %automatically find peak maxima
263     plotdata(:,pd_col), 1,filepath, 'delete_me.png', out_name, [], stand_para);
264     delete(fullfile(filepath, 'delete_me.png')); %delete output graphic of cjf_find_peak
265     maxima_mat=maxima_struct.maxima; %matrix with peak maxima information
266     if size(maxima_mat,1)<4
267         peak_num_ok=1;
268     else
269         warndlg('Too many peaks for one unit cell! Pick again - maximal 3!')
270         clear maxima_mat
271     end
272 end
273
274 if ~isempty(maxima_mat) && size(maxima_mat,1)>0
275     multiple_width=3; %VAR: multiple of width found by cjf_find_peak for integration
276     plotdata2=inQz(1,tfp:tlp)';
277
278     for i=1:size(maxima_mat,1) % i=i+1
279         int_pos(i,1)=maxima_mat(i,1)-(maxima_mat(i,1)-...
280         maxima_mat(i,3))*multiple_width+1); %start position of integration
281         if int_pos(i,1)<1, int_pos(i,1)=1; end
282         int_pos(i,2)=maxima_mat(i,1)+(maxima_mat(i,4)-...
283         maxima_mat(i,1))*multiple_width+1); %end position of integration
284         if int_pos(i,2)>size(plotdata,1), int_pos(i,2)=size(plotdata,1); end
285         int_pos(i,3)=maxima_mat(i,1); % position of maximum
286     end; clear multiple_width
287
288     for i=1:size(maxima_mat,1) % i=i+1
289         if i<size(maxima_mat,1) && int_pos(i,2) > int_pos(i+1,1) %if integration areas overlap
290             min_pos=find(plotdata(int_pos(i+1,1):int_pos(i,2),pd_col)==...
291             min(plotdata(int_pos(i+1,1):int_pos(i,2),pd_col)),1,'first');
292             int_pos(i,2)=int_pos(i+1,1)+min_pos-1;
293             int_pos(i+1,1)=int_pos(i,2);
294         end; clear min_pos
295         plotdata2(:,i+1)=mean(PSDNorm(int_pos(i,1):int_pos(i,2),min_int_lim:max_int_lim),1)';
296     end
297 else
298     plotdata2=[inQz(1,tfp:tlp) ' mean(PSDNorm(:,min_int_lim:max_int_lim),1)'];
299     int_pos=[];
300 end
301
302 if norm==1 %renormalise intensity if necessary
303     PSDNorm=PSDNorm-min(min(PSDNorm));
304     PSDNorm=PSDNorm./max(max(PSDNorm));
305     for i=2:size(plotdata2,2)
306         plotdata2(:,i)=(plotdata2(:,i)-min(plotdata2(:,i)))./...
307         max((plotdata2(:,i)-min(plotdata2(:,i))));
308     end
309 end
310
311 fig2=figure('Position',plot_size, 'color','w');
312 subplot(2,2,1) %plot Bragg peak profile including integration boundaries
313 plot(plotdata(:,1),plotdata(:,pd_col),'-xk','MarkerSize',4)
314 xlabel(['Q_{xy} / ' char(197) '^-\^1']); ylabel('integrated intensity / a.u.');
```

```

315 if norm==1
316     title('Integrated and normalized Q_{xy): integration boundaries');
317     ylim([-0.02 1.02]);
318 else
319     title('Integrated Q_{xy): integration boundaries');
320 end
321 hold on
322 for i=1:size(int_pos,1) %plot boundaries
323     x_pos=plotdata(int_pos(i,3),1);
324     plot([x_pos, x_pos],ylim,'-b')
325     x2_pos=plotdata(int_pos(i,1),1);
```

```

326     plot([x2_pos, x2_pos],ylim,':r')
327     x3_pos=plotdata(int_pos(i,2),1);
328     plot([x3_pos, x3_pos],ylim,'-g')
329 end; clear x_pos x2_pos x3_pos
330 hold off
331
332 if ~isempty(maxima_mat) && size(maxima_mat,1)>0 && size(maxima_mat,1)<4
333     for i=2:size(plotdata2,2) % plot all Bragg rods
334         figure(fig2)
335         subplot(2,2,i)
336         plot(plotdata2(:,1),plotdata2(:,i),'-sk','MarkerSize',4)
337         xlabel(['Q_{z} / ' char(197) '^^{-1}']); ylabel('integrated intensity / a.u. ');
338         title(['Integrated data around Q_{xy}-maximum @ ' ...
339             num2str(plotdata(int_pos(i-1,3),1)) ' ' char(197) '^{-1}']);
340         exportdata=[plotdata2(:,1),plotdata2(:,i)]; %#ok<NASGU>
341         temp_savename=cjf_generate_unique_filename(filepath,[out_name '_int_Qz_' ...
342             num2str(plotdata(int_pos(i-1,3),1)) '.dat']);
343         %export ASCII-data of integrated PSDNorm(Q_xy)
344         save(fullfile(filepath,temp_savename),'exportdata','-ASCII','-tabs');
345         clear exportdata temp_savename
346     end
347 else %if no Bragg peak was found
348     subplot(2,2,2)
349     plot(plotdata2(:,1),plotdata2(:,2),'-sk','MarkerSize',4)
350     xlabel(['Q_{z} / ' char(197) '^{-1}']); ylabel('integrated intensity / a.u. ');
351     title('Integrated data of complete dataset over Q_{xy}');
352     exportdata=[plotdata2(:,1),plotdata2(:,2)]; %#ok<NASGU>
353     temp_savename2=cjf_generate_unique_filename(filepath,[out_name '_int_Qz_all.dat']);
354     save(fullfile(filepath,temp_savename2),'exportdata','-ASCII','-tabs');
355     clear exportdata
356 end; clear tlp tfp
357
358 figure(fig2) %add overall title and export Bragg rod graphic to file
359 axes('Position',[0 0 1 1],'Xlim',[0 1],'Ylim',[0 1],...
360     'Box','off','Visible','off','Units','normalized','clipping','off');
361 text(0.5, 1,['Overview Bragg rods ' save_name_part1],'FontSize',18,...
362     'HorizontalAlignment','center','VerticalAlignment','top')
363 set(gcf,'PaperPositionMode','auto')
364 temp_savename=cjf_generate_unique_filename(filepath,...
365     [out_name '_overview_Bragg_rods.png']);
366 print('-dpng','-r300',fullfile(filepath,temp_savename))
367 close(fig2); clear temp_savename int_pos
368 end
369
370 man_cor_fac=1; %no_lv=50; %parameters for manual corrections
371 plotvec=mean(mean(PSDNorm))+num_std*mean(std(PSDNorm))*man_cor_fac:...
372     (max(max(PSDNorm))-mean(mean(PSDNorm))+num_std*mean(std(PSDNorm)))/(no_lv-1):...
373     max(max(PSDNorm)); %vector containing intensity levels for "multi-level-map"
374 plotvec=horzcat(plotvec,max(max(PSDNorm)));
375
376 title_text='data-history: '; %generate graphic title text for corrected map
377 if norm==1, title_text=[title_text '-> normalised ']; end %#ok<*AGROW>
378 if cut==1, title_text=[title_text '-> cutted ']; end
379 if sm==1, title_text=[title_text '-> smoothed ']; end
380 if strt==1, title_text=[title_text '-> straightened ']; end
381
382 figure(fig1)
383 subplot(2,2,2) % corrected level map with black lines
384 contour(inQy(:,firstpos:lastpos),Qz,PSDNorm,plotvec,'-k')
385 xlabel(['Q_{xy} / ' char(197) '^{-1}']); ylabel(['Q_{z} / ' char(197) '^{-1}']);
386 title(title_text);
387
388 figure(fig1)
389 subplot(2,2,3) % corrected level map in colour
390 [~,c]=contourf(inQy(:,firstpos:lastpos),Qz,PSDNorm,plotvec);
391 xlabel(['Q_{xy} / ' char(197) '^{-1}'],'fontSize',12);
392 ylabel(['Q_{z} / ' char(197) '^{-1}'],'fontSize',12);
393 h=colorbar; %ylim(h,[0 1])
394 set(get(h,'ylabel'),'String','intensity / a.u.', 'Rotation', 270,...
395     'VerticalAlignment','Bottom','fontSize',12)
396 set(get(c,'Children'),'LineStyle','none')
397 title(title_text);

```

```
398
399 figure(fig1) %add overall title and export Bragg rod graphic to file
400 axes('Position',[0 0 1 1],'Xlim',[0 1],'Ylim',[0 1],...
401      'Box','off','Visible','off','Units','normalized','clipping','off');
402 text(0.5, 1,['Overview Bragg peaks ' save_name_part1],'FontSize',18,...
403      'HorizontalAlignment','center','VerticalAlignment','top')
404 set(gcf,'PaperPositionMode','auto')
405 temp_savename=cjf_generate_unique_filename(filepath,...
406      [save_name_part1 '_overview_Bragg_peaks.png']);
407 print('-dpng', '-r300', fullfile(filepath,temp_savename))
408 close(fig1)
409
410 clear Qz c h plotvec save_name_part1 PSDNorm title_text int_pos temp_savename
411 end
412
413 disp(' '), disp('-----===== DONE ====='), disp(datestr(now)), disp(' ')
414 end
```

APPENDIX B

List of symbols and abbreviations

symbol	legend
a	length / magnitude of the first axis in a crystallographic unit cell
a	lattice constant of inverse hexagonal and cubic phases
\vec{a}	crystallographic lattice vector
\vec{a}^*	reciprocal lattice vector
A	scattering amplitude
a_0	area per lipid at cross section / at the interface
\AA	unit of length: 1 Ångström = 10^{-10} m
$A\beta$	peptide: beta amyloid
A_{cell}	area of a 2D unit cell
A_{chain}	area per hydrocarbon chain
AD	Alzheimer's disease
AFM	atomic force microscopy
A_1	interfacial area integrated over a single monolayer
A_{mol}	area per molecule
A_S	interfacial area between the particle surface and solvent in SAXS
A_{S0}	scaled surface area of a different triply periodic minimal surface
ATR	attenuated total reflectance
b	length / magnitude of the second axis in a crystallographic unit cell
b	coherent scattering length
\vec{b}	crystallographic lattice vector
\vec{b}^*	reciprocal lattice vector
bar	unit of pressure: 1 bar = 10^5 Pa
Be	chemical element: beryllium
BL9	beamline at DELTA
BW1	XRR and GIXD beamline at HASYLAB
BW4	SAXS beamline at HASYLAB
c	concentration
c	length / magnitude of the third axis in a crystallographic unit cell
c	speed of light (in vacuum) = $2,99792 \cdot 10^8$ m s $^{-1}$
\vec{c}	crystallographic lattice vector
\vec{c}^*	reciprocal lattice vector
C	correction term for short-distance density fluctuations and experimental fluctuations in SAXS
CCD	charge-coupled device

continued on the next page...

symbol	legend
cf.	confer (Latin) = compare
Chol	steroid: cholesterol ((3 β)-cholest-5-en-3-ol)
cmc	critical micelle concentration
cp.	compare
CPP	critical packing parameter
CPU	central processor unit
d	lamellar lattice constant
D	Schoen diamond periodic minimal surface
Da	unit of atomic mass: 1 Dalton = 1 u \approx 1,6605655 \cdot 10 ⁻²⁷ kg
DAM	dummy atom model
d_{av}	average dimension of a particle
DELTA	Dortmunder Elektronenspeicherring-Anlage – synchrotron source of TU Dortmund University
DESY	Deutsches Elektronen-Synchrotron
DHPC	lipid: 1,2-dihexanoyl- <i>sn</i> -glycero-3-phosphocholine
d_l	monolayer thickness of a lipid layer
D_{max}	maximal dimension of a particle
DMPC	lipid: 1,2-dimyristoyl- <i>sn</i> -glycero-3-phosphocholine
DNA	deoxyribonucleic acid
DOPC	lipid: 1,2-dioleoyl- <i>sn</i> -glycero-3-phosphocholine
DOPE	lipid: 1,2-dioleoyl- <i>sn</i> -glycero-3-phosphoethanolamine
DOPG	lipid: 1,2-dioleoyl- <i>sn</i> -glycero-3-phospho-(1'- <i>rac</i> -glycerol)
DPPC	lipid: 1,2-dipalmitoyl- <i>sn</i> -glycero-3-phosphocholine
DPPG	lipid: 1,2-dipalmitoyl- <i>sn</i> -glycero-3-phospho-(1'- <i>rac</i> -glycerol)
dPS	perdeuterated poly(styrene)
DR	dummy-residue
d_{sample}	thickness of a sample (-layer)
DSC	differential scanning calorimetry
d_{total}	total thickness of a layer system in XRR
d_w	thickness of the water layer in an MLV
E_0, E_1	energy of an X-ray beam
EDP	electron density profile
e.g.	exempli gratia (Latin) = for example
ESRF	European Synchrotron Radiation Facility
et al.	et alii (lat.) = and others
etc.	et cetera (Latin) = and other things
eV	unit of Energy: 1 eV = 1.602 \cdot 10 ⁻¹⁹ J
$f(variable)$	function of <i>variable</i>
f'	real part of the average atomic scattering factor
F	intra-particle form factor in SAXS
ff.	following pages
FP	fusion peptide
FTIR	Fourier transform infrared
FWHM	full width at half maximum
g	unit of mass: 1 g = 10 ⁻³ kg
G	Schoen gyroid periodic minimal surface
G	Gibbs energy
GDGT	glycerol dialkylglycerol tetraether – caldarchaeol
GDNT	glycerol dialkylcalditol tetraether – calditoglycerocaldarchaeol

continued on the next page...

symbol	legend
GIXD	grazing incidence X-ray diffraction
GlcN	N-acetylglucosamines
G_P	penalty function: measure of the connectivity of the overall <i>ab initio</i> model
$g(r)$	radial pair distance distribution function
GUI	graphical user interface
GUV	giant unilamellar vesicle
h	unit of time: hour
h	first Miller index
h	Planck constant: $6,62606 \cdot 10^{-34}$ J s
\hbar	Dirac's constant: $h/(2\pi)$
H	enthalpy
$\langle H \rangle$	surface averaged values of mean curvature
H_{\parallel}	inverse hexagonal phase
HA2	haemagglutinin = influenza virus subunit 2
HASYLAB	Hamburger Synchrotronstrahlungslabor
HFIP	1,1,1,3,3,3-hexafluoroisopropanol
HHP	high hydrostatic pressure
HHZ	Helmholtz-Zentrum Berlin
hIAPP	human islet amyloid polypeptide
$h(r)$	total correlation function
HMI	(Hahn-Meitner Institut Berlin); recently renamed to Helmholtz-Zentrum Berlin
HP	high pressure
i	$\sqrt{-1}$
i	index of a specific particle or layer
I	scattering intensity
$Ia3d$	Hermann-Mauguin symbol of the cubic space group 230
IAPP	peptide: amylin; islet amyloid polypeptide
IAPP-GI	[IAPP-[(N-Me)G24, (N-Me)I26]]
ID02	SAXS beamline at the ESRF
ID10B	XRR and GIXD beamline at the ESRF
i.e.	id est (Latin) = that is
$Im3m$	Hermann-Mauguin symbol of the cubic space group 229
I_{peak}	(integrated) peak intensity
IR	infrared
IRRAS	infrared reflection absorption spectroscopy
J	unit of energy: $1 \text{ J} = 1 \text{ kg m}^2 \text{ s}^{-2}$
$j_0(x)$	zero order spherical Bessel function
$J_1(x)$	the first order Bessel function
k	prefix: kilo = 10^3
k	second Miller index
\vec{k}	wave vector
k	magnitude of the wave vector
K	contrast factor in SAXS
$\langle K \rangle$	surface averaged values of Gaussian curvature
k_B	Boltzmann constant
Kdo	2-keto-3-deoxyoctonoic acid
l	unit of volume: $1 \text{ l} = 10^{-3} \text{ m}^3$
l	third Miller index

continued on the next page...

symbol	legend
l	length of a lipid (chain)
L	order of multipole harmonics
L16	non-fusogenic control peptide
L_α	lamellar liquid-crystalline phase
$L_{\beta'}$	lamellar lipid gel phase with tilted acyl chains
L_c	liquid ordered / crystalline lamellar lipid phase
l_d	disordered liquid lamellar lipid phase (= L_α)
l_o	liquid ordered lamellar lipid phase (= L_c)
LPS	lipopolysaccharide
LUV	large unilamellar vesicles
L_{xy}	vertical coherence length of the two-dimensional crystal
L_z	horizontal coherence length of the two-dimensional crystal
m	unit of length: meter
m	prefix: milli = 10^{-3}
m	mass
M	molecular mass
M	unit of concentration: 1 M = 1 mol·l ⁻¹
M	prefix: Mega = 10^6
MATLAB	programming language: matrix laboratory
min	unit of time: minute
MLV	multilamellar vesicle
MO	lipid: monoolein / 1-oleoyl- <i>rac</i> -glycerol
mol	unit for amount of substance
MTG	microbial transglutaminase
n	prefix: nano = 10^{-9}
n	refractive index
N	number of particles
N_A	Avogadro constant = $6.022 \cdot 10^{23}$ mol ⁻¹
N_D	number of dummy-atoms in the multi-bead modelling approach
n_e	number of electrons
n_l	number of lipid molecules per unit cell
NMR	nuclear magnetic resonance
N_P	number of modelling parameters
NR	neutron reflectometry
N_S	number of Shannon channels
N_{stack}	average number of stacked layers
n_x	integer numeric order of a diffraction reflex
p	pressure
P	scattering factor in SAXS
P	Schwarz primitive periodic minimal surface
Pa	unit of pressure: 1 Pa = 1 N m ⁻²
$P_{\beta'}$	lamellar lipid gel phase with tilted acyl chains
P_b	theoretical burst pressure
PDB	Protein Data Base
PLFE	polar lipid fraction E, archaeal lipids
$Pn3m$	Hermann-Mauguin symbol of the cubic space group 224
P_P	penalty function for the looseness or degree of isolation of each non-solvent dummy-atom
PPC	pressure perturbation calorimetry
$p(r)$	pair distance distribution function

continued on the next page...

symbol	legend
PSD	position sensitive device (detector)
PTFE	polytetrafluoroethylene
P_y	maximum yield pressure
PyrPC	1-palmitoyl-2-(10-pyrenyl)-decanoyl)- <i>sn</i> -glycero-3-phosphatidylcholine
q	magnitude of the wave vector transfer
Q	molar ratio of long-to-short-chain lipids
\vec{q}	wave vector transfer
\tilde{Q}	Porod invariant
q_c	magnitude of the critical wave vector transfer
q_{\max}	position of a diffraction maximum
q.v.	quod vide (Latin) = see also
\vec{q}_{xy}	horizontal component of the wave vector transfer
q_z	vertical component of the wave vector transfer
r	radius
r	reflectivity coefficient
R	reflectivity
R	ideal gas constant
\vec{r}	point at certain distance from the incident beam
\vec{R}	vector between two scattering points in a particle
r_e	classical electron radius ($2.82 \cdot 10^{-15}$ m)
R_F	Fresnel reflectivity
R_G	radius of gyration
RMSD	root mean square deviation
$R_{p0.2}$	0.2 % offset yield strength
r_w	radius of a water channel
s	unit of time: second
s	magnitude of the scattering vector
S	entropy
$S(q)$	structure factor
\vec{s}	scattering vector
SANS	small-angle neutron scattering
SAXS	small-angle X-ray scattering
Si	chemical element: silicon
SNARE	soluble N-ethylmaleimide-sensitive-factor attachment receptor
SNase	protein: staphylococcal nuclease
s_o	solid ordered lamellar lipid phase
SOLEIL	synchrotron source in Giv sur Yvette, France
SUV	small unilamellar vesicles
SWING	SAXS beamline at the synchrotron source Soleil
t	time
t	molecular tilt angle
T	temperature
$t_{66\%}$	time where 66 % of a progress is completed
$t_{95\%}$	time where 95 % of a progress is completed
T2DM	type 2 diabetes melitus
TBEV	tick-borne encephalitis virus
T_{crit}	critical temperature
TEM	transmission electron microscopy
TFE	2,2,2-trifluoroethanol

continued on the next page...

symbol	legend
T_{growth}	temperature of growth
T_{m}	main transition temperature of a lipid
TMD	trans-membrane domain
TPMS	triply periodic minimal surface
trSAXS	time-resolved small-angle X-ray scattering
T_{sub}	subphase temperature
u	unit of atomic mass: $1 \text{ u} = 1.6605 \cdot 10^{-27} \text{ kg}$
u	ratio of the outer and the inner high pressure cell diameters
ULV	unilamellar vesicle
uts	ultimate tensile strength
v	velocity
V	volume
V6	neutron reflectometry instrument at HHZ
v_l	molecular volume of a lipid
vol	based on the volume
V_p	volume of a scattering particle
V_{Porod}	volume of the dissolved and hydrated particle
VSV	vesicular stomatitis virus
wt	wild-type
w/v	weight per volume
x	general variable
x	first direction in space
X	string of bits describing the state of a multi-bead model
XRR	X-ray reflectometry
y	second direction in space
z	third direction in space
α	angle in space, e.g. in a crystallographic unit cell
α_c	critical angle in XRR
α_f	angle of the reflected beam in XRR
α_i	angle of the incident beam in XRR
α_t	angle of the refraction
α_w	weighting factor of penalty terms in multi-bead modelling
β	angle in space, e.g. in a crystallographic unit cell
β	imaginary part of the refractive index
γ	characteristic function in SAXS
γ	angle in space, e.g. in a crystallographic unit cell
γ	critical packing parameter or shape factor
γ_0	angle in the 2D monolayer plane included by the lattice vectors, \vec{a} and \vec{b}
δ	real part of the refractive index
δ_p	optical path difference
Δ +PHS	hyperstable SNase variant
ΔG°	standard Gibbs energy
$\Delta H^\#$	activation enthalpy
ΔH_m	main transition enthalpy of lipids
Δn_e	number of excess electrons
Δp	pressure-jump amplitude

continued on the next page...

symbol	legend
$\overline{\Delta\rho}$	average electron density contrast
ΔV	volume change
$\Delta V^\#$	activation volume
θ	(1/2) scattering angle
λ	wavelength of X-rays
Λ	total penetration depth
μ	prefix: 10^{-6}
μ	linear absorption coefficient
$\tilde{\nu}$	wave number
π	mathematical constant; US: 3.0; rest of the world: 3.14159...
π	surface pressure
ρ	scattering length density or electron density
ρ_e	electron density
ρ_0	homogeneous electron density of the solvent in SAXS
ρ_e	electron density
ρ_l	mass density of a lipid
ρ_n	density of nuclei
σ	RMSD roughness of an interface
ϕ_l	lipid volume fraction
ϕ_w	water volume fraction
χ	Euler-Poincaré characteristic
χ	lateral compressibility
χ^2	normalised discrepancy function between experimental and calculated data
Ψ	ratio of the particle volume to its number of electrons
ψ	azimuthal angle of hydrocarbon chains at the air-water interface
$\%_{\text{mol}}$	percent based on molecular mass
$\%_{\text{wt}}$	percent based on weight

APPENDIX C

List of publications

Scientific papers published during the PhD thesis at TU Dortmund University:

1. M. Puehse, C. Jeworrek, and R. Winter. The temperature-pressure phase diagram of a DPPC-ergosterol fungal model membrane – a SAXS and FT-IR spectroscopy study. *Chemistry and Physics of Lipids*, 152:57 - 63, 2008
2. C. Jeworrek, M. Puehse, and R. Winter. X-ray Kinematography of Phase Transformations of Three-Component Lipid Mixtures: A Time-Resolved Synchrotron X-ray Scattering Study Using the Pressure-jump Relaxation Technique. *Langmuir*, 24:11851 - 11859, 2008
3. R. Krivanek, C. Jeworrek, C. Czeslik, and R. Winter. Composition Fluctuations in Phospholipid-Sterol Vesicles – a Small-angle Neutron Scattering Study. *Zeitschrift für Physikalische Chemie - International Journal of Research in Physical Chemistry and Chemical Physics*, 222:1679 - 1692, 2008
4. C. Jeworrek, O. Hollmann, R. Steitz, R. Winter, and C. Czeslik. Interaction of IAPP and Insulin with Model Interfaces Studied Using Neutron Reflectometry. *Biophysical Journal*, 96:1115 - 1123, 2009
5. M. Puehse, R.T. Szweda, Y.Y. Ma, C. Jeworrek, R. Winter, and H. Zorn. Marasmius scorodoniensis extracellular dimeric peroxidase – Exploring its temperature and pressure stability. *Biochimica et Biophysica Acta – Proteins and Proteomics*, 1794:1091 - 1098, 2009
6. F. Evers, C. Jeworrek, S. Tiemeyer, K. Weise, D. Selin, M. Paulus, B. Struth, M. Tolan, and R. Winter. Elucidating the Mechanism of Lipid Membrane-Induced IAPP Fibrillogenesis and Its Inhibition by the Red Wine Compound Resveratrol: A Synchrotron X-ray Reflectivity Study. *Journal of the American Chemical Society*, 131:9516 - 9521, 2009
7. R. Winter and C. Jeworrek. Review: Effect of pressure on membranes. *Soft Matter*, 5:3157 - 3173, 2009
8. K. Vogtt, C. Jeworrek, V.M. Garamus, and R. Winter. Microdomains in Lipid Vesicles: Structure and Distribution Assessed by Small-Angle Neutron Scattering. *Journal of Physical Chemistry B*, 114:5643 - 5648, 2010
9. J.B. Rouget, M.A. Schroer, C. Jeworrek, M. Puehse, J.L. Saldana, Y. Bessin, M. Tolan, D. Barrick, R. Winter, and C.A. Royer. Unique Features of the Folding Landscape of a Repeat Protein Revealed by Pressure Perturbation. *Biophysical Journal*, 98:2712 - 2721, 2010
10. M.A. Schroer, M. Paulus, C. Jeworrek, C. Krywka, S. Schmacke, Y. Zhai, D.C.F. Wieland, C.J. Sahle, M. Chimenti, C.A. Royer, B. Garcia-Moreno, M. Tolan, and R. Winter. High-Pressure SAXS Study of Folded and Unfolded Ensembles of Proteins. *Biophysical Journal*, 99:3430 - 3437, 2010

11. R. Kitahara, K. Hata, A. Maeno, K. Akasaka, M.S. Chimenti, B. Garcia-Moreno, M.A. Schroer, C. Jeworrek, M. Tolan, R. Winter, J. Roche, C. Roumestand, K.M. de Guillen, and C.A. Royer. Structural plasticity of staphylococcal nuclease probed by perturbation with pressure and pH. *Proteins - Structure Function and Bioinformatics*, 79:1293-1305, 2011
12. C. Jeworrek, R. Steitz, C. Czeslik, and R. Winter. High pressure cell for neutron reflectivity measurements up to 2500 bar. *Reviews of Scientific Instruments*, 82:025106, 2011
13. C. Jeworrek, S. Uelner, and R. Winter. Phase behavior and kinetics of pressure-jump induced phase transitions of bicellar lipid mixtures. *Soft Matter*, 7:2709-2719, 2011
14. K. Weise, R. Mishra, S. Jha, D. Selin, D. Radovan, A. Gohlke, C. Jeworrek, J. Seeliger, S. Moebitz, and R. Winter. *Lipids and Cellular Membranes in Amyloid Diseases*, chapter 4: Interaction of hIAPP and Its Precursors with Model and Biological Membranes, page 93-120. Wiley-VCH, 2011
15. C. Jeworrek, F. Evers, J. Howe, K. Brandenburg, M. Tolan, and R. Winter. Effects of Specific versus Nonspecific Ionic Interactions on the Structure and Lateral Organization of Lipopolysaccharides. *Biophysical Journal*, 100:2169-2177, 2011
16. J. Seeliger, F. Evers, C. Jeworrek, S. Kapoor, M. Tolan, A. Kapurniotu, and R. Winter. Cross-amyloid interactions of A and IAPP at an anionic lipid raft monolayer and bilayer membranes. *Angewandte Chemie*, submitted, 2011
17. C. Jeworrek, F. Evers, M. Erilkamp, S. Grobelny, M. Tolan, and R. Winter. Structure and phase behavior of archaeal lipid monolayers. *Langmuir*, submitted, 2011
18. F. Evers, C. Jeworrek, K. Weise, M. Tolan, and R. Winter. Detection of lipid raft domains in Langmuir monolayers of complex lipid composition. *Soft Matter*, submitted, 2011
19. The interaction of different fusion peptides with monoolein, in preparation, 2011

D List of Figures

2.1	Kinematics of the scattering process and definition of the wave vector transfer \vec{q}	4
2.2	Representation of the protein lysozyme by the spherical harmonics method.	14
2.3	Reconstruction of a cylinder using DAMMIN and DAMMIF.	15
2.4	Comparison of different <i>ab initio</i> -methods.	17
3.1	Kinematics of the scattering processes at the air-water interface and definitions of the wave vector transfer, \vec{q} , for X-ray reflectometry and grazing incidence X-ray diffraction.	25
3.2	Oblique unit cell with lattice vectors (a , b), angles (γ_D , γ) and corresponding lattice spacings (d_a , d_b).	32
3.3	Three possible structures of crystalline packed hydrocarbon chains at the air-water interface and corresponding GIXD patterns.	35
4.1	The Schwarz diamond (D) minimal surface corresponding to the space group $Pn3m$	49
4.2	Phase diagram of the bicellar mixture DMPC/DHPC (3.2:1 molar ratio).	52
4.3	Chemical structure of cholesterol (IUPAC: (3 β)-cholest-5-en-3-ol).	53
4.4	Chemical structure of ergosterol (IUPAC: ergosta-5,7,22-trien-3 β -ol).	53
4.5	Chemical structure of the phospholipids DPPC and DOPG.	54
4.6	Chemical structure of 1-(cis-9-octadecenoyl)- <i>rac</i> -glycerol (DL- α -monoolein; IUPAC: 2,3-dihydroxypropylolate).	55
4.7	Chemical structure of lipopolysaccharide (LPS Re).	56
4.8	Chemical structure of archaeal lipid backbones.	57
5.1	Exploded and cross section view of the high pressure neutron reflectometry cell.	62
5.2	Exploded view and cross section view of the inner sample cell.	65
5.3	Schematic drawing of the high pressure network.	66
5.4	Neutron reflectivity curves of DOPE spincoated on an Si-wafer in D ₂ O.	67
5.5	Neutron reflectivities of an Si/perdeuterated poly(styrene)/protein adsorbate/protein solution interface at different pressures.	68
6.1	Small-angle X-ray scattering patterns of the lipid mixture DMPC / DHPC (3.2:1; 15 % _w t lipid content in pure water) between 6.0 and 61.9 °C at atmospheric pressure and pair distance distribution function, $p(r)$, at 9 °C.	74
6.2	Wave number of the symmetrical CH ₂ -stretching mode of the bicellar mixture DMPC / DHPC (3.2:1 molar ratio) as a function of temperature.	75
6.3	Temperature dependence of the wave number of the symmetrical carbonyl stretching mode of the bicellar mixture DMPC / DHPC (3.2:1 molar ratio) and relative degree of hydration of the lipid head groups as a function of temperature.	76

6.4	Pressure dependence of the small-angle X-ray scattering patterns of the lipid system DMPC / DHPC (3.2:1) at 61.9 °C.	77
6.5	Wave number of the symmetrical CH ₂ -stretching mode of the bicellar mixture DMPC / DHPC (3.2:1 molar ratio) at 35 °C as a function of pressure.	78
6.6	p, T -phase diagram of the binary lipid mixture DMPC / DHPC (3.2:1; 15 % _{wt} lipid content in water).	78
6.7	CH ₂ scissoring mode of the bicellar mixture DMPC / DHPC (3.2:1 molar ratio) at 20 °C showing a “correlation field splitting” at elevated pressures.	79
6.8	Diffraction patterns of the lipid mixture DMPC / DHPC (3.2:1) during a pressure-jump from 2.60 to 0.42 kbar (bicellar to lamellar) at $T = 61$ °C.	80
6.9	RMSDs of the scattering patterns from the final scattering pattern as a function of time after pressure-jumps between lamellar to nematic phase in the system DMPC / DHPC (3.2:1) at $T = 61$ °C.	82
6.10	RMSDs for the transition from the nematic to the lamellar phase of the system DMPC / DHPC (3.2:1) in the depressurising direction for various p -jump amplitudes.	83
6.11	Small-angle X-ray scattering patterns of the temperature-dependent measurement of DPPC / ergosterol (22 % _{mol}) at atmospheric pressure.	88
6.12	Temperature dependence of the lamellar lattice constants d and integrated peak areas of DPPC / ergosterol (22 % _{mol}).	89
6.13	Pressure dependence of the lamellar lattice constants of DPPC / ergosterol (22 % _{mol}).	89
6.14	Tentative p, T -phase diagram of the binary lipid mixture DPPC / ergosterol (22 % _{mol}) in excess water.	91
6.15	Small-angle X-ray scattering patterns of the ternary lipid mixture DOPC / DPPC / Chol (1:2:1 molar ratio) between 10.5 and 64.9 °C at atmospheric pressure.	94
6.16	Temperature dependence of the lamellar lattice constants and peak areas of DOPC / DPPC / Chol (1:2:1 molar ratio).	95
6.17	Small-angle X-ray scattering patterns of the pressure-dependent measurement on the ternary lipid mixture DOPC / DPPC / Chol (1:2:1) at 60 °C.	95
6.18	Pressure dependence of the lamellar lattice constant of the three phases s_o , l_o and l_d in the ternary lipid mixture DOPC / DPPC / Chol (1:2:1) at 61 °C.	96
6.19	p, T -phase diagram of the ternary lipid mixture DOPC / DPPC / Chol (1:2:1 molar ratio) in excess water.	97
6.20	Two-dimensional contour plot of the intensity, $I(q_{xy}, q_z)$, GIXD pattern, $I(q_{xy})$, and Bragg rod intensity profile, $I(q_z)$, of a lipid raft monolayer (DOPC / DPPC / Chol, molar ratio 1:2:1).	98
6.21	X-ray reflectometry data, best fits and electron density profiles of a lipid raft monolayer (DOPC / DPPC / Chol, molar ratio 1:2:1) at a film pressure of $\pi = 30$ mN m ⁻¹ and a temperature of 10 °C on the air-water interface.	99
6.22	Diffraction patterns of the ternary lipid mixture DOPC / DPPC / Chol (1:2:1 molar ratio) during the first 4 s of a pressure-jump from 1.6 kbar to 0.3 kbar at $T = 61$ °C.	100
6.23	Lamellar lattice constants and integrated peak intensities of the ternary lipid mixture DOPC / DPPC / Chol (1:2:1) upon a pressure-jump from 1.6 to 0.3 kbar at 61 °C.	101
6.24	Comparison of lamellar lattice constants and intensities of two pressure-jumps in opposing directions between 1.6 kbar and 0.8 kbar at 61 °C.	102
6.25	Lamellar lattice constants and intensities of a pressure-jump from 2.62 to 1.35 kbar at $T = 61$ °C.	102
6.26	Lamellar lattice constants and intensities of the ternary lipid mixture DOPC / DPPC / Chol (1:2:1) upon a pressure-jump from 2.2 to 0.4 kbar at $T = 61$ °C.	103

6.27	Two-dimensional contour plot of the intensity, $I(q_{xy}, q_z)$, as obtained from an anionic lipid raft monolayer (15 % DOPC, 10 % DOPG, 40 % DPPC, 10 % DPPG and 25 % cholesterol, molar ratio).	108
6.28	GIXD pattern, $I(q_{xy})$, and Bragg rod intensity profile of an anionic lipid raft monolayer.	109
6.29	GIXD pattern, $I(q_{xy})$, of an anionic lipid raft monolayer at 20 °C as a function of the film pressure, π	110
6.30	SAXS scattering patterns of monoolein (17 % _{wt} water content) at 60 °C between atmospheric pressure and 2.0 kbar.	113
6.31	The Schoen gyroid (G) triply periodic minimal surface corresponding to the space group $Ia3d$	113
6.32	Lattice constant and integrated peak intensity of monoolein (17% _{wt} water) at 60 °C between atmospheric pressure and 2 kbar.	114
6.33	p, T -phase diagram of pure monoolein (17 % _{wt} water content)	115
6.34	Scattering patterns after a pressure-jump of monoolein from 1.0 kbar to 2.0 kbar at 63.7 °C.	118
6.35	Pressure-jump of monoolein from 1.0 kbar to 2.0 kbar at 63.7 °C.	119
6.36	Pressure-jump of monoolein from 2.00 kbar to 0.95 kbar at 63.7 °C.	120
6.37	X-ray reflectivity data and electron density profiles obtained from archaeal lipid monolayers (PLFE grown at 68 °C) at the air-water interface.	123
6.38	Influence of subphase temperature on the PLFE monolayer structure at different surface pressures.	124
6.39	Two-dimensional contour plot of the intensity, $I(q_{xy}, q_z)$, GIXD pattern, $I(q_{xy})$, and Bragg rod intensity profile as obtained from an archaeal lipid monolayer.	125
6.40	Compression isotherms of LPS monolayers spread on subphases of various ion content.	130
6.41	X-ray reflectometry data and corresponding normalised electron density profiles obtained from LPS monolayers at the air-water interface.	132
6.42	Electron density profiles of LPS on three different aqueous subphases at different lateral film pressures.	133
6.43	Two-dimensional contour plots, $I(q_{xy}, q_z)$, as obtained from a LPS monolayer.	134
6.44	GIXD pattern, $I(q_{xy})$, and Bragg rod intensity profile for different LPS monolayers.	135
6.45	Coherence length, L_{xy} , calculated from the {10} peak as a function of the lateral film pressure of LPS spread on four different subphases.	137
7.1	<i>Ab initio</i> structures of Δ +PHS at pH 7.0, ambient pressure and temperature.	142
7.2	<i>Ab initio</i> structures of Δ +PHS V66K at pH 6.0, ambient temperature and pressure.	143
7.3	<i>Ab initio</i> structures of Δ +PHS/V66K at different pressures and pH-values (6.0 and 4.5).	145
7.4	<i>Ab initio</i> structures of Δ +PHS at pH 7.0 and ambient temperature calculated at 1 bar, 2 kbar and 3 kbar.	146
7.5	<i>Ab initio</i> structures of Δ +PHS/V66K at pH 6.0, ambient temperature and high pressure of 3 kbar.	147
7.6	<i>Ab initio</i> structures of Δ +PHS/V66K at pH 4.5, ambient temperature and 1 kbar.	147
7.7	<i>Ab initio</i> structures of different Δ +PHS mutants at ambient pressure and temperature.	149
7.8	SAXS scattering patterns and pair-distance distribution functions of the protein MsP1 at selected pressures ($T = 30$ °C).	152
8.1	X-ray reflectometry data and derived electron density profiles obtained from archaeal lipid monolayers containing 2% _{wt} gramicidin D at the air-water interface.	157

8.2	Scattering patterns of monoolein containing the fusion peptide TBEV as a function of pressure at 5.7 °C.	161
8.3	Lattice constants and integrated peak intensities of monoolein containing the fusion peptide TBEV as a function of pressure at 5.7 °C.	162
8.4	Scattering patterns of monoolein containing 2% _{wt} of the fusion peptide TMD as a function of pressure at 24.3 °C.	163
8.5	Lattice constants and integrated peak intensities of monoolein containing the fusion peptide TMD as a function of pressure at 24.3 °C.	164
8.6	p, T -phase diagrams of monoolein including 2% _{wt} of different fusion peptides.	165
8.7	The Schwarz primitive (P) triply periodic minimal surface, corresponding to the space group $Im3m$	167
8.8	Scattering patterns of monoolein and 2% _{wt} L16 after a pressure-jump from 2.0 kbar to 0.9 kbar at 64.0 °C.	171
8.9	Lattice constants and phase intensities of pressure-jumps from 2.0 kbar to 0.9 kbar and 1.0 kbar to 2.0 kbar, respectively, at 63.7 °C of monoolein including 2% _{wt} L16.	172
8.10	Lattice constants and phase intensities of pressure-jumps between 0.7 kbar and 1.7 kbar as well as 1.6 kbar and 0.7 kbar at 58.2 °C of monoolein including 2% _{wt} HA2.	174
8.11	Lattice constants and phase intensities of pressure-jumps in pressurising direction with different pressure-jump amplitudes at 48.7 °C of monoolein including 2% _{wt} HA2.	176
8.12	Lattice constants and phase intensities of pressure-jumps in depressurising direction with different pressure-jump amplitudes at 48.7 °C of monoolein including 2% _{wt} HA2.	177
8.13	Scattering patterns of a pressure-jump of monoolein and 2% _{wt} TBEV from 1 bar to 2.4 kbar at 4.8 °C.	178
8.14	Lattice constants and phase intensities of a pressure-jump at 4.8 °C of monoolein including 2% _{wt} TBEV.	179
8.15	XRR curves and electron density profiles of the association of IAPP with an anionic DOPC / DOPG (7:3 molar ratio) lipid film as well as schematic illustration of the time-evolution of the underlying lipid-induced IAPP aggregation process.	182
8.16	Time evolution of normalised electron density profiles of resveratrol as well as a equimolar mixture of resveratrol and IAPP in the presence of a negatively charged DOPC / DOPG monolayer.	182
8.17	Schematic illustration of resveratrol interacting with a lipid monolayer in the presence and absence of IAPP.	183
8.18	GIXD patterns of an anionic lipid raft monolayer on different peptide subphases.	186
8.19	Lateral film pressure as a function of time of an anionic lipid raft monolayer spread on subphases containing different peptides.	186
8.20	Time evolution of the normalised electron density profiles for the interaction of IAPP, A β , and both A β and IAPP with anionic lipid raft monolayers.	187
8.21	Two-dimensional contour plots of the intensity, $I(q_{xy}, q_z)$, as obtained from an anionic lipid raft monolayer (15% DOPC, 10% DOPG, 40% DPPC, 10% DPPG and 25% cholesterol, molar ratio) in the presence of A β and a mixture of IAPP / A β	188
A.1	Graphical user interface (GUI) of a program to identify different crystallographic space groups from SAXS Bragg peak patterns.	a4
A.2	GUI of a program identifying space groups automatically from Bragg peak patterns.	a15

E List of Tables

2.1	Miller indices leading to Bragg peaks of the seven cubic lipid phases.	20
4.1	Properties of class I, class II, and class III fusion proteins.	41
4.2	Triply periodic minimal surface, typical label, space group, and ratio of periodic distances in the TPMS of the three basic cubic phases.	48
4.3	Crystallographic space groups, Hermann-Mauguin symbols of symmetry operations, and point symmetry groups of the seven bicontinuous cubic lipid phases.	50
4.4	Euler-Poincaré characteristic, χ , and the scaled surface area, A_0 , of the different triply periodic minimal surfaces (TPMS).	50
6.1	Fitting parameters of the X-ray reflectivity curve of a lipid raft monolayer (DOPC/DPPC/Chol, molar ratio 1:2:1) at the air-water interface.	99
6.2	Calculated parameters of grazing incidence X-ray diffraction measurements of different lipid raft monolayers at the air-water interface.	108
6.3	Parameters of the cubic $Ia3d$ unit cell of pure monoolein (17% _{wt} hydration).	115
6.4	Parameters of lamellar phases calculated for pure monoolein (17% _{wt} hydration).	116
6.5	Calculated parameters of grazing incidence diffraction measurements of different archaeal lipid monolayers at the air-water interface.	126
6.6	Fitting parameters of the X-ray reflectometry curves obtained from LPS monolayers at the air-water interface.	131
6.7	Calculated parameters of grazing incidence diffraction measurements obtained from LPS monolayers at the air-water interface.	135
7.1	Radii of gyration of different SNase variants.	142
8.1	Calculated parameters of grazing incidence diffraction measurements of an archaeal lipid monolayer containing 2% _{wt} gramicidin D at the air-water interface.	157
8.2	Estimated numbers of measurements taken from monoolein samples containing different fusion peptides.	161
8.3	Parameters of lamellar phases of monoolein (17% _{wt} hydration) including 2% _{wt} of different fusion peptides as a function of temperature and pressure.	168
8.4	Unit cell parameters of cubic phases in the system monoolein (17% _{wt} hydration) including 2% _{wt} of different fusion peptides as a function of temperature and pressure.	169
8.5	Parameters of the hexagonal unit cell of monoolein (17% _{wt} hydration) including 2% _{wt} of different fusion peptides as a function of pressure and temperature.	170
A.1	Prefixes of different user-programmed MATLAB files.	a1

APPENDIX F

Curriculum vitae

Contact Details

Name: Christoph Jeworrek
Adress: Teutoburgerstr. 27
44149 Dortmund
Germany

Phone: 00 49 231 / 56 84 980
Mobile: 00 49 176 / 23 819 736
Email: christoph.jeworrek@tu-dortmund.de

Personal Information

Date of Birth: 05th of July 1982
Place of Birth: Duisburg, Germany
Nationality: German
Marital Status: single

Education

08/1989–07/1993 primary school “Grundschule Hülsdonk”
08/1993–05/2002 secondary school “Städtisches Gymnasium Kamp-Lintfort”

University Studies

10/2002–08/2005 Gerhard-Mercator University, Department of Chemistry, Duisburg, Germany
Bachelor Degree Programme: Chemistry and Molecular Materials
Bachelor Thesis: ^{129}Xe NMR Spectroscopic Investigation of
Multi Wall Carbon Nanotubes

10/2005–10/2007 University of Dortmund, Department of Chemistry, Dortmund, Germany
Master Degree Programme: Chemistry
Master thesis: Protein Adsorption on Lipid Membranes
and Physical-Chemical Properties of Lipid-Sterol Mixtures

10/2007–03/2008 University of Dortmund, Department of Chemistry, Dortmund, Germany
student research assistant, Biophysical Chemistry I

04/2008–06/2011 TU Dortmund University, Department of Chemistry, Dortmund, Germany
PhD Programme in Biophysical Chemistry, Group: Prof. Dr. R. Winter

Research interests

My research interests are proteins under high hydrostatic pressure, the structure and dynamics of biological model membranes as well as the interaction of model biomembranes with steroids and proteins by using different scattering methods such as X-ray -, synchrotron - and neutron - small-angle scattering, grazing incidence diffraction and reflectometry.

Skills and Qualifications

Languages: German (native), English (business fluent)

Computing Skills

Operating Systems: MS DOS, Windows 95 - 7

Programming Languages: MATLAB, Mathematica, Fortran, LabTalk

Other: \LaTeX , JabRef, MS Office, ChemOffice, Origin, VMD, Solid Edge

Dortmund, 5th July 2011

Selbstständigkeitserklärung

Erklärung

Ich versichere, dass ich die vorliegende Promotionsarbeit selbstständig verfasst und alle in Anspruch genommenen Quellen und Hilfen in der Dissertation vermerkt habe. Alle Stellen im Text, die anderen Werken im Wortlaut oder sinngemäß entnommen sind, wurden kenntlich gemacht. Die Dissertation wurde in der gegenwärtigen oder in einer anderen Fassung noch nicht an der Technischen Universität Dortmund oder an einer anderen Hochschule im Zusammenhang mit einer staatlichen oder akademischen Prüfung vorgelegt.

Dortmund, den 05.07.2011

